Investigating the Dust Distribution in Galaxy Disks with DustPedia and NIKA2

By

RUTH EVANS

School of Physics and Astronomy
CARDIFF UNIVERSITY

A thesis submitted to Cardiff University in accordance with the requirements of the degree of DOCTOR OF PHILOSOPHY

JANUARY 2019

Dedication

This thesis is dedicated to each and every person who has helped me along this roller-coaster of a degree. For every low point, we've had twice as many laughs, pub trips, and excuses to celebrate with some good food and a bottle of champagne.

Firstly, to my Mumma Straker who has stood by me every step of the way. You never bogged me down with questions like "so when are you going to get a real job?", "how long have you been in University now?!" and "maybe it's about time to to enter the real world, no?", but instead offered so much support over the last 8 years of my university life. I can honestly say that I wouldn't be submitting this thesis without your continued guidance and emotional support, thank you for being there every step of the way.

Thank you to Alice, Ian and baby Ruben for always keeping me entertained when I'm in Essex, there's never a dull day when you're around (next time we'll *definitely* just have one drink and then get a taxi home though).

I can't begin to express my appreciation for the friends I've made in Cardiff. To Eleni and Rosie, thank you for the hours of chats over coffee, retail therapy, crochet lessons and amazing dinners we've shared together. To Aris and Penny for putting up with short-notice sleepovers, and your never-ending hospitality. Thank you to Greg and Elisa for the awesome Thanksgiving dinners (Joanne too!) and numerous evenings gathered in your flat. To Valeriu who has opened my eyes to the world of brewskis and tanks, Adam for the pub trips and art chats, Chinmay for your awful jokes, and everyone part of 'Brewskis and the Beast' for all the evenings that I wish I could remember better...

To Max, there are many things that I'd like to say that may not be appropriate for a thesis dedication, but thank you for putting up with me. Who'd have thought three years ago that we'd end up living together in Sheffield? I'm forever grateful for your no-frills pep talks and giving me the motivation I needed to complete the thesis, and I'm so happy that I got to share this adventure with you. There are too many great memories to thank you for, but a special mention goes to looking after me during the last few weeks of the write up, for the delicious food and essentially becoming a house-husband for a month, which allowed me to get this written while keeping some shred of sanity (and also for pointing out how many times I wrote "this allowed me to..." in the thesis). You cool.

I would like to thank all of my colleagues and supervisory team for answering a multitude of stupid questions, and providing valuable insight to this project. To name everyone would take a thesis in itself, but a special thank you has to go to Chris Clark for being an excellent conference buddy with the best beer recommendations, and for your never-ending patience. To Matt Smith, many thanks for your help and advice throughout this project (and for the awesome BBQs and bonfire night parties). To the galaxies group as a whole, thank you for providing the ultimate procrastination when I needed it most. The mini-golf tournaments and afternoon pub trips were great ways to avoid doing work.

Lastly, but definitely not least, to Prof. Jonathan Davies. Thank you for your continued support and guidance, and for the opportunities you've provided me with over the last few years. Apologies for all the hours you've spent trying to understand the weird and wonderful methodology used throughout my research, especially after your retirement when there are so many better things to be doing. But we got there in the end. Here's to you nearly being rid of dust, and having time to research the things that are really interesting!

Diolch yn fawr.

Acknowledgements

This PhD was made possible due to funding from the Science and Technology Facilites Council.

This work made use of Astropy, a community-developed core Python package for astronomy (Astropy Collaboration et al., 2013). All plots in this thesis made use of both the MatPlotLib15 (Barrett et al., 2005) and Seaborn (Waskom et al., 2014) packages for Python, and the majority of scripts written as part of this research make use of NumPy16 (van der Walt et al., 2011) and SciPy17.

This research made use TOPCAT (Taylor, 2005), which was initially developed under the UK Starlink project, and has since been supported by PPARC, the VOTech project, the Astro- Grid project, the AIDA project, the STFC, the GAVO project, the European Space Agency, and the GENIUS project.

This research has made use of the NASA/IPAC Extragalactic Database (NED) which is operated by the Jet Propulsion Laboratory, California Institute of Technology, under contract with the National Aeronautics and Space Administration.

This research made use of NASA's Astrophysics Data System and NASA's Astrophysics Data System Bibliographic Services.

This research made use of Montage. It is funded by the National Science Foundation under Grant Number ACI-1440620, and was previously funded by the National Aeronautics and Space Administration's Earth Science Technology Office, Computation Technologies Project, under Cooperative Agreement Number NCC5-626 between NASA and the California Institute of Technology.

All observations included in this thesis were viewed in SAOImage DS9, developed by the Smithsonian Astrophysical Observatory with support from the Chandra X-ray Science Center (CXC), the High Energy Astrophysics Science Archive Center (HEASARC), and the JWST Mission office at the Space Telescope Science Institute (STSI).

This research made use of the DustPedia databse. DustPedia is a collaborative focused research project supported by the European Union under the Seventh Framework Programme (2007-2013) call (proposal no. 606847). The participating institutions are: Cardiff University, UK; National Observatory of Athens, Greece; Ghent University, Belgium; Universite Paris Sud, France; National Institute for Astrophysics, Italy and CEA (Paris), France.

PACS has been developed by a consortium of institutes led by MPE (Germany) and including UVIE (Austria); KU Leuven, CSL, IMEC (Belgium); CEA, LAM (France); MPIA (Germany); INAF-IFSI/OAA/OAP/OAT, LENS, SISSA (Italy); IAC (Spain). This development has been supported by the funding agencies

BMVIT (Austria), ESAPRODEX (Belgium), CEA/CNES (France), DLR (Germany), ASI/INAF (Italy), and CICYT/MCYT (Spain). SPIRE has been developed by a consortium of institutes led by Cardiff University (UK) and including Univ. Lethbridge (Canada); NAOC (China); CEA, LAM (France); IFSI, Univ. Padua (Italy); IAC (Spain); Stockholm Observatory (Sweden); Imperial College London, RAL, UCL-MSSL, UKATC, Univ. Sussex (UK); and Caltech, JPL, NHSC, Univ. Colorado (USA). This development has been supported by national funding agencies: CSA (Canada); NAOC (China); CEA, CNES, CNRS (France); ASI (Italy); MCINN (Spain); SNSB (Sweden); STFC, UKSA (UK); and NASA (USA).

This publication makes use of data products from the Wide-field Infrared Survey Explorer, which is a joint project of the University of California, Los Angeles, and the JPL/Caltech, funded by NASA (USA).

I would like to thank the IRAM staff and NIKA2 collaboration for their support during the NIKA2 campaign.

ABSTRACT

This thesis presents the results of a multi-wavelength study into the 3D distribution of dust in the haloes of galaxies.

A sample of 31 nearby, edge-on galaxies from the DustPedia database is used to measure the vertical extent of dust above the central plane of galaxy disks at the *Herschel* PACS 100 & 160 μm and SPIRE 250, 350 & 500 μm bands. I generate a 3D model of the dust to match each galaxy based on the exponential TRIPLEX function, which ensures that line-of-sight effects of inclination can be accounted for when measuring the vertical scaleheight. The brightness profiles of each galaxy are plotted against the models, an inclined thin disk, and the stellar disk to measure the extent to which the dust is distributed. 11 of the sample galaxies show evidence of an extraplanar dust component, with NGC 4222 exhibiting the most extended structure out to 4 kpc.

The galaxy maps and models are stacked at each wavelength to increase the sensitivity of the observations over that of a single map. I carry out the same procedure on WISE 3.4 μm data which traces the oldest, and most extended, stellar population for comparison of the dust scaleheight versus stellar scaleheight (β_d/β_s). I find that the dust is more vertically extended than the stellar disk by at least a factor of 1-1.3 at each wavelength.

I fit two-component modified blackbody SEDs to the stacked maps, and find a total dust mass for the sample of $9.54^{+0.90}_{-2.67} \times 10^9 M_\odot$, an order of magnitude greater than previous estimates. At 500 μm, the flux is in excess of that predicted by the model (assuming β = 1.7). These results may indicate the presence of a large cold dust reservoir that has been previously unaccounted for in the literature. I test the dust temperatures required to account for the sub-millimetre excess and find that a very cold dust component of around ~7 K fits well to the data, however the dust mass increases by a further 2 orders of magnitude which is likely to be unphysical.

The dust temperature at increasing distance up to 2 kpc from the plane is found increase slightly yet with a relatively flat gradient, in line with radiative transfer models, although large errors at vertical distances greater than ~2 pixels have

hindered further analysis of temperature dependence on scale height.

I also utilise the first high-resolution 1.2 and 2 mm NIKA2 observations of NGC 891 and M99 as science verification for the IMEGIN Large Programme. A two-component blackbody spectrum is fitted to the data and dust temperatures and masses estimated. I find a cold to warm dust ratio of 42.6 and 41.3 for the galaxies respectively, and total dust masses of $8.5 \pm 0.4 \times 10^7 M_\odot$ and $1.0 \pm 0.6 \times 10^8 M_\odot$. The temperatures of the cold and warm components are found to be 20.9 and 34.9 K for NGC 891, and 21.2 and 37.7 K for M99. These values are consistent with the literature, and we do not find evidence of a hidden cold dust component at the NIKA2 wavelengths or any sub-mm/mm excess.

TABLE OF CONTENTS

List of Tables

List of Figures

CHAPTER 1

INTRODUCTION

1.1 Cosmic Dust

The obscuring nature of cosmic dust was observed as early as 1785 by William Herschel, upon noting that some regions of the sky were devoid of stars and unevenly distributed, describing the phenomenon as 'star voids' or 'holes in the heavens' (Herschel, 1785). The discovery was further investigated by Struve (1847) who stated that the apparent number of stars per unit volume of space declines in all directions with distance from the Sun. Jacobus Kapteyn proposed that the nature of the phenomenon could arise from a light-absorbing medium between the stars (Kapteyn, 1909), a discovery that was considered to be the birth of interstellar dust extinction studies. This work wasn't widely accepted however, and it wasn't until 1930 that the presence of cosmic dust was unambiguously established by confirming the occurrence of interstellar absorption and reddening (Trumpler, 1930).

Cosmic dust, especially within our own galaxy, was typically considered a hindrance to astronomical observations as it obscures our view of stellar light and can potentially deem optical studies of stars, galaxies and the interstellar medium (ISM) futile. During the early years of dust studies, the only scientific merit attributed to dust was to account for the reddening of objects; a nuisance to be accounted for and discarded. According to Gaustad (1971), as far as an astronomer was concerned, "if you simply tell him the reddening law, particularly the ratio of total to selective extinction, he can unredden his clusters, correct the distance moduli, find the turnoff points, determine the age of the galaxy, and

be happy!". More recently, however, the study of cosmic dust itself has been considered a useful probe for studying star formation, chemical evolution, galaxy evolution, and therefore leading to a better understanding of the Universe itself.

1.1.1 Origin and Growth of Cosmic Dust

Shortly after the birth of the Universe, only the very basic elements of hydrogen, helium and lithium were in existence; a leftover from the Big Bang. As stars began to form from interstellar clouds, and subsequently lived and died, the nuclear processes taking place throughout their evolution produced heavier elements. Such metals can be contained within solid particles at sub-micron scales, and give rise to the cosmic dust we observe today. The mass of dust accounts for just 1% of the total mass of the interstellar medium (ISM), yet plays a major role in our view of galaxies; it has the ability to scatter, absorb and re-radiate stellar light, and as such, dust re-radiates typically 30% of the optical light emitted by stars (Popescu and Tuffs, 2002; Davies et al., 2012).

1.1.1.1 Dust Production in Asymptotic Giant Branch Stars

The largest contributors to the interstellar dust mass are post-main sequence stars, including giant, supergiant and asymptotic giant branch (ABG) stars that lie on the upper right corner of the Hertsprung-Russel (HR) diagram (see Figure 1.1).

Some regions of evolved stars have temperatures too high for the formation of solid particles, but we observe a 'dust shell' extending to ~ 1 - 2 times the stellar radii, in which temperatures are low enough for the condensation of matter. Particles are not considered to be ionised, as positively charged ions will repel one another and thus prevent condensation from occurring. In the inner dust shell regions, density, temperature and pressure conditions are optimum for the nucleation of dust particles from gas, where gas particles begin to form into clusters due to random movement until a critical size is reached. After this point, it becomes energetically favourable for these clusters to grow in size until grains or droplets of metals form - and become dust. The grains are expelled from the stars into the ISM via stellar winds and ejecta which are particularly prevalent in evolved stars as stability decreases, as well as through lengthy periods of constant mass loss during the stars' lifetimes (Whittet, 2002). Figure 1.2 shows the interstellar lifecycle including the production and destruction of dust in the ISM. The figure shows the interactions between molecular clouds, massive stars and supernovae with respect to the dust produced and/or destroyed in each scenario.

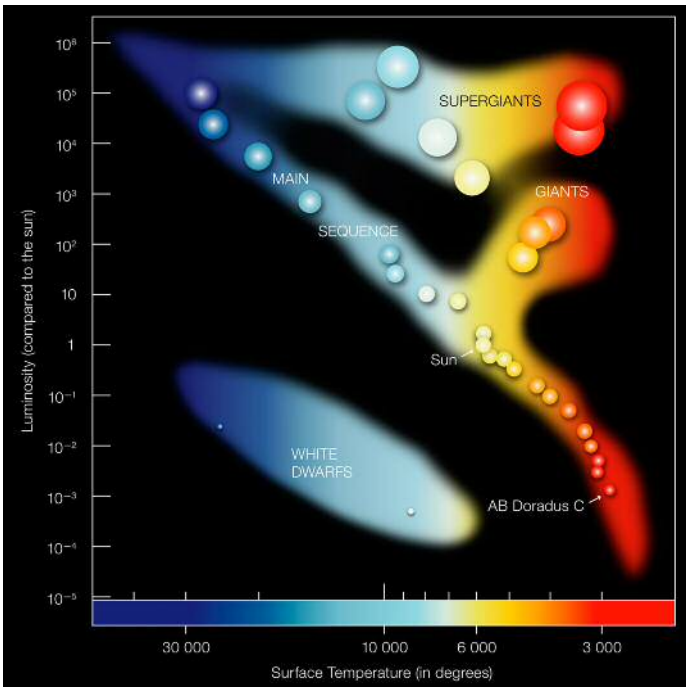

Figure 1.1: A Hertzsprung-Russell diagram showing the evolution of stars with relative temperature and luminosity. Image taken from ESO (2007), https://www.eso.org/public/images/eso0728c/.

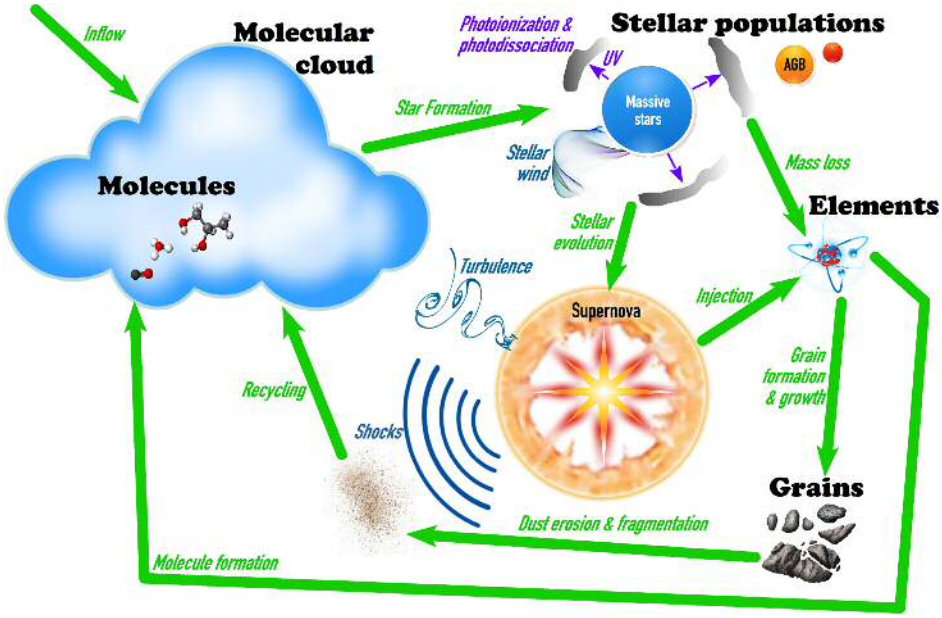

Figure 1.2: Schematic view of the interstellar lifecycle. Image taken from Galliano (2017).

1.1.1.2 Dust Production in Supernovae

When measuring the quantity of dust in the Universe, we find a budget crisis, whereby the total mass of dust is not accounted for by production in AGB stars alone. This discovery led to the search for new producers of dust previously not considered; particularly the study of dust production in supernovae (SNe).

A high mass star ($\geq 8\ M_\odot$) will end its life in the form of supernova, a destructive explosion that expels material at speeds of to 2000 km s^{-1} and temperatures high enough to destroy dust on impact (Gomez, 2013). Despite the damaging nature of SNe to the surrounding ISM, we see evidence that dust is in fact produced in the ejected material which is abundant in heavy elements. These metals combined with the high densities produced by shockwaves, and the rapidly decreasing temperature over time, make SNe prime candidates for dust production, with some models predicting 0.1 - 2 $M_\odot$ of dust to be produced in a single explosion (Todini and Ferrara, 2001; Bianchi and Schneider, 2007; Kozasa et al., 2009). More recent studies show that nearly 100% of the ejecta metals will be converted to dust and molecules within a few hundred years of the initial explosion (Gomez, 2013).

According to Gomez (2013), there are four key ways in which we can observe the presence of dust in SNe; (i) a decrease in the luminosity due to obscuration by dust, (ii) a red-blue asymmetry in optical line profiles originating from red-shifted material being reddened by ejecta dust more than blue-shifted material, (iii) detecting the onset of dust formation via increased IR emission, (iv) polarised emission from dust aligned with the magnetic field of the remnant. Dust has been observed via these methods in the Crab Nebula, Cassiopeia A and SN1987A with the *Hershcel* and ALMA telescopes, yeilding dust masses of 0.1-0.2 $M_\odot$ (Gomez et al., 2012), 0.1 $M_\odot$ (Barlow et al., 2010) and 0.4-0.7 $M_\odot$ (Matsuura et al., 2011) respectively.

The formation and destruction of dust is highly dependent on the supernova type; classified by the mechanisms that fuelled the explosion. Core-collapse SNe (CCSNe) are trigged by the gravitational collapse of a $\geq 8\ M_\odot$ main sequence star, and thermonuclear SNe are triggered by the explosive thermonuclear burning (Kozasa et al., 2009).

There is little evidence that dust is produced in Type Ia SNe, but CCSNe provide a wealth of evidence for dust formation. Kozasa et al. (2009) modelled the dust production in numerous types of CCSNe based on the composition, density and temperature of the ejecta. They assume that dust forms in the He-core where the density is high enough for the coagulation of molecules to form via nucleation, and find newly-formed dust masses ranging from 0.1 to 0.7 $M_\odot$.

1.1.1.3 Dust Grain Growth in the ISM

Growth of dust grains occurs via two methods; coagulation and mantle growth (Whittet, 2002). Coagulation occurs via low-velocity collisions between already present grains, and as such, higher grain growth occurs with increasing cloud density. Mantle growth occurs on already present grains via 'depletion' of elements from interstellar gas. The process is generally considered to have three stages: (i) the collision of atoms or ions of the element with the pre-existing grains, (ii) it must be bound in a way such that it can survive in the presence of destructive UV radiation, (iii) the grains will be subject to heavy UV irradiation and any grains that survive will be present in the ISM that we view today (Draine, 2009). The process of mantle growth significantly alters the size and composition of the dust initially ejected by evolved stars and SNe.

It is clear that in some galaxies, grain growth is the dominant mechanism for dust mass production (Asano et al., 2013). However, as the dust mass growth in the ISM is regulated by metallicity, the critical metallicity[1] of a galaxy indicates whether grain growth in the ISM is the main source or whether it is due to ejecta from evolved stars and SNe.

1.1.2 Chemical Composition

98% of the total observable matter in the Universe is made up of hydrogen and helium produced during the big bang. The other 2% is composed of heavier elements, including C, N, O, Mg, Si, and Fe which are the six elements assumed to contribute the most mass to interstellar dust grains. The mass of these elements in interstellar gas clouds is significantly smaller than in the stars that produce the elements, giving evidence for the depletion of the material from gas by grains. The chemical combinations of the six aforementioned elements lead to the assumption that there are two main dust compositions; C-rich and O-rich. Large variations in composition and grain size arise from the differing abundances of elements in the local ISM where dust increases in size by mantle growth, and variations are highly dependent on environment (Jones et al., 2017).

Figure 1.3 shows the variations in composition between the diffuse ISM and dense molecular clouds, giving an indication to the role environment can play on dust grain composition.

[1]below which dust condensation becomes inefficient due to low partial pressures for many metals, leading to less nucleation and slow accretion (Mattsson et al., 2014).

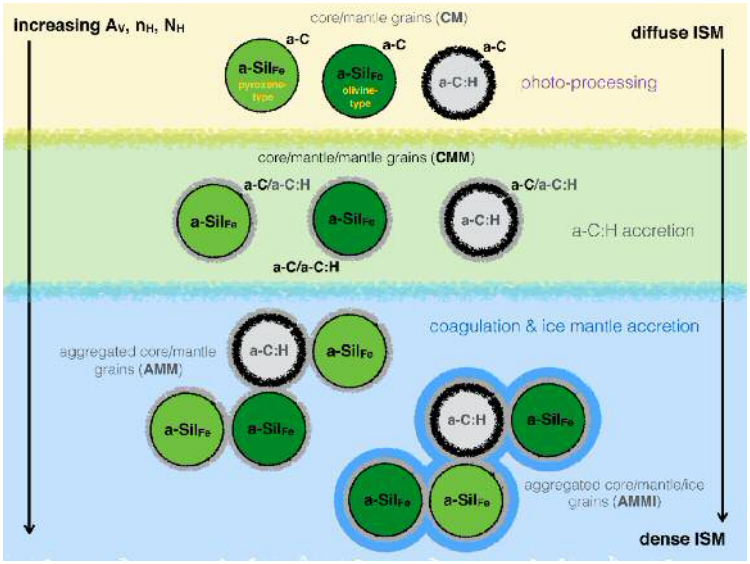

Figure 1.3: Schematic view of the dust composition and stratification between diffuse ISM and dense molecular clouds. The major evolutionary processes acting on the dust in each region are indicated on the right, i.e., photo-processing, accretion and coagulation with increasing density and extinction from top to bottom (Jones et al., 2017).

1.1.3 Dust Destruction

There are numerous ways in which dust can be destroyed, from absorption of high energy photos to grain-grain collisions in supernovae shockwaves. To fully explain each process in detail would require a study by itself, hence we direct your attention to Jones (2004) and references therein for a more detailed review.

Dust destruction is characterised by "any interaction between a grain and another ‘particle’ (grain, atom, ion, atomic nucleus, electron or photon) that leads to a net baryon loss from the grain - the resultant grain mass loss may be total" (Jones, 2004). "Sputtering" is the process by which atoms or ions are removed from the surface of the dust grain and thus returning it to its gas phase. The process is usually classified as either "chemical sputtering" or "thermal sputtering", depending on whether the removal of atoms is due to chemical interactions from incident particles or because of an increase in temperature of the grain, which then leads to sublimation or vaporisation.

Chemical sputtering occurs in a number of situations where chemical bonds between a surface particle and incident particle cause desorption of material from the grain back into the surrounding environment, such as through the low-energy collision of gas-phase atoms with the grain. The process is thought to be reliant on warm, dense environments such as compact envelopes surrounding young stars

(Whittet, 2002).

Thermal sputtering can be caused by a number of scenarios, including the absorption of high-energy photons (UV - γ-ray wavelengths). Dust grains will absorb such photons, increasing their temperature to the point of sublimation. It is also possible for the dust to be destroyed via expulsion of ions when the high-energy photon is absorbed ("charging"), as well as through "coulomb explosions" whereby the coulombic forces overcome the tensile strength of the grain (this is particularly pertinent for grains with impurities that contribute to low-tensile strength). We see the same effect of "charging" a dust grain for all sources of high-energy of ionised interactions with grains. For example, cosmic rays will incur similar effects to that of high-energy photons, increasing temperature, charging the grain and causing the ionisation of atoms attached to the grain. This is also the case for electron-grain interactions that induce a negative charge on the grain.

One type of event that can give rise to all the above instances of dust destruction are supernovae explosions, which not only destroy but produce cosmic dust in the interstellar medium (ISM) (see Section 1.1.1).

After a supernova explodes, high-velocity shockwaves are expelled from the centre that sweep up surrounding material as they expand. We observe hot gas bubbles around supernovae with temperatures reaching up to 10^6 K, resulting in the thermal sputtering of dust grains. Chemical sputtering is caused by the presence of gas-phase atoms, ions, photons and other particles that are expelled from the supernova, each of which interact with the grain and aid the process of removing surface particles. These events make supernovae an important factor in the life cycle of dust.

When modelling the production and destruction of dust in the ISM, it is predicted that the destruction timescale of dust cannot extend beyond $\sim 10^8$ years. However, the dust production rate is predicted to be in the region of 10^9 years, an order of magnitude above the destruction timescale. This result is problematic as we observe a vast amount of dust in the Universe that must have survived these events. For this reason, it is assumed that the majority of dust growth must occur in the interstellar environment rather than from stars themselves. Despite theories surrounding dust growth in the ISM, we still observe an imbalance whereby the mass of observable dust cannot be accounted for by current dust production models alone (see reviews in Draine (2009); Jones and Nuth (2011); Dunne et al. (2011); Rowlands et al. (2014)). Therefore, we require a more thorough model of dust production and destruction, as well as evolution throughout its lifetime.

1.2 The Radio to Far Infrared Spectra of Galaxies

The spectra of galaxies at wavelengths between a few metres down to micron levels provides a wealth of information about the internal processes that give rise to infrared and radio emission. Despite the scientific value of observations at these wavelengths, this region of the spectral energy distribution (SED) is the least explored, and more observations are needed at long wavelengths to further constrain the individual components that constitute emission from galaxies.

The radio to infrared spectrum is formed by both thermal and non-thermal emission mechanisms. The thermal emission is derived from two main constituents; free-free radiation and re-radiation of light by dust. Synchrotron radiation is the dominant mechanism for the non-thermal SED component. Figure 1.4 shows the radio to infrared spectrum for the starburst galaxy M82 and each of the three components is included. The x-axis represents the frequency (c/λ) of the emitted light.

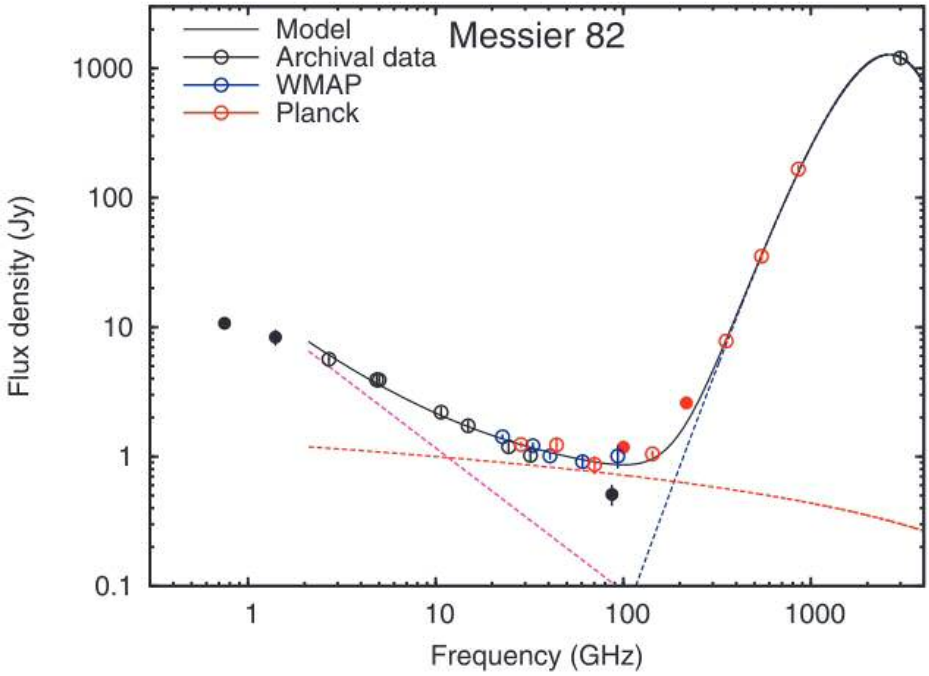

Figure 1.4: The SED of the starburst galaxy M82. The blue dotted line represents thermal radiation from dust, the red dotted line represents free-free emission and the purple dotted line represents synchrotron emission. The black solid line is the composite spectrum. Image taken from Peel et al. (2011).

1.2.1 Thermal Emission

1.2.1.1 Free-Free Radiation

There are relatively few studies on free-free emission due to the lack of available data at millimetre wavelengths, hence our understanding of the mechanism and its contribution to the spectrum is not well understood. According to Kaastra et al. (2008) and Burke and Graham-Smith (2010), free-free emission arises from the interaction between two oppositely charged particles within an ionised medium; or plasma. It is caused by the acceleration of charged particles, notably electrons due to their low mass, as their path is deflected by an oppositely charged particle. As the trajectory of an electron is diverted, a photon is released whose frequency is dependent on the initial energy of the electron. It is so-called 'free-free' radiation as the charged particle is not captured but is free both before and after the interaction. It is considered to be thermal as the medium must be ionised to form the plasma, and therefore the effective temperature is relatively high. For free-free emission within our own galaxy, typical electron temperatures (T_e) are in the region of $5{\times}10^3$ to 10^4 K (Condon, 1992). The emission coefficient, ϵ, can be described by

$$\epsilon = B_\nu \kappa, \tag{1.1}$$

where B_ν is the Planck function which is approximately equal to $2kT_e\nu^2/c^2$ at radio frequencies and κ is the absorption coefficient. The production rate of Lyman continuum photos [2] (N_{uv}), as presented by Condon (1992), can be derived using the following equation;

$$\frac{N_{uv}}{s^{-1}} \geq 6.3 \times 10^{52} \left(\frac{T_e}{10^4 K}\right)^{-0.45} \left(\frac{\nu}{GHz}\right)^{0.1} \frac{L_T}{10^{20} WHz^{-1}}, \tag{1.2}$$

where T_e is the electron temperature, ν is the observing frequency and L_T is the thermal spectral luminosity, which is defined as the total power per unit bandwidth radiated by the source (Condon and Ransom, 2010). This theory was originally formulated by Rubin (1968) and developed by Condon (1992) on the basis that the number of Lyman photos is loosely related to electron temperature, and approximately 65% of recombinations will produce Lyman continuum photons.

At frequencies between 30 - 100 GHz (λ 3 - 10 mm), free-free is the dominant source of emission in galaxies (Condon, 1992) (Figure 1.4). The radiation is predominantly emitted from HII regions that have been ionised by massive O-type

[2] Lyman continuum photons are produced when the photon energy is above the Lyman limit. This limit describes the amount of energy required for an electron in the ground state of a hydrogen atom to escape, thus creating a hydrogen ion.

stars. According to Condon (1992) and Beswick et al. (2015), free-free emission can be considered a direct tracer of star-formation (SF) within the radio regime as the intensity of free-free emission indicates the photoionisation rate, which therefore represents the number of the most massive and short-lived stars present. This fact is generally accepted for normal galaxies and is assumed in many studies, for example in the recent paper by Harper et al. (2015). Other sources of free-free emission are intergalactic gas in large clusters or groups of galaxies, and accretion discs around black holes.

1.2.1.2 The Thermal Dust Component

Absorption

Typically 30% of the bolometric luminosity of a galaxy is processed by dust into the infrared from stellar light, although this value can vary for different galaxy morphologies, luminosities and activity levels (Calzetti, 2001; Popescu and Tuffs, 2002; Davies et al., 2012). The process by which photons are reddened is known as extinction, which takes into account both the absorption and scattering of stellar light by dust grains.

In the case of absorption, a dust grain will absorb an energetic photon, temporarily raising the energy level of an electron in the grain, and therefore raising the dust temperature. When the grain loses energy, the photon will be re-emitted with a lower energy, i.e. a longer wavelength (see below for a brief outline of dust emission).

Scattering is the process by which stellar photons are 'reflected' by dust grains, redirecting their path out of the line-of-sight. When the incident stellar light hits a dust grain, the electric charges in the grain are set into oscillatory motion, radiating electromagnetic energy in all directions. This removes energy, therefore reddens, the incident stellar light. The direction and amount of scattering is highly dependent on grain size, density, composition and shape (Li, 2008).

The transfer of radiation through dust is defined by the following equation (Chandrasekhar and Subrahmanyan, 1960; Sobolev and Viktorovich, 1963),

$$\frac{dI_\lambda}{ds} = -\kappa_\lambda I_\lambda(s,\theta,\phi) + \epsilon_\lambda(s,\theta,\phi) + \kappa_\lambda \frac{\omega_\lambda}{4\pi} \int_\Omega I_\lambda(s,\theta',\phi')\Phi_\lambda(cos\Theta)d\Omega', \tag{1.3}$$

where $I_\lambda(s,\theta,\phi)$ is the radiation intensity, ds is the element of linear distance along the direction of propagation, $d\Omega'$ is the element of solid angle as seen by the dust grain, κ_λ is the opacity (absorption plus scattering) of the dust per unit separation s, $\epsilon_\lambda(s,\theta,\phi)$ is the emissivity of the sources along the direction of propagation, ω_λ is the albedo, i.e., the fraction of the opacity due to scattering, and $\Phi_\lambda(cos\Theta)$ is the phase function of the dust grains expressed as a function of Θ, the angle between the directions determined by the incident radiation (θ,ϕ) and the scattered radiation (θ',ϕ'). One commonly used expression of the scattering phase function, the Henyey-Greenstein function (Henyey and Greenstein, 1941), is characterised by a single parameter, the asymmetry parameter $g_\lambda = \langle cos\Theta \rangle$, which is the average of the cosine of the scattering angle (Calzetti, 2001).

Emission

Due to its obscuring nature, studies of direct emission from dust were greatly hindered until the advent of infrared space telescopes such as *IRAS* (Infrared Astronomy Telescope, Hedden (1976)) and the *Herschel Space Observatory* (Pilbratt et al., 2010), which allowed us to observe this emission directly at infrared wavelengths from 12μm up to 500μm.

Kirchhoff's law (Kirchhoff, 1860) states that "at thermal equilibrium, the power radiated by an object must be equal to the power absorbed" for a body at a particular frequency. This implies that the rate of energy absorption from the local radiation field is equal to the rate of energy emitted by dust. The Planck function characterises the spectrum of true blackbody emission, and is described in terms of frequency, ν, by

$$B_\nu(T) = \frac{2h\nu^3}{c^2} \frac{1}{e^{\frac{h\nu}{k_B T}} - 1}, \tag{1.4}$$

where B_ν is the Planck function spectral radiance, h is the Planck constant, and k_B is the Boltzmann constant. To characterise the dust emission spectrum, we can first consider a perfect blackbody emitter in radiative equilibrium with the local radiation field. The object will have temperature T, found by

$$T^4 = \frac{Uc}{4\sigma}, \tag{1.5}$$

where U is the energy density of the local radiation field, c is the speed of light, and σ is the Stefan-Boltzmann constant. Dust, however, is not an ideal blackbody and as such, the Planck function must be modified to account the emission efficiency of dust grains. The efficiency term is known as Q_ν, which represents the ratio of emitting power of an object, to the emitting power of a perfect blackbody at the same equilibrium temperature, at a given frequency. For far-infrared (FIR, 50 - 500 μm) and submm (250μm - 1mm) wavelengths, the term is typically characterised by a power law such that

$$Q_\nu \propto \nu^\beta \propto \lambda^{-\beta}, \tag{1.6}$$

where λ is the wavelength, and β is the spectral index of the dust emission slope (Tielens, 2005). Therefore dust, an imperfect blackbody, can be described by a modified blackbody function, such that

$$S_\nu \propto \nu^\beta B_\nu(T), \tag{1.7}$$

where S_ν is the observed flux at a given frequency.

For typical galaxies, the spectrum has peak temperatures between 20-200 K (Blain et al., 2002) dependent on the morphology and optical properties of the dust molecules as well as the spectrum and intensity of the interstellar radiation field (ISRF)[3].

Dust sublimates between approximately 1500-2000 K (Vaidya et al., 2009) but high temperatures at the top of this range are observed, particularly for small dust grains in regions affected by a powerful radiation source such as an O or B-type star emitting UV light. Dust temperatures lower than 20 K are also possible in regions of the ISM where grains are shielded from radiation, although heating from the cosmic microwave background (CMB) provides a minimum dust temperature limit of 2.7 K. If dust is not heated by the ISRF and solely by the CMB then the dust in the galaxy is undetectable (Blain et al., 2002).

1.2.2 Non-Thermal Emission

1.2.2.1 Synchrotron Radiation

At frequencies below ~30 GHz (λ ~10 mm) non-thermal synchrotron emission accounts for around 90% of the radio emission from a normal galaxy (Condon,

[3]The ISRF represents the global emission from a galaxy over all wavelengths.

1992). Synchrotron emission is caused by relativistic Cosmic-Ray Electrons (CREs) spiralling through an interstellar magnetic field. The centripetal force from the approximately circular orbit causes electromagnetic radiation to be released in the form of a photon. The intensity of the resulting photon is dependent only on the number and energy spectrum of cosmic-ray electrons and the magnetic field strength perpendicular to the line of sight (Strong et al., 2014). The frequency (ν) of an emitted photon can be calculated from the following equation taken from Condon (1992);

$$\left(\frac{\nu}{GHz}\right) = 0.016\left(\frac{Bsin\theta}{\mu G}\right)\left(\frac{E}{GeV}\right)^2, \tag{1.8}$$

where B is the magnetic field strength, θ is the pitch angle and E is the energy of the cosmic ray electron. At microwave wavelengths, thermal emission mechanisms such as free-free and re-radiation by dust become the dominant features in galaxy spectra and it becomes more difficult to separate each component.

Radio supernovae (RSNe) and supernova remnants (SNRs) are thought to be the dominant mechanism by which synchrotron radiation is emitted in galaxies. CREs are accelerated by the shock waves when stars become core-collapse supernovae (CCSNe - type Ibc and type II). The electrons interact with the circumstellar material as a shell begins to form around the explosion and the magnetic fields produced by the event produce synchrotron radiation. Radio emission is detected for thousands of years after the explosion in SNRs as the CREs meet the ISM and undergo re-brightening, also producing synchrotron radiation (Beswick et al., 2015).

According to Condon (1992) and Westcott (2015), it is possible to get a measure of the star formation rate (SFR) from the non-thermal radio luminosity of a galaxy using the following equation

$$L_\nu = 5.3 \times 10^{21} \cdot \nu^{-\alpha} \cdot SFR, \tag{1.9}$$

where L_ν is the radio luminosity in W Hz^{-1}, ν is the frequency, α is the spectral index and SFR is measured in $M_\odot$ yr^{-1}. By assuming a typical synchrotron spectral index of 0.8 at a frequency of 1.5 GHz (20 cm), this equation becomes

$$SFR = \frac{L_{1.5GHz}}{3.83 \times 10^{21}}, \tag{1.10}$$

where $L_{1.5GHz}$ is the luminosity of the galaxy in W Hz^{-1} at 1.5 GHz. Because of this link between non-thermal emission and supernovae, synchrotron emission can be used as a direct tracer of star formation and therefore the non-thermal component of a galaxy's SED can provide crucial information about their internal processes.

1.2.3 Anomalous Microwave Emission

Some galaxies exhibit excess emission in the microwave region of the spectrum. Within the dusty thermal spectral line profile (blue dotted line in Figure 1.4), there may be an excess in microwave emission called Anomalous Microwave Emission (AME) which can be seen in Figure 1.5. According to a study by Harper et al. (2015), AME has been observed at typical frequencies of 10 - 60 GHz (λ = 5 - 30 mm) and exhibits a spectrum that can be differentiated from the usual free-free, thermal dust and synchrotron components as can be seen in Figure 1.5. AME has so far been found in a number of environments such as HII regions (Dickinson et al., 2009; Tibbs et al., 2012), Lynds dark clouds (Casassus et al., 2006; AMI Consortium et al., 2009), diffuse galactic dust (Peel et al., 2012) and one extragalactic source (NGC 6946) (Murphy et al., 2010).

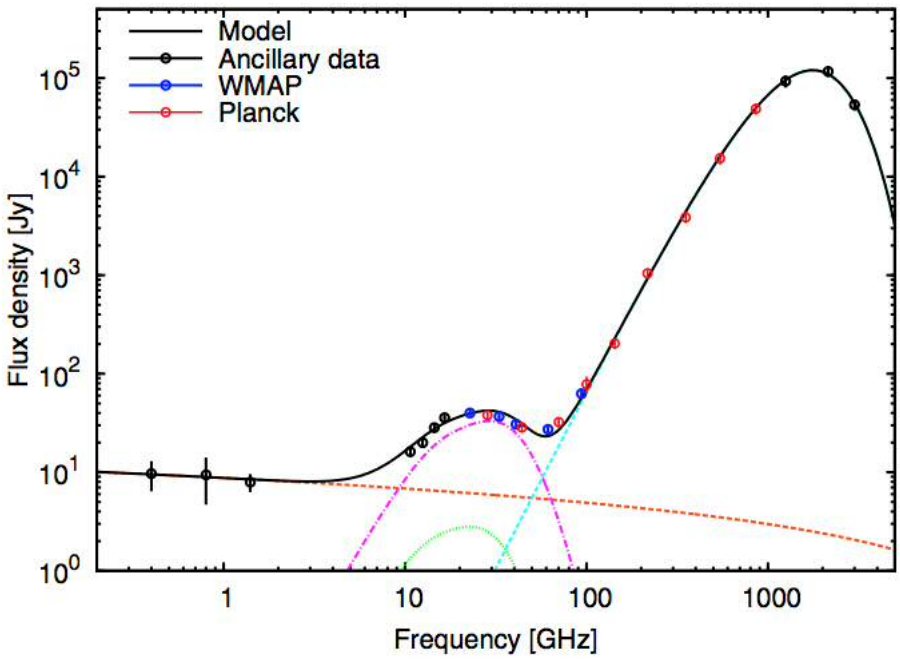

Figure 1.5: Spectral profile of AME which gives rise to an excess in the spectral dust slope. The vibrational dust corresponds to normal thermal emission from dust at a temperature of 19 K and a β of 1.55. Image taken from Planck Collaboration et al. (2011).

There are a number of models currently available to explain the AME anomaly, such as excess free-free emission from shock-heated gas, flat spectrum synchrotron emission and magnetic dipole emission from dust grains. The most widely accepted theory is that of spinning dust which represents the rapid rotation of dust grains that generate electric dipoles.

It was initially suggested that AME arises from free-free processes although there was no evidence of Hα being present in the observations, which is expected in regions where free-free emission is present. The lack of Hα would require temperatures greater than 10^6 K which was considered not possible by Draine and Lazarian (1998), who instead suggested that the phenomenon could be caused by electric dipole emission from dust grains. Dust grains are generally split into three main groups; big grains (BGs) with diameters greater than 0.1 μm, very small grains (VSGs) with diameters less than 0.1 μm and Polycyclic Aromatic Hydrocarbons (PAHs) which are disc-like dust molecules. The VSGs produce mid-infrared (MIR) continuum emission and PAHs emit at several MIR bands between 1-12 μm, hence both are possible sources of AME although it is still unknown which is the main contributor.

A study by Hensley and Draine (2015) suggests that contrary to this theory, there is no correlation between fluctuations in AME intensity and fluctuations in PAH emission. Their work finds a strong correlation between AME and all tracers of thermal dust emission which is also found by von Hausegger and Liu (2015), although they find that AME strength is strongly correlated with both dust radiance and radiation field strength as opposed to PAH emission. They conclude that other theories must be considered such as magnetic dipole emission, and more polarisation observations are needed to explore the phenomenon further. Another paper by Hensley et al. (2015) both agrees and contradicts with the work by Hensley and Draine (2015). Although the paper concludes that spinning dust must be affected by environmental factors to account for AME, it also states that there is no correlation between the radiation field strength and AME strength which is in disagreement with the later paper. Although they are both presented within the same year, there is still much debate over the source of AME and the processes that give rise to it. This shows that there is still a lot of confusion over the spinning dust theory and AME despite the abundance of research and current interest in the subject.

1.2.4 Modelling and Decomposing the Radio to Far-Infrared SED

1.2.4.1 The Thermal Radio Component

Free-free emission differs from other components of the SED as it has a relatively flat spectrum with a spectral index of ≤ 0.1, whereas thermal dust emission has a higher spectral index of ~1.7 (Verstappen et al., 2013) and the non-thermal synchrotron spectral index is 0.8. It should therefore be distinguishable from the steeper synchrotron and dust components in the SED by taking flux density measurements at two or more wavelengths (Condon, 1992).

To isolate the thermal free-free contribution in galaxies, it is possible to consider the ratio of the thermal flux density over the total radio flux density (S_T/S) which is generally small. Studies by Klein and Emerson (1981) and Gioia et al. (1982) observed this ratio in a sample of galaxies at 10.4 GHz and consistently found a value for S_T/S of ~ 0.4 assuming a non-thermal spectral index of $\alpha = 0.8$. There is a strong correlation between the thermal and non-thermal radio components in normal galaxies if multiple frequencies are measured, assuming a non-thermal spectral index range of $0.6 \leq \alpha \leq 1.0$. There is also a strong correlation between the thermal free-free emission at 1.4 GHz and the Hα emission line. When an extinction correction has been applied, we get a thermal fraction in normal galaxies of ~ 0.1 (Condon, 1992).

Although the thermal fraction seems to vary depending on what constraints are used, the relation between the thermal and non-thermal radio components can be generally quantified by the following equation

$$S/S_T \sim 1 + 10(\nu)^{0.1-\alpha}, \tag{1.11}$$

where ν is the observed frequency in GHz and α is the spectral index, typically assumed to be 0.8 for non-thermal emission (Condon, 1992). To decompose the radio spectrum globally is much more difficult as the free-free radiation from HII regions is clumpier than the smooth synchrotron emission from galactic spiral arms, but studies by Klein et al. (1989) and Graeve et al. (1990) among others have used the above formula to isolate the thermal radio component on smaller scales.

1.2.4.2 Dust Emission Models

To better understand dust as a whole, we require accurate models of the dust spectrum. The most commonly cited dust model was proposed by Draine and

Li (2007), which characterises the amorphous silicate and graphitic grains with varying contributions of poly-aromatic hydrocarbons (PAHs). This model has the benefit of being finely tuned to observations where certain properties are known or can be inferred, such as: wavelength-dependent extinction of starlight, abundance constraints, polarization of starlight, scattering of starlight, scattering of X-rays, infrared emission and microwave emission (Draine, 2011).

Despite the advantages of such models as Draine and Li (2007), recent observations show that the composition and evolution of cosmic dust is significantly more complex than originally assumed, and in most cases it is beneficial to have laboratory-measured observations of ISM-like dust to remove biases that occur when dust properties are adjusted to fit astronomical observations. While empirically based dust models such as Draine and Li (2007) can be finely tuned to the observations and thereby advance astrophysical understanding, in achieving this they tend to sacrifice some physical understanding of the dust itself (Jones et al., 2017).

A newer dust model, THEMIS (The Heterogeneous dust Evolution Model for Interstellar Solids), was suggested by Jones et al. (2017) for the purposes of the DustPedia project (Davies et al., 2017) and is therefore the model used during the scope of this thesis. THEMIS incorporates the structure, composition and evolution of dust in a cohesive model to study how the dust constituents interact with each other and with gas in the ISM. The framework is based on laboratory research of ISM-like compounds that are physically reflective of interstellar dust, particularly hydrogenated amorphous carbon-like dust particles.

The model considers three key stages of dust evolution;

1). Sources of Dust Production - how dust is produced in environments such as evolved stars and supernovae, as well as production and growth of dust in dense molecular clouds. This measure is derived from the star formation properties of individual galaxies (star formation rate, initial mass function and star formation history), enabling the exploration of input rates in a range of environments, and testing whether current theories surrounding production are accountable for the observed quantity of dust.

2). Dust Evolution - existing dust models have been compared with the laboratory-measured dust properties for amorphous hydrocarbon and silicate dust analogues to measure the reliability of previous models. THEMIS accounts for the nature of dust and how SEDs are affected by quantifying emission and absorption of light by dust. Furthermore, this allows the estimation of important physical parameters of dust, such as extinction and the dust mass in galaxies. The model provides a

link between the physical properties of dust grains to the observed SEDs of dust in galaxies.

3). Dust Destruction - dust destruction is modelled in a number of environments, such as supernova shockwaves, photo-dissociation regions and other intense UV-radiation fields. By quantifying the dust destruction rate in many different environments, this value can be compared to the production rate in galaxies to better answer questions surrounding the dust budget crisis. In addition, THEMIS aims to assess the importance of ram pressure stripping, how the stripped dust responds to the stripping process, how the dust evolves and how long it can survive in the hot tenuous inter-galactic medium (IGM).

1.3 Dust in Galactic Disks

Edge-on galaxies provide us with an excellent opportunity to study the distribution of dust in both the vertical and radial directions in galaxy disks. Dalcanton et al. (2004) show that spiral galaxies with high baryonic masses exhibit a concentrated disk of dust that lays on the same plane as the stellar and gaseous components. For galaxies with a lower mass, the dust morphology remains flocculent and shows a more vertically fractured structure as turbulence in the ISM outweighs the effect of gravitational collapse (Holwerda et al., 2012b). The galactic dust in both cases causes extinction of the optical and UV light from background stars due to absorption and scattering of light at these wavelengths. As a result, in high mass spirals we observe an optically thick dust lane when mapping edge-on galaxies with inclinations close to 90°. Previously, resolution issues hindered observations of dust lanes and vertical distributions until the launch of the *Herschel Space Observatory* which observed at FIR and sub-millimetre wavelengths (from 70 - 500 μm).

1.3.1 Galaxy Disk Models

The majority of galaxies that are classified as 'edge-on' are not inclined at a 90° angle, but are instead inclined at various degrees around this projection. For this reason, we need to understand how surface brightness, colour and FIR output vary as a function of inclination to properly study edge-on galaxies.

In real terms, galaxy disks are multi-layered with the stellar and dust components rising to different scale heights and extended to different scale lengths. The optical depth throughout the disk will change along the radius and the obscuration of light by dust is not consistent along the plane. To analyse the observed data of

galaxy disks we must first be able to model these variations to avoid systematic effects. Disney et al. (1989) provide a comprehensive outline of galaxy disk models that offers insight into the above effects and how we can realistically model them.

1.3.1.1 The Sandwich Model

One of the earlier galaxy disk models is the sandwich model; introduced by Disney et al. (1989). In the model they explain that the dissipative nature of dust relative to stars means that the dust will generally sink into an obscuring layer that is ξ times thinner than the stellar disk (where $\xi \leq 1$). This is the case for the Milky Way, where the scale height of the dust is smaller than the scale height of the stars (Cowie and Songaila, 1986; Drimmel and Spergel, 2001), more recently measured at 90 pc and 160 pc respectively (Misiriotis et al., 2006). Assuming the thickness of the stellar 'slab' is T, they find the optical depth τ to be

$$\tau = \xi T/\lambda \tag{1.12}$$

where λ is the mean free path of the stellar photons. The sandwich model is relatively simplistic, and can model a vertically layered disk with upper and lower regions of unobscured stars (a fraction of $(1-\xi)/2$ of the total), a patchy disk, a disk where the optical depth falls off exponentially or a combination of all three (see Figure 1.6).

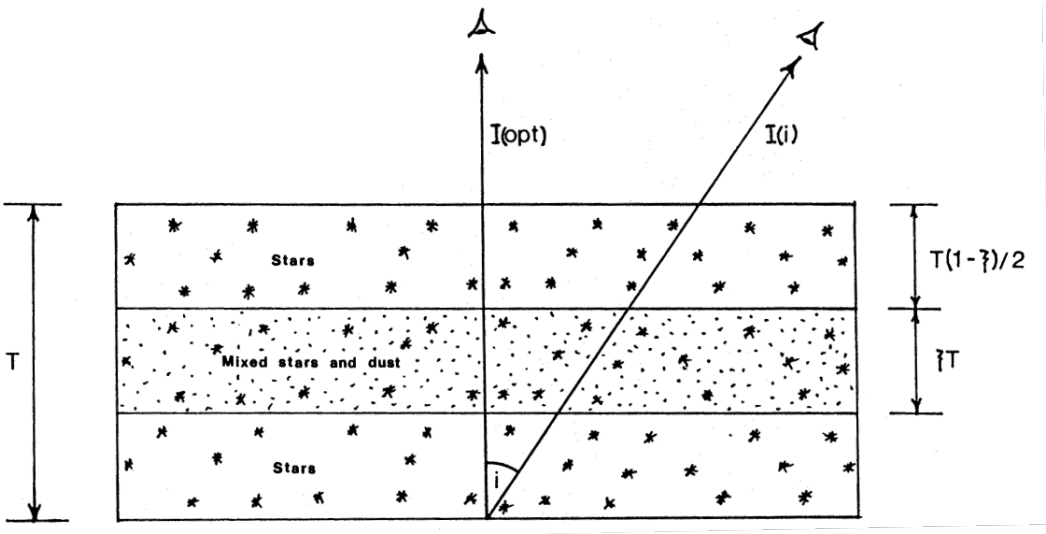

Figure 1.6: Geometry of the Sandwich model from Disney et al. (1989).

Viewed from face-on, the upper layer will be unobscured and the bottom layer will be undetectable through the central layer (if optically thick), through which

we could see to a distance of λ. Each sandwich model has just two parameters for characterisation; the layering parameter and the face-on optical depth. For $\lambda < \xi T$, the surface brightness, I_{opt}, as seen face-on will be

$$I_{opt} \approx E^* T(1-\xi)/2 + E^* \lambda \tag{1.13}$$

where E^* is the volume emissivity (in starlight), and the bolometric brightness, I_{bol}, is

$$I_{bol} = E^* T, \tag{1.14}$$

therefore

$$I_{opt} = I_{bol}[(1-\xi)/2 + \xi/\tau], \quad exp(-\tau) \gg 1. \tag{1.15}$$

Provided that

$$\xi < \tau/(2+\tau), \quad exp(-\tau) \ll 1 \tag{1.16}$$

or

$$\tau > 2\xi/(1-\xi), \quad exp(-\tau) \ll 1, \tag{1.17}$$

in the optical regime, an optically thick sandwich will appear like an optically thin disk. The thick upper crust of stars will dominate even when the crust thickness comprises just one-sixth of the total (i.e. $\xi < 2/3$), and as such a disk will behave as if it is optically thin, regardless of how large the optical depth. Therefore, optical observations of disk galaxies and extinction will return values that are systematically low, as detectors will preferentially pick up radiation from the least obscured areas of the disk.

1.3.1.2 TRIPLEX: The Triple Exponential Disk Model

Disney et al. (1989) expand on the sandwich disk model, outlining a triple-exponential model (TRIPLEX) that can compare better with observations. It considers the exponential fall-off of surface intensity in radius, as well as for stars and dust in the z-direction. Within the model, the scale length in radial directions for

both stars and dust is denoted as α_s and α_d respectively, the scale height in the z-direction of stars is β_s and for the dust is $\beta_d = \xi\beta_s$. They use the same layering parameter, ξ as for the sandwich model.

The full derivation of the model for dust absorption in a galactic disk is given in Disney et al. (1989), although we refer to the work by Davies et al. (1997) who provide results of the derivation. Solving the TRIPLEX model for the Milky Way disk, they find that the energy received over a wavelength range $\Delta\lambda = \lambda_2 - \lambda_1$ per unit area per second from a volume element of angular size Ω steradians and length Δd is

$$F^T_{\lambda_1-\lambda 2} \approx \frac{\Omega}{4\pi} n_d \alpha \Delta d \int_{\lambda_1}^{\lambda_2} Q(\lambda) B(\lambda, T_d) d\lambda, \tag{1.18}$$

where n_d is the dust number density, α is the emitting area of a dust grain, T_d is the dust temperature, $Q(\lambda)$ is the emissivity law, and $B(\lambda, T_d)$ is the Planck function. They assume that the dust number density and temperature vary with position, as described by the TRIPLEX model.

The way in which dust is distributed throughout a disk, $n_d(x, y, z)$, can be solved by the TRIPLEX model as

$$n_d(x, y, z) = n_d(0)\ exp\left[-\frac{\sqrt{x^2 + y^2}}{\alpha_d} + \frac{z}{\beta_d}\right], \tag{1.19}$$

where $n_d(0)$ is measured at the centre of the galaxy. This function provides us with a 3-dimensional solution to show how dust can be dispersed in galaxies, and as such we refer to this model in Chapters 2 and 3.

1.3.1.3 Radiative Transfer Modelling

Dust grains play an important role in shielding molecules from dissociating and are a critical factor in the heating and cooling balance of galaxies, with about 98% of the total FIR flux emitted by dust (Andreani et al., 2002). These grains regulate the cooling of gas in the ISM, a process that allows the gas in a galaxy to condense into stars. On the other hand, the extinction of stellar photons by dust makes it difficult to accurately view and study the stars within galaxies. Thus, it is important to understand the radiative transfer through dust so that we can better understand galaxy evolution processes such as star formation, and to determine the specific amount of stellar light reprocessed by dust particles (De Looze et al., 2012). Radiative transfer modelling predicts the relative influence of dust, gas and

stars and how these components affect one another, as well as the observational signatures they produce.

The equation of radiative transfer (Chandrasekhar and Subrahmanyan, 1960) describes light travelling in a dusty medium along a path of length s and direction κ, and the change in intensity I_λ of radiation (see Section 1.2.1.2). It can be written as

$$\frac{dI_\lambda}{ds} = -\kappa_\lambda I_\lambda + j_\lambda + \kappa_\lambda \frac{\omega_\lambda}{4\pi} \int I_\lambda(\kappa')\Phi_\lambda(\kappa,\kappa')d\Omega. \tag{1.20}$$

The first term represents the light that is removed from the beam, either because of absorption by or scattering of dust grains (both effects included in the extinction coefficient κ_λ). The opacity of a medium is characterized by the optical depth τ_λ, the integral of κ_λ along the whole radiation path. The other two terms in Eq. 1.20 are positive contributions to I_λ, due to direct sources of radiation (the emission coefficient j_λ) or to light coming from different directions κ' that is scattered into the direction κ. The last term depends on the dust phase function Φ_λ (stating the directionality of the scattering) and the albedo ω_λ (the fraction of extinguished light that is scattered) (Bianchi, 2004).

If the scattering term is removed, it is relatively simple to numerically solve the equation. However, due to the large amount of scattering by dust of optical light, the scattering term must be included when considering radiative transfer modelling using optical observations.

One solution as interpreted by Bianchi et al. (1995); Wood and Jones (1997); Baes et al. (2003) is to use a Monte Carlo method, which defines the path of a photon in a probabilistic way using random numbers. The model assigns a path direction for each photon emitted as well as its position when it is emitted. The probability for a photon to avoid absorption or scattering is $e^{-\tau}$ therefore the probable optical depth along a path can be derived. If this value is larger than the total optical depth along the direction of travel, the photon will escape the dust and can be recorded by an observer. Otherwise, it encounters a dust grain within the disk where it will be absorbed or scattered, altering the direction of travel. If scattering occurs, the new path is treated as before and the same process is undertaken.

Previous radiative transfer models have determined the dust content of edge-on galaxies from optical and near-infrared (NIR) observations (Xilouris et al., 1997; De Looze et al., 2012), which suggest that the dust disk is vertically thinner but horizontally more extended than the stellar disk with 10% of the stellar radiation

being absorbed by the dust. However upon observing the FIR/sub-mm spectrum of galaxies it was noted that the emission profile of dust at these wavelengths was not consistent with the radiative transfer estimates, and typically 30% of the UV and optical radiation is absorbed by dust (Davies et al., 2012). In fact, the dust mass required to produce the observed SEDs is at least twice as large as the mass estimated by the models (Bianchi, 2008; Baes et al., 2010; De Looze et al., 2012).

One solution to this dust-energy balance problem is to include a secondary thick disk of dust which extends further than that of the thin disk assumed by the radiative transfer models. Another proposed cause of the imbalance is the presence of high-density, clumpy dust clouds that hardly contribute to the attenuation of stellar light, and can therefore not be distinguished from optical observations (Popescu et al., 2000; Tuffs et al., 2004; Misiriotis et al., 2004; Bianchi, 2008; Popescu et al., 2010; De Looze et al., 2012). In this case, it is worthwhile to investigate the presence of a thick dusty disk that could account for the missing mass, and therefore search for dust above and below the plane of galaxies that has not been previously detected.

1.4 Detecting Extraplanar Dust

Despite continued efforts to model galaxy disks, it still remains relatively unclear to what extent the dust disk extends vertically beyond the stellar component. There are four key methods by which we can study dust in the haloes of galaxies; (1) using optical and UV emission as a tracer of dust, (2) direct imaging of the dust emission, (3) measuring the extinction of background light from the foreground dust and (4), modelling galaxies such that we are able to test the distribution of dust in disks via radiative transfer modelling. These processes and relevant studies are explained further in the following sections 1.4.1 - 1.4.4.

1.4.1 Optical and UV Emission as a Tracer of Dust

Detecting the emission from extraplanar dust in the FIR/sub-mm regime was considered difficult due to the poor resolution of infrared (IR) telescopes, and a faint IR background that can makes it difficult to define low-luminosity foreground sources of emission due to poorly constrained background subtraction techniques (Howk, 2012). Instead, optical and UV emission are often used as tracers of the presence of dust, as UV photons are scattered by particles in the dusty medium. This allows us to view optical emission originating from planar and background stars and detecting it in regions where there are no stars, but instead dust. The UV

and optical backgrounds are less bright and easier to subtract than the problematic IR background, hence they were considered the optimum wavelengths through which to detect extraplanar dust.

There are extensive studies that measure the optical emission scattered by dust against background stars. They show that many galaxies exhibit dense dusty clouds out to heights of z ~2 kpc (Howk, 2012). Rossa and Dettmar (2003) use the method to study the dust distribution in 74 galaxies, and find evidence of extraplanar dust extending to z ~2 kpc in 35% of their sample. Although optical imaging does provide evidence for an extraplanar dust component, it biases clumpy clouds of dust that have a density much greater than their surroundings and therefore increase the scattering effects, hence why they are detectable via this method. Optical imaging introduces a difficulty in quantifying the dust as we are prone to detect only dense clouds on the near-side of disks, and exclude any less-dense extraplanar dust as well as clouds on the far side of the galaxy (Howk, 2005, 2012).

This is partially resolved by UV imaging of extended galaxy haloes in which the dust is generally detected in a smooth distribution rather than in clumpy structures extending from the disk itself. Hodges-Kluck and Bregman (2014) use the UV emission observed by *Swift* and GALEX to trace the scattering or 'reflection' of light from stars, and they detect this radiation in late-type galaxies up to 5-20 kpc from the galactic disk.

Although for both UV and optical imaging methods there is evidence of dust above the plane of galaxies, it is difficult to quantify its mass using these methods independently due to their dependence on the dust morphology. With the advent of high resolution FIR/sub-mm telescopes such as *Herschel* and *Spitzer*, it is possible to overcome the limitations set by optical and UV imaging and enable us to observe the direct thermal emission from dust.

1.4.2 Direct Detection of FIR and Sub-mm Dust Emission

As well as scattering, dust particles also absorb optical and UV light from stars and re-emit the light at longer wavelengths such as infrared and sub-mm where emission from cold dust grains dominates the spectrum. We can detect this second-hand thermal emission by taking observations at these wavelengths and measuring the height above the disk at which the dust is still visible. Studies of nearby spiral galaxies in the FIR and sub-mm have revealed a more detailed picture of dust morphology and constrained the scale lengths and height of dust for individual galaxies, although there is little agreement between studies on these parameters.

Holwerda et al. (2012a) use *Herschel* SPIRE observations of the nearby, highly-inclined galaxy NGC 4244 and find that the dusty ISM is confined within the stellar disk, concluding that the vertical distributions of the dusty and stellar components are similar. They state that the cold dust component is consistent with the thin HI disk, finding no evidence for extraplanar dust.

On the contrary, the HEROES (HERshel Observations of Edge-on Spirals) project (Verstappen et al., 2013) surveyed seven nearby spiral galaxies observed with *Herschel*, utilising auxiliary data at other wavelengths. In their study, they find that 3 galaxies from the total sample show some evidence of an extended dust distribution in the vertical direction. For 2 of these galaxies, they attribute the extension to inclination effects; whereby the disk is not viewed exactly edge-on. For the other galaxy, NGC 4013, they find dust emission above the stellar disk which has previously been observed in optical observations and with radiative transfer modelling (Howk and Savage, 1999; Xilouris et al., 1999; Bianchi, 2007), extending up to 2.9 kpc from the plane. They conclude that the scale height of dust is loosely proportional to the 'clumpiness' of the dust morphology, whereby clumpier distributions are found closer to the disk than smooth distributions.

The work of Bocchio et al. (2016) traces dust emission from multi-wavelength observations of the nearby edge-on galaxy NGC 891 and detect extraplanar dust emission to at least 1.44 kpc from the plane, in agreement with previous studies of this galaxy (Burgdorf et al., 2007; Kamphuis et al., 2007; Whaley et al., 2009; Seon et al., 2014). They conclude that up to 3% of the galaxy's total dust mass is contained at heights above ~2 kpc from the plane.

Although UV and optical direct imaging approaches find traces of extraplanar dust in a large percentage of galaxies, this value is much lower for FIR/sub-mm emission methods. This may be due to lower signal to noise ratio (SNR) at longer wavelengths, or the still better resolution of UV and optical telescopes that allow the detection of clumpy dust clouds extending from the plane via indirect methods.

1.4.3 Extinction by Dust

Light from distant objects is scattered and absorbed by foreground dust in galaxies, and causes reddening, whereby this light appears redder and dimmer due to the effects of dust. The first attempt to look for dust in galactic halos by observing the effects of reddening was made by Zaritsky (1994), who discovered a significant colour change of background galaxies around two nearby spirals. More recently, Ménard et al. (2010) have studied the brightness of ~ 85,000 distant ($z > 1$) quasars and how this parameter changes with angular proximity to a foreground galaxy.

Their work shows that the quantity of diffuse dust in halos is comparable to the denser dust distribution contained in the disk, as quasars are reddened comparably by foreground objects directly along the line of sight, and close to the line of sight.

Observing the extinction of background radiation by dust is an efficient method to determine the dust morphology due to the excellent resolution achieved by UV, optical and near infrared (NIR) telescopes as opposed to the FIR, and because the extinction signatures of dust are fairly well determined at these wavelengths. However, the downside to this approach is that it is not straightforward to determine accurate dust masses when the only background light source is the galaxy itself (De Geyter et al., 2015).

1.4.4 Radiative Transfer Modelling

Radiative transfer models are used to define the quantity and distribution of dust in galaxies to test for the presence of extraplanar dust. Modelling was carried out by Bianchi (2007) on a sample of seven nearby highly-inclined galaxies, including NGC 891. The results (from optical V and K-band imaging) show that the event of the dust disk in the radial direction is greater than that of the stellar disk, by a ratio of $\alpha_d/\alpha_s \sim 1.5$. Their results also show, however, that the height of the dust is less than that of the stars, with a ratio of $\beta_d/\beta_s \sim 1/3$. This is consistent with previous radiative transfer modelling studies (Xilouris et al., 1997, 1998, 1999; Alton et al., 2004; Bianchi, 2007; Baes et al., 2010; De Looze et al., 2012). Although radiative transfer modelling allows us to quantify and predict the distribution of dust within the thin disk, the results so far show that an extended dust disk is poorly modelled from the optical data, and would benefit from exploration of extended dust disks in edge-on galaxies.

1.5 The Source of Extraplanar Dust

It is clear that dust is expelled from galactic disks, and according to Davies et al. (1998) up to 90% of the total dust produced within a galaxy could be expelled over its lifetime. However, not all galaxies with extraplanar dust have the same distribution of material above the plane, with some exhibiting dust in dense filamentary structures and others showing a more evenly extended cloud throughout the galaxy halo (Davies et al., 1998; Rossa and Dettmar, 2003). This is confirmed by optical and UV direct-imaging methods that give evidence of these two key types of extraplanar dust. For this reason, we consider both of the dust distributions independently.

1.5.1 Filamentary Clouds of Dust

Dense filaments in the thick disk of galaxies are relatively less extended and are found within a few kpc of the disk (see Figure 1.7 for an example of these structures). It is generally agreed that the dust has been expelled from the disk itself (Howk, 2012; Verstappen et al., 2013). Howk and Savage (1999) undertake a study of nearby edge-on galaxies and conclude that there are many processes by which dust can be expelled, including hydrodynamic or magnetohydrodynamic fountains (Howk and Savage, 1997) whereby the dust is driven upwards due to the convection of hot gas and/or magnetic fields. They also state that it is likely that dust can be expelled in the 'bubbles' of supernovae remnants. Although the initial shockwaves from SNe have high velocities and can destroy dust grains, the slower expansion of SNRs will carry dust from the disk into the halo as it sweeps up considerable mass. The 'chimney' model by Norman and Ikeuchi (1989) shows that if the supernovae remnant bubble is sufficiently long-lived, the resulting morphology will take the shape of chimney-shaped walls of material extending vertically from the disk with a possible dust component. Howk and Savage (1997) also show that dust grains can be "photolevitated" to a few hundred parsecs above the plane by the effects of radiation pressure from stellar winds. The effects of radiation pressure on dust are also confirmed by Davies et al. (1998), who show that this process is highly dependent on local surface mass and luminosity density, disk opacity and grain size. Therefore, radiation pressure may be responsible for both local high-density dust filaments, and for extended emission in the halo.

1.5.2 Extended Dust Emission in the Halo

The diffuse distribution of dust extends much further than the dense clouds, and has been shown to extend up to 1 Mpc from the planes of galaxies (Ménard et al., 2010). Studies debate whether this distribution originates from the disk itself, whether it is the result of interactions and mergers between galaxies which cause tidal disruptions and force material into the halos, or whether the dust is pulled gravitationally into the halo from the IGM. Ferrara et al. (1991) state that the dust grains originate from the disk itself, and can be expelled > 100 kpc into the halo due to radiation pressure. According to Howk (2012) however, the dust originates from extragalactic sources and not from the thin disk. They state that the continuing star formation in the Universe requires the constant infall of low-metallicity matter from outside of the star forming disks of spirals (LARSON and B., 1972; Chiappini et al., 1997; Wolfe et al., 2005). This material can originate

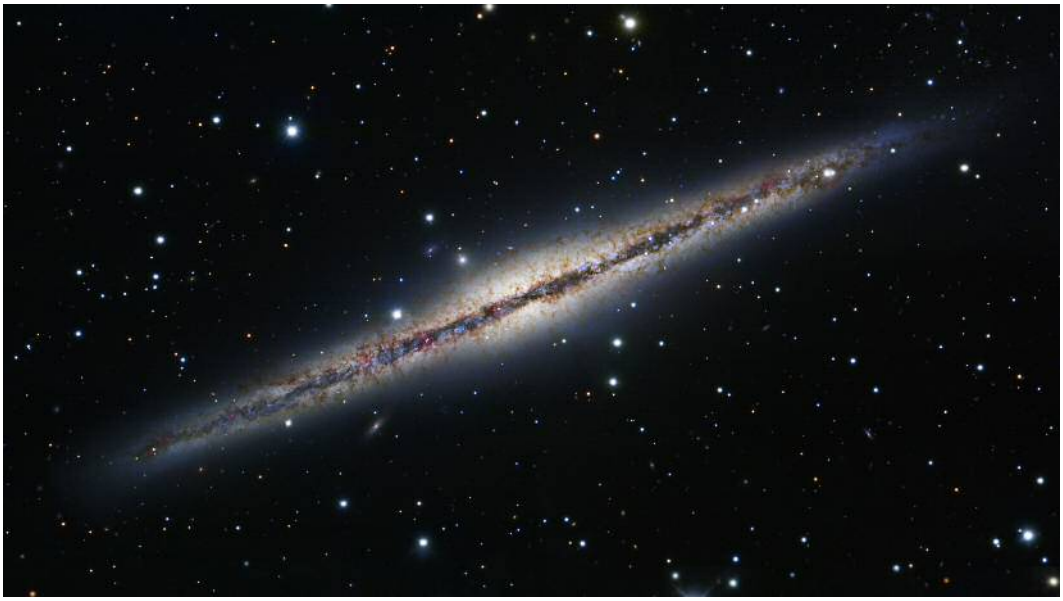

Figure 1.7: Composite optical observation of the nearby edge-on galaxy NGC 891, in which dust columns extending from the disk can be seen (Joner et al., 2012).

.

from primordial intergalactic gas, such as high velocity clouds condensed from a galactic corona (Peek et al., 2008), or dwarf galaxies may contribute some materials (although this is disputed by studies such as Peek (2009)).

1.6 Summary

The study of cosmic dust has only recently become a topic of interest rather than a nuisance to astronomers, and as such there are many unexplored issues that arise when researching dust in galaxies.

If up to 90% of dust produced in galaxies is expelled into the halo at some point in its lifetime (Davies et al., 1998), this has important implications on the extinction of background sources and the infrared background. For example, if our galaxy has produced $4{\times}10^8$ $M_\odot$ of dust, then over $3{\times}10^8$ $M_\odot$ of dust is currently in the halo or has been expelled further into the IGM. Previous studies (Davies et al., 1997; Ménard et al., 2010) show an excess in FIR emission at high redshifts, often assumed to be caused by greater dust production at earlier epochs. It is possible, however, that this excess could be caused by a large mass of cool dust in the IGM and haloes of foreground galaxies.

A recent study by Smith et al. (2016) explores this issue by considering the extinction and reddening of high redshift quasars as viewed through the disks of face-on galaxies. The aim of their study is to directly detect the FIR emission

from dust in 110 face-on galaxies by averaging maps of these galaxies at *Herschel* wavelengths, increasing the signal-to-noise by more than an order of magnitude over that of a single object. Previous studies attempting to detect radial emission from dusty disks find that the dust is confined to approximately 1-1.5 times the optical radius of the stellar disk, however Smith et al. (2016) find that in their sample the dust extends out to at least twice the radius of the stellar disk. The extent of dust in the disk is massive enough to conclude that the reddening of distant quasars can be attributed to Milky-Way type dust alone, and hence could provide evidence against higher dust production in high-redshift galaxies as the observed reddening may be due to foreground extinction (as evidenced by the reddening of quasars at high-redshift), rather than internal dust emission.

Further evidence suggesting a large mass of dust not contained within galaxy disks comes from the dust energy balance problem, whereby the dust mass measured by radiative transfer modelling does not account for the FIR contribution to galaxy SEDs. This indicates that there could be a hidden dust component that is not yet well constrained, hence our models must be progressed to better predict the distribution and contribution of dust in the interstellar and intergalactic media.

Now that the face-on distribution of dust in disks has been more reliably probed by Smith et al. (2016), it is important to measure the same for edge-on disks to get a fully 3-dimensional view of the dust in galaxies. If we can find evidence of a hidden dust component in galaxy haloes from observations of edge-on disks, it may well solve the dust energy balance problem and answer questions about the chemical evolution of galaxies from high redshifts to nearby galaxies.

In this thesis, we aim to study this topic by analysing *Herschel* 100 - 500 μm data for a sample of 31 nearby, edge-on galaxies. In Chapter 2, the vertical dust profiles of the sample galaxies are compared against an infinitely thin disk, a 3D dust model and the stellar disk profiles to measure the vertical extent of dust. In Chapter 3, similar methods to those discussed in Smith et al. (2016) are used to stack the maps with the aim of increasing the signal-to-noise ratio (SNR) of the data and potentially detecting an extraplanar dust component that is more extended than the values we find in Chapter 2.

We also utilise brand new data from the NIKA2 detector on the IRAM 30 m telescope at 1.2 and 2 mm for two nearby galaxies, NGC0891 (edge-on) and M99 (face-on), to measure the distribution of the very cold dust component for galaxies at different inclinations. It is this cold dust component that carries the majority of the total dust mass, making it an important contributor to the sub-mm/mm spectrum, and may enable us to identify a significant dust mass that is so-far

unconstrained.

As well as giving us a new view of the cold dust reservoir, there are generally very few observations of galaxies at the NIKA2 wavelengths. NGC 891 and M99 have never before been observed at 2 mm, and previous observations at 1.3 mm have such poor resolution that it is not possible to study the dust on local scales. These new observations may well open the window to mm-astronomy for nearby galaxies, giving us new insights to the local dust heating mechanisms and enabling us to disentangle the radio-infrared spectrum. These observations and the NIKA2 project are discussed in Chapter 4.

Chapter 5 presents a conclusion of the work undertaken for this thesis, discussing the main results from our analysis and outlining any issues that arose, as well as plans for future work to better aid our understanding of dust in galactic disks.

CHAPTER 2

A STUDY OF EDGE-ON GALAXIES IN THE DUSTPEDIA SAMPLE

DustPedia (Davies et al., 2017) is an EU-funded project whose aim is to provide the scientific community with a definitive study of cosmic dust in the local Universe. The database exploits observations from both the *Herschel* and *Planck* space telescopes, as well as other available data from ground and space-based observatories at a variety of wavelengths from UV to sub-mm. The DustPedia project enables the development of tools and computer models to relate observed cosmic dust emission to its physical properties (chemical composition, size distribution, and temperature), its origins (evolved stars, supernovae, and growth in the ISM), and the processes that destroy it (high-energy collisions and shock heated gas). Objectives of the project include SED fitting, radiative transfer modelling, the study of dust evolution, and formation of a global dust model.

The advent of *Herschel* provided us with a new wealth of information about long-wavelength dust emission. The only previous notable space observatory to observe at wavelengths greater than 350 μm was *Planck*, whose wavelength coverage ranged from 350 μm to 1 cm. However, the *Herschel* resolution is more than an order of magnitude higher than that of *Planck* at 350 μm. This high-resolution data opens a window to study the FIR spectrum on local galactic scales, such that had never been possible before.

As discussed in Section 1.4, the light emitted by dust particles at FIR wavelengths is notoriously hard to directly detect above the plane for edge-on galaxies. This is partly due to the relatively low resolution of FIR detectors compared to UV or optical, and to the low signal to noise ratio (SNR) of cold dust emission

against the IR background. Although there is evidence of extraplanar dust in a number of nearby galaxies (Verstappen et al., 2013; Bocchio et al., 2016), we are yet to fully quantify the dust contribution above and below the plane for a large enough sample to perform adequate statistics. The quantity and distribution of dust contained above the thin disk is a vital piece of information required to accurately determine the fidelity of current chemical evolution models, and solve the dust energy balance problem (see Section 1.3.1.3).

This thesis aims to shed light on the issue by conducting a large study of nearby, edge-on galaxies to measure the extent and mass of dust contained above and below the plane, and hence its contribution to the FIR/Sub-mm spectrum. In this Chapter, the vertical dust profiles of a sample edge-on galaxies are measured and compared against a 3D dust model, an infinitely thin disk, and the stellar disk profiles. The aim of the study is to measure to what extent the dust is detectable in FIR observations. In Chapter 3, the sample of galaxies is stacked in an attempt to increase the SNR of the data, and decipher whether we see an increase in the value of β_d via the stacking method versus analysis of the galaxies individually.

This chapter presents the DustPedia *Herschel* and The Wide-field Infrared Survey Explorer (WISE) observations used to analyse the dust distribution in a sample of nearby, edge-on galaxies. Overviews of *Herschel* and WISE are discussed in Sections 2.1 and 2.2, and the sample selection is outlined in Section 2.3. I introduce a 3D galaxy disk model in Section 2.6 and explain the methodology in Section 2.7, and results are presented in Section 2.8.

2.1 The *Herschel Space Observatory*

The *Herschel Space Observatory* was a satellite-based telescope operated by the European Space Agency (ESA) for the purposes of observing at far-infrared (FIR) to submillimetre wavelengths (55 to 672 μm), and was the first space telescope to cover wavelengths as long as ~700 μm (Pilbratt, G. L. et al., 2010; Pilbratt et al., 2010). *Hershcel* is the largest mirror of any space observatory at 3.5 metres in diameter, 50% greater than that of the *Hubble Space Telescope*. By operating in space, *Herschel* was able to avoid issues caused by the absorption of FIR light by the Earth's atmosphere. FIR wavelengths are notoriously hard to observe due to the absorption of the light by atmospheric particles and background emission, even at particularly dry, high altitude locations on Earth. As a result, the FIR and submillimetre wavelengths are the least explored by astronomers, hence this field has much to gain from *Herschel* observations.

The lifetime of the *Herschel* mission was limited by its liquid helium reserves - used to cool the telescope's instruments down to 1.7 K, and its detectors to 300 mK. Over time the helium evaporates into space and its resources eventually ran out on the 29th April 2013, the total operating lifetime of the telescope being just under 4 years.

On board the telescope were 3 instruments that provide full spectroscopic and photometric coverage of the 55 - 672 μm wavelength range; HIFI (Heterodyne Instrument for the Far Infrared), PACS (Photodetector Array Camera and Spectrometer) and SPIRE (Spectral and Photometric Imaging REceiver). For the purposes of this thesis I discuss only the PACS and SPIRE instruments (Sections 2.1.1 and 2.1.2 respectively) as we do not make use of data taken by the HIFI instrument.

2.1.1 PACS

PACS (Photodetector Array Camera and Spectrometer, (Poglitsch, A. et al., 2010)) is an imaging photometer and medium resolution grating spectrometer that observes in the 51-220 μm wavelength range, the region of the spectrum where emission from cold interstellar dust peaks.

The PACS instrument uses a bolometer system to detect incident light. This consists of a cryogenically-cooled thermistor acting as an absorption element, which is heated slightly by absorbing the incoming radiation and so the resistive properties of the thermistor are measurably changed. PACS has two bolometer arrays, one with 2048 elements (for shorter wavelengths) and one with 512 elements (for longer wavelengths). Both arrays have a field of view of 1.75′ x 3.5′. The photometer observes at three bands centred on 70, 100 and 160 μm with a relative bandwidth of $\frac{\Delta\lambda}{\lambda} \sim \frac{1}{3} - \frac{1}{2}$, despite having just two arrays. This design means that simultaneous observations can be taken at 160 μm and *either* 70 or 100 μm. Therefore, each observing region must be covered twice if all three bands are required. The spectrometer has a spectral resolution of λ / Δ λ ~ 1000-4000 and has a 47" x 47" field of view resolved into 5 x 5 pixels. Further specifications of the PACS instrument can be seen in Table 2.1.

2.1.2 SPIRE

SPIRE (Spectral and Photometric Imaging REceiver) (Griffin, M. J. et al., 2010) is an imaging photometer and an imaging Fourier transform spectrometer and is the longest wavelength instrument on board the satellite, observing from 190-670

μm. This region of the spectrum is particularly under-explored, yet covers the beginning of the Rayleigh-Jeans slope of interstellar dust emission, making SPIRE observations vital to this thesis and more generally to the study of cosmic dust.

The SPIRE bolometers are arranged in a spider-web pattern to reduce bulk in construction yet ensure adequate coverage. These bolometers act as temperature sensors to detect incoming radiation.

The spectrometer comprises of a small mirror which changes position, causing the different wavelengths of light to undergo different patterns of interference. This interference pattern is then de-coded and transformed into a spectrum, with a spectral resolution of λ / Δ λ ~ 370-1300 and wavelength coverage in two bands; 194-313 μm and 303-671 μm.

The photometer has three wavelength bands that are centred on 250, 350 and 500 μ, each with a relative bandwidth of $\frac{\Delta\lambda}{\lambda} \sim \frac{1}{3}$. The field of view on the sky of SPIRE is 4′ x 4′, and all three bands are observed simultaneously by the use of a dichroic filter which splits the incoming light beam into the three bands. The photometer has three observing modes; point source photometry, small area maps (for small objects with diameter < 5′), and large area maps (for covering large areas of sky or extended sources). Further specifications of the SPIRE instrument can be seen in Table 2.1.

Instrument	Wavelength (μm)	PSF Major Axis (")	PSF Axial Ratio	Pixel Size (")	Calibration Error (± %)
PACS	70	5.8 / 9.0 / 12.2	1.06 / 1.55 / 2.11	3.2	12
	100	6.9 / 9.7 / 12.7	1.03 / 1.41 / 1.81	3.2	12
	160	12.1 / 13.3 / 15.7	1.12 / 1.18 / 1.35	6.4	12
SPIRE	250	18.3	1.08	6	7
	350	24.7	1.06	8	7
	500	37.0	1.11	12	7

Table 2.1: Parameters of both the PACS and SPIRE instruments on board the *Herschel Space Observatory*. In each PACS band, the PSF characteristics are changeable depending upon the mapping mode. The order of which these are listed is slow scan (20" s^{-1}), fast scan (60" s^{-1}) and parallel scan mode (60" s^{-1}). Table courtesy of Clark (2015).

2.2 The Wide-field Infrared Survey Explorer

The *Wide-field Infrared Survey Explorer* (WISE; Wright et al. (2010)) is a space-based survey instrument providing NIR and MIR coverage of the entire sky, observing at 3.4 μm, 4.6 μm, 12 μm, and 22 μm with a sensitivity hundreds to hundreds of thousands times better than previous all-sky surveys at these wavelengths. The single WISE instrument consists of a 40cm focal telescope, a two-stage solid hydrogen cryostat, a scan mirror mechanism, and reimaging optics giving 6" FWHM (Liu et al., 2011).

WISE was placed into a Sun-synchronous polar orbit on a Delta II 7320 launch vehicle on December 14, 2009, and began surveying the sky in January 2010, completing its first full coverage of the sky on July 17 2010. After the solid hydrogen cryostat was exhausted in 2011, WISE was still able to use the 3.4 and 4.6 μm detectors to survey the main asteroid belt and search for near-Earth objects (NEOs), asteroids whose orbits cross that of Earth. The WISE mission ended on February 17, 2011. The angular resolution of the instrument is 6.1, 6.4, 6.5, and 12.0 arcseconds at 3.4, 4.6, 12, and 22μm respectively.

2.3 Sample Selection

The DustPedia sample consists of 4259 galaxies initially selected from the LEDA database with $v_{rad} < 3000$ km s^{-1} and $d_{25} > 1$ arcmin, where v_{rad} is the measured radial velocity either from an optical or 21 cm spectrum and d_{25} is the major axis diameter (Davies et al., 2017).

There are 864 galaxies with *Herschel* detections, and it is this smaller subsample with *Herschel* data that is used to create the galaxy sample for this project. Galaxies were selected if they were detected by the DustPedia photometry pipeline (i.e. pixels with SNR>3 at the co-ordinates of the target source have been detected in at least one band, Clark et al. (2018)), with d_{25} values greater than 2.5′ (so that sources are sufficiently resolved for later analysis).

Galaxies were excluded if they had t-type values less than 0 (where 0 indicates a morphological type of S0/Sa, and values above 0 are representative of late-type galaxies) to exclude early-type galaxies that are typically spheroidal and hence do not have a disk-like structure.

At this stage the sample was reduced to only contain galaxies with relatively high inclinations, i.e. above 80°, based on the inclination values for the sample as measured by Mosenkov et al. (2018). In their study, they used the GALFIT

programme with WISE W1 (3.4 μm) maps to measure the inclination by fitting an ellipse to each galaxy, and the inclination is found from the ratio of the semi-minor to -major axes as follows;

$$sin^2 i = \frac{1 - 10^{\,2\ log\ q}}{1 - 10^{\,2\ log\ q_0}}, \tag{2.1}$$

where q is the ratio of the apparent minor to major axes of a galaxy outer disc and q_0 is the intrinsic disc flattening. According to Mosenkov et al. (2018), the average value for late type galaxies is $\langle q_0 \rangle \approx 0.14$.

The resulting sample contained 67 galaxies, 6 of which were removed due to their proximity to the Galactic plane. Galaxies within 15° of the Galactic plane were excluded as the data is likely to be contaminated by radiation from foreground Milky Way dust.

After these cut-offs, the sample then consisted of 61 galaxies, at which point each map was analysed by eye to find any non detections or other sources of error. 27 sources were removed because they either; (i) were not detected in one or more of the PACS and SPIRE bands, (ii) were face-on rather than edge-on, (iii) appeared point-like due to detection only of the central bulge. The Sombrero galaxy was also removed from the sample as its morphological type is ambiguous, possibly due to previous mergers or interactions that give the galaxy both elliptical and spiral morphological qualities (McQuinn et al., 2016).

The sample consists of 33 galaxies (4% of the original DustPedia sample with *Herschel* detections) with inclinations ≥ 80°, t-type values > 0 and Galactic latitudes l < -15° and l > 15°. The distribution of the final sample on the sky can be seen in Figure 2.1, and a table of sources and their properties is presented in Table 2.2.

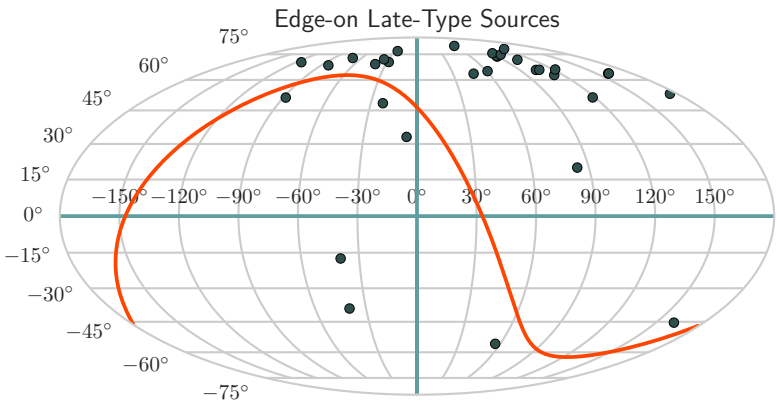

Figure 2.1: The distribution of the sample as a function of their galactic co-ordinates. Note that galaxies within 15° of the Galactic plane have been removed in case of contamination from foreground dust emission. The red line indicates the celestial equator projected onto the sky.

Name	SFR ($M_\odot yr^{-1}$)	Stellar Mass ($M_\odot$)	Dust Mass ($M_\odot$)	Dust Temp (K)	Dist (Mpc)	RA	Dec	Hubble Type	d25 (")	Position Angle (°)
IC2233	0.21	1.36×10^{9}	1.01×10^{6}	19.84	14.00	123.50	45.74	SBc	2.88	83.66
NGC0678	0.09	6.57×10^{10}	1.01×10^{7}	18.24	27.87	27.35	22.00	SBb	3.09	-12.67
NGC0891	1.96	3.48×10^{10}	4.90×10^{7}	22.22	9.86	35.64	42.35	Sb	13.18	113.77
NGC1351A	0.09	3.93×10^{9}	4.35×10^{6}	17.80	19.41	52.20	-35.18	SBbc	2.51	43.11
NGC3079	5.25	3.85×10^{10}	3.42×10^{7}	24.67	16.52	150.49	55.68	SBcd	8.13	73.78
NGC3501	0.52	1.39×10^{10}	1.12×10^{7}	20.11	22.59	165.70	17.99	Sc	4.27	118.45
NGC3628	1.76	3.15×10^{10}	3.87×10^{7}	22.45	10.81	170.07	13.59	Sb	10.96	12.99
NGC4013	0.31	3.72×10^{10}	1.98×10^{7}	22.22	18.79	179.63	43.95	Sb	4.9	-23.87
NGC4183	0.32	2.95×10^{9}	8.04×10^{6}	17.83	16.67	183.32	43.70	Sc	4.27	79.70
NGC4206	0.35	6.61×10^{9}	1.18×10^{7}	17.06	18.88	183.82	13.02	Sbc	4.68	91.68
NGC4216	0.13	8.34×10^{10}	2.07×10^{7}	18.66	13.80	183.98	13.15	SABb	7.76	111.00
NGC4217	1.59	3.45×10^{10}	2.94×10^{7}	22.45	18.54	183.96	47.09	Sb	5.37	133.33
NGC4222	0.27	4.39×10^{9}	8.21×10^{6}	19.12	19.77	184.09	13.31	Scd	2.82	-31.84
NGC4244	0.11	1.01×10^{9}	2.84×10^{6}	16.76	4.35	184.37	37.81	Sc	16.22	-42.52
NGC4289	1.18	4.30×10^{10}	2.18×10^{7}	22.01	45.08	185.26	3.72	Sc	4.27	82.82
NGC4302	0.42	2.72×10^{10}	1.49×10^{7}	20.16	14.32	185.43	14.60	Sc	6.03	88.15
NGC4402	0.38	6.08×10^{9}	6.46×10^{6}	22.43	12.42	186.53	13.11	Sb	3.55	-0.32
NGC4437	0.46	8.94×10^{9}	1.38×10^{7}	18.75	8.39	188.19	0.11	Sc	9.12	-7.94
NGC4445	0.03	5.74×10^{9}	1.90×10^{6}	19.55	18.03	187.07	9.44	Sab	2.51	12.67
NGC4758	0.09	2.35×10^{9}	3.32×10^{6}	18.28	13.49	193.18	15.85	SBm	2.75	64.89
NGC5023	0.03	3.70×10^{8}	1.52×10^{6}	14.01	6.58	198.05	44.04	Sc	6.17	115.05
NGC5301	0.88	1.34×10^{10}	1.51×10^{7}	20.27	20.89	206.60	46.11	SBc	3.98	56.66
NGC5348	0.10	1.69×10^{9}	3.54×10^{6}	17.02	15.92	208.55	5.23	SBbc	3.89	83.92
NGC5356	0.10	1.00×10^{10}	7.96×10^{6}	18.44	19.50	208.74	5.33	SABb	2.82	107.17
NGC5529	2.86	1.45×10^{11}	1.04×10^{8}	18.82	44.46	213.89	36.23	Sc	5.75	23.47
NGC5746	0.07	2.95×10^{11}	7.53×10^{7}	18.31	27.04	221.23	1.95	SABb	7.24	79.99
NGC5907	3.04	9.01×10^{10}	7.10×10^{7}	20.22	17.22	228.97	56.33	SABc	11.22	63.88
NGC7090	0.45	5.78×10^{9}	6.76×10^{6}	20.27	9.51	324.12	-54.56	Sc	8.13	37.04
UGC07321	0.24	4.20×10^{9}	8.87×10^{6}	16.34	23.33	184.39	22.54	Scd	4.79	-4.29
UGC07522	0.45	2.41×10^{10}	2.10×10^{7}	18.15	35.48	186.49	3.43	Sc	2.63	36.35
UGC07982	0.06	4.88×10^{9}	4.53×10^{6}	17.55	19.23	192.46	2.85	Sc	2.88	90.22

Table 2.2: Galaxies included in the sample alongside their properties, all values taken from Nersesian, A. et al. (2019) as part of the DustPedia database, which were calculated via the SED-fitting software `CIGALE` (Noll et al., 2009).

2.3.1 Inclination Errors in the Sample

During the sample selection phase, it became apparent that some galaxies had lower inclinations than measured by Mosenkov et al. (2018), therefore the inclinations quoted for the rest of the sample may be inaccurate. To remedy this, new values for the galaxy inclinations have been measured as part of this study.

Similar to the methods developed in the GALFIT programme (Peng et al., 2002), I have written an automated routine to fit an ellipse to each of the galaxies out to a threshold of SNR ≥ 2, and then use the method as shown in Eq. 2.1 which uses the ratio of semi-minor to -major axes of each ellipse. This process is done for each galaxy over a number of wavelengths, from DSS B-band (optical) to SPIRE 500 μm (FIR) as can be seen in Figure 2.2. The purpose of sampling the inclination at multiple wavelengths is to find a waveband that is consistent and representative of the true inclination, as the values obtained by Mosenkov et al. (2018) were measured at the W1 band and subsequently shown to be inaccurate at high inclinations. The new inclinations are plotted for 10 sample galaxies whose inclinations are known to be >85°. From Figure 2.2, it was concluded that the most consistent band is the *Herschel* PACS 100 μm as all values are found to be ≥85° and therefore representative of the sample.

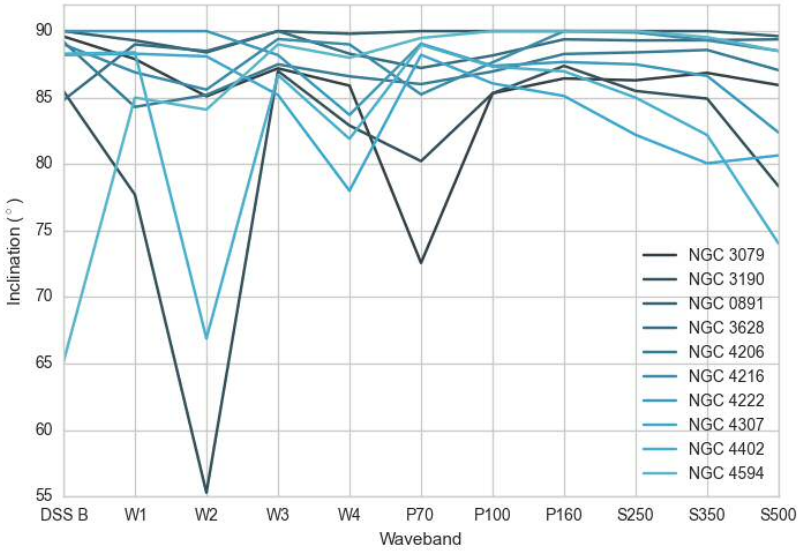

Figure 2.2: Inclination of some of the sample galaxies at each wavelength ranging from the DSS B-band, through all 4 WISE bands, all 6 *Herschel* PACS bands and SPIRE bands. Inclinations of the ten galaxies are known to be >85°.

I compare the new inclination values against those of Mosenkov et al. (2018) and a plot of this comparison can be seen in Figure 2.3. The values obtained by Mosenkov et al. (2018) overestimate the inclinations in the majority of cases and most of the sample are measured at exactly 90°. The lower measurements obtained from this thesis mean that when modelling the galaxies (see Section 2.6), the tilt is better accounted for and inclination effects are therefore not underestimated in the analysis.

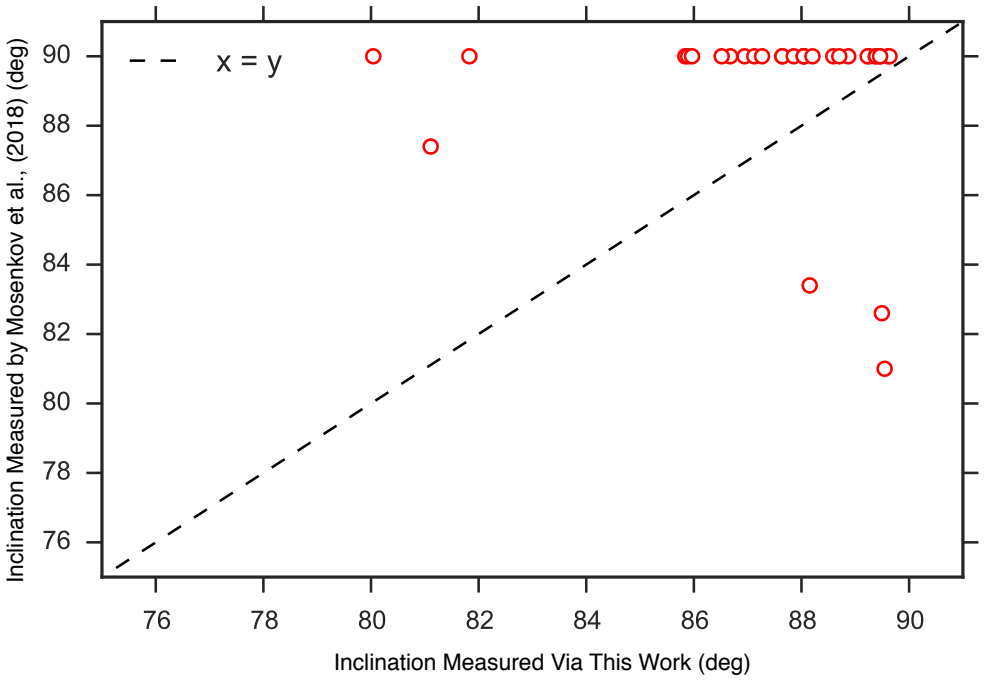

Figure 2.3: Inclination of the sample galaxies as found by our ellipse fitting routine on the x-axis, compared to those published in Mosenkov et al. (2018) on the y-axis. Red circles represent the galaxies in the sample, and the black dashed line represents a 1:1 correlation.

Two of the sample galaxies were found to have inclinations between 60° and 70°, hence they were removed from the sample due to their relatively low inclination. *The sample at this stage now consists of 31 galaxies*.

The inclinations measured from the PACS 100 μm maps were cross-referenced with the literature for galaxies with which this information is available. Results show that the measurements agree to within 5% of the published values (Dahlem et al., 2005; Verstappen et al., 2013; Banerjee and Bapat, 2017). It is worth noting that although the inclination of the 31 sample galaxies have been tested and verified, there may yet be galaxies in the DustPedia database whose true inclinations would make them eligible for this study. Further work would redefine the inclinations

for all DustPedia galaxies to ensure that upcoming studies do not omit possible eligible sources.

2.4 Data

The data used throughout this chapter consists of 31 galaxies with detections in all 3 SPIRE bands and at the 100 and 160 μm PACS bands. Data were obtained from the DustPedia database (http://dustpedia.astro.noa.gr/) with their respective photometric and physical measurements (http://dustpedia.astro.noa.gr/Photometry) for all galaxies selected in this sample, as well as their error maps which contain the instrumental error for each pixel in the source map, as measured by the instrument.

WISE data is utilised for the purpose of measuring the vertical scale height of the stellar disk for each galaxy, which is later used for comparison against the dust emission. The WISE W1 (3.4 μm) band was chosen as it traces the older stellar populations in a galaxy, which are typically found furthest from the central mid-plane (Lagattuta et al., 2013). This ensures that the dust distribution is compared against the most extended possible distribution of the stellar disk.

2.4.1 PACS Data

The data reduction procedure for DustPedia galaxies is outlined in Davies et al. (2017) and Clark et al. (2018). Level-0 data was is obtained from the *Herschel* Space Archive (HSA) and processed to the Level-1 stage using the HIPE v13 package, which is then processed to Level-2 data (final maps) using the Scanamorphous pipeline (Roussel 2012, 2013). This process takes into account whether the PACS data was taken in scan map, mini map or parallel mode. If more than one mode is available for any given galaxy, the optimum map is chosen based upon depth, coverage sky area and scan speed. The final maps have pixel sizes of 3 and 4 arcseconds for the 100 and 160 μm maps respectively.

At 100 μm, the Full Width Half Maximum (FWHM) beam size of 6.9" equates to 0.62 kpc at 18.5 Mpc (the mean distance of the sample galaxies), and at 160 μm the 12.1" FWHM equates to 1.09 kpc.

2.4.2 SPIRE Data

The Level-0 data is acquired from the HSA and processed up to Level-1 with the HIPE v13 package. It is then processed to Level-2 data which consists of the final

maps using the Bright Galaxy Adaptive Element pipeline (BriGAdE, Smith 2012). The final timelines were refined with the HIPE v13 package, which was also used to produce the final maps via the naive map-maker with pixel sizes of 6, 8, and 12 arcseconds at 250, 350 and 500 μm respectively, and with beam areas of 469.7, 831.7 and 1793.5 arcsec^2.

At 250 μm, the FWHM beam size of 18.3" equates to 2.22 kpc at 18.5 Mpc (the mean distance of the sample galaxies), at 350 μm the 24.7" FWHM equates to 1.09 kpc, and at 500 μm the 37.0" FWHM equates to 3.32 kpc.

2.4.3 WISE Data

The Wide-field Infrared Survey Explorer (WISE; Wright et al. (2010)) provides NIR and MIR coverage of the entire sky, observing at 3.4 μm, 4.6 μm, 12 μm, and 22 μm. WISE maps were obtained from the DustPedia database, described in Clark et al. (2018). For the database, WISE imagery was obtained from the AllWISE data release Image Atlas, which combines WISE cryogenic and NEOWISE (Near Earth Object WISE; Mainzer et al. (2014)) survey phases. AllWISE Atlas images in the vicinity of the DustPedia *Herschel* galaxies were identified and retrieved from IRSA. The final WISE cutouts retain the standard AllWISE Image Atlas pixel size of 1.375". The map pixel units were rendered in Jy pix^{-1} by using the zero-point magnitudes provided in the headers of the AllWISE Atlas images to convert pixel units to Vega magnitudes, which were then converted to AB magnitudes, and finally to Jy.

2.5 Data Preparation

I obtained the data products described in sections 2.4.2 through 2.4.3 from the DustPedia archive and completed the following steps for each galaxy map at the 5 *Herschel* wavelengths, WISE1 maps, and for their corresponding error maps to ensure consistency between observations:

2.5.1 Background Subtraction

An estimate of the image background is required to accurately measure the photometry and morphological properties of galaxies. Background noise arises from both the sky and the detector itself (and must be subtracted from the galaxy maps before analysis.

Background estimation was completed using the `photutils` package for *Python* which finds the mean value of pixels within various 'meshes' or sub-regions, the size of which is specified by the user. Mesh sizes were selected for each galaxy based on the aperture dimensions selected by the automated photometry routine, CAAPR, used for the DustPedia database photometry (Clark et al., 2018). The input box size provides a limit to the proximity in which background meshes are placed to the galaxy, ensuring we do not inadvertently sample actual source flux. This procedure is can be seen in Figure 2.4 in which the meshes are plotted over the NGC 3079 SPIRE 250μm map.

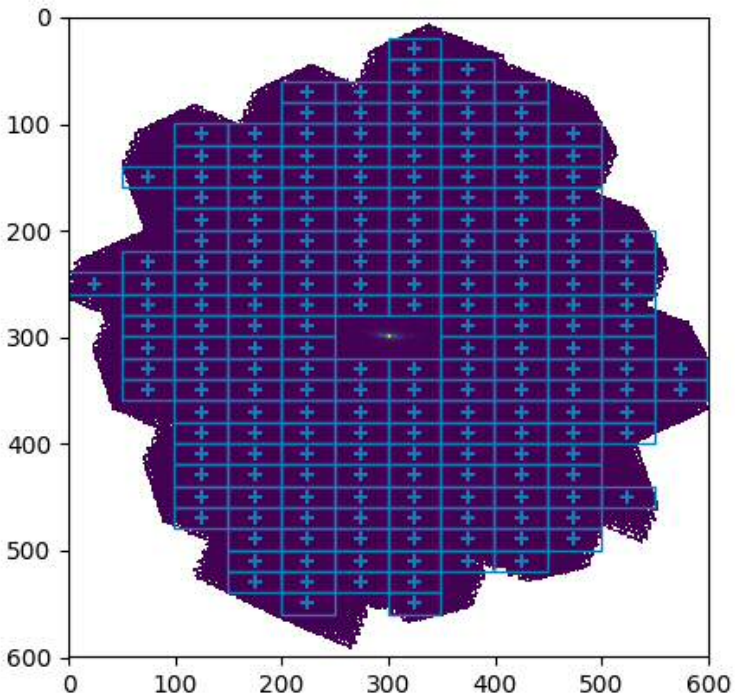

Figure 2.4: `photutils` background estimation technique, showing meshes in which the background is calculated over the SPIRE 250μm map of NGC 3079. Light blue boxes represent the meshes, or sub-regions, in which the sigma-clipped mean is calculated. The galaxy is visible at the centre of the image, and is not contained within a mesh hence its flux is not considered during the background estimation.

The procedure calculates the sigma-clipped mean in each mesh of a grid that covers the input data to create a low-resolution background image. This background image can then be subtracted from the original galaxy maps. The method was applied to all galaxies in the sample at all 5 *Herschel* wavelengths and in the W1 band.

2.5.2 Image Rotation

To ease analysis when comparing and stacking the data, each map is rotated so that the major axis of all galaxies are aligned to the horizontal plane according to their position angles[1]. To do this, the `Montage` wrapper for *Python* is used which produces a new `.fits` header file for each map, specifying the angle by which each galaxy should be rotated. The maps are then reprojected to match the new header file with the `montage.wrappers.reproject` function; a flux-conserving algorithm that re-samples data to a projection specified by the input header file.

2.5.3 Convolution

Direct comparison of images with structures ranging over multiple angular and spatial scales obtained with different PSFs can result in intensity ratios (i.e. colours) that are unphysical. To preserve the true colours, we must compare these data with a common PSF, and therefore require convolution kernels that can transform the observations from several instruments to this state. The result is a series of images expressed in the same co-ordinate grid, in which each pixel corresponds to the same sky region for all instruments used.

I make use of the common-resolution convolution kernels provided by Aniano et al. (2011) for this task[2]. Aniano et al. (2011) have generated convolution kernels that allow the conversion from shorter wavelength data to the SPIRE 500 μm resolution via a series of image processing techniques outlined in. The series involves resampling, circularisation and resizing of the PSF before computing its Fourier transform (FT). The FT of the PSF is then filtered and inverted, before the FT of the filtered kernel is computed. The kernel is then again circularised, resampled and a final trim is completed. At this stage the kernels are ready to be used and openly available to the public.

By utilising these kernels, the 100, 160, 250 and 350 μm band images have been degraded to match the 500 μm resolution using the `image_convolve.pro` script in *IDL*, also provided by Aniano et al. (2011). All maps at all wavelengths now have a common resolution and can be compared against one another without the influence of improper colour ratios.

[1] Position angles of each target were produced during the photometry stage, see Clark et al. (2018) for detailed information.

[2] Convolution kernels and the useful `image_convolve.pro` *IDL* script can be obtained from https://www.astro.princeton.edu/~ganiano/Kernels/Ker_012/Kernels_fits_Files/Hi_Resolution/

2.5.4 Image Resampling

As well as convolving the shorter wavelength maps to the same resolution as the 500 μm data, the maps must also be re-gridded to match the same pixel size to allow meaningful comparison during the analysis stage. As I intend to eventually stack the data, it is ensured that each galaxy map has the same number of pixels per half-light radius to aid fair comparison of the galaxies which lie at a range of distances and have varied morphologies.

To measure the half-light radius of each galaxy in the sample, the following equation for exponential disk galaxies is used:

$$r_{1/2} = 1.67835 r_d, \tag{2.2}$$

where $r_{1/2}$ is the half-light radius and r_d is the scale length of the galaxy. The scale length this case it is defined as the radius at which the brightness of the galaxy has fallen off by a factor of e (~ 2.71828) from the centre. The brightness follows the functional form

$$b = b_0 \times e^{-r/r_d} \tag{2.3}$$

where b_0 is the brightness in the centre of the galaxy (Ho et al., 2014).

To find the half-light radii of the sample galaxies, the brightness profile of each galaxy at 500 μm was measured from the central pixel along the major axis out to a SNR of 2 at, providing a value for r. I then find at what distance the brightness of the profile is equal to $b_0 \sim 2.718$, resulting in a value for the scale length of the galaxy. Once the scale length is known, or r_d, Equation 2.2 is used to measure the half-light radius. For all galaxies to have the same pixels per half-light radius for later stacking, I find the ratio of each galaxy's $r_{1/2}$ to the smallest $r_{1/2}$ in the sample, and then change the pixel size according to this ratio.

The map resampling was completed using the `Montage` wrapper for *Python*, which produces a header file implementing the new pixel sizes for the 500 μm data. The `montage.wrappers.reproject` function was then used to resample the maps according to the new header files. At this stage all of the 500 μm maps have the same number of pixels per half-light radius (26 pixels/$r_{1/2}$).

The data at 3.4, 100, 160, 250 and 350 μm were resampled to the same pixel size as these 500 μm maps, using the `Montage` wrapper as before. After this is completed, all maps for each sample galaxy have the same angular rotation, resolution, pixel size and pixels per half-light radius.

Now that the basic preparations of the data have been completed, models are generated for each of the galaxies in the sample at all 5 wavelengths.

2.6 A 3D TRIPLEX Model of Dust in Galaxies

If a galaxy is not exactly edge-on, issues arise when attempting to measure the z-directional distribution of dust. Consider a galaxy inclined a few degrees towards the observer; when we observe directly along the line of sight we begin to detect the rear side of the disk as it rises with increasing inclination. This can be problematic when searching for extraplanar dust, as the dust within the disk can appear above or below the plane relative to our line of sight.

As an example of this, Verstappen et al. (2013) mathematically predict at which point the thin disk will appear as vertical structure along the line of sight. The apparent height of dust above the plane, β_d^{app}, is related to the radial length of the galaxy, α_d and the inclination, i by the following;

$$\beta_d^{app} = 1.8137\ \alpha_d\ cos\ i. \tag{2.4}$$

If we assume, for example, that $\alpha_d/\beta_d \approx 12$, where β_d is the actual scale height of the galaxy (although this value varies from galaxy to galaxy, see Mosenkov et al. 2018), we find that $\beta_d^{app} \approx 0.083\alpha_d$. In this case, β_d is greater than β_d^{app} when $\beta_d^{app} = 1.8137\alpha_d\ cos\ i \leq 0.038\alpha_d$, or $cos\ i \leq 0.046$, or $\mathbf{i \geq 87.4}°$.

From this example, a galaxy with an axial ratio of 12 will begin to exhibit observational signatures of extraplanar dust at an inclination lower than 87.4°, despite the origin of the dust being planar. This angle is dependent on the ratio of the z and radial scale lengths. This highlights the need for well-modelled disks when considering geometries that are not exactly edge-on, to counteract the line-of-sight effects.

Here I introduce a full rotatable 3-dimensional model based on the TRIPLEX function (Disney et al., 1989; Davies et al., 1997) (see Section 1.3.1.2), which describes the distribution of dust in x, y and z-directions ($n_d(x,y,z)$) as

$$n_d(x,y,z) = n_d(0)\ exp\left[-\frac{\sqrt{x^2+y^2}}{\alpha_d} + \frac{z}{\beta_d}\right], \tag{2.5}$$

where α_d is the radial scale length of dust and β_d is the z-directional scale height of dust. The aim is to build a model for each of the galaxies in the sample

(at the 5 *Herschel* wavelengths) from the TRIPLEX function. To do this, there are certain parameters which must be known about the galaxies prior to generating the models. Firstly, we must be able to model the inclination of the real galaxy so that the line-of-sight effects can be properly accounted for. Secondly, we require an estimate of β_d as an initial parameter for the model to be generated upon. The inclination of each sample galaxy has already been measured via the ellipse fitting procedure, hence this parameter is constrained. To measure β_d, the same ellipse fitting method is implemented out to a SNR of 2, as described in Section 2.3.1, to measure the scale height for each of the (pre-convolved & re-gridded) galaxy maps. The value of β_d obtained for each galaxy can be seen in Table 2.3. A value for the dust scale length (α_d) is also obtained during the ellipse fitting procedure, which provides a further geometric constraint that is used when building the models.

Now that the inclination, β_d and α_d for all galaxies are known, the next step is to generate the models. The TRIPLEX function (Eq. 2.5) is defined in *Python*, from which the probability density of dust particles existing at any co-ordinate in the x, y or z-directions is found. This is done using the `Seaborn` package. Figure 2.5 shows the probability density function for the dust distribution at a particular radius from the centre of the disk. I calculate this probability for x, y and z.

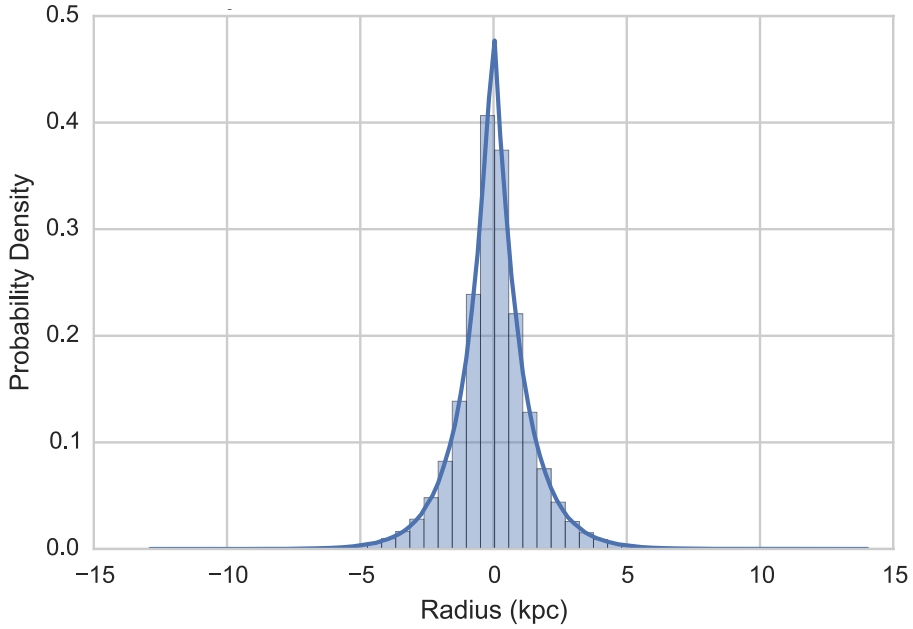

Figure 2.5: The probability density of the TRIPLEX model for the dust distribution in radial direction, i.e. the likelihood of finding dust particles at a particular radius from the centre of the disk.

The estimated values of β_d and α_d are implemented to specify the geometry of

the output model, i.e. how far should the dust extend in the z and radial directions, which can later be scaled to match the physical co-ordinates of the real galaxy. This ensures that the geometry of the modelled disk is as close to the real galaxy as possible for comparison. The model is generated by randomly sampling 1 million points each from the x, y and z dimensional probability densities, out to a distance limited by α_d and β_d. This results in 3 million dust 'particles' each represented by a point in 3D space. Together, these points represent the distribution of dust through a plane as defined by the TRIPLEX model. An example of the 3D view can be seen in Figure 2.6 and it's column density in the vertical direction is presented in Figure 2.7.

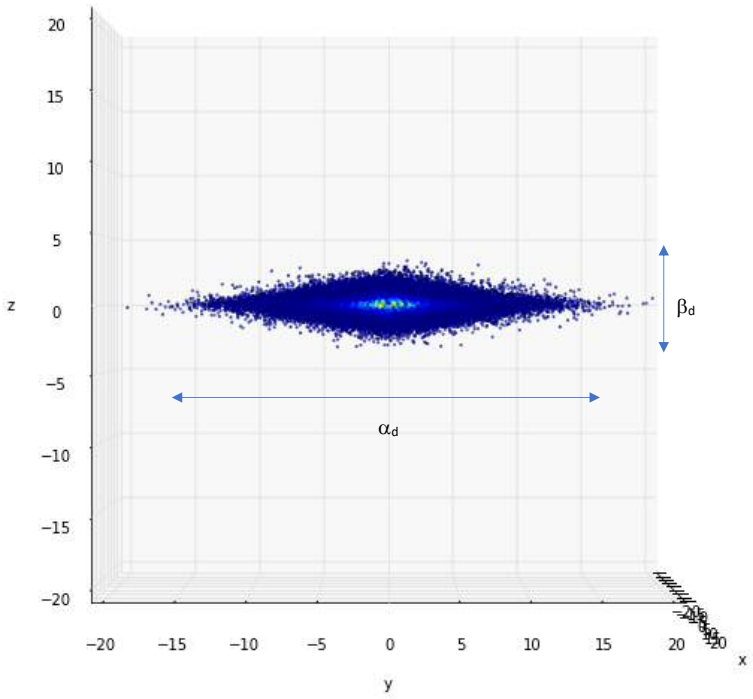

Figure 2.6: A 3D projection of the TRIPLEX model used throughout this study for an example axial ratio $\alpha_d/\beta_d = 6$, as viewed at an inclination angle of 90° (3 million data points) with arbitrary units. β_d and α_d are labelled in the diagram.

Once the points have been generated for each galaxy, the model is inclined by the same angle as the real galaxies by altering the plane on which the model is generated. At this stage I can then flatten the 3D model to a 2D plane.

An array of random noise is generated with the same median values (in Jy) as the real maps for each galaxy at each wavelength, and the 2D model is superimposed onto this array to simulate the real *Herschel* data. The model is then output to a `.fits` file with the same arsecond per pixel scale as that of the original data.

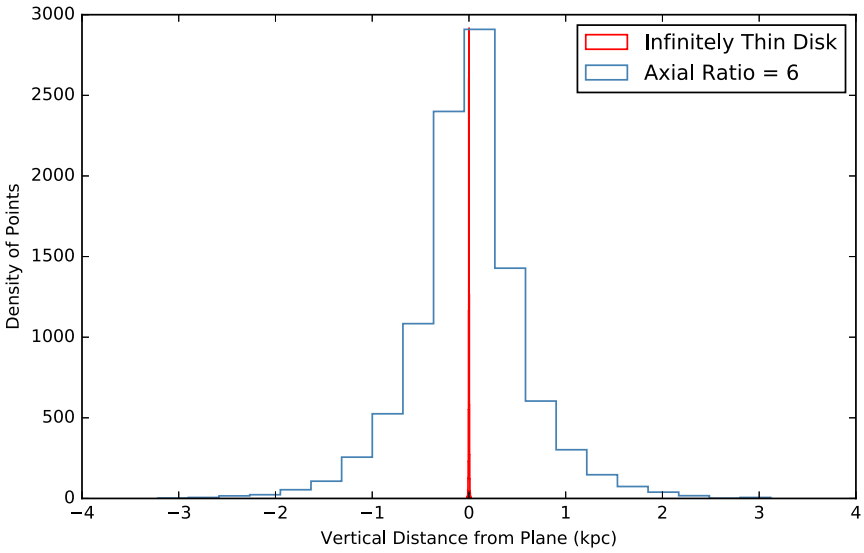

Figure 2.7: A 2D projection of the TRIPLEX model column density at y=0 for an example axial ratio $\alpha_d/\beta_d = 6$ in blue, and for an infinitely thin disk in red, as viewed at an inclination angle of 90°.

To simulate the effect of the instrument PSF, each model is convolved to match the corresponding wavelength PSF as per Section 2.5.

At this stage I have generated a series of models that match the pre-processed data in terms of inclination, β_d, α_d, and background noise. To be able to compare the models against the processed data, all models are re-convolved to match the resolution of the 500 μm beam using the convolution kernels and IDL script `convolve_image.pro` provided by Aniano et al. (2011), and the maps are resampled so the pixel scales are equal (via the same method as in Section 2.5). There now exists a set models that were produced to match the original, high-resolution data, but convolved to the worst resolution and with the same arcseconds-per-pixel as the processed data.

2.7 Individual Brightness Profiles

In this section, the processed galaxy data is compared with the generated models at each wavelength by plotting their brightness profiles in the z-direction. This allows us to characterise how well the exponential TRIPLEX model matches the real galaxies and whether the initial measurements for the value of β_d are accurate. The minimum value of β_d above which dust emission can be considered resolved is found by convolving the 500 μm PSF with an infinitely thin disk for comparison against the data.

2.7.1 A Convolved, Infinitely Thin Disk

Edge-on galaxy disks are typically thin and may be unresolved in observations if the instrument resolution is not smaller than the angular scale height of the disk. If the disk is unresolved, the detected emission can not be considered "real", but is instead due to a smearing effect of the instrument's PSF. To combat this issue, I compare the observations against an infinitely thin disk convolved with the longest wavelength (500 μm) beam. This provides a lower limit for the scale height, above which dust emission is considered to be real and not an effect of the PSF.

An infinitely thin disk is modelled using the TRIPLEX function assuming β_d = 0 which is then projected onto a 2D plane. An array is generated and filled with random noise equivalent to that of the *Herschel* maps, and the infinitely thin disk is superimposed in the centre. This array is then convolved with the 500 μm PSF to create a profile of the minimum height above which we can confidently detect resolved dust emission from the galaxies. I measure a value of β_d for the convolved thin disk (measured at an equivalent distance to each sample galaxy) by fitting an ellipse to the data and measuring the semi-minor axis of the ellipse at SNR = 2.

The measured values of β_d for the infinitely thin disk and real galaxies (at the 5 *Herschel* wavelengths) can be seen in Figure 2.8, and are listed in Table 2.3.

From Figure 2.8 it is apparent that all galaxies except four (IC2233, NGC 1351A, NGC 5023, UGC 07321) exhibit dust scale heights above what is expected from a convolved infinitely thin disk, and therefore detected emission above this limit is real and these galaxies are considered resolved. According to Figure 2.8 and Table 2.3, the galaxies IC2233, NGC 1351A, NGC 5023 and UGC 70321 are not fully resolved in the PACS 100 μm band, hence extended emission at this wavelength is assumed to be influenced by the instrument's PSF.

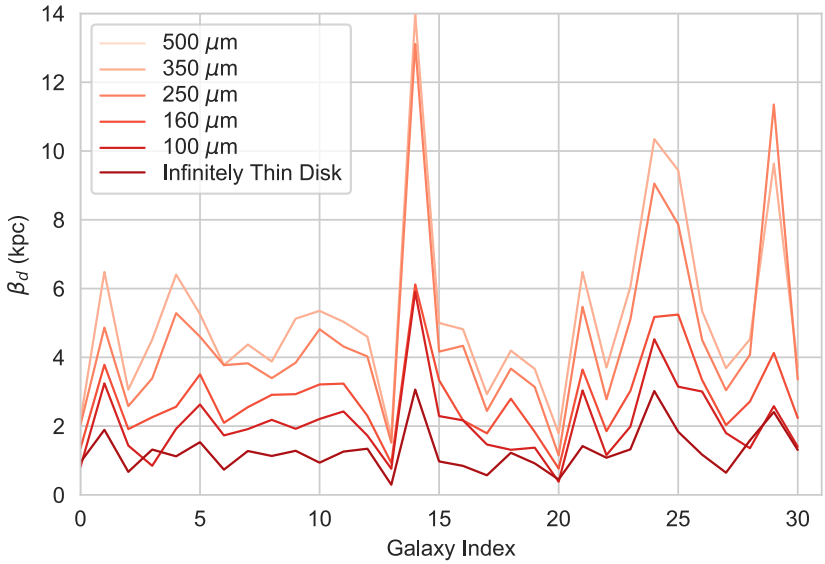

Figure 2.8: Measured values of β_d for each galaxy in the sample at each wavelength. The x-axis corresponds to the index of each galaxy in the sample (i.e. 0 - 30) and the y-axis shows the height of dust measured by the ellipse fitting procedure in kpc.

In Figure 2.8 and Table 2.3 we see an increase in the value of β_d at longer wavelengths. This relationship is presented in Figure 2.9 in which I plot the kernel density estimate of the measured values of β_d at each of the 5 *Herschel* wavelengths.

The increase in scale height at longer wavelengths may be due to a more extended cold dust distribution that is only detected at the longer wavelength bands. Bocchio et al. (2016) undertake a study of NGC 891 and find a similar gradient in the scale height at increasing wavelength. They conclude that the cause of the gradient is either due to the presence of cold dust and a steep temperature gradient, or due to a super thin disk which is unresolved in the observations. The effect of increasing scale height with wavelength is also observed by Verstappen et al. (2013), however they argue that the phenomenon is probably due to the limited and gradually worsening resolution of the *Herschel* images for increasing wavelengths.

2.7.2 Generating the Profiles

For each galaxy and model at the 5 *Herschel* wavelengths, I sum the value of all pixels along the major axis out to the half-light radius of the galaxy (a total of 26 pixels). This provides an integrated value of the flux along the plane for both the galaxy and model. This same process is carried out for each row of pixels

Galaxy	Index	β_d (kpc)						
		100 μm	160 μm	250 μm	350 μm	500 μm	3.4 μm	Thin Disk
IC2233	1	0.81	1.36	2.04	2.17	1.63	0.07	0.95
NGC0678	2	3.24	3.78	4.86	6.49	6.49	2.97	1.89
NGC0891	3	1.43	1.91	2.58	3.06	4.02	1.67	0.67
NGC1351A	4	0.85	2.26	3.39	4.52	4.52	0.56	1.32
NGC3079	5	1.92	2.56	5.29	6.41	7.69	2.08	1.12
NGC3501	6	2.63	3.50	4.60	5.26	5.26	1.42	1.53
NGC3628	7	1.73	2.10	3.77	3.77	5.03	2.52	0.73
NGC4013	8	1.91	2.55	3.83	4.37	6.56	3.19	1.28
NGC4183	9	2.18	2.91	3.39	3.88	4.85	0.40	1.13
NGC4206	10	1.92	2.93	3.84	5.13	5.49	1.28	1.28
NGC4216	11	2.21	3.21	4.82	5.35	5.62	3.28	0.94
NGC4217	12	2.43	3.24	4.31	5.03	6.47	1.53	1.26
NGC4222	13	1.73	2.30	4.03	4.60	5.75	1.00	1.34
NGC4244	14	0.76	0.93	1.52	1.69	2.02	0.36	0.3 0
NGC4289	15	5.90	6.12	13.11	13.99	13.11	2.84	3.06
NGC4302	16	2.29	3.33	4.17	5.00	5.00	1.74	0.97
NGC4402	17	2.17	2.17	4.34	4.82	6.50	1.08	0.84
NGC4437	18	1.46	1.79	2.44	2.93	3.42	0.57	0.57
NGC4445	19	1.31	2.80	3.67	4.20	4.20	0.61	1.22
NGC4758	20	1.37	1.83	3.14	3.66	4.71	0.39	0.92
NGC5023	21	0.38	0.77	1.15	1.79	1.53	0.03	0.45
NGC5301	22	3.04	3.65	5.47	6.48	7.29	1.11	1.42
NGC5348	23	1.16	1.85	2.78	3.70	3.70	0.08	1.08
NGC5356	24	1.99	3.03	5.11	6.05	5.67	1.80	1.32
NGC5529	25	4.53	5.17	9.05	10.35	12.93	3.23	3.02
NGC5746	26	3.15	5.24	7.87	9.44	12.58	4.19	1.84
NGC5907	27	3.01	3.34	4.51	5.34	6.01	2.84	1.17
NGC7090	28	1.80	2.03	3.04	3.69	4.43	0.28	0.65
UGC07321	29	1.36	2.71	4.07	4.52	5.43	0.11	1.58
UGC07522	30	2.58	4.13	11.35	9.63	12.38	2.24	2.41
UGC07982	31	1.40	2.24	3.36	3.73	4.48	0.37	1.31

Table 2.3: Galaxy names, indices and β_d measured for each galaxy in the sample at all 5 wavelengths, the stellar disk at W1 3.4 μm, and for an infinitely thin disk convolved with the 500 μm beam.

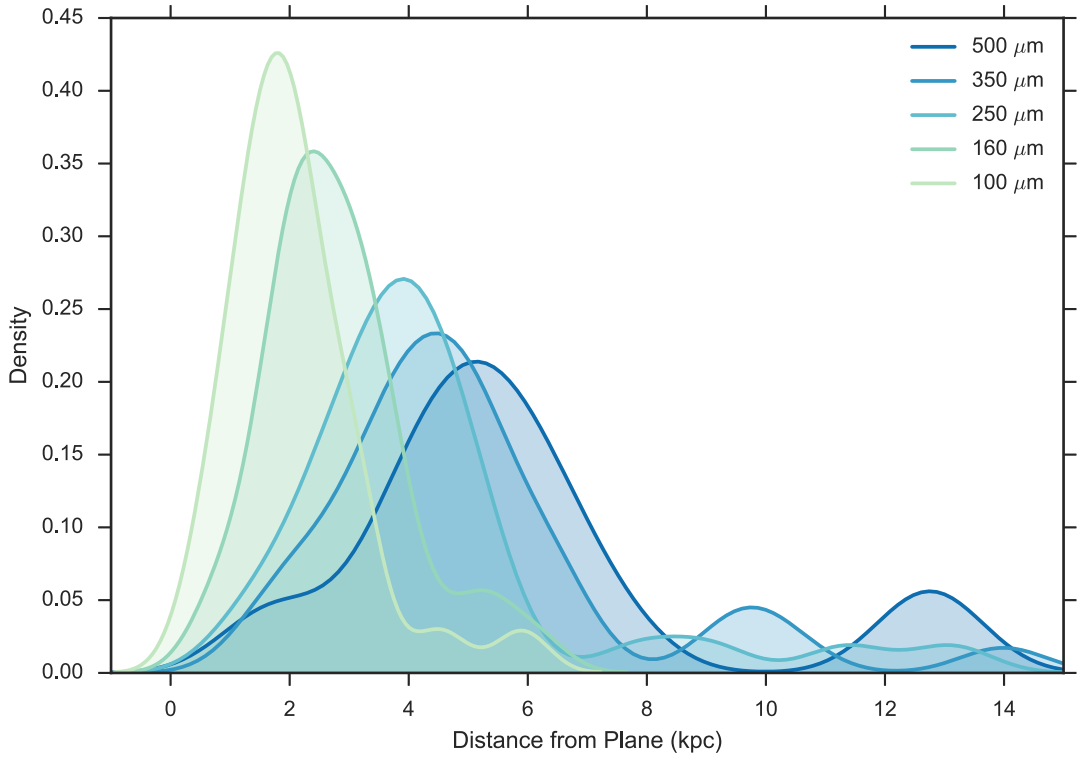

Figure 2.9: Kernel density estimation of the measured β_d for the 5 *Herschel* bands.

above and below the plane out to an arbitrary distance of 20 pixels (equating to a mean distance of 13.46 kpc). These values are then summed and plotted against distance from the plane, resulting in brightness profiles for each galaxy and matching model at each wavelength, as can be seen in Figures 2.10 through 2.14. An exponential curve is fitted to the model and galaxy profiles individually using the *Scipy.curve_fit* routine in Python.

The brightness profiles of the infinitely thin disk convolved with the 500 μm beam are also plotted for comparison, however for the purposes of comparing the true profile of an infinitely thin disk, I rotate the thin disks prior to analysis to match the inclination of the real galaxies. This ensures that the galaxy flux is compared against the minimum dust height at which an inclined, thin disk could exhibit. For reference here I present only one of the sample galaxies at all 5 wavelengths from 100 to 500 μm. The full set of brightness profiles can be seen in Appendix A.

2.7.2.1 Uncertainty Estimation

Uncertainties are assumed to arise from two main sources; the instrumental noise (σ_{instr}, quantified in the error maps) and sky noise. The instrumental noise is calculated by adding in quadrature the flux of the error map pixels within an aperture corresponding to the same measured region of the galaxy map, i.e. a row of 26 pixels equal to the half-light radius of the galaxy. The sky noise, σ_{sky} is calculated using the following formula (Hughes et al., 2014);

$$\sigma_{sky}^2 = N_{ap}\sigma_{skypix}^2 + N_{ap}^2\sigma_{skymean}^2 \tag{2.6}$$

where N_{ap} is the number of pixels in the aperture, σ_{skypix} is the rms of fluxes in the chosen aperture and $\sigma_{skymean}$ is the mean background standard deviation (output by the `photutils` package as described in Section 2.5. We therefore calculate the total uncertainty as $\sigma_{tot} = \sqrt{\sigma_{sky}^2 + \sigma_{instr}^2}$. As we are not comparing the fluxes at different wavelengths here, calibration errors are not accounted for. They are however included in the total uncertainties calculated in Chapter 3.

The confusion noise is also considered, particularly for the longest wavelength 500 μm band. The confusion noise is defined as the stochastic fluctuations of the background sky brightness, below which sources cannot be detected individually. Hence increasing the integration time of an observation will not yield an increase in sensitivity. At 500 μm, the confusion limit is estimated to be 6.8 mJy (Nguyen et al., 2010). For the sample galaxies, the estimated errors are at least an order of magnitude greater than the confusion limit, hence we find its effects to be negligible.

2.7.2.2 Profiles

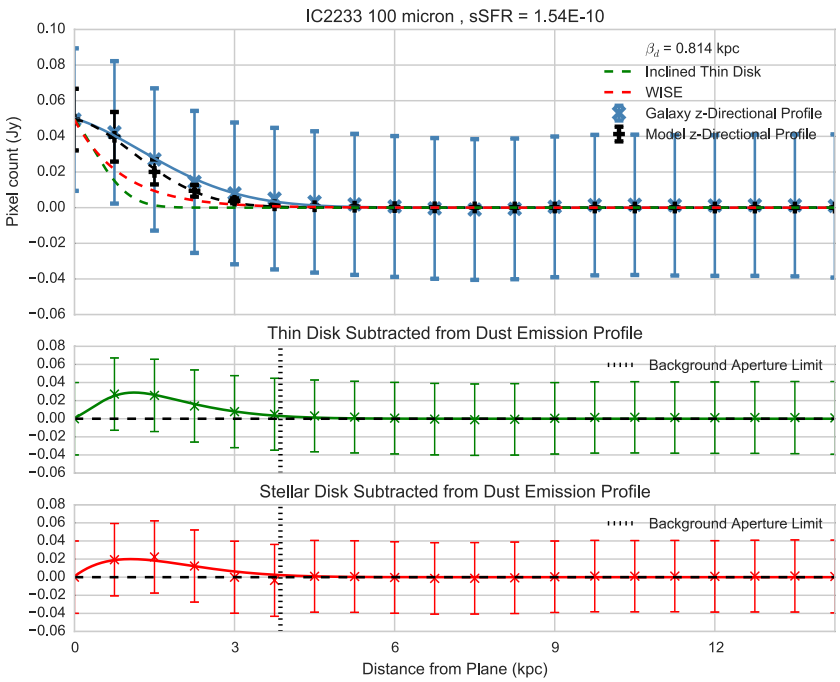

Figure 2.10: Vertical profile of the galaxy IC 2233 at 100 μm in blue, and model profile for comparison in black. An exponential curve has been fitted to each profile. Red and green dashed lines represent the brightness profiles of the stellar and inclined thin disks respectively. The x-axis shows the distance of each pixel row from the central plane of the galaxy. The y-axis represents the summed pixel value for each row of pixels above the plane in Jy. The profiles have been normalised to match at the peak. Lower: We subtract the inclined thin disk and stellar disk profiles from the galaxy profile to see the difference in detected emission.

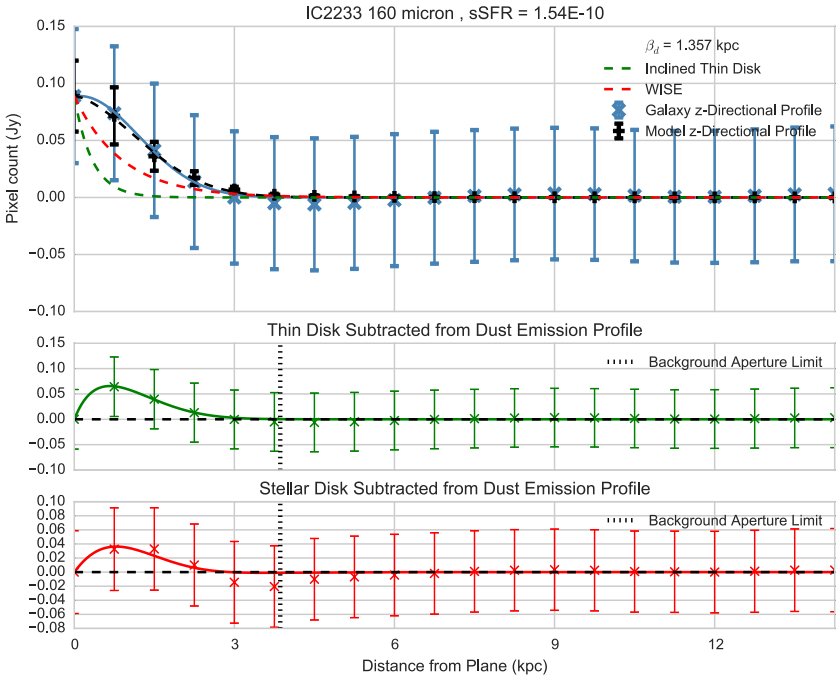

Figure 2.11: Vertical profile of the galaxy IC 2233 at 160 μm. See Figure 2.10 for full description.

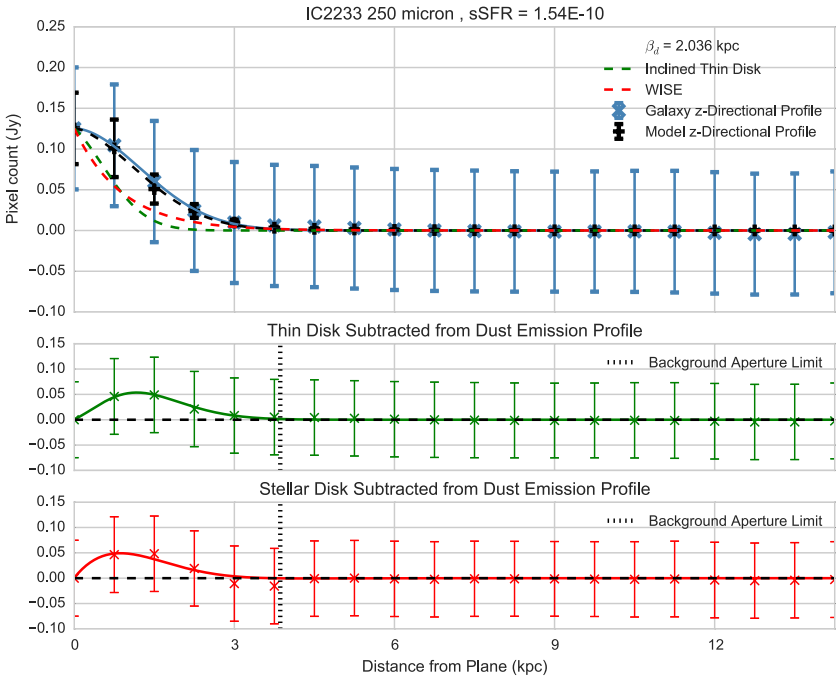

Figure 2.12: Vertical profile of the galaxy IC 2233 at 250 μm. See Figure 2.10 for full description.

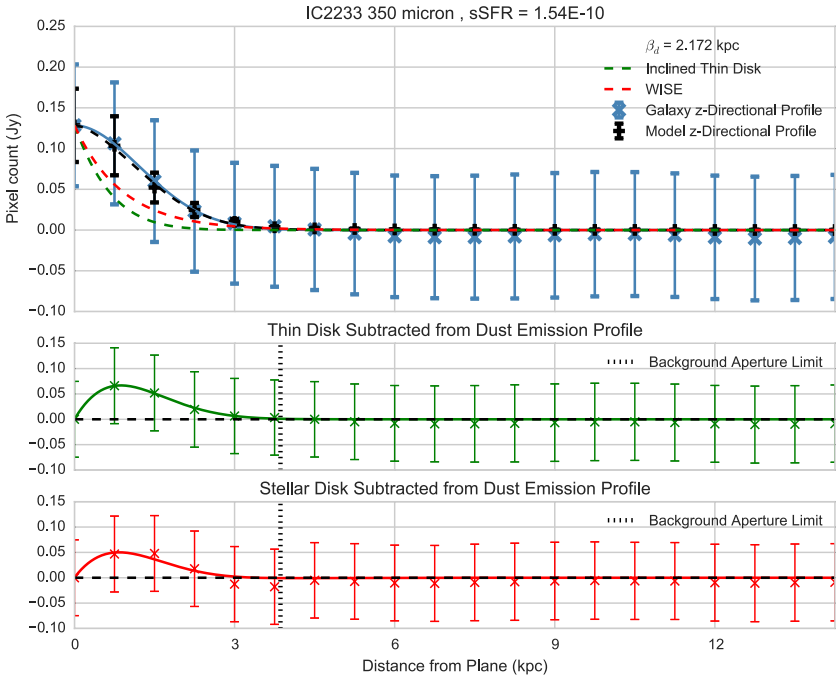

Figure 2.13: Vertical profile of the galaxy IC 2233 at 350 μm. See Figure 2.10 for full description.

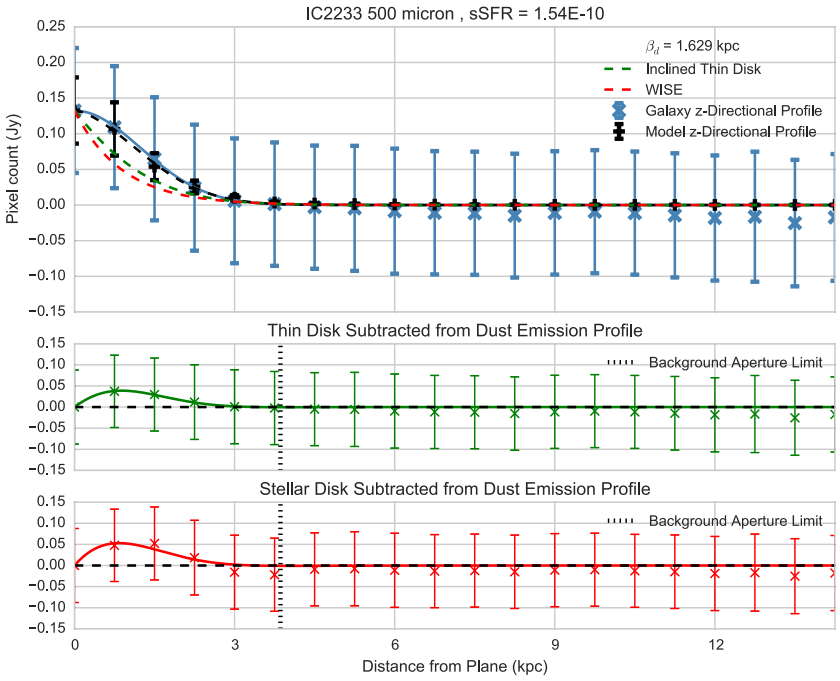

Figure 2.14: Vertical profile of the galaxy IC 2233 at 500 μm. See Figure 2.10 for full description.

The brightness profiles provide a more accurate determination of the values of β_d and β_s than were estimated via the ellipse fitting method. Results of the profile analysis for each galaxy in comparison to their original estimated values for β_d are presented in Section 2.8.

2.8 Results

2.8.1 Individual Galaxies

Maps are available for each galaxy at the 5 *Herschel* wavelengths in Appendix A that show grid lines with an equivalent scale of 2 kpc, and include a scale bar that corresponds to the estimated values for β_d from the ellipse fitting procedure. Appendix A also includes the brightness profiles for each individual galaxy. Here, we discuss the results of the brightness profile fitting briefly for each galaxy and show images of each source at the optical DSS B-band and at the SPIRE 500 μm band for comparison.

2.8.1.1 IC 2233

As presented in Table 2.3, IC2233 does not show evidence of extraplanar dust above the convolved thin disk, hence we consider observations of this galaxy to be unresolved.

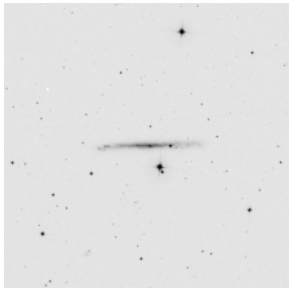

Figure 2.15: DSS B-Band

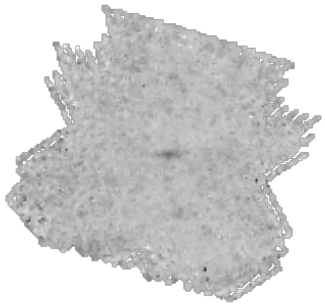

Figure 2.16: SPIRE 500 μm

Results of the brightness profile fitting (see Section A.1) show that any excess in emission above both the stellar disk is within the errors and cannot be considered extraplanar.

2.8.1.2 NGC 678

In Table 2.3, NGC 678 shows evidence of an extended dust distribution above the convolved thin disk and stellar disk, therefore we consider this source to be resolved and a possible source of extraplanar dust. The dust scale height measured at 100 μm is 3.24 kpc, versus 2.97 kpc for the stellar disk.

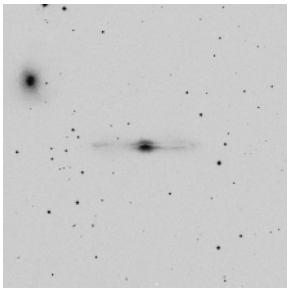

Figure 2.17: DSS B-Band

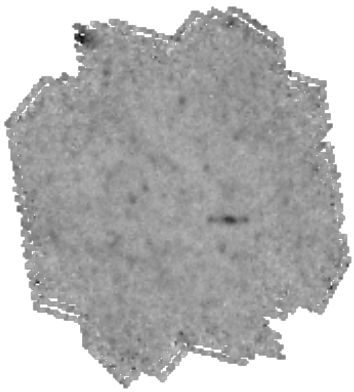

Figure 2.18: SPIRE 500 μm

From the brightness profile fitting (see Section A.2), excess dust emission above the stellar disk is within the errors, and therefore we conclude that there is not a significant extraplanar dust component.

2.8.1.3 NGC 891

Ellipse fitting results at 100 μm show the dust scale height to be 1.43 kpc, consistent with Bocchio et al. (2016). The measured scale height is greater than that of the infinitely thin disk (0.67 kpc) hence we consider the source resolved in the observations. However, the stellar disk is found to extend further out to 1.67 kpc. The dust disk appears to be more extended than the stars at the longer wavelengths of 160μm and above.

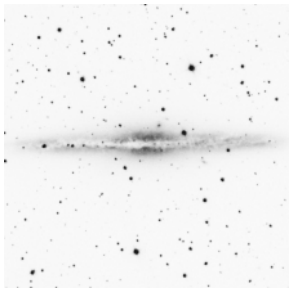

Figure 2.19: DSS B-Band

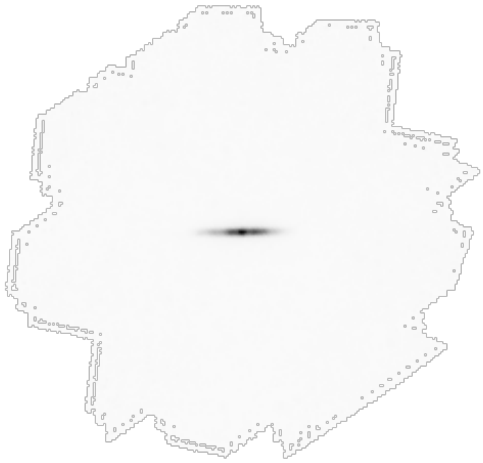

Figure 2.20: SPIRE 500 μm

From the brightness profile fitting (Section A.3), the excess dust emission above the stellar disk is within the errors at all wavelengths, therefore we do not conclude that NGC 891 has a considerable extraplanar dust component above the noise.

2.8.1.4 NGC 1351A

As presented in Table 2.3, NGC 1351A does not show evidence of extraplanar dust above the convolved thin disk, hence we consider observations of this galaxy to be unresolved.

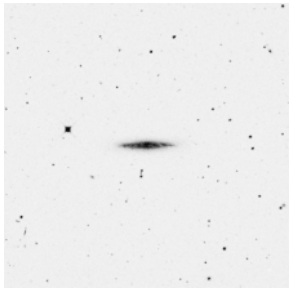

Figure 2.21: DSS B-Band

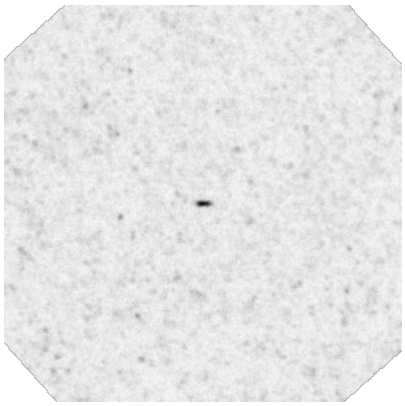

Figure 2.22: SPIRE 500 μm

From the brightness profile fitting (Figure A.4), the excess dust emission above the stellar disk is within the errors.

2.8.1.5 NGC 3079

From the ellipse fitting procedure, the measured scale height of dust at 100 μm exceeds the thin disk, hence we consider the observations to be resolved. The scale height of the dust disk at 1.92 kpc is less than that of the stellar disk at 2.08 kpc, however we begin to see evidence of extraplanar dust at wavelengths of 160 μm and above.

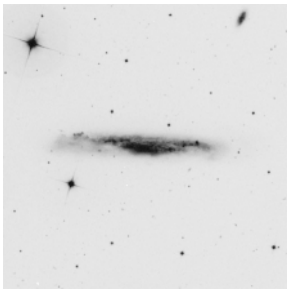

Figure 2.23: DSS B-Band

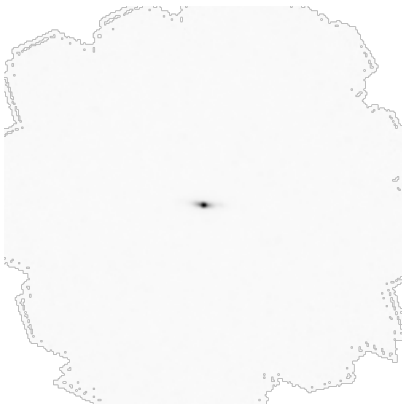

Figure 2.24: SPIRE 500 μm

From the brightness profiles of NGC 3079 (see Section A.5), we see an excess in the dust emission above the stellar disk out to a maximum distance of 1 kpc at all 5 of the *Herschel* wavelengths.

2.8.1.6 NGC 3501

The ellipse fitting-measured scale height of dust at 100 μm exceeds the thin disk, hence we consider the observations to be resolved. The scale height of the dust disk at 2.63 kpc is greater than that of the stellar disk at 1.42 kpc, hence this galaxy exhibits evidence for extraplanar dust even at the shortest wavelength of 100 μm.

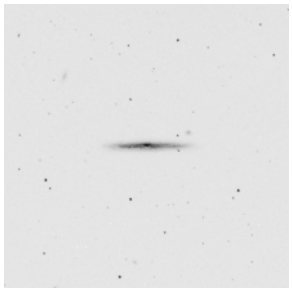

Figure 2.25: DSS B-Band

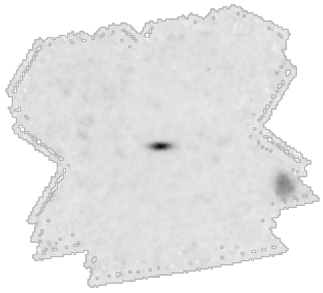

Figure 2.26: SPIRE 500 μm

From the brightness profiles of NGC 3501 (see Section A.6), we see an excess in the dust emission above the stellar disk out to a maximum distance of 2 kpc at the 160-500 μm bands.

2.8.1.7 NGC 3628

The measured scale height of dust at 100 μm exceeds the thin disk from the ellipse fitting method, hence we consider the observations to be resolved. The scale height of the dust disk at 1.73 kpc is less than that of the stellar disk at 2.52 kpc, however we begin to see evidence of extraplanar dust at wavelengths of 250 μm and above.

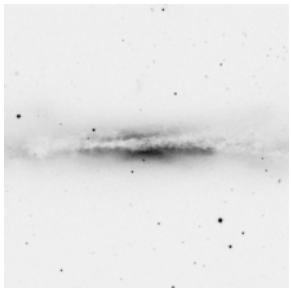

Figure 2.27: DSS B-Band

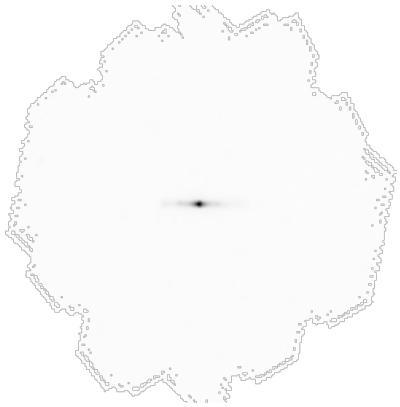

Figure 2.28: SPIRE 500 μm

From the brightness profile fitting (Figure A.7), the excess dust emission above the stellar disk is within the errors and therefore we cannot conclude that the galaxy has a significant extraplanar dust component.

2.8.1.8 NGC 4013

The measured scale height of dust from the ellipse fitting at 100 μm exceeds the thin disk, hence we consider the observations to be resolved. The scale height of the dust disk at 1.91 kpc is less than that of the stellar disk at 3.19 kpc, however we begin to see evidence of extraplanar dust at wavelengths of 250 μm and above.

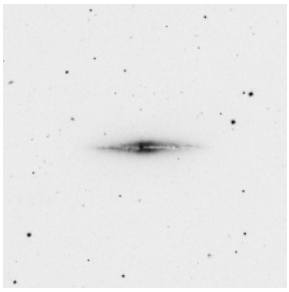

Figure 2.29: DSS B-Band

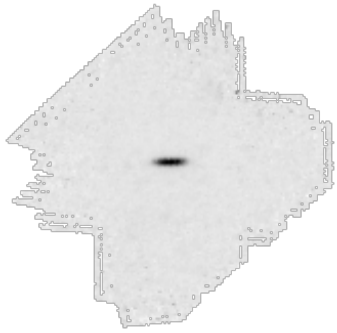

Figure 2.30: SPIRE 500 μm

From the brightness profiles of NGC 4013 (see Section A.8), we see an excess in the dust emission above the stellar disk out to a maximum distance of 2 kpc at the SPIRE 250-500 μm bands.

2.8.1.9 NGC 4183

The measured scale height of dust from the ellipse fitting at 100 μm exceeds the thin disk, hence we consider the observations to be resolved. The scale height of the dust disk at 2.18 kpc is greater than that of the stellar disk at 0.40 kpc, hence this galaxy exhibits evidence for extraplanar dust even at the shortest wavelength of 100 μm.

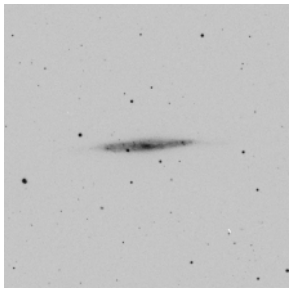

Figure 2.31: DSS B-Band

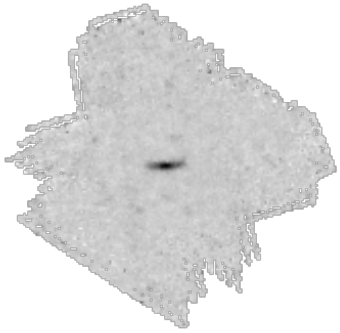

Figure 2.32: SPIRE 500 μm

From the brightness profile fitting (Figure A.9), the excess dust emission above the stellar disk is within the errors.

2.8.1.10 NGC 4206

The measured scale height of dust from the ellipse fitting at 100 μm exceeds the thin disk, hence we consider the observations to be resolved. The scale height of the dust disk at 1.92 kpc is greater than that of the stellar disk at 1.28 kpc, hence this galaxy exhibits evidence for extraplanar dust even at the shortest wavelength of 100 μm.

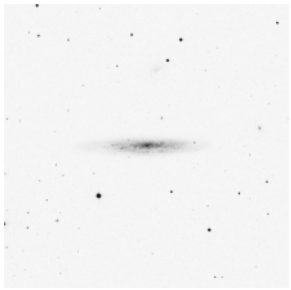

Figure 2.33: DSS B-Band

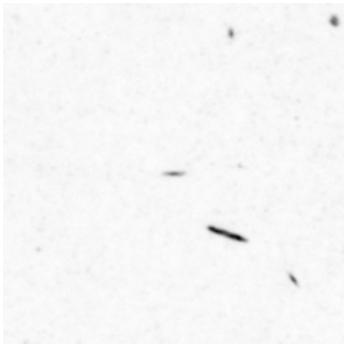

Figure 2.34: SPIRE 500 μm

In the resulting brightness profiles for NGC 4206 (see Section A.10), there appears to be an artefact or a miscalculation of the stellar disk profile. Because of this, we cannot make an accurate conclusion regarding the extent of any dust emission above the stellar disk.

2.8.1.11 NGC 4216

The measured scale height of dust from the ellipse fitting at 100 μm exceeds the thin disk, hence we consider the observations to be resolved. The scale height of the dust disk at 2.21 kpc is less than that of the stellar disk at 3.28 kpc, however we begin to see evidence of extraplanar dust at wavelengths of 250 μm and above.

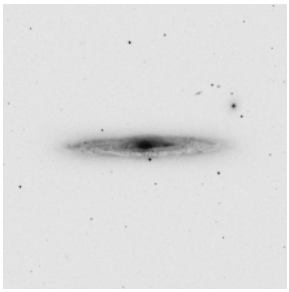

Figure 2.35: DSS B-Band

Figure 2.36: SPIRE 500 μm

From the brightness profile fitting (Section A.11), the excess dust emission above the stellar disk is within the errors.

2.8.1.12 NGC 4217

The measured scale height of dust from the ellipse fitting at 100 μm exceeds the thin disk, hence we consider the observations to be resolved. The scale height of the dust disk at 2.43 kpc is greater than that of the stellar disk at 1.53 kpc, hence this galaxy exhibits evidence for extraplanar dust even at the shortest wavelength of 100 μm.

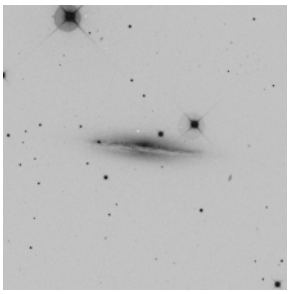

Figure 2.37: DSS B-Band

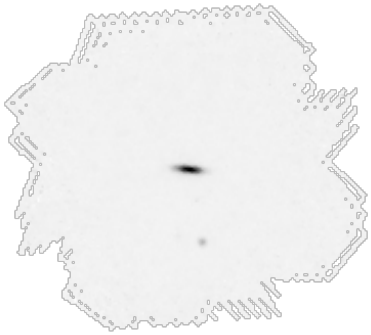

Figure 2.38: SPIRE 500 μm

From the brightness profiles of NGC 4217 (see Section A.12), we see an excess in the dust emission above the stellar disk out to a maximum distance of 2 kpc at all *Herschel* bands.

2.8.1.13 NGC 4222

The measured scale height of dust from the ellipse fitting at 100 μm exceeds the thin disk, hence we consider the observations to be resolved. The scale height of the dust disk at 1.73 kpc is greater than that of the stellar disk at 1.00 kpc, hence this galaxy exhibits evidence for extraplanar dust even at the shortest wavelength of 100 μm.

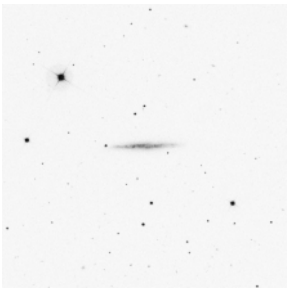

Figure 2.39: DSS B-Band

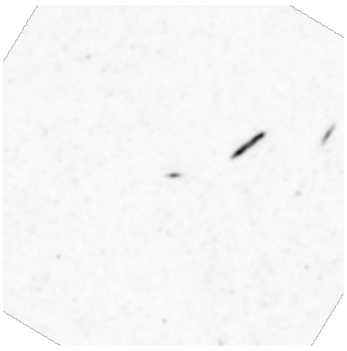

Figure 2.40: SPIRE 500 μm

From the brightness profiles of NGC 4222 (see Section A.13), we see an excess in the dust emission above the stellar disk out to a maximum distance of 4 kpc at the 250-500 μm bands.

2.8.1.14 NGC 4244

The measured scale height of dust from the ellipse fitting at 100 μm exceeds the thin disk, hence we consider the observations to be resolved. The scale height of the dust disk at 0.76 kpc is greater than that of the stellar disk at 0.36 kpc, hence this galaxy exhibits evidence for extraplanar dust even at the shortest wavelength of 100 μm.

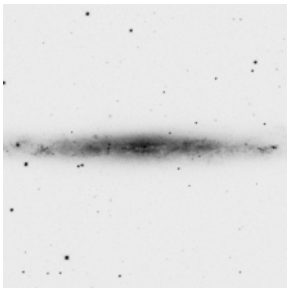

Figure 2.41: DSS B-Band

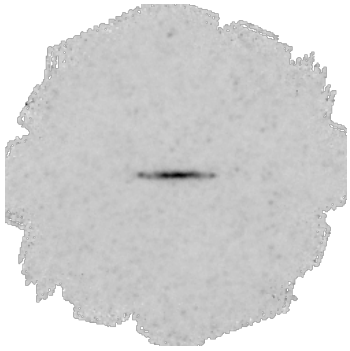

Figure 2.42: SPIRE 500 μm

It is difficult to draw conclusions from the brightness profiles of NGC 4244 (see Section A.14) due to the negative bowls exhibited in the WISE maps, hence I do not consider this galaxy to exhibit evidence for any extraplanar dust component.

2.8.1.15 NGC 4289

The measured scale height of dust from the ellipse fitting at 100 μm exceeds the thin disk, hence we consider the observations to be resolved. The scale height of the dust disk at 5.90 kpc is greater than that of the stellar disk at 2.84 kpc, hence this galaxy exhibits evidence for extraplanar dust even at the shortest wavelength of 100 μm.

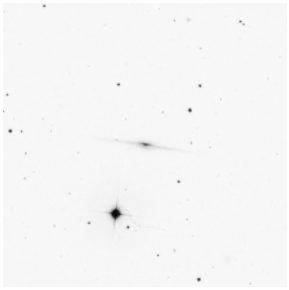

Figure 2.43: DSS B-Band

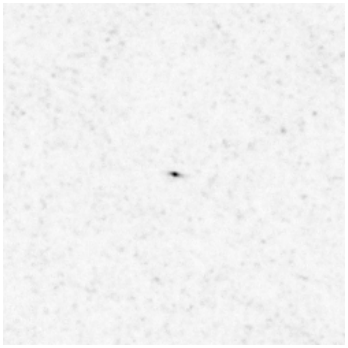

Figure 2.44: SPIRE 500 μm

From the brightness profiles of NGC 4289 (see Section A.15), we see an excess in the dust emission above the stellar disk out to a maximum distance of 4 kpc at the 250-500 μm bands.

2.8.1.16 NGC 4302

The measured scale height of dust from the ellipse fitting at 100 μm exceeds the thin disk, hence we consider the observations to be resolved. The scale height of

the dust disk at 2.29 kpc is greater than that of the stellar disk at 1.74 kpc, hence this galaxy exhibits evidence for extraplanar dust even at the shortest wavelength of 100 μm. It is apparent that there is another bright source within close proximity to the galaxy which may contribute to the dust emission above the plane. This is seen in the brightness profiles as a bump in the dust emission profile between 7-12 kpc (see Figures A.151 to A.155).

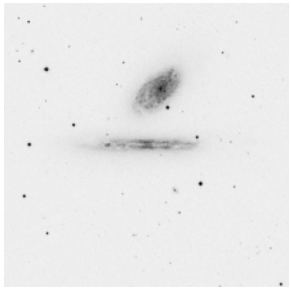

Figure 2.45: DSS B-Band

Figure 2.46: SPIRE 500 μm

From the brightness profile fitting (Figure A.16), the excess dust emission above the stellar disk is within the errors hence we do not consider the galaxy to have an extraplanar dust component from these observations.

2.8.1.17 NGC 4402

The measured scale height of dust from the ellipse fitting at 100 μm exceeds the thin disk, hence we consider the observations to be resolved. The scale height of the dust disk at 2.17 kpc is greater than that of the stellar disk at 1.08 kpc, hence this galaxy exhibits evidence for extraplanar dust even at the shortest wavelength of 100 μm.

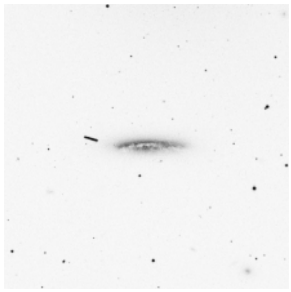

Figure 2.47: DSS B-Band

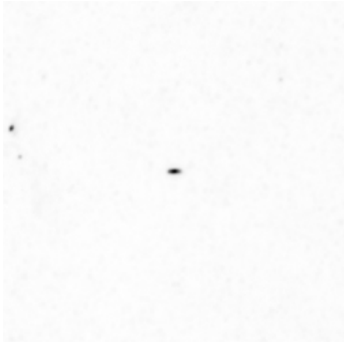

Figure 2.48: SPIRE 500 μm

From the brightness profiles of NGC 4402 (see Section A.17), we see an excess in the dust emission above the stellar disk out to a maximum distance of 1 kpc at the 160-500 μm bands.

2.8.1.18 NGC 4437

The measured scale height of dust from the ellipse fitting at 100 μm exceeds the thin disk, hence we consider the observations to be resolved. The scale height of the dust disk at 1.46 kpc is greater than that of the stellar disk at 0.57 kpc, hence this galaxy exhibits evidence for extraplanar dust even at the shortest wavelength of 100 μm.

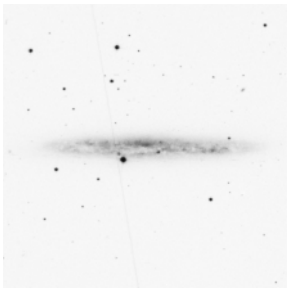

Figure 2.49: DSS B-Band

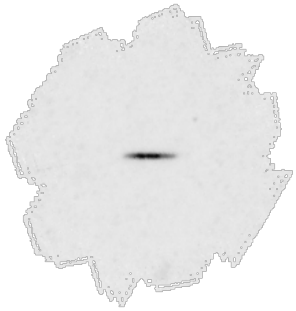

Figure 2.50: SPIRE 500 μm

It is difficult to draw conclusions from the brightness profiles of NGC 4437 (see Section A.18) due to the negative bowls exhibited in the WISE maps, hence I do not consider this galaxy to exhibit evidence for any extraplanar dust component.

2.8.1.19 NGC 4445

The measured scale height of dust from the ellipse fitting at 100 μm exceeds the thin disk, hence we consider the observations to be resolved. The scale height of the dust disk at 1.31 kpc is greater than that of the stellar disk at 0.61 kpc, hence this galaxy exhibits evidence for extraplanar dust even at the shortest wavelength of 100 μm.

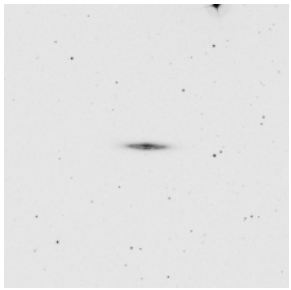

Figure 2.51: DSS B-Band

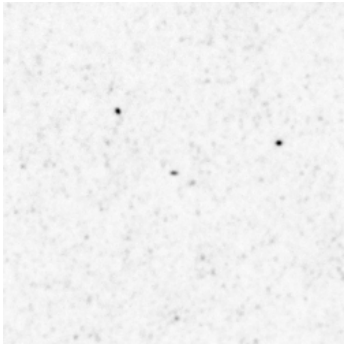

Figure 2.52: SPIRE 500 μm

From the brightness profiles of NGC 4445 (see Section A.19), we see an excess in the dust emission above the stellar disk out to a maximum distance of 1.5 kpc at the 250-500 μm bands.

2.8.1.20 NGC 4758

The measured scale height of dust from the ellipse fitting at 100 μm exceeds the thin disk, hence we consider the observations to be resolved. The scale height of the dust disk at 1.37 kpc is greater than that of the stellar disk at 0.39 kpc, hence this galaxy exhibits evidence for extraplanar dust even at the shortest wavelength of 100 μm.

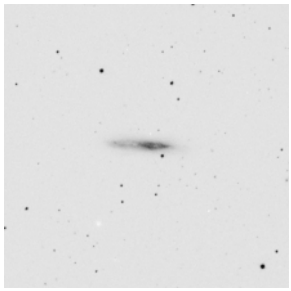

Figure 2.53: DSS B-Band

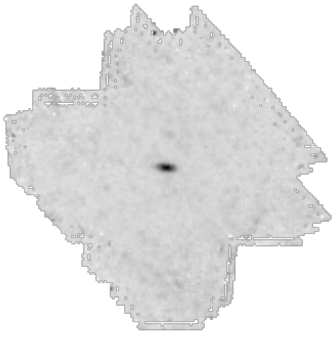

Figure 2.54: SPIRE 500 μm

From the brightness profiles of NGC 4758 (see Section A.20), we see an excess in the dust emission above the stellar disk out to a maximum distance of 1 kpc at the 250-500 μm bands.

2.8.1.21 NGC 5023

As presented in Table 2.3, NGC 5023 does not show evidence of extraplanar dust above the convolved thin disk, hence we consider observations of this galaxy to be unresolved.

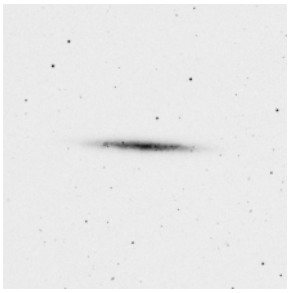

Figure 2.55: DSS B-Band

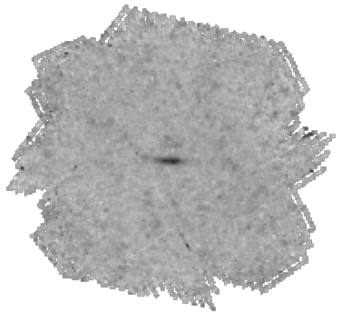

Figure 2.56: SPIRE 500 μm

We do not see an excess of dust emission above the stellar disk for NGC 5023 (see Section A.21), hence we do not consider this galaxy to have an extraplanar dust component.

2.8.1.22 NGC 5301

The measured scale height of dust from the ellipse fitting at 100 μm exceeds the thin disk, hence we consider the observations to be resolved. The scale height of the dust disk at 3.04 kpc is greater than that of the stellar disk at 1.11 kpc, hence this galaxy exhibits evidence for extraplanar dust even at the shortest wavelength of 100 μm.

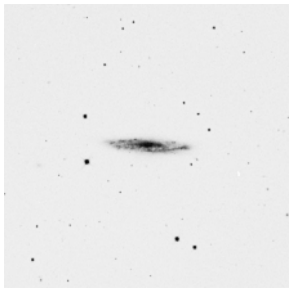

Figure 2.57: DSS B-Band

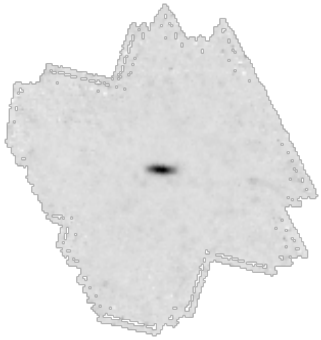

Figure 2.58: SPIRE 500 μm

From the brightness profile fitting (Figure A.22), the excess dust emission above the stellar disk is within the errors hence we do not consider the galaxy to have an extraplanar dust component from these observations.

2.8.1.23 NGC 5348

The measured scale height of dust from the ellipse fitting at 100 μm exceeds the thin disk, hence we consider the observations to be resolved. The scale height of the dust disk at 1.16 kpc is greater than that of the stellar disk at 0.08 kpc, hence this galaxy exhibits evidence for extraplanar dust even at the shortest wavelength of 100 μm.

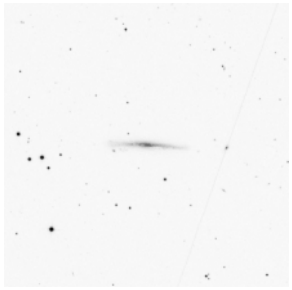

Figure 2.59: DSS B-Band

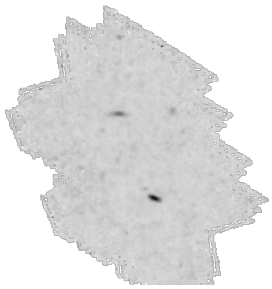

Figure 2.60: SPIRE 500 μm

From the brightness profile fitting (Figure A.23), the excess dust emission above the stellar disk is within the errors hence we do not consider the galaxy to have an extraplanar dust component from these observations.

2.8.1.24 NGC 5356

The measured scale height of dust from the ellipse fitting at 100 μm exceeds the thin disk, hence we consider the observations to be resolved. The scale height of the dust disk at 1.99 kpc is greater than that of the stellar disk at 1.80 kpc, hence this galaxy exhibits evidence for extraplanar dust even at the shortest wavelength of 100 μm.

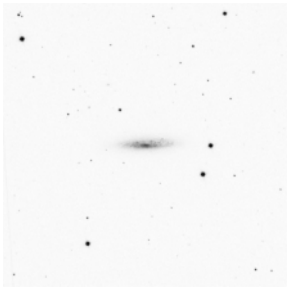

Figure 2.61: DSS B-Band

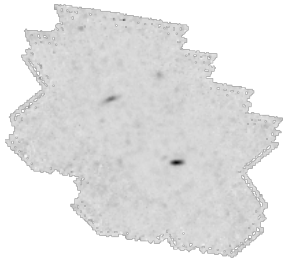

Figure 2.62: SPIRE 500 μm

From the brightness profiles of NGC 4758 (see Section A.20), we see an excess in the dust emission above the stellar disk out to a maximum distance of 1.5 kpc at the 250-500 μm bands.

2.8.1.25 NGC 5529

The measured scale height of dust from the ellipse fitting at 100 μm exceeds the thin disk, hence we consider the observations to be resolved. The scale height of the dust disk at 4.53 kpc is greater than that of the stellar disk at 3.23 kpc, hence this galaxy exhibits evidence for extraplanar dust even at the shortest wavelength of 100 μm.

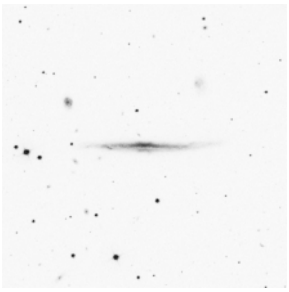

Figure 2.63: DSS B-Band

Figure 2.64: SPIRE 500 μm

From the brightness profile fitting (Figure A.25), the excess dust emission above the stellar disk is within the errors hence we do not consider the galaxy to have an extraplanar dust component.

2.8.1.26 NGC 5746

The measured scale height of dust from the ellipse fitting at 100 μm exceeds the thin disk, hence we consider the observations to be resolved. The scale height of the dust disk at 3.15 kpc is less than that of the stellar disk at 4.19 kpc, however we begin to see evidence of extraplanar dust at wavelengths of 250 μm and above.

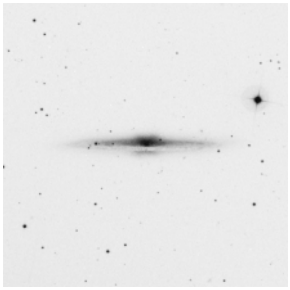

Figure 2.65: DSS B-Band

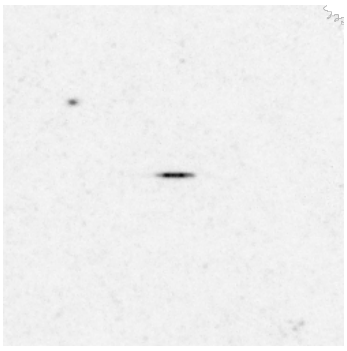

Figure 2.66: SPIRE 500 μm

From the brightness profile fitting (Figure A.26), the dust emission closely follows the stellar disk profile, hence we do not consider the galaxy to have an extraplanar dust component.

2.8.1.27 NGC 5907

The measured scale height of dust from the ellipse fitting at 100 μm exceeds the thin disk, hence we consider the observations to be resolved. The scale height of the dust disk at 3.01 kpc is greater than that of the stellar disk at 2.84 kpc, hence this galaxy exhibits evidence for extraplanar dust even at the shortest wavelength of 100 μm.

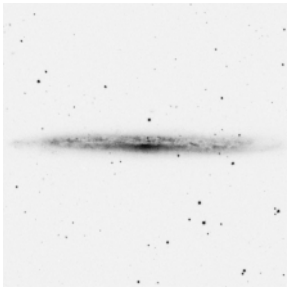

Figure 2.67: DSS B-Band

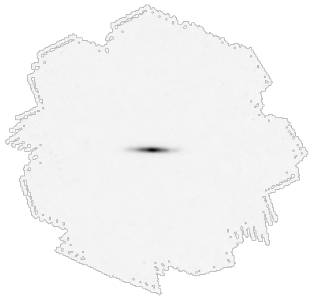

Figure 2.68: SPIRE 500 μm

From the brightness profile fitting (Figure A.27), the excess dust emission above the stellar disk is within the errors hence we do not consider the galaxy to have an extraplanar dust component.

2.8.1.28 NGC 7090

The measured scale height of dust from the ellipse fitting at 100 μm exceeds the thin disk, hence we consider the observations to be resolved. The scale height of the dust disk at 1.80 kpc is greater than that of the stellar disk at 0.28 kpc, hence this galaxy exhibits evidence for extraplanar dust even at the shortest wavelength of 100 μm.

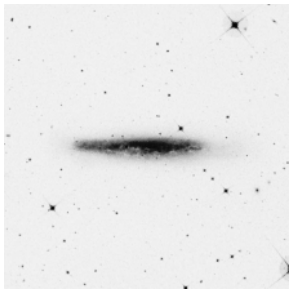

Figure 2.69: DSS B-Band

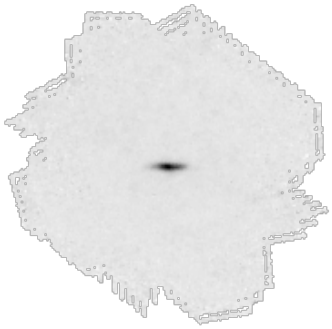

Figure 2.70: SPIRE 500 μm

The negative bowls apparent in the WISE emission profile (see Section A.28) may have affected the brightness profile closer to the plane, hence we cannot consider this galaxy as a candidate for exhibiting an extraplanar dust component.

2.8.1.29 UCG 7321

As presented in Table 2.3, UGC 7321 does not show evidence of extraplanar dust above the convolved thin disk, hence we consider observations of this galaxy to be unresolved.

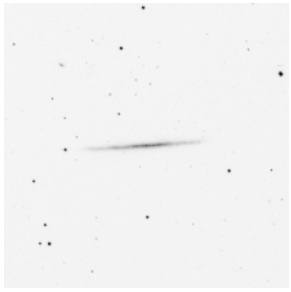

Figure 2.71: DSS B-Band

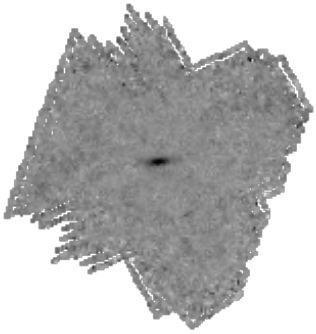

Figure 2.72: SPIRE 500 μm

From the brightness profile fitting (Figure A.29), the dust emission closely follows the stellar disk profile and any excess emission is within the errors, hence we do not consider the galaxy to have an extraplanar dust component.

2.8.1.30 UGC 7522

The measured scale height of dust from the ellipse fitting at 100 μm exceeds the thin disk, hence we consider the observations to be resolved. The scale height of the dust disk at 2.58 kpc is greater than that of the stellar disk at 2.24 kpc, hence this galaxy exhibits evidence for extraplanar dust even at the shortest wavelength of 100 μm.

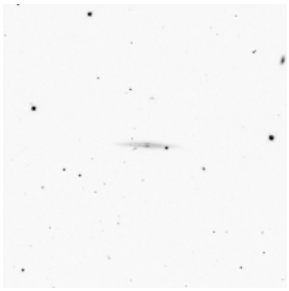

Figure 2.73: DSS B-Band

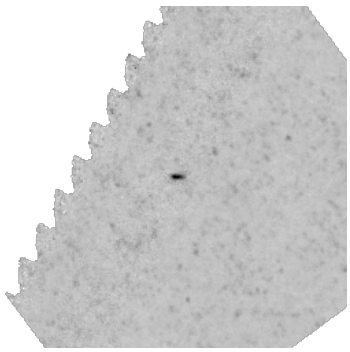

Figure 2.74: SPIRE 500 μm

From the brightness profiles of UGC 7522 (see Section A.30), we see an excess in the dust emission above the stellar disk out to a maximum distance of 3 kpc at the 250-500 μm bands.

2.8.1.31 UGC 7982

The measured scale height of dust from the ellipse fitting at 100 μm exceeds the thin disk, hence we consider the observations to be resolved. The scale height of the dust disk at 1.40 kpc is greater than that of the stellar disk at 0.37 kpc, hence this galaxy exhibits evidence for extraplanar dust even at the shortest wavelength of 100 μm.

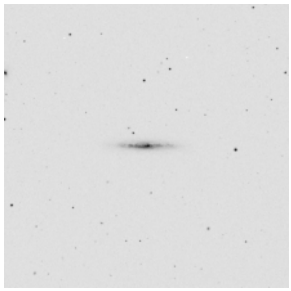

Figure 2.75: DSS B-Band

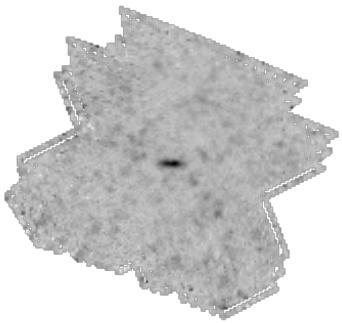

Figure 2.76: SPIRE 500 μm

From the brightness profile fitting (Section A.31), the excess dust emission above the stellar disk is within the errors, hence we do not consider the galaxy to have an extraplanar dust component.

2.8.2 Galaxies with Evidence for Extraplanar Dust

11 of the 31 (35%) galaxies in the sample show evidence of an extraplanar dust component above the stellar disk. These galaxies are presented in Table 2.4 alongside the maximum distance above the plane at which an excess of the dust emission over stellar emission is observed. Errors are estimated as one pixel (expressed in kpc) and are propagated for the value of β_d/β_s by the following formula:

$$\Delta R = R \times \sqrt{\left(\frac{\Delta x}{x}\right)^2 + \left(\frac{\Delta y}{y}\right)^2}, \tag{2.7}$$

where ΔR is the error on the resulting value, R is the resulting value, Δx is the error on x, and Δy is the error on y.

Name	Distance (kpc)	β_s (kpc)	β_d/β_s
NGC 3079	1.0 ± 0.5	1.0 ± 0.5	1.0 ± 0.7
NGC 3501	2.0 ± 1.0	1.0 ± 1.0	2.0 ± 2.2
NGC 4013	2.0 ± 1.0	1.0 ± 1.0	2.0 ± 2.2
NGC 4217	2.0 ± 1.0	1.0 ± 1.0	2.0 ± 2.2
NGC 4222	4.0 ± 0.8	1.5 ± 0.8	2.7 ± 1.5
NGC 4289	3.8 ± 1.3	2.5 ± 1.3	1.5 ± 0.9
NGC 4402	1.0 ± 0.5	0.5 ± 0.5	2.0 ± 2.2
NGC 4445	1.5 ± 0.5	1.0 ± 0.5	1.5 ± 0.9
NGC 4758	1.0 ± 0.5	1.0 ± 0.5	1.0 ± 0.7
NGC 5356	1.5 ± 0.8	1.5 ± 0.8	1.0 ± 0.8
UGC 7522	3.0 ± 1.5	1.5 ± 1.5	2.0 ± 2.2

Table 2.4: Galaxies that show evidence for an extraplanar dust component from their brightness profiles and their ratio of β_d to β_s.

In all cases except NGC 4222, the estimated uncertainty on β_d/β_S brings the resulting value below 1, hence we cannot conclude that these galaxies show a considerable extraplanar dust component. NGC 4222 however does show evidence of an extended dust distribution despite the large errors.

2.8.3 Relationship Between Star Formation Rate and β_d

The specific star formation rate (sSFR) of each galaxy is included at the top of each profile to test any correlation between active star formation and the expulsion of dust over greater distances. As dust is produced and expelled from the galaxy disk by processes related to star formation (see Section 1.1.1), we may expect to find a relationship between dust scale height and star formation rate.

Values for the current star formation rate (SFR) have been obtained by Nersesian et al. (2019) as part of the DustPedia project, in which they use the SED fitting algorithm `CIGALE` (Noll et al., 2009) on all 817 DustPedia galaxies with *Herschel* detections to measure their dust properties. Parameters such as the SFR, stellar mass and dust mass are estimated by the CIGALE model given the input fluxes of each galaxy. They calculate the SFR as a function of time, t, to be

$$SFR(t) \approx t \times \exp(-t/\tau_{main}), \tag{2.8}$$

where τ_{main} is the e-folding time of the main stellar population model assuming a delayed star-formation history. They compare the results of the CIGALE SFR

parameter estimation against other methods to derive SFR, such as polycyclic aromatic hydrocarbon (PAH) features at the WISE 12 μm band, and via the mid-infrared (MIR) emission observed at the WISE 22 μm band. In the case of PAH features, the following formula is used to calculate SFR:

$$log\left(\frac{SFR}{M_{\odot}yr^{-1}}\right) = (0.66 \pm 0.01)\,[\log(L_{12}) - 22.25], \tag{2.9}$$

where L_{12} is the luminosity at 12 μm (Davies et al., 2016). Chang et al. (2015) derive the SFR from the MIR emission using

$$log\left(\frac{SFR}{M_{\odot}yr^{-1}}\right) = \log(L_{22}\,/\,L_{\odot}) - 9.08, \tag{2.10}$$

where L_{22} is the luminosity at 22 μm. Comparisons with the above derivations against CIGALE results show that the 12 μm flux calibration overestimates the SFR of early-type galaxies from CIGALE which has also been shown in the literature (Davis et al., 2014). The 22 μm calibration underestimates the SFR of late-type galaxies while also overestimating the early-types. In both cases, it is apparent that MIR derivations are not sufficient to get good estimates of the current SFR thus the CIGALE estimations are used throughout the DustPedia project and this thesis. To find the sSFR I use

$$sSFR = \frac{SFR(M_{\odot}yr^{-1})}{M_{\star}(M_{\odot})}, \tag{2.11}$$

where $M_{\star}$ is the stellar mass also obtained by Nersesian et al. (2019). To compare the star formation against dust expulsion I plot sSFR vs β_d, which can be seen in Figure 2.77.

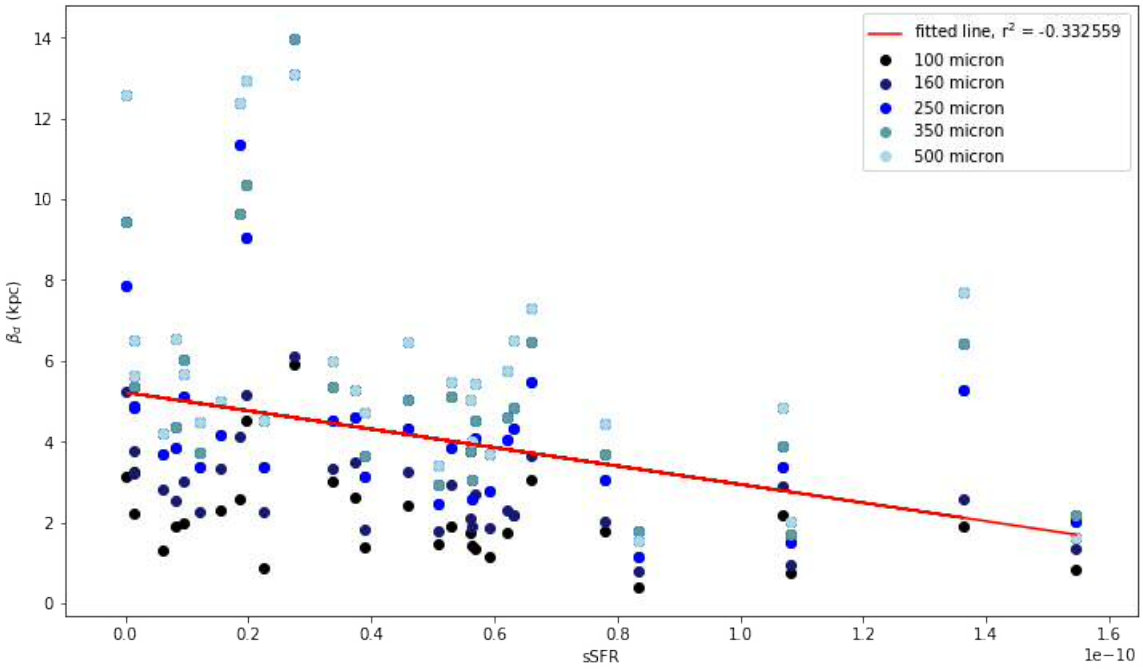

Figure 2.77: Relationship between the specific star formation rate (sSFR), which is the SFR in $M_\odot yr^{-1}$ per unit stellar mass in $M_\odot$, versus β_d for all galaxies in the sample at each wavelength. The red line represents the line of best fit calculated via linear regression, resulting in an R^2 value of -0.33.

The line of best fit was calculated using the `scipy.stats.linregress` function in *Python*, which outputs the linear least-squares regression for two sets of measurements including an R^2 value. The R^2 value measures how close the data are to the fitted regression line. A value of 0 indicates that the model explains none of the variability of the response data around its mean.

The sSFRs appear to be lower estimates due to the value being derived from the current SFR rather than an integrated value. For comparison against the Milky Way, the current sSFR is $2.71 \pm 0.59 \times 10^{-11}$ (Licquia and Newman, 2015), within the range of the late-type edge-on DustPedia galaxies in this sample. From the plot and R^2 value of -0.33, there is a weak negative correlation between the sSFR and β_d, although due to the small number of data points we are unable to make a confident conclusion regarding this relationship. A larger sample size would be more statistically significant and better able to probe any correlation between these two parameters.

2.8.4 Goodness of Fit of the Models

I test the goodness of fit of the models against the data via χ^2 minimization using the equation

$$\chi^2 = \sum_{i=1}^{n} \frac{(O_i - E_i)^2}{E_i}, \tag{2.12}$$

where O_i is the observed data, and E_i is the modelled data. To compute this for each profile, I use the `scipy.stats.chisquare` package in *Python*, which returns the actual value of χ^2 and the p-value (the probability of the model matching the data set). For the vast majority of sample galaxies, the returned p-value from this test is, or is very close to, 1. This indicates that the models are well matched to the data.

For 3 galaxies in the sample (NGC3628, NGC4206 and NGC4222), the p-value was much lower. Upon inspection of their brightness profiles, these galaxies exhibit brightness profiles that extend further than their model counterparts. This indicates the presence of an extended, low SNR dust distribution that was not detected during the initial measurements of β_d via our ellipse fitting procedure.

There are few studies of the dust distribution in the disks of NGC 4206 and 4222, however a study by Baes and Viaene (2016) provides evidence for an extraplanar dust component in NGC 3268 contained within the thick disk via radiative transfer modelling. It may be this extended component that is underestimated by the models, indicating that the dust emission is below the detection threshold of our ellipse fitting procedure (SNR = 2). This emission is not detected above the errors in this analysis. We show in Section 2.8 that NGC 4222 exhibits an extended dust distribution, however this was not detected for NGC 3628.

As there is evidence of a hidden dust component that was not predicted by the models for NGC 4222, it is possible that other galaxies in the sample have low-surface brightness extraplanar dust that has so-far been undetected in the individual maps. Due to the sensitivity of the *Herschel* maps, it is difficult to detect the presence of a further extended dust disk via direct detection of a single map. But by averaging a number of maps together however, we may be able to boost the signal of the dust emission while the random background noise remains fairly constant.

2.9 Summary

In this Chapter, I have presented the targets used to investigate the dust distribution in a sample of nearby, edge-on galaxies in the DustPedia database. An ellipse fitting procedure is used to estimate the inclination of each galaxy and their values of β_d and α_d.

I have generated models for the distribution of dust in x, y, z planes for each galaxy in the sample at the 100, 160, 250, 350 and 500 μm bands which are used as a comparison against the real galaxies, and to account for line-of-sight effects that occur when a disk is not exactly edge-on. The vertical brightness profile of each galaxy, its matching model, a modelled inclined thin disk, and the stellar disk are plotted to compare the relative scale heights of each of these parameters.

The results show that the models are well matched to the galaxy profiles in all but 3 galaxies; one of which has been shown to exhibit a vertically extended dust distribution via radiative transfer modelling (NGC 3268, Baes and Viaene (2016)), and another which has been shown to exhibit an extended dust distribution by this analysis. The presence of a more vertically extended distribution than their models predict may indicate a hidden dust component that was not detected in the initial ellipse fitting procedure. To test this hypothesis, I follow the procedure set out in Smith et al. (2016) for the 31 sample galaxies at each of the 5 *Herschel* wavelengths.

CHAPTER 3

GALAXY AND MODEL STACKING

A recent study by Smith et al. (2016) introduces the stacking method used on a sample of 110 face-on galaxies included in the *Herschel* Reference Survey. By averaging their observations, they improve the sensitivity of the data by more than an order of magnitude over that of a single map, allowing the detection of low-surface brightness dust emission that was previously unobserved.

The aim of this chapter is to follow the methods outlined in Smith et al. (2016) for the edge-on sample galaxies presented in Chapter 2.3. I follow the averaging procedure for data at at the 100, 160, 250, 350 and 500 μm *Herschel* bands to measure the extent of dust above the mid-plane. WISE 3.4 μm data is also used for this study as a comparison against the stellar disk height.

The stacking procedure is outlined in Section 3.1. Section 3.2 describes the method used to characterise the stellar disk from the WISE data, and the resulting brightness profiles are presented in section 3.3. The results are explained in Section 3.4 and a discussion and summary are provided in Sections 3.5 and 3.6.

A description of the data products used throughout this chapter can be seen in Section 2.4

3.1 Stacking the Data

Each galaxy is first weighted by their peak flux, hence the brightest galaxies were weighted down so that each galaxy contributes an equal impact on the final stacked brightness profiles, and there is not one particularly bright galaxy that dominates the result.

To average the maps at each wavelength, each pixel in the 31 galaxy images (which have been cropped to the same 180x180 pixel size) are assigned an x and y co-ordinate value based on their distance from the central plane in both the x and y directions. All pixels at the same co-ordinates are then placed into radial bins, and the summed value of all pixels in each bin is calculated. This is carried out individually at 3.4, 100, 160, 250, 350 and 500 μm. Images of the stacked maps at each wavelength can be seen in Figures 3.1 through 3.6. We do not see any obvious background sources or irregularities in the stacked maps.

I carry out the same stacking process for an infinitely thin disk convolved with the SPIRE 500 μm beam profile (outlined in Section 2.7.1). This provides a value of the detection limit above which any excess emission is considered real and not an effect of the instrument PSF.

Figure 3.1: WISE 3.4 μm stacked map.

The errors at each co-ordinate value are calculated ($\sigma/\sqrt{N}$, where N is the number of data points, i.e. 31, and σ is the standard deviation), hence by measuring σ for each radial bin we obtain a minimum error at each co-ordinate of the averaged map. Background subtraction is carried out on the stacked maps via the same process as in Section 2.5.1. To ensure the uncertainties included in the stacked maps are robust, the stacking technique outlined above is also applied to the error maps, and we calculate the resulting errors as per Section 2.7.2.1, including calibration uncertainties of 7% for both the PACS and SPIRE data.

Figure 3.2: PACS 100 μm stacked map.

Figure 3.3: PACS 160 μm stacked map.

Figure 3.4: SPIRE 250 μm stacked map.

Figure 3.5: SPIRE 350 μm stacked map.

Figure 3.6: SPIRE 500 μm stacked map.

3.2 Characterising the Stellar Disk

To gain a measure of the stellar disk versus the dust disk height, the WISE 3.4 μm averaged map is used. By utilising the same ellipse-fitting procedure as mentioned in Section 2.1, I have been able to obtain a value of the stellar scale height (β_s) by measuring the semi-minor axis of the ellipse. Although this parameter does not have a physical value and is instead measured in pixels due to the varying distance of each galaxy that has been co-added to the map, we can compare this value against the dust scale height (β_d) directly to measure how far the dust extends beyond the stars in terms of a ratio between the two parameters.

As the light from background stars is used as a way to measure the foreground extinction from dust (and therefore how far the dust extends), we can use our value of β_s as an upper limit at which extinction could be measured. Because we are probing the oldest and most extended stellar population, we would not expect dust extinction to be observed above this limit (except for in the case of using background galaxies or quasars as a light source).

β_s from the WISE maps was measured to be 3 pixels, equal to ~3 kpc at the sample mean distance of 18.8 Mpc. As the stellar disk has been convolved with the 500 μm beam, this profile does not represent the true height of stars but that measured after the convolution and therefore provides a considerable upper limit on the stellar scale height.

3.3 Stacked Brightness Profiles

Once the stacking is completed, I plot the brightness profiles of the real dust emission, the modelled dust emission, the stellar component and convolved thin disk for the *Herschel* wavelengths, via the same process as in Section 2.7.2. The stellar disk profile is subtracted from the dust emission profile, and the result plotted on a subplot. The difference of these two profiles gives us a measure of the flux of the dust emission above the stellar disk and how far above the stellar component it extends to.

The brightness profiles are displayed β_d/β_s (where $\beta_s = 3$ pixels from the plane). Therefore, at $\beta_d/\beta_s = 1$, the dust scale height is equal to the maximum stellar disk scale height. At $\beta_d/\beta_s > 1$, we directly detect extraplanar dust emission above the stellar disk.

The results of the brightness profile fitting are shown in Figures 3.7 through 3.11.

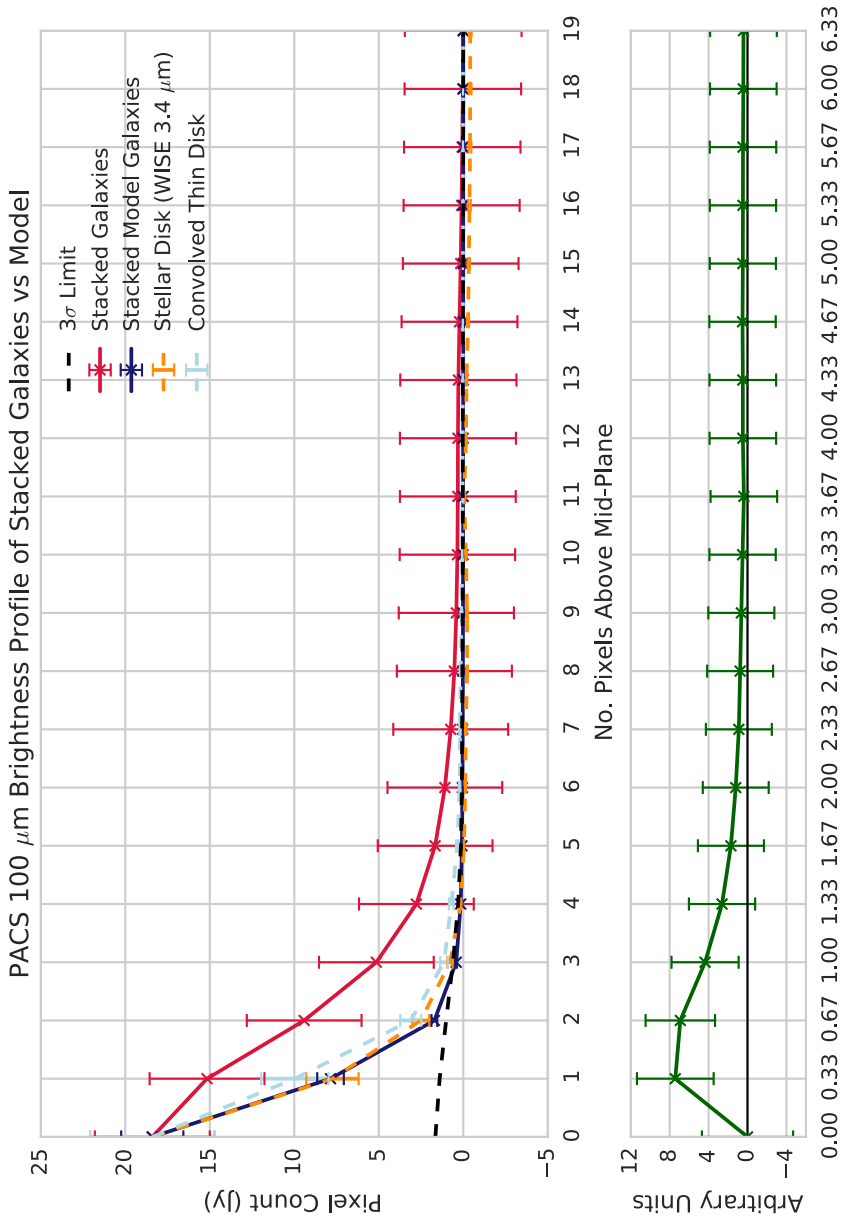

Figure 3.7: Upper: Vertical profile of all 31 averaged galaxies and models at 100 μm. The profiles have been normalised to match at the peak. The red line shows the value of the summed real galaxy maps using the *Herschel* data, the dark blue line shows the value of the summed models, and the orange dashed line shows the stellar disk profile from the WISE maps. The light blue dashed line represents the profile of an infinitely thin disk convolved with the 500 μm beam processed using the same method, and the black dashed line shows the 3σ noise detection limit. Lower: We subtract the stellar disk profile from the galaxy dust disk profile to see the difference in detected emission and how far the dust extends above the stellar component.

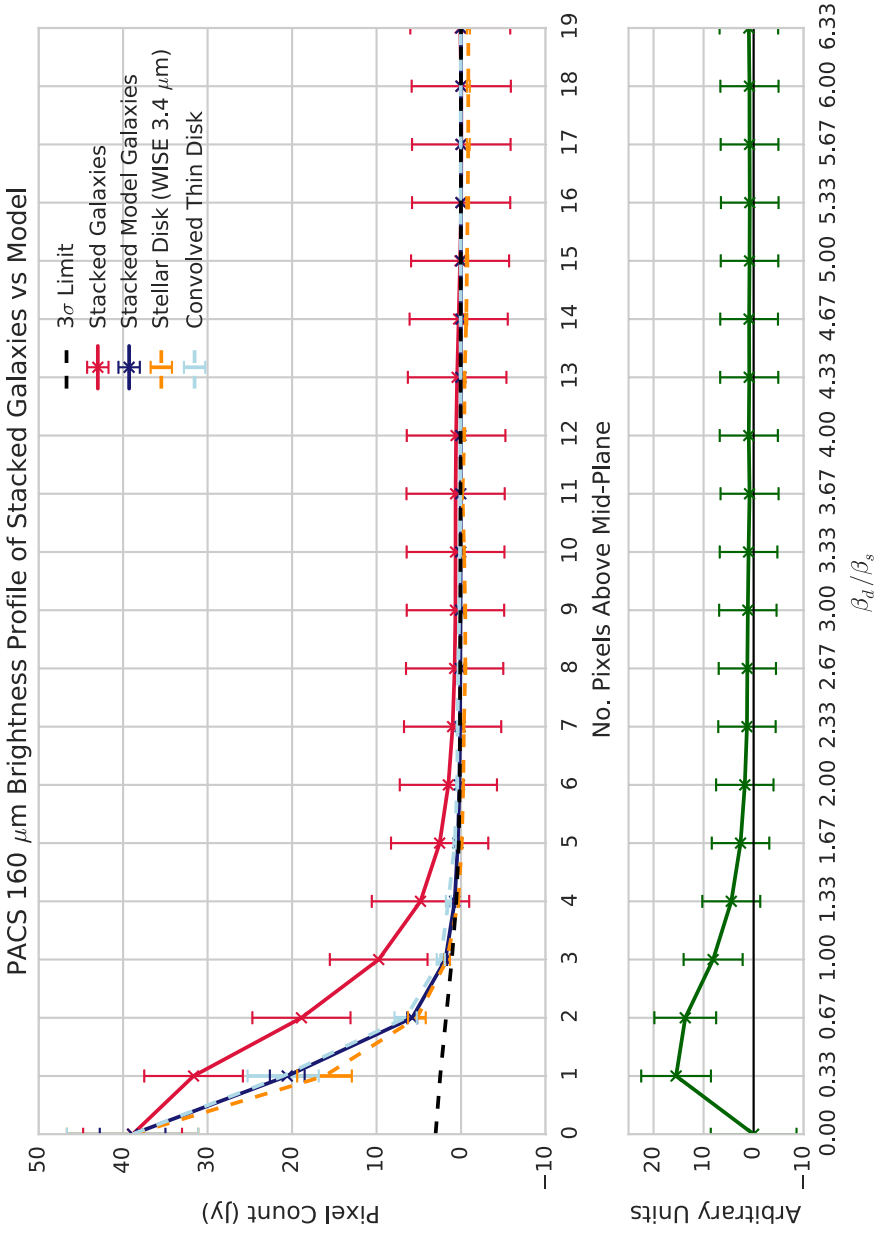

Figure 3.8: Upper: Vertical profile of all 31 averaged galaxies and models at 160 μm. The profiles have been normalised to match at the peak. The red line shows the value of the summed real galaxy maps using the *Herschel* data, the dark blue line shows the value of the summed models, and the orange dashed line shows the stellar disk profile from the WISE maps. The light blue dashed line represents the profile of an infinitely thin disk convolved with the 500 μm beam processed using the same method, and the black dashed line shows the 3σ noise detection limit. Lower: We subtract the stellar disk profile from the galaxy dust disk profile to see the difference in detected emission and how far the dust extends above the stellar component.

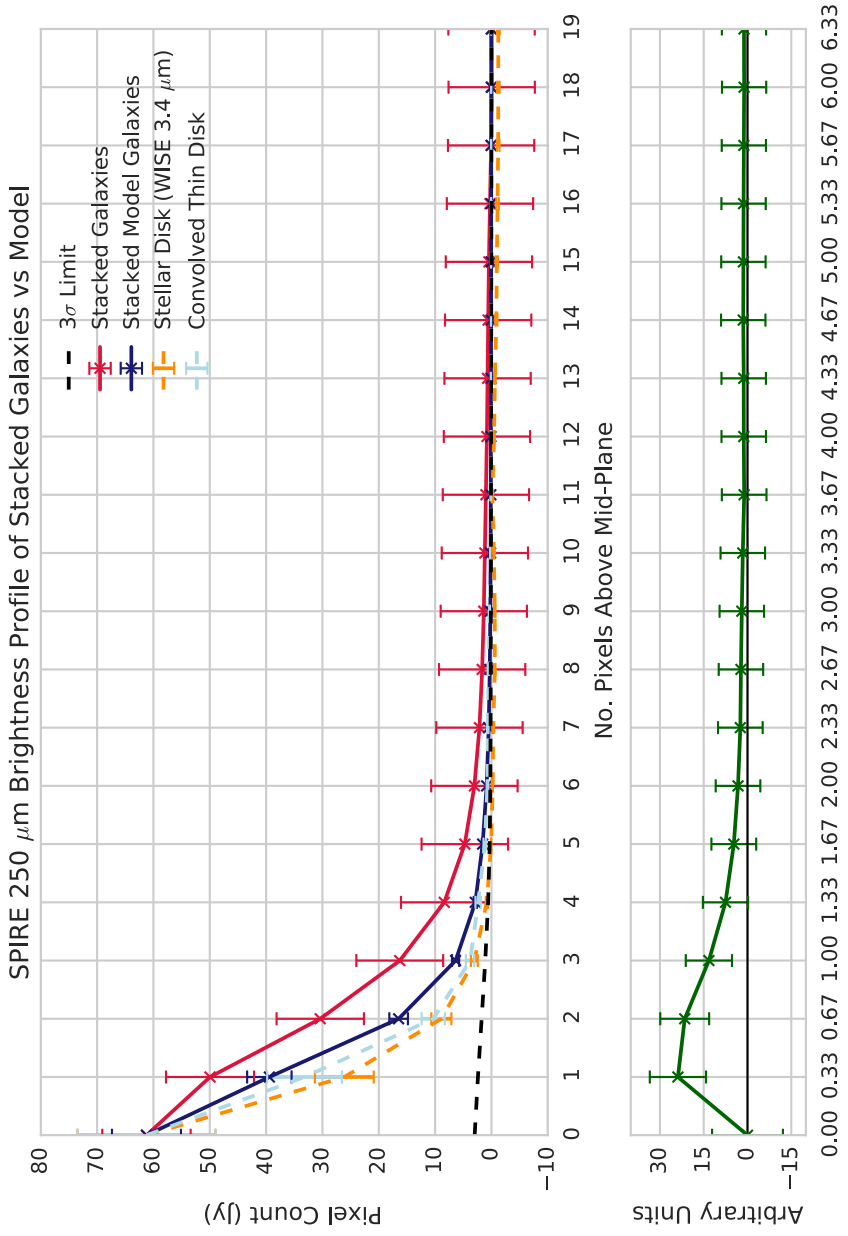

Figure 3.9: Upper: Vertical profile of all 31 averaged galaxies and models at 250 μm. The profiles have been normalised to match at the peak. The red line shows the value of the summed real galaxy maps using the *Herschel* data, the dark blue line shows the value of the summed models, and the orange dashed line shows the stellar disk profile from the WISE maps. The light blue dashed line represents the profile of an infinitely thin disk convolved with the 500 μm beam processed using the same method, and the black dashed line shows the 3σ noise detection limit. Lower: We subtract the stellar disk profile from the galaxy dust disk profile to see the difference in detected emission and how far the dust extends above the stellar component.

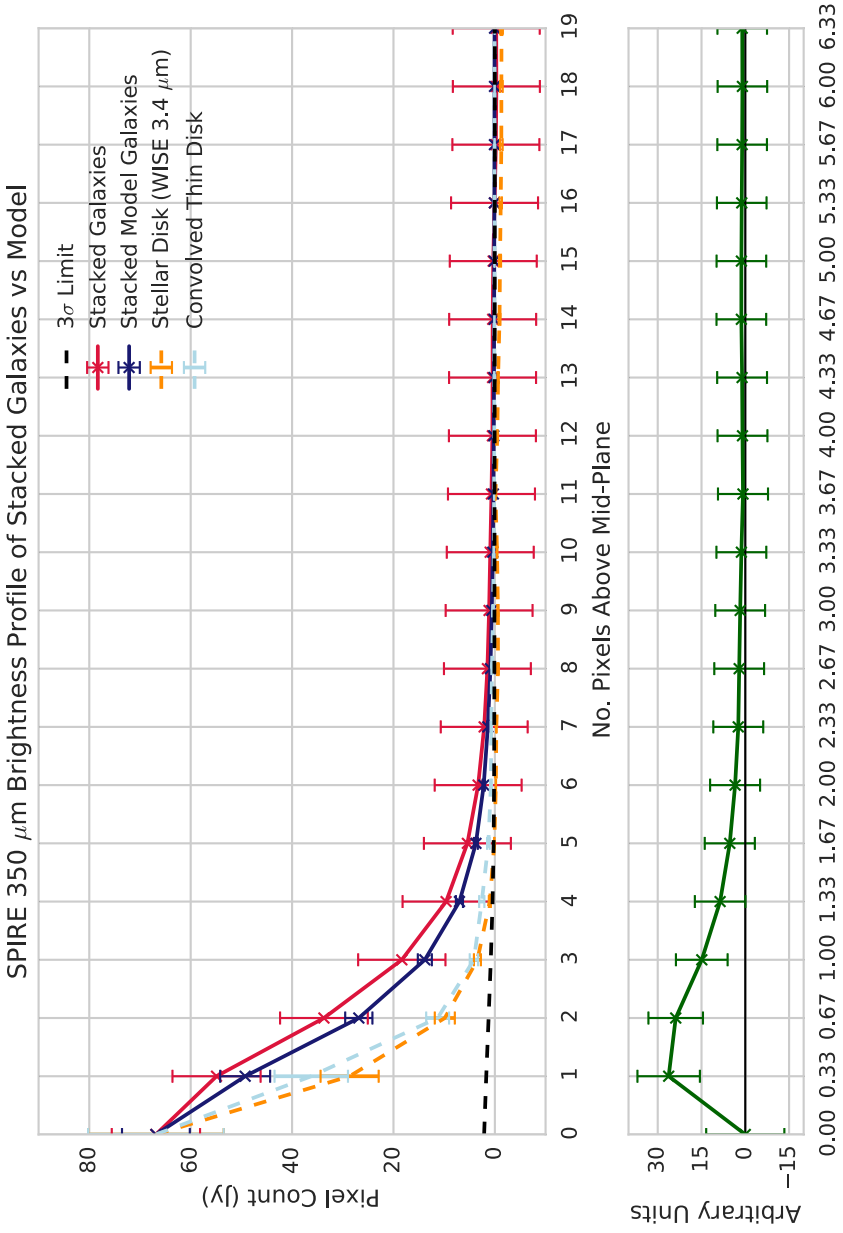

Figure 3.10: Upper: Vertical profile of all 31 averaged galaxies and models at 350 μm. The profiles have been normalised to match at the peak. The red line shows the value of the summed real galaxy maps using the *Herschel* data, the dark blue line shows the value of the summed models, and the orange dashed line shows the stellar disk profile from the WISE maps. The light blue dashed line represents the profile of an infinitely thin disk convolved with the 500 μm beam processed using the same method, and the black dashed line shows the 3σ noise detection limit. Lower: We subtract the stellar disk profile from the galaxy dust disk profile to see the difference in detected emission and how far the dust extends above the stellar component.

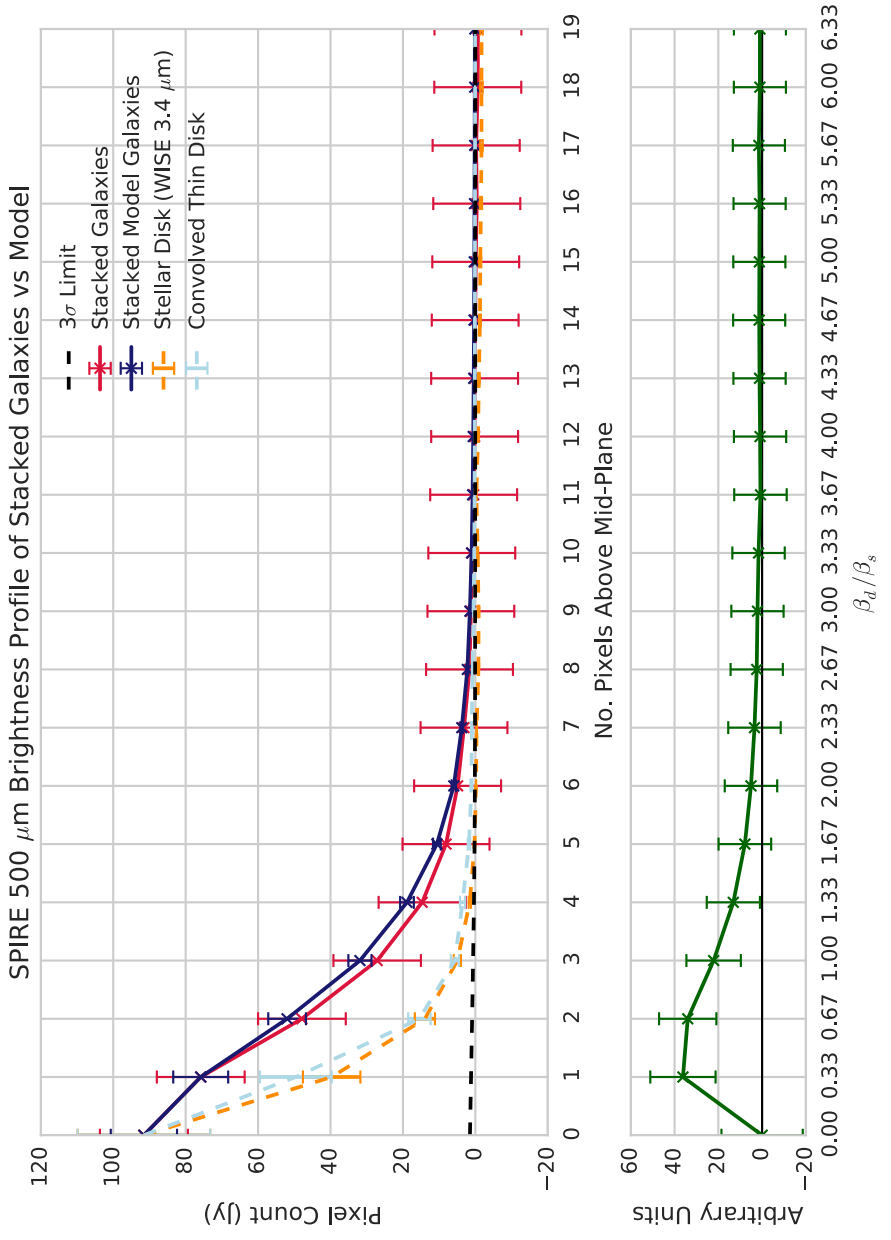

Figure 3.11: Upper: Vertical profile of all 31 averaged galaxies and models at 500 μm. The profiles have been normalised to match at the peak. The red line shows the value of the summed real galaxy maps using the *Herschel* data, the dark blue line shows the value of the summed models, and the orange dashed line shows the stellar disk profile from the WISE maps. The light blue dashed line represents the profile of an infinitely thin disk convolved with the 500 μm beam processed using the same method, and the black dashed line shows the 3σ noise detection limit. Lower: We subtract the stellar disk profile from the galaxy dust disk profile to see the difference in detected emission and how far the dust extends above the stellar component.

3.4 Results

3.4.1 Testing the Robustness of the Stacked Profiles

To test the robustness of the results, I 'jackknife' the sample by splitting it in two and re-averaging the data for each new sample, one with 15 galaxies and the other with 16. The brightness profiles of the two new samples are produced to test whether the results from the full sample are consistent. I include here the brightness profiles for the jackknifed sample at 100 μm in Figures 3.12 and 3.13

=

The results of jacknifing the sample show that we obtain the same results as for the full sample and therefore results of the full analysis are statistically robust, however the 3σ limit becomes the dominant source of error at closer distances to the plane. By stacking the full sample, we increase the SNR above this limit. Jackknifed plots at all 5 wavelengths are included in Appendix B.

3.4.2 Excess Emission Above the Model

At 100 - 250 μm, we detect a higher flux density in the data compared to the model prediction. For the individual brightness profiles, the χ^2 minimization showed that for all except 3 galaxies, the models were well matched to the data. As the stacked brightness profiles provide evidence of excess dust emission that was not detected for the individual galaxies, we conclude that the stacking technique has increased the sensitivity of the data, and enabled the detection of emission that was previously hidden in the individual maps. In the 350 μm profile we see a less significant excess in the dust emission over the modelled emission, indicating that there is a small increase in sensitivity by stacking at this wavelength. In Figure 2.14 the modelled emission and the real dust emission profiles are well matched and we do not detect an excess as in the shorter wavelength data. This indicates that at 500 μm, we gain negligible sensitivity by stacking the maps over a single observation.

3.4.3 β_d versus β_s

At 100-250 μm, the data show a dust emission profile that is extended to the same distance as the convolved stellar disk, i.e. $\beta_d/\beta_s = 1.00 \pm 0.33$. This is highlighted in the lower plots, whereby we subtract the WISE flux from the *Herschel* profiles.

At 350 and 500 μm, we detect dust emission that is more extended than the stellar component by at least a factor of 1/3 (i.e. $\beta_d/\beta_s = 1.33 \pm 0.33$). One possible

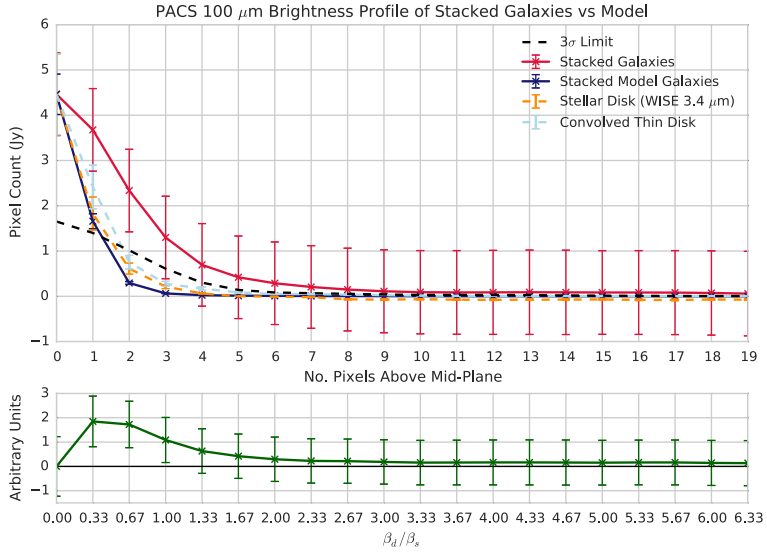

Figure 3.12: Upper: Vertical profile of 15 averaged galaxies and models at 100 μm. The profiles have been normalised to match at the peak. The red line shows the value of the summed real galaxy maps using the *Herschel* data, the dark blue line shows the value of the summed models, and the orange dashed line shows the stellar disk profile from the WISE maps. The light blue dashed line represents the profile of an infinitely thin disk convolved with the 500 μm beam processed using the same method, and the black dashed line shows the 3σ noise detection limit. Lower: We subtract the stellar disk profile from the galaxy dust disk profile to see the difference in detected emission and how far the dust extends above the stellar component.

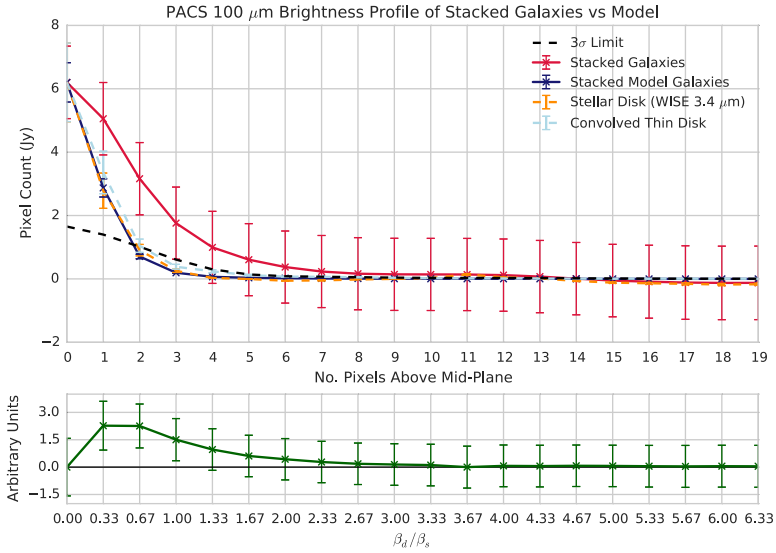

Figure 3.13: Caption as for Fig. 3.12 but for 16 of the sample galaxies.

reason for the scale height gradient could be due to background confusion in the longer wavelength data, however as shown in Section 2.7.2.1, the estimated uncertainties on the source fluxes are more than an order of magnitude greater than the confusion noise itself, hence its effect is considered to be negligible. This effect should also have been counteracted via the background subtraction methods used, and upon measuring the background emission after subtraction, we find a zero value. An alternative reason why we may detect a more extended distribution at the longer wavelengths is due to a cold dust component that is more extended than the warm dust detected at the shorter wavelengths, or perhaps due to an unresolved thin disk with high dust temperatures (Bocchio et al., 2016).

3.4.4 Influence of Galaxy Bulges

All pixels along the plane are summed to build the galaxy brightness profiles, hence the presence of a bulge that is vertically extended could influence the scale length measured across the whole disk. To test whether the results are biased by a bulge in the centre of the disk, we measure the brightness profile of the stacked maps at each wavelength at different radii from the centre. We present here profiles measured at 0.25, 0.5, and 0.75 $r_{1/2}$ from the centre of the plane, where instead of summing all pixels along the plane we measure just one column of the data at each radius. These results for the 100 μm data are presented in Figure 3.14.

By measuring the brightness profiles at different radii along the plane, we are able to conclude whether or not our initial results from summing all pixels along the plane are reliable or influenced by the presence of a vertically extended bulge. A significantly higher extension in the centre of the galaxy (0.5 $r_{1/2}$) would indicate that much of the emission is coming from the bulge itself, however we see from these plots that the scale height of the dust remains mostly constant along the disk. Therefore, we conclude that the galaxies do not exhibit a prominent bulge feature that would bias our results.

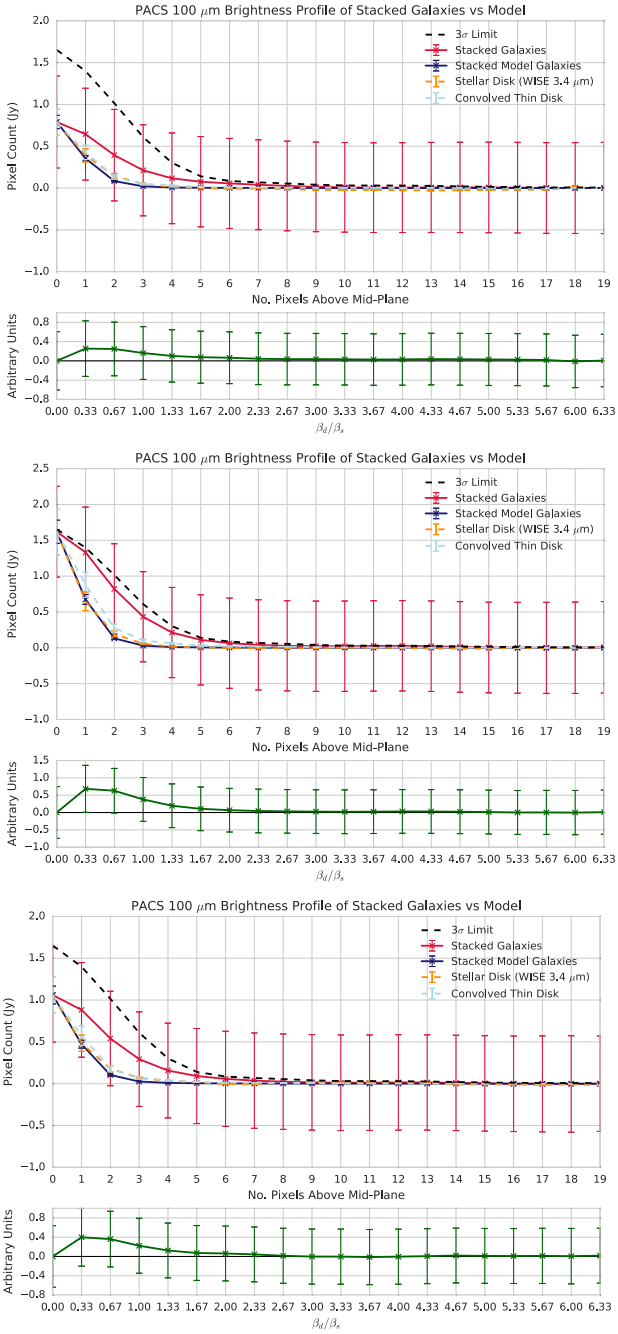

Figure 3.14: Brightness profiles of the stacked maps at 100 μm for a radius of 0.2 (upper), 0.5 (middle) and 0.75 (lower) $r_{1/2}$. For a full description of the profiles, see Figure 3.7.

3.4.5 SED Fitting of the Stacked Maps

Fluxes and errors were obtained via the brightness profile fitting for each row of pixels above the plane and are listed in Table 3.1. Note that we only include values up to 3 pixels from the plane as noise above this distance was too large to perform accurate SED fitting on the data.

	Flux (Jy)			
	Midplane	+1 pixel	+2 pixels	+3 pixels
100 μm	19.92 ±3.35	16.43 ±3.35	10.18 ±3.35	5.56 ±3.36
160 μm	46.47 ±6.68	38.08 ±6.66	23.04 ±6.63	12.11 ±6.66
250 μm	61.2 ±3.15	50.00 ±3.12	30.4 ±3.06	16.3 ±3.10
350 μm	53.2 ±7.06	43.5 ±7.04	26.6 ±7.01	14.3 ±7.05
500 μm	47.1 ±7.58	38.7 ±7.56	23.9 ±7.55	13.00 ±7.57

Table 3.1: Measured flux densities of the stacked map at increasing distance from the midplane.

A single component modified blackbody fit was first tested so as to be consistent with the THEMIS model which states that the FIR emission can be fit well with a single temperature blackbody (Jones et al., 2013; Nersesian et al., 2019), using the following function (Pearson et al., 2013):

$$S_\nu = A[B_\nu(T_c)]\nu^\beta], \tag{3.1}$$

where S_ν is the flux density at rest frame frequency ν, A is a normalisation factor, B_ν is the Planck function, β is the dust emissivity index, T_c and T_h are the cold and warm dust temperatures and α is the ratio of cold to warm dust mass. In the model, the temperature and normalisation factor parameters remain free and the optimum value is estimated, whereas the frequency and value of β are fixed (we set $\beta = 1.7$ to be consistent with the THEMIS dust model (Köhler et al., 2015)).

A Markov Chain Monte Carlo method is used to find the optimum parameters. This model outputs a fit to the data over all wavelengths. χ^2 is a sum over all available wavelengths, and for each combination of the free parameters, the model finds the values that gave the minimum value of χ^2. Our best-fitting model was the set of T and A that gave the lowest value of χ^2 overall.

However, the resulting SED did not fit the data at wavelengths greater than 250 μm and at the 100 μm band. See Figure 3.15 as an example.

Due to the observed excess emission at the shortest and longest wavelengths from the one-component fit, I instead fit a two-component modified blackbody

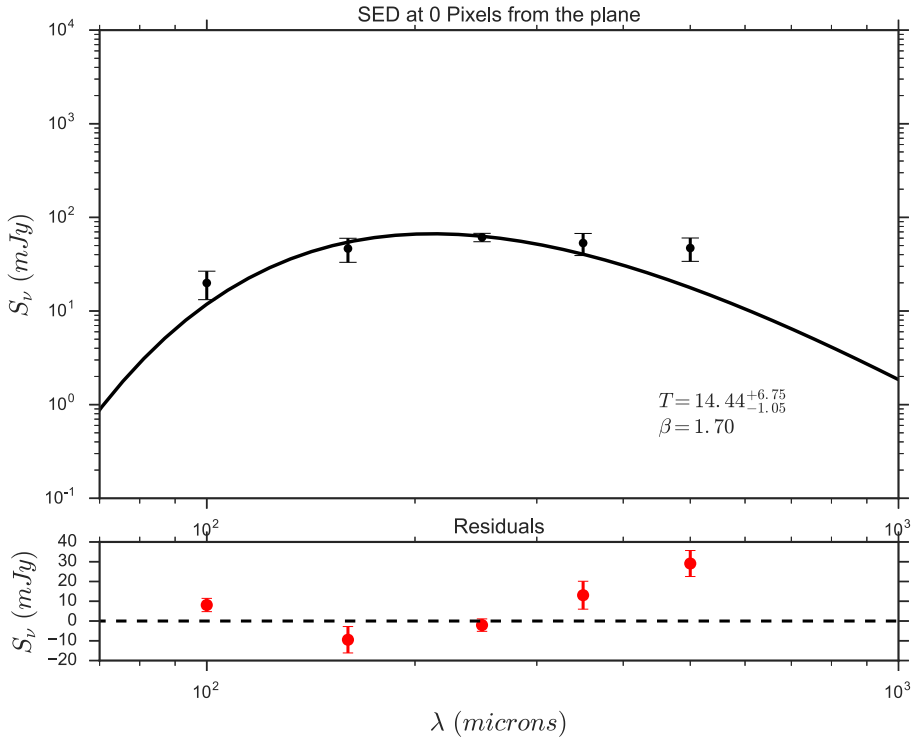

Figure 3.15: Upper: Poorly-fitted one-component SED of the averaged maps from 100 to 500 μm at a distance of 4 pixels from the plane, where the x-axis represents the wavelength and the y-axis represents the flux of the observations in Jy. Black markers indicate the data points, and the solid black line shows the fitted spectrum to the data. Lower: Residuals between the predicted model and data have been plotted as red points.

SED to the stacked maps to obtain a value for the warm and cold dust temperature and mass from the FIR emission at incremental distances above the stellar disk. The two-component model is recommended for FIR SED fitting by Clark et al. (2016) and Mattsson et al. (2014). I fit the spectrum given the following blackbody function (Pearson et al., 2013):

$$S_\nu = A[B_\nu(T_c)]\nu^\beta + \alpha B_\nu(T_h)]\nu^\beta], \tag{3.2}$$

An example of the SED fitting results can be seen in Figure 3.16.

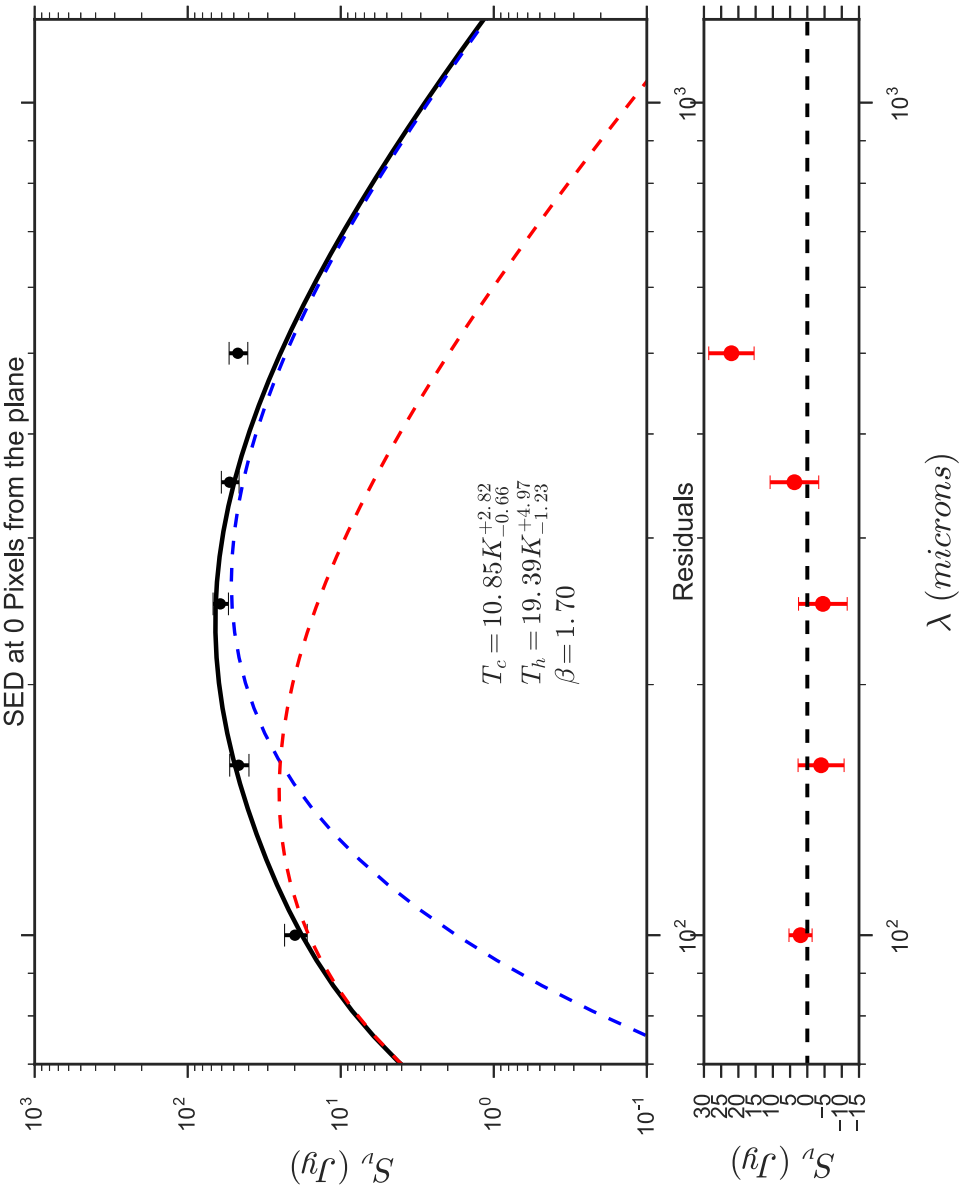

Figure 3.16: Upper: SED of the averaged maps from 100 to 500 μm along the plane where the x-axis represents the wavelength and the y-axis represents the flux of the observations in Jy. Black markers indicate the data points, and the solid black line shows the fitted spectrum to the data. Lower: Residuals between the predicted model and data have been plotted as red points.

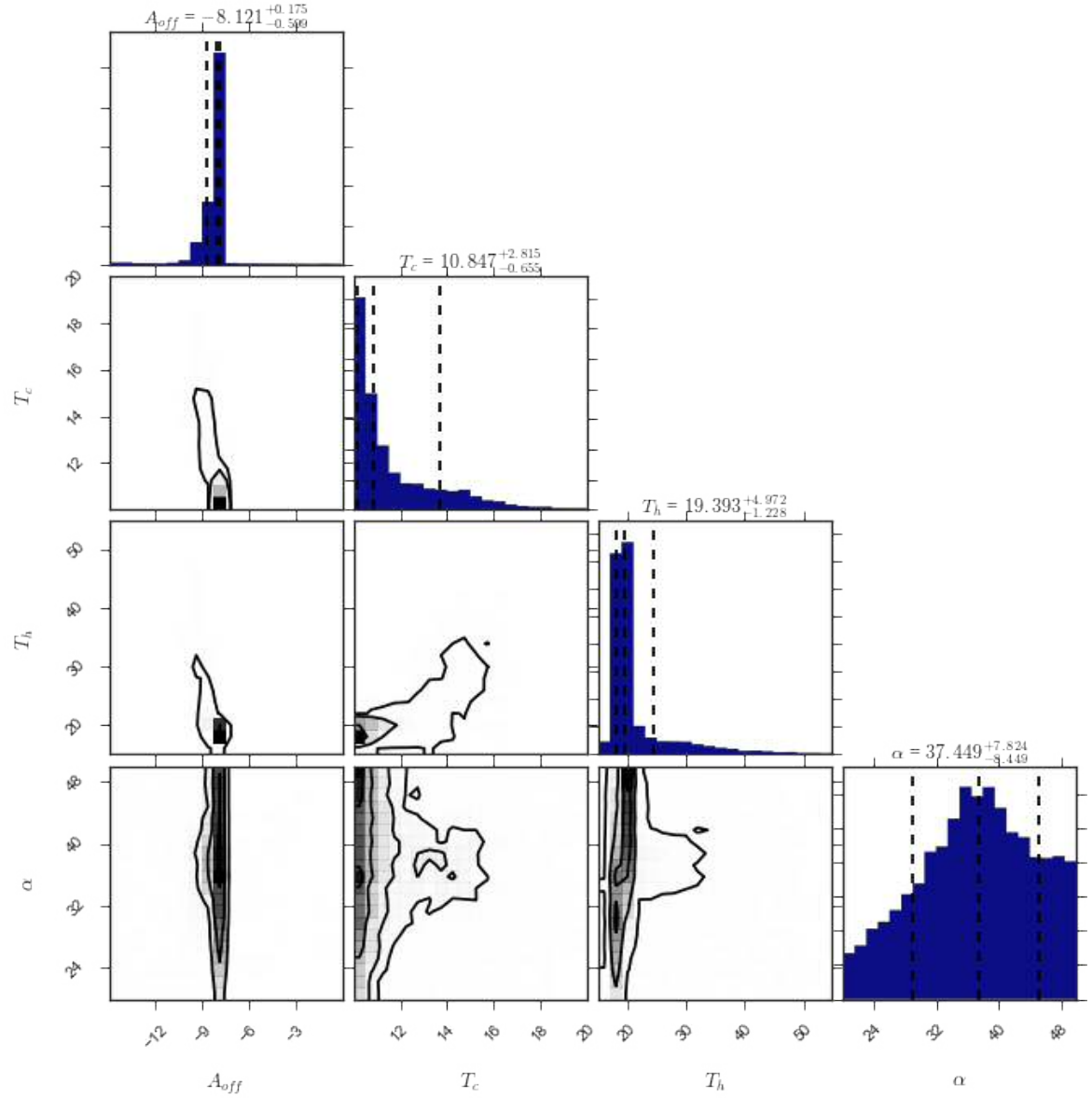

Figure 3.17: Corner plot produced by the MCMC SED fitting method for the averaged data along the plane. Contours represent the 16, 50 and 84th percentile estimates.

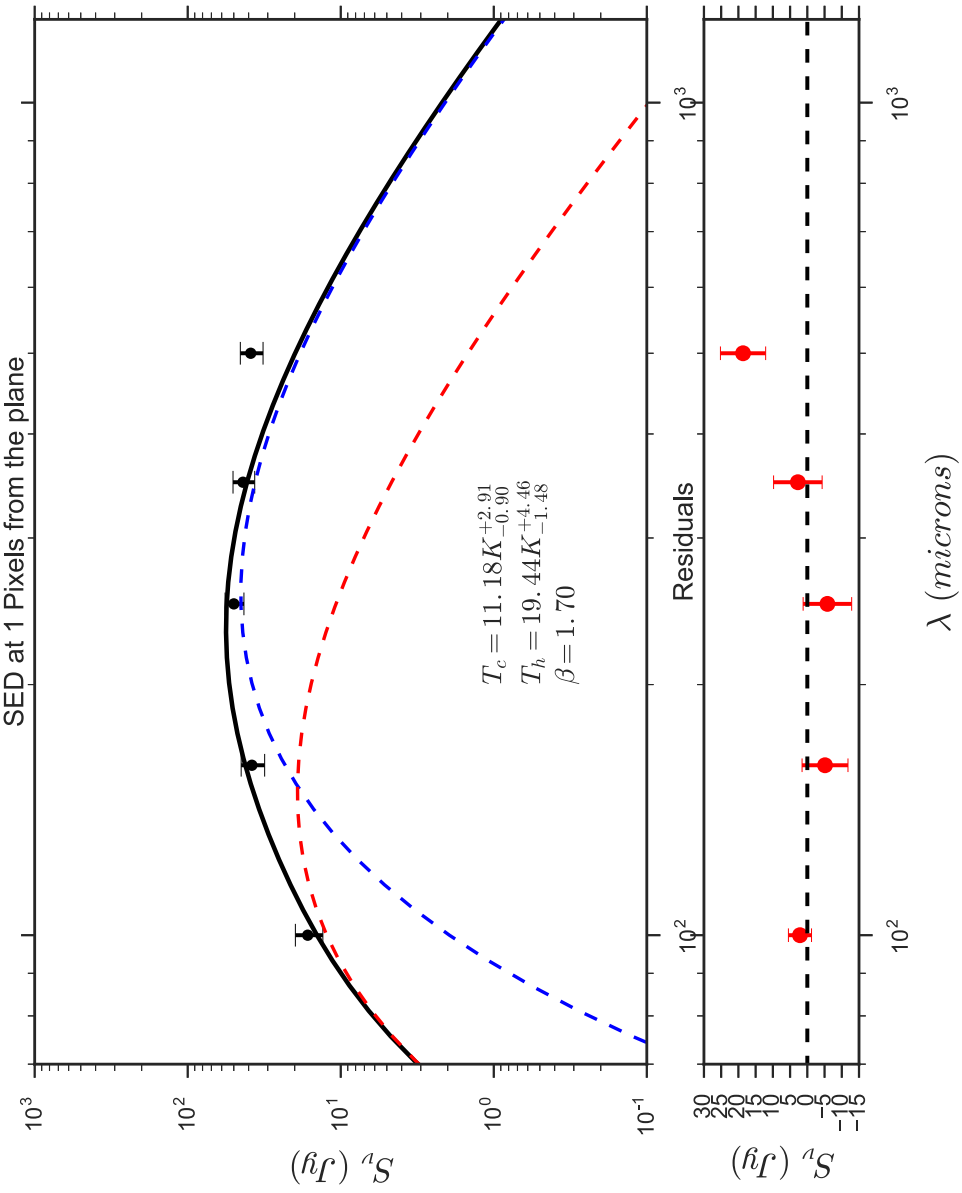

Figure 3.18: Upper: SED of the averaged maps from 100 to 500 μm at 1 pixel from the planewhere the x-axis represents the wavelength and the y-axis represents the flux of the observations in Jy. Black markers indicate the data points, and the solid black line shows the fitted spectrum to the data. Lower: Residuals between the predicted model and data have been plotted as red points.

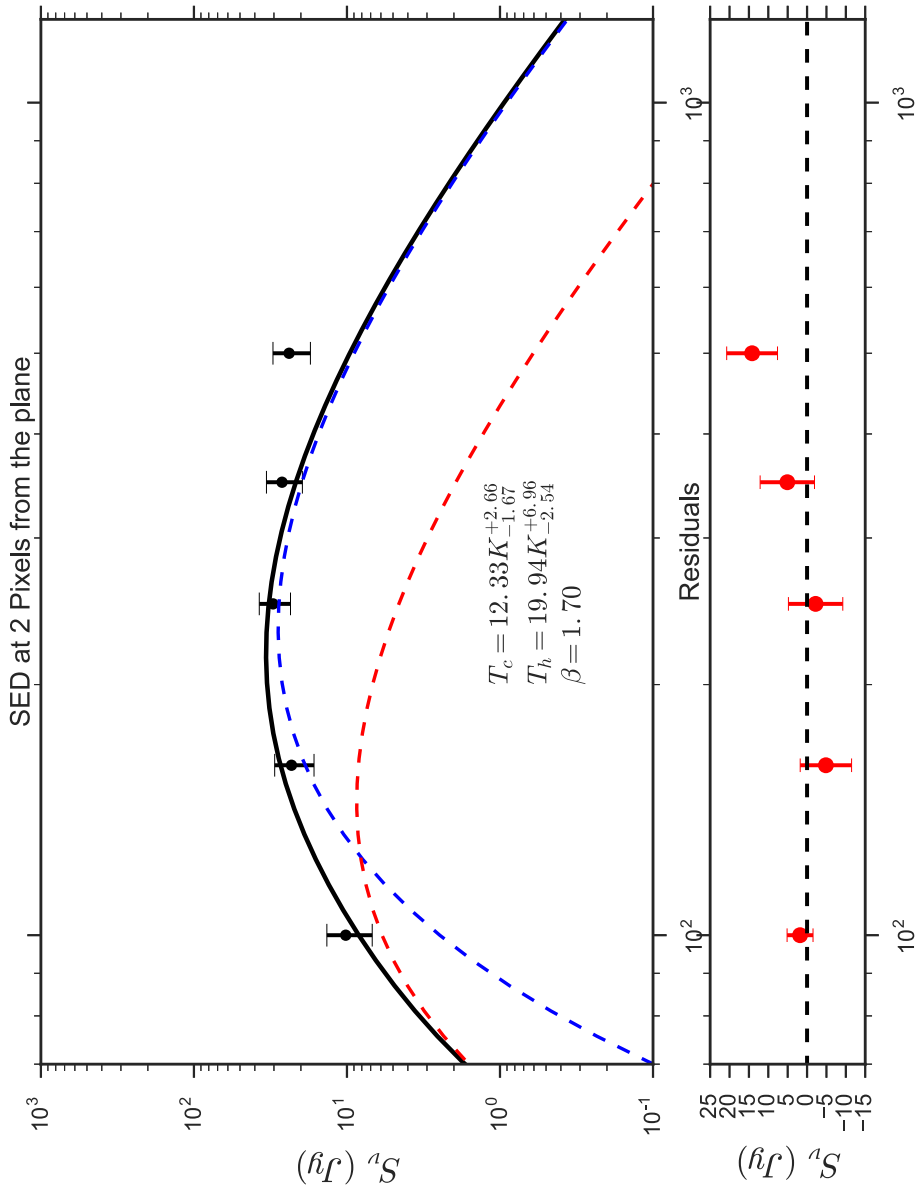

Figure 3.19: Upper: SED of the averaged maps from 100 to 500 μm at 2 pixels from the plane where the x-axis represents the wavelength and the y-axis represents the flux of the observations in Jy. Black markers indicate the data points, and the solid black line shows the fitted spectrum to the data. Lower: Residuals between the predicted model and data have been plotted as red points.

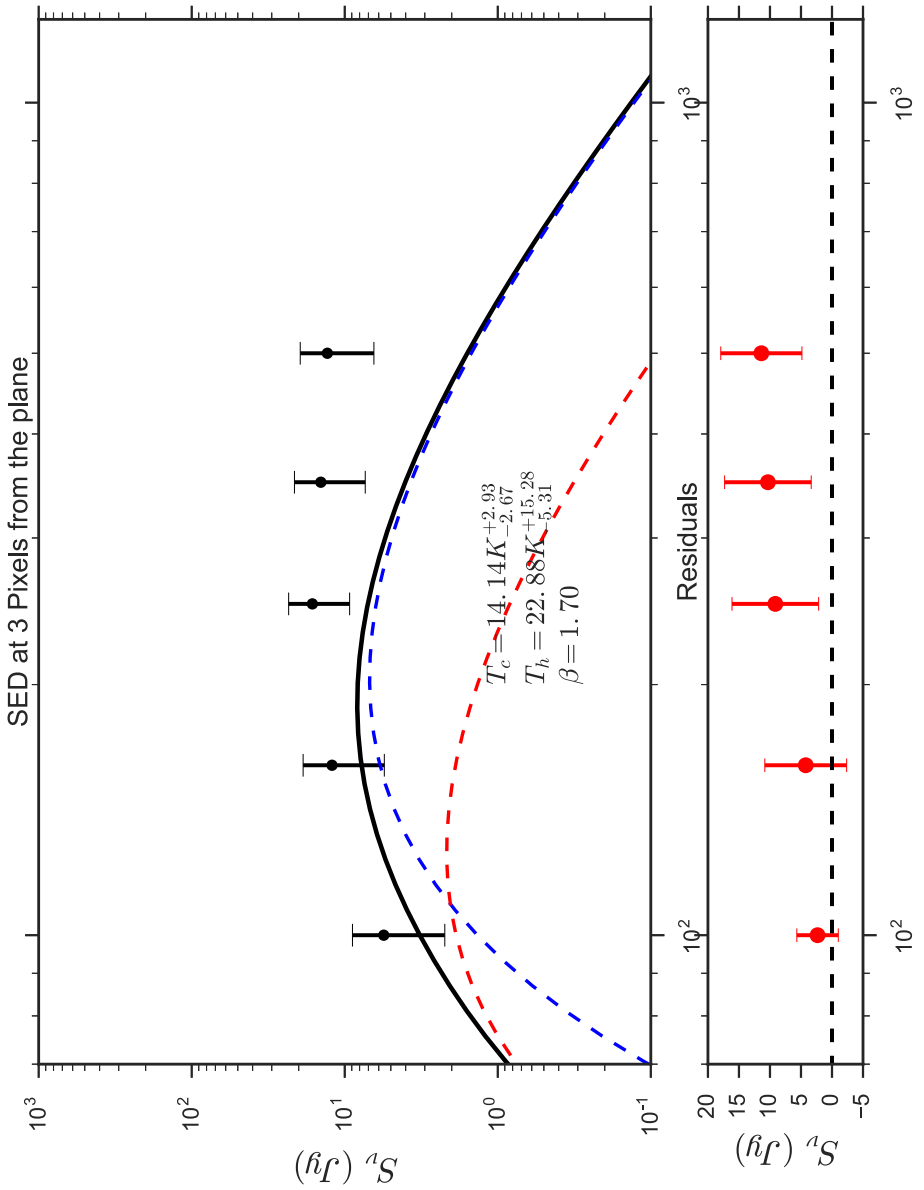

Figure 3.20: Upper: SED of the averaged maps from 100 to 500 μm at 3 pixels from the plane where the x-axis represents the wavelength and the y-axis represents the flux of the observations in Jy. Black markers indicate the data points, and the solid black line shows the fitted spectrum to the data. Lower: Residuals between the predicted model and data have been plotted as red points.

At 3 pixels from the plane, the errors on the data become too large to gain an accurate fit to the data. For this reason, we exclude this results from further analysis.

Derived dust temperatures for the warm and cold components range between 19.94-19.34 K and 10.85-12.33 K respectively, consistent with the temperatures found for the DustPedia sample by Nersesian et al. (2019) (~11-37 K). Due to the large errors at distances greater than 2 pixels, I am unable to study the effect of dust temperature on extended vertical scaleheight. Radiative transfer models have shown that vertical gradients in T due to diffuse dust heating are generally very shallow. Previous work by Bianchi et al. (1999) models the temperature gradient of dust both radially and vertically for the nearby galaxy NGC 6946 via radiative transfer modelling. They do not observe a steep temperature gradient in the z-direction, but do find the temperature increases slightly above the plane before plateauing, as is consistent with the results that we have managed to obtain.

From the SED fits at 0-2 pixels from the plane (mean distance = ~2 kpc), we observe a significant excess in emission at longer wavelength of 500 μm. This excess is well documented in the literature (Galliano et al., 2003, 2005; Bot et al., 2010; Galametz et al., 2011; Ciesla et al., 2014) where the 500 μm flux is systematically underestimated by SED models. The sub-millimetre excess has also been observed in late-type galaxies in the DustPedia sample by Nersesian et al. (2019), who state that the excess may be due to the presence of cold dust and therefore account for a dust mass component that is currently underestimated by the CIGALE SED fitting.

I note that although the observed excess could be interpreted as background confusion in the long wavelength data, I have aimed to counteract this effect via the background subtraction methods used, and upon measuring the background emission after subtraction, I find a zero flux value in the map background.

Suggested physical causes for the excess include a very cold dust component (which would result in higher derived dust masses), temperature-dependent emissivity changes with wavelength, and the presence of free-flying grains (Ciesla et al., 2014). To test whether the excess is due to very cold (<10 K) dust, I re-fit SEDs to the data but allow the cold dust component to fluctuate between 5 and 10 K.

3.4.5.1 Introducing a Very Cold Dust Component

In an attempt to model the sub-millimetre excess seen in the 500 μm observations, I introduce a very cold dust component to the model. The cold component is allowed to fluctuate between 5 and 10 K, whereas the warmer component may

fluctuate between 15 and 30 K. The results of this test can be seen in Figures 3.21 through 3.25. Note that at distances greater than 3 pixels from the plane, the errors become increasingly problematic and the fitting technique becomes unusable. Hence we only measure the SEDs from 0-3 pixels from the plane. An example corner plot for the SED generated at 0 pixels from the plane can be seen in Figure 3.22.

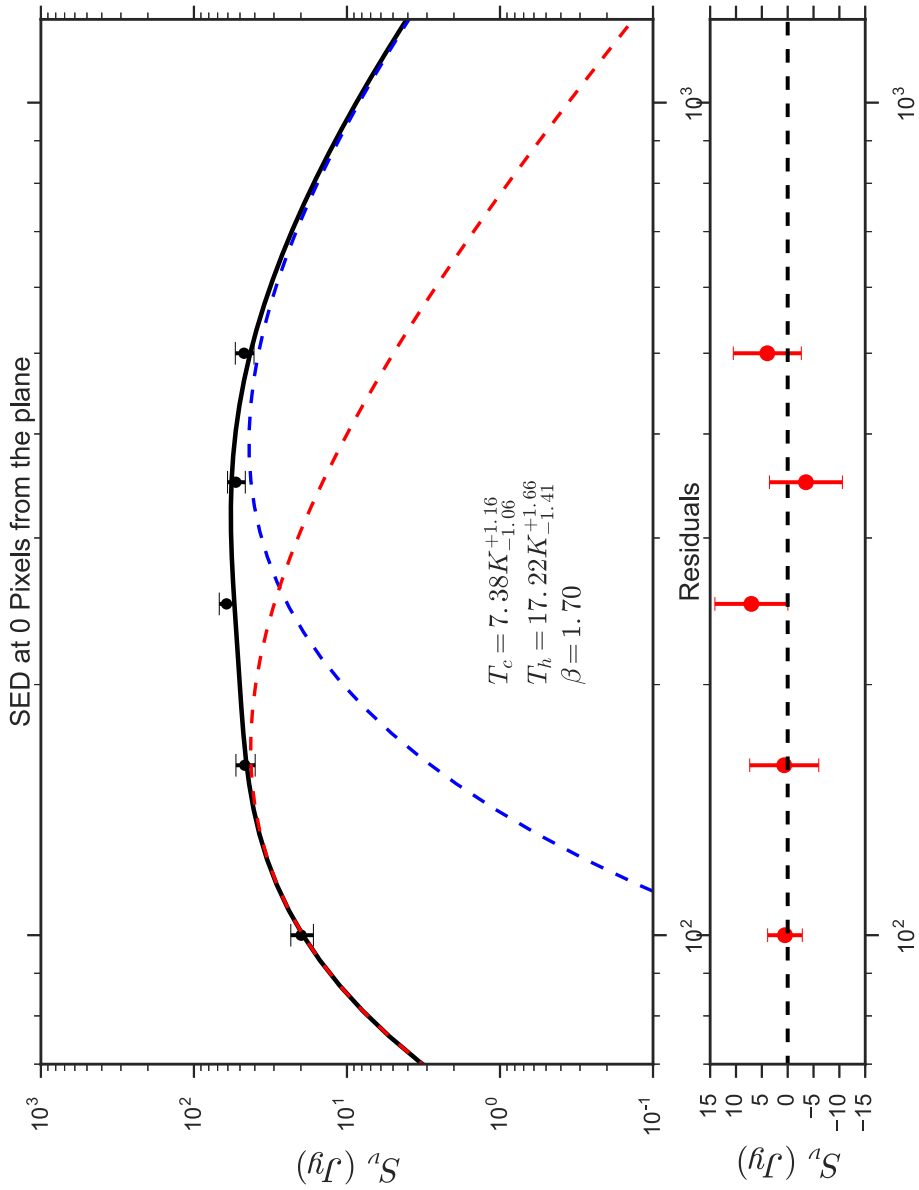

Figure 3.21: Upper: SED of the averaged maps from 100 to 500 μm at 0 pixels from the plane where the x-axis represents the wavelength and the y-axis represents the flux of the observations in Jy. Black markers indicate the data points, and the solid black line shows the fitted spectrum to the data. Lower: Residuals between the predicted model and data have been plotted as red points.

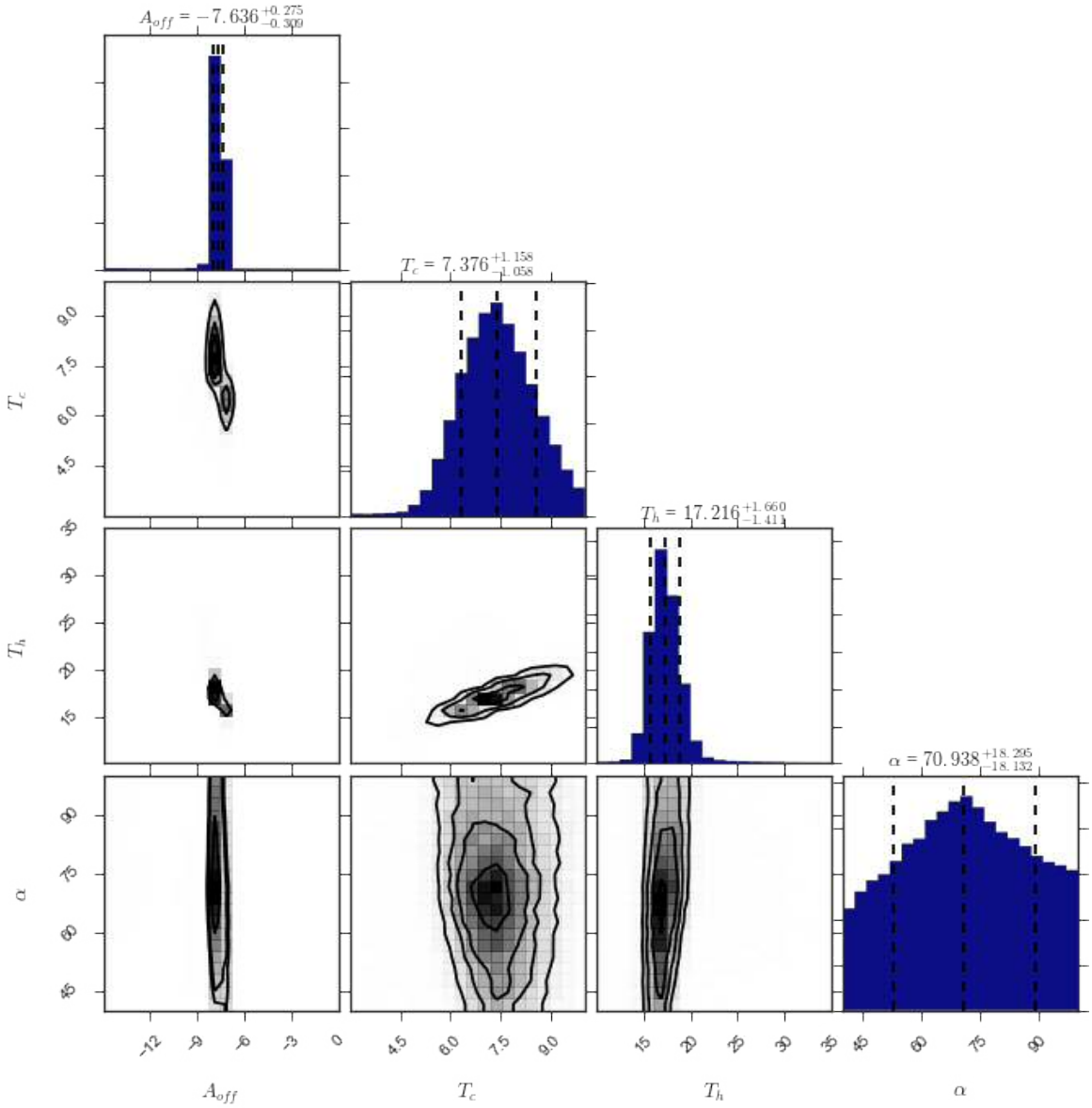

Figure 3.22: Corner plot produced by the MCMC SED fitting method for the averaged data along the plane when a very cold dust component is introduced. Contours represent the 16, 50 and 84th percentile estimates.

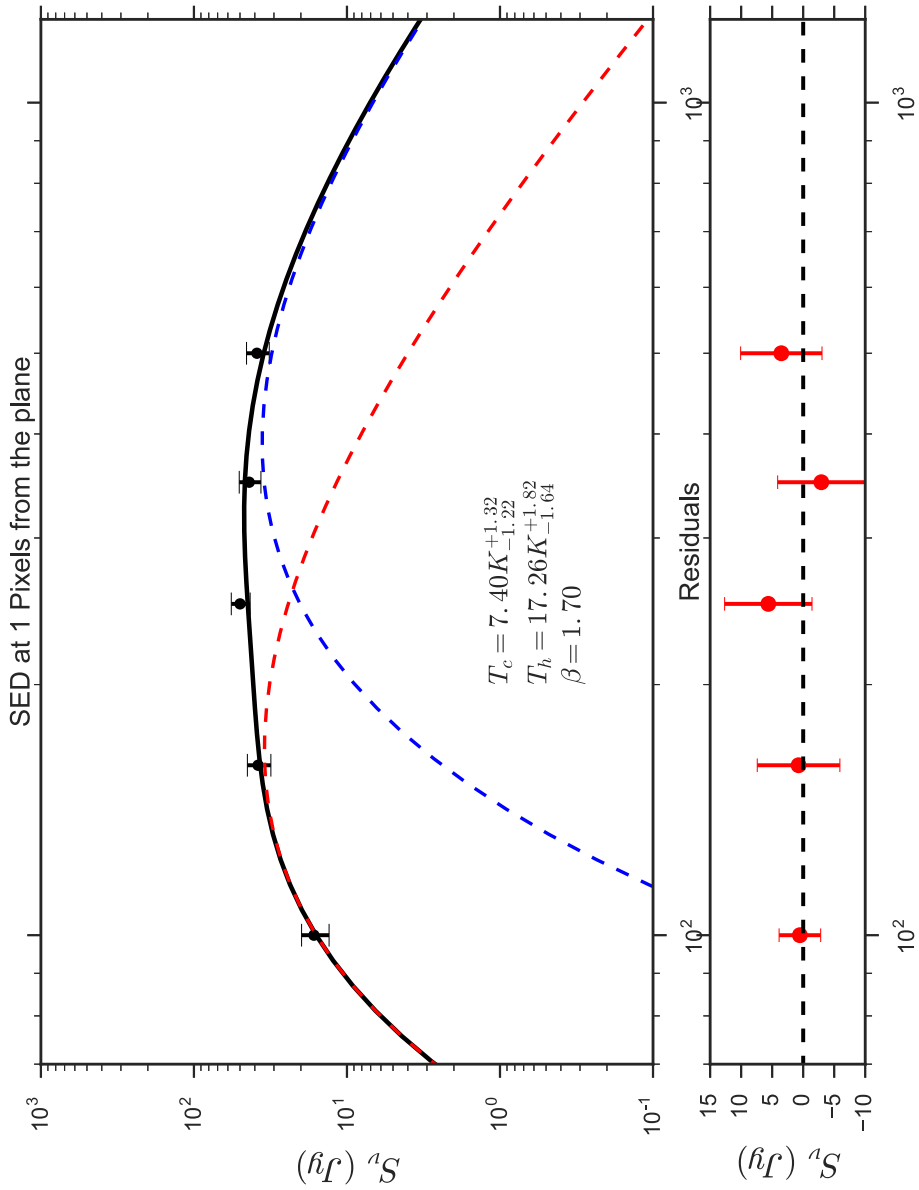

Figure 3.23: Upper: SED of the averaged maps from 100 to 500 μm at 1 pixels from the plane where the x-axis represents the wavelength and the y-axis represents the flux of the observations in Jy. Black markers indicate the data points, and the solid black line shows the fitted spectrum to the data. Lower: Residuals between the predicted model and data have been plotted as red points.

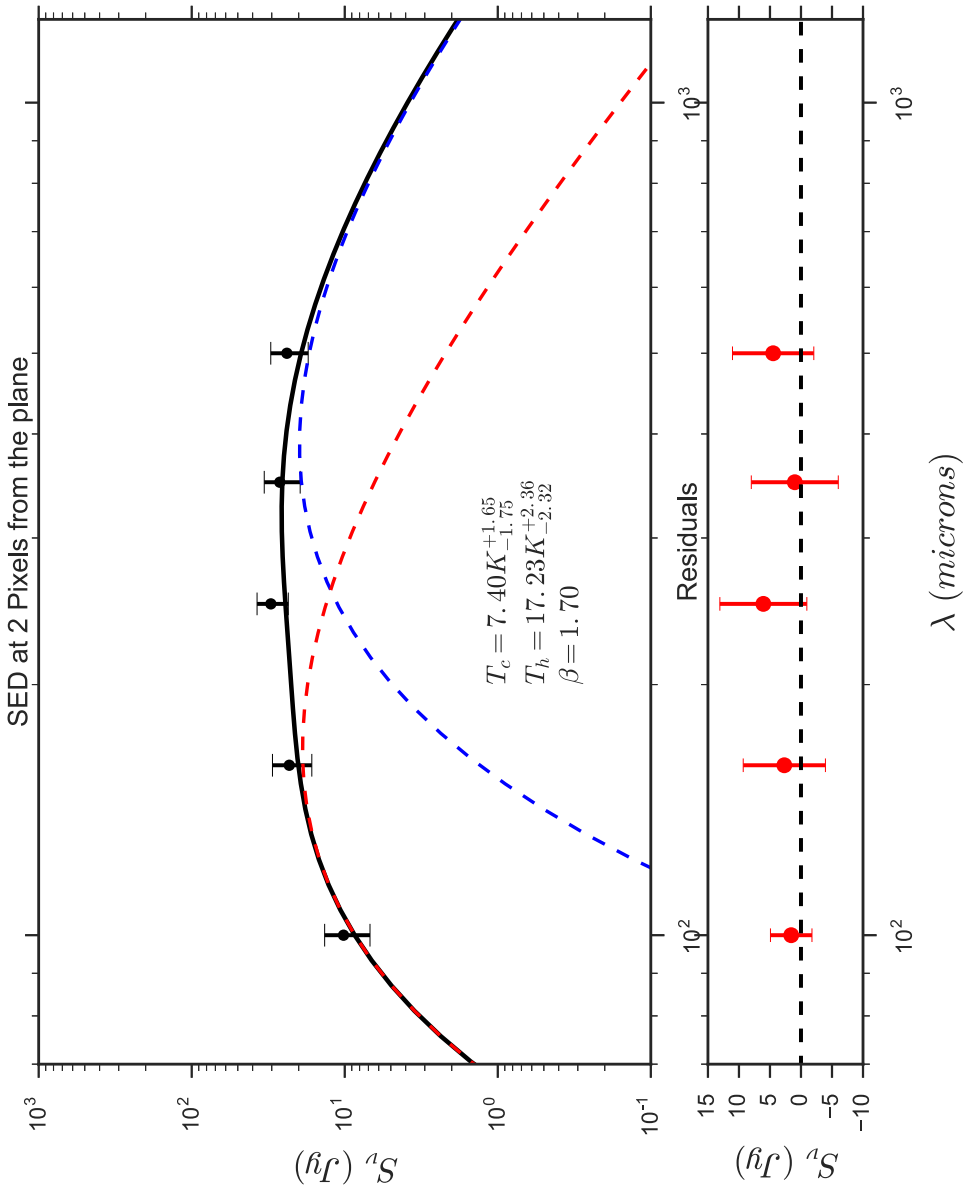

Figure 3.24: Upper: SED of the averaged maps from 100 to 500 μm at 2 pixels from the plane where the x-axis represents the wavelength and the y-axis represents the flux of the observations in Jy. Black markers indicate the data points, and the solid black line shows the fitted spectrum to the data. Lower: Residuals between the predicted model and data have been plotted as red points.

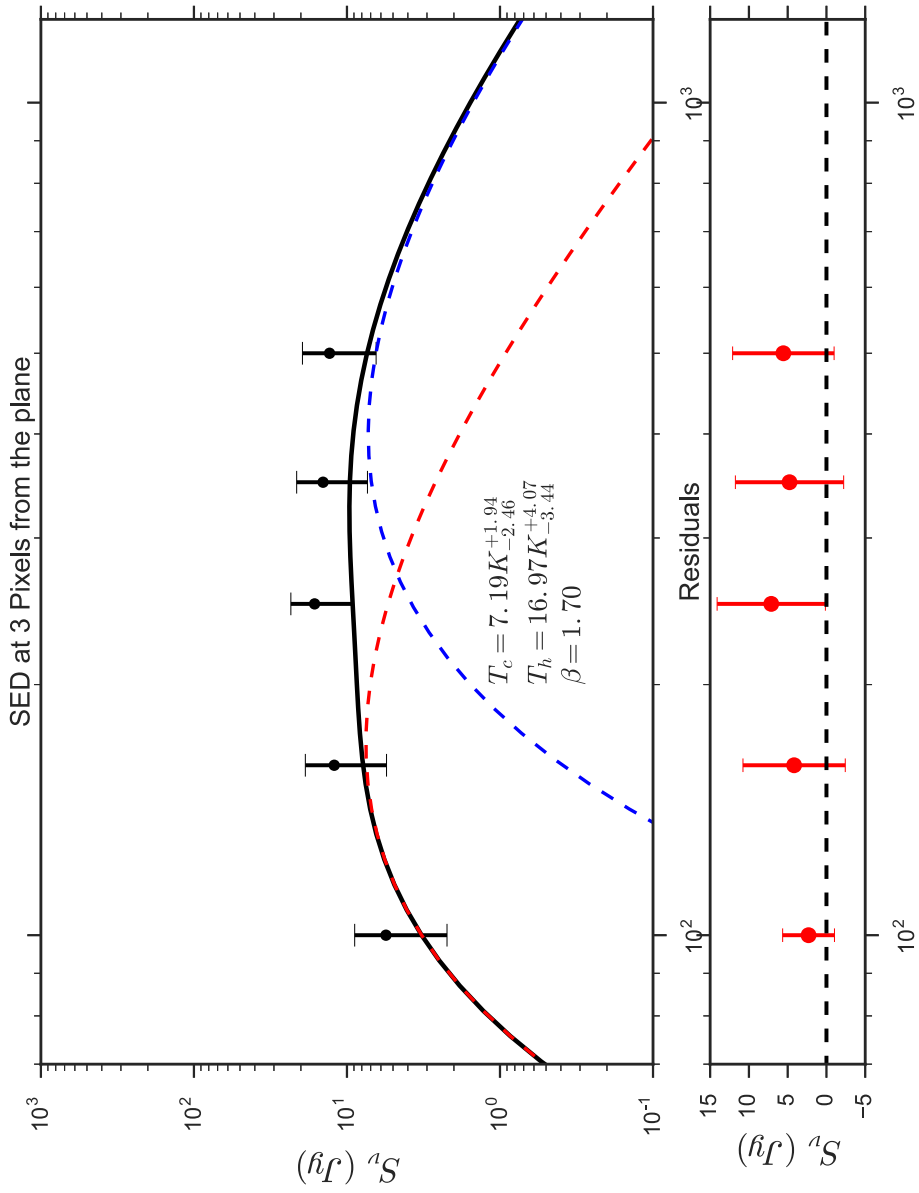

Figure 3.25: Upper: SED of the averaged maps from 100 to 500 μm at 3 pixels from the plane where the x-axis represents the wavelength and the y-axis represents the flux of the observations in Jy. Black markers indicate the data points, and the solid black line shows the fitted spectrum to the data. Lower: Residuals between the predicted model and data have been plotted as red points.

I find that introducing a very cold dust component removes the sub-millimetre excess in the SEDs. This is consistent with the work by Galametz et al. (2011) in which they find that a ~10 K component successfully accounts for the excess. We find the very cold component to range between 7.19 and 7.40 K, with a warmer dust component ranging between 16.97 and 17.26 K.

If the observed excess is in fact due to a very cold dust component, we would expect to find higher dust masses than previously estimated. To test this, I measure the total dust mass contained within all 31 galaxies out to a height of 2 pixels (~2 kpc at the mean sample distance of 18.8 Mpc) for both the two-component and the very-cold component fits.

3.4.6 Dust Masses

To estimate the dust mass, I use

$$M_d = \frac{S_\nu d^2}{\kappa_\nu B(\nu, T)}, \tag{3.3}$$

where M_d is the dust mass, S_ν is the flux density at frequency ν, d is the distance and κ_υ is the dust emissivity, where according to Clark (2015),

$$\kappa_\upsilon = \kappa_0 (\frac{\lambda_0}{\lambda \nu})^\beta, \tag{3.4}$$

where κ_0 is measured at a given frequency, λ_0. We assume the value of κ_0 to be 6.40âĂĘcm^2 g$^-$1 at 250 μm to be consistent with Nersesian et al. (2019) and therefore the THEMIS dust model. The total dust mass for each row of pixels above the plane is calculated out to a height of 3 pixels (β_d/β_s = 1). I calculate the mass at the median sample distance of 18.80 Mpc, the closest distance of 4.35 and the furthest distance of 45.08 Mpc. Masses are estimated for both the two-component and very cold dust methods outlined above.

3.4.6.1 Two-Component Model

Using equation 3.2 on the fitted spectra assuming dust temperatures greater than 10 K, we find the mass to be $9.54^{+0.90}_{-2.67} \times 10^9 M_\odot$ at the median distance of the sample. At the closest galaxy distance of 4.35 Mpc, this mass reduces to $5.11^{+0.48}_{-1.43} \times 10^8 M_\odot$ and at the furthest distance of 45.08 the mass increases to $5.48^{+2.55}_{-1.26} \times 10^{10} M_\odot$.

As part of the work carried out by Nersesian et al. (2019), they measure the dust mass for all galaxies with *Herschel* detections in the DustPedia database.

The summed values obtained for the galaxies included in this thesis equate to $6.31 \times 10^8 M_\odot$, an order of magnitude lower than the values derived from our stacked maps. They state that the current CIGALE-THEMIS fitting method underestimates the dust masses for the DustPedia sample (possibly due to the sub-millimetre excess), hence our method may have recovered some of the cold dust mass that is not detected by the THEMIS dust model. This may be due to the increased sensitivity of the averaged data in which an extended cold dust component has been discovered, that was not detected in the individual maps analysed by Nersesian et al. (2019). As the 500 μm excess is still observed in the averaged maps despite the higher dust mass, we may not have recovered the full extent of the dust mass contained within the sample.

3.4.6.2 Very Cold Dust Model

When we include a very cold dust component, the dust masses increases to $6.79^{+1.32}_{-1.72} \times 10^{11} M_\odot$ at the mean distance of 18.8 Mpc, 2 orders of magnitude greater than the first estimate. At a distance of the closest sample galaxy (4.35 Mpc), this mass reduces to $3.63^{+1.32}_{-1.70} \times 10^{10} M_\odot$ and increases at the maximum distance (45.08 Mpc) to $3.90^{+1.32}_{-1.70} \times 10^{12} M_\odot$.

The resulting dust mass is much higher in comparison to the masses obtained when the very cold component is not included. One explanation for the dust mass excess could be the presence of a very cold, extended dust distribution that has been discovered via the increased SNR of the stacked maps over the single observations. However, according to Galliano (2017), the observed 500 μm excess typically arises in diffuse regions, whereas a very cold (< 10 K) dust component would have to be contained within dense clumps. Due to the poor resolution of our observations and the stacking technique used, it is not possible to measure the excess emission on spatially resolved scales, hence we cannot decipher whether the source of excess is in diffuse or dense regions. Due to this reason, I am unable to make a reliable conclusion regarding whether the inclusion of a very cold component and increased dust masses in our fitting method provides a reliable explanation for the 500 μm excess, however the resulting cold dust mass appears un-physically high. Future work would aim to carry out a similar analysis on the gas and metal content of the galaxies in this sample to study the gas-to-dust ratio and dependency of the dust mass and sub-millimetre on metalicity.

3.5 Discussion

3.5.1 Vertical Scale Height of the Dust

The final results of the measurements of β_d/β_s at each of the 5 *Herschel* wavelengths can be seen in Table 3.2. From these values obtained via fitting the brightness profiles of the stacked galaxies, I conclude that at FIR wavelengths the scale height of the dust disk is at least equal to the scale height of the stellar disk, and extends up to at least 1.3x the stellar disk height at the longer wavelengths.

The final values are calculated as the vertical scale height measured via the brightness profile fitting of the stacked maps, above which the signal is dominated by the errors. The errors are obtained from the relative size of 1 pixel expressed in β_d/β_s, equating to the distance between two data points and therefore the lower limit of the resolution. Because all data are scaled to the resolution of the 500 μm band, the uncertainties are large in comparison to the scale heights observed.

Wavelength (μm)	β_d/β_s
100	1.0 ± 0.33
160	1.0 ± 0.33
250	1.0 ± 0.33
350	1.33 ± 0.33
500	1.33 ± 0.33

Table 3.2: Final results of the stacking technique used to measure the brightness profiles of the sample galaxies.

Previous studies of the direct detection of dust emission provide evidence for an extended vertical distribution of dust for a number of edge-on galaxies, such as NGC 891. Hughes et al. (2014) measure the dust distribution from 3.6 μm to 250 μm, and find dust out to at least β_d/β_s = 1.3 at the SPIRE 250 μm band for this galaxy, as is consistent with my results. For the same galaxy, Bocchio et al. (2016) measure the extent of the dust component out to 1.44 kpc from the plane via direct detection of the FIR emission. Our initial measurement of β_d for NGC 891 at 100 μm is 1.43 kpc in agreement with Bocchio et al. (2016). At longer wavelengths, our measurements of the dust scale height for this individual galaxy are larger, extending up to 4 kpc, although it is not clear if the scale height gradient is due to and extended cold dust distribution, and effect of the increasing PSF with wavelength, or due to an unresolved thin disk.

Compared to radiative transfer modelling of edge on galaxies, we find a more extended distribution than has been previously modelled. Studies such as Xilouris

et al. (1997, 1998, 1999); Alton et al. (2004); Bianchi (2007); Baes et al. (2010); De Looze et al. (2012) find that the ratio of stellar to dust scale heights is ~ 1/3, indicating that the stellar disk is more extended that the dust. This is contrary to our findings which show that there is an extended dust component above and below the planes of galaxies out to at least β_d/β_s = 1-1.3.

3.5.2 SED Fitting

We observe a significant excess in emission at 500 μm above that predicted by a two-component modified blackbody fit. This excess has been well documented in the literature (Galliano et al., 2003, 2005; Bot et al., 2010; Galametz et al., 2011; Ciesla et al., 2014), and its cause is as-yet unidentified. Proposed hypotheses for the excess include a very cold dust component that would yield significantly higher (and perhaps unphysical) dust masses, free-flying dust particles, and changes in the dust emissivity properties at increasing wavelengths.

I include a very-cold dust component (<10 K) in the model and find that the resulting SED provides a good fit to the data and the estimated dust mass increases by two orders of magnitude up to $6.79^{+1.32}_{-1.72} \times 10^{11} M_{\odot}$. Although the extra dust mass would account for the sub-millimetre excess observed in a large number of galaxies, the result is likely unphysical. Future work would aim to carry out the stacking analysis but for both gas, stellar and metalicity maps to probe the full content if the ISM for the sample. In any case, Casey (2012) show that as dust mass is highly dependent on temperature, it is unwise to attempt dust mass estimations when the true cause of the 500 μm excess is unaccounted for and may have a large temperature dependence in itself.

A more likely explanation for the 500 μm excess may be due to changes in β values at longer wavelengths, leading to a flattening of the sub-millimetre spectrum, and thus mimicking a cold dust component (Dupac et al., 2003). Galametz et al. (2012) showed that modelling the FIR emission with a modified blackbody with β = 1.5 can increase the dust masses up to 50% compared to when β = 2.

Due to the limited data available at wavelengths longer than 500 μm, it is difficult to properly constrain the contribution from cold dust, as there may be significant emission from free-free or synchrotron radiation that arises at longer wavelengths. Further observations at millimetre wavelengths may help to model the spectrum and better understand the contribution of dust, free-free and synchrotron emission to this region and therefore the cause of the sub-millimetre excess.

3.5.3 The Dust Energy Balance Problem

A recent study by Mosenkov et al. (2018) explores the dust energy balance problem for 7 edge-on galaxies that form the HEROES (*HERschel*Observations of Edge-on Spirals) sample. They fit radiative transfer models to optical and NIR images of the galaxies based on the THEMIS dust model, and compare their findings to the real *Herschel* observations. Their results show that the RT models underestimate the true FIR emission by a factor of 1.4 - 4, and the dust mass by 1.5 - 2 times. These results are consistent with previous studies that explore the energy balance problem (Baes et al., 2010; De Looze et al., 2012; De Geyter et al., 2015). They conclude that the cause of the discrepancy in measured emission may be due to complex dust morphologies such as spiral arms, star forming regions and an extended vertical structure.

RT modelling has not been undertaken as part of this thesis, and hence we cannot directly compare any RT model results with our findings, however we can conclude that there is a vertically extended dust component that is currently underestimated by RT models. As one of the causes of the dust energy balance problem is considered to be due to an extended dust component (Saftly et al., 2015; Mosenkov et al., 2018), there is a strong likelihood that the findings of this thesis would, in part, account for the discrepancy between RT models and the observations.

3.5.4 The Source of Extraplanar Dust

As described in Section 1.5, we generally observe two types of extraplanar dust; a filamentary structure and a more diffuse and extended structure. Due to the nature of the stacking methods used throughout this work and the relatively poor resolution achieved after convolving and resampling the data, we are unable to conclude whether the dust has a filamentary or diffuse structure. Due to the degraded resolution, our pixel scales are such that filamentary dust columns would not be resolved for the galaxies. Also, as we are averaging the observations of multiple galaxies, any dust columns that may exist would be smoothed by the summing of multiple galaxies of varying morphologies. Because of this, it can be difficult to conclude the origin of extraplanar dust and the process via which it is expelled from the galaxy via the results of this study.

3.6 Summary

For this study I utilise a sample of 31 galaxies from the DustPedia database which have been detected at the *Herschel* PACS 100 and 160 μm and SPIRE 250, 350 and 500 μm bands.

Three of the sample galaxies exhibit an excess in the measured flux above what the model predicts (see Chapter 2.8.4). Comparing this result to the literature reveals that for one of these galaxies, NGC 4222, the vertical profile of the dust is observed to be extended (to a distance of 4 kpc) and provides evidence for a thick dust disk. As we have evidence that our initial values of β_d may be underestimating the true scale height of dust, it may be possible that there is an extended dust distribution in more of the sample galaxies that is undetected in the individual observations.

To test this, all galaxy maps were stacked at each of the 5 *Herschel* wavelengths to increase the SNR of the data, with the aim of detecting low surface brightness dust emission in the haloes. Brightness profiles of the stacked maps are plotted, and compared against WISE 3.4 μm data which traces the oldest, most extended distribution of stars. By comparing the extent of FIR emission to stellar emission, it is possible to measure the vertical scale height of the dust versus the stars, β_d/β_s. We find that at 100-250 μm, the dust scale height is consistent with the stars. At 350 and 500 μm, the dust scale height is greater than that of the stars by at least a factor of 1.3. I note that as the WISE data is convolved to match the 500 μm resolution, this result represents the *minimum* value of β_d/β_s that could be measured via this method. It is possible, and highly likely, that the actual extent of this ratio is much greater.

The temperature and mass of dust is measured via SED fitting of the data at intervals above the plane. Due to the large errors at increasing scale height, I was unable to accurately fit an SED above 3 pixels from the plane. This means that we are unable to obtain likely temperature and mass values above this distance. The dust mass of all galaxies in the sample is found to be $9.54^{+0.90}_{-2.67} \times 10^9 M_\odot$ when assuming a two-temperature modified blackbody, and increases to $6.79^{+1.32}_{-1.72} \times 10^{11} M_\odot$ when a very cold (<10 K) dust component is introduced.

These results overall indicate the presence of an extended dust component that is undetected by direct-detection of the FIR emission in the individual observations. By stacking the data, I have increased the sensitivity and find an extended distribution of dust out to vertical scale heights of *at least* 1-1.3 times β_d/β_s.

CHAPTER 4

DUST EMSSION FROM NEARBY GALAXIES WITH NIKA2

The results presented in Chapters 2 and 3 provide evidence of a vertically extended dust component, the mass of which are currently underestimated by dust models such as THEMIS. The fitted SEDs of the averaged maps reveal an excess of emission at the longer wavelength 500 μm *Herschel* band than is expected. The discovery of this dust component has major implications for our dust evolution models, however there is very little data available at wavelengths longer than 500 μm with which to explore this region of the spectrum. There are few general-purpose platforms such as NIKA2 currently available to astronomers. Detectors such as Artemis (Revéret et al., 2014), SCUBA2 (Holland et al., 2013) on JCMT, and MUSTANG2 (Dicker et al., 2014) on the Green Bank Telescope are all based on bolometric system principles. Kinetic Inductance Detector (KID) technology has demonstrated its competitiveness particularly in terms of spacial resolution, hence NIKA2, a KID-based detector, may open a new window to high-resolution millimetre astronomy.

In this chapter I present the first high resolution 1.2 and 2 mm observations for two nearby galaxies; NGC 891 which is edge-on, and M99 (NGC 4254) which is face-on. These observations were obtained as part of the NIKA2 Nearby Galaxies Large Programme, with the aim of using these longer wavelength observations to characterise the dust emission in the mm-region of the spectrum.

The New IRAM Kid Arrays 2 (NIKA2) is composed of three dual-band Kinetic Inductance Detectors (KIDs) on the IRAM 30 m telescope with observing wavelengths of 1.2 and 2 mm, and a 6.5′ field of view (FOV). The telescope itself

is well suited to host high-resolution spectroscopes and broad-band continuum photometric instruments which are used to detect very faint sources. The 30 m dish has a diffraction limited resolution of 10" and 17" for the 1.2 and 2 mm bands respectively. To sample the 6.5′ FOV, a photometric camera requires arrays containing ~10^3 pixels with an intrinsic noise below or comparable to the photon noise expected at the dish. Only recently has this been made possible with the NIKA2 detector. The instrument is a development of the original NIKA camera, which consisted of 365 pixels over the two wavelength bands, and its success has lead to the approval of the NIKA2 camera. The upgrade to the original instrument includes replacement and modification of the previous mirrors, and the addition of two new mirrors. The band splitting is carried out by a dichroic[5], and the 1.2 mm light is further split by a wire-grid polarizer allowing polarization measurements to be taken.

NIKA2 is currently undergoing its commissioning phase, whereby it is undertaking observations as science verification for 5 Large Programmes, which aim to utilise the instrument for a number of science topics ranging from high-redshift studies to observing our own galactic plane. For our Nearby Galaxies Large Programme, we aim to study a sample of nearby galaxies to answer three key science topics. This project is described in further detail in Section 4.1. The sample selection is described in Section 4.1.4, and preliminary observations and analysis for NGC891 and M99 are presented in Sections 4.2 and 4.2.2 respectively. We then discuss the implications of the findings and plans for future work in Section 4.4.

4.1 Interpreting the Millimetre Emission from Galaxies with IRAM and NIKA2 (IMEGIN)

The IMEGIN Large Programme has been granted 200 hours of guaranteed observing time with the NIKA2 detector. NIKA2 observations at 1.2 and 2 mm have the potential to measure the dust thermal spectrum in this little explored region of the SED, as long as we can also remove the emission from other physical processes. At wavelengths beyond 500 μm we expect, to varying degrees, synchrotron emission due to charged particles moving in the magnetic field of the galaxy and free-free emission from ionised particles primarily associated with star forming regions. The relative contributions of the three physical processes to the NIKA2 flux density in these bands will vary with galaxy morphology and position in an individual

[5] A colour filter that passes some wavelengths and reflects others.

galaxy, and for this reason spatial resolution is a key factor to improve our understanding. In addition, all three of the emission mechanisms that contribute to the radio-infrared spectrum (radio continuum, free-free and thermal dust) offer the opportunity to measure the star formation rate in different ways, resulting from different physical processes.

To make full use of the high-resolution millimetre observations that are possible with NIKA2, the IMEGIN project has three key science goals with which we hope to explore the long wavelength emission. These science themes are outlined in Sections 4.1.1 through 4.1.3.

4.1.1 Dust Emissivity

The dust properties of the local universe will be explored by combining the NIKA2 observations with those from *Herschel* at shorter wavelengths. *Herschel* has given us a new view of the cold dust reservoir across individual galaxies and over a wide variety of galaxy types (Galametz et al., 2012; Davies et al., 2013) (see Chapter 2.1). It is the cold dust component (≤30 K) that carries most of the dust mass in galaxies, making it a major contributor to the sub-mm/mm spectrum. Observations at 1.2 and 2 mm by NIKA2 are critical for determining a more accurate and reliable dust mass by enabling us to identify a distinct cold (≤15 K) dust component or by looking for changes in the dust emissivity properties.

Excess above our usual dust SED models can, at around 500 μm to 1 mm, leave us with an ambiguity in quantifying dust masses (e.g. Galliano et al. (2003, 2005); Galametz et al. (2011); Rémy-Ruyer et al. (2013); Kirkpatrick et al. (2014); Hunt et al. (2014)). With the NIKA2 data we will be able to determine the strength of any sub-mm excess or deficit within galaxies and across a wide range of galaxy types. This can be correlated with local conditions and so provide input into models designed to determine its origin. Some explanations for any excess/deficit include: a very cold dust component (e.g. Galliano et al. (2003)); non-dust contamination (molecules or free-free emission); spinning grains (e.g. Draine and Lazarian (1998); Bot et al. (2010); Ade et al. (2011)) and varying dust optical properties (e.g. Meny et al. (2007); Jones et al. (2013)). For example, in the small and large Magellanic Clouds, Bot et al. (2010) found excess emission at 1.9 mm and 2.2 mm respectively. We will be able to consider this issue over a much broader range of galaxies and over very different environments within galaxies.

Accurate SED modelling is also required to address the issue of how dust is heated locally throughout galaxies, which is not straightforward as the heating sources may not be spatially coincident with the dust (e.g. Lu and Helou (2008);

Bendo et al. (2012)). With spatially resolved observations, it is possible to compare the local heating with the local emission. By studying local galactic properties, the galaxy morphology can also be considered including its effect on dust heating, i.e. how much of the various components of the dust is heated by evolved stars or how much is heated by radiation from ionizing stars. While some work on this has been done on integrated galaxy scales, with NIKA2 we will be able to consider these issues over a much broader range of galaxies and over very different environments within galaxies.

Critical to the above is our knowledge of dust emissivity. Not having an accurate value for the emissivity throughout the MIR to FIR/sub-mm region has an effect on extinction at every wavelength. Again, it is almost certainly local conditions such as the temperature, density, and dust evolution (grain composition, growth and/or destruction) that regulate dust emissivity within galaxies. Measurements of long-wavelength thermal dust emission are an important factor when constraining the value of the emissivity slope (β) for SED modelling. A more accurate value of β will lead to better dust and SED models and therefore a greater understanding of the role that dust plays in galaxy evolution.

While *Herschel* left us with new insights into the cold dust characteristics of galaxies, it has also left us with some questions due to the long wavelength limit of 500 μm. These issues can be addressed by using the NIKA2 observations.

4.1.2 Disentangling Spatially Resolved Galaxy SEDs

To obtain an accurate measure of the thermal dust emission at 1.2 and particularly 2 mm, measurements of the synchrotron and free-free components are required. At wavelengths greater than 2 mm, we expect the spectrum to be dominated by the synchrotron component. As such, data at these longer wavelengths has been assembled as part of the IMEGIN project to enable us to model the synchrotron component (see Section 4.1.4 below). Once combined with the *Herschel* and NIKA2 data, this will enable us to decompose the far-infrared to radio SED into its three constituents parts using the procedure described in Peel et al. (2011). By carrying out pixel-by-pixel IR to radio SED modelling and utilising previously derived independent calibrations, we can measure the local star formation rate in three ways using the far-infrared, radio continuum and free-free emission and compare with values obtained from Hα measurements (which are available for all galaxies in the sample). The ratio of synchrotron to free-free emission can be used as a measure of the diffuse timescale of electrons into the ISM. These different SFR estimators measure recent, although different, star formation timescales.

4.1.3 How Does the Gas-to-Dust Mass Ratio (G/D) Evolve?

All the galaxies in the IMEGIN are also part of HERACLES (Leroy et al., 2009), and all but six are included within the KINGFISH sample. Hence we are able to combine sub-mm to radio data with maps of the atomic and molecular gas (HI, CO and CII). These data will provide measures of the gas-to-dust ratio, both globally and its variation with spatial position and local conditions. Gas-to-dust mass ratio (G/D) is also an important input into chemical evolution models (Groves et al., 2014). While early work in this field suggests a linear relationship between the G/D ratio and metallicity (Boselli et al., 2002; Leroy et al., 2009), a recent survey of 100 galaxies over 2 dex in metallicity range shows that the evolution of the G/D ratio appears to be non-linear and governed either by the dust production, dominated by condensation of metals in stars, or the growth of dust in the ISM (possibly both) (Rémy-Ruyer et al., 2014; De Vis et al., 2017; De Vis, P. et al., 2019). This will again depend on local physical conditions and the galactic star formation and dust processing history (Zhukovska, 2014). One goal of the IMEGIN project is to investigate the dependence of G/D with metallicity using state-of-the-art LBT/MODS measurements of the gas phase metallicity from the CHAOS survey (PI: Croxall), which finely samples the disk of 13 face-on galaxies in our sample. For the rest of our target galaxies, we aim to investigate whether there are covarying radial variations in G/D and metallicity using the metallicity gradients provided by the Spitzer Space Telescope (SINGS) obtained by Moustakas et al. (2010).

4.1.4 IMEGIN Sample Selection

To carry out the IMEGIN science goals, I have selected 39 galaxies that are accessible from IRAM and are well-matched to other recent Legacy Programmes. The galaxies are selected according to the following criteria:
1. Full MIR to sub-millimetre continuum wavelength coverage to constrain accurate dust SED models.
2. Longer radio observations to constrain the non-dust components.
3. CO and HI measurements to obtain G/D ratio measurements.
4. Distances less than 30 Mpc to ensure adequate linear resolution scales to fulfil the science aims (30 Mpc equates to 2.5 kpc and 1.5 kpc resolution at NIKA2 1.2 and 2 mm bands respectively).

The HERA CO-Line Extragalactic Survey (HERACLES) is comprised of 48 nearby galaxies that have high quality resolved CO and HI observations (Leroy

et al., 2009). From the HERACLES sample, 38 galaxies have been selected that satisfy requirements 1 to 4 above and hence are the target sample for this NIKA2 large programme (see Table 4.1). I have also included NGC 891 in the sample, which does not form part of HERACLES, but has been detected and resolved in both CO and HI as well as the other bands. As NGC 891 is also included in the analysis outlined in Chapters 2 and 3 and has been well studied in the literature, it provides a useful comparison between the archival data and the new NIKA2 observations.

The sample galaxies range in stellar mass from $\log(M_\star)$ = 8.18 to 11.06 $M_\odot$, star formation rate from (log(SFR)) = -1.09 to 1.04 $M_\odot yr^{-1}$ and have morphologies of Sa to Irr. The average angular size of the sample galaxies is 8.6 arcmin, only slightly larger than the 6.5 arcmin field-of-view of NIKA2.

Each galaxy in the sample has been detected in all *Herschel* SPIRE (250, 350 and 500 μm) and PACS (70, 100 and 160 μm) bands, as well as all 4 WISE (3.4-22 μm) bands. Archival data is available for all galaxies at the *Spitzer* MIPS wavebands of 24, 70 and 160 μm and most have *Spitzer* IRS and *IRAC* detections (3.6-39.9 μm).

Each galaxy has extensive UV and optical data available, as well as Planck detections extending from 343 μ to 1.38 μ for most targets, which will allow us to obtain full coverage of the global SEDs.

As well as the sub-mm availability, each galaxy has been detected with the VLA at 20 cm and deep (6hr) radio continuum observations from e-MERLIN at both 6 and 20 cm are available for all but 11 of the targets.

Given the 200 hours observing time limit of the programme, I have prioritised each galaxy based on the quality of radio data available, range of right ascensions, SFR range and mass range. Each galaxy was ranked as A (high priority), B, or C (low priority), and only A-priority galaxies had their required integration times calculated. Further details of the sample galaxies including their priority rank are given in Table 4.1.

Table 4.1: The Nearby Galaxies Large Programme Sample. Unless otherwise stated all M_* values are taken from Skibba et al. (2011) and all other values from Leroy et al. (2009). † = Lee et al. (2009). * = Davies et al. (2012), ** = Munoz-Mateos et al. (2007), ^{F} = Fischer et al. (2011), ^{S} = Schmidt et al. (1993).

Name	**RA (J2000)**	**Dec (J2000)**	**Hubble Type**	**D_{25} (arcmin)**	**Distance (Mpc)**	**i (°)**	**log M_* ($M_\odot$)**	**log SFR ($M_\odot$ yr^{-1})**	**Rank**	**Integration Time (hrs)**
NGC 0337	00 59 50.1	-07 34 41	SBd	2.9 × 1.8	20.971 ± 2.466	52	9.47 ± 0.22	0.11*	A	15.4
NGC 0628	01 36 41.7	+15 47 01	SAc	10.5 × 9.5	9.006 ± 1.140	25	9.57 ± 0.13	0.3†	B	
NGC 0891	02 22 33.4	+42 20 57	SAb	13.3 × 2.5	9.963 ± 1.377	89	-	0.58	A	0.22
NGC 0925	02 27 16.9	+33 34 45	SABd	10.5 × 5.9	8.583 ± 1.472	66	9.48 ± 0.14	0.42†	A	15.4
NGC 2146	06 18 37.7	+78 21 25	SBab pec	6.0 × 3.4	21.883 ± 4.832	57	10.30 ± 0.13	0.90*	A	2.7
NGC 2366	07 28 54.6	+69 12 57	IBm	8.1 × 3.3	3.338 ± 0.865	67^{S}	8.19 ± 0.06*	-1.09†	C	
NGC 2403	07 36 51.4	+65 36 09	SABcd	21.9 × 12.3	3.487 ± 0.656	56**	9.43^{F}	0.01†	B	
NGC 2798	09 17 22.8	+41 59 59	SBa pec	2.6 × 1.0	26.371 ± 5.611	68	10.04 ± 0.13	0.53*	B/C	
NGC 2841	09 22 02.6	+50 58 35	SAb	8.1 × 3.5	17.620 ± 4.980	74	10.17 ± 0.14	0.70	A	11.9
NGC 2976	09 47 15.4	+67 54 59	SAc	5.9 × 2.7	3.955 ± 0.942	59^{S}	9.13 ± 0.09*	-0.76†	A	10.4
NGC 3034	09 55 52.7	+69 40 46	I0	11.2 × 4.3	3.992 ± 0.721	84^{S}	10.04^{F}	0.75†	B	
NGC 3049	09 54 49.5	+09 16 16	SBab	2.1 × 1.1	24.843 ± 7.208	61	8.58 ± 0.04	-0.22	C	
NGC 3077	10 03 19.1	+68 44 02	I0 pec	5.4 × 4.5	3.611 ± 0.555	33	9.29 ± 0.07	-1.00	B/C	
NGC 3184	10 18 16.8	+41 25 27	SABcd	7.4 × 6.9	12.037 ± 2.552	16	9.24 ± 0.17	0.08	A	15.4
NGC 3190	10 18 05.6	+21 49 56	SAap	4.4 × 1.5	24.500 ± 3.028	73	10.03 ± 0.14	-1.00	C	
NGC 3198	10 19 54.9	+45 32 59	SBc	8.5 × 3.3	13.972 ± 1.720	72	9.85 ± 0.11	-0.05	A	11.5
NGC 3351	10 43 57.7	+11 42 14	SBb	3.1 × 2.9	10.085 ± 1.058	48**	10.28 ± 0.12	0.20†	B	
NGC 3521	11 05 48.6	-00 02 09	SABbc	11.0 × 5.1	11.839 ± 3.215	73	10.78 ± 0.12	0.28	A	6.1

Table 4.1: The Nearby Galaxies Large Programme Sample. Unless otherwise stated all M_* values are taken from Skibba et al. (2011) and all other values from Leroy et al. (2009). † = Lee et al. (2009). * = Davies et al. (2012), ** = Munoz-Mateos et al. (2007), ^{F} = Fischer et al. (2011), ^{S} = Schmidt et al. (1993).

Name	**RA (J2000)**	**Dec (J2000)**	**Hubble Type**	**D_{25} (arcmin)**	**Distance (Mpc)**	**i (°)**	**log M_* ($M_\odot$)**	**log SFR ($M_\odot$ yr^{-1})**	**Rank**	**Integration Time (hrs)**
NGC 3627	11 20 14.9	+12 59 30	SABb	9.1 × 4.2	9.793 ± 1.897	62	10.57 ± 0.13	0.69†	A	2.5
NGC 3938	11 52 49.4	+44 07 15	SAc	5.4 × 4.9	19.800 ± 2.746	25	9.12 ± 0.04	0.08	A	14.4
NGC 4214	12 15 39.2	+36 19 37	Irr	8.5 × 6.6	3.323 ± 0.921	38^{S}	8.65 ± 0.04*	-0.65†	B	
NGC 4236	12 16 42.1	+69 27 45	SBdm	21.9 × 7.2	3.770 ± 1.236	72	8.18 ± 0.08	-0.55†	B/C	
NGC 4254	12 18 49.6	+14 24 59	SAc	5.4 × 4.7	15.425 ± 1.537	29	9.61 ± 0.15	1.04	A	4.2
NGC 4321	12 22 54.8	+15 49 19	SABbc	7.4 × 6.3	16.558 ± 3.088	32	10.36 ± 0.11	0.74	A	5.2
NGC 4536	12 34 27.0	+02 11 17	SABbc	7.6 × 3.2	15.305 ± 2.677	67	9.49 ± 0.11	0.57	B	
NGC 4559	12 35 57.6	+27 57 36	SABbc	10.7 × 4.4	8.915 ± 2.460	66	8.93 ± 0.20	-0.40*	A	11.4
NGC 4569	12 36 49.8	+13 09 47	SABab	9.5 × 4.4	12.277 ± 3.363	64	10.38 ± 0.12	0.28	A	13.6
NGC 4579	12 37 43.5	+11 49 05	SABb	5.9 × 4.7	19.786 ± 2.799	37**	9.96 ± 0.23	0.30	B	
NGC 4594	12 39 59.4	-11 37 23	SAa	8.7 × 3.5	11.118 ± 3.904	69	11.06 ± 0.12	-0.30†	B	
NGC 4625	12 41 52.7	+41 16 26	SABm	1.3 × 1.2	8.200	33**	8.72 ± 0.14	-0.78†	A	11.9
NGC 4631	12 42 08.0	+32 32 29	SBd	15.5 × 2.7	5.829 ± 1.499	83	9.76 ± 0.14	0.72†	C	
NGC 4725	12 50 26.6	+25 30 03	SABab	10.7 × 7.6	13.638 ± 2.613	45	10.58 ± 0.12	-0.4*	A	3.5
NGC 4736	12 50 53.0	+41 07 14	SAab	11.2 × 9.1	5.152 ± 0.828	37**	10.34 ± 0.13	0.07†	A	15.4
NGC 5055	13 15 49.3	+41 07 14	SAbc	12.6 × 7.2	8.011 ± 1.772	59	10.76 ± 0.12	0.48†	A	15.4
NGC 5194	13 29 52.7	+47 11 43	SABbc	11.2 × 6.9	7.898 ± 1.230	53**	10.93^{F}	0.88†	B	
NGC 5474	14 05 01.6	+53 39 44	SAcd	4.8 × 4.3	5.948 ± 0.968	27**	8.70± 0.11	-0.52†	A	4.5

Table 4.1: The Nearby Galaxies Large Programme Sample. Unless otherwise stated all M_* values are taken from Skibba et al. (2011) and all other values from Leroy et al. (2009). † = Lee et al. (2009). * = Davies et al. (2012), ** = Munoz-Mateos et al. (2007), ^{F} = Fischer et al. (2011), ^{S} = Schmidt et al. (1993).

Name	**RA (J2000)**	**Dec (J2000)**	**Hubble Type**	**D_{25} (arcmin)**	**Distance (Mpc)**	i (°)	**log M_* ($M_\odot$)**	**log SFR ($M_\odot$ yr^{-1})**	**Rank**	**Integration Time (hrs)**
NGC 5713	14 40 11.5	-00 17 20	SABbc	2.8 × 2.5	21.411 ± 5.310	27**	10.07 ± 0.11	0.40*	B	
NGC 6946	20 34 52.3	+60 09 14	SABcd	11.5 × 9.8	5.620 ± 1.626	33	9.96 ± 0.40	0.34	A	3.9
NGC 7331	22 37 04.0	+34 24 56	SAb	10.5 × 3.7	14.276 ± 2.189	76	10.58 ± 0.12	0.62	A	4.1

4.1.5 Observing Strategy

We predicted the dust emission from each 'A' priority source at 1 and 2 mm by reprojecting 250 μm *Herschel* SPIRE observations to NIKA2 pixel sizes, and estimating the flux in each pixel assuming modified blackbody emission, using conservative values of β = 2 and T = 17K. An 'ideal' target sensitivity was calculated for each galaxy by finding the depth required for resolved detection with SNR>5 at 1 mm out to 1/3 of the optical D25. However, as we intended to observe all 22 priority A galaxies during the guaranteed 200 hours observing time, we do not expect to observe deeper than a 'floor' sensitivity of 0.625 mJy/beam at 1 mm. This floor sensitivity applies to half our targets, and for these we may not achieve high-SNR detections out to the full 1/3 optical D25, but we still expect strong global detections and some degree of good-SNR resolved detection. Also, note that we do not incorporate non-thermal emission into our flux predictions; as such, all of our predicted fluxes, particularly at 2 mm, should represent lower limits.

Table 4.2 shows the expected flux that should be obtained from the high priority galaxies as well as the 'floor' sensitivity we hope to achieve and Figure 4.1 shows an example of two predicted maps at 1.2 mm for the galaxies NGC 3521 and NGC 5194.

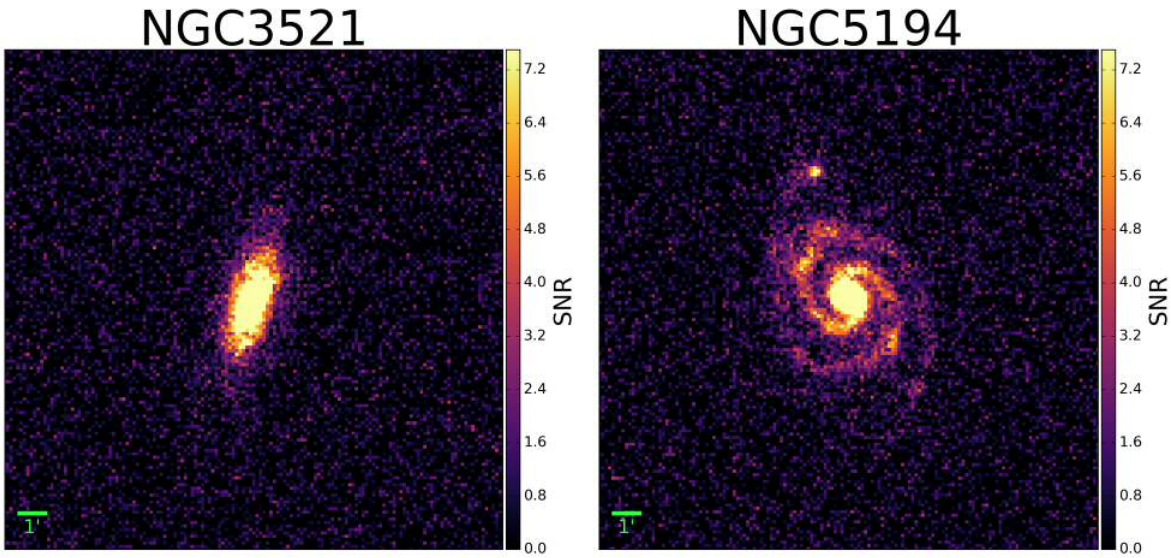

Figure 4.1: Predicted NIKA2 maps of the sample galaxies NGC 3521 and NGC 5194 at 1.2 mm. The green bar represents the angular scale of 1 arcminute.

Galaxy Name	Id	1.2 mm Flux	1.2mm RMS	2mm Flux	2mm RMS
NGC 0628	1	2.77	0.65	0.83	0.36
NGC 0891	2	51.72	4.1	15.11	2.25
NGC 0925	3	2.26	0.65	0.69	0.36
NGC 2146	4	82.75	1.26	24.52	0.69
NGC 2841	5	2.81	0.65	0.9	0.36
NGC 2976	6	6.86	0.65	2.17	0.36
NGC 3184	7	3.36	0.65	0.98	0.36
NGC 3198	8	4.33	0.65	1.33	0.36
NGC 3521	9	12.76	0.94	4.08	0.52
NGC 3627	10	19.24	1.38	5.6	0.76
NGC 3938	11	5.96	0.65	2.91	0.36
NGC 4254	12	12.78	1.08	4.07	0.59
NGC 4321	13	16.77	1.04	5.31	0.57
NGC 4536	14	24.39	0.65	7.48	0.36
NGC 4559	15	3.35	0.65	1.07	0.36
NGC 4631	16	28.16	1.05	8.55	0.58
NGC 4725	17	3.18	0.65	0.92	0.36
NGC 4736	18	11.26	0.65	3.4	0.36
NGC 5194	19	22.41	1.11	7.02	0.61
NGC 6946	20	47.49	1.2	14.74	0.66
NGC 7331	21	16.81	1.04	5.29	0.57
NGC 4954	22	4.13	0.65	1.33	0.36

Table 4.2: Expected flux densities of the IMEGIN sample galaxies at 1.2 and 2 mm in mJy/beam, as well as the required RMS (root mean square) sensitivity for each galaxy in mJy/beam.

4.1.6 Delays to the Project

I have undertaken proprietary work for this project with an observing start date of late-2016 in mind. The work involved writing and submitting the observing proposal, generating the sample, obtaining archival data, predicting the NIKA2 fluxes and maps, and calculating the observing time needed for each map to achieve the floor RMS. Unfortunately the IMEGIN project was delayed by the NIKA2 consortium and observations for the Large Programme will not begin until late-2019.

During the commissioning phase for the detector however, we submitted two IMEGIN pilot proposals for the galaxies NGC 891 (edge-on) and NGC 4254 (or M99, face-on) which were accepted. These galaxies were chosen due to their orientations. The edge-on galaxy will provide us with measures of the cold dust, free-free and synchrotron emission above and below the plane of the galaxy which can be combined with the work in Chapters 2 and 3 to better constrain the excess

dust emission that we observe in our sample. A face-on galaxy was chosen to gain a measure of these emission processes at a resolved scale in morphological features of a spiral galaxy, such as the central bulge, spiral arms and outer regions.

Observations and analysis of the two preliminary galaxies, NGC 891 and M99, can be seen in Sections 4.2 and 4.2.2 respectively.

4.2 Preliminary Observations of NGC 891 and M99

4.2.1 NGC 891 - A Nearby Edge-On Galaxy

Edge-on spiral galaxies are excellent candidates with which to study stellar, gaseous and dusty regions of nearby galaxies. This is due to their high surface brightness, which enables them to be better detected in infrared observations than lower surface brightness, face-on galaxies.

NGC 891 is an edge-on spiral galaxy with an inclination angle of 89° (consistent with the inclination measured in Chapter 2). With its morphological type classed as SA(s)b and a rotational velocity of 225 km/s, the physical characteristics are considered similar to our own galaxy and provide excellent means with which to study stars, gas and dust in spiral disks. Table 4.3 shows some other basic properties of NGC 891 and Figure 4.2 shows an optical Digital Sky Survey 2 (DSS2) image of the galaxy.

Property	**Value**
RA (J2000)	2h 22m 33.0s
Dec (J2000)	+42d 20′ 57.2"
Morphology	SA(s)b
Distance	9.6 Mpc
Major Axis	13.5′
Minor Axis	2.5"
Inclination Angle	89°
Rotational Velocity	225 km/s
Mass	1.4×10^{11} $M_\odot$
Star Formation Rate	3.8 $M_\odot$/yr
Major Axis Angle	22.5°

Table 4.3: The basic properties of the edge-on spiral NGC 891 (Hughes et al., 2014).

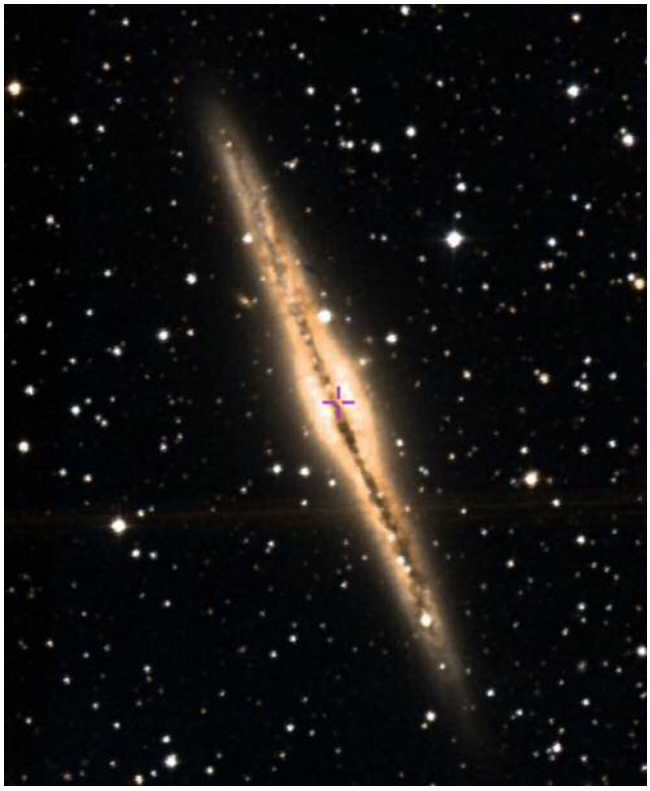

Figure 4.2: Optical image of NGC 891 from DSS2.

The stellar content of NGC 891 appears to be relatively symmetric along the galactic plane, while the HI gas distribution shows a slight north-south asymmetry in both disk and halo thickness, extending up to 22 kpc above the plane. H_2 is often traced from CO observations, and in this particular case is found in a much narrower disk with a thickness of ~400 pc, although traces of H_2 are seen in the halo up to 1.4 kpc above the plane. Hα observations are a useful tool to trace ionized gas and therefore study star formation characteristics of galaxies. In NGC 891, Hα detections show that ionized gas is more prominent and extended in the z-plane on the northern side of the galaxy than on the southern side. The cause of the north-south asymmetries is as-yet unknown, although recent theories suggest that it could be due to either higher star formation rates in the north, or higher attenuation by dust in the spiral arms along the line of sight through the disk. By observing the cold dust (~ 15K) properties of the galaxy, it may be possible to determine a solution to this problem (Hughes et al., 2014).

As part of the comissioning phase of the NIKA2 detector, we have obtained observations of NGC891 at 1.2 and 2 mm for an integration time totalling ~ 2 hours. These observations can be seen in Figures 4.3 and 4.4.

Data was taken on the nights of 28th Oct - 9th Nov 2015, consisting of ~2

hours observation time. Four scans were completed; two of which were carried out in polarimetry mode and the other two of which were parallel-scans (both 1 mm arrays were used and the resulting observations are combined). The data reduction was completed using the `nk pipeline Rev 9881` with a single point source as a mask and a single common mode removal. Both 1 mm arrays are used and co-added in a single map. The data at both wavelength bands have pixel sizes of 6".

Although the ~2 hours of integration time is greater than we calculated would be necessary for NGC 891, the observations were taken before significant improvements to the detector were undertaken, hence if the same observations were done now, the required integration time would be less. Also due to poor weather conditions at the telescope and an inconsistent atmospheric opacity during the commissioning phase, these observations are not considered complete and more time is needed to reach the requested RMS. The requested RMS noise sensitivity for NGC 891 was 4.1 and 2.25 mJy/beam at 1.2 and 2 mm respectively, however the obtained RMS is equal to 7 and 3 mJy/beam at these bands. For this reason, we are unable to carry out analysis of the source on a pixel-by-pixel basis but can study the global properties of the galaxy.

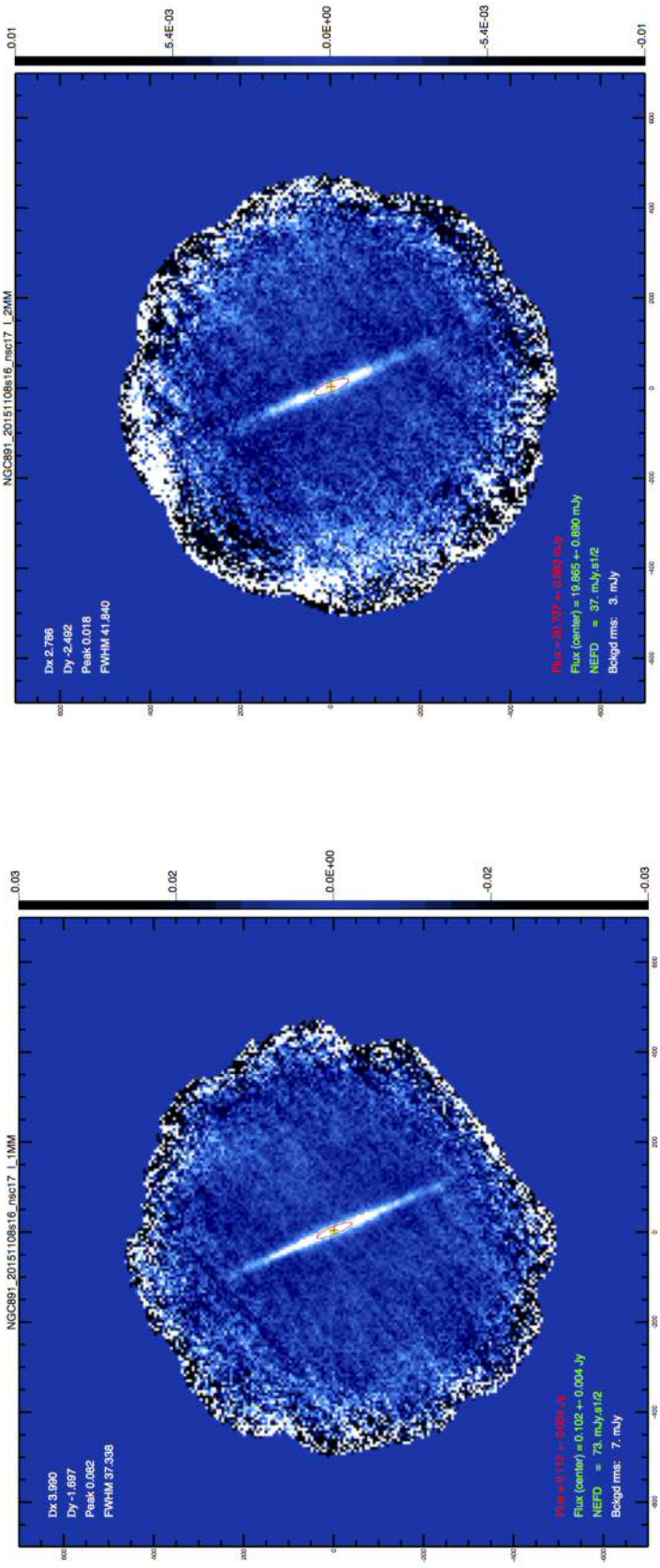

Figure 4.3: NIKA2 observations of the edge-on spiral galaxy NGC 891. Left: 1mm observation. Right: 2mm observation.

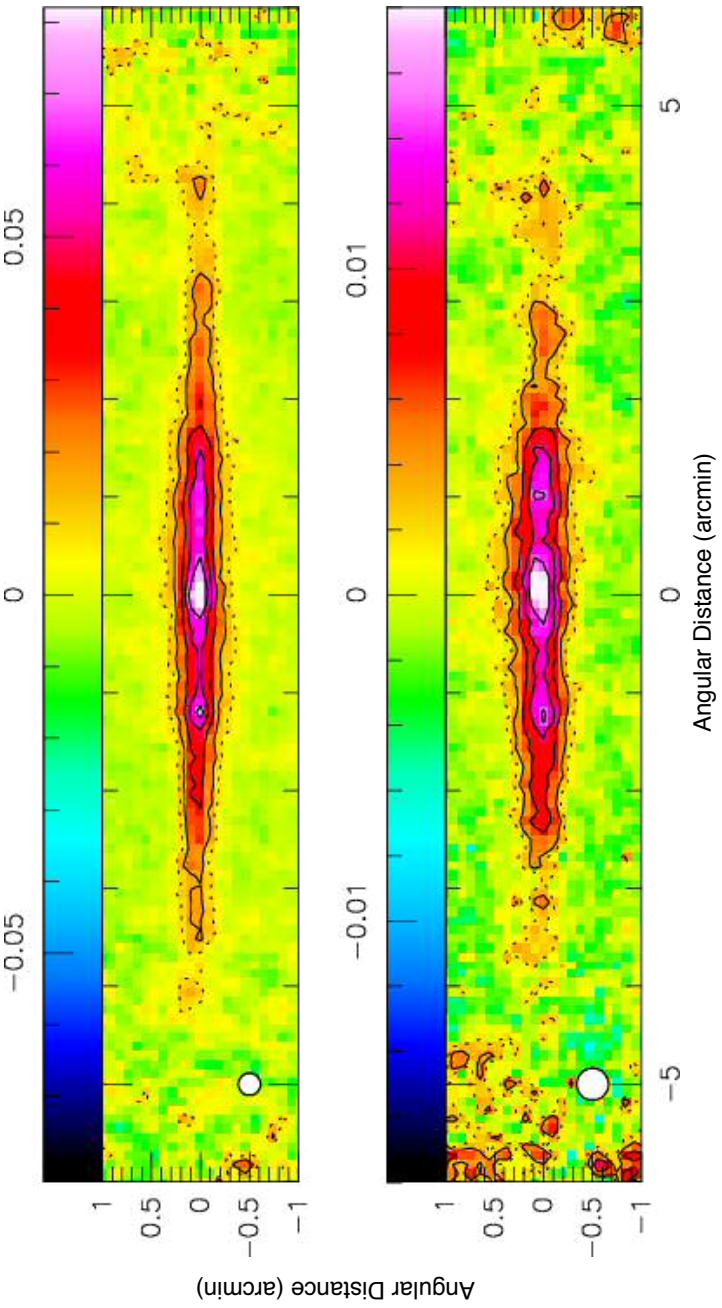

Figure 4.4: NIKA2 maps of NGC 891 at 1 mm (upper) and at 2 mm (lower) after correction for the position angle of 22.5°. The maps cover 12′ x 2′. Half-power beamwidths of 12" and 18" are shown as white circles in the bottom left corners. Contours are at 10% (dashed line), and 20% to 80% in steps of 20% (solid lines) of the peak flux densities (82mJy/beam at 1mm and 18mJy/beam at 2mm). The colour bar is represented in units of Jy. The vertical structure seen in the NIKA2 maps looks smooth, qualitatively similar to the *Herschel* maps shown in Hughes et al. (2014).

4.2.2 M99 (NGC 4254) - A Nearby Face-On Galaxy

M99 is a nearby, asymmetric, face-on spiral which was chosen for preliminary observations due to its orientation. To study the 3D distribution of cold dust in disks we require observations of galaxies at a range of inclinations from face-on to edge-on. NIKA2 observations will provide the first high-resolution maps at 1 and 2 mm for the galaxy, which can be used to study the spiral arm regions on spatially resolved scales. Table 4.4 shows the basic properties of the galaxy and Figure 4.5 shows an optical DSS2 image of the galaxy.

Property	Value
RA (J2000)	12h 18m 49.6s
Dec (J2000)	+14d 24′ 59.4"
Morphology	SAc
Distance	15.4 Mpc
Major Axis	5.4′
Minor Axis	4.7′
Inclination Angle	29°
Rotational Velocity	278 km/s
Mass	4.1×10^9 $M_\odot$
Star Formation Rate	10.96 $M_\odot$/yr
Major Axis Angle	-35.7°

Table 4.4: The basic properties of the face-on spiral M99.

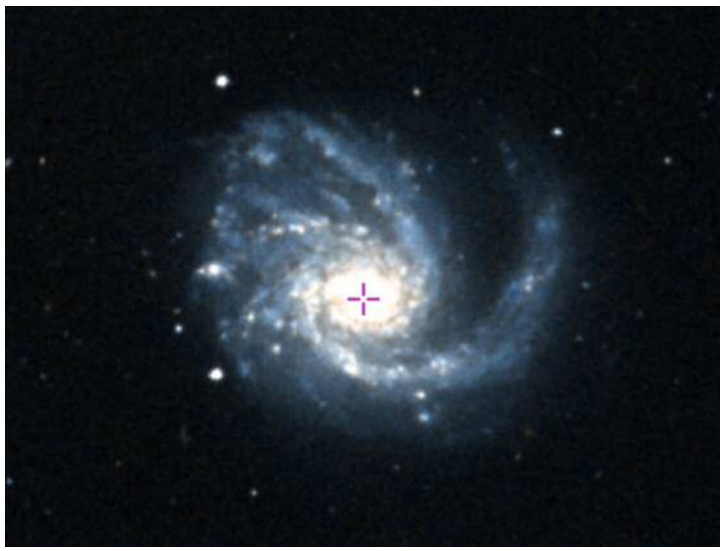

Figure 4.5: Optical image of M99 from DSS2

.

Science verification observations of M99 were completed on the nights of 13th - 20th March 2018, consisting of ~3.2 hours observation time during which 47 scans were completed. The data reduction was completed using the `nk pipeline Rev 9881` with a single point source as a mask and a single common mode removal. Both 1 mm arrays are used and co-added in a single map. The data at both wavelength bands have pixel sizes of 6".

We proposed to observe M99 as part of the NIKA2 science verification for a total integration time of 6 hours. Unfortunately due to bad weather we were unable to observe for the total time proposed, but we have observations for ~ 3.2 hours. These observations can be seen in Figure 4.6. In the 1.2 mm maps, we see a southern spiral arm and we begin to detect the northern arm. The southern arm is barely detected in the 2 mm maps, and the northern arm is not visible in the observations.

We requested a minimum RMS of 1.08 and 0.59 mJy/beam at the 1.2 and 2 mm bands respectively, however the obtained values were 1.2 and 0.89 mJy/beam. For this reason, we are unable to carry out analysis of the source on a pixel-by-pixel basis but can study the global properties of the galaxy via SED fitting with the first ever recorded 2 mm observations for M99.

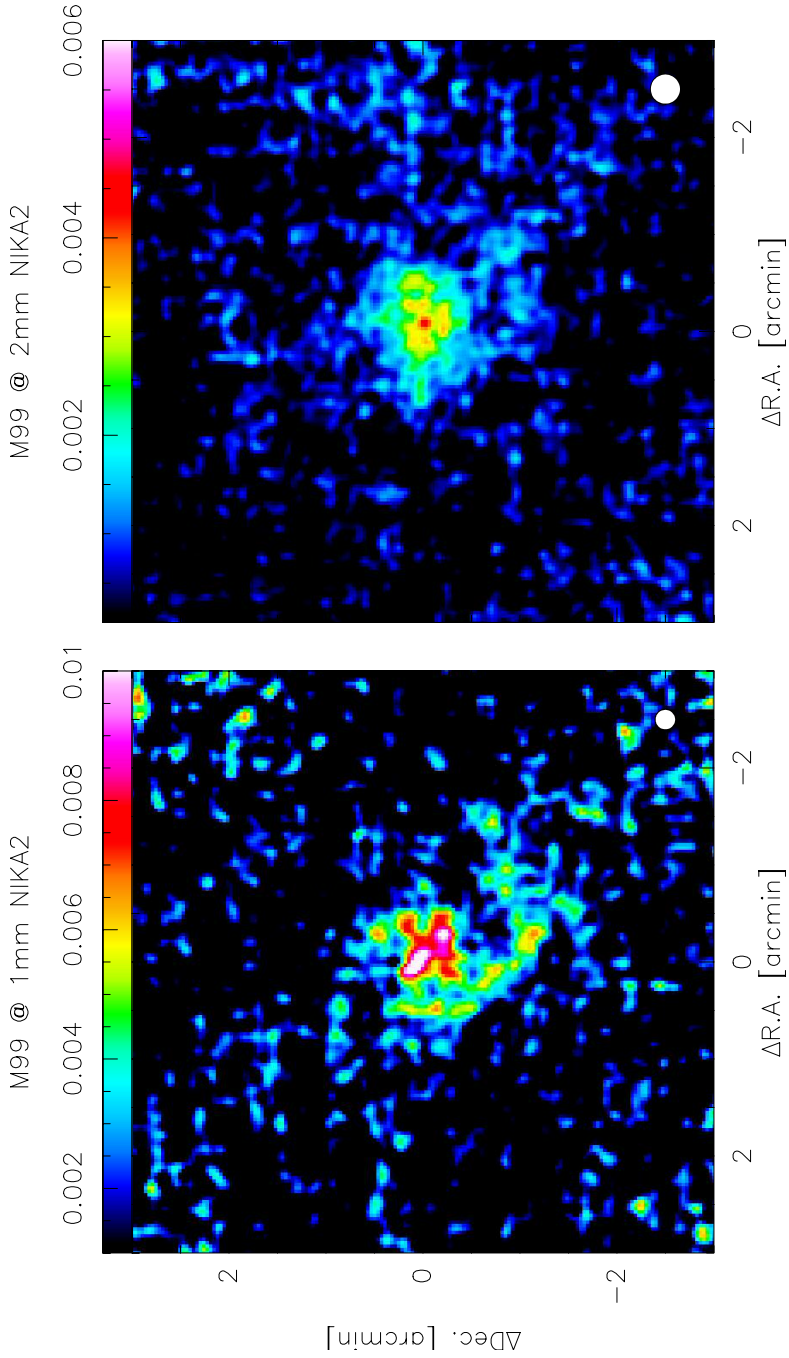

Figure 4.6: NIKA2 observations of the face-on galaxy M99. Left: 1.2 mm observations. The white circle represents the detector beam size of 12". Right: 2 mm observations of the same source, the white circle represents the detector beam size of 18". The total integration time of these observations is ~3.2 hours, resulting in a sensitivity of ~ 1.2 mJy/beam. The colour bars are represented in units of Jy.

4.3 Global Analysis of the NIKA2 Data

We make use of the DustPedia (Davies et al., 2017) database which contains a wealth of observations for the galaxy, including the *Herschel* SPIRE and PACS observations which are necessary to properly sample the dust slope. See Chapter 2.1 for a detailed discussion of the instrument. We utilise PACS 70, 100 and 160 μm and SPIRE 250, 350 and 500 μm data, which is processed via the same method in Chapter 2.4.

4.3.1 Brightness Profiles of NGC 891

As in Chapter 2.7, we generate a brightness profile for the NGC 891 NIKA2 1.2 and 2 mm observations by summing the values of each row of pixels above and below the plane, out to a radius of the scale length of the galaxy. We ensure that the detected emission has been resolved above the instrument PSF by convolving an infinitely thin disk with the beam of the instrument. As the true PSF for the NIKA2 bands is not fully constrained, we generate convolution kernels with the `scipy.convolution.Gaussian2D` package in *Python*, which models the diffraction pattern of a circularised aperture given the FWHM of the beam to be convolved with (10" and 17" at 1.2 and 2 mm, corresponding to 0.47 & 0.79 kpc for NGC 891 and 0.75 & 1.27 kpc for M99). We then convolve this kernel with the data to gain the minimum limit above which the emission is considered to be resolved.

Figure 4.7 shows the vertical profile of the galaxy for the 1 and 2 mm observations. We see from this figure that the detected emission lies above the PSF, therefore we consider the observations to be resolved.

From the profile, we measure the scale height of dust (β_d) by measuring the distance from the plane at which the profile falls below zero. For 1.2 and 2 mm respectively these values are 1.12 and 1.68 kpc.

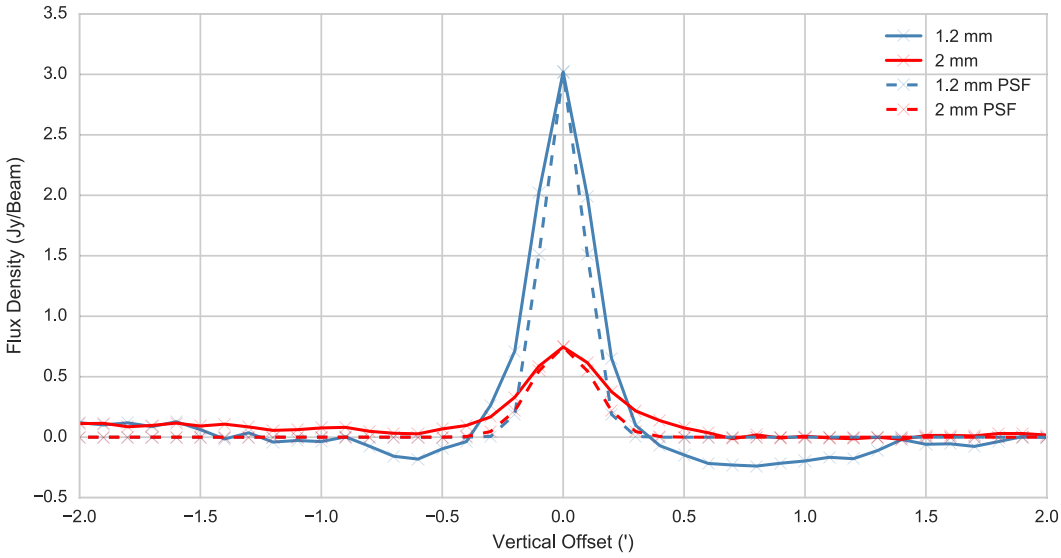

Figure 4.7: Brightness profile of NGC 891 in the z-direction. The blue solid line represents the 1.2 mm data and the blue dashed line shows the 1.2 mm PSF. The 2 mm galaxy flux is shown by the solid red line, and the red dashed line represents the 2 mm PSF.

4.3.2 SED Fitting

A spectrum is fitted to the global emission from the galaxies at all 6 *Herschel* and both NIKA2 wavelengths to measure their temperature and mass, and test for any excess emission in the NIKA2 bands. Background subtraction and uncertainty estimation are carried out using the same process as in Sections 2.5.1 and 2.7.2.1.

Convolution and Resampling

To properly compare the data at all wavelengths we must ensure that each map has a common resolution and pixel size, hence each pixel corresponds to the same sky co-ordinates as the same pixel in every other map. Each map is first convolved to the match that of the worst resolution, the 500 μm band with a FWHM of 37".

As the Aniano et al. (2011) convolution kernels used in Chapter 2 do not cover the NIKA2 bands, we instead use the `astropy.convolution.Gaussian2DKernal` module in *Python* to generate kernels as in Section 4.3.1. We can then convolve the data with this kernel to obtain matched-resolution images for the galaxy at all 8 wavelengths.

Pixels in each map are then regridded to match that of the 500 μm map

(12" per pixel). The `montage.wrappers.MHdr` package for *Python* generates a new header file for each of the images, specifying the appropriate pixel size. The `montage.wrappers.reproject` package is a flux-conserving reprojection package that is used to regrid the maps to the larger pixel size as specified by the new header files.

Aperture Photometry

Once the maps have been convolved and re-gridded to match the 500 μm data, aperture photometry is carried out which will allow us to measure the total flux of the galaxy at all 8 wavelengths within a pre-defined aperture.

Here we make use of the photometry performed by Clark et al. (2018) for the DustPedia database. The Comprehensive & Adaptable Aperture Photometry Routine (CAAPR) uses matched-aperture photometry for all galaxies in the DustPedia database, including NGC 891 and M99, for which there is a large quantity of auxiliary data available. CAAPR's aperture fitting process generates an elliptical aperture in every band for a given target; these apertures are then combined to provide a final aperture for the target. The photometric measurements made by CAAPR take the form of standard aperture photometry, with local background subtraction conducted using an elliptical background annulus around the elliptical master aperture, both centred on the coordinates of the target source. The flux of the source is measured within the ellipse as well as the errors.

As the NIKA2 data is not available in the DustPedia database, we perform our own aperture photometry at all 8 wavelengths via the `ds9` software and compare the *Herschel* fluxes against those obtained through CAAPR. We use the same ellipse major and minor axes as from Clark et al. (2018) and fit these along the major plane of the galaxy in each band, and sum the total flux within the aperture using the `ds9` software. We find that the values are consistent with those measured by CAAPR within the errors as can be seen in Figure 4.8. Errors on CAAPR measurements are provided in the DustPedia database, and errors for this work are calculated by the `ds9` software. Errors were estimated via the same method as in Section 2.7.2.1, however as error maps were not available for the NIKA2 observations, I include both the calibration uncertainty and the noise-equivalent flux density (NEFD) at each pixel that is calculated via the NIKA2 data reduction pipeline. Calibration errors included are 7% for the PACS and SPIRE data, and 9 & 7% for the NIKA2 1.2 and 2 mm bands respectively. NIKA2 uncertainties are particularly large in comparison to the *Herschel* data due to the low SNR of the observations

which results from an insufficient integration time on the sources and sub-optimal instrument calibration during the science verification runs.

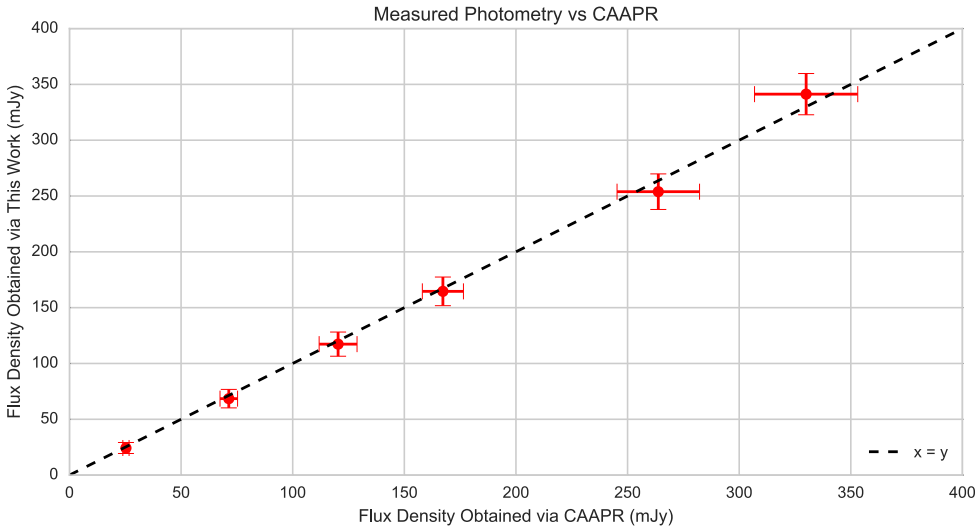

Figure 4.8: Our photometric measurements of NGC 891 for the *Herschel* bands versus those obtained via CAAPR. The black dashed line represents a 1:1 relation.

Building the SED

The fluxes measured during the aperture photometry stage are used to fit a spectrum to the data. We model the data to a two-component spectrum given the following blackbody function (Pearson et al., 2013):

$$S_\nu = A[B_\nu(T_h)\,\nu^\beta + aB_\nu(T_c)\,\nu^\beta], \tag{4.1}$$

where S_ν is the flux density at rest frame frequency ν, A is a normalisation factor, B_ν is the Planck function, β is the dust emissivity index, T_h and T_c are the temperatures of the hot and cold dust components, and a is the ratio of the mass of cold dust to the mass of hot dust. We assume a value for β of 1.7, consistent with the THEMIS model and Verstappen et al. (2013).

As in Chapter 3, a Markov Chain Monte Carlo method is used to find the optimum parameters for the hot and cold dust temperatures, ratio of cold to hot dust and the normalisation factor. This model outputs a fit to the data for the dust components, as well as the composite fit over all wavelengths. χ^2 is a sum over all

available wavelengths, and for each combination of T_c, T_h and a, we found the values that gave the minimum value of χ^2. Our best-fitting model was the set of T_c, T_h and a that gave the lowest value of χ^2 overall, resulting in the templates shown in Figures 4.10 and 4.12.

4.3.3 Results

4.3.3.1 NGC 891

The results of the SED fitting are shown below in Figures 4.9 and 4.10. We obtain values of 20.9 K and 34.9 K for the cold and hot dust components respectively. The dust masses are calculated as in Chapter 3.4.6 for both the hot and cold components individually, as well as the total dust mass. We find the total mass to be 8.5±0.4 $\times 10^7 M_\odot$, consistent with results by Hughes et al. (2014) who find the dust mass to be 8.5±2.0 $\times 10^7 M_\odot$. The ratio of cold to hot dust α was calculated by the model to be 42.6, and our resulting cold and hot dust masses are 8.3±0.4 $\times 10^7 M_\odot$ and 2.0±4$\times 10^6 M_\odot$ respectively. One aspect of the IMEGIN science goals is to explore the long wavelength spectrum to look for an excess in emission at 1.2 and particularly 2 mm. From the NGC 891 SED and residual plot, we do not observe a significant excess at these wavelengths, and the data points follow the dust emission slope according to the value of β = 1.7.

4.3.3.2 M99

The results of the SED fitting are shown below in Figures 4.11 and 4.12. The residual plot shows that the data is well fitted by the spectrum, and we do not see a significant excess in emission at the NIKA2 wavelengths. We obtain values of 21.2 K and 37.7 K for the cold and hot dust components respectively. The resulting dust mass for M99 is 1.01±0.6 $\times 10^8 M_\odot$; consistent with the published value of 1.0±0.1 $\times 10^8 M_\odot$ (Corbelli et al., 2012). The ratio of cold to hot dust α was estimated by the MCMC script to be 41.3, hence the cold mass is equal to 9.8±0.6 $\times 10^7 M_\odot$, and the hot mass was found to be 2.4±6 $\times 10^6 M_\odot$.

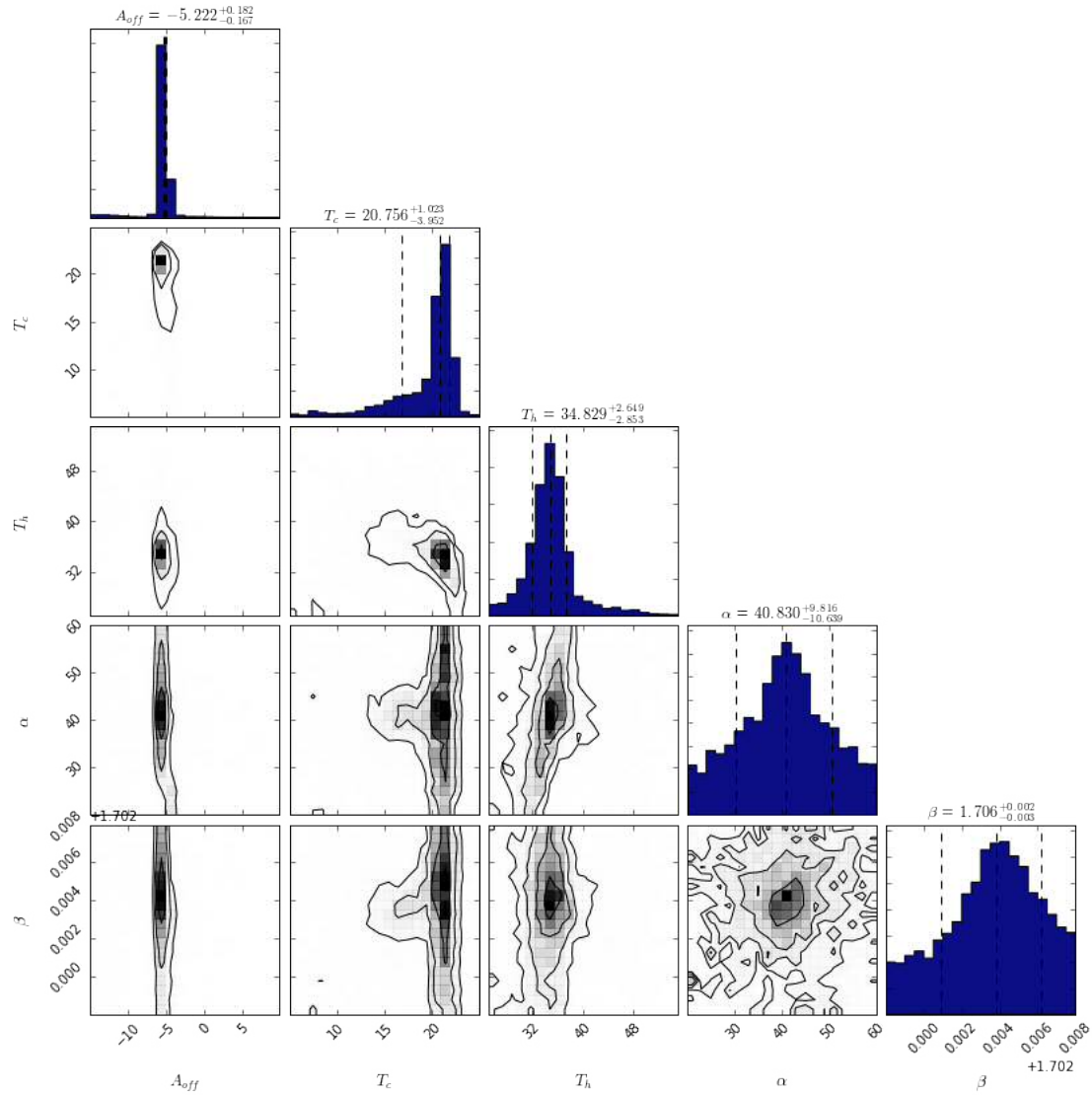

Figure 4.9: MCMC corner plot for the NGC 891 SED fit with the derived values of the normalisation factor A, cold and hot dust temperatures T_c and T_c, ratio of cold to hot dust mass α and dust emissivity index β. Contours represent the 16th, 50th and 84th percentile.

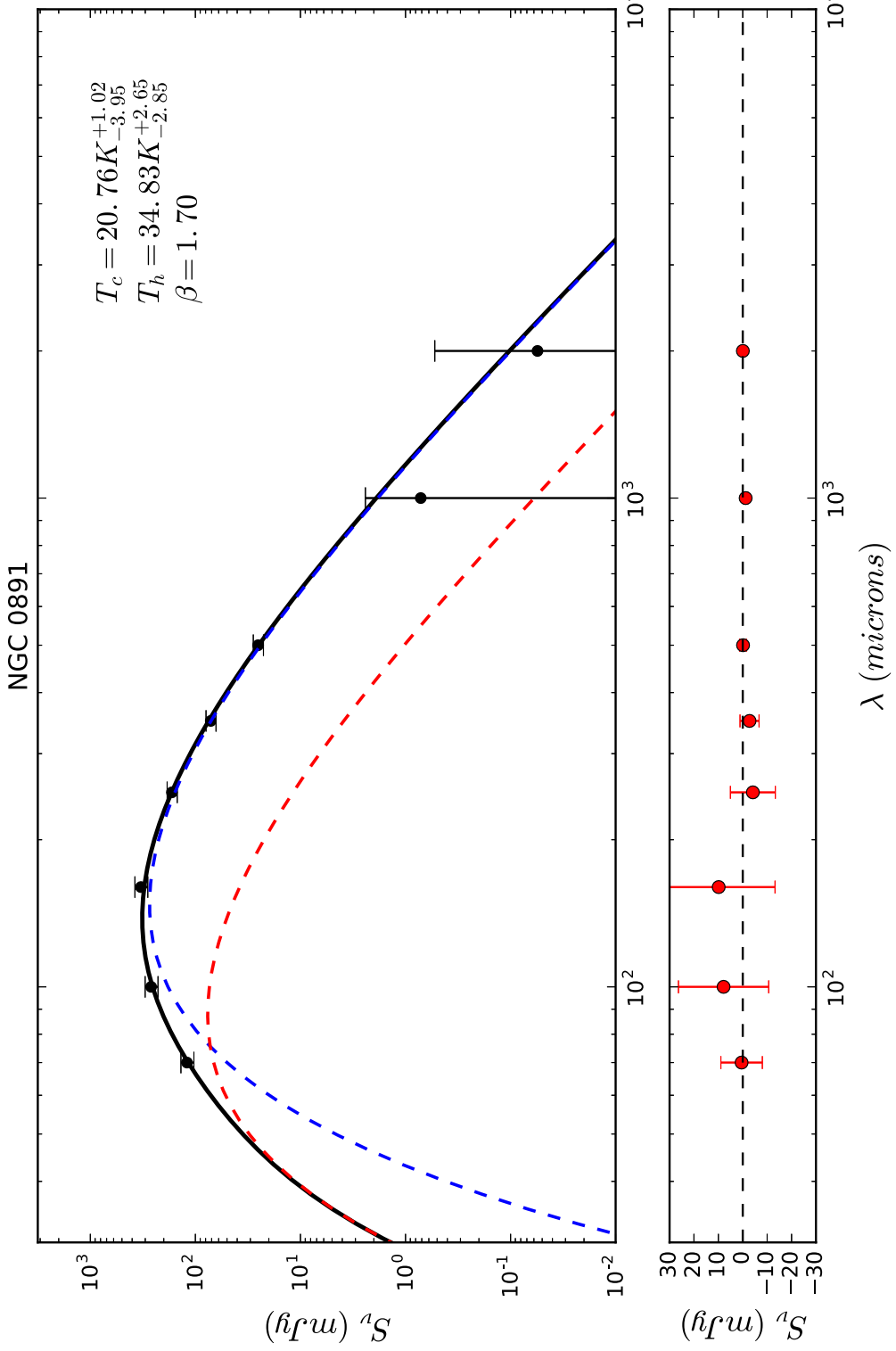

Figure 4.10: The spectral energy distribution of the galaxy NGC891. The dashed blue line represents the cold dust component (measured temperature of 20.9 K), and the red dashed line represents the warm dust component (measured temperature of 34.9 K). The solid black line is the composite of these two components. The lower plot represents the residuals between the data and the model.

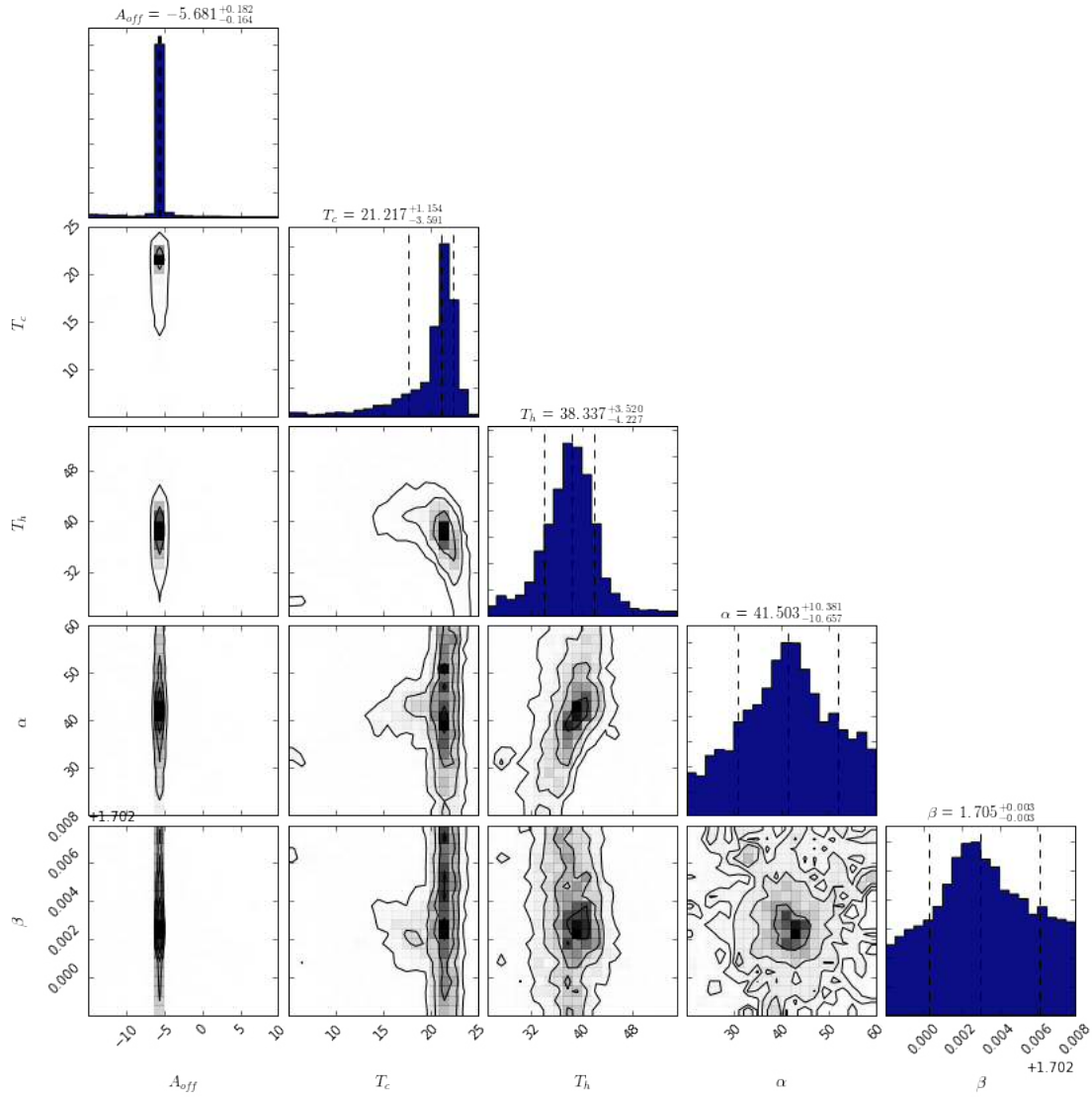

Figure 4.11: MCMC corner plot for the M99 SED fit with the derived values of the normalisation factor A, cold and hot dust temperatures T_c and T_c, ratio of cold to hot dust mass α and dust emissivity index β. Contours represent the 16th, 50th and 84th percentile.

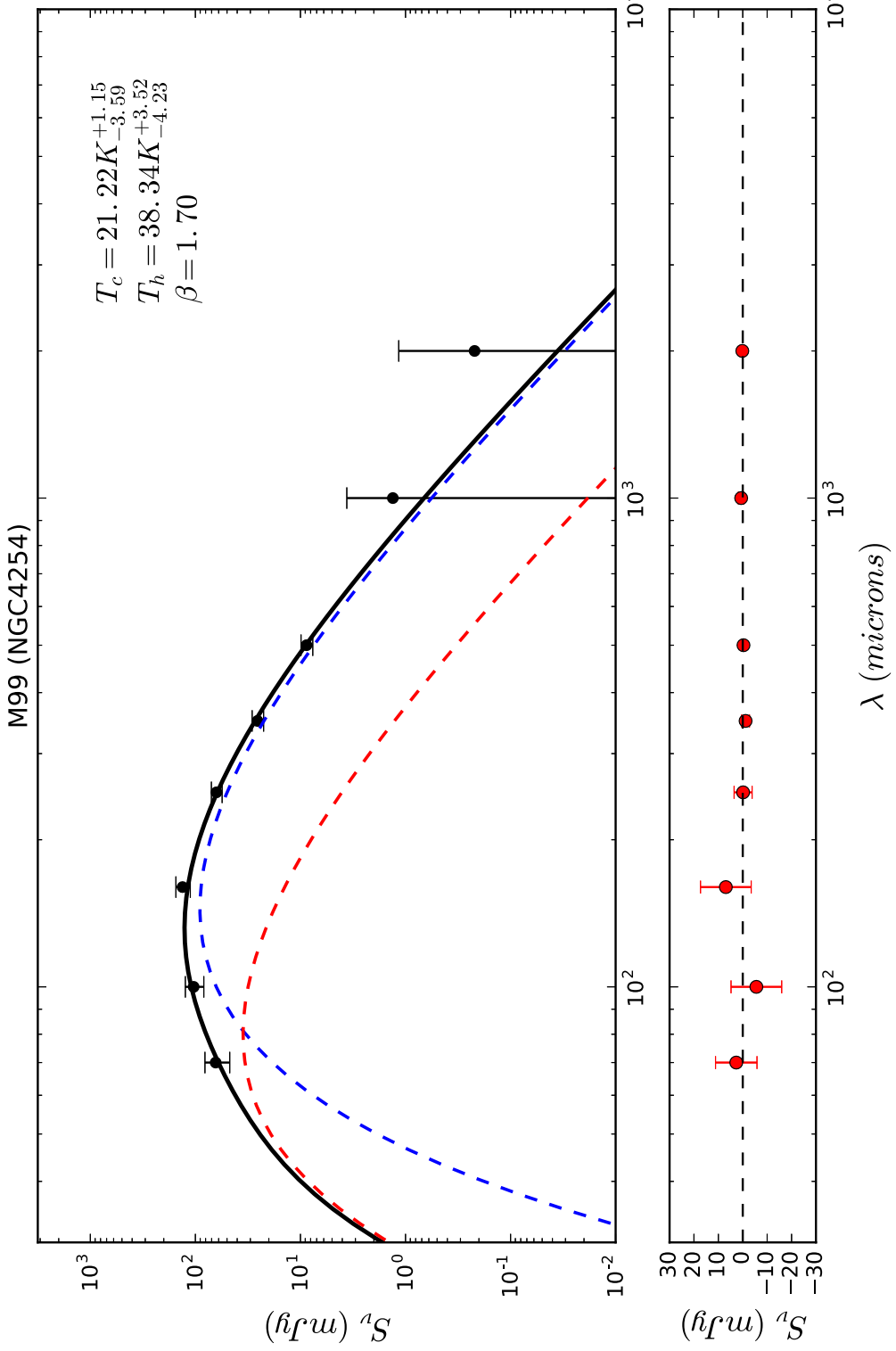

Figure 4.12: The spectral energy distribution of the galaxy M99. The dashed blue line represents the cold dust component (measured temperature of 21.2 K), and the red dashed line represents the warm dust component (measured temperature of 37.7 K). The solid black line is the composite of these two components. The lower plot represents the residuals between the data and the model.

4.4 Discussion

4.4.1 Observations

The results of the preliminary observations provide the first high-resolution data for both NGC891 and M99 at 1.2 and 2 mm.

Due to the low sensitivity of the NIKA2 data, I am unable to complete the majority of the IMEGIN science goals for these preliminary observations, as the SNR of the data is insufficient for more complex analysis on local scales.

The requested RMS noise sensitivity for NGC 891 was 4.1 and 2.25 mJy/beam at 1.2 and 2 mm respectively, however the obtained RMS is equal to 7 and 3 mJy/beam at these bands. For M99, we requested a minimum RMS of 1.08 and 0.59 mJy/beam, however the obtained values were 1.2 and 0.89 mJy/beam.

In the case of M99, we encountered difficulties observing the galaxy due to its orientation to us. Edge-on galaxies have a higher surface brightness than their face-on counterparts and hence are relatively easily detected in millimetre observations. Face-on galaxies require deeper observations to detect the extended emission, and we would need more time observing M99 to measure the true extent of the dust disk. This is an issue that must be accounted for in the remaining observations taken as part of the IMEGIN project. Although the observation time required for each galaxy is calculated based on their requested RMS, these values will need updating in the future to account for the changing nature of the observing opacity and sensitivity of the detector.

Results of parameters derived from the SED fits can be seen in Table 4.5.

	NGC 891	M99
Cold Dust Temp. (K)	20.9 ±3.31	21.2 ±4.38
Hot Dust Temp. (K)	34.9 ±3.15	37.7 ±4.14
Total Dust Mass ($M_\odot$)	$8.5 \pm 0.4 \times 10^7$	$1.0 \pm 0.6 \times 10^8$
Cold Dust Mass ($M_\odot$)	$8.3 \pm 0.4 \times 10^7$	$9.8 \pm 0.6 \times 10^7$
Hot Dust Mass ($M_\odot$)	$2.0 \pm 4 \times 10^6$	$2.4 \pm 6 \times 10^6$

Table 4.5: Results of the SED fitting for NGC 891 and M99.

4.4.2 Future Prospects for IMEGIN

IMEGIN observations are scheduled to start in late-2019, by which time it is expected that the observing strategy (particularly for face-on targets) will be optimised for the sample. The purpose of the NGC 891 and M99 science verification

observations was to test the robustness of the project and data reduction techniques to ensure that the project runs smoothly once observations begin.

From the current observations, it is clear that face-on targets may need a significantly longer on-source time than originally estimated to detect the full extent of the diffuse emission. The time required is highly dependent on current conditions at the telescope, hence it may be worthwhile to incorporate more conservative overheads when building the observing strategy, or prioritise face-on targets when conditions are optimum.

Difficulties arose in testing the science goals of IMEGIN based on the NGC 891 and M99 data due to their high RMS noise, which was below the requested sensitivity for both galaxies. For this reason, I was unable to perform analysis on local or pixel-by-pixel scales due to the low SNR of the data. Instead, I have measured the global dust characteristics of the galaxies and found results consistent with the literature. It is hoped, however, that with the future observations we can fully utilise the NIKA2 data for the scope of this project.

4.5 Summary

We analyse the first millimetre observations of two galaxies; NGC891 and M99, at 1.2 and 2 mm with the NIKA2 detector on the IRAM 30 m telescope. The data was take as part of the commissioning phase of the detector, and so are of insufficient quality to perform a full analysis as per the science goals of IMEGIN. It was possible, however, to estimate the global SEDs of these two galaxies to measure their dust masses and temperatures.

I find that for NGC891, the temperatures of the hot and cold dust components are 34.9 and 20.9 K respectively, and the dust mass is 8.5 $\times 10^7 M_\odot$. For M99, the hot and cold dust temperatures are 37.7 and 21.2 K respectively, and the dust mass is 1.0 $\times 10^8 M_\odot$. These values obtained from the SED fitting are consistent with previous observations. We do not see any significant dust excess at the NIKA2 wavelengths and hence find no evidence of a hidden cold dust component in either of the galaxies.

CHAPTER 5

CONCLUSION

Research shows that as much as 90% of cosmic dust is expelled from galactic disks over the course of their lifetime (Davies et al., 1998), yet we have little understanding about the process by which it is expelled and where the dust eventually resides. Tracing the dust above and below the planes of galaxies aids in quantifying the total dust mass held within galactic haloes, and understanding how it is distributed. In turn, we can learn much about the evolution of dust throughout the lifetime of a galaxy, including its production, expulsion and destruction. These are crucial parameters required to build accurate chemical evolution models.

An excess of FIR emission is observed in galaxies at high redshifts (Davies et al., 1997; Ménard et al., 2010) which is typically thought to be due to a higher dust production rate at earlier epochs. It is unknown how much of the emission comes from the galaxy itself, and how much is due to the reddening of light by foreground dust contained within the haloes of closer galaxies. It is possible that there is a vast quantity of cold dust within the IGM that has so far been under-represented in cosmic dust studies and RT models.

Evidence of an extended extraplanar dust component has been found via a number of methods; direct-detection of the FIR emission (Howk and Savage, 1999; Xilouris et al., 1999; Bianchi, 2007; Verstappen et al., 2013; Bocchio et al., 2016), using UV light as a tracer of dust scattering (Rossa and Dettmar, 2003; Howk, 2012; Hodges-Kluck and Bregman, 2014), measuring extinction of background light by foreground dust (Zaritsky, 1994; Ménard et al., 2010), and via radiative transfer modelling (Xilouris et al., 1997, 1998, 1999; Alton et al., 2004; Bianchi, 2007; Baes et al., 2010; De Looze et al., 2012). In some cases, dust has been found at scale

heights of up to a few Mpc (Ménard et al., 2010). However, there are numerous issues involved when quantifying the mass of dust not contained within the disk.

For direct-detection methods, low SNR in FIR observations provides a limit at which the cold dust emission can be measured. By using UV light as a tracer of dust particles, it is not straightforward to correlate the detected light with the mass of dust. Extinction studies are limited by the extent of the background light sources, hence there may be large quantities of dust that are hidden because there is no background source with which the extinction can be measured, and radiative transfer models vastly underestimate the emission at FIR wavelengths, and as a result underestimate the dust mass in galaxies.

In this thesis, I directly measure the FIR dust emission for a sample of 31 galaxies both individually and by averaging the observations at multiple wavelengths (PACS 100 & 160 μm, and SPIRE 250, 350, & 500 μm), therefore increasing sensitivity and reducing the impact of issues caused by the low SNR of IR observations.

I consider the emission from dust at the little-explored wavelengths of 1.2 and 2 mm using the new NIKA2 detector on the IRAM 30 m telescope for the edge-on galaxy NGC 891, and face-on M99. Observations at millimetre wavelengths can offer a unique view into the interactions between cold dust, free-free and synchrotron emission in the radio-infrared region of the spectrum, and may help quantify the cold dust mass at long wavelengths.

The conclusions and future prospects for all chapters of the thesis are described in Sections 5.1 and 5.2.

5.1 Dust Distribution in Edge-On Galaxies with DustPedia

In Chapters 2 and 3, I use a sample of 31 nearby galaxies that are detected in the 100 & 160 μm PACS and 250, 350 & 500 μm SPIRE bands to measure the vertical extent of the dust distribution both individually and by following the method outlined in Smith et al. (2016) to stack the maps at each wavelength. By averaging multiple observations, I have increased the sensitivity and SNR of the observations, enabling the direct detection of FIR dust emission above and below the planes of galaxies.

5.1.1 Inclination Errors

One of the key issues for this part of the project was determining an accurate value for the inclination for each sample galaxy. Previously, the inclinations for DustPedia galaxies had been taken from HyperLEDA, which proved unreliable. They were then updated via the ellipse fitting procedure (Mosenkov et al., in prep) `GALFIT` which uses WISE 3.4 μm observations to measure the axial ratio and therefore the inclination of the galaxies. Upon inspection, some of the sample galaxies were not edge-on, but were instead face on or had relatively low inclinations. Incorrect measurements of inclination would deem our results inaccurate, as line-of-sight effects that arise as inclination is decreased would bias our results.

I measure the inclinations via an ellipse-fitting procedure over a number of wavelengths from optical to FIR. We found the most consistent band at which the inclination was measured (100 μm) and compared the findings to literature values. Our results were consistent with the literature (within 5%), hence the PACS 100 μm observations were used throughout the project to measure the inclination of each sample galaxy.

5.1.2 Individual Galaxy Analysis

The *Herschel* observations are compared against a new 3D galaxy model based on the TRIPLEX function (Disney et al., 1989), which is generated for each galaxy in the sample to match their inclination and morphology. To generate the models, I first obtain prior values for the scale height (β_d) of each sample galaxy via our ellipse fitting procedure out to SNR = 2.

I measure the brightness profiles of each galaxy against the model to test its robustness, as well as against an infinitely thin disk convolved with the 500 μm beam to measure the minimum scale height above which we consider the *Herschel* observations to be resolved. The profiles are also compared against WISE 3.4 μm observations which measure the oldest and most extended stellar component. In the case of 11 galaxies, I find that the dust is either equal to, or more extended than the stellar disk. For NGC 4222, the dust extends out to ~4 kpc above the midplane.

5.1.3 β_d versus sSFR

I compare the values of β_d obtained for each galaxy against their specific star formation rate (sSFR) as measured by Nersesian et al., (2019). I find a weak negative correlation between the two, however there are too few data points for this

relationship to be statistically significant. Future work on this topic would aim to expand the sample and probe for any relationship between the two parameters.

5.1.4 Galaxy and Model Stacking

The maps and models are averaged at each of the *Herschel* wavelengths and their brightness profiles are measured. I compare these against the averaged stellar disk profile measured at the WISE 3.4 μm band which traces the oldest, most extended stellar component.

By comparing the dust profile against the stellar profile, I am able to present the results as a fraction of the stellar disk height. Our results show a significant amount of extraplanar dust that extends to **at least 1 - 1.3** β_d/β_s.

I carried out two-component modified blackbody SED fitting to the data at incremental distances from the plane, and find the mass of dust to be $9.54^{+0.90}_{-2.67} \times 10^9 M_\odot$, an order of magnitude higher than Nersesian et al. (2019) measure for the DustPedia galaxies in this sample. The evidence for a vertically extended dust component may help account for the reddening of distant quasars, the FIR excess at high redshifts, and contribute to the discrepancy in dust masses observed from FIR observations and via radiative transfer modelling.

A sub-millimetre excess was found in the SEDs, as is well documented in the literature. Explanations for the phenomenon include a very cold dust component, free-flying grains, and a dust emissivity dependence on wavelength. I re-fit the SEDs with a very cold dust component included, and find that a dust temperature of ~7 K accounts well for the 500 μm excess. However, the dust masses derived from these fits increases by two orders of magnitude, an un-physically high value. Further work is required to study the metal and gas content of the sample galaxies via the same analysis methods used in this thesis to compare the sub-millimetre excess to physical properties.

From the SED modelling, we measure the temperature of the dust at increasing distances from the plane. I find that the results are in agreement with those by Bianchi et al. (1999) in that the temperature gradient is shallow (at least to a distance of ~3 kpc), with an increase of 1 K in the first ~1 kpc above the disk.

5.1.5 Possible Sources of Error

One issue that was considered throughout this project was whether the results are influenced by the presence of galaxy bulges that may bias our results. I plot the brightness profiles of the averaged maps at intervals along the plane of the galaxy

to measure the scale height of the dust at different radii. The results show that the dust extends to a vertical scale height of 0.67-1 β_d/β_s consistently across the disk, hence I conclude that there is not evidence of a more extended dust distribution at the centre of the galaxies.

It is also worth considering that the SED fitting is not well constrained due to having just 5 data points and 4 free parameters in the model; two temperatures, α and A. A fixed value of β = 1.7 is used to be consistent with the THEMIS dust model which is utilised throughout the DustPedia project. The spectrum is not well fitted to the data at 500 μm, where the dust emission slope is shallower than the model predicts. The project would benefit from including data at longer wavelengths to better constrain the value of β.

At each wavelength, the data is convolved to match the resolution of the 500 μm beam. As a result, the shorter wavelength data is considerably degraded, hence one pixel in the map equates to a mean angular distance of ~ 0.96 kpc. When considering an extended dust component, it would be useful to probe the dust emission at better resolution to obtain smaller errors on our measurements and more precisely constrain the vertical scale height of the dust.

5.1.6 Future Prospects

This is the first study of its kind that finds a significant extended cold dust component above and below the planes of a large sample of galaxies via direct detection of its FIR emission.

The results of this thesis represent the most sensitive study of extraplanar dust emission in edge-on galaxies to date. It is unlikely that the results could be improved by observations from ground-based telescopes due to the fluctuating atmospheric emission which make it almost impossible to obtain data at 50 - 200 μm. We may, however, improve the sensitivity further with a larger sample than the 31 galaxies used throughout this thesis.

It would be beneficial to the project if a study of the metallicity was completed to measure the surface brightness gradient of the dust versus metals. This parameter can determine whether the dust originates from grain growth or via other methods (in closed box chemical evolution methods (Smith et al., 2016)). By probing the metal content for the sample of galaxies we can learn more about how dust is produced, and therefore the methods via which it is expelled from galaxy disks. Due to the low resolution of our data and the method by which we average the observations, it has proven difficult to explore the ways in which dust is expelled from the disk. Further investigation into the expulsion and retention

of dust grains with the new evidence for an extended dust disk would greatly expand our understanding of the topic.

Further work on this topic would also aim to quantify the reddening contribution from the extraplanar dust to background quasars in line with the work by Smith et al. (2016), as we would then have a more thorough understanding of the 3D structure of dust in galaxies and how this effects our view of objects at high redshifts.

Perhaps the most important result of this project is the evidence for a vertically extended cold dust component. As the results indicate this component may contribute a large fraction of the total dust mass in galaxies, it would be worthwhile to compare our findings against radiative transfer models, such as was undertaken by Mosenkov et al. (2018). We may find that the hidden dust component accounts for much of the dust-energy balance problem, allowing the development of future radiative transfer models that account for the hidden dust mass.

5.2 The IMEGIN Large Programme

In Chapter 4 I present brand new observations taken with the NIKA2 detector for two galaxies, NGC891 and M99, as part of the IMEGIN Large Programme.

The aim of the IMEGIN project is to analyse a large sample of galaxies observed with NIKA2, comprising the first ever observations at these wavelengths for a number of galaxies. There are three key science goals that we hoped to answer with these observations, however due to a delay in the IMEGIN programme we were unable to obtain data for the full sample. The proposed start-date for observations was late 2016, however the project was pushed back repeatedly until a date of late 2019 was agreed on. Unfortunately these timings did not coincide with the lifespan of this degree, hence we do not have observations for the majority of the sample with which to use for this project.

Two galaxies have been observed as part of the NIKA2 science verification phase; NGC 891 and M99, although the acquired sensitivity is less than the required value for these observations. As a result, I have been unable to carry out a resolved analysis of the data, but instead consider the global properties. We fit a two-component modified blackbody SED model to the data to probe the dust emission at 1.2 and 2 mm. We derive temperatures and dust masses that are consistent with previous studies for these galaxies.

For NGC 891 we measure temperatures of the hot and cold dust components to be 34.9 and 20.9 K respectively, and the dust mass is 8.5 $\times 10^7 M_\odot$, consistent

with Hughes et al. (2014). Results of the M99 SED fitting show that the hot and cold dust temperatures are 37.7 and 21.2 K respectively, and the dust mass is 1.0 $\times 10^8 M_\odot$, in agreement with Corbelli et al. (2012). We do not find evidence of a previously-hidden cold dust component at the NIKA2 wavelengths, nor do we see any significant dust excess above what the SED predicts at these bands.

Although the delay to the IMEGIN start date has been detrimental to this study, the observations presented in this thesis show the potential of even low-SNR NIKA2 data, and hence the future prospects of the project are encouraging. With more observing time and better observing conditions, we expect that the observations will be sufficient to explore the goals as outlined in the IMEGIN project.

5.2.1 Future Prospects

As observations have not officially begun for IMEGIN, the key prospects of this project would be to obtain the data for each galaxy in the sample, and carry out research for our main science goals. It is hoped that with better sensitivity observations than we have for NGC891 and M99, we will be able to carry out a more thorough investigation of the topic and probe the galaxies on spatially resolved scales.

The current observations have also enabled us to better explore our observing strategy, particularly for face-on galaxies that can be problematic to detect at millimetre wavelengths. Future work would aim to optimise the observing strategy and data reduction techniques to ensure the extended emission is detected in the NIKA2 bands.

Once the project is completed, we will have the first ever 1.2 and 2 mm observations of the majority of the sample. This will allow us to learn more about the cold dust component and emissivity in a wide variety of galaxy types and morphologies, decompose the FIR-radio spectrum into its three constituent parts, as well as to study the evolution of the Gas-to-Dust ratio with better estimates of the dust mass in galaxies.

BIBLIOGRAPHY

Ade, P. A. R., Aghanim, N., Arnaud, M., et al. Planck early results. I. The Planck mission. *A&A*, 536:A1, December 2011.

Alton, P., Xilouris, E., Misiriotis, A., Dasyra, K., and Dumke, M. The emissivity of dust grains in spiral galaxies. *A&A*, 425:109–120, October 2004.

AMI Consortium, Scaife, A., Hurley-Walker, N., et al. AMI observations of Lynds dark nebulae: further evidence for anomalous cm-wave emission. *MNRAS*, 400: 1394–1412, December 2009.

Andreani, P., Fosbury, R. A. E., van Bemmel, I., and Freudling, W. Far-infrared/millimetre emission in 3C sources. *A&A*, 381(2):389–400, January 2002.

Aniano, G., Draine, B. T., Gordon, K. D., and Sandstrom, K. Common-Resolution Convolution Kernels for Space- and Ground-Based Telescopes. *PASP*, 123:1218, June 2011.

Asano, R. S., Takeuchi, T. T., Hirashita, H., and Inoue, A. K. Dust formation history of galaxies: A critical role of metallicity dust mass growth by accreting materials in the interstellar medium. *Earth, Planets Sp.*, 65(3):213–222, March 2013.

Astropy Collaboration, Robitaille, T. P., Tollerud, E. J., et al. Astropy: A community Python package for astronomy. *A&A*, 558:A33, October 2013.

Baes, M. and Viaene, S. The nature of the UV halo around the spiral galaxy NGC 3268. *A&A*, 587:86, 2016.

Baes, M., Davies, J. I., Dejonghe, H., et al. Radiative transfer in disc galaxies âĂŤ III. The observed kinematics of dusty disc galaxies. *MNRAS*, 343(4):1081–1094, August 2003.

Baes, M., Fritz, J., Gadotti, D., et al. Herschel-ATLAS: The dust energy balance in the edge-on spiral galaxy UGC 4754. *A&A*, 518:L39, July 2010.

Banerjee, A. and Bapat, D. Mass modelling of superthin galaxies: IC5249, UGC7321 and IC2233. *MNRAS*, 466(3):3753–3761, April 2017.

Barlow, M. J., Krause, O., Swinyard, B. M., et al. A Herschel PACS and SPIRE study of the dust content of the Cassiopeia A supernova remnant. *A&A*, 518: L138, 2010.

Barrett, P., Hunter, J., Miller, J. T., Hsu, J.-C., and Greenfield, P. matplotlib – A Portable Python Plotting Package. In Shopbell, P., Britton, M., and Ebert, R., editors, *Astronomical Data Analysis Software and Systems XIV*, volume 347 of *Astronomical Society of the Pacific Conference Series*, page 91, December 2005.

Bendo, G. J., Boselli, A., Dariush, A., et al. Investigations of dust heating in M81, M83, and NGC 2403 with the Herschel Space Observatory. *MNRAS*, 419: 1833–1859, September 2012.

Beswick, R., Brinks, E., Perez-Torres, M., et al. SKA studies of nearby galaxies: star-formation, accretion processes and molecular gas across all environments. *Adv. Astrophys. with Sq. Km. Array*, page 70, 2015.

Bianchi, S. Radiative Transfer in Spiral Galaxies. Technical report, 2004.

Bianchi, S. The dust distribution in edge-on galaxies. Radiative transfer fits of V and K'-band images. *A&A*, 471:765–773, September 2007.

Bianchi, S. Dust Extinction and Emission in a Clumpy Galactic Disk. An Application of the Radiative Transfer Code TRADING. *A&A*, 490:461–475, July 2008.

Bianchi, S. and Schneider, R. Dust formation and survival in supernova ejecta. *MNRAS*, 378(3):973–982, July 2007.

Bianchi, S., Ferrara, A., and Giovanardi, C. Monte Carlo simulations of dusty spiral galaxies: extinction and polarization properties. *ApJ*, 465:127, December 1995.

Bianchi, S., Alton, P. B., and Davies, J. I. ISO observations of spirals: modelling the FIR emission. *ISO Beyond Point Sources Stud. Ext. Infrared Emiss. Sept. 14-17, 1999, ISO Data Centre, Villafranca del Castillo, Madrid, Spain. Ed. by R. J. Laureijs, K. Leech M. F. Kessler, ESA-SP 455, 2000. p. 149.*, 455:149, October 1999.

Blain, A., Smail, I., Ivison, R., Kneib, J.-P., and Frayer, D. Submillimeter galaxies. *Phys. Rep.*, 369:111–176, October 2002.

Bocchio, M., Bianchi, S., Hunt, L., and Schneider, R. Halo dust detection around NGC 891. *A&A*, 586:A8, February 2016.

Boselli, A., Lequeux, J., and Gavazzi, G. The CO to H2 Conversion Factor in Normal Late-Type Galaxies. *Ap&SS*, 281(1/2):127–128, July 2002.

Bot, C., Ysard, N., Paradis, D., et al. Submillimeter to centimeter excess emission from the Magellanic Clouds. *A&A*, 523:A20, November 2010.

Burgdorf, M., Ashby, M., and Williams, R. Mid-Infrared Photometry of Dust in the Thick Disk of NGC 891. *ApJ*, 668:918–923, October 2007.

Burke, B. and Graham-Smith, F. *An Introduction to Radio Astronomy*. Cambridge University Press, Cambridge: UK, 2010.

Calzetti, D. The Dust Opacity of Star-forming Galaxies. *PASP*, 113(790):1449–1485, December 2001.

Casassus, S., Cabrera, G., Förster, F., et al. Morphological Analysis of the Centimeter-Wave Continuum in the Dark Cloud LDN 1622. *ApJ*, 639:951–964, March 2006.

Casey, C. M. Far-infrared spectral energy distribution fitting for galaxies near and far. *MNRAS*, 425(4):3094–3103, Oct 2012.

Chandrasekhar, S. and Subrahmanyan. *Radiative transfer*. New York, Dover, 1960.

Chang, Y.-Y., van der Wel, A., da Cunha, E., and Rix, H.-W. Stellar Masses and Star Formation Rates for 1M Galaxies from SDSS+WISE. *The Astrophysical Journal Supplement Series*, 219(1):8, jul 2015.

Chiappini, C., Matteucci, F., and Gratton, R. The Chemical Evolution of the Galaxy: The TwoâĂŘInfall Model. *ApJ*, 477(2):765–780, March 1997.

Ciesla, L., Boquien, M., Boselli, A., et al. Dust spectral energy distributions of nearby galaxies: an insight from the Herschel Reference Survey. *A&A*, 565:A128, May 2014.

Clark, C. J. R. *On the origins of cosmic dust and the evolution of nearby galaxies with the Herschel Space Observatory*. PhD thesis, Cardiff University, 2015.

Clark, C. J. R., Schofield, S. P., Gomez, H. L., and Davies, J. I. An empirical determination of the dust mass absorption coefficient, Îžd, using the Herschel

Reference Survey. *Monthly Notices of the Royal Astronomical Society*, 459(2):1646–1658, 03 2016.

Clark, C. J. R., Verstocken, S., Bianchi, S., et al. DustPedia: Multiwavelength photometry and imagery of 875 nearby galaxies in 42 ultraviolet-microwave bands. *A&A*, 609:A37, January 2018.

Condon, J. Radio emission from normal galaxies. *ARA&A*, 30:575–611, 1992.

Condon, J. and Ransom, S. Essential Radio Astronomy. NRAO Online Course, URL: http://www.cv.nrao.edu/course/astr534/ERA.shtml, 2010.

Corbelli, E., Bianchi, S., Cortese, L., et al. The Herschel Virgo Cluster Survey: X.The relationship between cold dust and molecular gas content in Virgo spirals âŃĘ. Technical report, 2012.

Cowie, L. L. and Songaila, A. High-Resolution Optical and Ultraviolet Absorption-Line Studies of Interstellar Gas. *ARA&A*, 24(1):499–535, September 1986.

Dahlem, M., Ehle, M., Ryder, S. D., Vlajicvlajic, M., and Haynes, R. F. Astrophysics Neutral hydrogen gas in 7 high-inclination spiral galaxies I. The data. *A&A*, 432: 475–489, 2005.

Dalcanton, J., Yoachim, P., and Bernstein, R. The Formation of Dust Lanes: Implications for Galaxy Evolution. *ApJ*, 608:189–207, June 2004.

Davies, J., Bianchi, S., Baes, M., et al. The Herschel Fornax Cluster Survey - I. The bright galaxy sample. *MNRAS*, 428:834–844, January 2013.

Davies, J., Baes, M., Bianchi, S., et al. DustPedia: A Definitive Study of Cosmic Dust in the Local Universe. *PASP*, 129(4):44102, April 2017.

Davies, J. I., Phillipps, S., Trewhella, M., and Alton, P. Luminosity evolution, extragalactic background light and the opacity of the Universe. *MNRAS*, 291(1): 59–64, October 1997.

Davies, J. I., Alton, P., Bianchi, S., and Trewhella, M. The expulsion and retention of dust grains by galactic discs. *MNRAS*, 300(4):1006–1014, November 1998.

Davies, J. I., Bianchi, S., Cortese, L., et al. The Herschel Virgo Cluster Survey - VIII. The Bright Galaxy Sample. *MNRAS*, 419(4):3505–3520, February 2012.

Davies, L. J. M., Driver, S. P., Robotham, A. S. G., et al. GAMA/H-ATLAS: a meta-analysis of SFR indicators - comprehensive measures of the SFR - M⋆ relation and cosmic star formation history at z<0.4. *Monthly Notices of the Royal Astronomical Society*, 461(1):458–485, 06 2016.

Davis, T., Young, L., Crocker, A., et al. The atlas3d project - xxviii. dynamically driven star formation suppression in early-type galaxies. *Monthly Notices of the Royal Astronomical Society*, 444:3427–3445, 11 2014.

De Geyter, G., Baes, M., De Looze, I., et al. Dust energy balance study of two edge-on spiral galaxies in the Herschel-ATLAS survey. *MNRAS*, 451:1728–1739, August 2015.

De Looze, I., Baes, M., Bendo, G., et al. The dust energy balance in the edge-on spiral galaxy NGC 4565. *MNRAS*, 427:2797–2811, December 2012.

De Vis, P., Gomez, H. L., Schofield, S. P., et al. Using dust, gas and stellar mass-selected samples to probe dust sources and sinks in low-metallicity galaxies. *Monthly Notices of the Royal Astronomical Society*, 471(2):1743–1765, 05 2017.

De Vis, P., Jones, A., Viaene, S., et al. A systematic metallicity study of dustpedia galaxies reveals evolution in the dust-to-metal ratios. *A&A*, 623:A5, 2019.

Dicker, S., Ade, P., Aguirre, J., et al. Mustang 2: a large focal plane array for the 100 m green bank telescope. *Journal of Low Temperature Physics*, 176(5-6):808–814, 2014.

Dickinson, C., Davies, R., Allison, J., et al. Anomalous Microwave Emission from the H II Region RCW175. *ApJ*, 690:1585–1589, January 2009.

Disney, M., Davies, J., and Phillipps, S. Are galaxy discs optically thick? *MNRAS*, 239(3):939–976, August 1989.

Draine, B. and Lazarian, A. Electric Dipole Radiation from Spinning Dust Grains. *ApJ*, 508:157–179, November 1998.

Draine, B. T. Interstellar Dust Models and Evolutionary Implications. *ASP Conf. Ser.*, 414, 2009.

Draine, B. T. Spitzer View of the Center of the Milky Way. Technical report, 2011.

Draine, B. T. and Li, A. Infrared Emission from Interstellar Dust. IV. The Silicate-Graphite-PAH Model in the Post-Spitzer Era. *ApJ*, 657:810–837, July 2007.

Drimmel, R. and Spergel, D. N. Three-dimensional Structure of the Milky Way Disk: The Distribution of Stars and Dust beyond 0.35 R⊙. *ApJ*, 556(1):181–202, July 2001.

Dunne, L., Gomez, H. L., da Cunha, E., et al. Herschel-ATLAS: rapid evolution of dust in galaxies over the last 5 billion years. *MNRAS*, 417(2):1510–1533, October 2011.

Dupac, X., del Burgo, C., Bernard, J.-P., et al. The Complete Submillimetre Spectrum of NGC 891. *MNRAS*, 344(1):105–109, September 2003.

ESO. Hertzsprung-russell diagram, Jun 2007.

Ferrara, A., Ferrini, F., Barsella, B., and Franco, J. Evolution of dust grains through a hot gaseous halo. *ApJ*, 381:137, November 1991.

Galametz, M., Madden, S., Galliano, F., et al. Probing the dust properties of galaxies up to submillimetre wavelengths. II. Dust-to-gas mass ratio trends with metallicity and the submm excess in dwarf galaxies. *A&A*, 532:A56, August 2011.

Galametz, M., Kennicutt, R., Albrecht, M., et al. Mapping the cold dust temperatures and masses of nearby KINGFISH galaxies with Herschel. *MNRAS*, 425: 763–787, September 2012.

Galliano, F. Some insights on the dust properties of nearby galaxies, as seen with Herschel. *Planet. Space Sci.*, 149:38–44, 2017.

Galliano, F., Madden, S., Jones, A., et al. ISM properties in low-metallicity environments. II. The dust spectral energy distribution of NGC 1569. *A&A*, 407:159–176, August 2003.

Galliano, F., Madden, S., Jones, A., Wilson, C., and Bernard, J.-P. ISM properties in low-metallicity environments. III. The spectral energy distributions of II Zw 40, He 2-10 and NGC 1140. *A&A*, 434:867–885, May 2005.

Gaustad, J. E. The Composition of Interstellar Dust. *Dark Nebul. Globul. Protostars, Proc. a Symp. held Tucson, March 26-27, 1970. Ed. by B.T. Lynds. Tucson, Arizona Univ. Arizona Press. 1971., p.91*, page 91, 1971.

Gioia, I., Gregorini, L., and Klein, U. High frequency radio continuum observations of bright spiral galaxies. *A&A*, 116:164–174, December 1982.

Gomez, H. Pos (lcdu 2013) 146 dust in supernovae remnants. 2013.

Gomez, H. L., Krause, O., Barlow, M. J., et al. A Cool Dust Factory in the Crab Nebula: A Herschel Study of the Filaments. *ApJ*, 760(12pp), 2012.

Graeve, R., Klein, U., and Wielebinski, R. A multi-frequency radio continuum study of the galaxy M101. *A&A*, 238:39–49, November 1990.

Griffin, M. J., Abergel, A., Abreu, A., et al. The herschel-spire instrument and its in-flight performance*. *A&A*, 518:L3, 2010.

Groves, B. A., Schinnerer, E., Leroy, A., et al. Dust continuum emission as a tracer of gas mass in galaxies. *ApJ*, 799, November 2014.

Harper, S., Dickinson, C., and Cleary, K. Observations of free-free and anomalous microwave emission from LDN 1622 with the 100 m Green Bank Telescope. *MNRAS*, 453:3375–3385, November 2015.

Hedden, R. L. A Telescope For The Infrared Astronomical Satellite (IRAS). volume 0095, pages 8–12. International Society for Optics and Photonics, November 1976.

Hensley, B. and Draine, B. A Case Against Spinning PAHs as the Source of the Anomalous Microwave Emission. *ArXiv e-prints*, May 2015.

Hensley, B., Murphy, E., and Staguhn, J. Characterizing extragalactic anomalous microwave emission in NGC 6946 with CARMA. *MNRAS*, 449:809–819, May 2015.

Henyey, L. C. and Greenstein, J. L. Diffuse radiation in the Galaxy. *ApJ*, 93:70, January 1941.

Herschel, W. On the Construction of the Heavens. *Philos. Trans. R. Soc. London, Vol. 75, pp. 213-266*, 75:213–266, 1785.

Ho, I.-T., Kudritzki, R.-P., Kewley, L. J., et al. Metallicity gradients in local field star-forming galaxies: Insights on inflows, outflows, and the coevolution of gas, stars and metals. Technical Report 0000, 2014.

Hodges-Kluck, E. and Bregman, J. Detection of Ultraviolet Halos around Highly Inclined Galaxies. *ApJ*, 789:131, July 2014.

Holland, W., Bintley, D., Chapin, E., et al. Scuba-2: the 10 000 pixel bolometer camera on the james clerk maxwell telescope. *Monthly Notices of the Royal Astronomical Society*, 430(4):2513–2533, 2013.

Holwerda, B., Bianchi, S., Böker, T., et al. Herschel/SPIRE observations of the dusty disk of NGC 4244. *A&A*, 541:L5, May 2012a.

Holwerda, B. W., Dalcanton, J. J., Radburn-Smith, D., et al. Evolution in the Dust Lane Fraction of Edge-on L* V Spiral Galaxies Since z = 0.8. *ApJ*, 753(1):25, 2012b.

Howk, J. Extra-planar Dust as a Tracer of Cold Dense Gas in the Thick Disks of Spiral Galaxies. In Braun, R., editor, *Extra-Planar Gas*, volume 331 of *Astronomical Society of the Pacific Conference Series*, page 287, June 2005.

Howk, J. Extraplanar Dust in Spiral Galaxies: Tracing Outflows in the Disk-Halo Interface. In de Avillez, M., editor, *EAS Publ. Ser.*, volume 56 of *EAS Publications Series*, pages 291–298, September 2012.

Howk, J. and Savage, B. Extraplanar Dust and Star Formation in Nearby Edge-On Galaxies. In Ossenkopf, V., Stutzki, J., and Winnewisser, G., editors, *Phys. Chem. Interstellar Mediu.*, August 1999.

Howk, J. C. and Savage, B. D. Extraplanar Dust in the Edge-On Spiral NGC 891. *AJ*, 114:2463, September 1997.

Hughes, T. M., Baes, M., Fritz, J., et al. Astrophysics A resolved analysis of cold dust and gas in the nearby edge-on spiral NGC 891. *A&A*, 565, 2014.

Hunt, L. K., Draine, B. T., Bianchi, S., et al. Cool dust heating and temperature mixing in nearby star-forming galaxies. *A&A*, 576(33), September 2014.

Joner, M., Laney, D., and Gendler, R. APOD: 2012 May 26 - At the Edge of NGC 891, 2012.

Jones, A., Fanciullo, L., Köhler, M., et al. The evolution of amorphous hydrocarbons in the ISM: dust modelling from a new vantage point. *A&A*, 558:A62, October 2013.

Jones, A. P. Dust Destruction Processes. *Astrophys. Dust ASP Conf. Ser.*, 309, 2004.

Jones, A. P. and Nuth, J. A. Astronomy Astrophysics Dust destruction in the ISM: a re-evaluation of dust lifetimes. *A&A*, 530:44, 2011.

Jones, A. P., Köhler, M., Ysard, N., Bocchio, M., and Verstraete, L. The global dust modelling framework THEMIS. *A&A*, 602:A46, June 2017.

Kaastra, J., Paerels, F., Durret, F., Schindler, S., and Richter, P. Thermal Radiation Processes. *Space Sci. Rev.*, 134:155–190, February 2008.

Kamphuis, P., Holwerda, B., Allen, R., Peletier, R., and van der Kruit, P. A dust component ~2 kpc above the plane in NGC 891. *A&A*, 471:L1–L4, August 2007.

Kapteyn, J. C. *On the absorption of light in space, by J. C. Kapteyn.* Contributions from the Mount Wilson Solar Observatory; no. 31, 42, Chicago, 1909.

Kirkpatrick, A., Calzetti, D., Kennicutt, R., et al. Untangling the Nature of Spatial Variations of Cold Dust Properties in Star Forming Galaxies. *ApJ*, 789(2):130, June 2014.

Klein, U. and Emerson, D. A Survey of the Distributions of 2.8-CM Radio Continuum in Nearby Galaxies - Part One - Observations of 16 Spiral. *A&A*, 94:29, January 1981.

Klein, U., Wielebinski, R., Haynes, R., and Malin, D. A new radio continuum survey of the Magellanic Clouds at 1.4 GHz. II - The radio morphology, and thermal and nonthermal emission of the LMC. *A&A*, 211:280–292, March 1989.

Köhler, M., Ysard, N., and Jones, A. P. Dust evolution in the transition towards the denser ISM: impact on dust temperature, opacity, and spectral index. *A&A*, 579:A15, July 2015.

Kozasa, T., Nozawa, T., Tominaga, N., and Nomoto, K. Dust in Supernovae: Formation and Evolution. *ASP Conf. Ser.*, 414, 2009.

Lagattuta, D. J., Mould, J. R., Staveley-Smith, L., et al. WIE TF: A Mid-Infrared, 3.4 μm Extension od the Tully-Fisher Relation Using WISE Photometry. *ApJ*, 771(2): 88, June 2013.

LARSON, R. B. and B., R. Infall of Matter in Galaxies. *Nature*, 236(5340):21–23, March 1972.

Leroy, A., Walter, F., Bigiel, F., et al. Heracles: The HERA CO Line Extragalactic Survey. *AJ*, 137:4670–4696, June 2009.

Li, A. Optical Properties of Dust. *arXiv e-prints*, art. arXiv:0808.4123, Aug 2008.

Licquia, T. C. and Newman, J. A. IMPROVED ESTIMATES OF THE MILKY WAY's STELLAR MASS AND STAR FORMATION RATE FROM HIERARCHICAL BAYESIAN META-ANALYSIS. *The Astrophysical Journal*, 806(1):96, jun 2015.

Lu, N. and Helou, G. Global Star Formation and Mid-Infrared Emission Features in Galaxies. Technical report, 2008.

Mainzer, A., Bauer, J., Cutri, R. M., et al. Initial Performance of the NEOWISE Reactivation Mission. *ApJ*, 792(1):30, August 2014.

Matsuura, M., Dwek, E., Meixner, M., et al. Herschel detects a massive dust reservoir in supernova 1987A. *Science*, 333(6047):1258–61, September 2011.

Mattsson, L., De Cia, A., Andersen, A. C., and Zafar, T. On the (in)variance of the dust-to-metals ratio in galaxies. *MNRAS*, 440(2):1562–1570, May 2014.

McQuinn, K. B. W., Skillman, E. D., Dolphin, A. E., Berg, D., and Kennicutt, R. The Distance to M104. *AJ*, 152(5):144, October 2016.

Ménard, B., Scranton, R., Fukugita, M., and Richards, G. Measuring the galaxy-mass and galaxy-dust correlations through magnification and reddening. *MNRAS*, 405:1025–1039, June 2010.

Meny, C., Gromov, V., Boudet, N., et al. Far-infrared to millimeter astrophysical dust emission. *A&A*, 468(1):171–188, June 2007.

Misiriotis, A., Papadakis, I. E., Kylafis, N. D., and Papamastorakis, J. Dust masses and star formation in bright IRAS galaxies. *A&A*, 417(1):39–50, April 2004.

Misiriotis, A., Xilouris, E. M., Papamastorakis, J., Boumis, P., and Goudis, C. D. The distribution of the ISM in the Milky Way A three-dimensional large-scale model. *A&A*, 459:113–123, 2006.

Mosenkov, A. V., Allaert, F., Baes, M., et al. HERschel Observations of Edge-on Spirals (HEROES) IV. Dust energy balance problem. *A&A*, 616:120, 2018.

Moustakas, J., Kennicutt, R. C., Tremonti, C. A., et al. Optical Spectroscopy and Nebular Oxygen Abundances of the Spitzer/SINGS Galaxies. *{ApJS*, 190:233–266, July 2010.

Murphy, E., Helou, G., Condon, J., et al. The Detection of Anomalous Dust Emission in the Nearby Galaxy NGC 6946. *ApJ*, 709:L108–L113, February 2010.

Nersesian, Xilouris, E. M., Bianchi, S., et al. Old and young stellar populations in dustpedia galaxies and their role in dust heating. *A&A*, 624:A80, 2019.

Nersesian, A., Xilouris, E. M., Bianchi, S., et al. Old and young stellar populations in dustpedia galaxies and their role in dust heating. *A&A*, 624:A80, 2019.

Nguyen, H. T., Schulz, B., Levenson, L., et al. Hermes: The spire confusion limit*. *A&A*, 518:L5, 2010.

Noll, S., Burgarella, D., Giovannoli, E., et al. Analysis of galaxy SEDs from far-UV to far-IR with CIGALE: Studying a SINGS test sample. *A&A*, 507:1793–1813, September 2009.

Norman, C. A. and Ikeuchi, S. The disk-halo interaction - Superbubbles and the structure of the interstellar medium. *ApJ*, 345:372, October 1989.

Pearson, E. A., Eales, S., Dunne, L., et al. H-ATLAS: estimating redshifts of Herschel sources from sub-mm fluxes. *MNRAS*, 435:2753–2763, 2013.

Peek, J. E. G. Hitting the Bull's-eye: The Radial Profile of Accretion and Star Formation in the Milky Way. *ApJ*, 698:1429–1436, April 2009.

Peek, J. E. G., Putman, M. E., and SommerâĂŘLarsen, J. Ongoing Galactic Accretion: Simulations and Observations of Condensed Gas in Hot Halos. *ApJ*, 674(1): 227–236, February 2008.

Peel, M., Dickinson, C., Davies, R., Clements, D., and Beswick, R. Radio to infrared spectra of late-type galaxies with Planck and Wilkinson Microwave Anisotropy Probe data. *MNRAS*, 416:L99–L103, September 2011.

Peel, M., Dickinson, C., Davies, R., et al. Template fitting of WMAP 7-year data: anomalous dust or flattening synchrotron emission? *MNRAS*, 424:2676–2685, August 2012.

Peng, C. Y., Ho, L. C., Impey, C. D., and Rix, H.-W. Detailed Structural Decomposition of Galaxy Images. *AJ*, 124:266–293, April 2002.

Pilbratt, G. L., Riedinger, J. R., Passvogel, T., et al. Special feature Herschel Space Observatory An ESA facility for far-infrared and submillimetre astronomy. *A&A*, 518:1, 2010.

Pilbratt, G. L., Riedinger, J. R., Passvogel, T., et al. Herschel space observatory* - an esa facility for far-infrared and submillimetre astronomy. *A&A*, 518:L1, 2010.

Planck Collaboration, Ade, P. A. R., Aghanim, N., et al. Planck early results. xx. new light on anomalous microwave emission from spinning dust grains. *A&A*, 536:A20, 2011.

Poglitsch, A., Waelkens, C., Geis, N., et al. The photodetector array camera and spectrometer (pacs) on the herschel space observatory*. *A&A*, 518:L2, 2010.

Popescu, C. C. and Tuffs, R. J. The percentage of stellar light re-radiated by dust in late-type Virgo Cluster galaxies. *MNRAS*, 335(2):L41–L44, September 2002.

Popescu, C. C., Misiriotis, A., Kylafis, N. D., Tuffs, R. J., and Fischera, J. Modelling the spectral energy distribution of galaxies. I. Radiation fields and grain heating in the edge-on spiral NGC 891. *A&A*, 362:138, October 2000.

Popescu, C. C., Tuffs, R. J., Dopita, M. A., et al. Modelling the spectral energy distribution of galaxies. V. The dust and PAH emission SEDs of disk galaxies. *A&A*, 527, November 2010.

Rémy-Ruyer, A., Madden, S., Galliano, F., et al. Revealing the cold dust in low-metallicity environments. I. Photometry analysis of the Dwarf Galaxy Survey with Herschel. *A&A*, 557:A95, September 2013.

Rémy-Ruyer, A., Madden, S. C., Galliano, F., et al. Gas-to-Dust mass ratios in local galaxies over a 2 dex metallicity range. *A&A*, 563, December 2014.

Revéret, V., André, P., Le Pennec, J., et al. The artémis wide-field sub-millimeter camera: preliminary on-sky performance at 350 microns. In *Millimeter, Submillimeter, and Far-Infrared Detectors and Instrumentation for Astronomy VII*, volume 9153, page 915305. International Society for Optics and Photonics, 2014.

Rossa, J. and Dettmar, R.-J. An Hα survey aiming at the detection of extraplanar diffuse ionized gas in halos of edge-on spiral galaxies. II. The Hα survey atlas and catalog. *A&A*, 406:505–525, August 2003.

Rowlands, K., Gomez, H. L., Dunne, L., et al. The dust budget crisis in high-redshift submillimetre galaxies. *MNRAS*, 441(2):1040–1058, June 2014.

Rubin, R. A Discussion of the Sizes and Excitation of H II Regions. *ApJ*, 154:391, October 1968.

Saftly, W., Baes, M., De Geyter, G., et al. Large and small-scale structures and the dust energy balance problem in spiral galaxies. *A&A*, 576:A31, April 2015.

Seon, K.-i., Witt, A., Shinn, J.-h., and Kim, I.-j. Diffuse Extraplanar Dust in NGC 891. *ApJ*, 785:L18, April 2014.

Smith, M., Eales, S., De Looze, I., et al. Far-reaching dust distribution in galaxy discs. *MNRAS*, 462:331–344, October 2016.

Sobolev, V. V. and Viktorovich, V. A treatise on radiative transfer. *Princeton, N.J., Van Nostrand [1963]*, 1963.

Strong, A., Dickinson, C., and Murphy, E. Synchrotron radiation from molecular clouds. *ArXiv e-prints*, December 2014.

Struve, F. G. W. Etudes d'Astronomie Stellaire: Sur la voie lactee et sur la distance des etoiles fixes. *St. Petersbg. Tip. Acad. Imper., 1847; IV, 165 p. ; 8.; DCCC.4.211*, 1847.

Taylor, M. B. TOPCAT and STIL: Starlink Table/VOTable Processing Software. In Shopbell, P., Britton, M., and Ebert, R., editors, *Astronomical Data Analysis Software and Systems XIV*, volume 347 of *Astronomical Society of the Pacific Conference Series*, page 29, December 2005.

Tibbs, C., Paladini, R., Compiègne, M., et al. A Multi-wavelength Investigation of RCW175: An H II Region Harboring Spinning Dust Emission. *ApJ*, 754:94, August 2012.

Tielens, A. G. G. M. *The Physics and Chemistry of the Interstellar Medium*. Cambridge University Press, Cambridge, 2005.

Todini, P. and Ferrara, A. Dust formation in primordial Type II supernovae. *MNRAS*, (325):726–736, 2001.

Trumpler, R. J. Absorption of Light in the Galactic System. *PASP*, 42:214, August 1930.

Tuffs, R. J., Popescu, C. C., Völk, H. J., Kylafis, N. D., and Dopita, M. A. Modelling the spectral energy distribution of galaxies. *A&A*, 419(3):821–835, June 2004.

Vaidya, B., Fendt, C., and Beuther, H. Accretion Disks Around Massive Stars: Hydrodynamic Structure, Stability, and Dust Sublimation. *ApJ*, 702:567–579, September 2009.

van der Walt, S., Colbert, S. C., and Varoquaux, G. The NumPy Array: A Structure for Efficient Numerical Computation. *Computing in Science and Engineering*, 13: 22–30, March 2011.

Verstappen, J., Fritz, J., Baes, M., et al. HERschel Observations of Edge-on Spirals (HEROES). I. Far-infrared morphology and dust mass determination. *A&A*, 556: A54, August 2013.

von Hausegger, S. and Liu, H. The morphology of the Anomalous Microwave Emission in the Planck 2015 data release. *J. Cosmology Astropart. Phys.*, 8:29, August 2015.

Waskom, M., Botvinnik, O., Hobson, P., et al. Seaborn: statistical data visualization. *URL: https://seaborn. pydata. org/(visited on 2017-05-15)*, 2014.

Westcott, J. A High-Resolution Radio Continuum Study of the Dwarf Irregular Galaxy IC10. Master's thesis, University of Hertfordshire, Hertfordshire: UK, 2015.

Whaley, C. H., Irwin, J. A., Madden, S. C., Galliano, F., and Bendo, G. J. A multi-wavelength infrared study of NGC 891. *MNRAS*, 395(1):97–113, 2009.

Whittet, D. *Dust in the Galactic Environment*. IOP, London, 2002.

Wolfe, A. M., Gawiser, E., and Prochaska, J. X. Damped Lyman alpha Systems. *ARA&A*, 43:861–918, September 2005.

Wood, K. and Jones, T. J. Modeling Polarization Maps of External Galaxies. *AJ*, 114:1405, October 1997.

Wright, E. L., Eisenhardt, P. R. M., Mainzer, A., et al. The Wide-field Infrared Survey Explorer (WISE): Mission Description and Initial On-orbit Performance. *ApJ*, 140:1868–1881, July 2010.

Xilouris, E., Kylafis, N., Papamastorakis, J., Paleologou, E., and Haerendel, G. The distribution of stars and dust in spiral galaxies: the edge-on spiral UGC 2048. *A&A*, 325:135–143, September 1997.

Xilouris, E., Alton, P., Davies, J., et al. Optical and NIR modelling of NGC 891. *A&A*, 331:894–900, March 1998.

Xilouris, E., Byun, Y., Kylafis, N., Paleologou, E., and Papamastorakis, J. Are spiral galaxies optically thin or thick? *A&A*, 344:868–878, April 1999.

Zaritsky, D. Preliminary evidence for dust in galactic halos. *Astronomical Journal*, 108(5):1619–1626, November 1994.

Zhukovska, S. Dust origin in late-type dwarf galaxies: ISM growth vs. type II supernovae. *A&A*, 562:A76, February 2014.

APPENDIX A

This Appendix presents the full results of the brightness profile fitting for all 31 galaxies in the edge-on sample at the 5 *Herschel* wavelengths, as per Chapter 2.

In each galaxy section, the brightness profiles are presented at 100, 160, 250, 350 and 500 μm. In each case, the galaxy profiles are presented in blue, and model profiles for comparison in black. An exponential curve has been fitted to each profile. The x-axis shows the distance of each pixel row from the central plane of the galaxy. The y-axis represents the summed pixel value for each row of pixels above the plane in Jy. The profiles have been normalised to match at the peak. In the lower plots, we subtract the thin disk and stellar profiles from the galaxy profile to see the difference in detected emission. If this value is above 0, we detect dust emission that is above what we expect from either an inclined thin disk or stellar disk.

Images of each galaxy at the same 5 wavelengths are shown. The grid lines represent a scale of 2 kpc, and the red bar in each case represents the value for β_d calculated for each galaxy via the ellipse fitting procedure.

A.1 IC2233

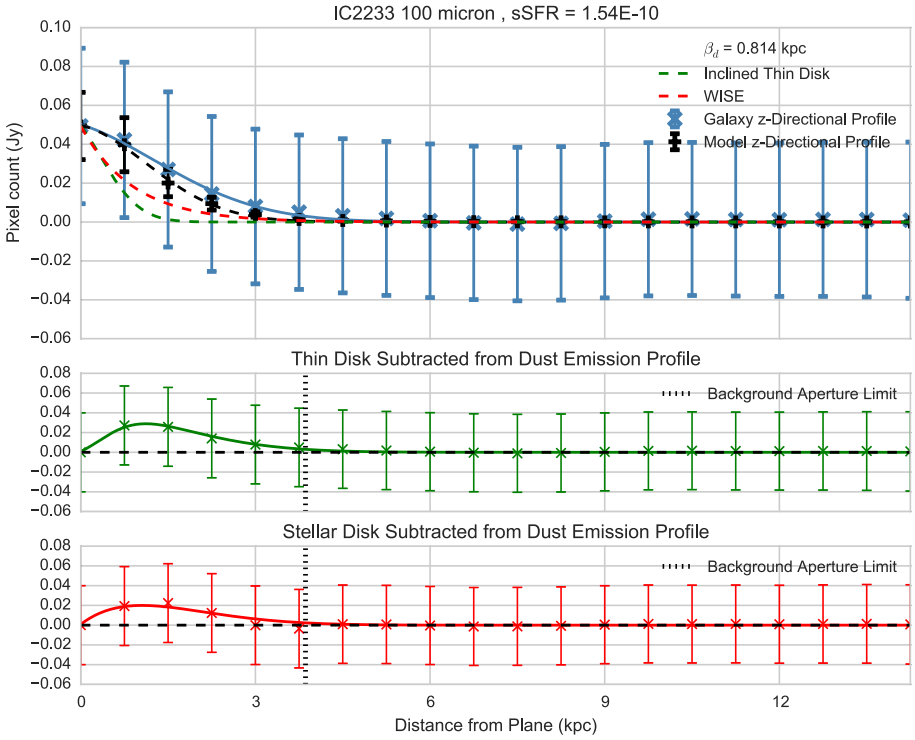

Figure A.1

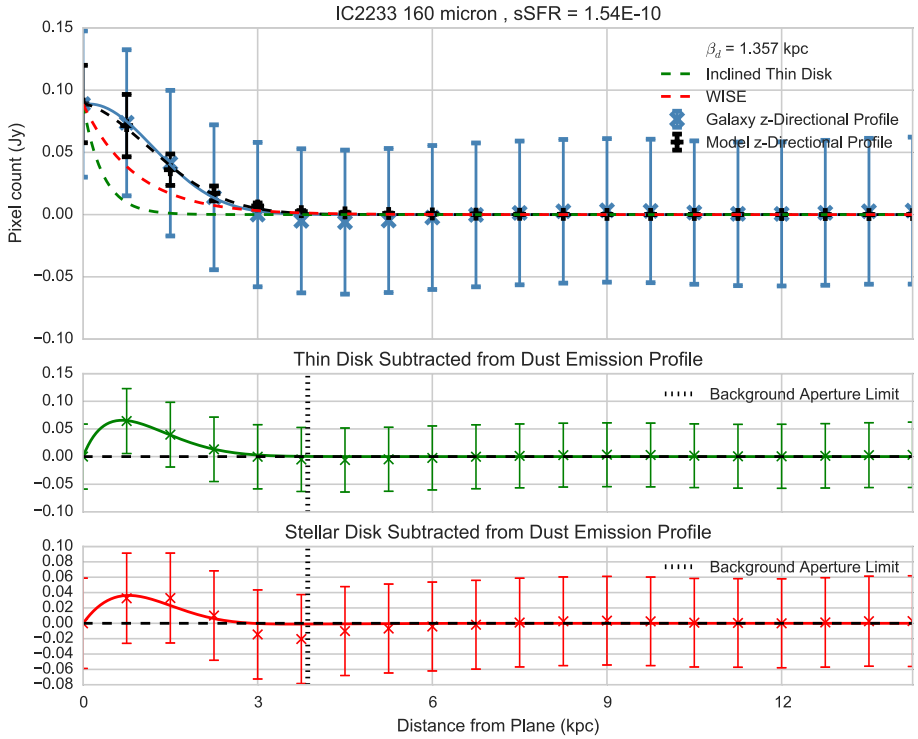

Figure A.2

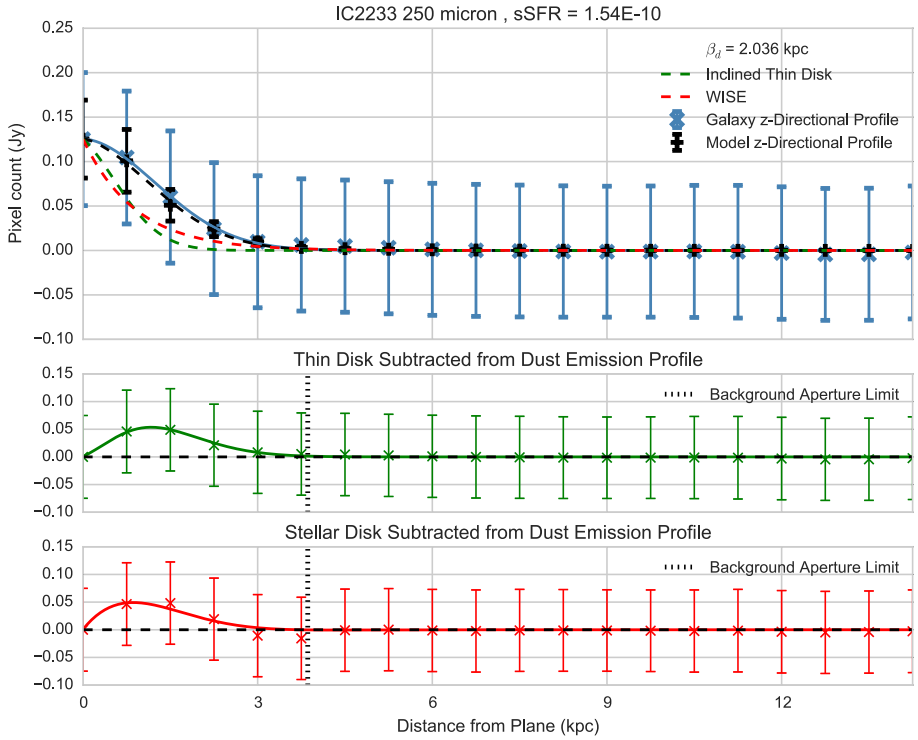

Figure A.3

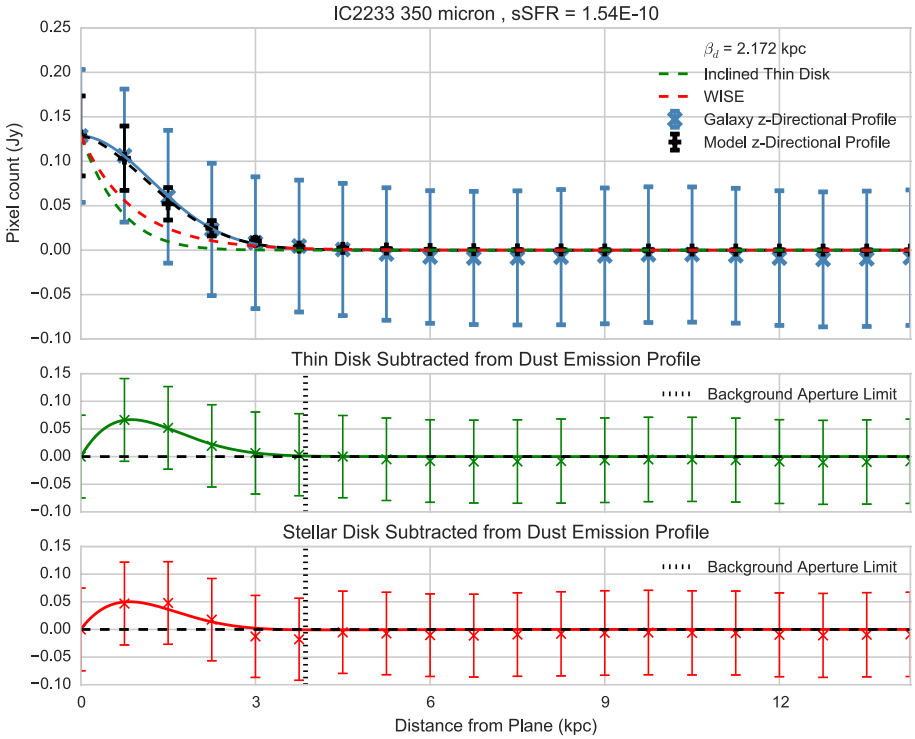

Figure A.4

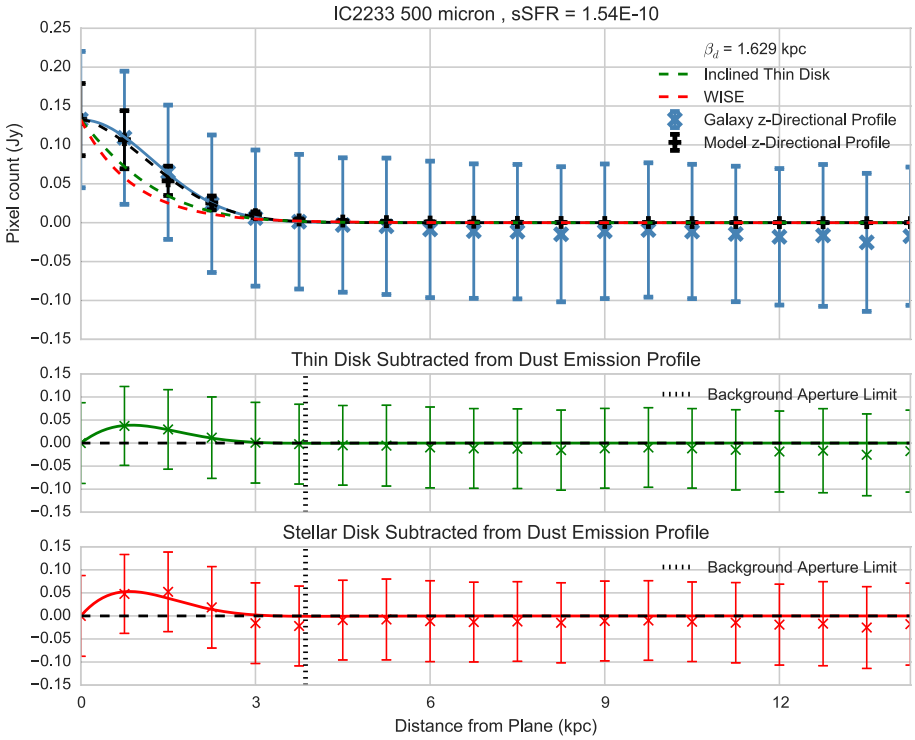

Figure A.5

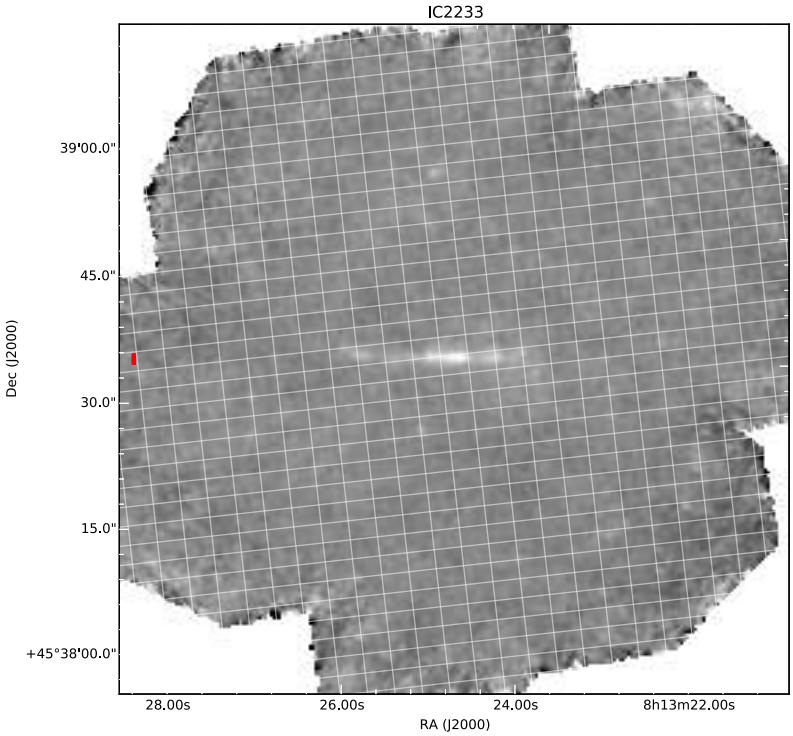

Figure A.6: 100 μm

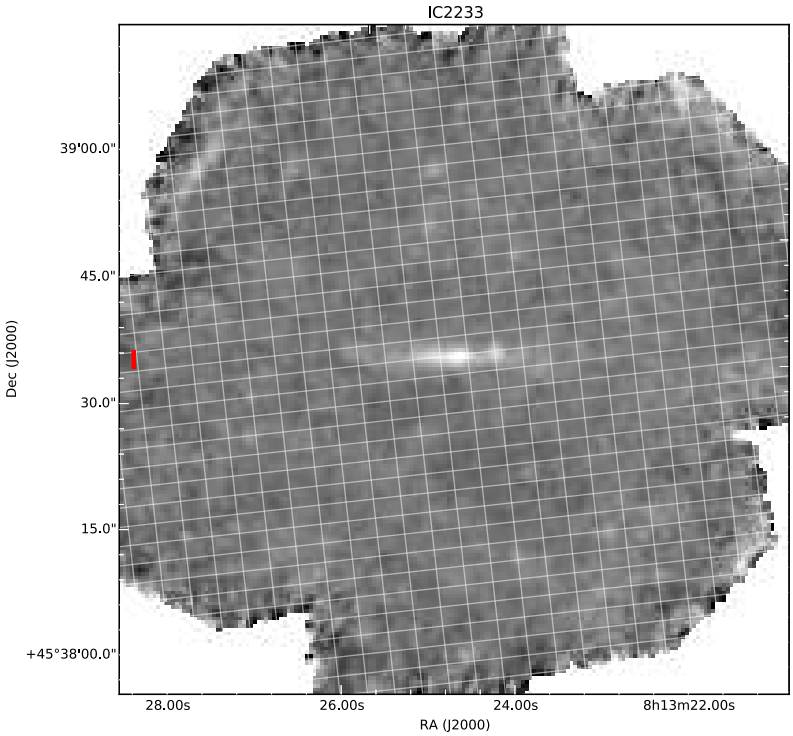

Figure A.7: 160 μm

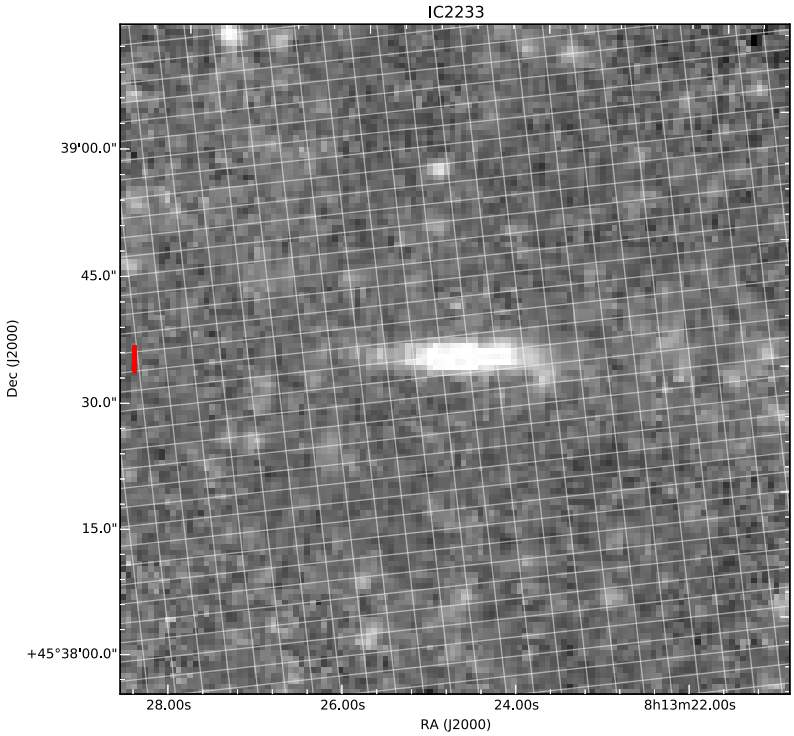

Figure A.8: 250 μm

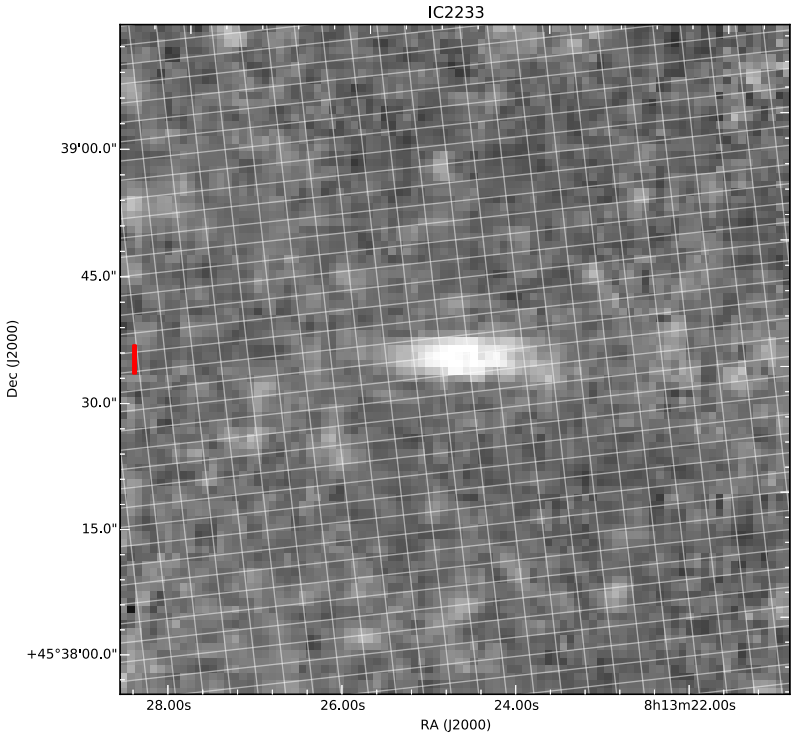

Figure A.9: 350 μm

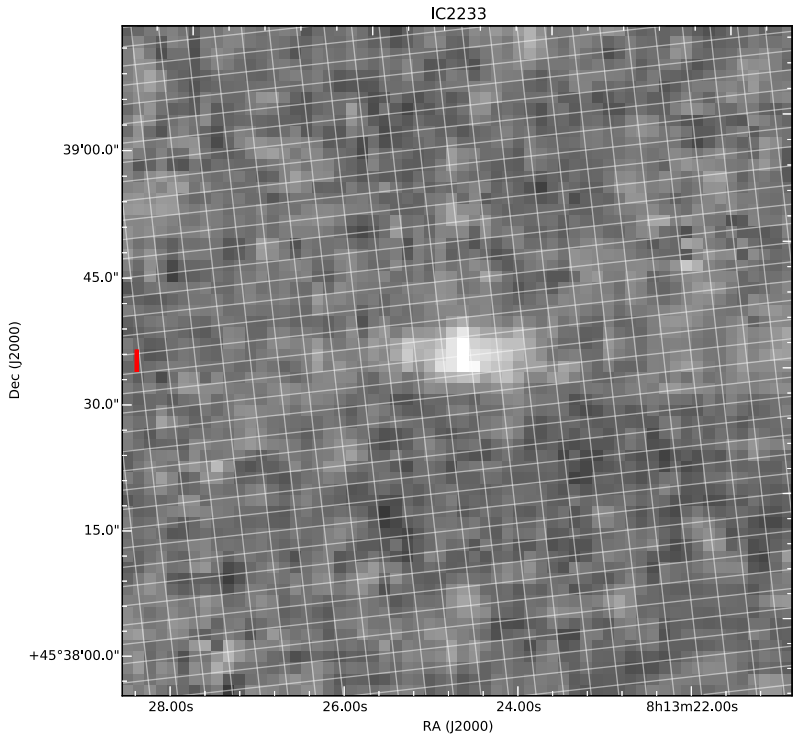

Figure A.10: 500 μm

A.2 NGC0678

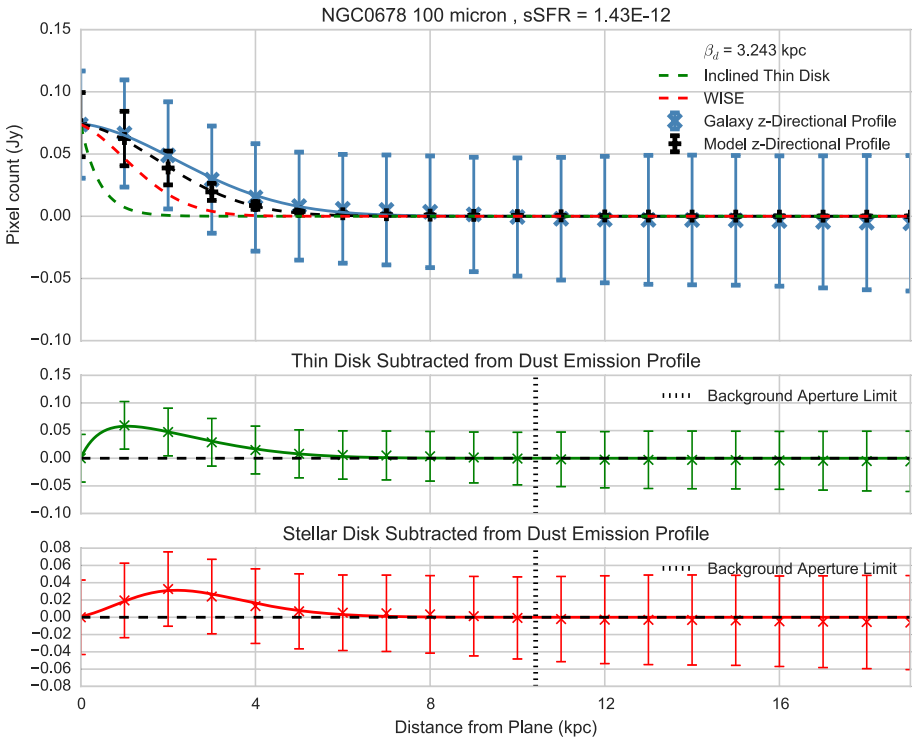

Figure A.11

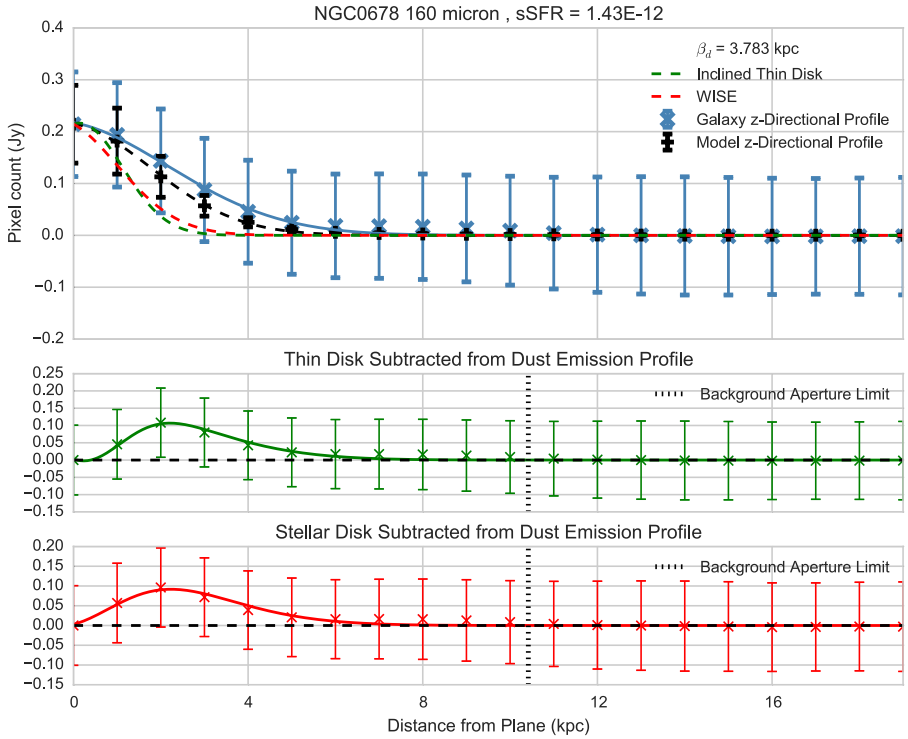

Figure A.12

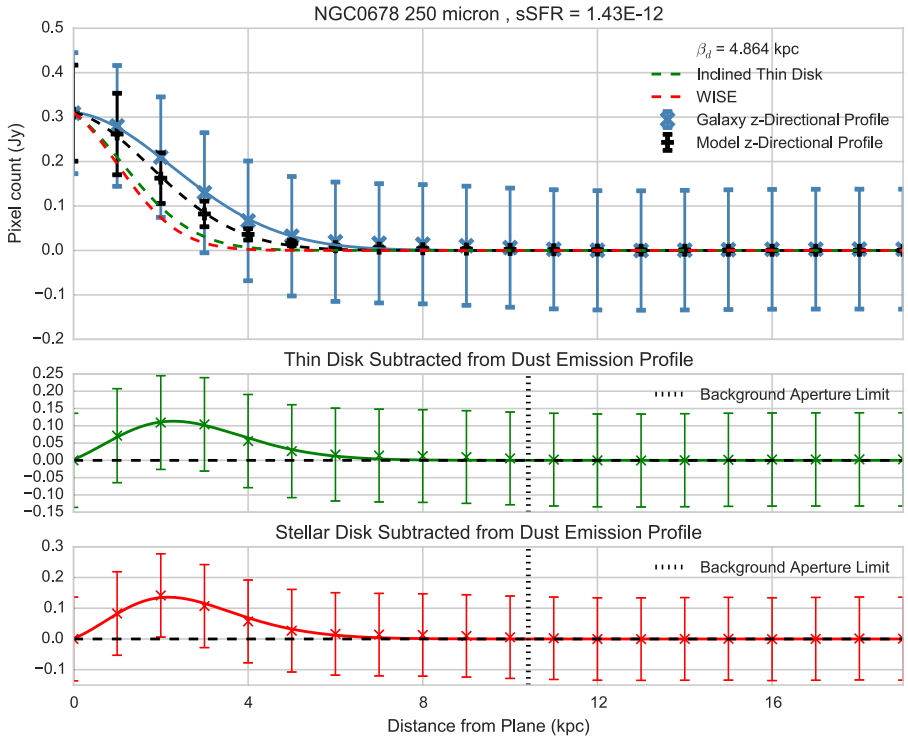

Figure A.13

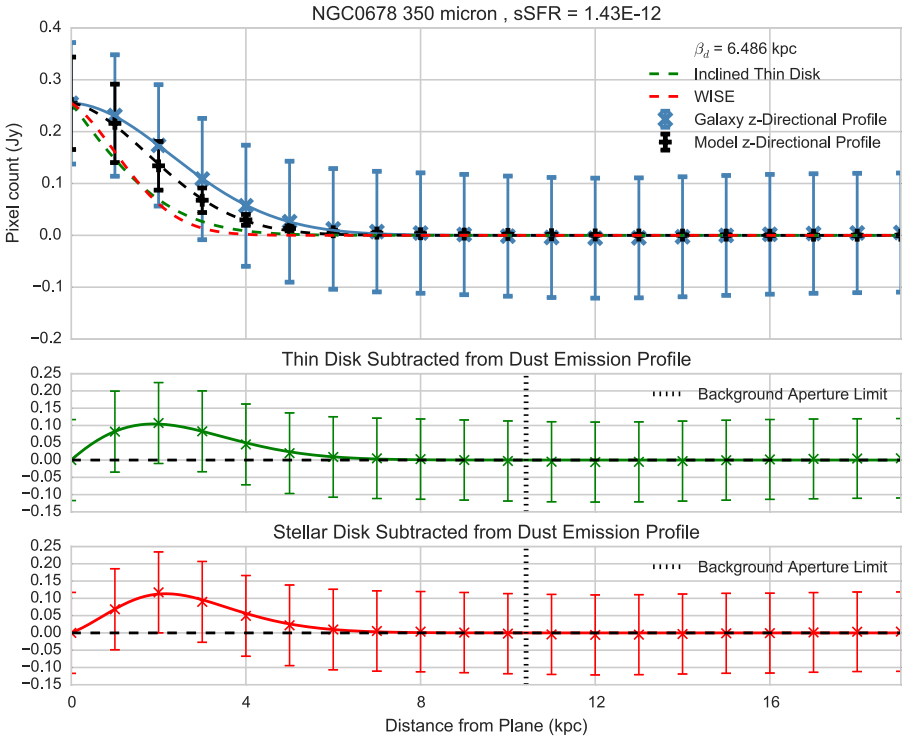

Figure A.14

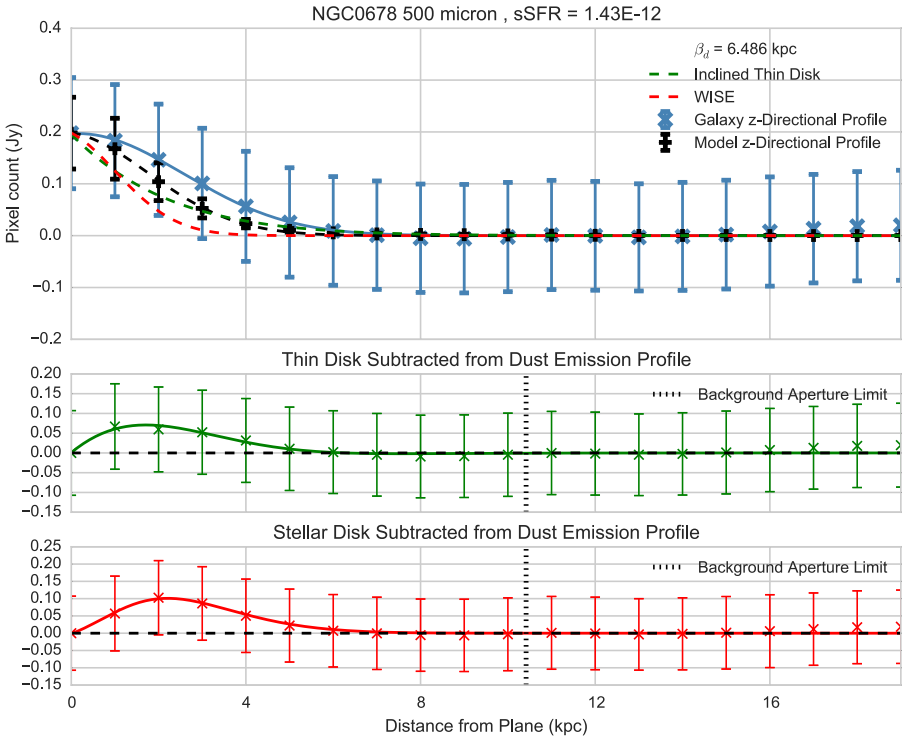

Figure A.15

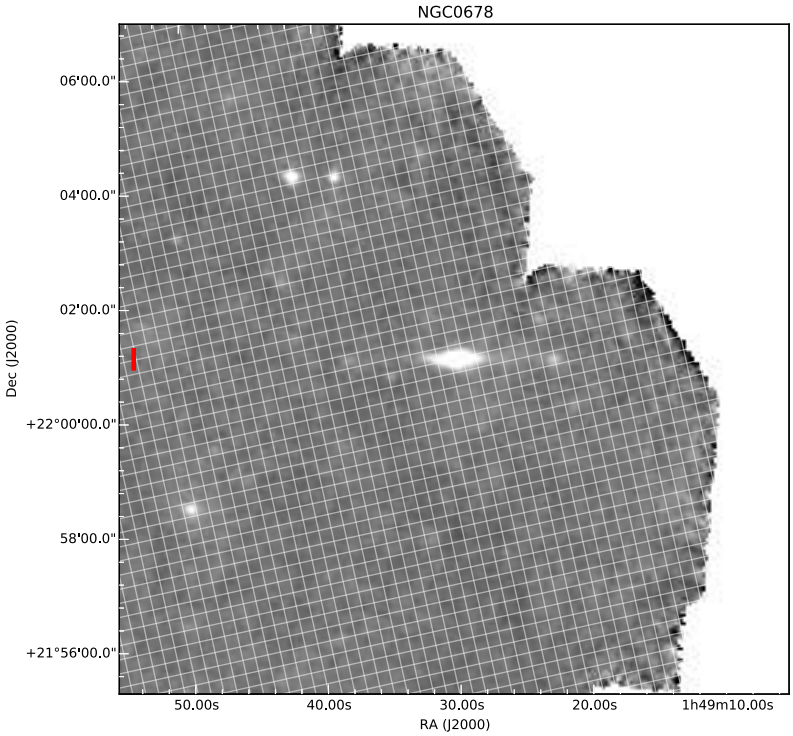

Figure A.16: 100 μm

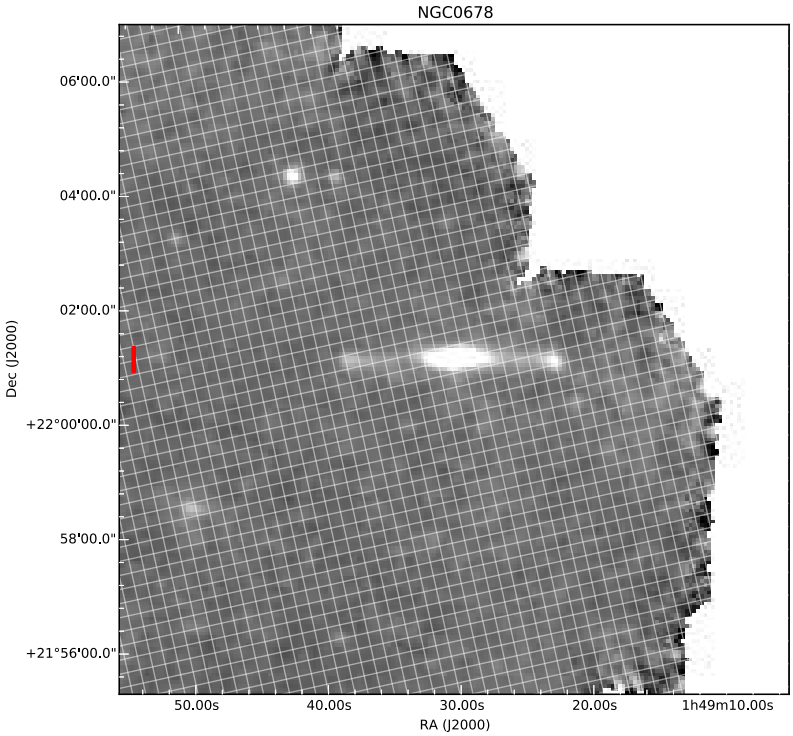

Figure A.17: 160 μm

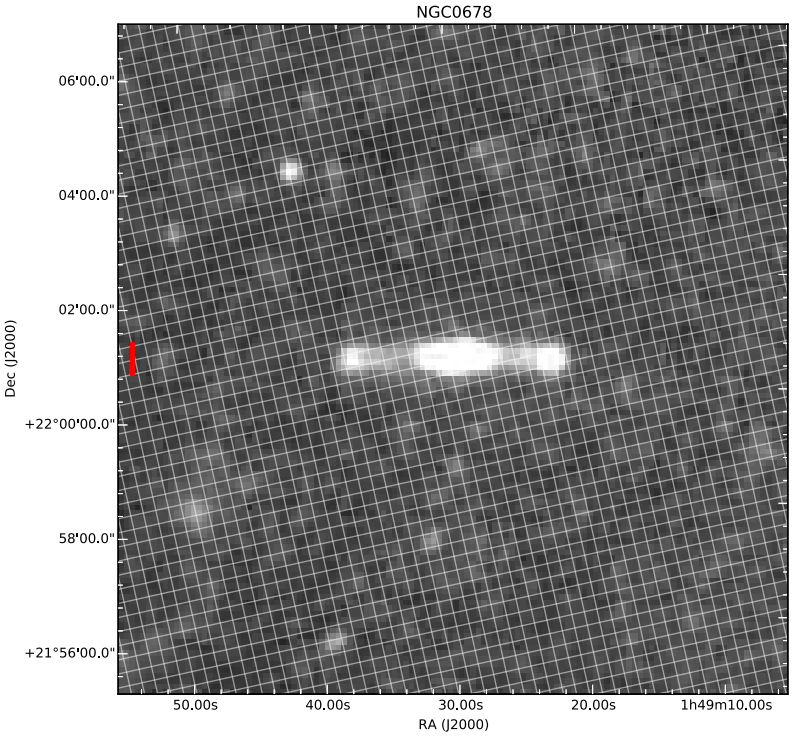

Figure A.18: 250 μm

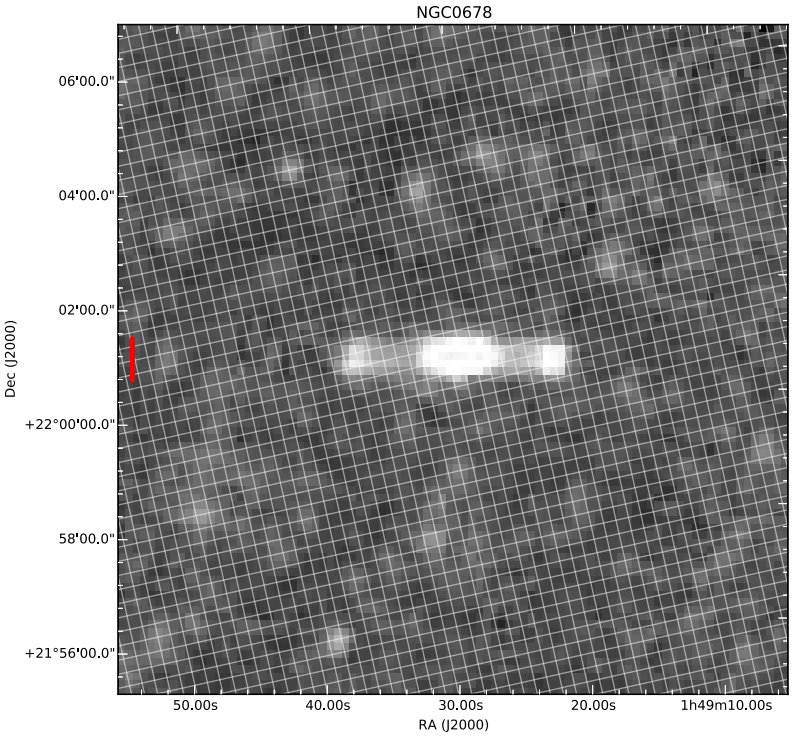

Figure A.19: 350 μm

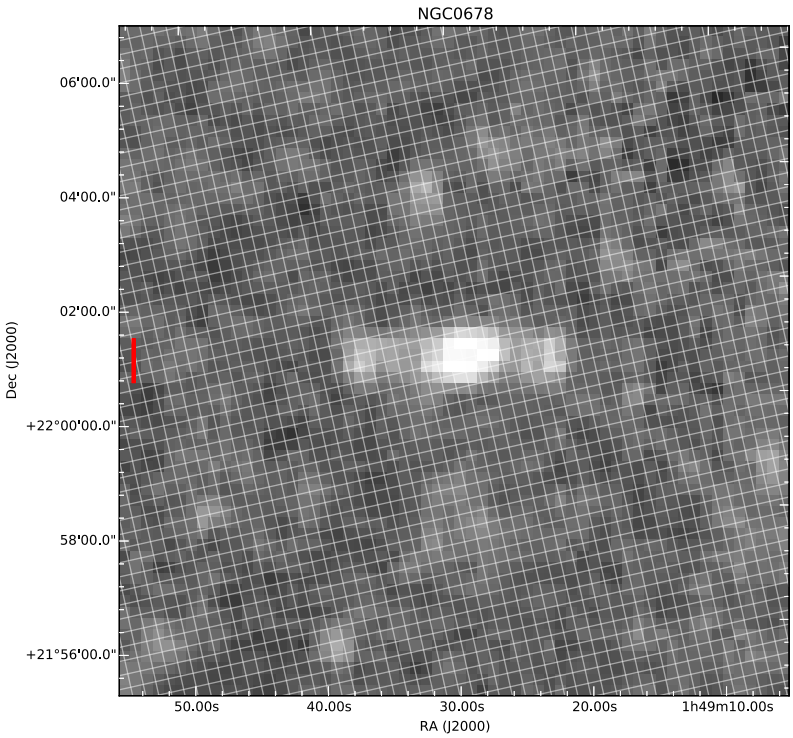

Figure A.20: 500 μm

A.3 NGC0891

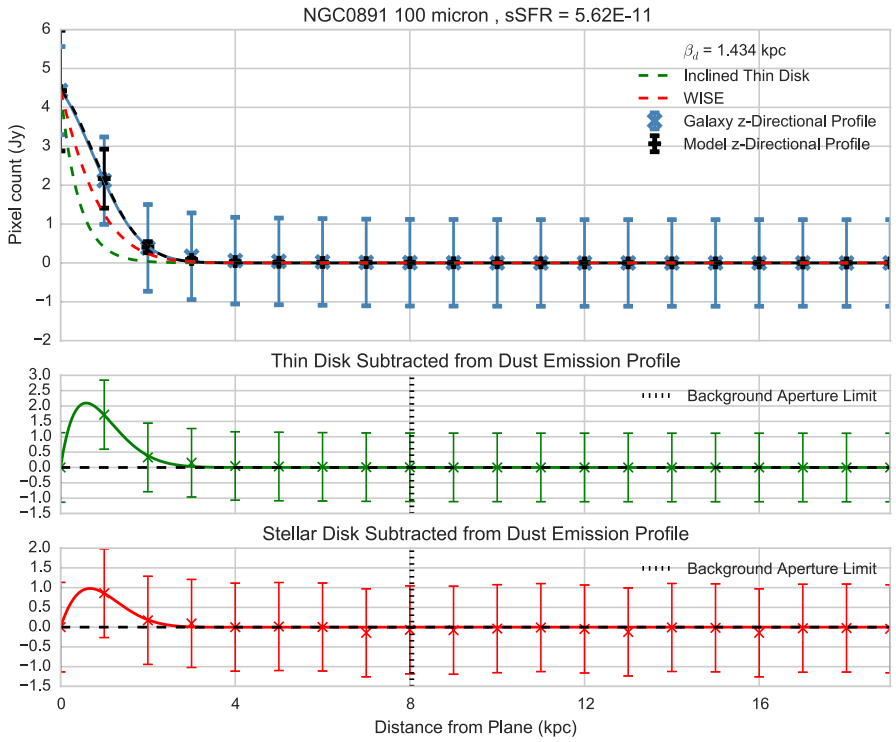

Figure A.21

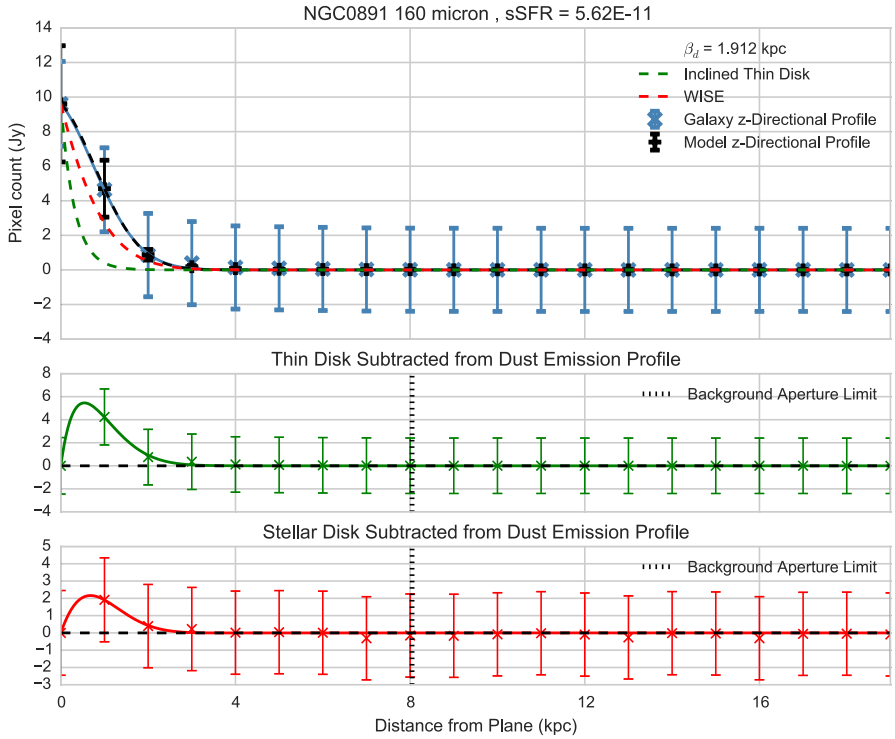

Figure A.22

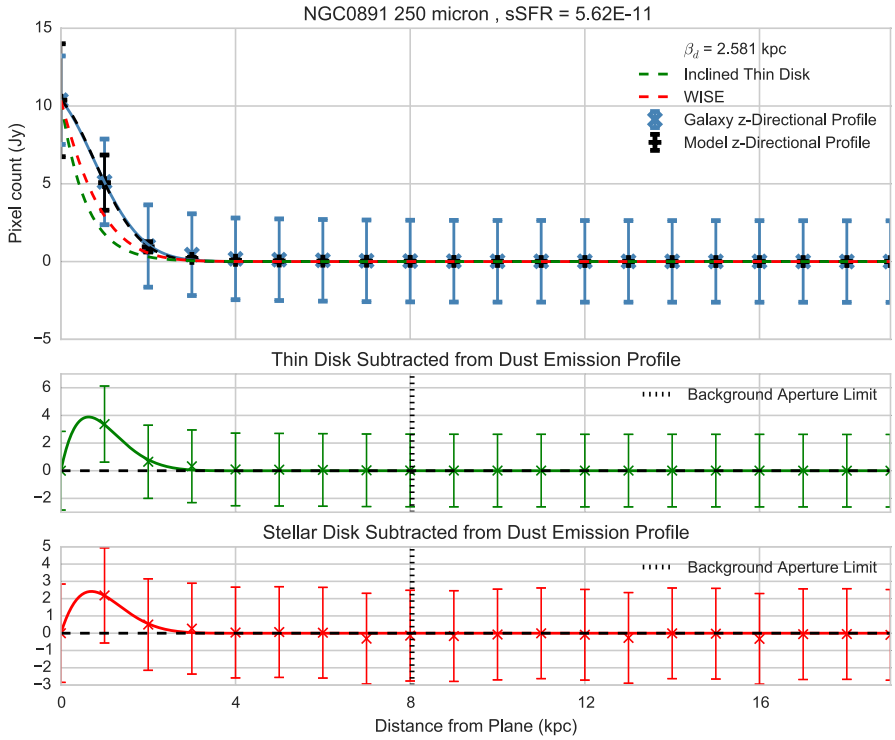

Figure A.23

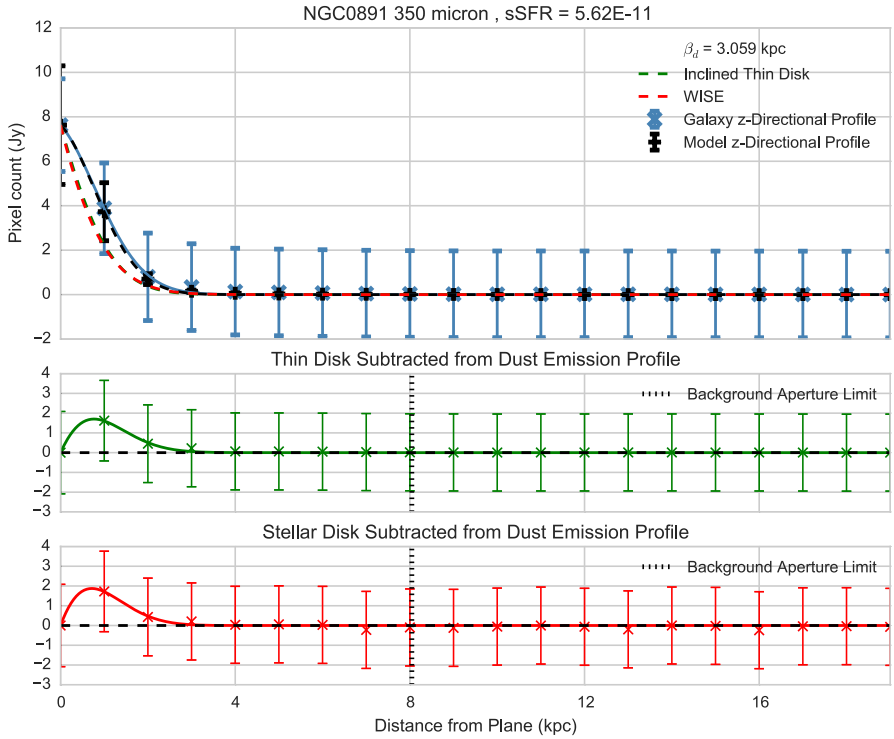

Figure A.24

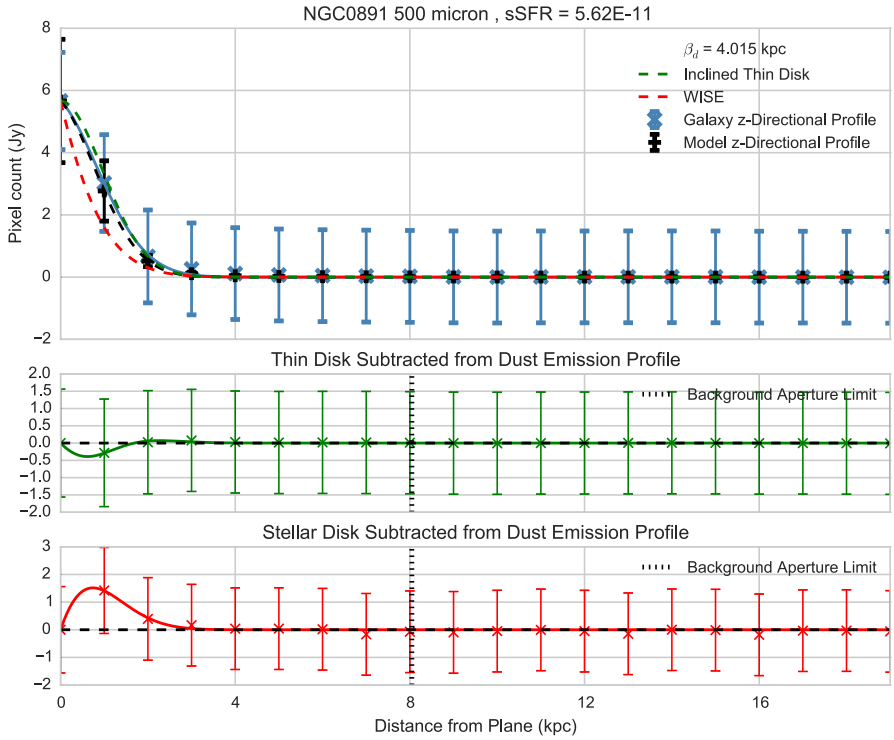

Figure A.25

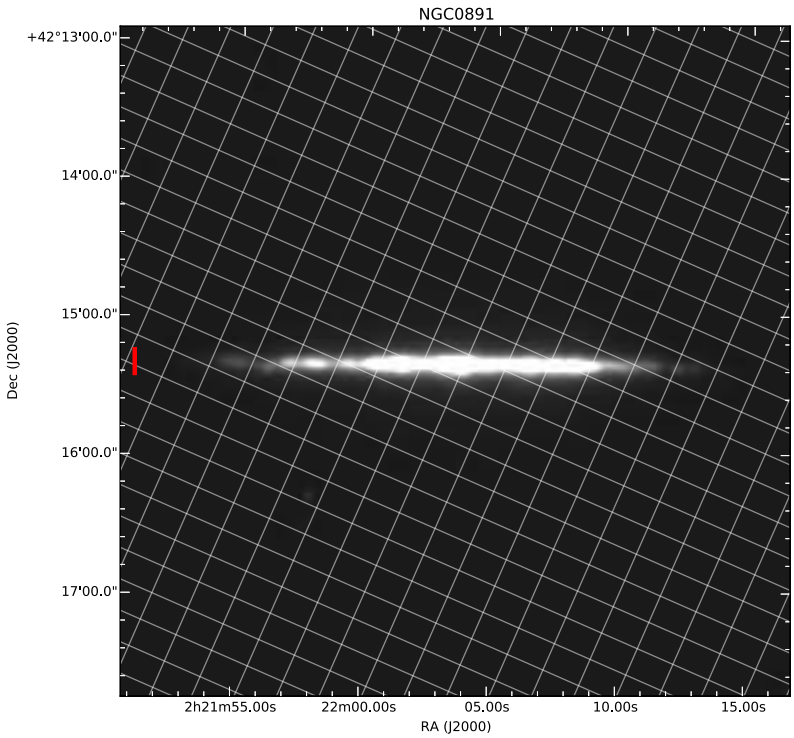

Figure A.26: 100 μm

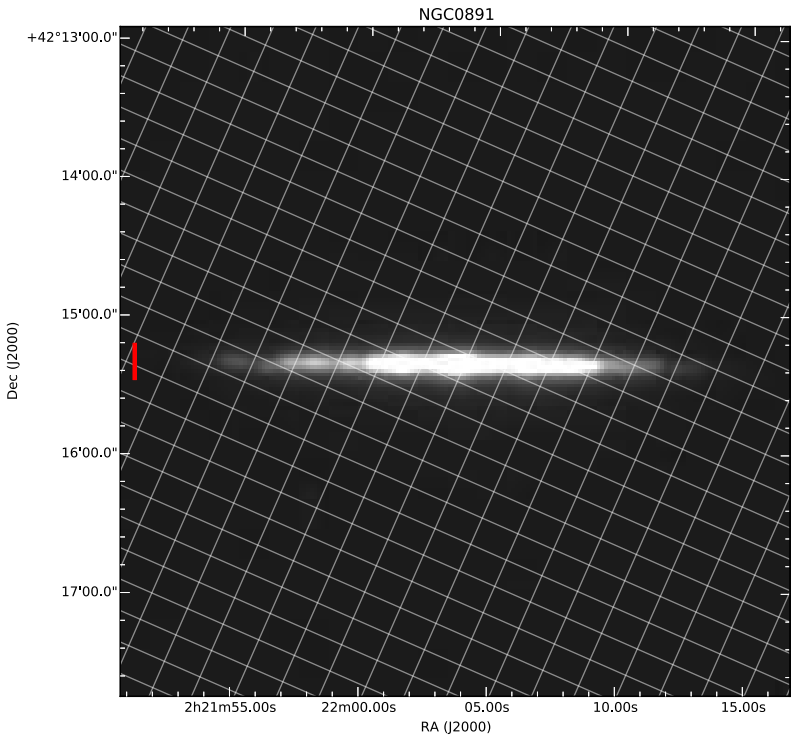

Figure A.27: 160 μm

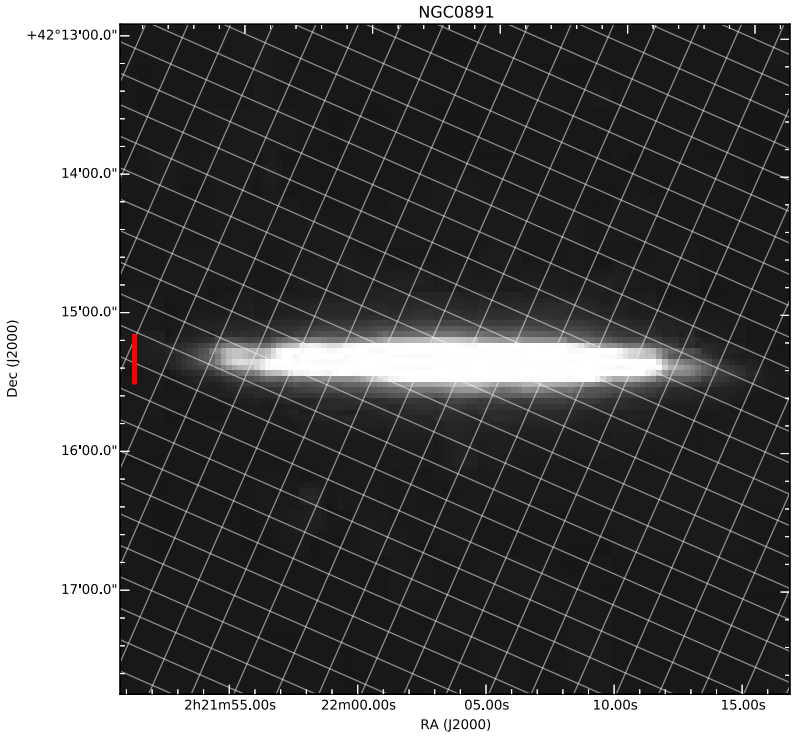

Figure A.28: 250 μm

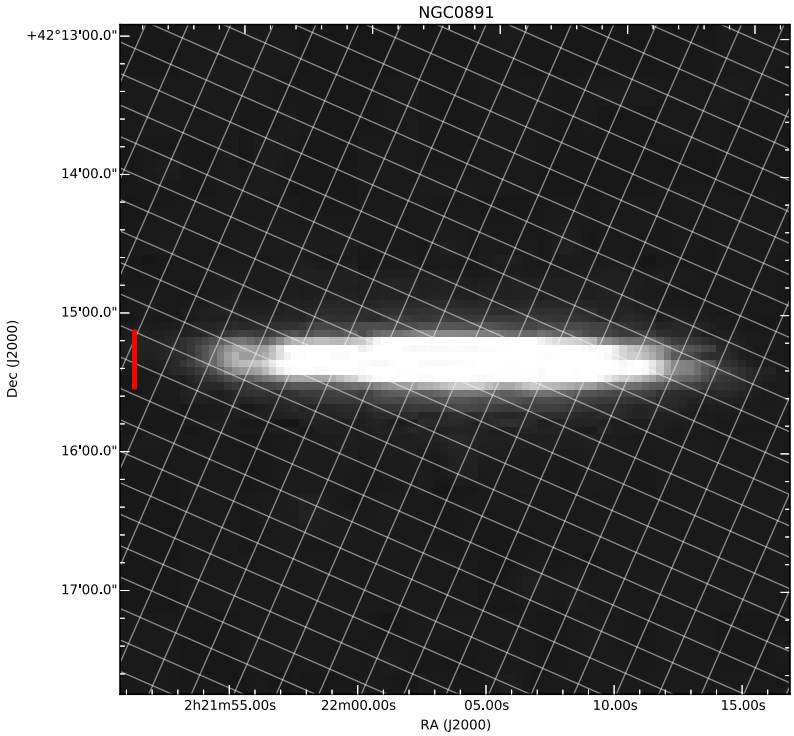

Figure A.29: 350 μm

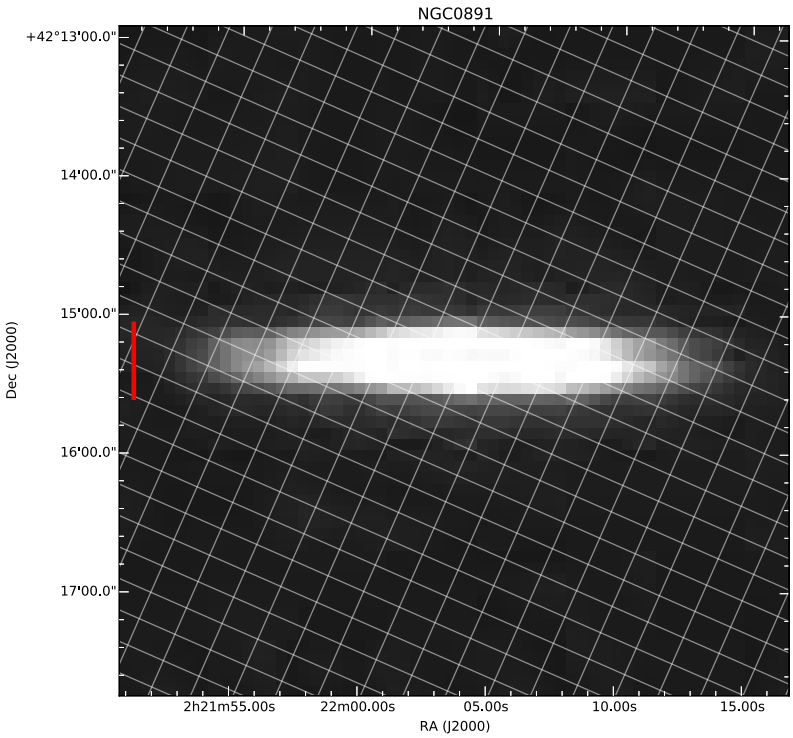

Figure A.30: 500 μm

A.4 NGC1351A

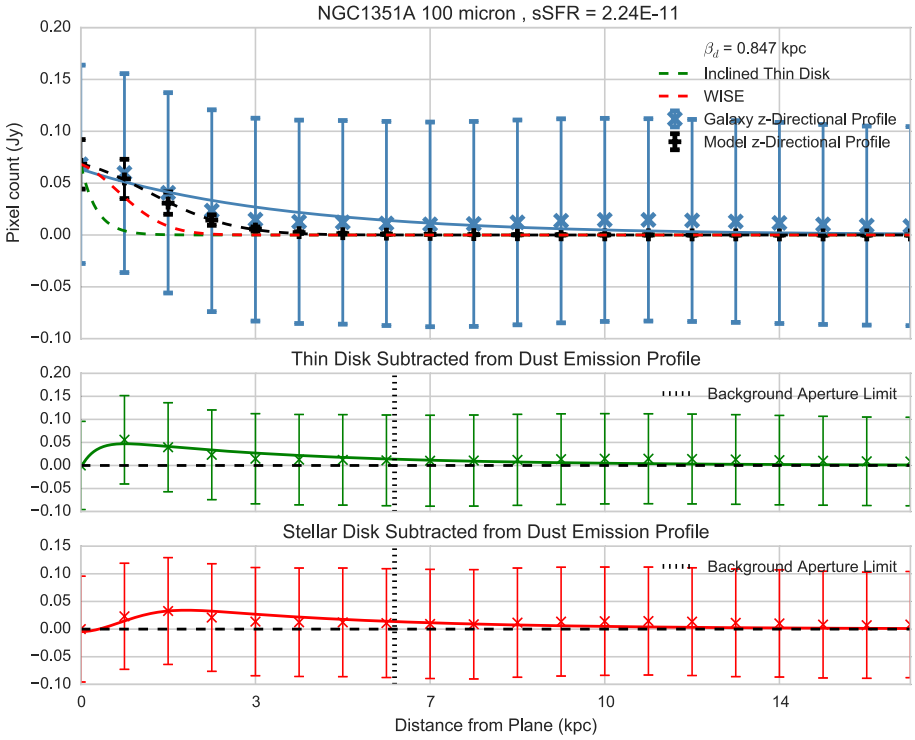

Figure A.31

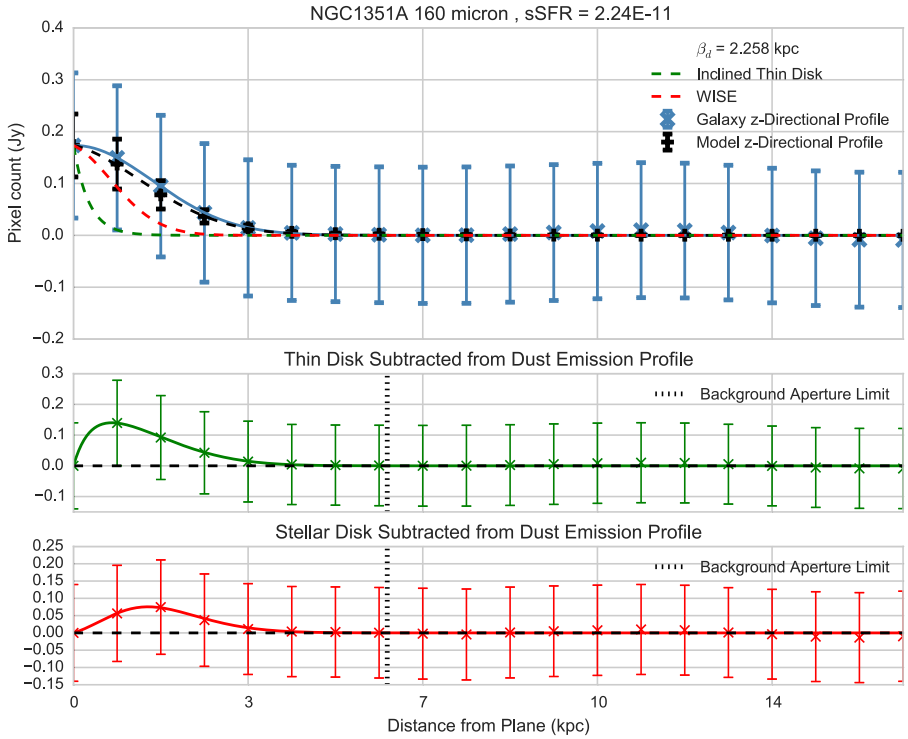

Figure A.32

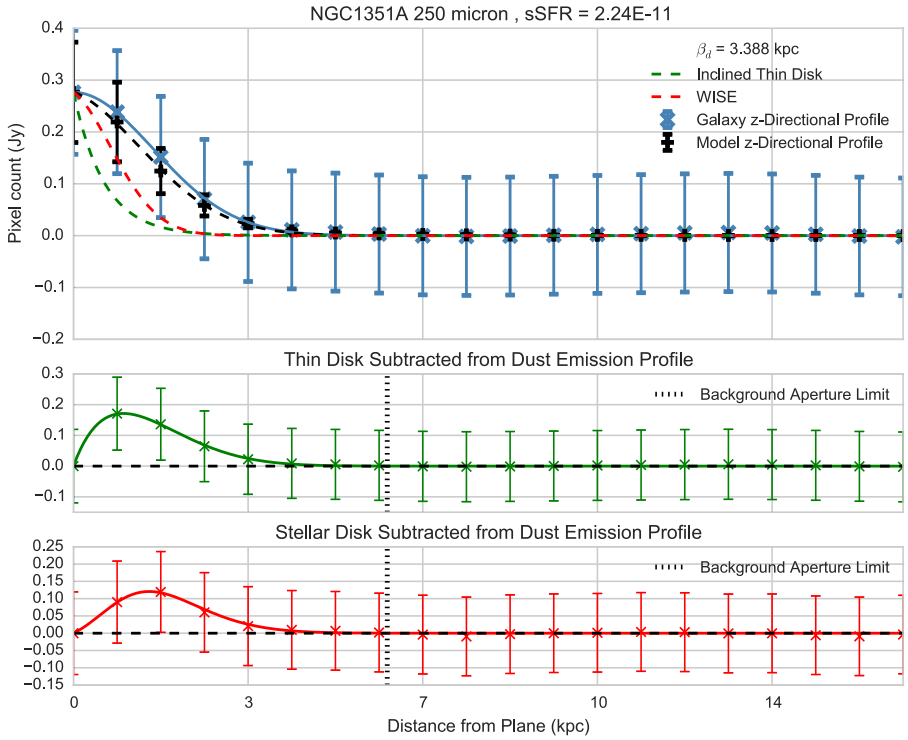

Figure A.33

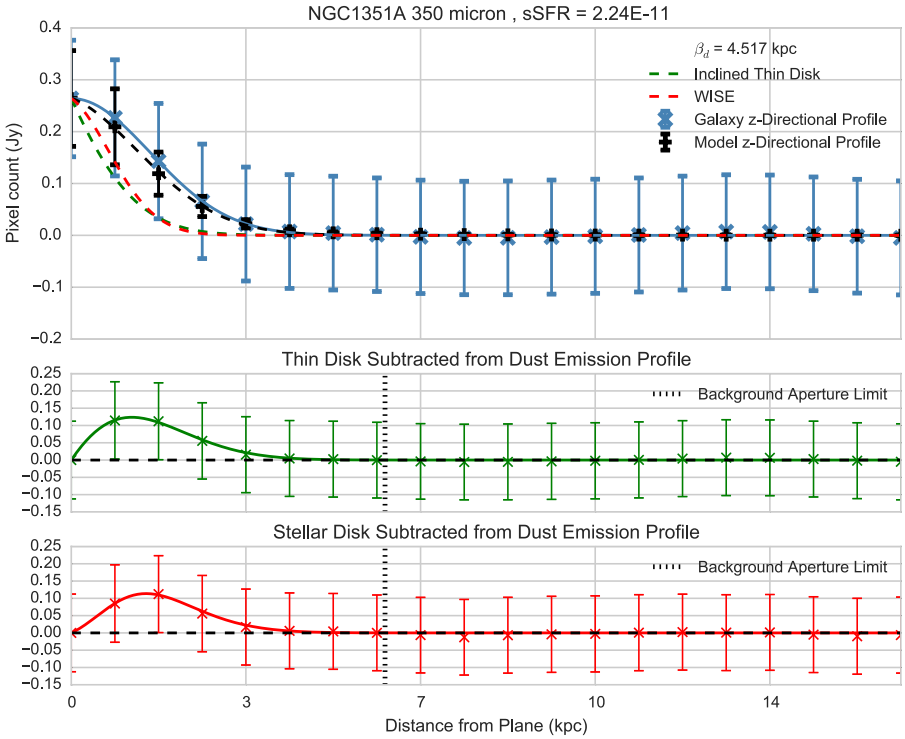

Figure A.34

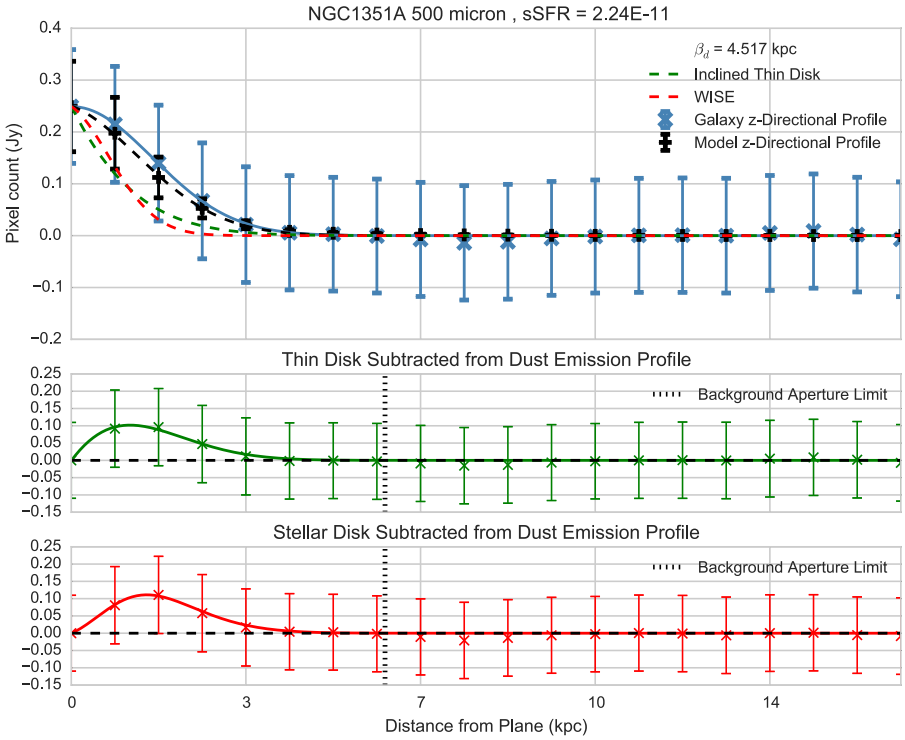

Figure A.35

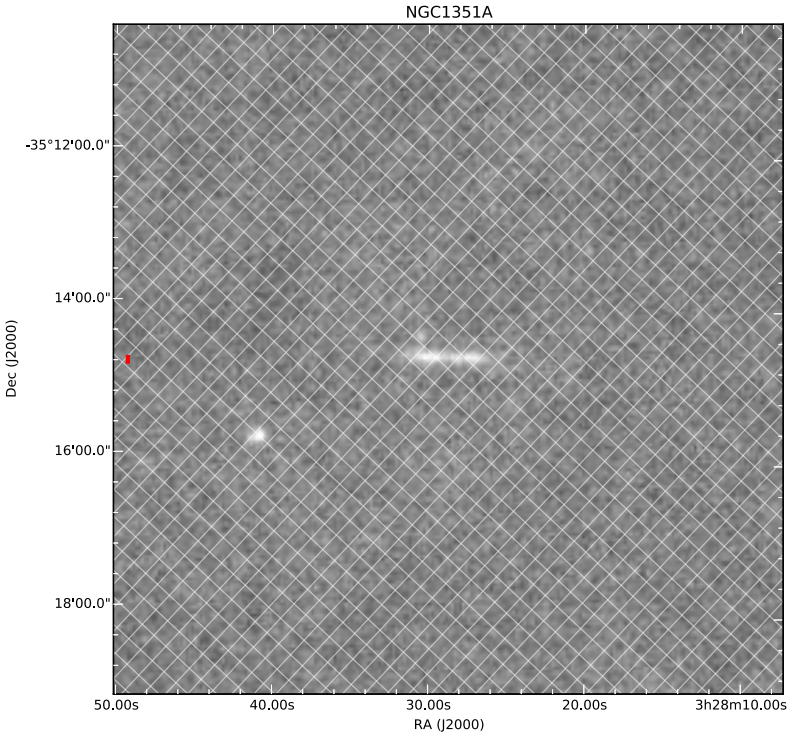

Figure A.36: 100 μm

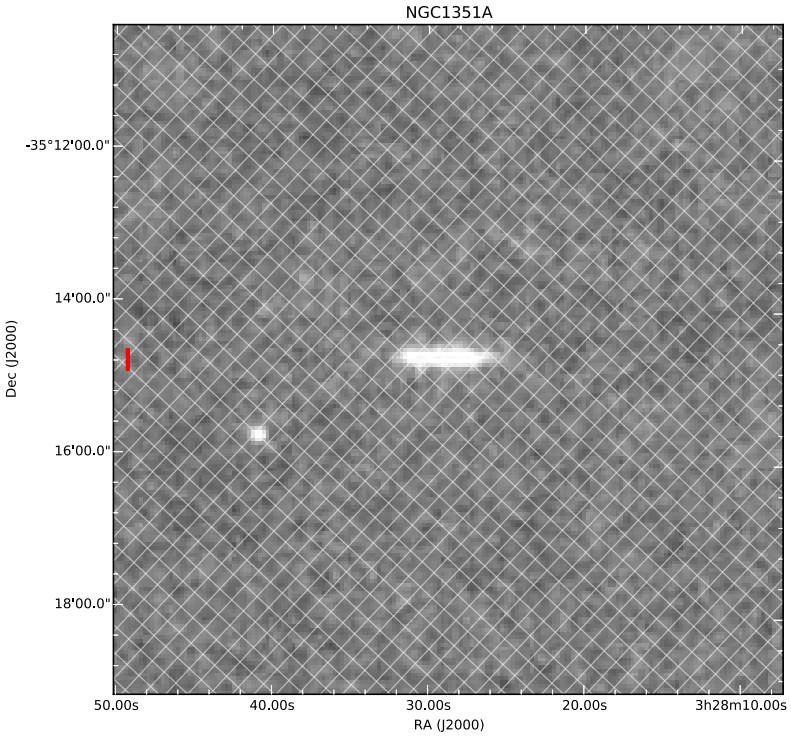

Figure A.37: 160 μm

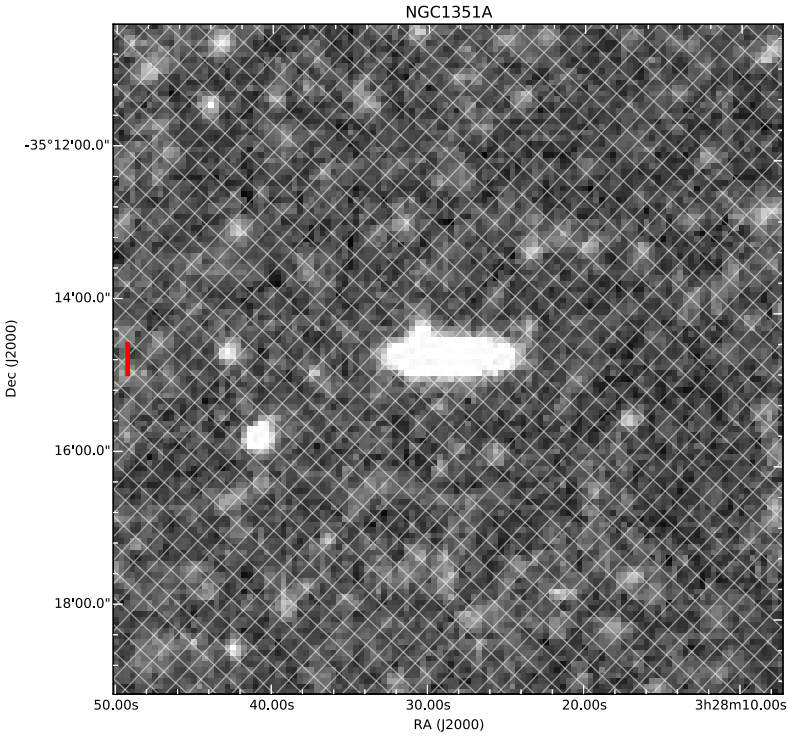

Figure A.38: 250 μm

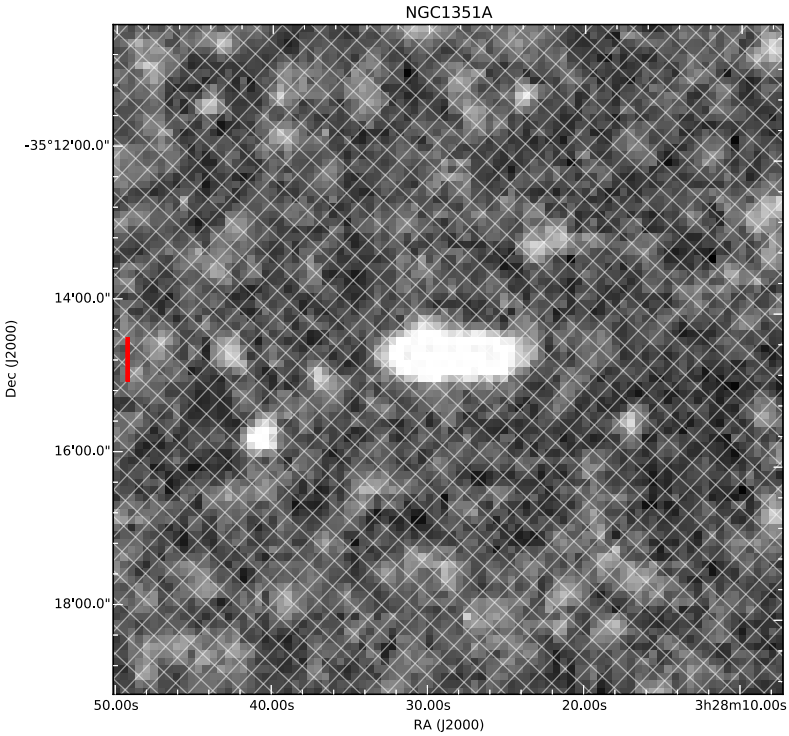

Figure A.39: 350 μm

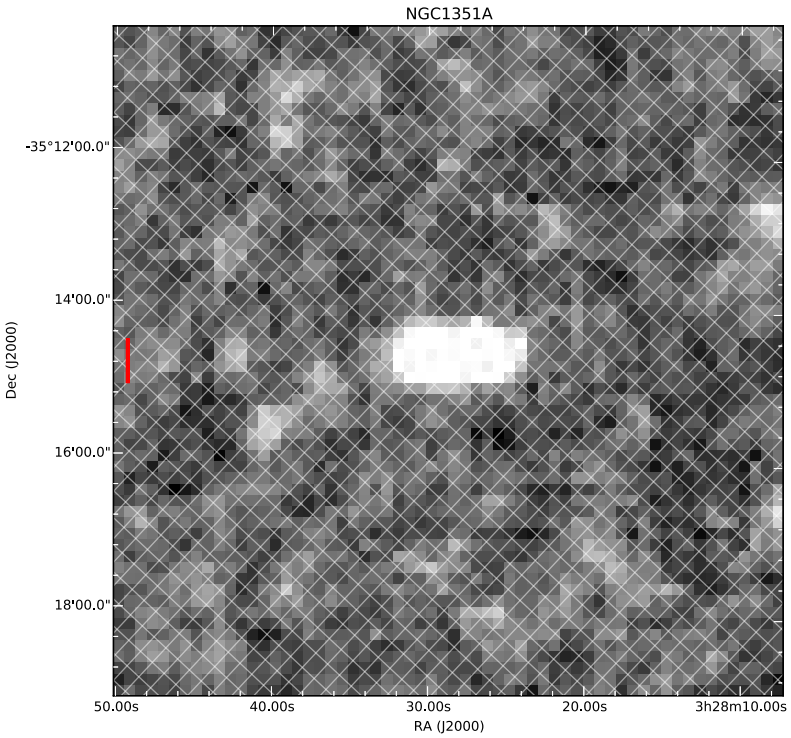

Figure A.40: 500 μm

A.5 NGC3079

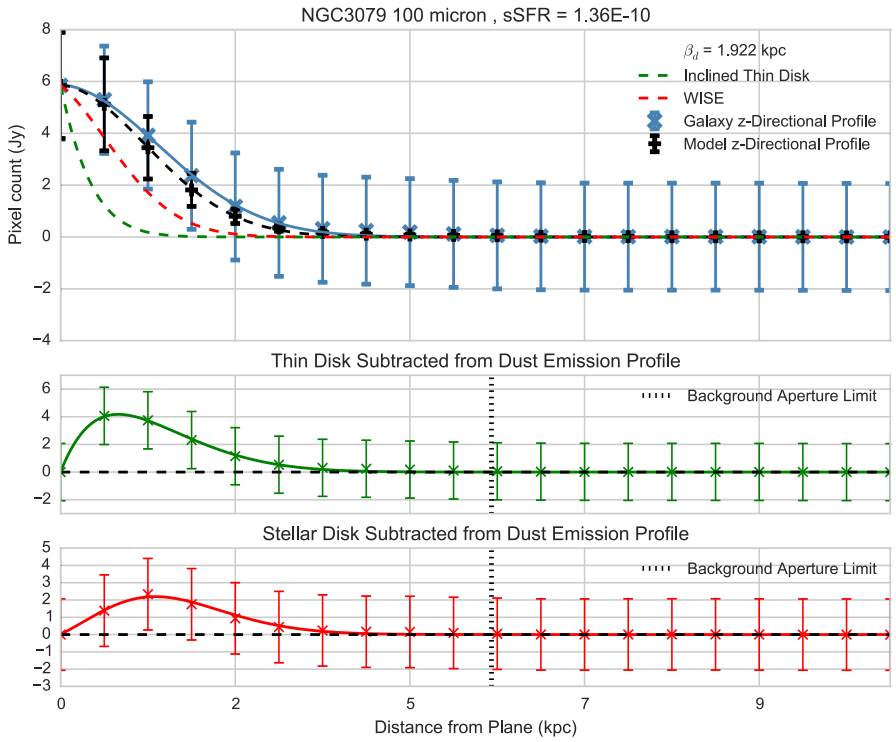

Figure A.41

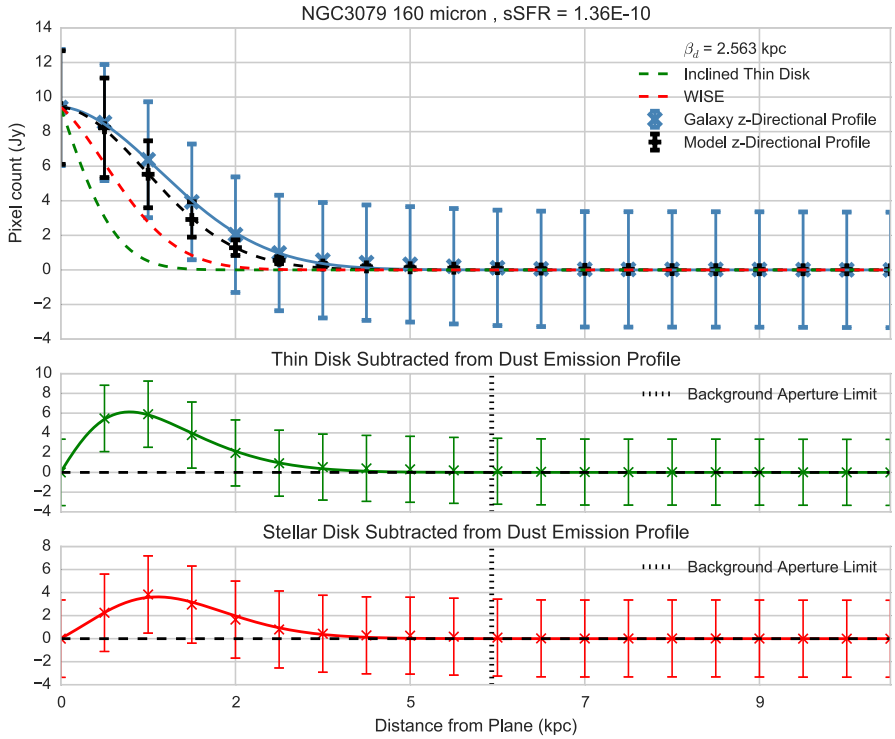

Figure A.42

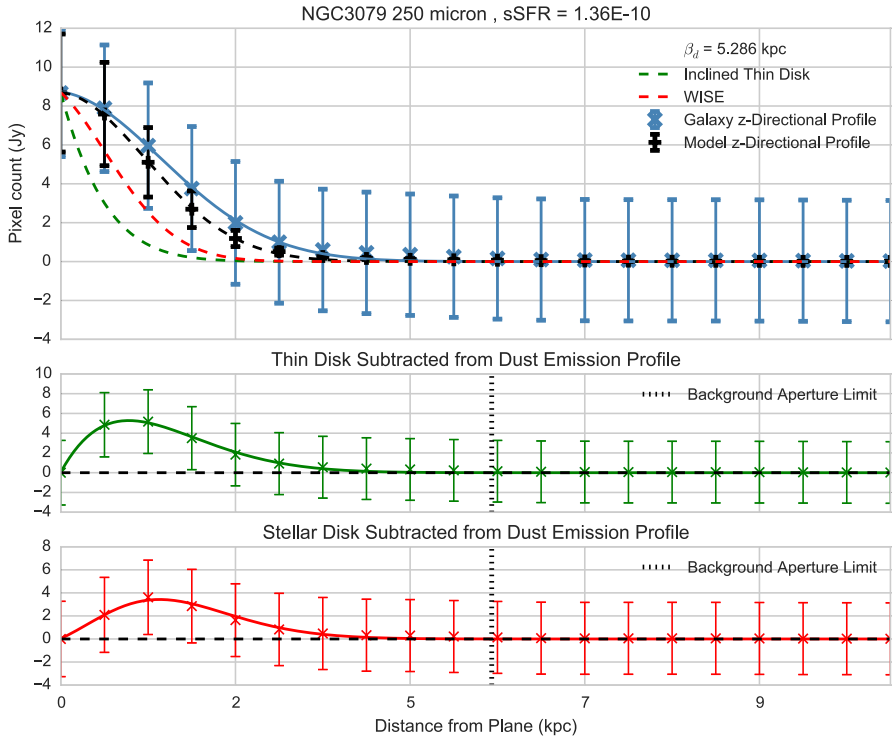

Figure A.43

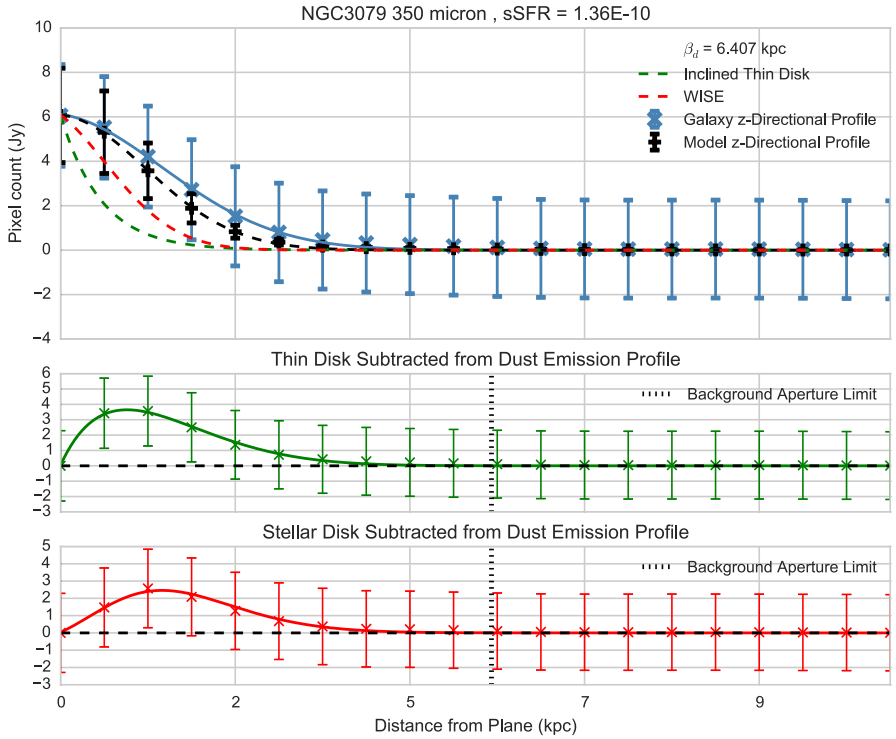

Figure A.44

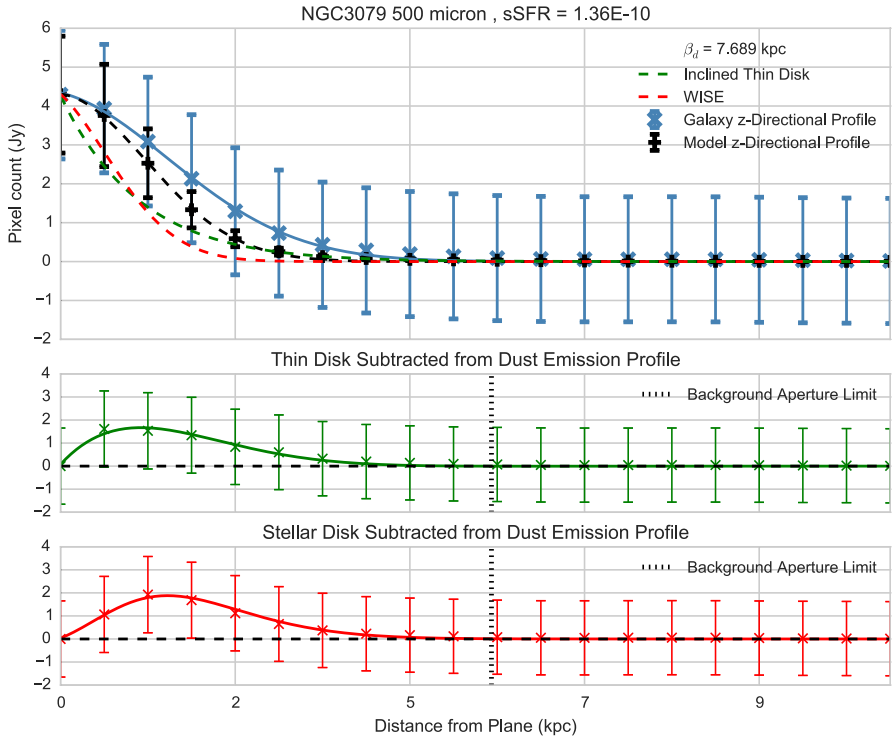

Figure A.45

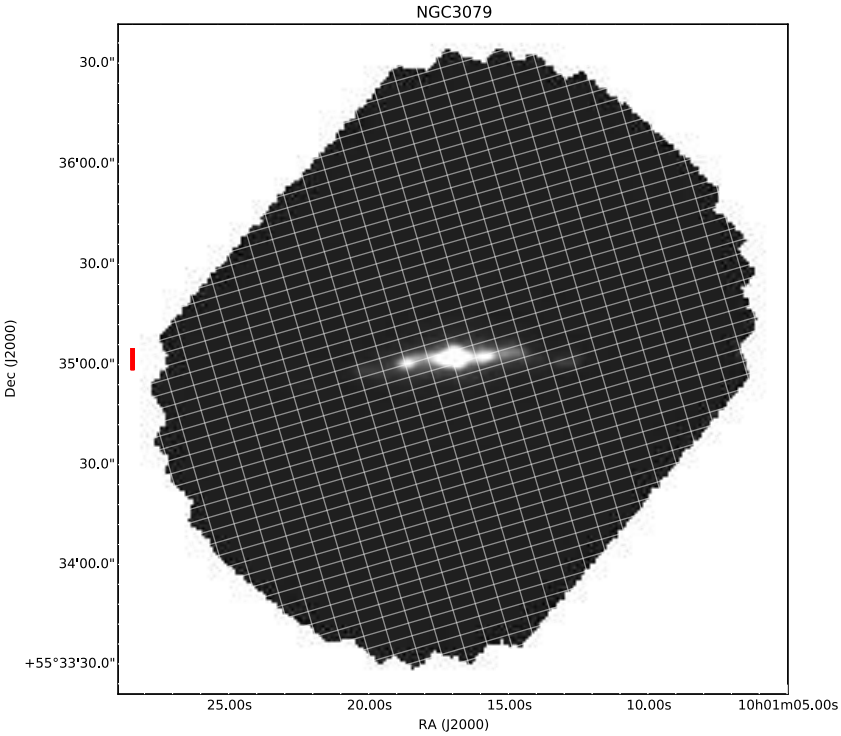

Figure A.46: 100 μm

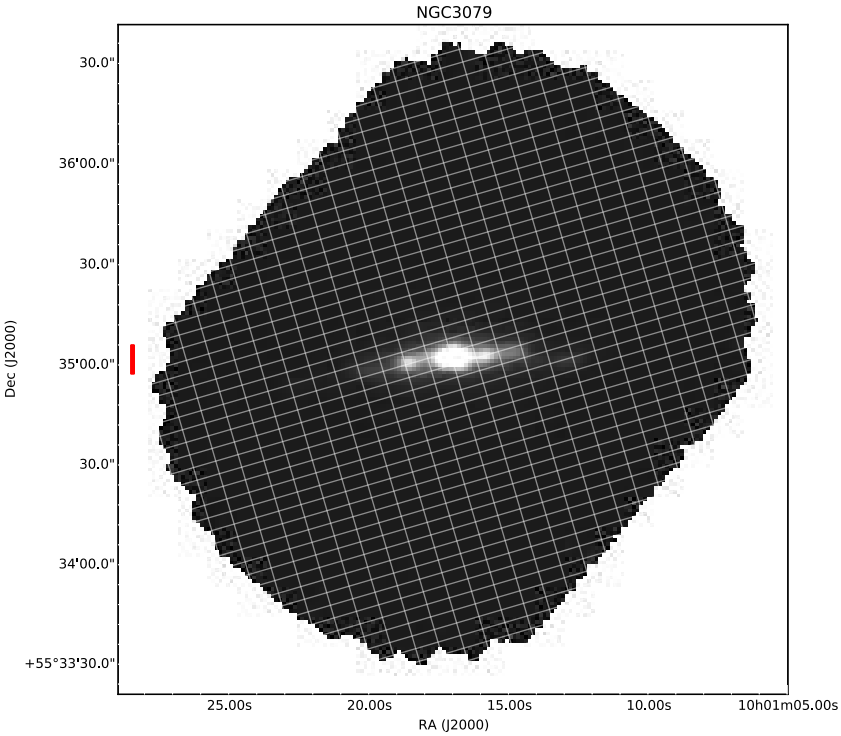

Figure A.47: 160 μm

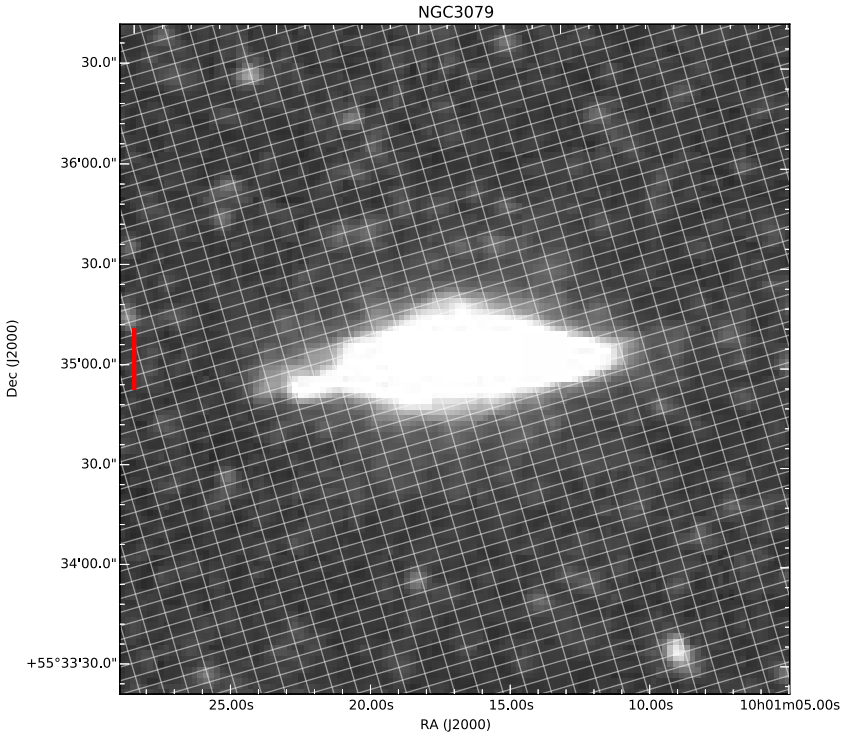

Figure A.48: 250 μm

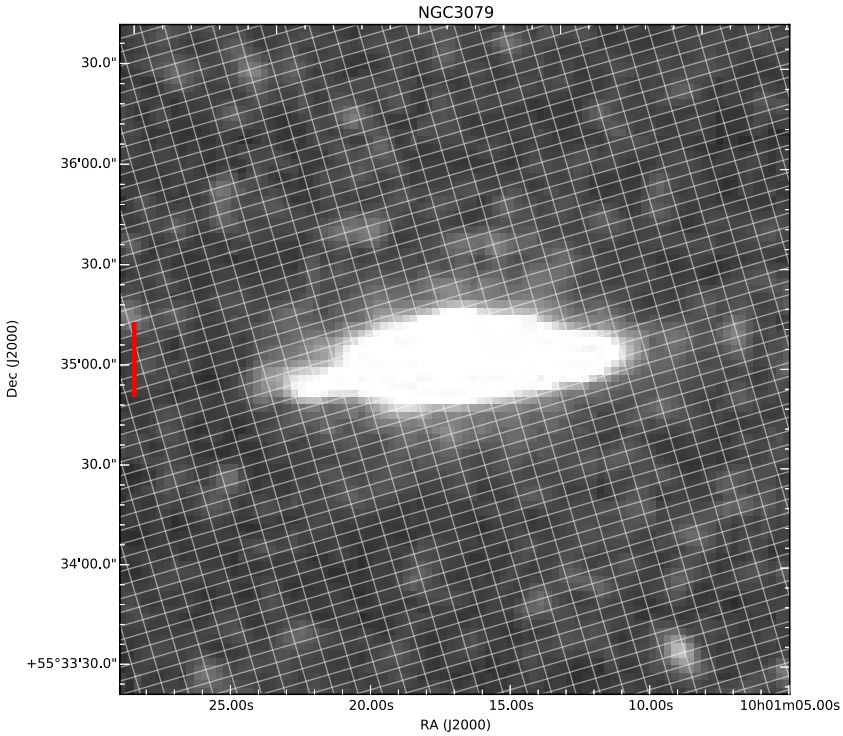

Figure A.49: 350 μm

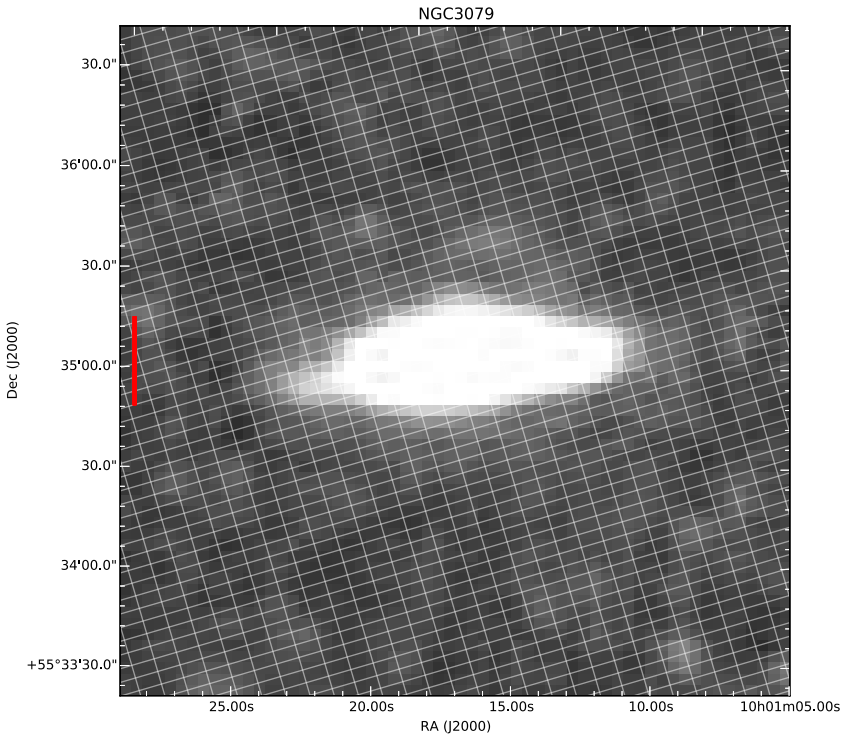

Figure A.50: 500 μm

A.6 NGC3501

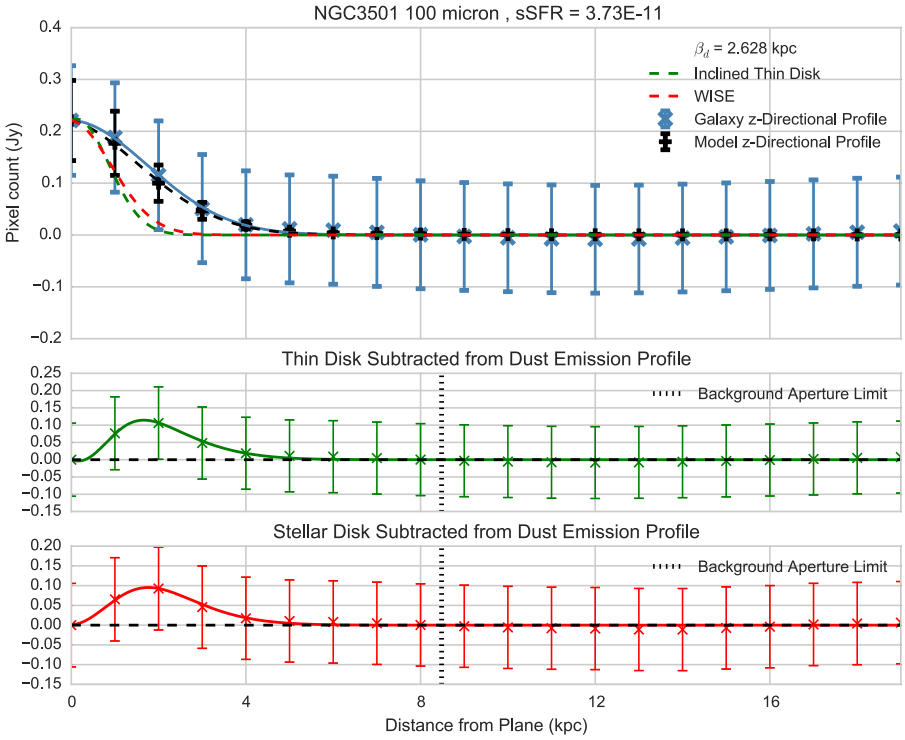

Figure A.51

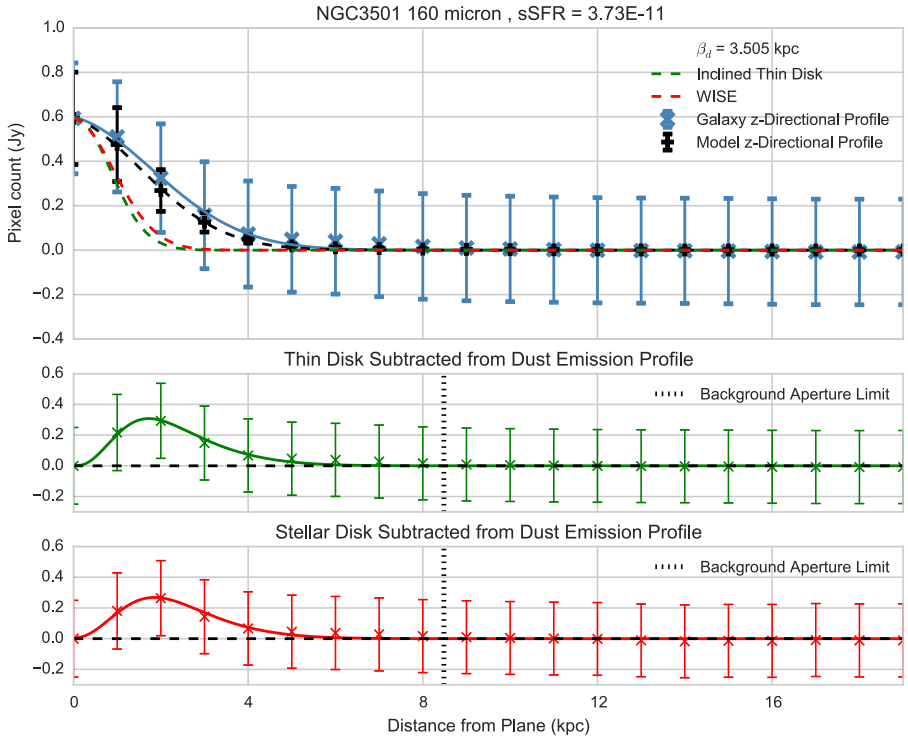

Figure A.52

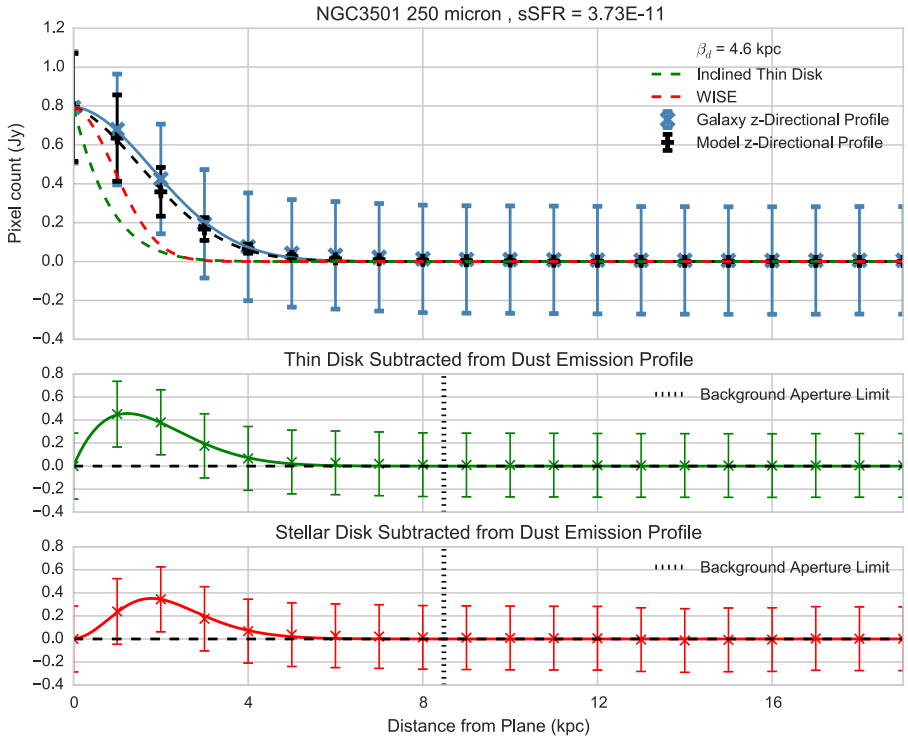

Figure A.53

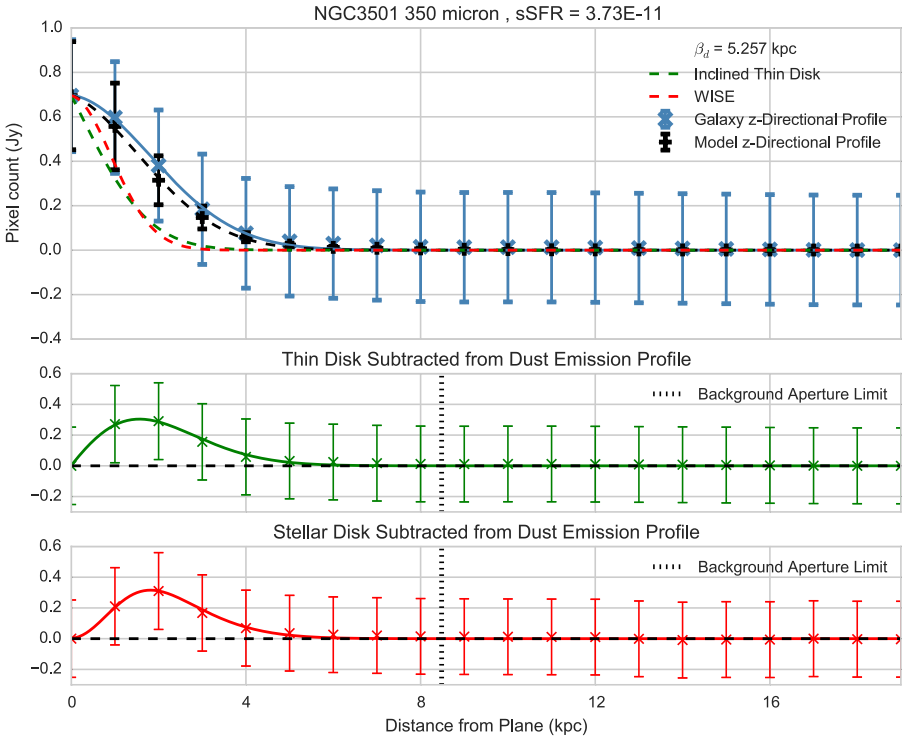

Figure A.54

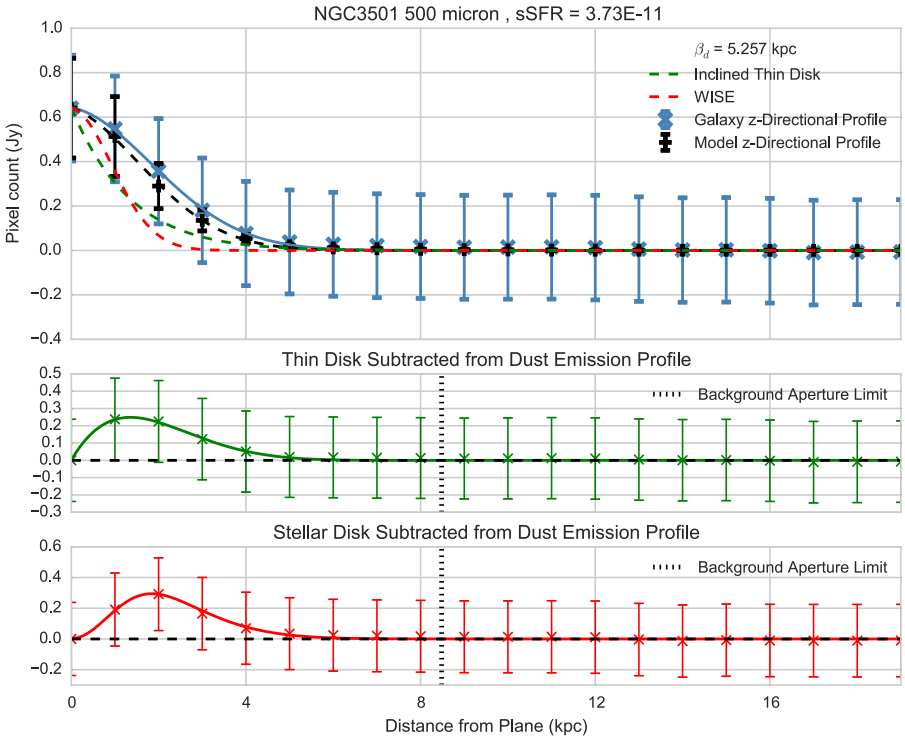

Figure A.55

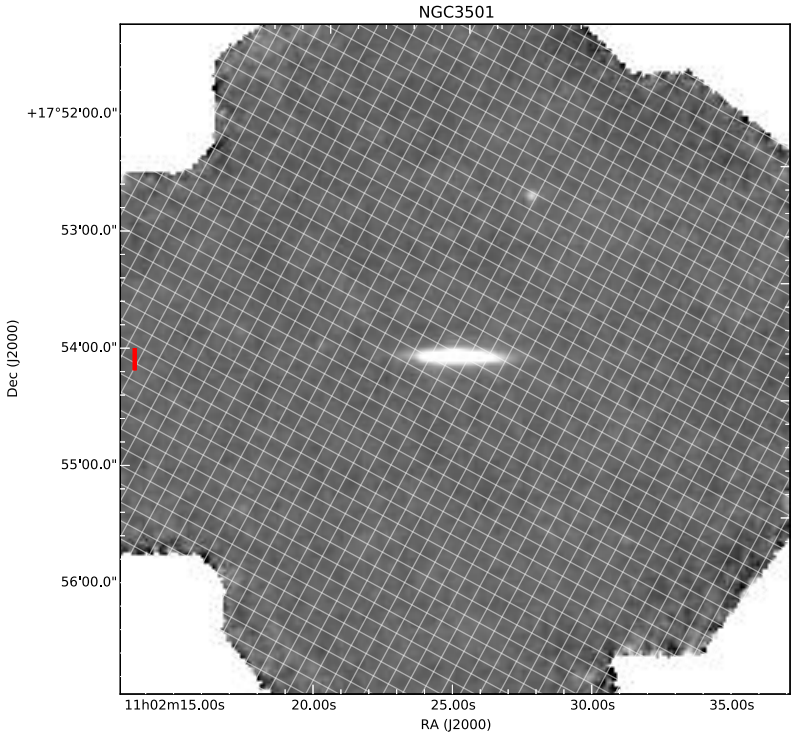

Figure A.56: 100 μm

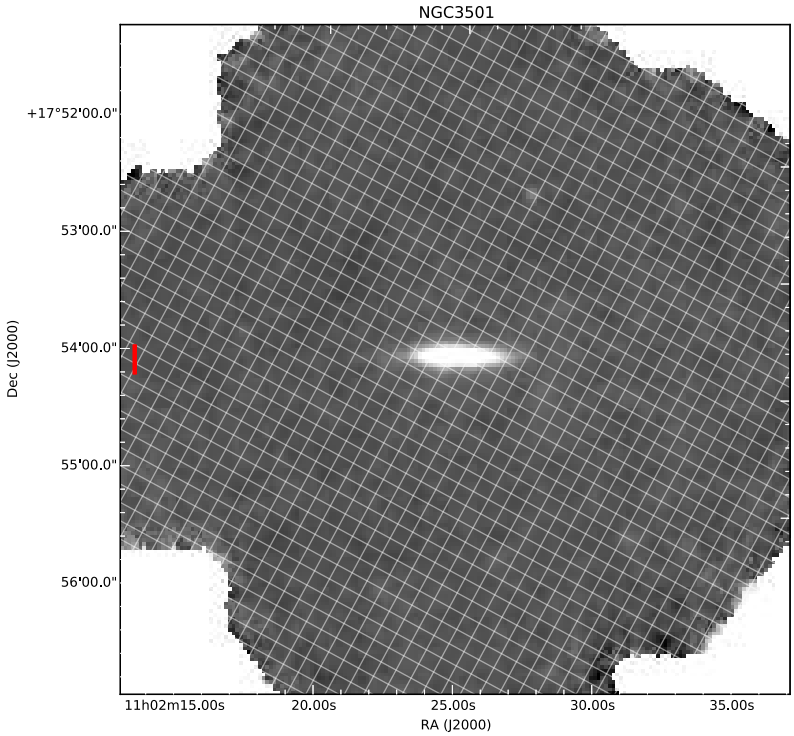

Figure A.57: 160 μm

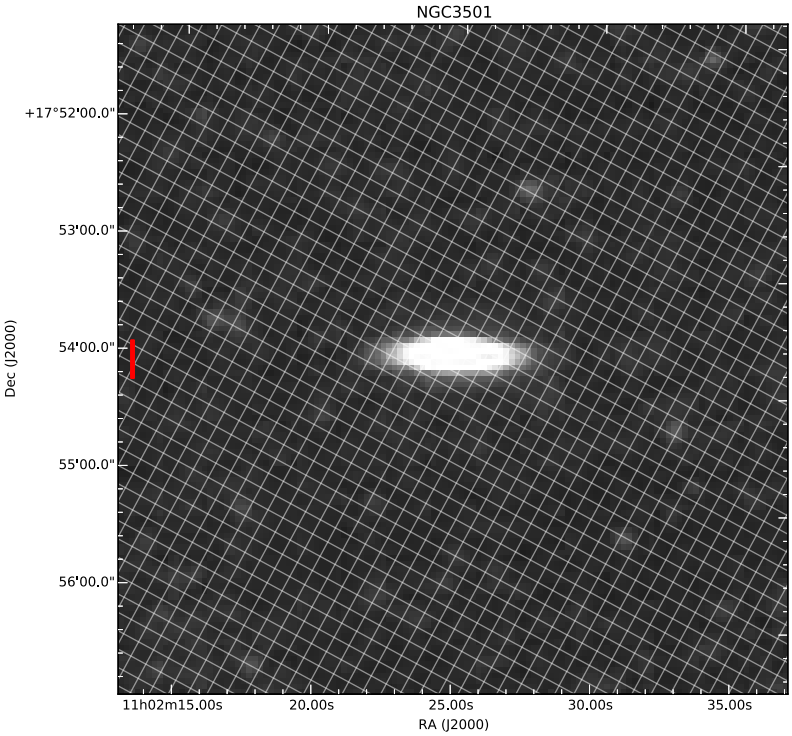

Figure A.58: 250 μm

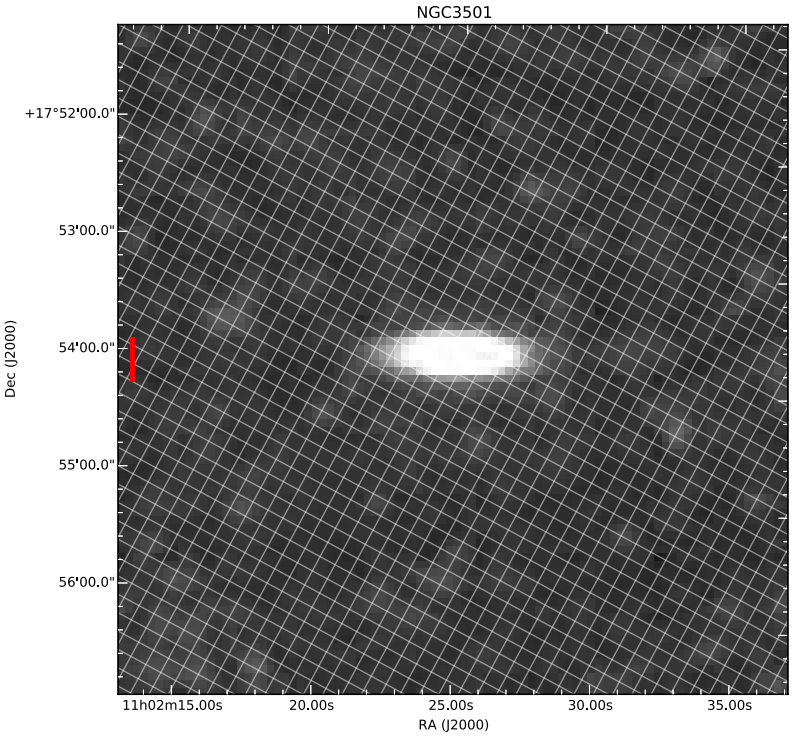

Figure A.59: 350 μm

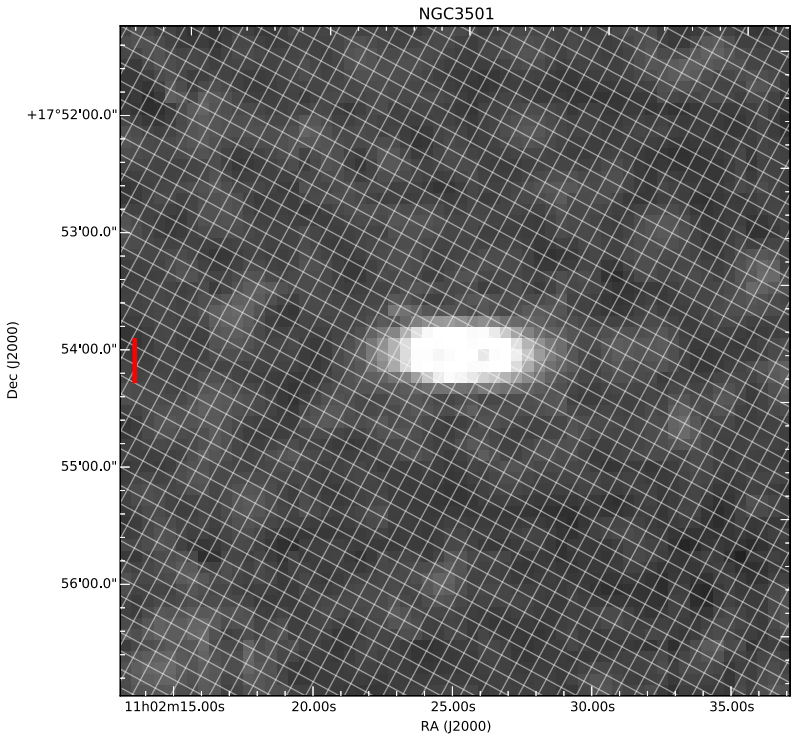

Figure A.60: 500 μm

A.7 NGC3628

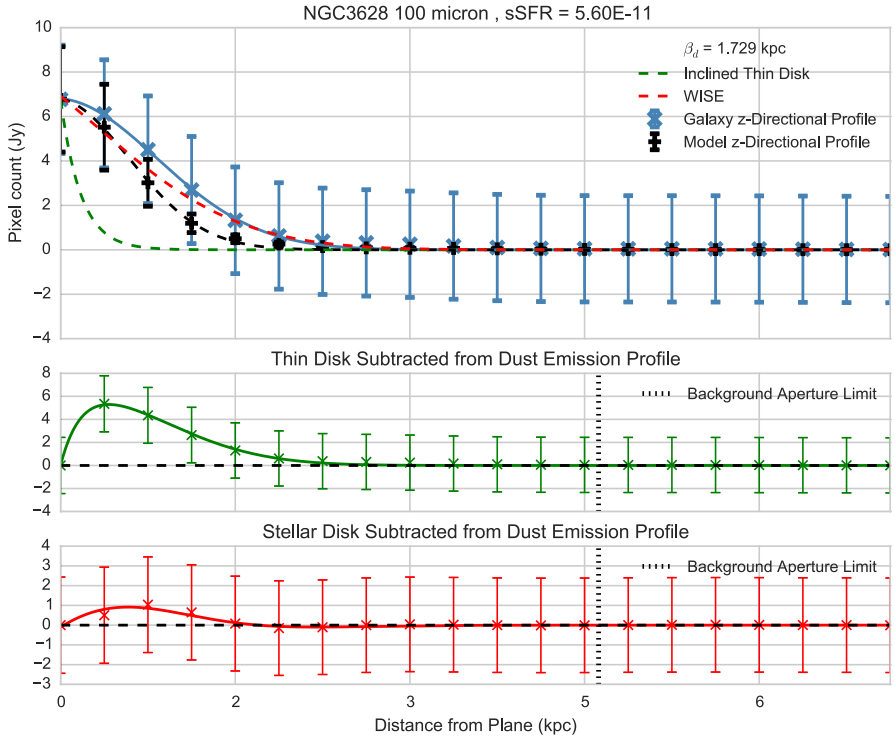

Figure A.61

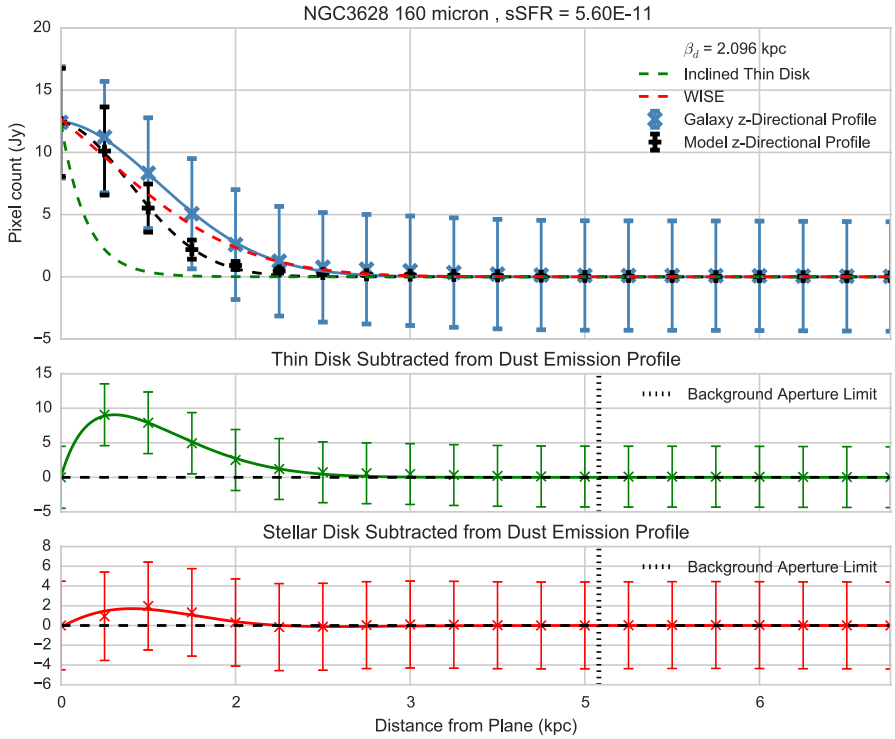

Figure A.62

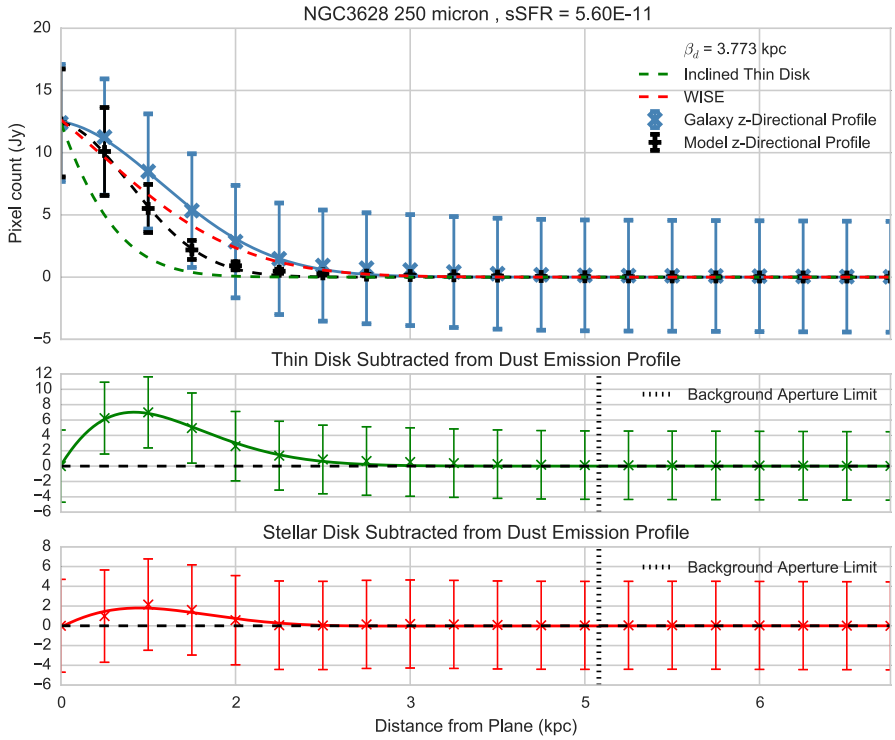

Figure A.63

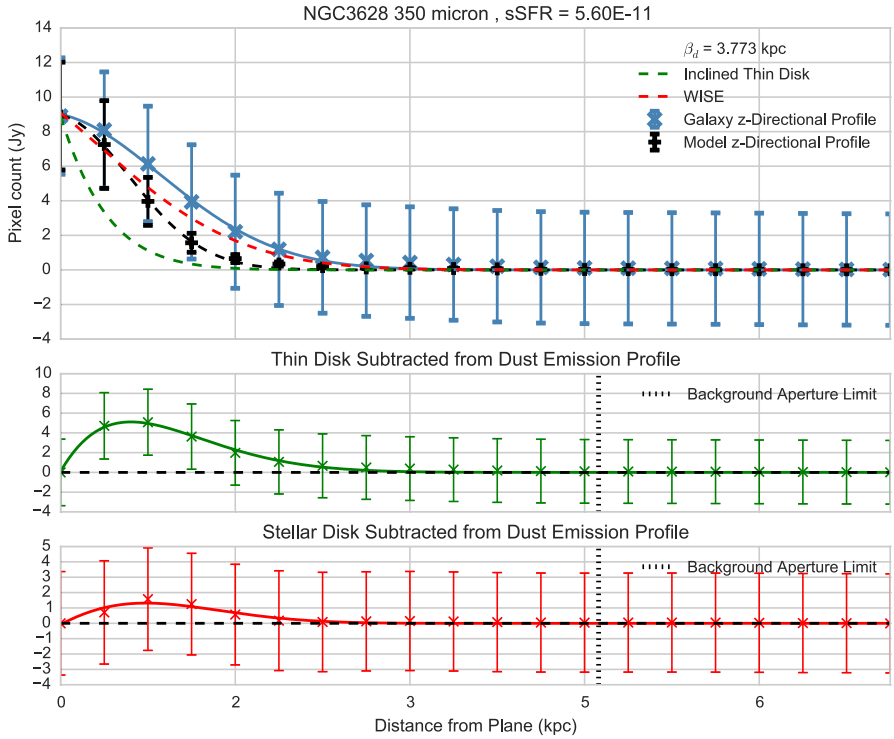

Figure A.64

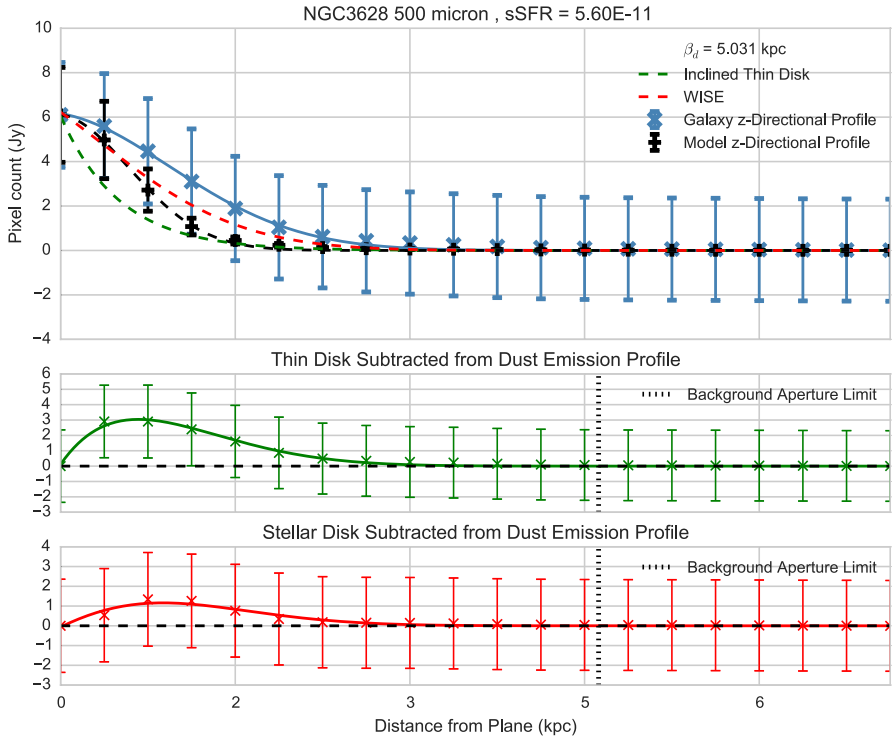

Figure A.65

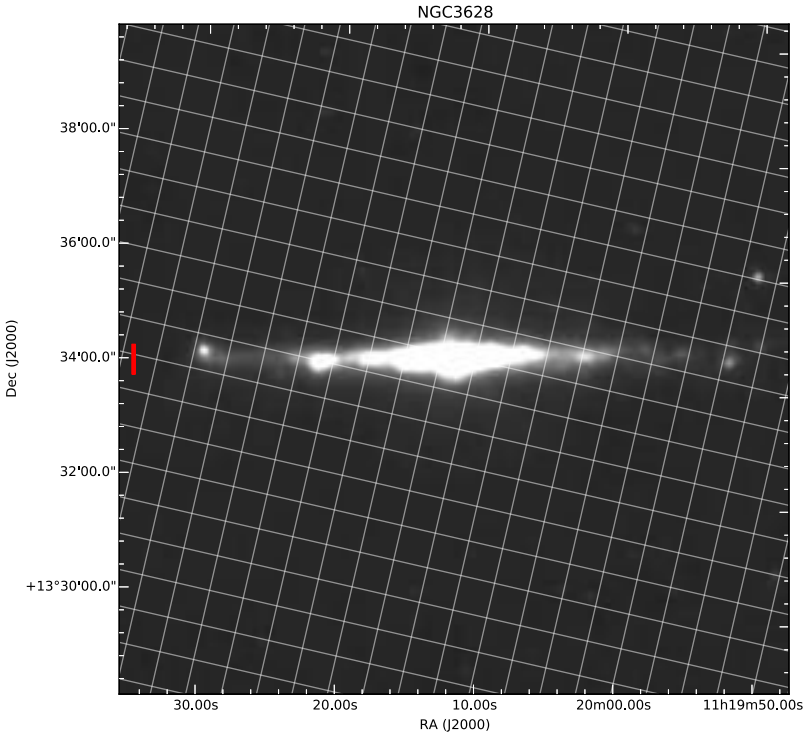

Figure A.66: 100 μm

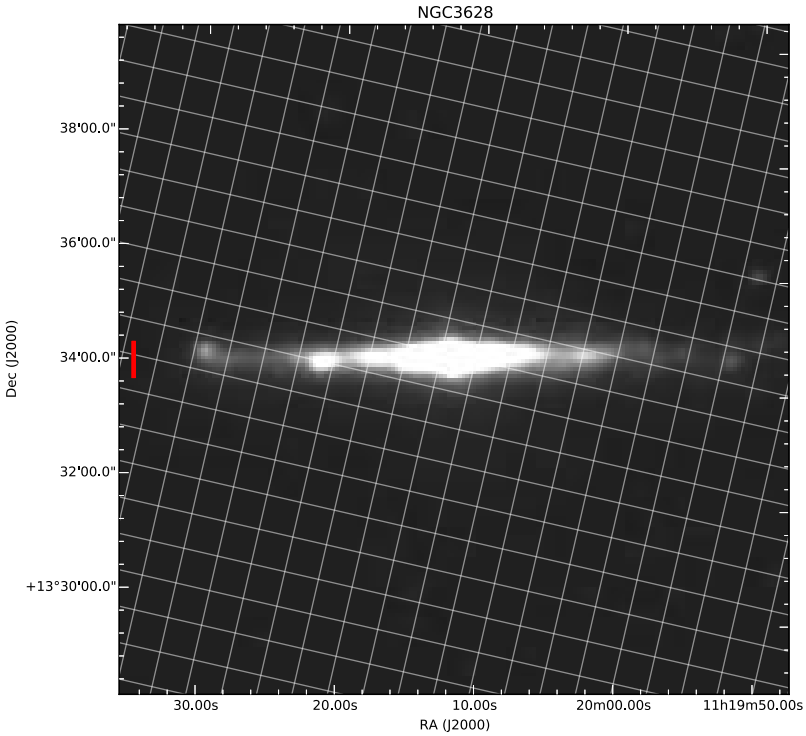

Figure A.67: 160 μm

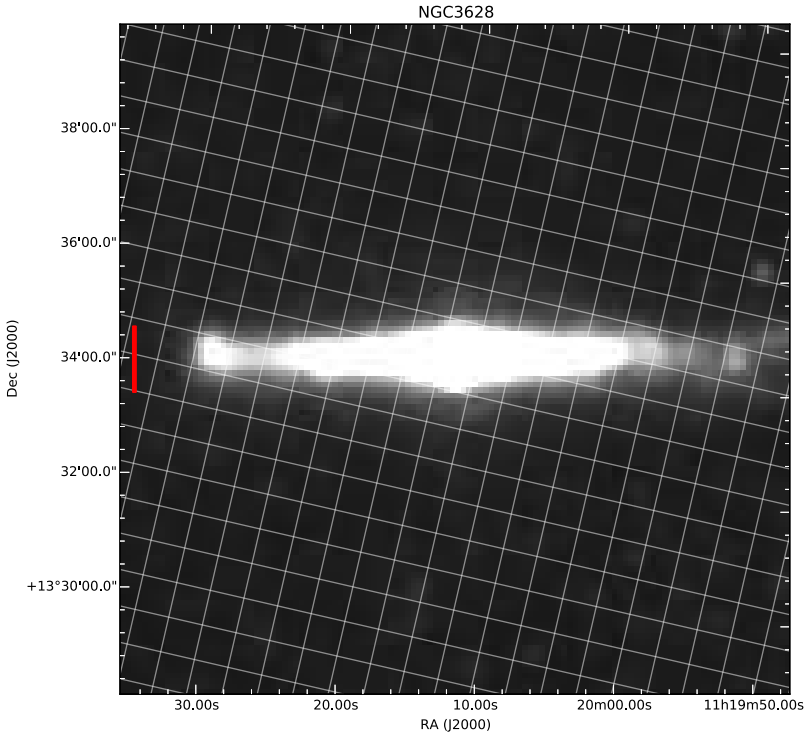

Figure A.68: 250 μm

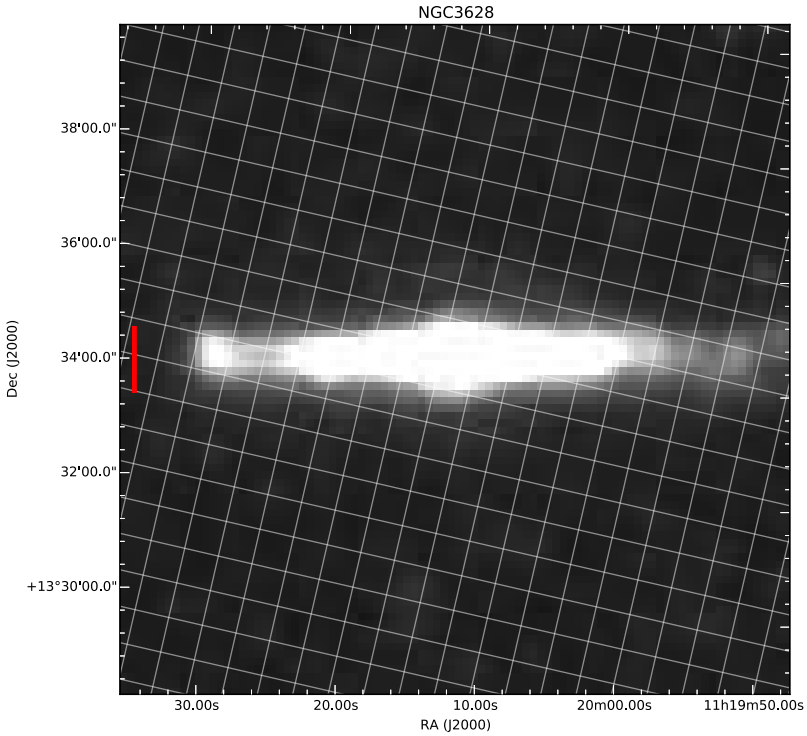

Figure A.69: 350 μm

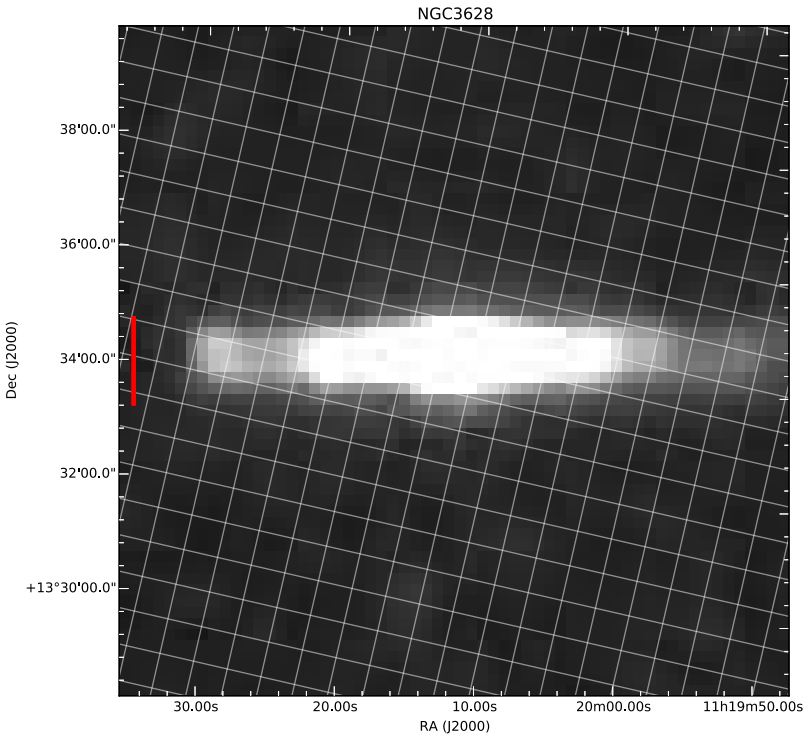

Figure A.70: 500 μm

A.8 NGC4013

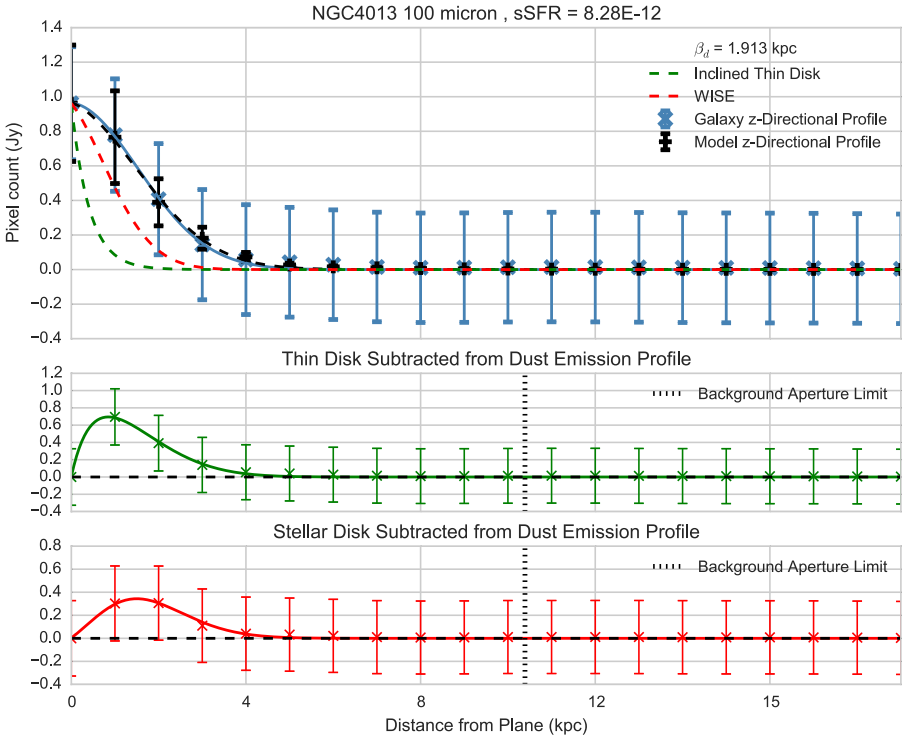

Figure A.71

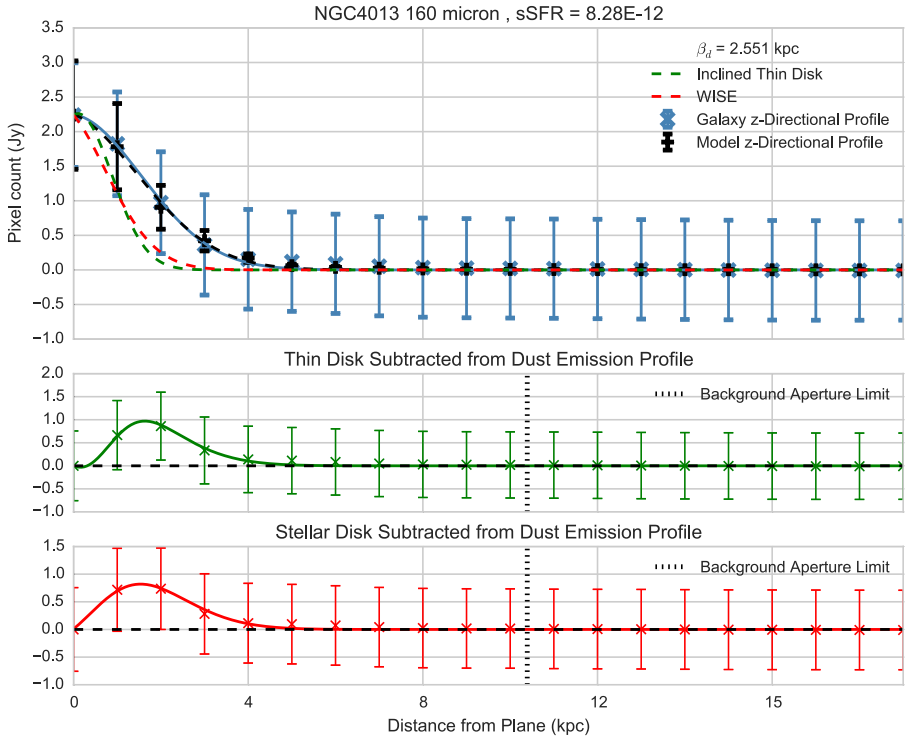

Figure A.72

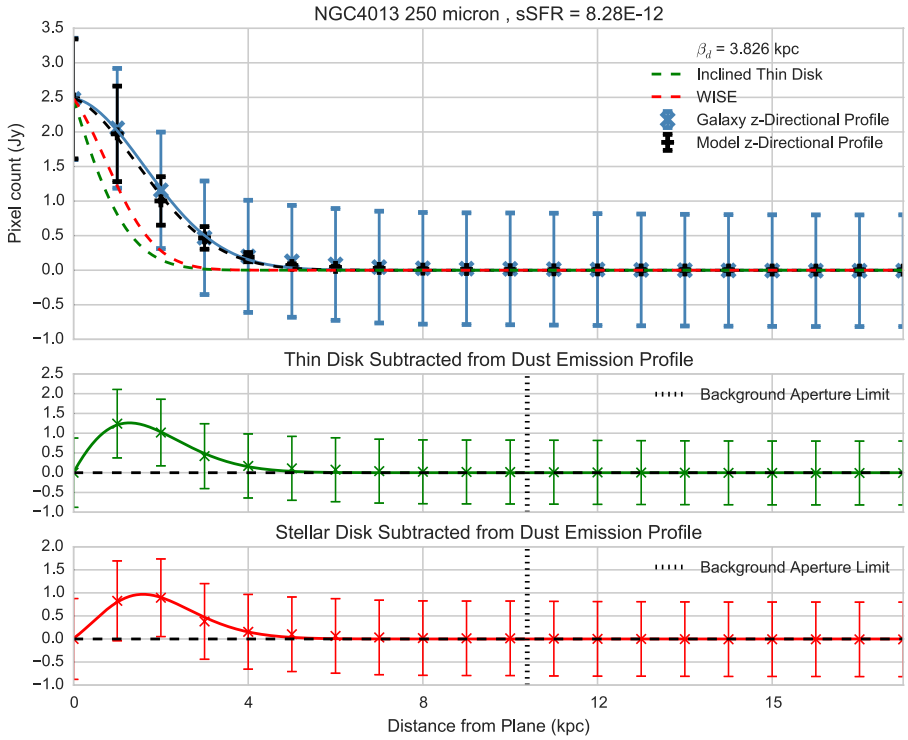

Figure A.73

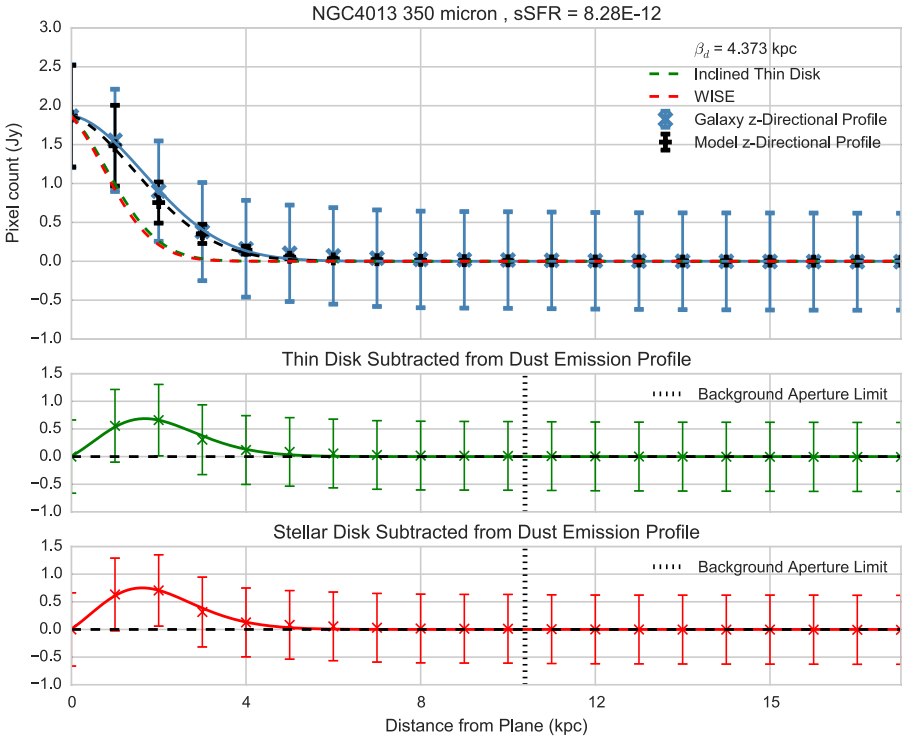

Figure A.74

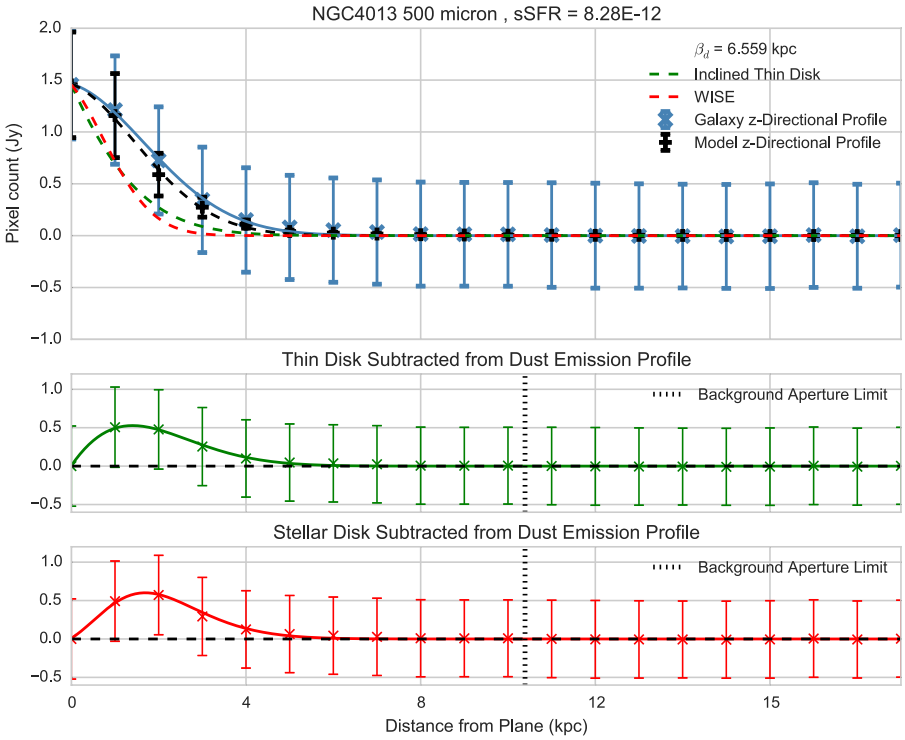

Figure A.75

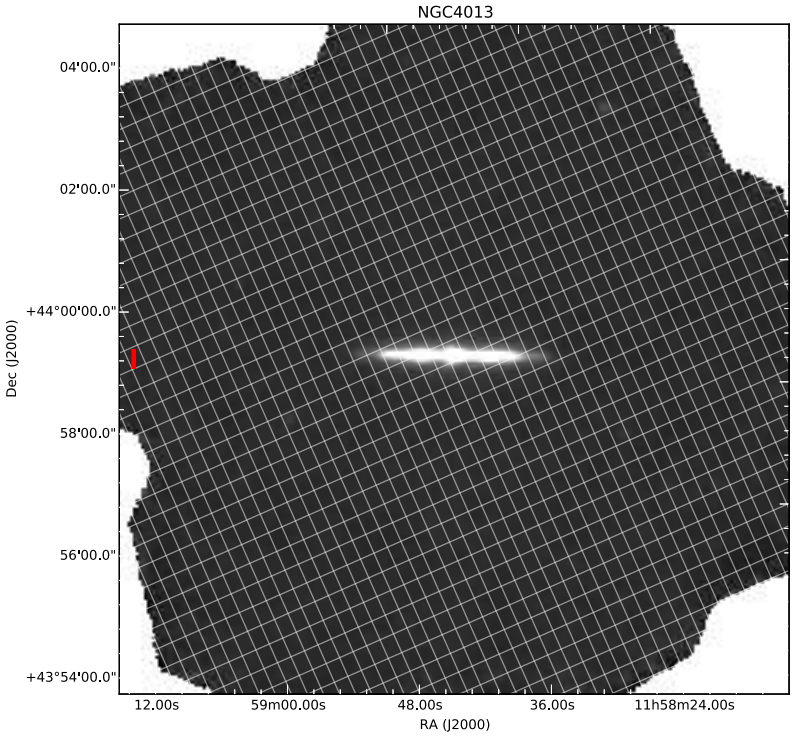

Figure A.76: 100 μm

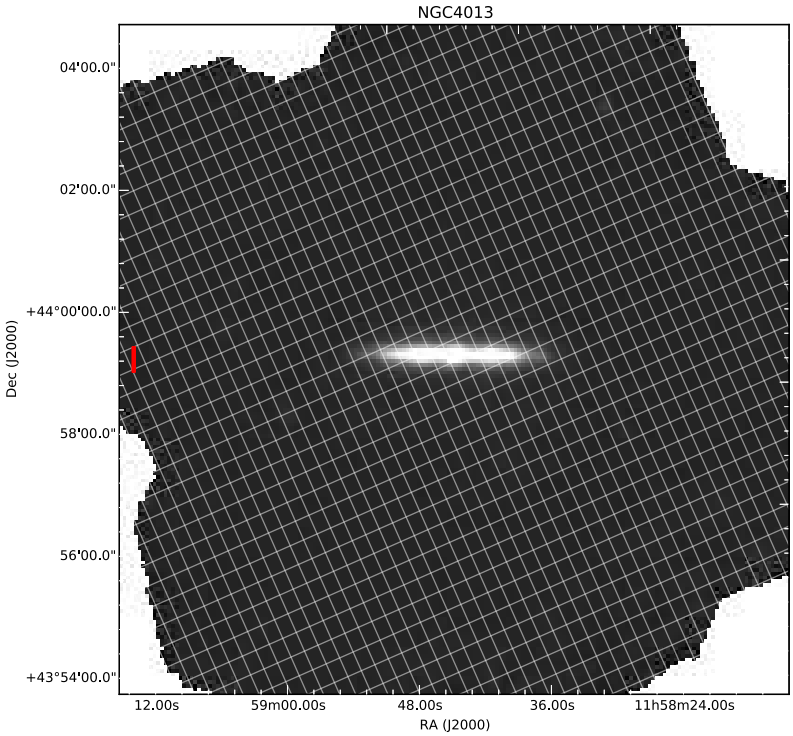

Figure A.77: 160 μm

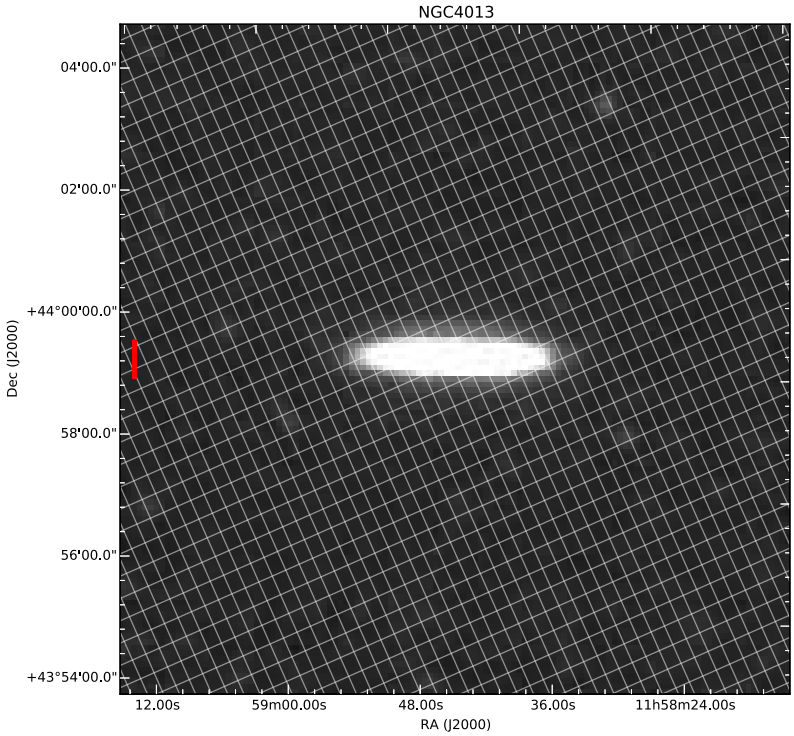

Figure A.78: 250 μm

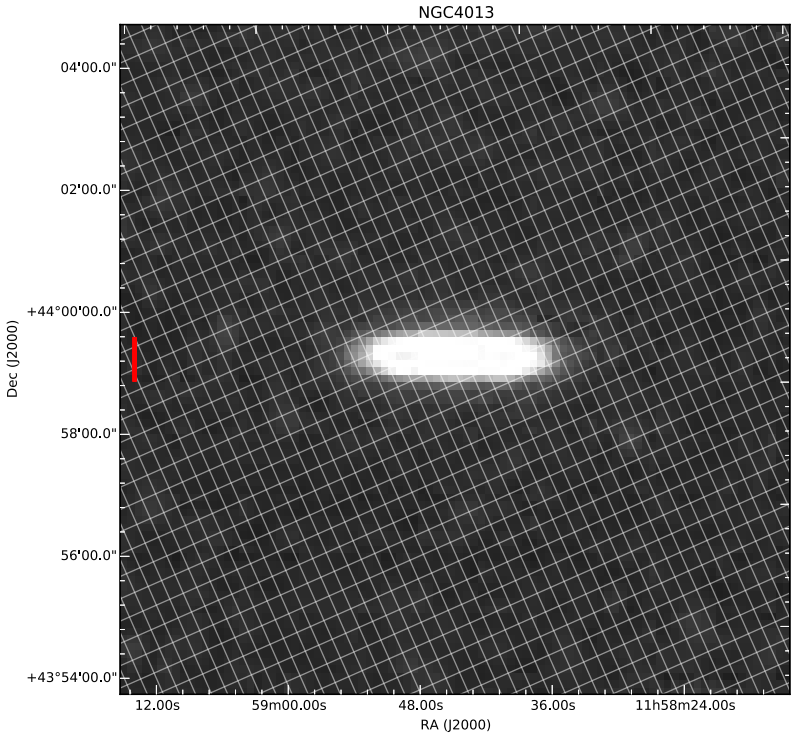

Figure A.79: 350 μm

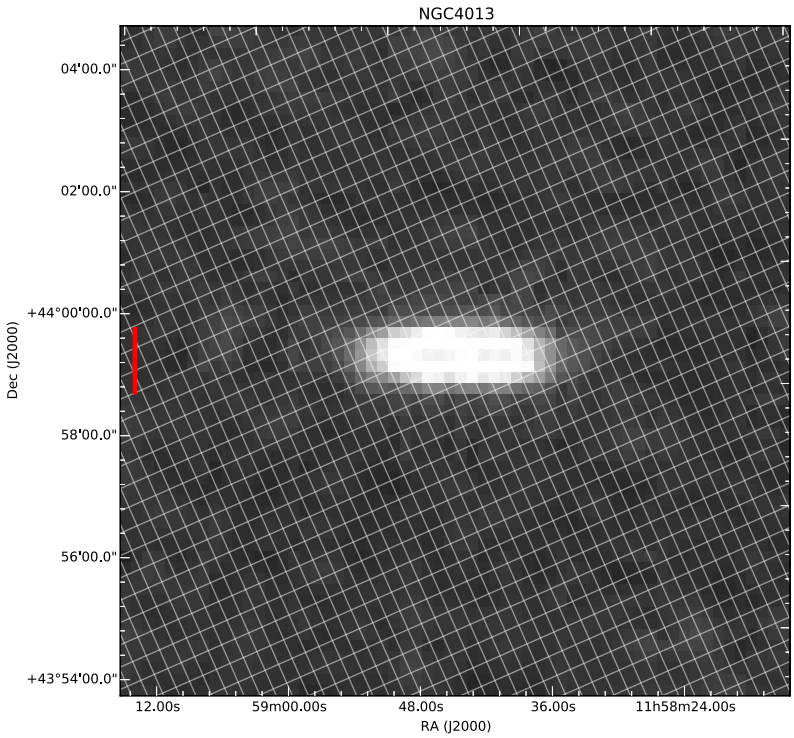

Figure A.80: 500 μm

A.9 NGC4183

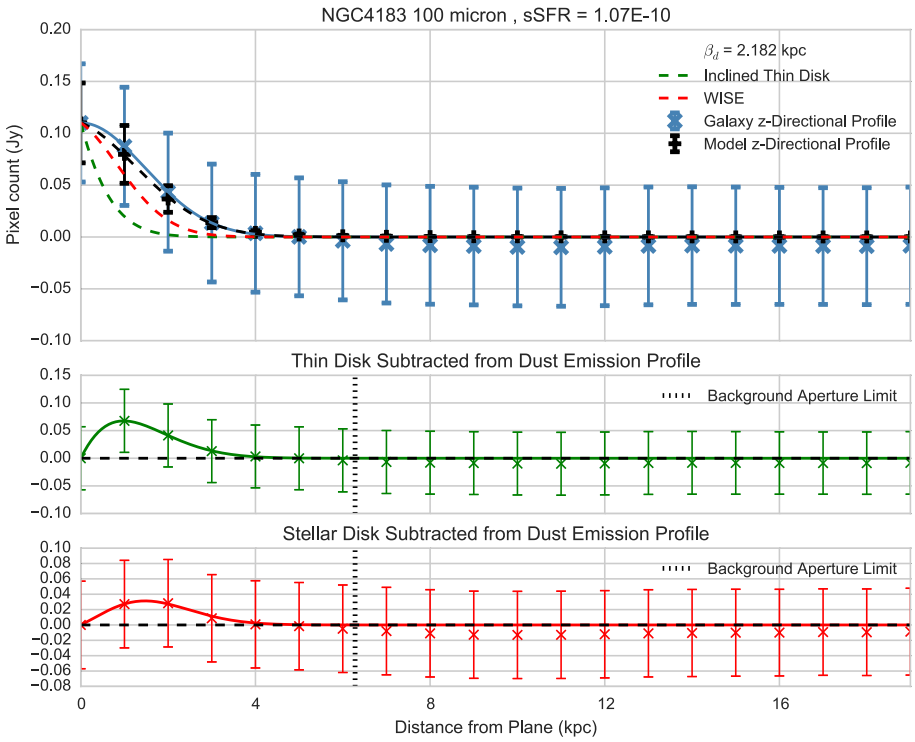

Figure A.81

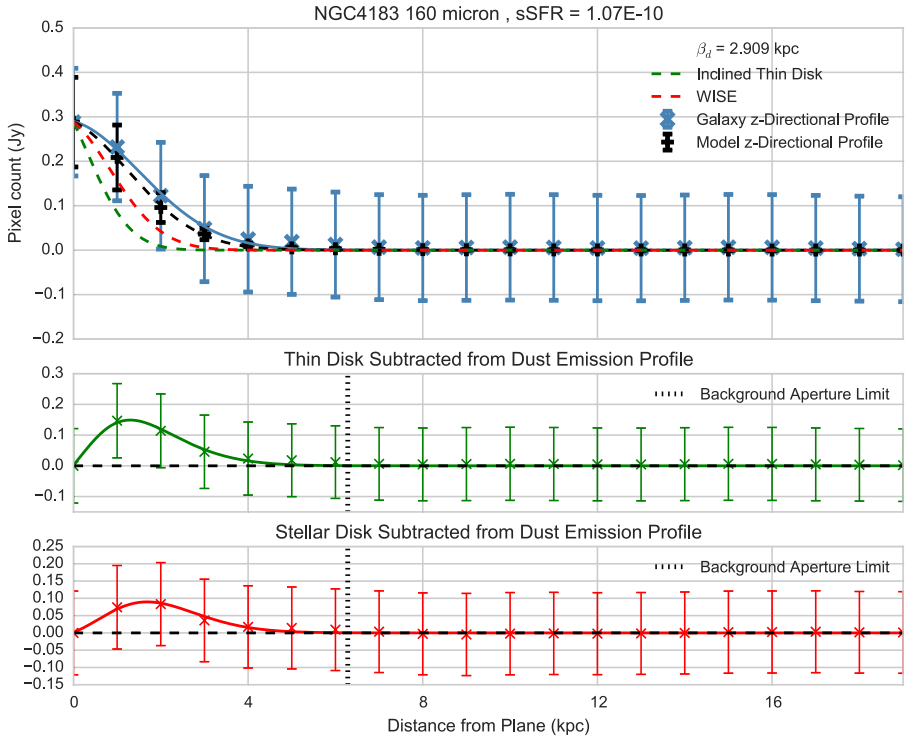

Figure A.82

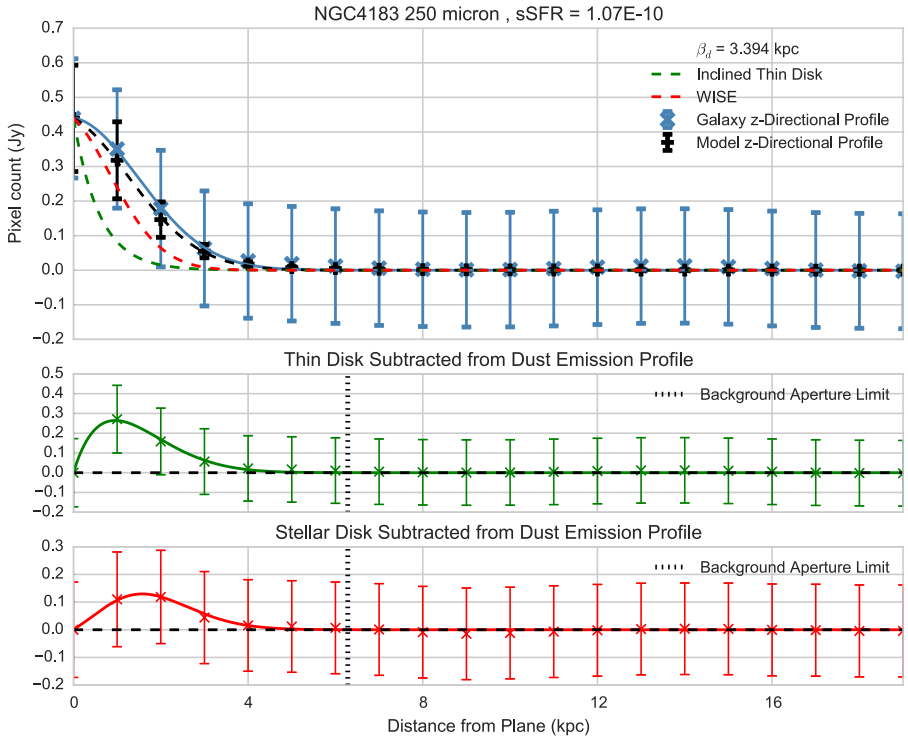

Figure A.83

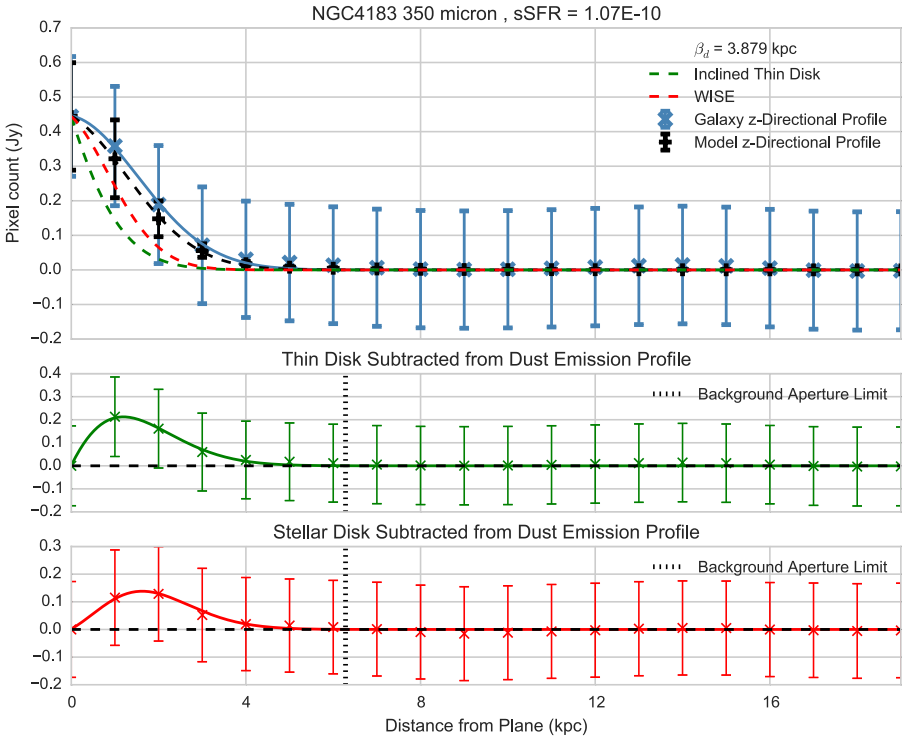

Figure A.84

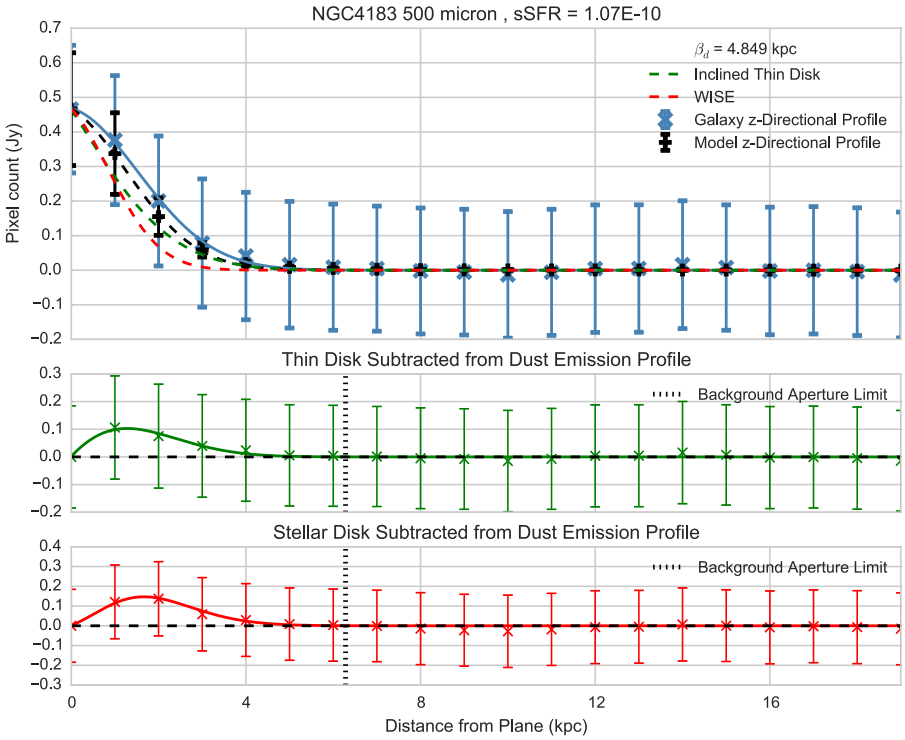

Figure A.85

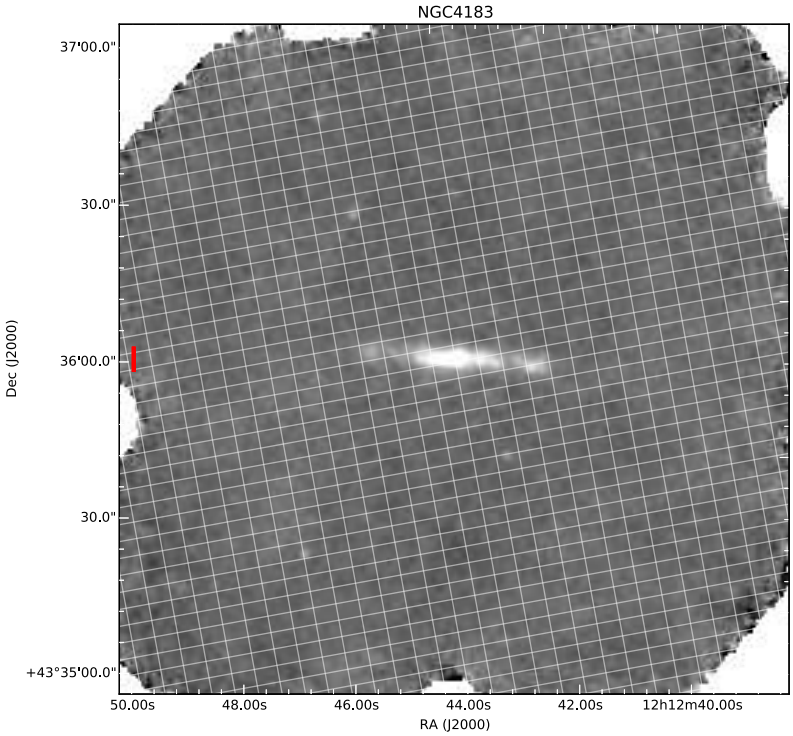

Figure A.86: 100 μm

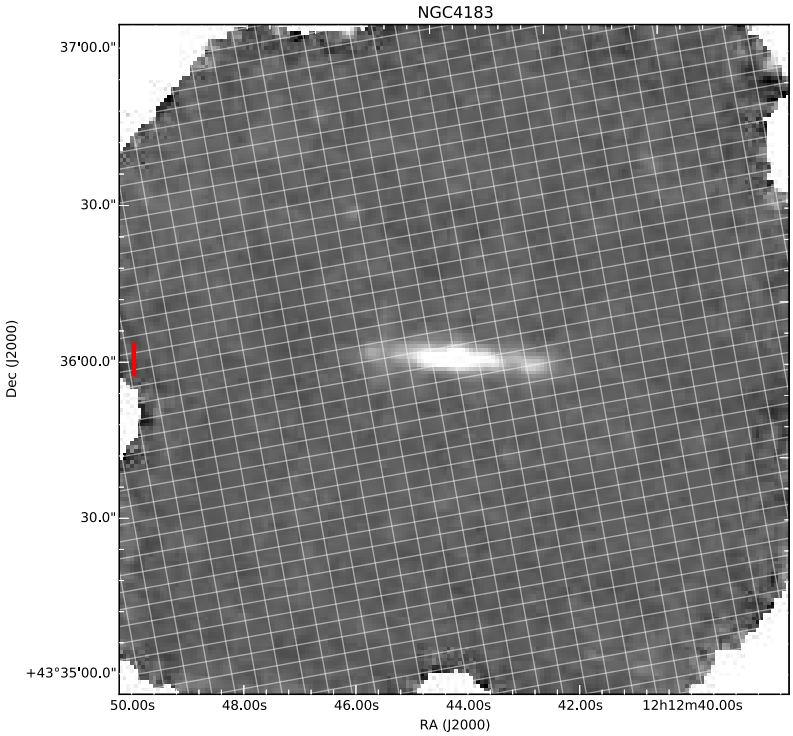

Figure A.87: 160 μm

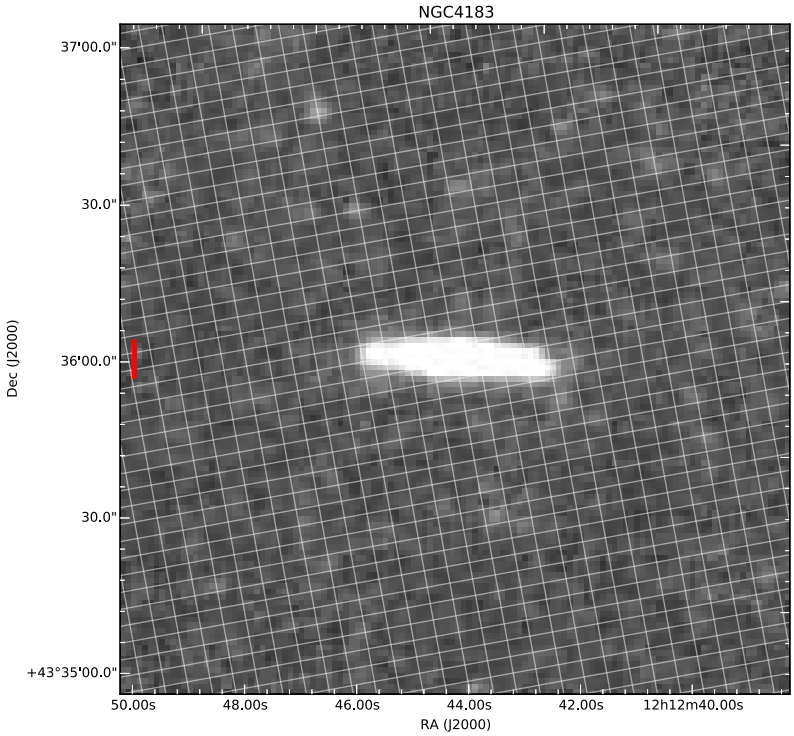

Figure A.88: 250 μm

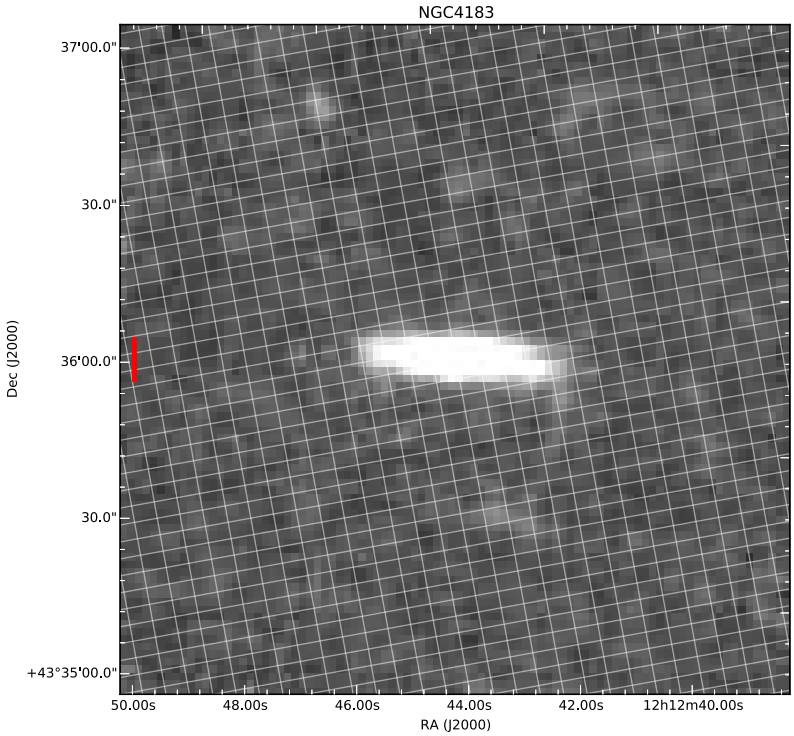

Figure A.89: 350 μm

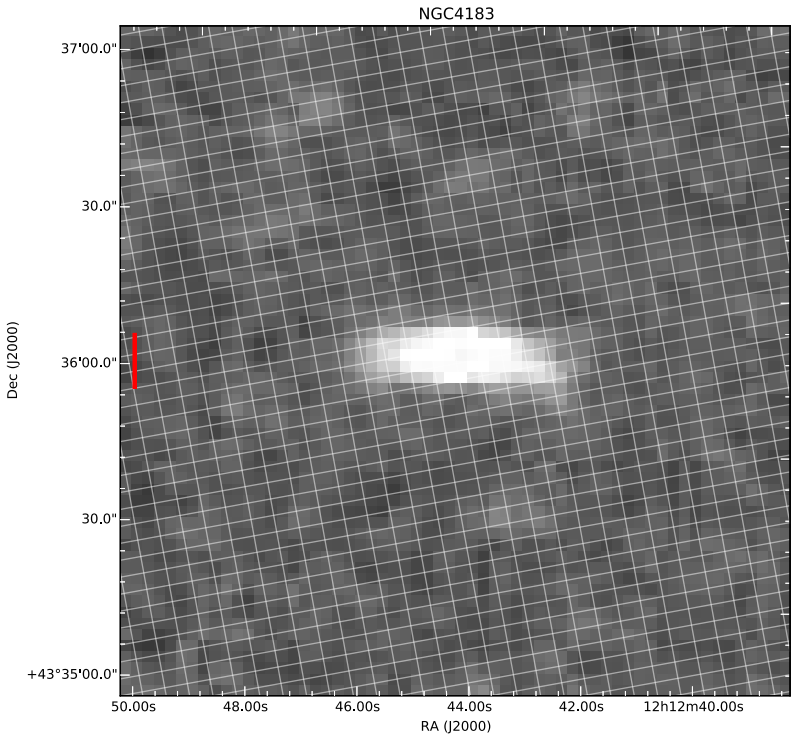

Figure A.90: 500 μm

A.10 NGC4206

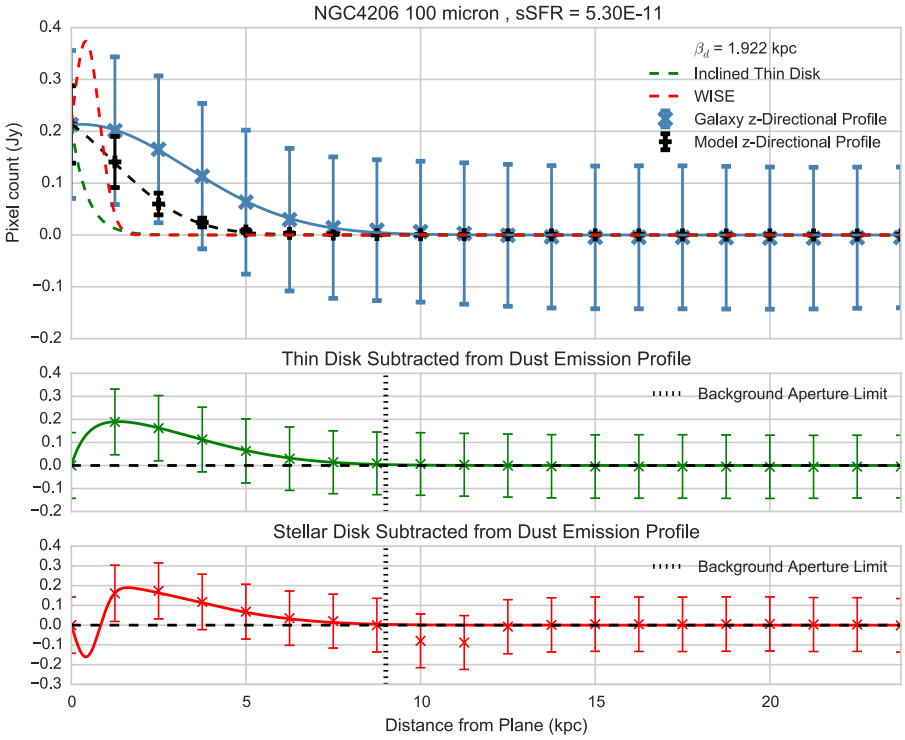

Figure A.91

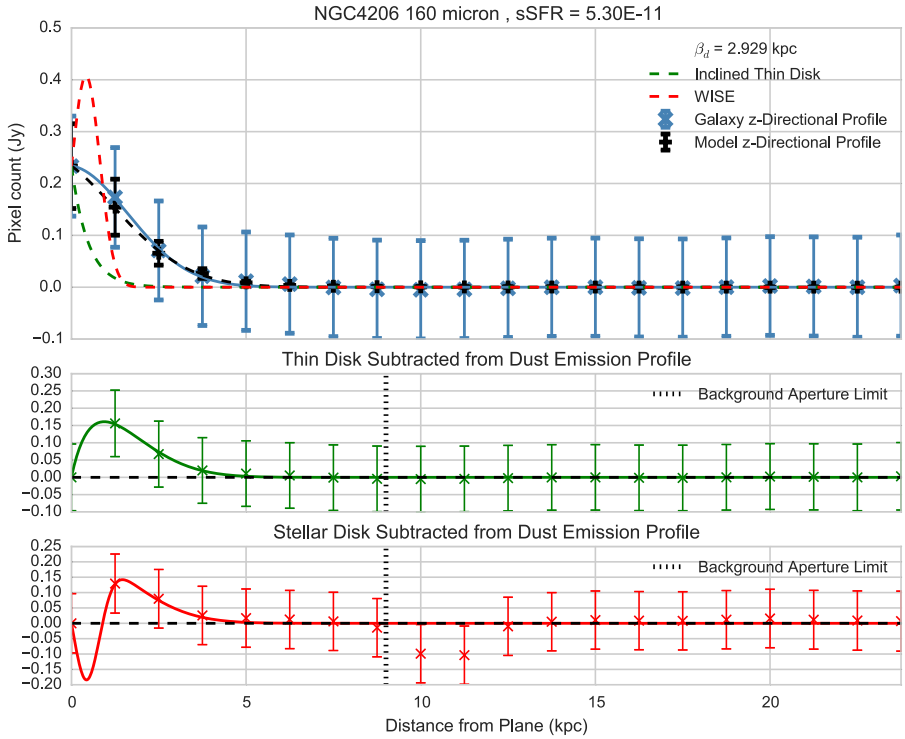

Figure A.92

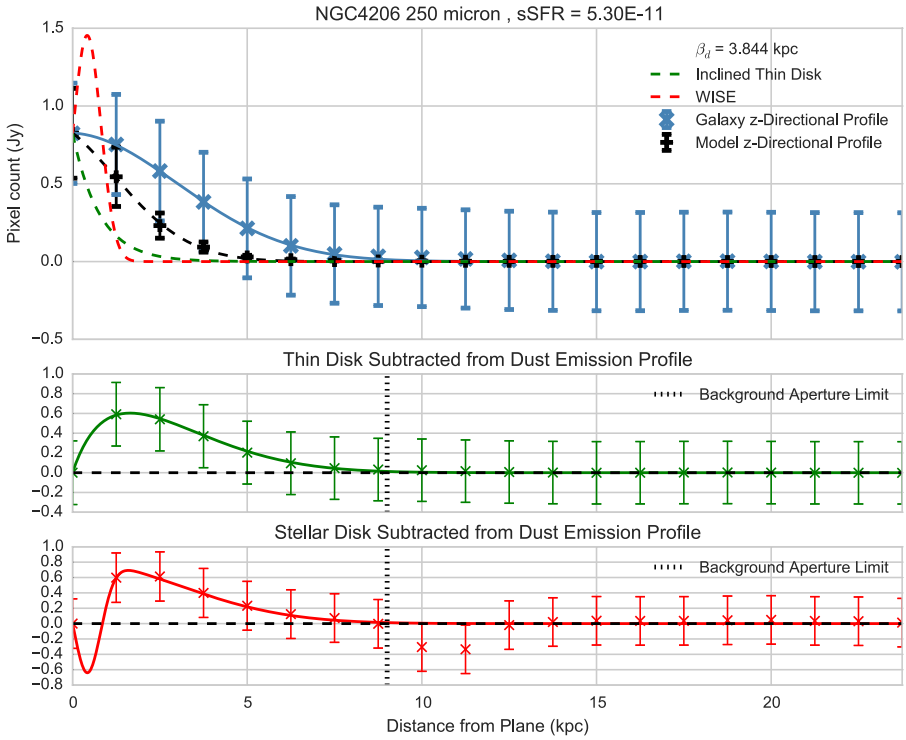

Figure A.93

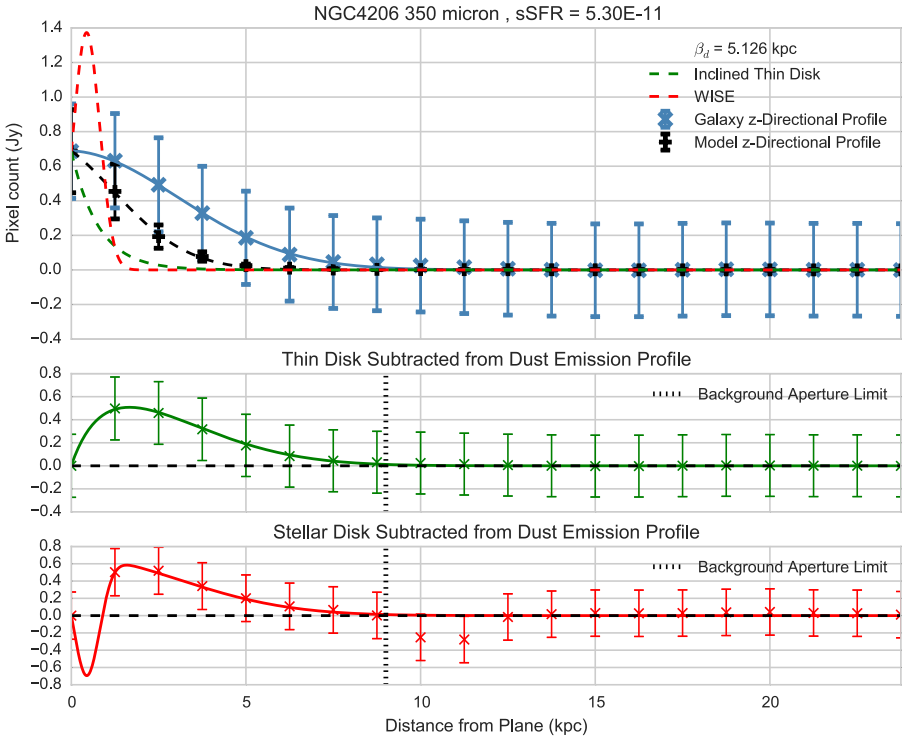

Figure A.94

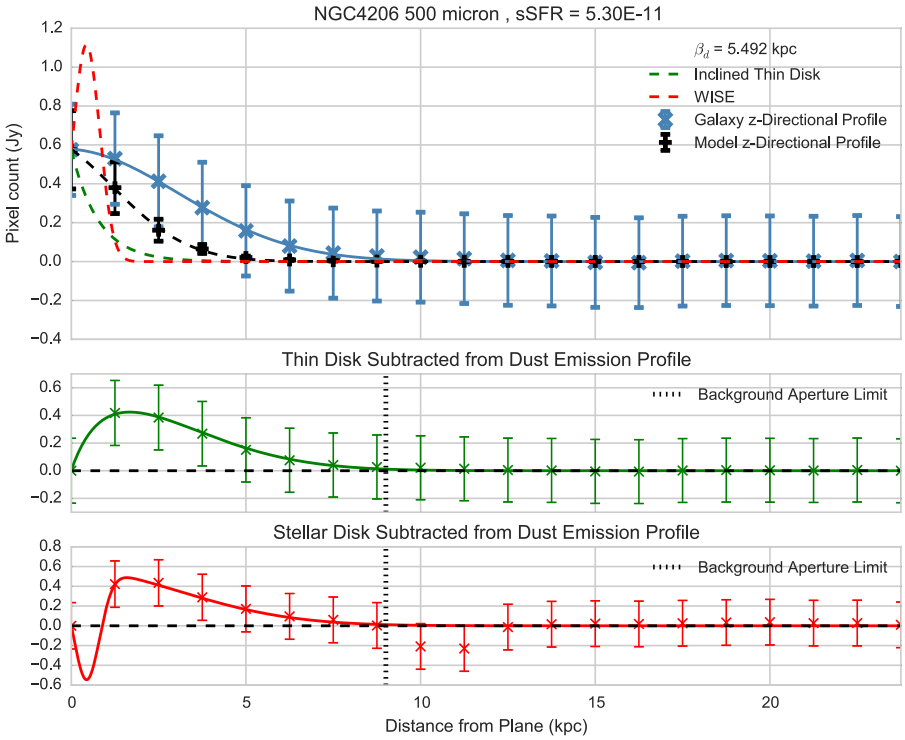

Figure A.95

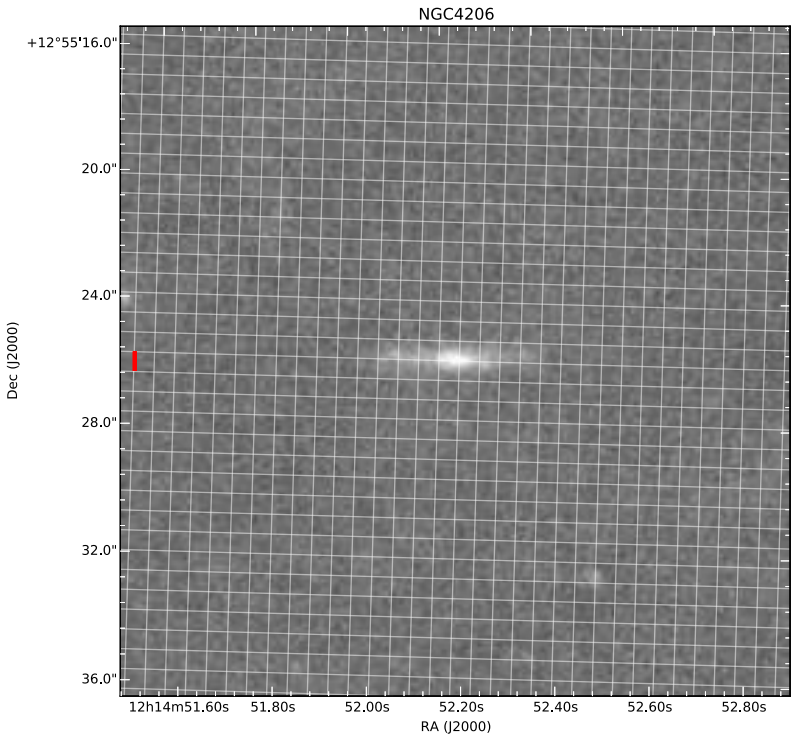

Figure A.96: 100 μm

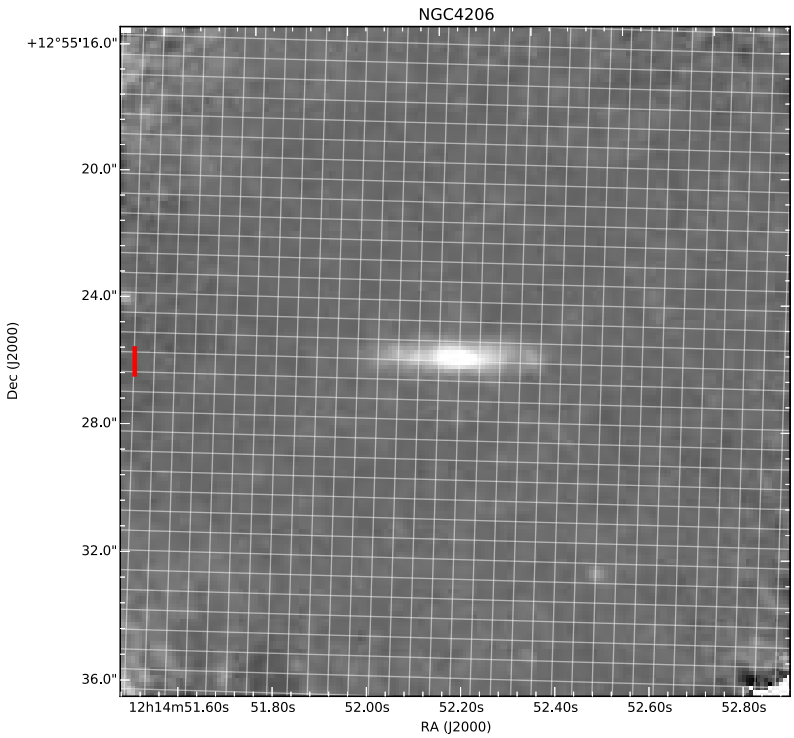

Figure A.97: 160 μm

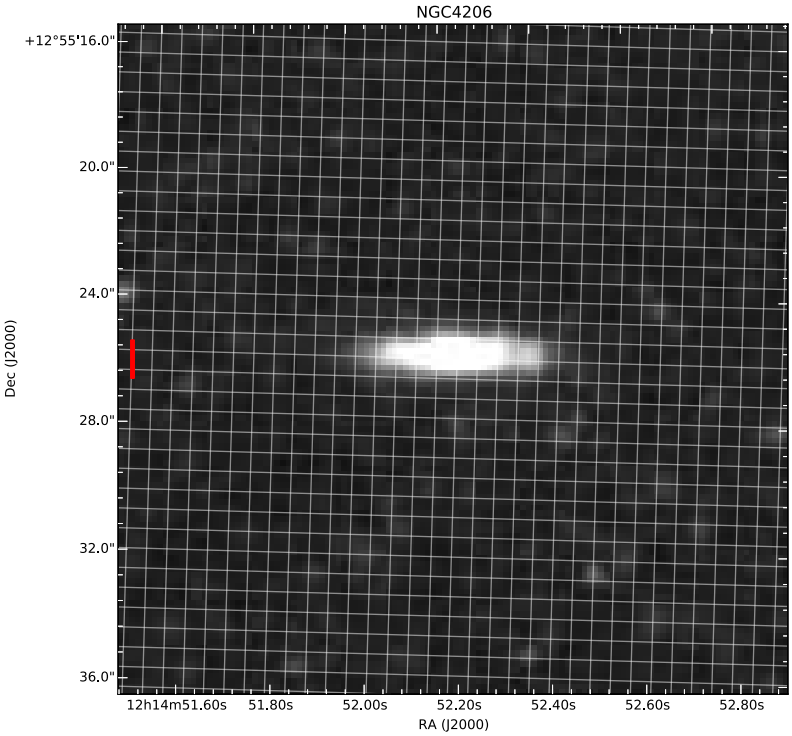

Figure A.98: 250 μm

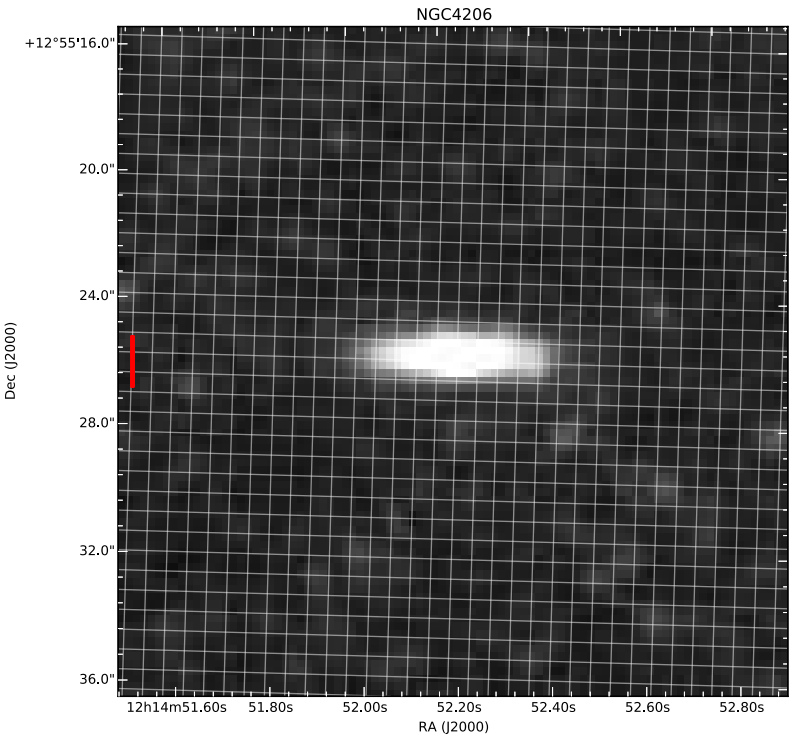

Figure A.99: 350 μm

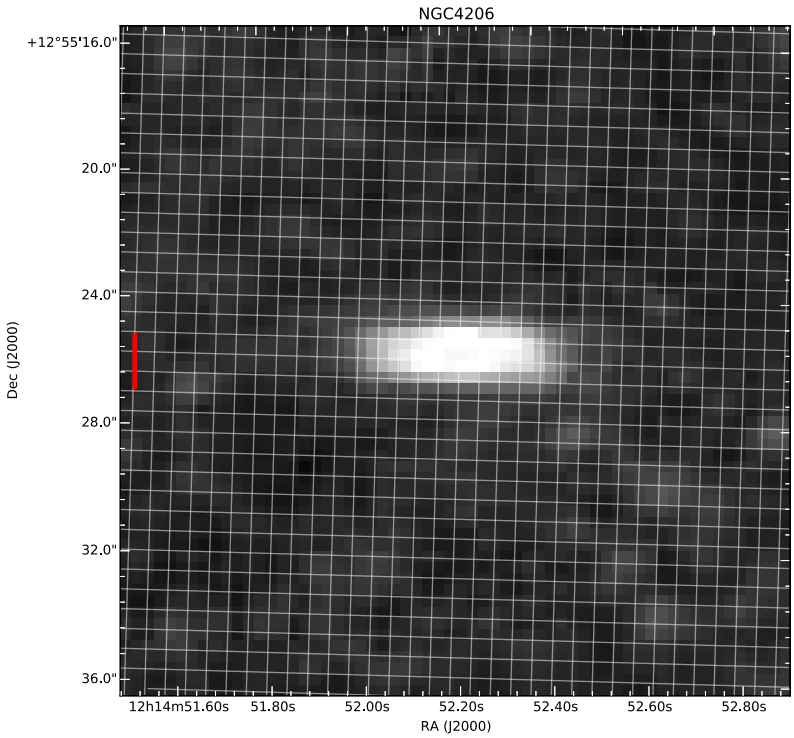

Figure A.100: 500 μm

A.11 NGC4216

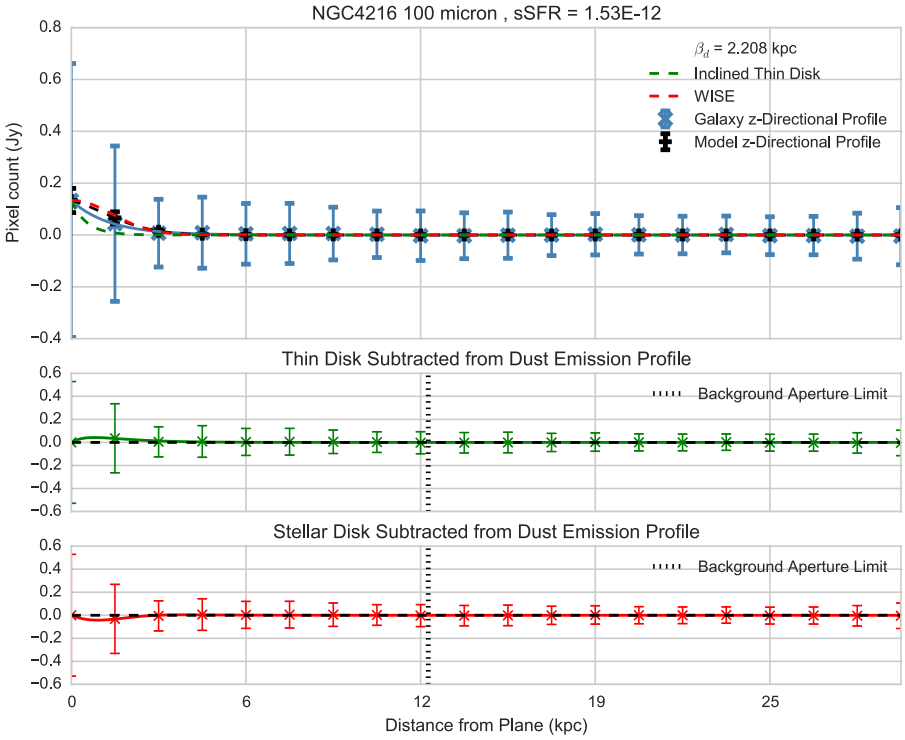

Figure A.101

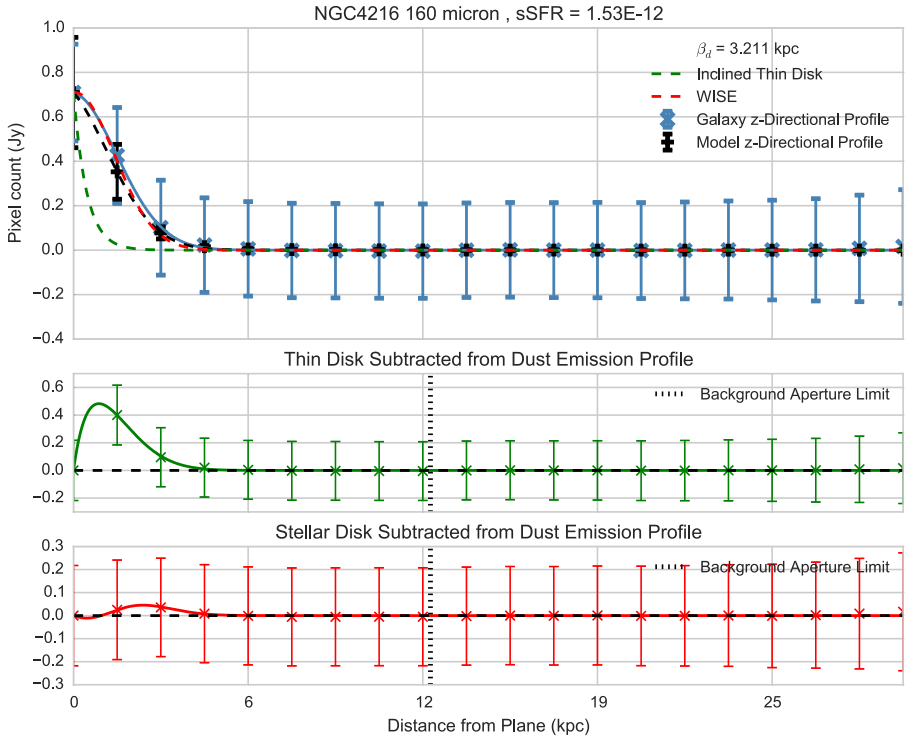

Figure A.102

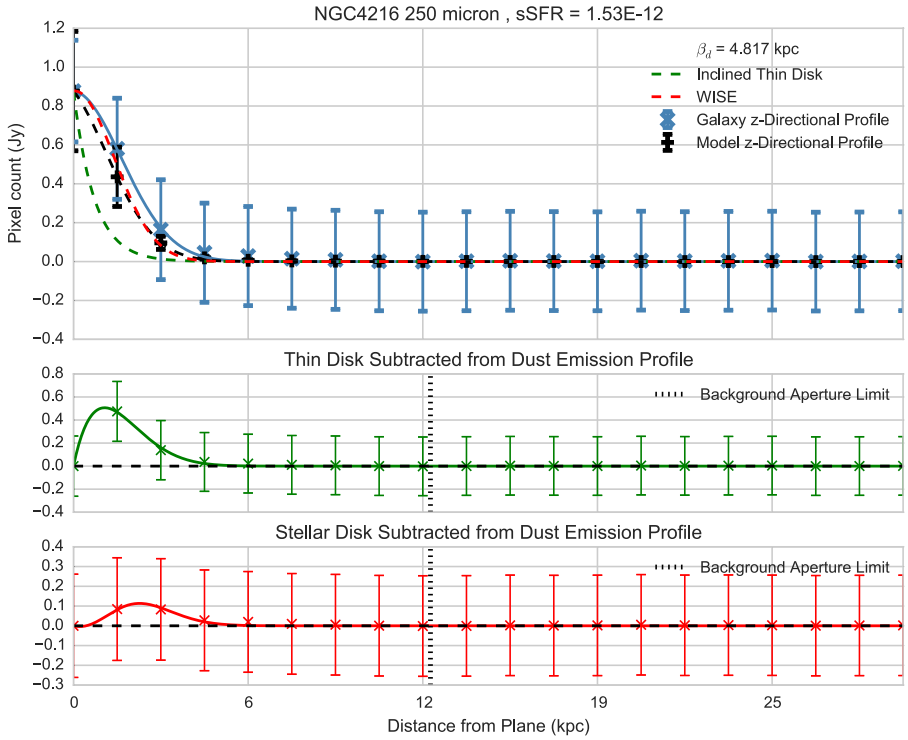

Figure A.103

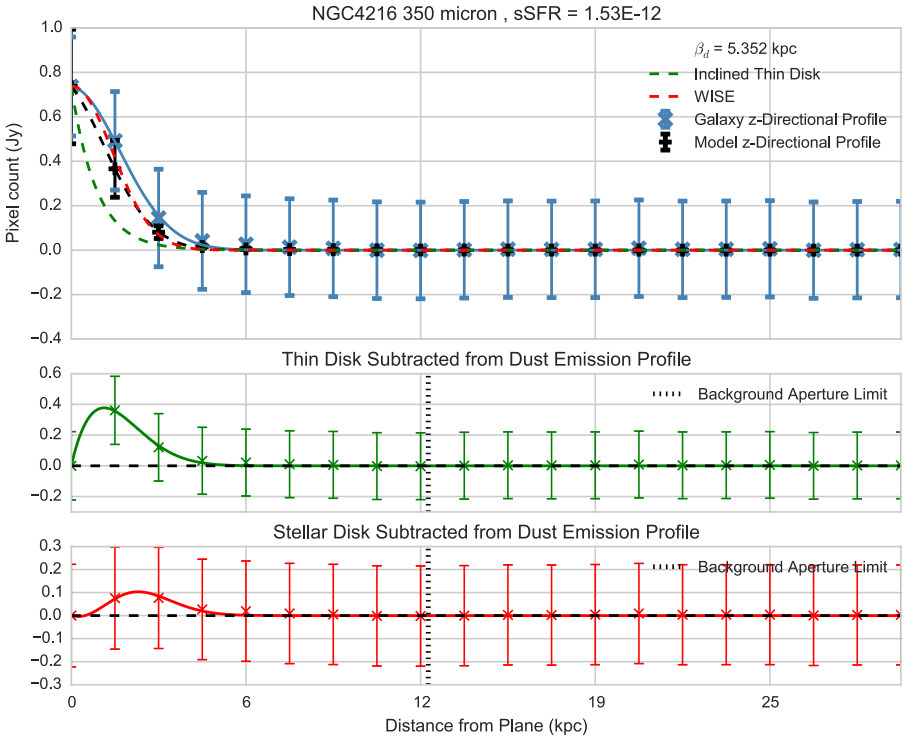

Figure A.104

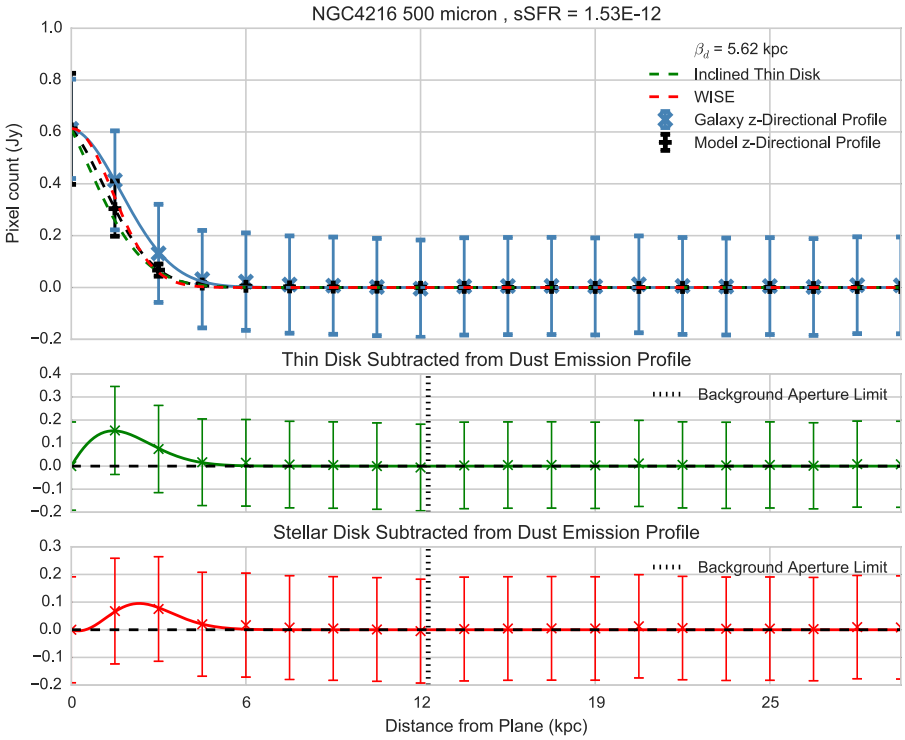

Figure A.105

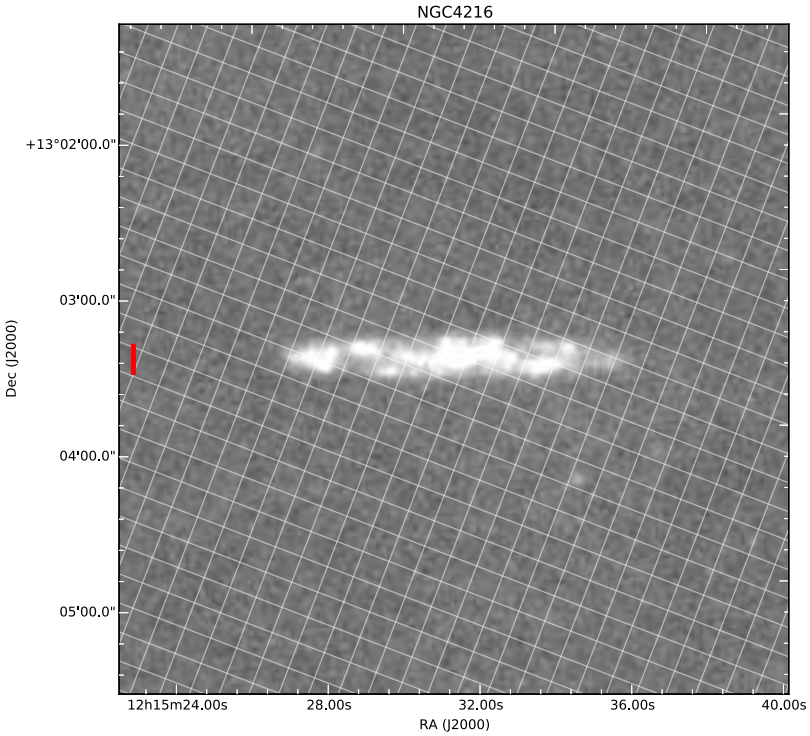

Figure A.106: 100 μm

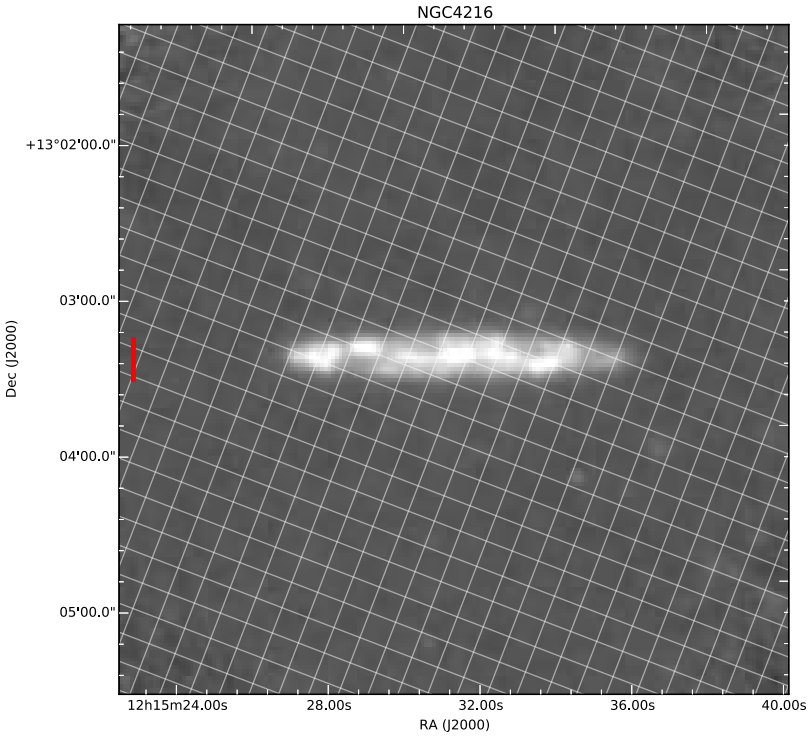

Figure A.107: 160 μm

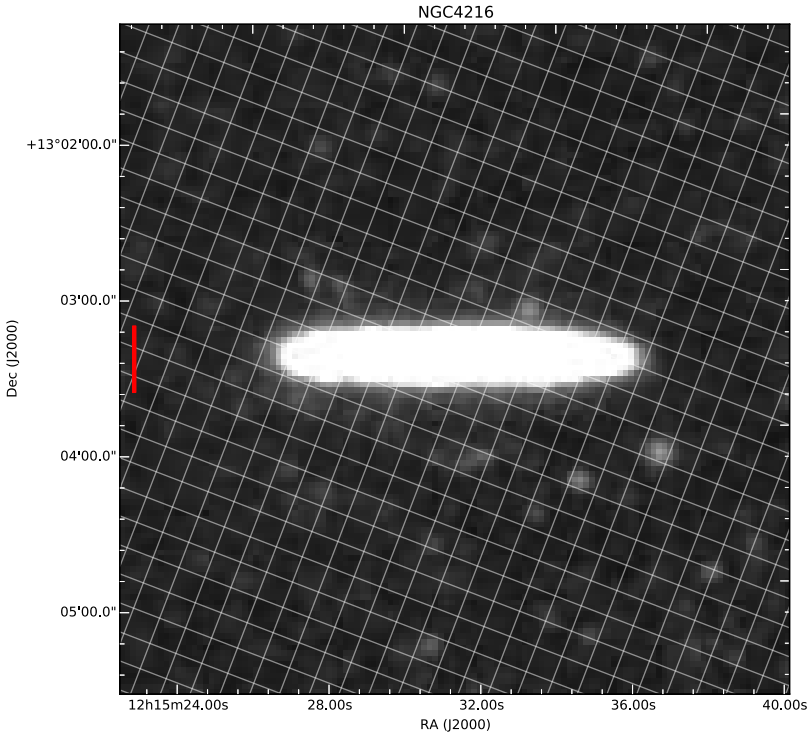

Figure A.108: 250 μm

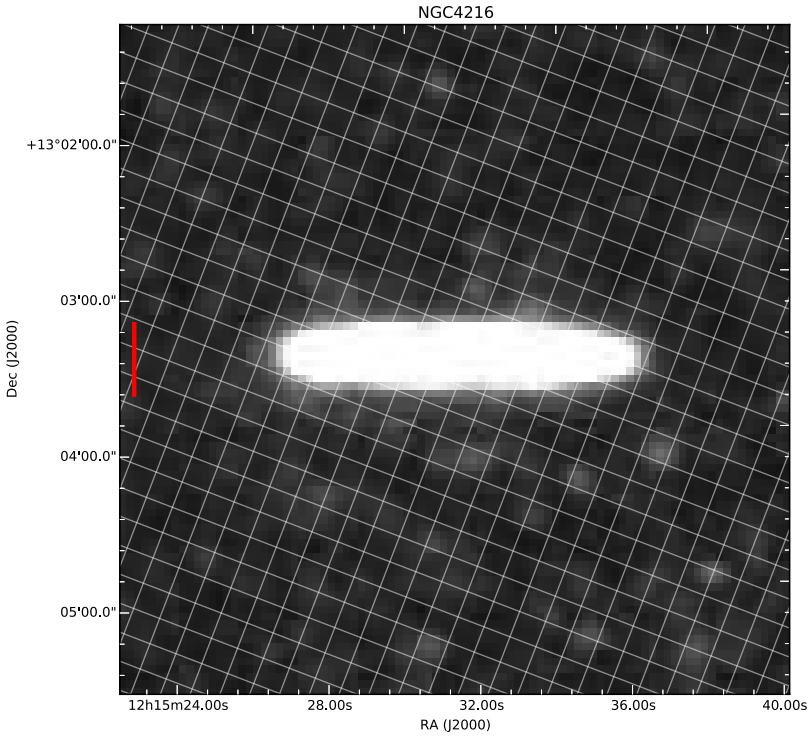

Figure A.109: 350 μm

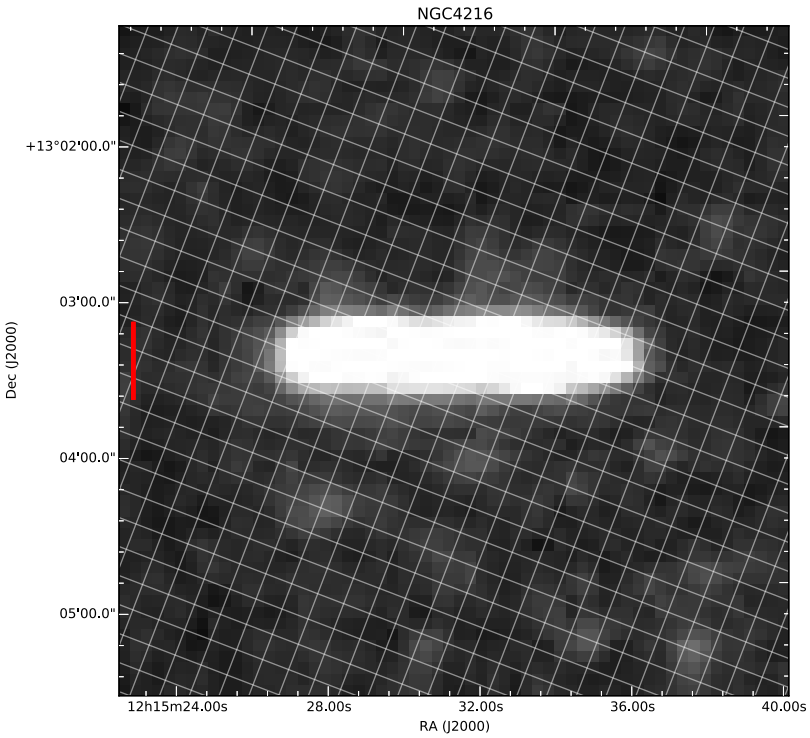

Figure A.110: 500 μm

A.12 NGC4217

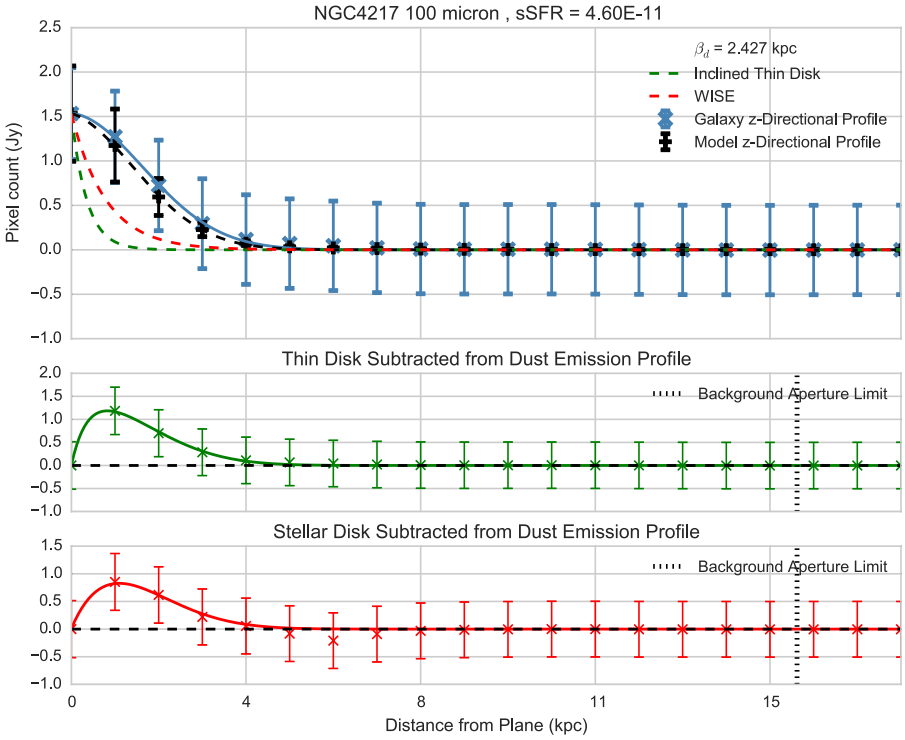

Figure A.111

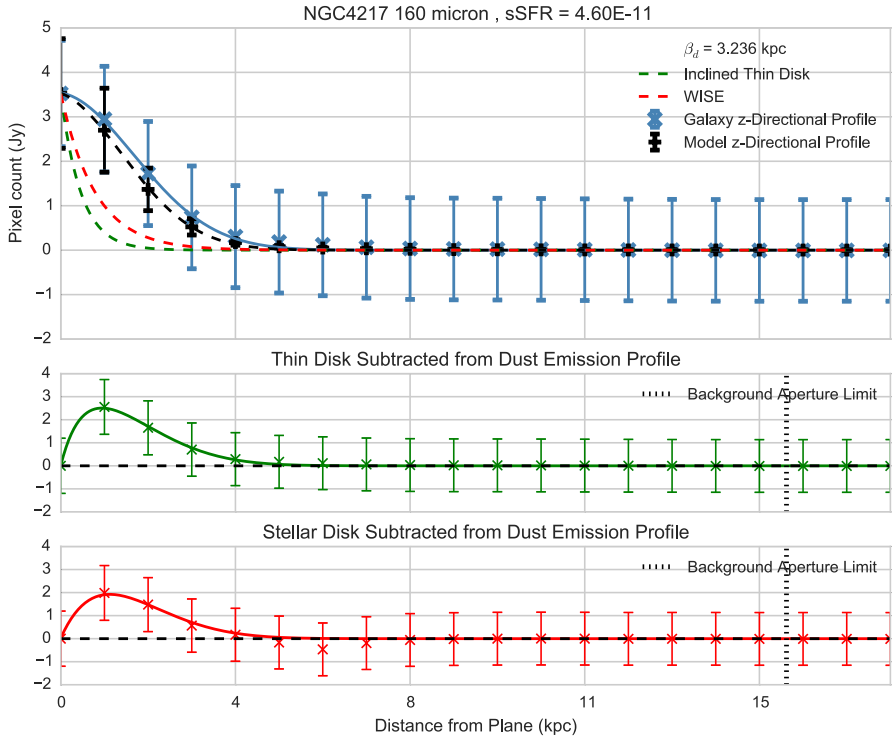

Figure A.112

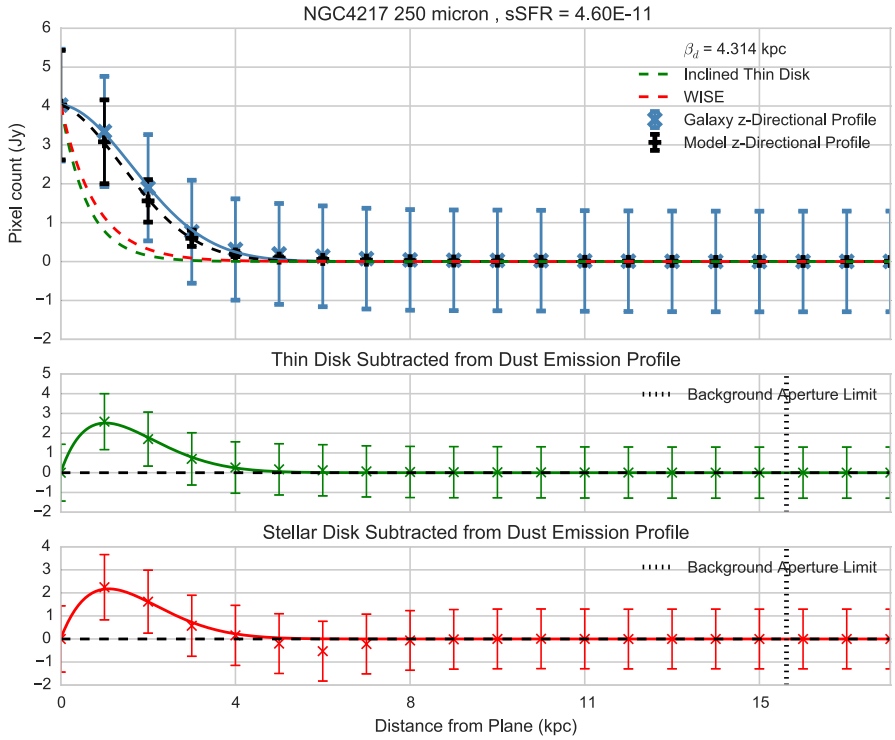

Figure A.113

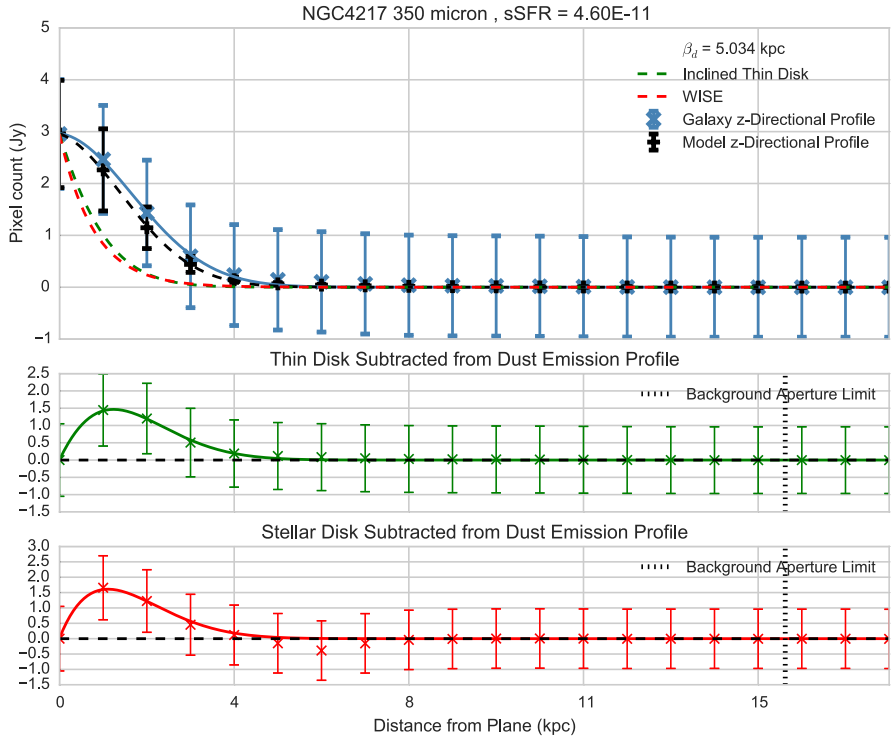

Figure A.114

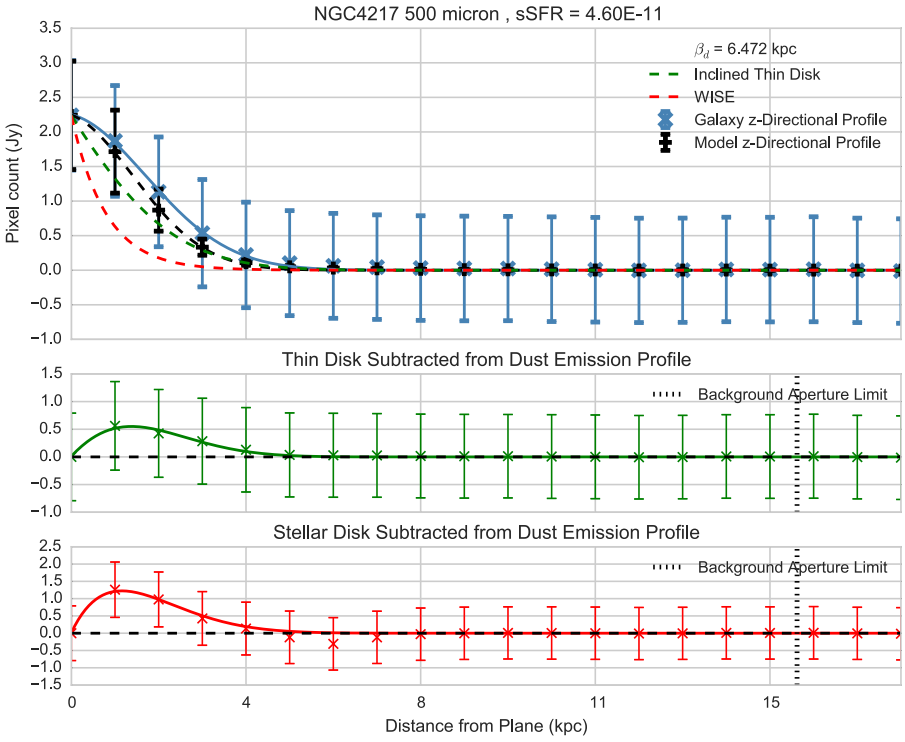

Figure A.115

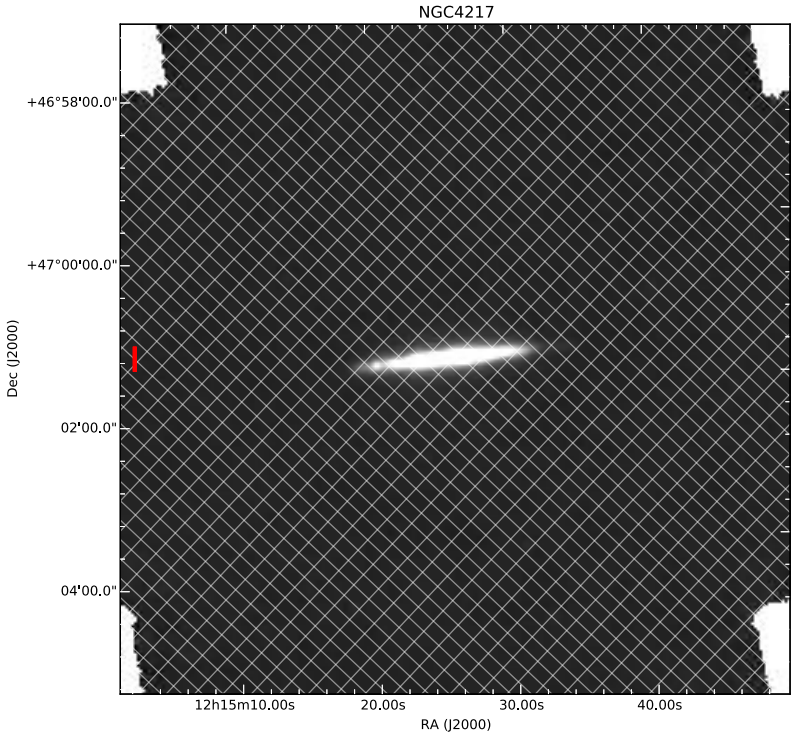

Figure A.116: 100 μm

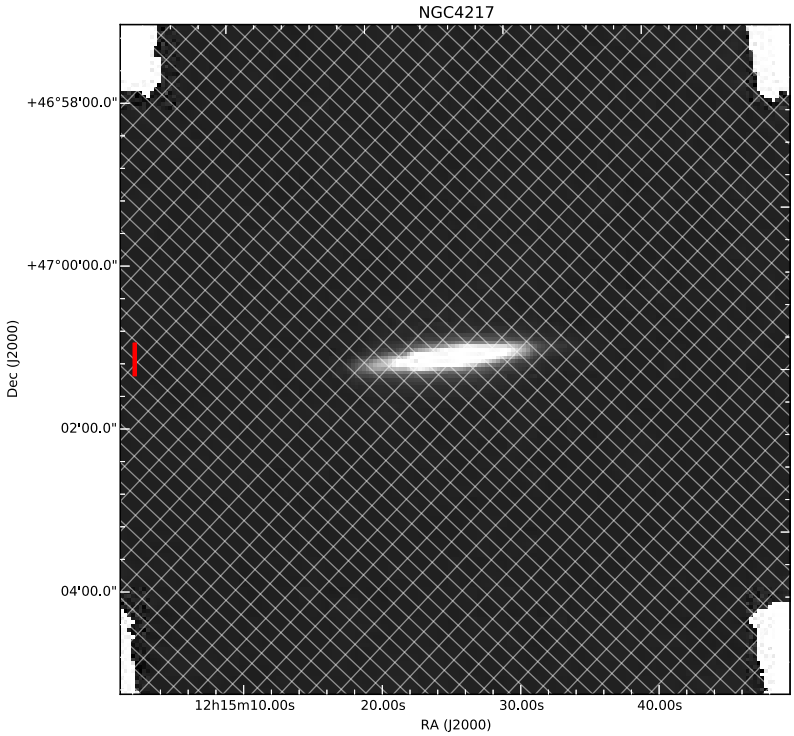

Figure A.117: 160 μm

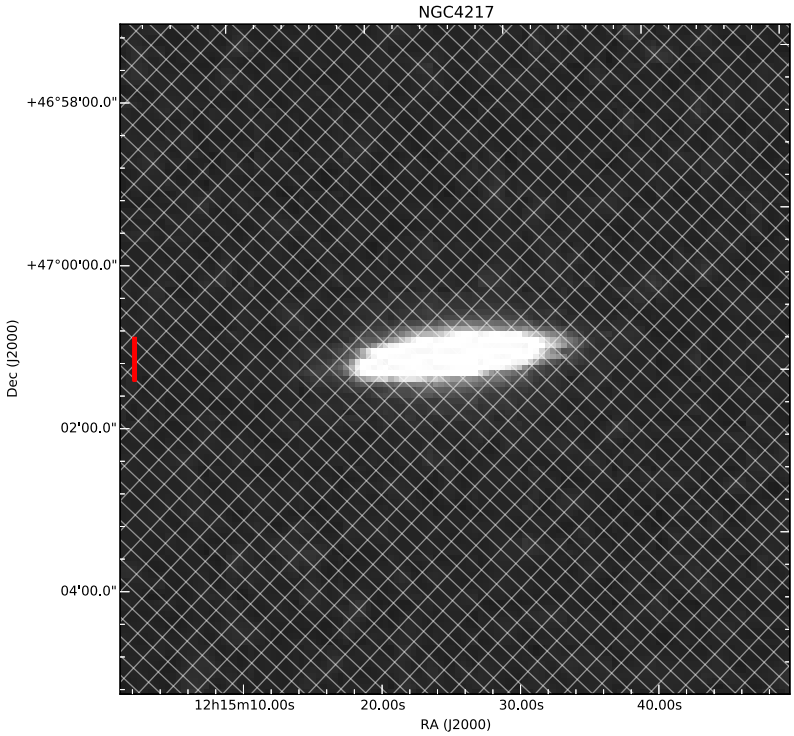

Figure A.118: 250 μm

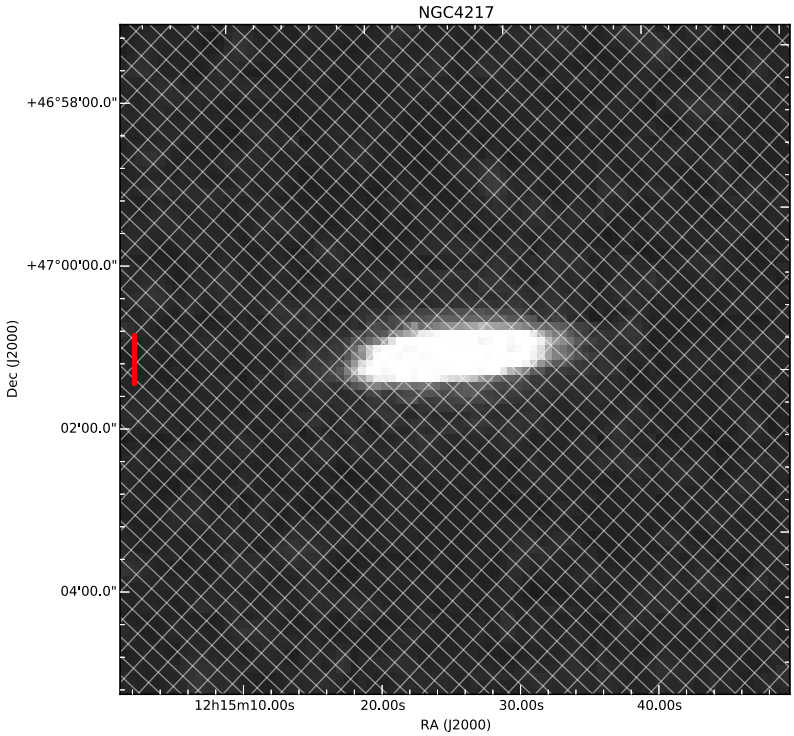

Figure A.119: 350 μm

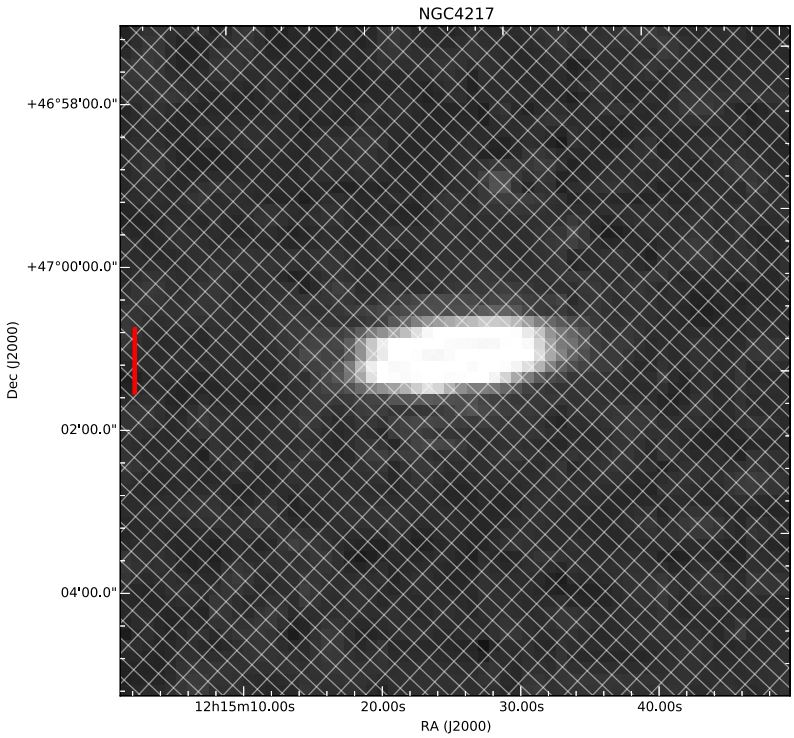

Figure A.120: 500 μm

A.13 NGC4222

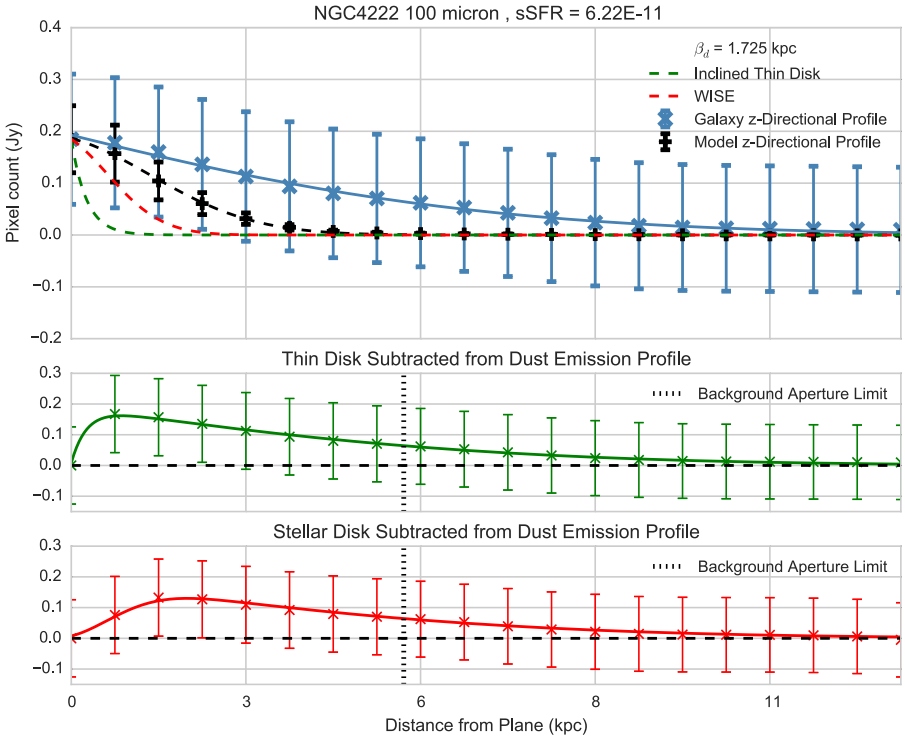

Figure A.121

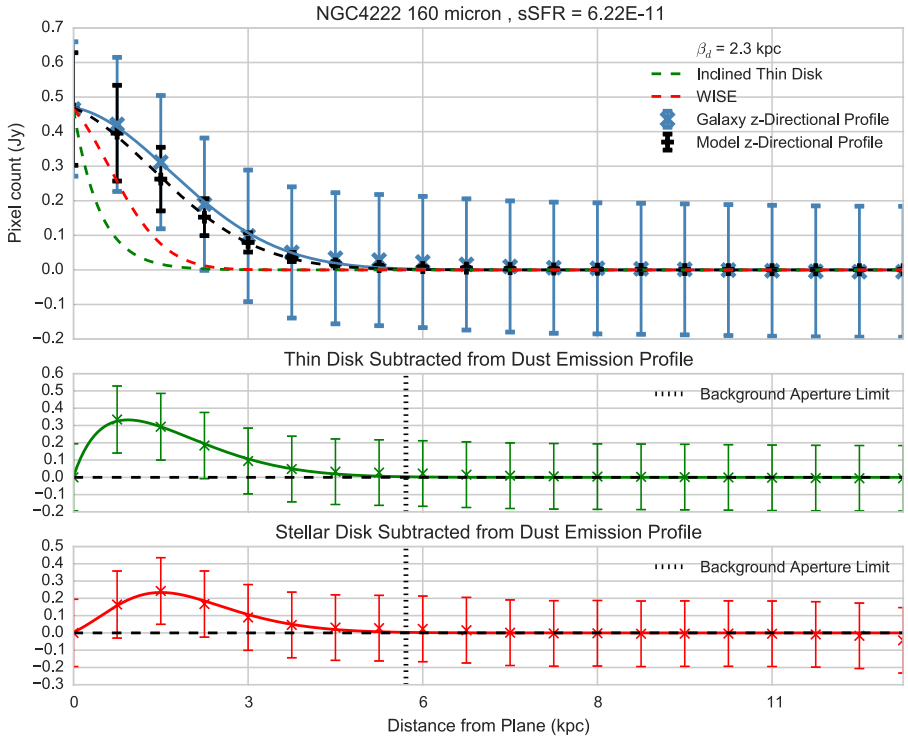

Figure A.122

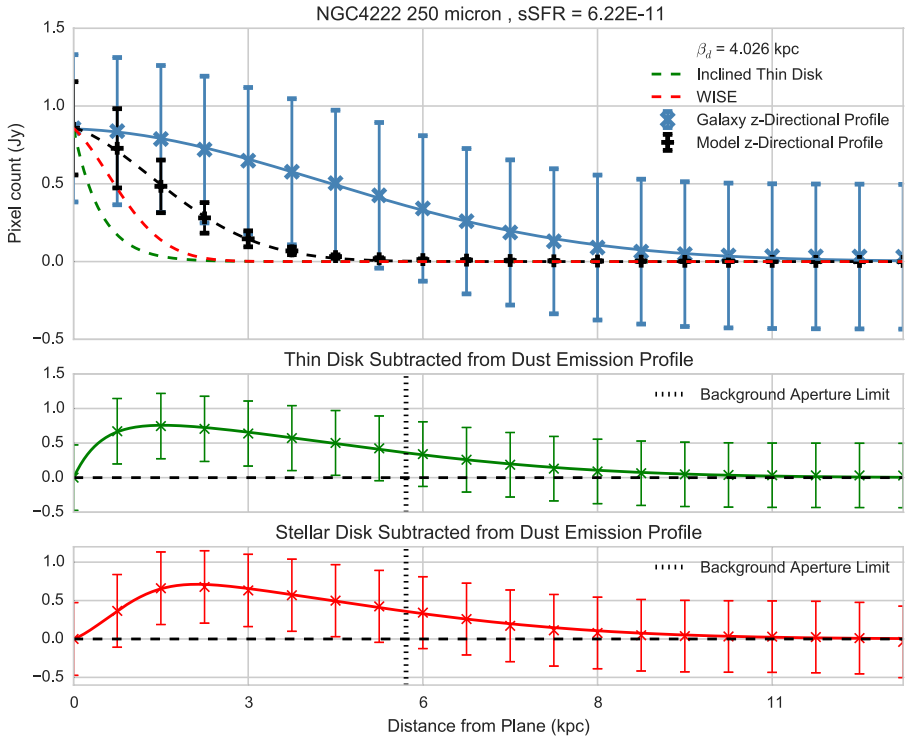

Figure A.123

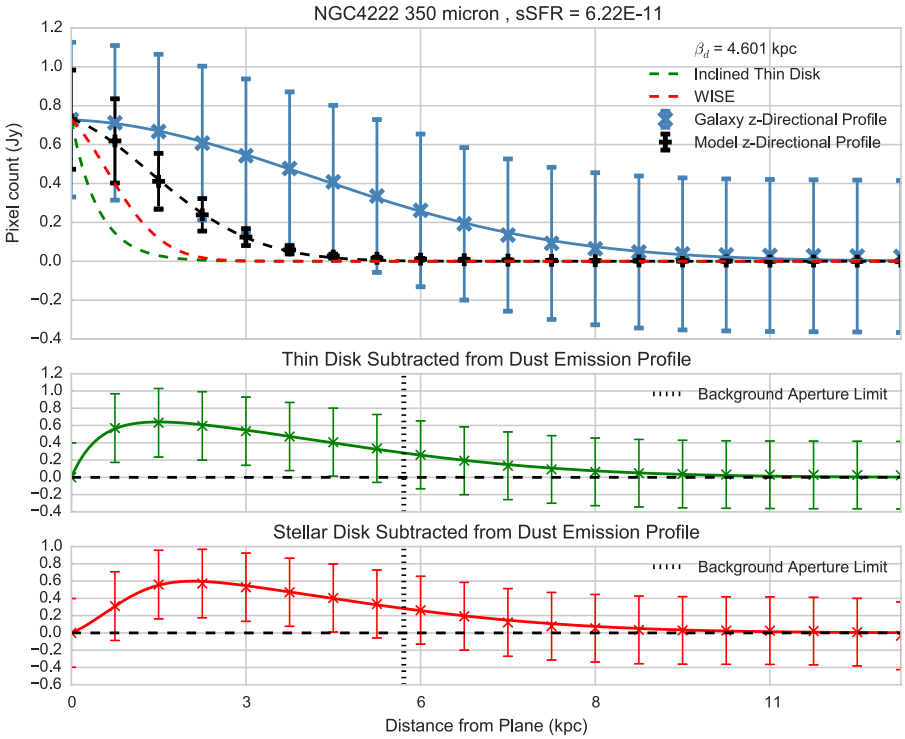

Figure A.124

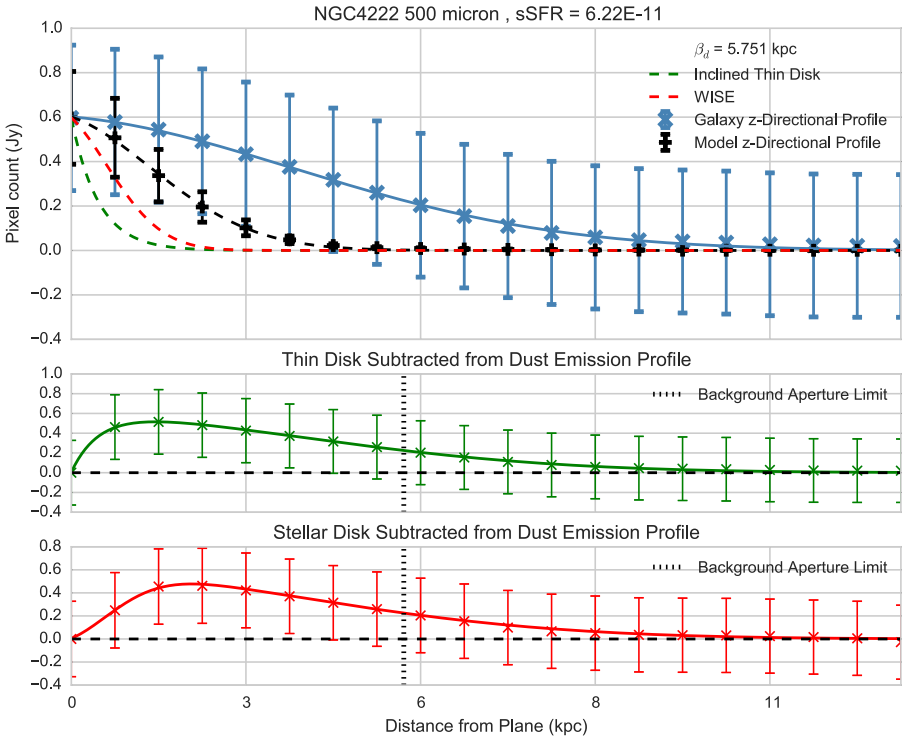

Figure A.125

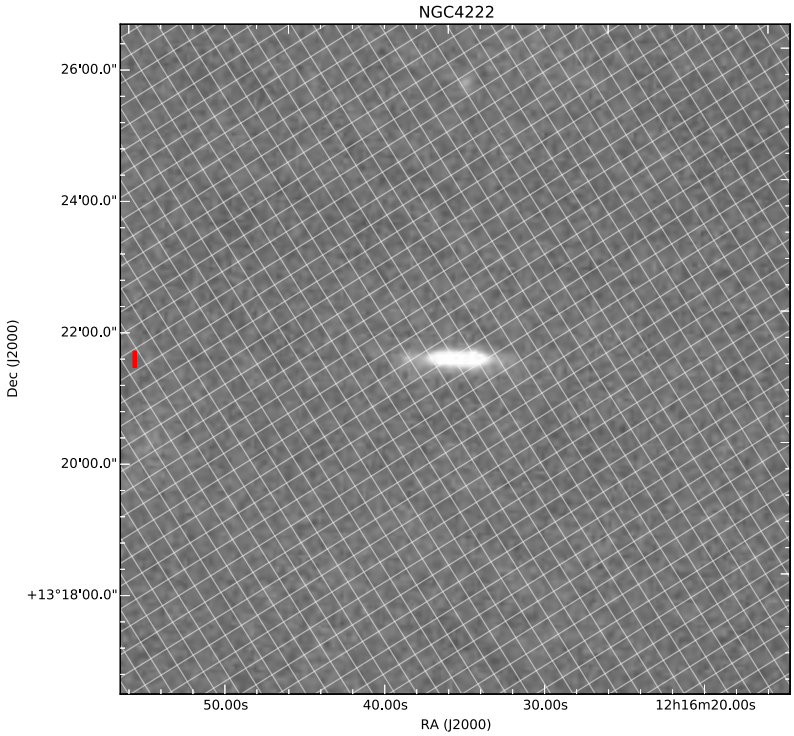

Figure A.126: 100 μm

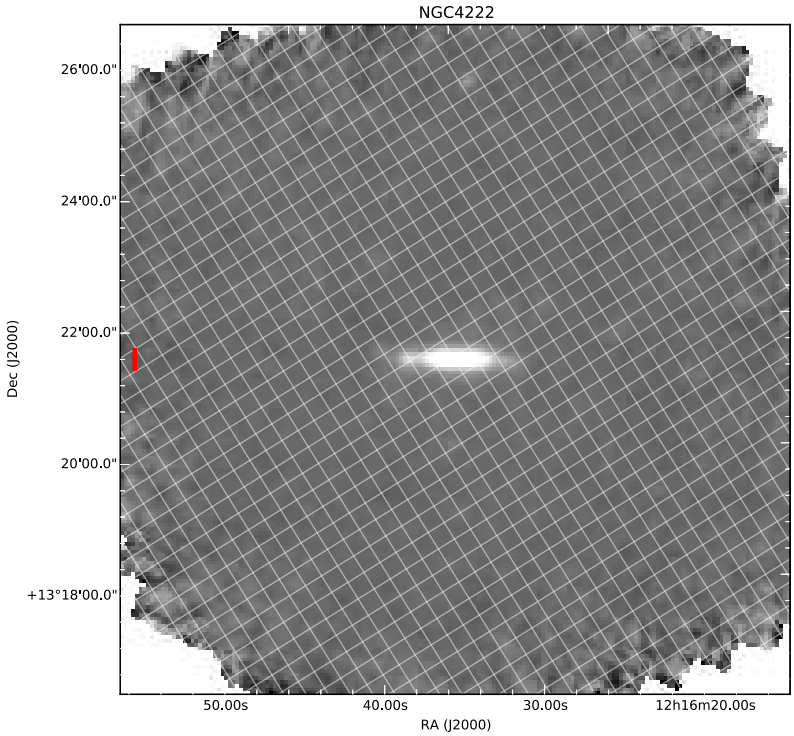

Figure A.127: 160 μm

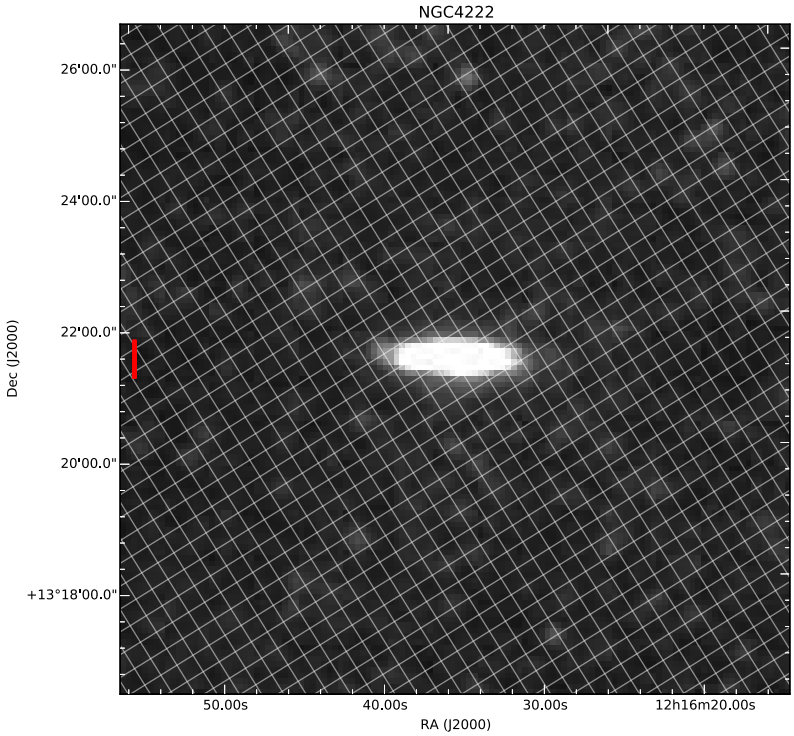

Figure A.128: 250 μm

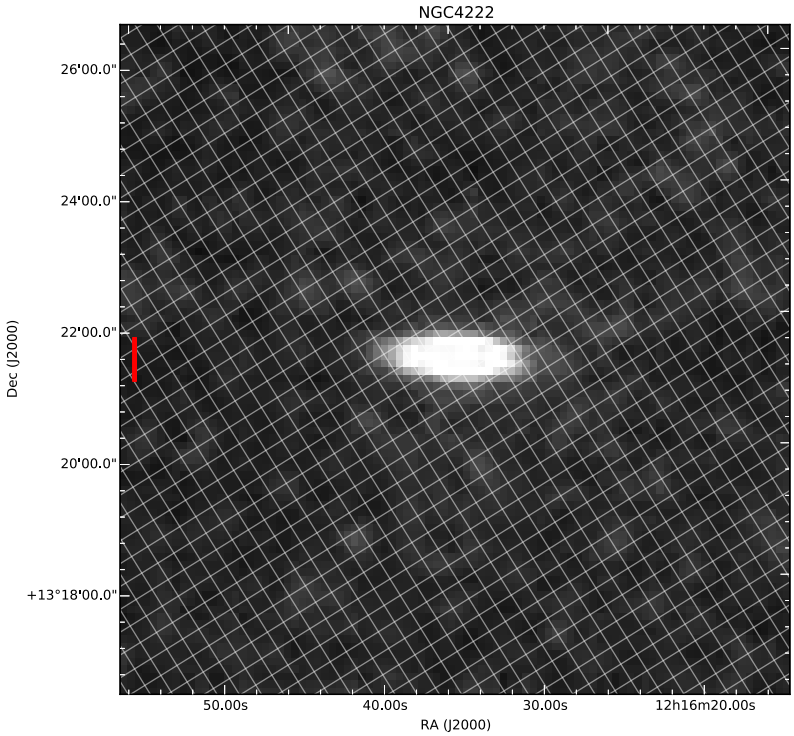

Figure A.129: 350 μm

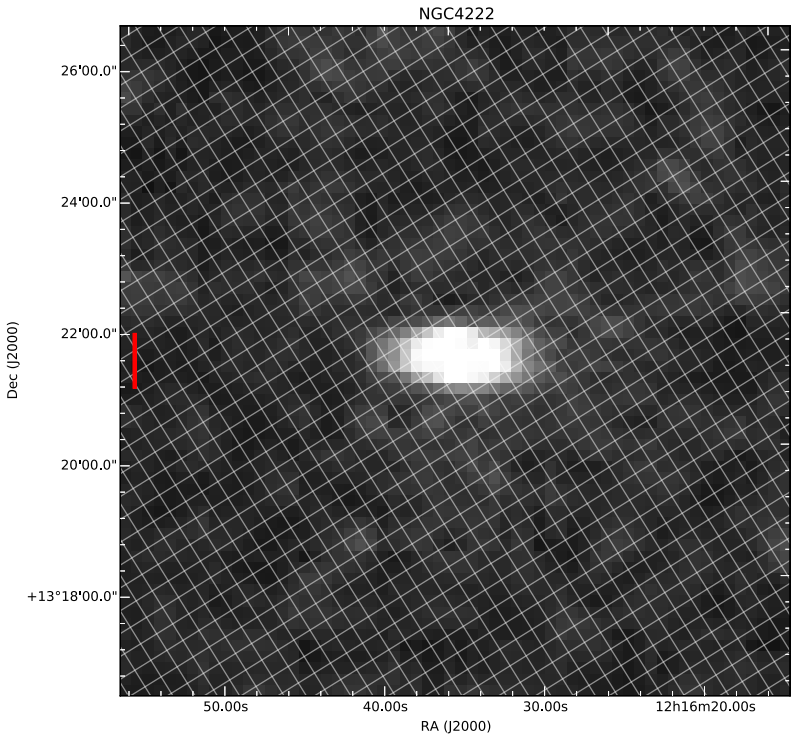

Figure A.130: 500 μm

A.14 NGC4244

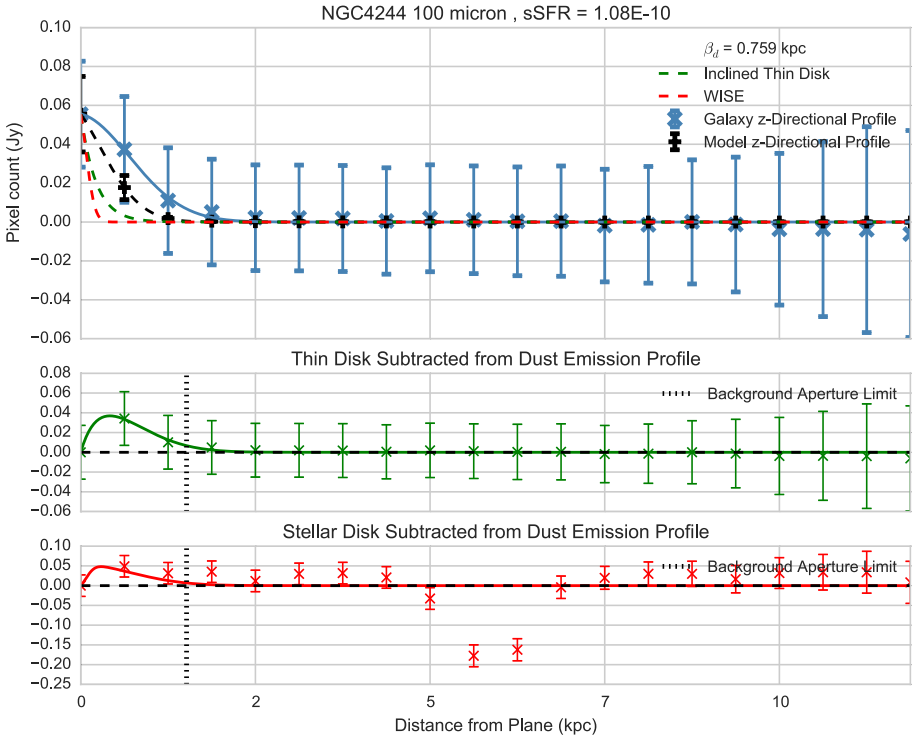

Figure A.131

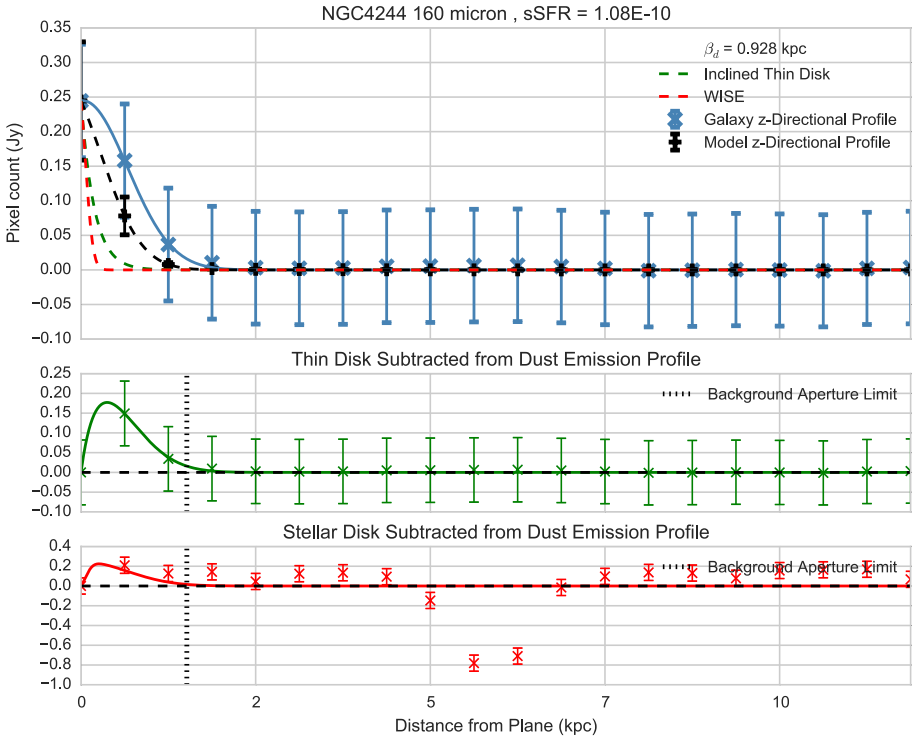

Figure A.132

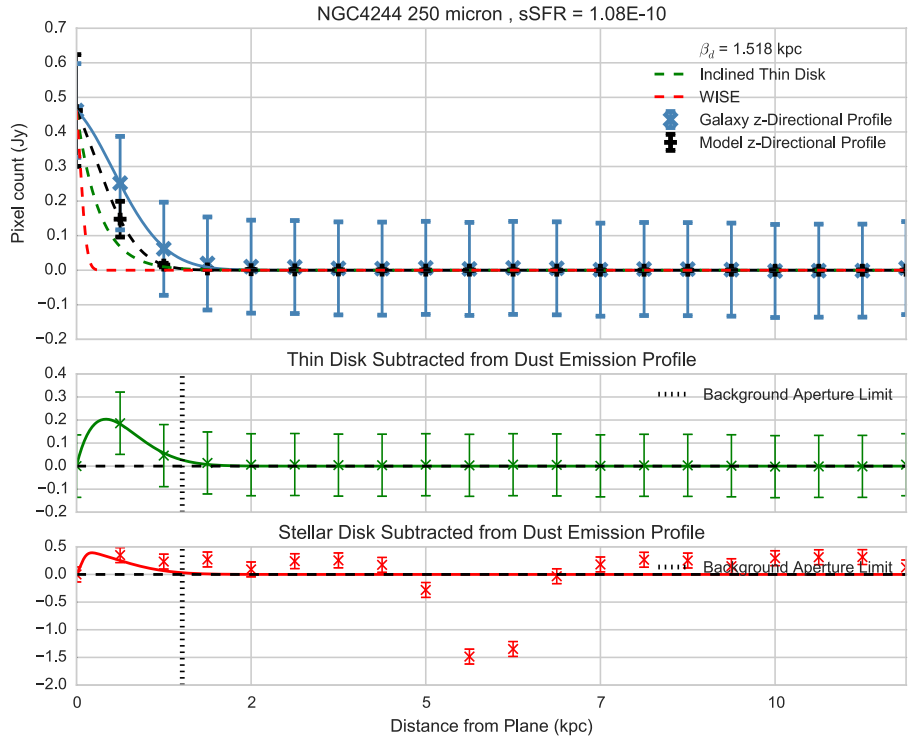

Figure A.133

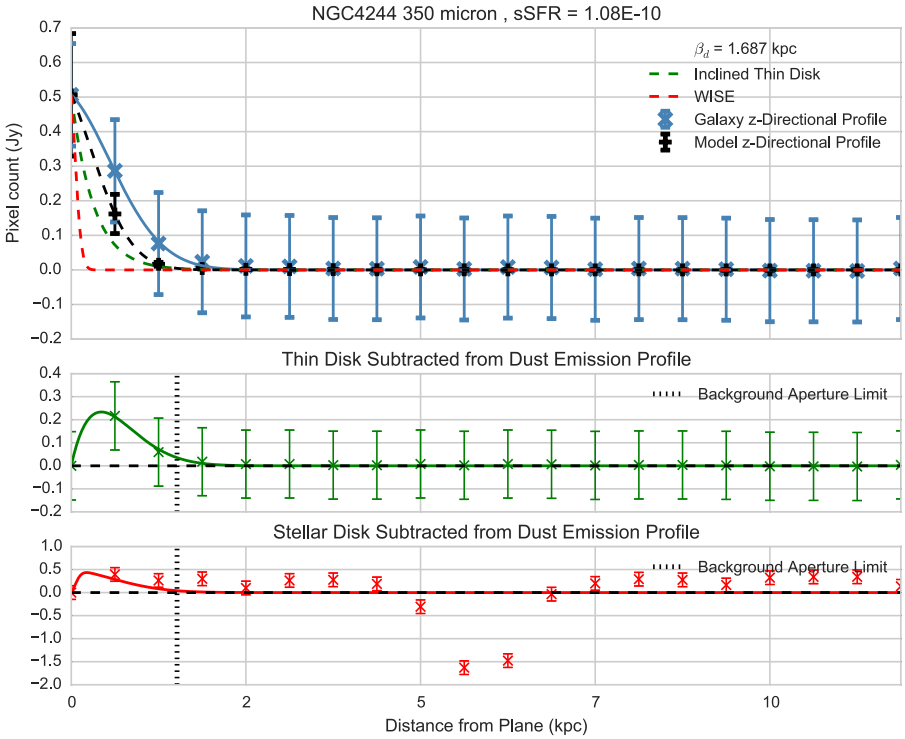

Figure A.134

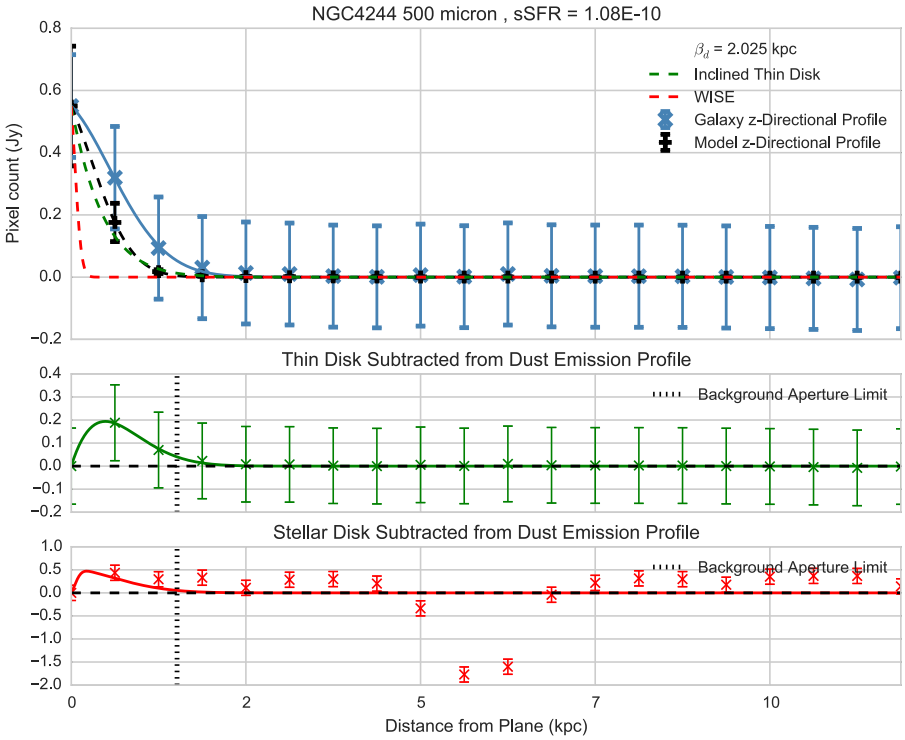

Figure A.135

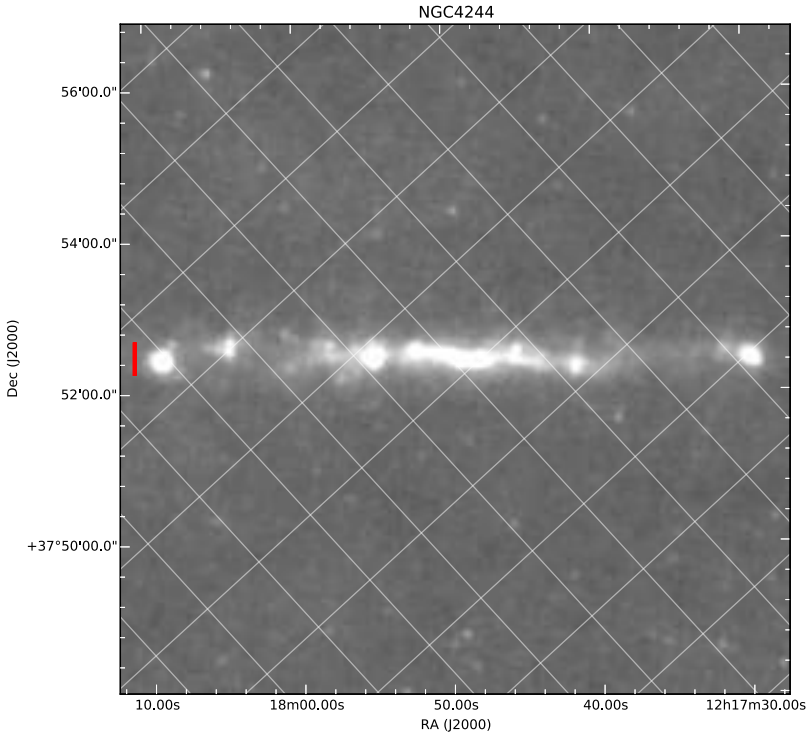

Figure A.136: 100 μm

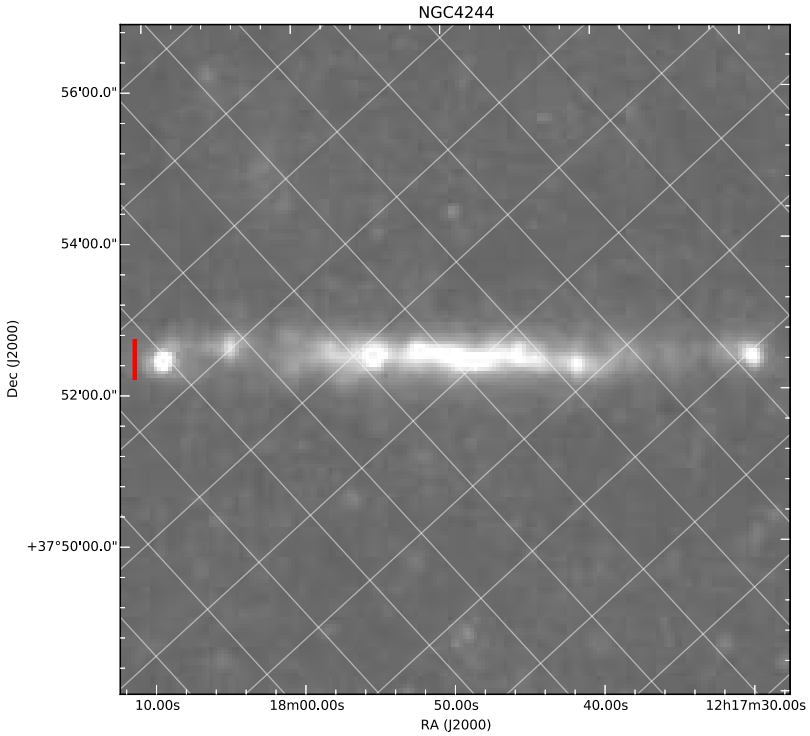

Figure A.137: 160 μm

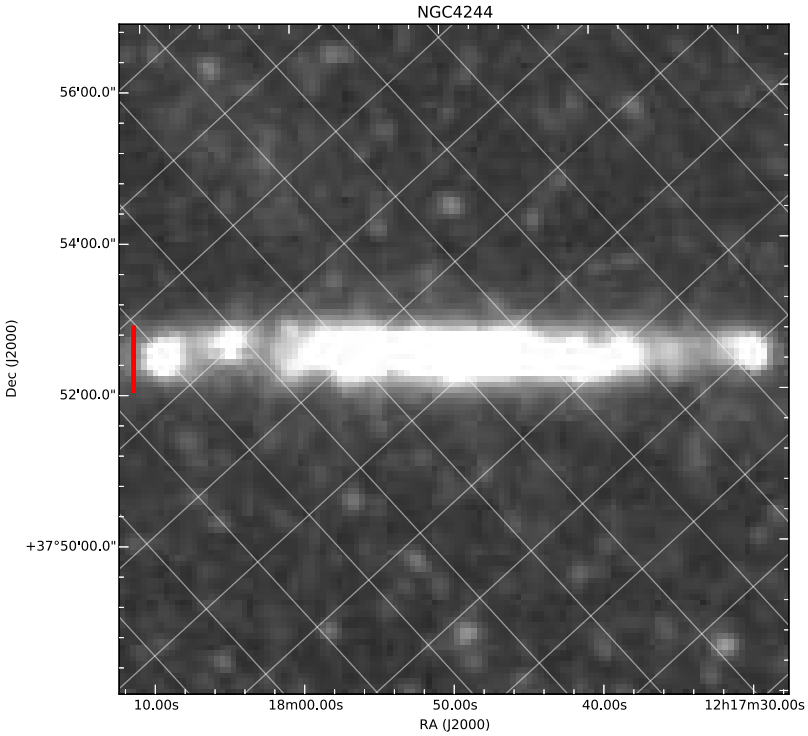

Figure A.138: 250 μm

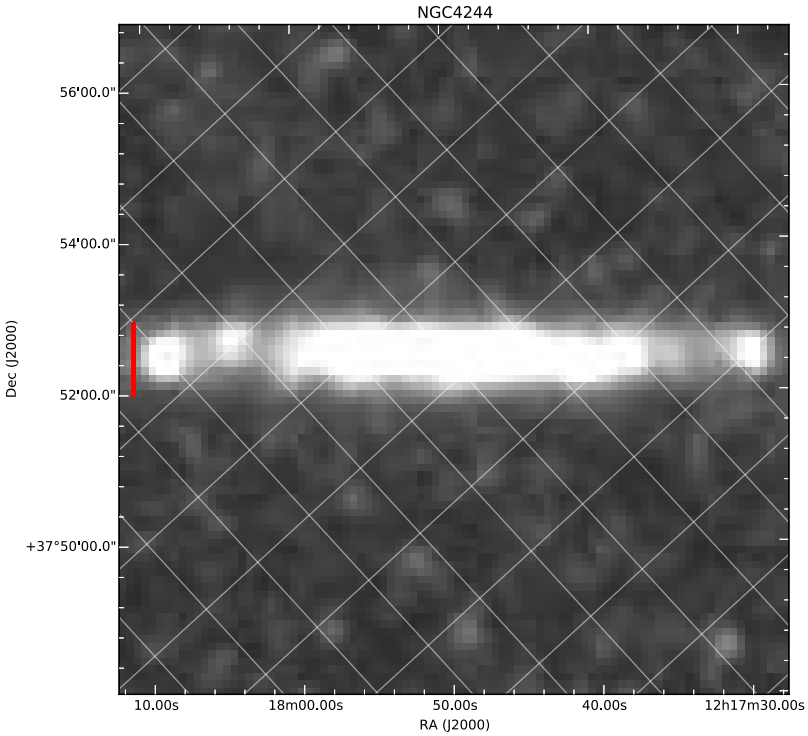

Figure A.139: 350 μm

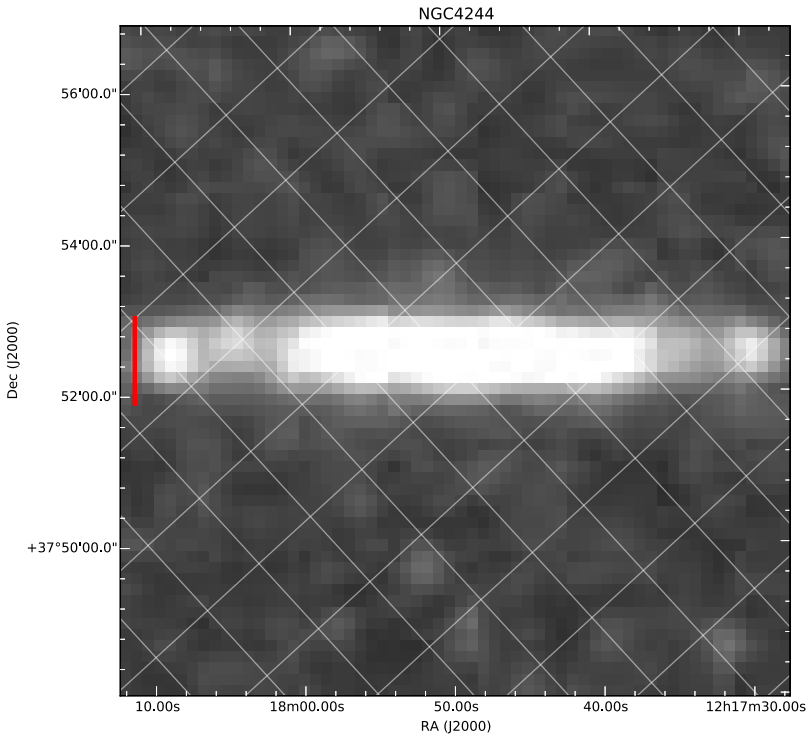

Figure A.140: 500 μm

A.15 NGC4289

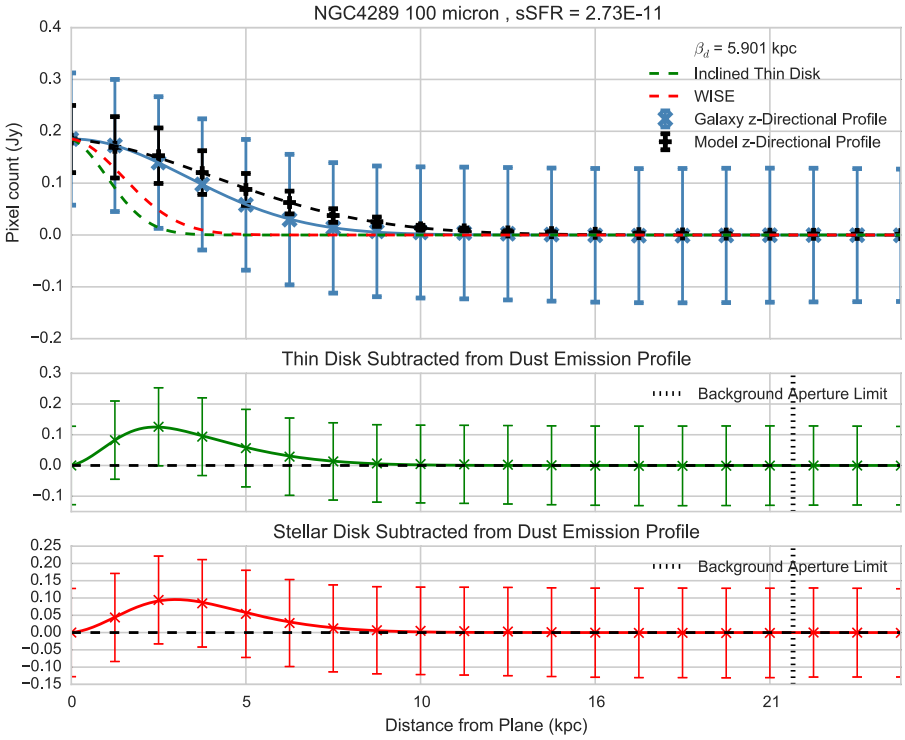

Figure A.141

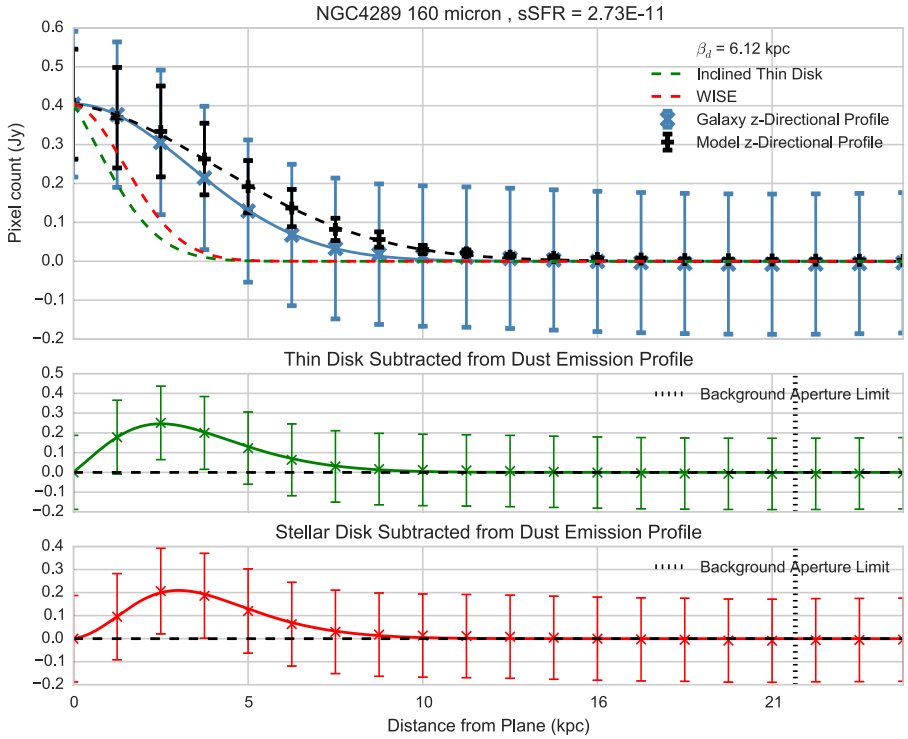

Figure A.142

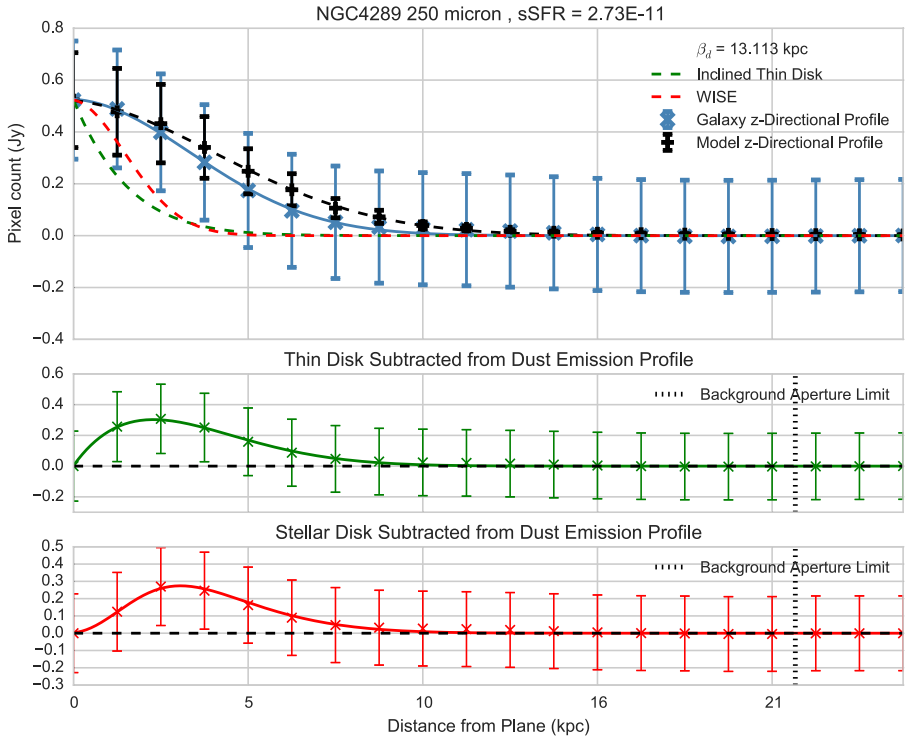

Figure A.143

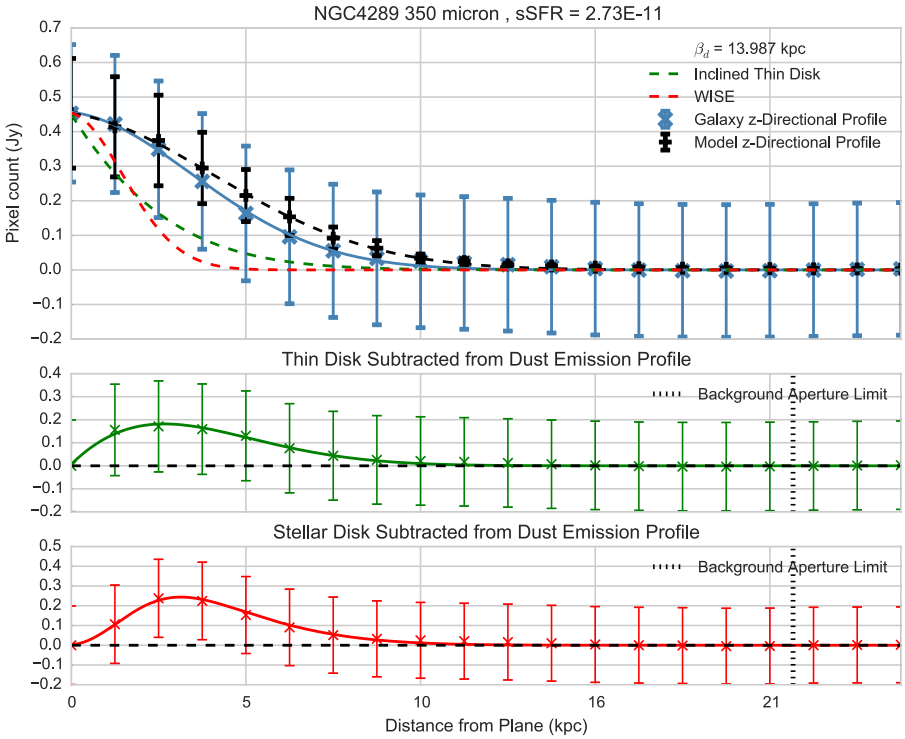

Figure A.144

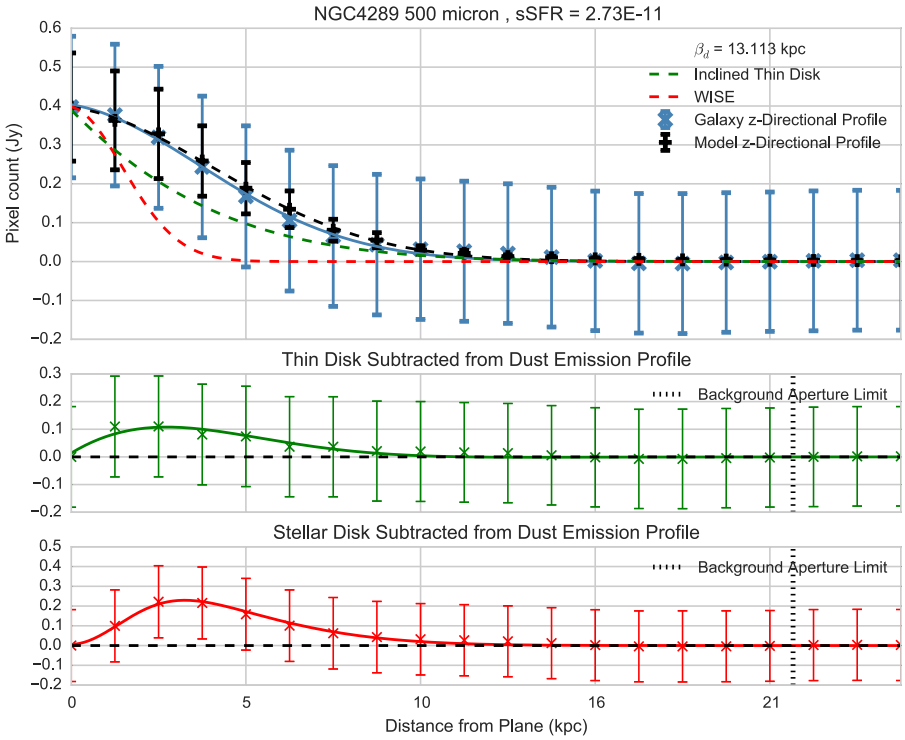

Figure A.145

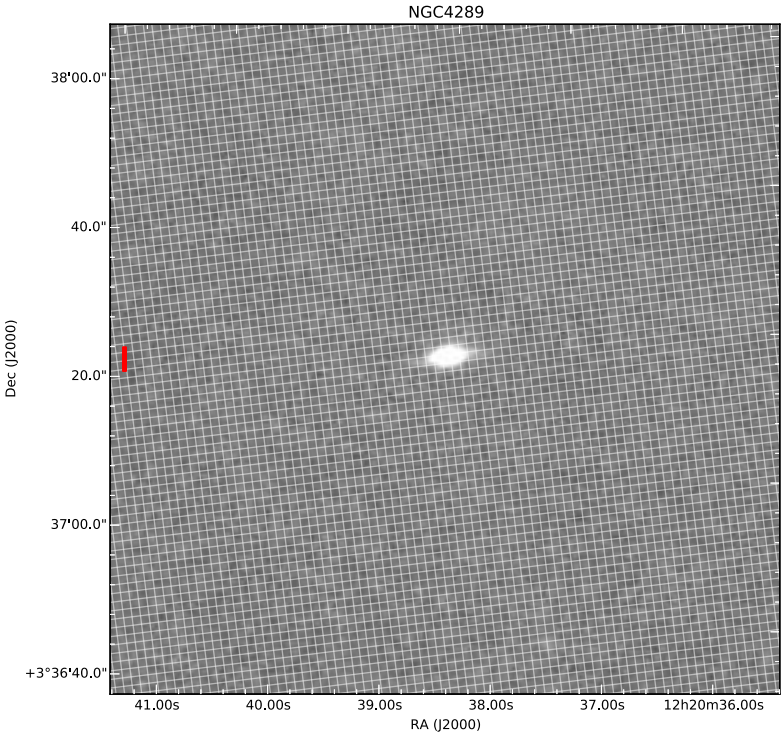

Figure A.146: 100 μm

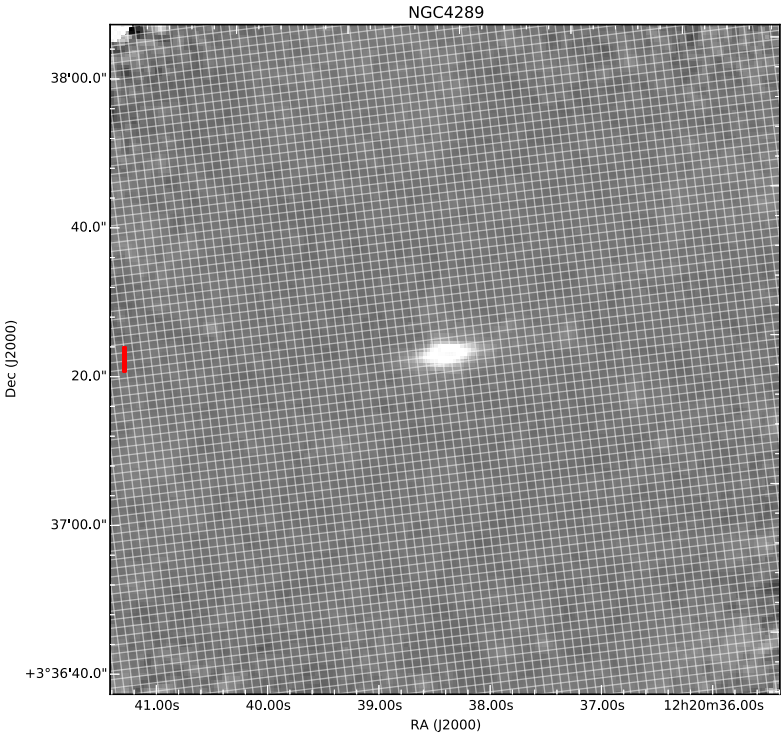

Figure A.147: 160 μm

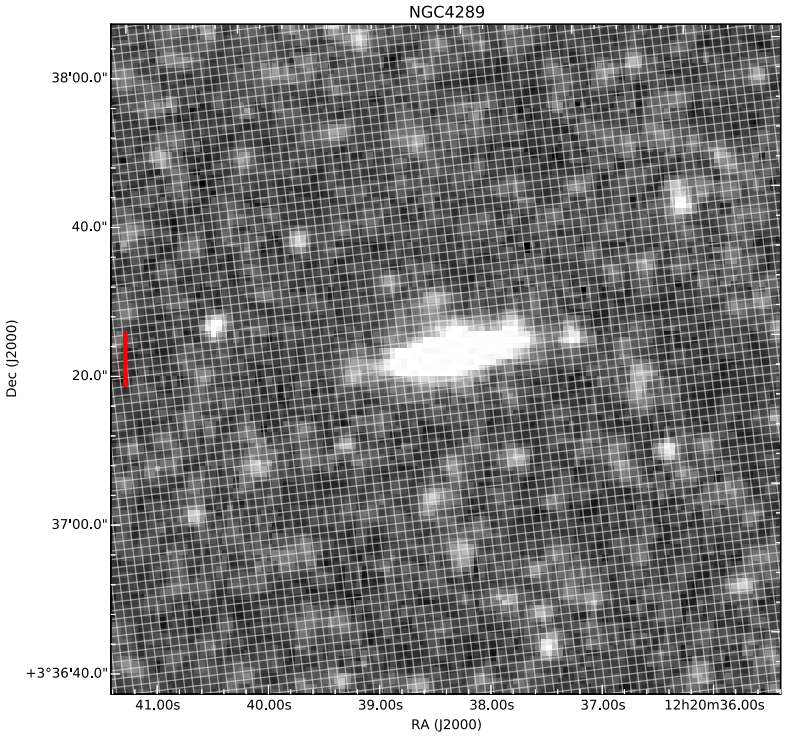

Figure A.148: 250 μm

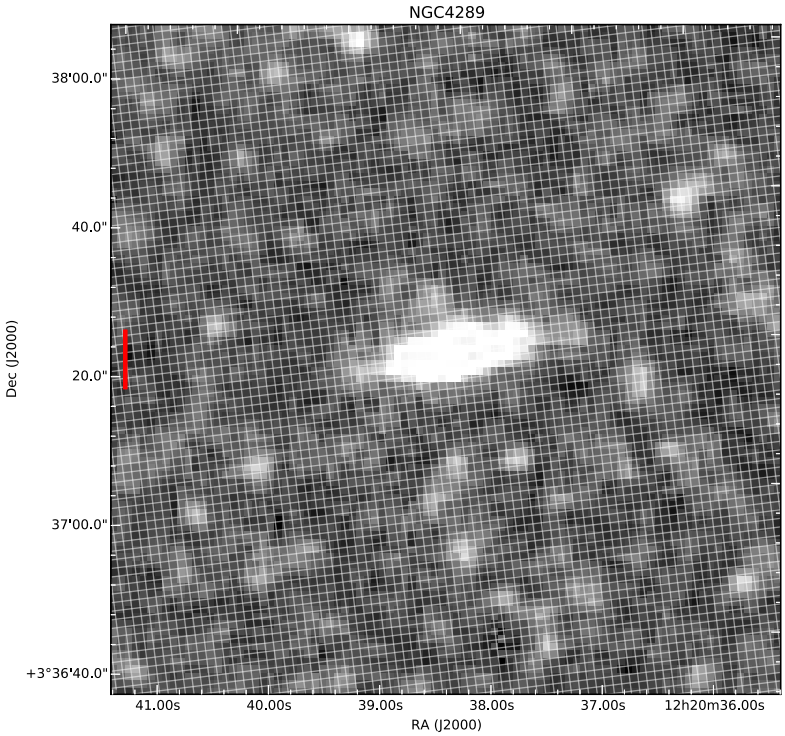

Figure A.149: 350 μm

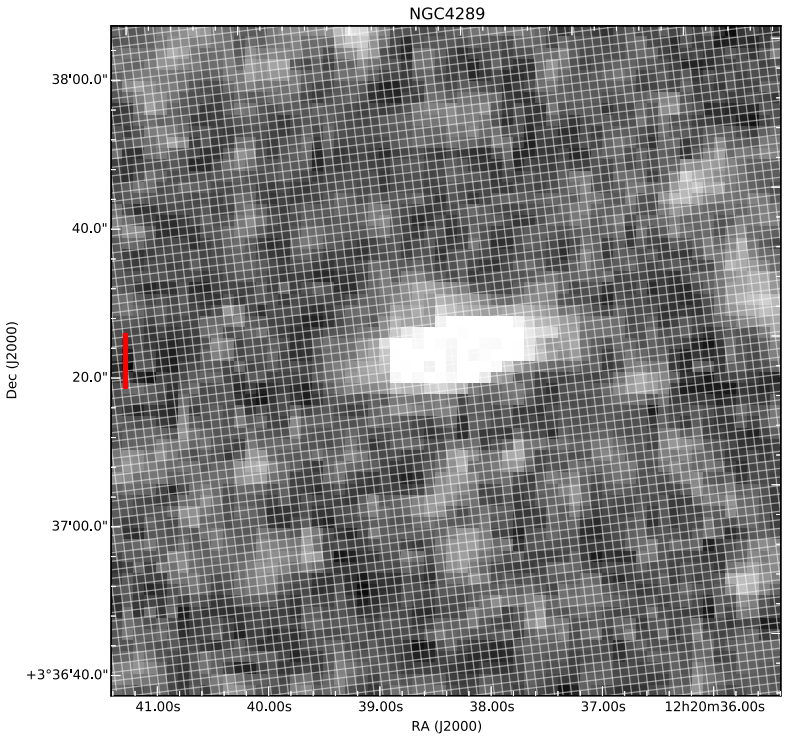

Figure A.150: 500 μm

A.16 NGC4302

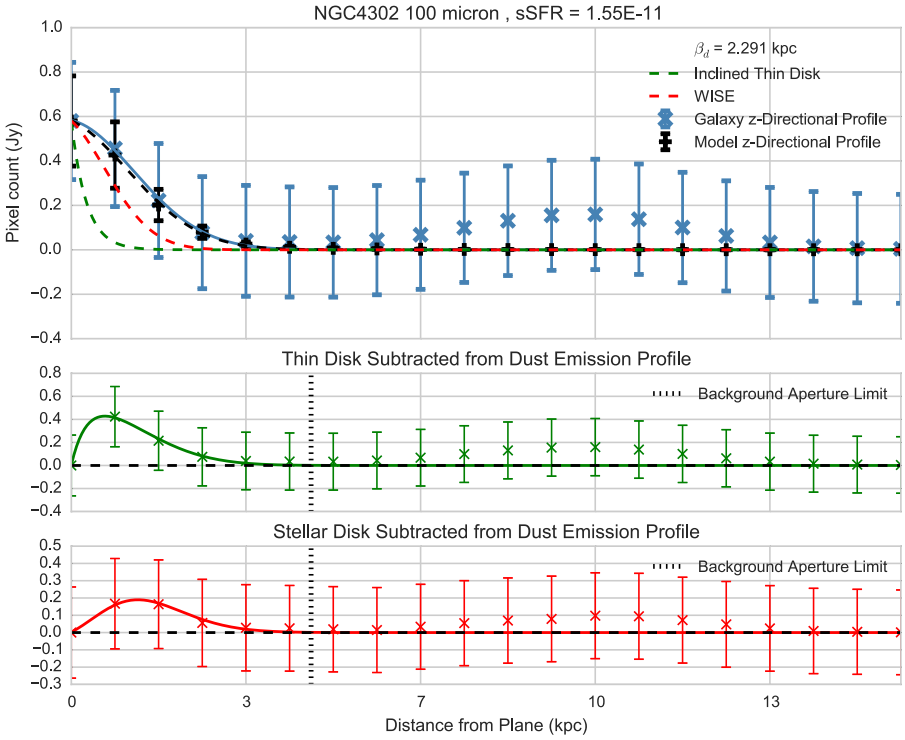

Figure A.151

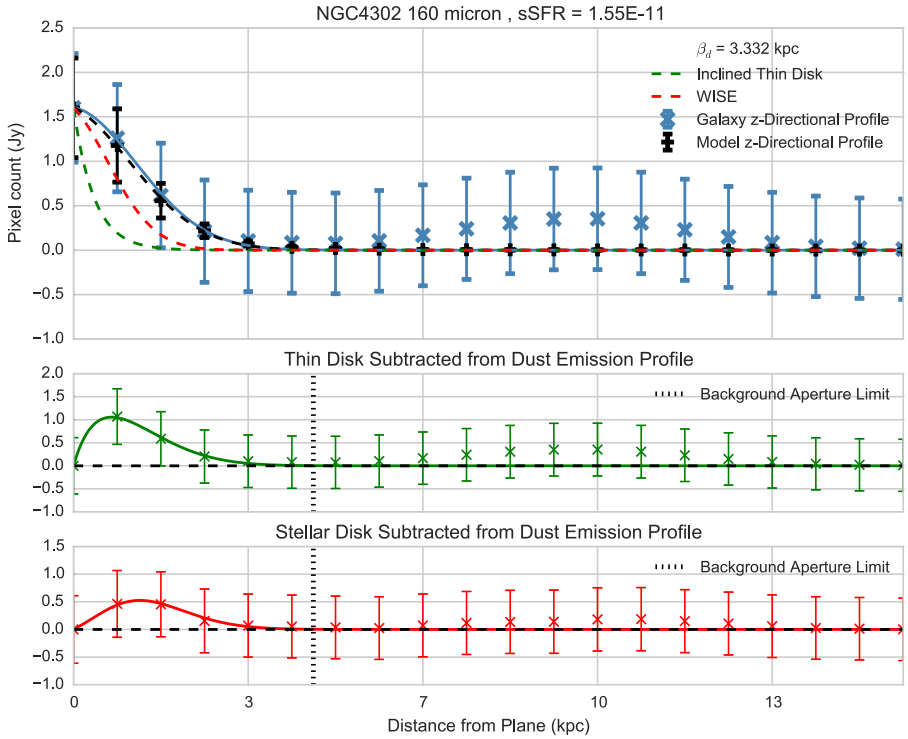

Figure A.152

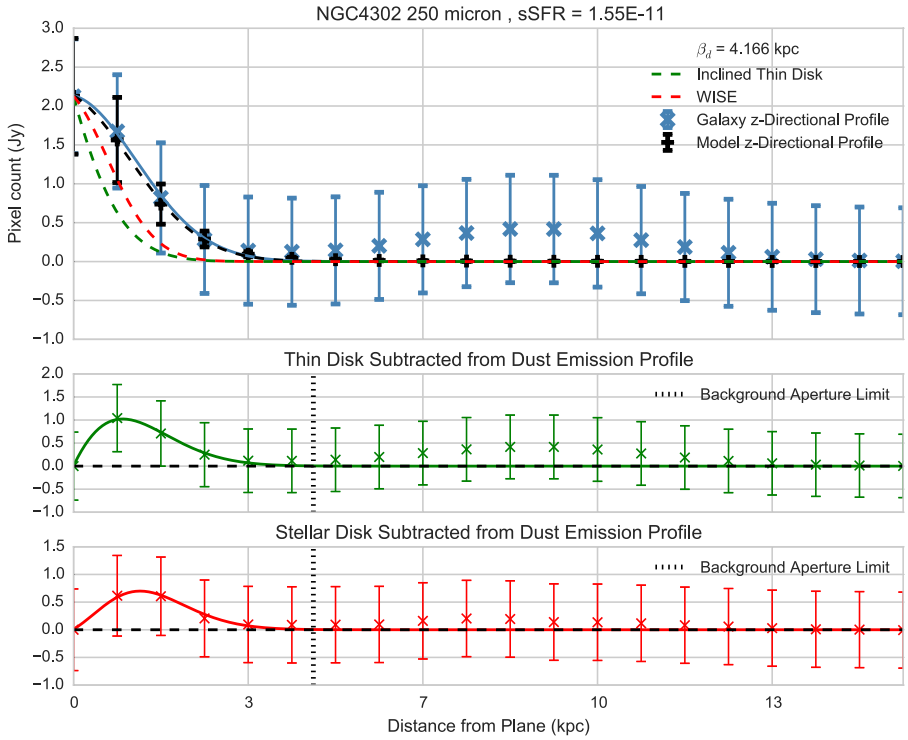

Figure A.153

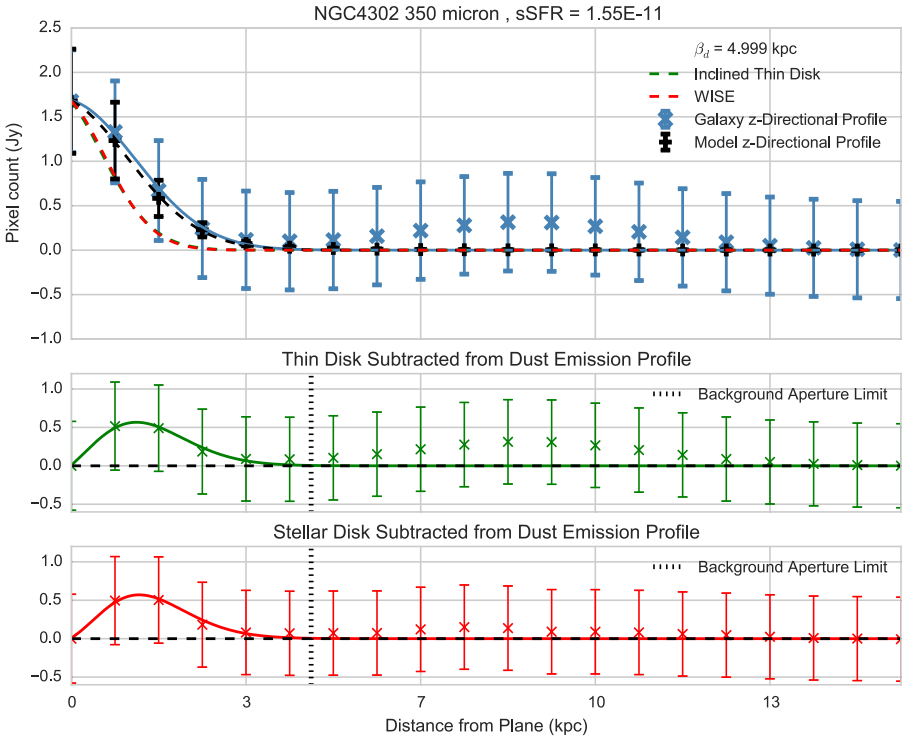

Figure A.154

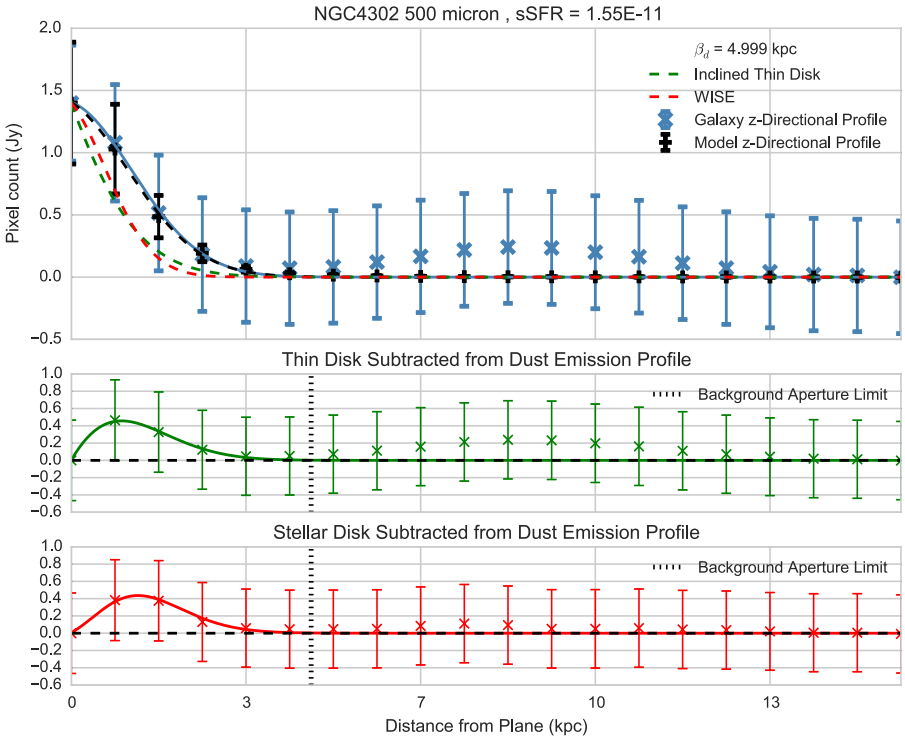

Figure A.155

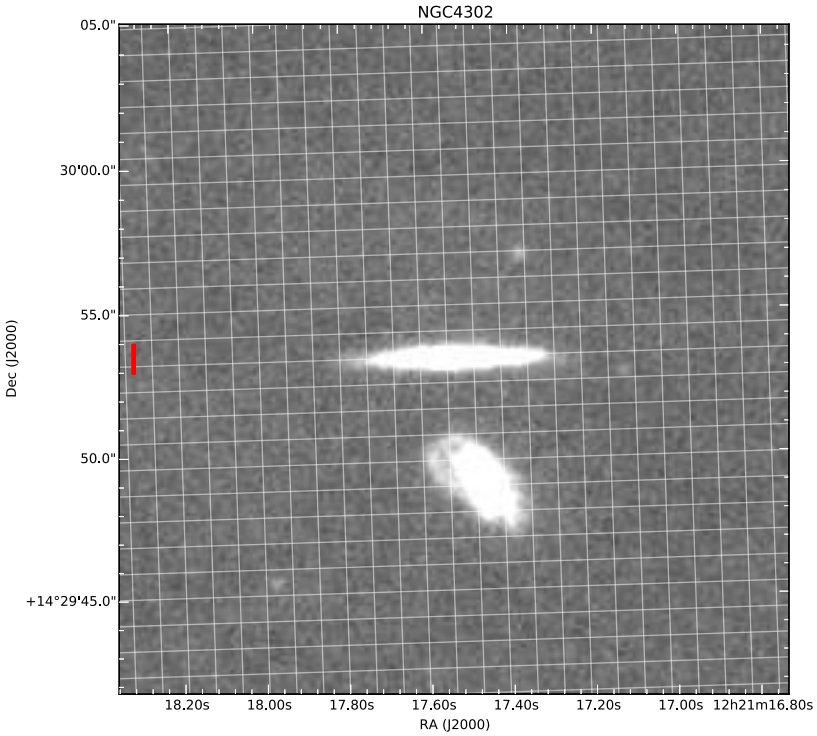

Figure A.156: 100 μm

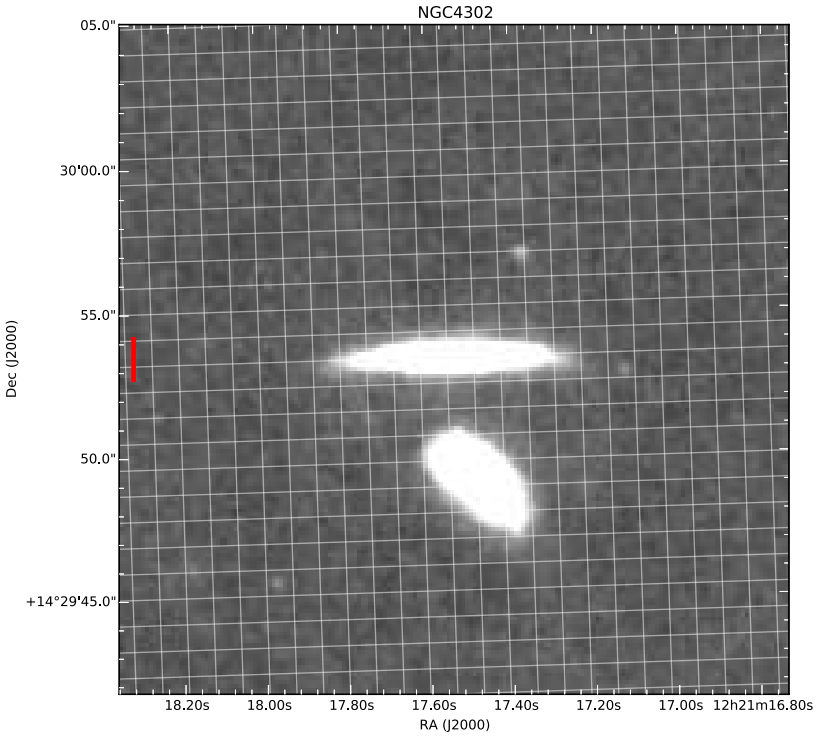

Figure A.157: 160 μm

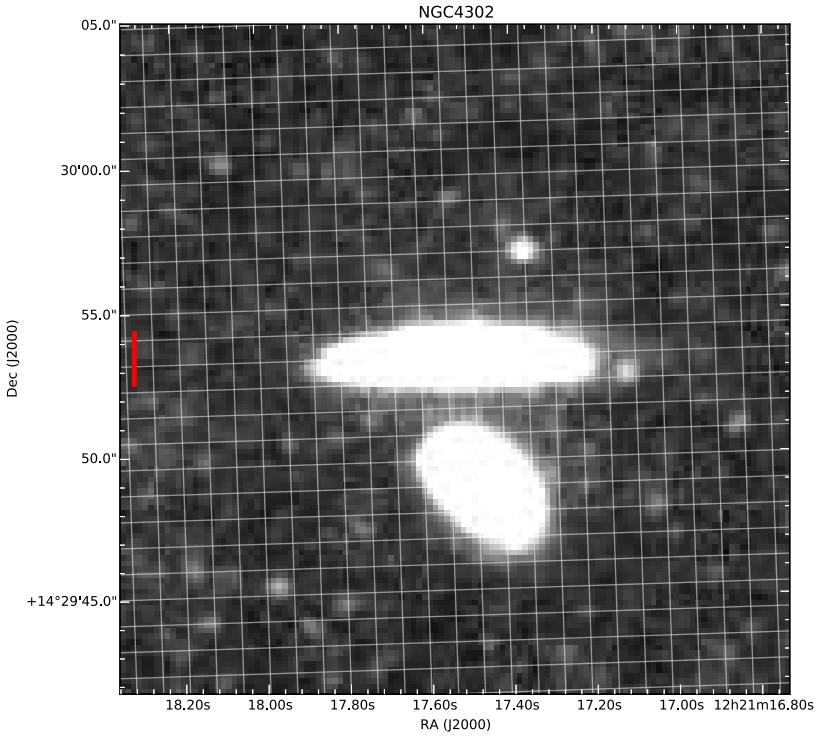

Figure A.158: 250 μm

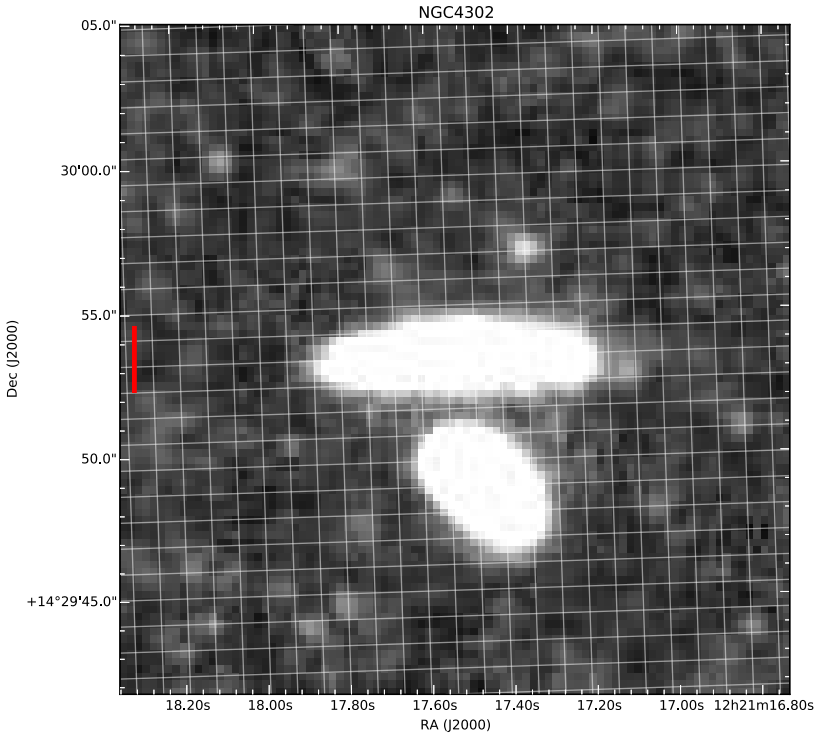

Figure A.159: 350 μm

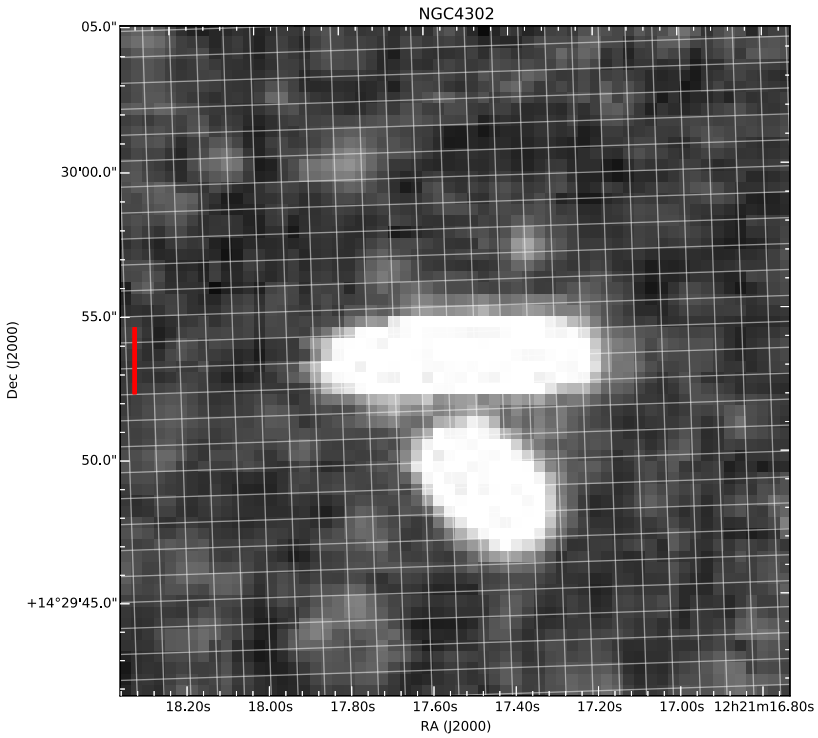

Figure A.160: 500 μm

A.17 NGC4402

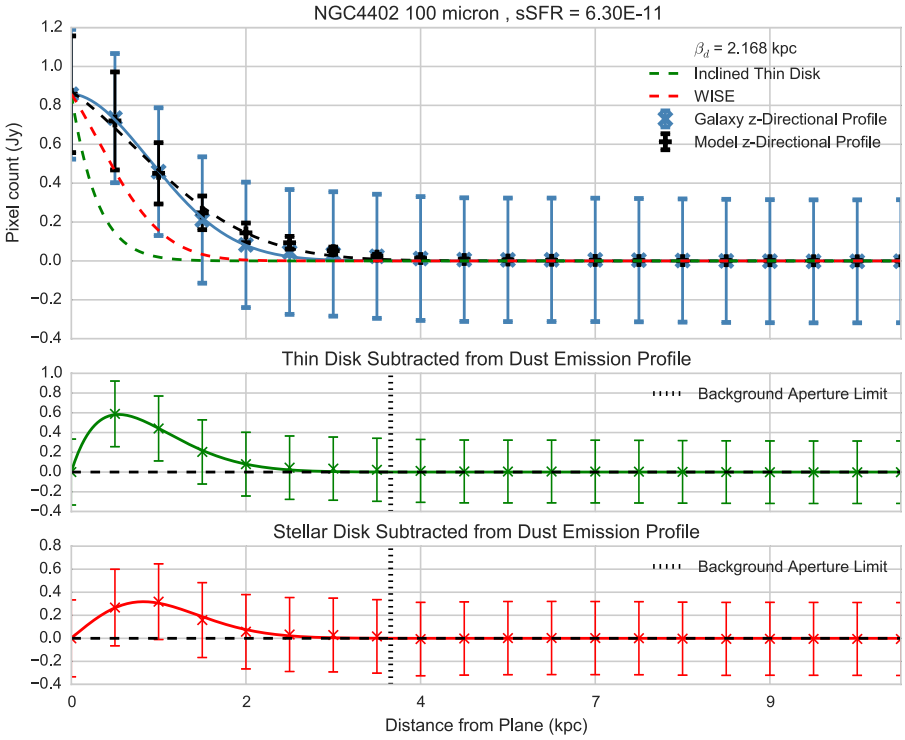
NGC4402 100 micron , sSFR = 6.30E-11
β_d = 2.168 kpc
Inclined Thin Disk
WISE
Galaxy z-Directional Profile
Model z-Directional Profile
Pixel count (Jy)
Thin Disk Subtracted from Dust Emission Profile
Background Aperture Limit
Stellar Disk Subtracted from Dust Emission Profile
Background Aperture Limit
Distance from Plane (kpc)

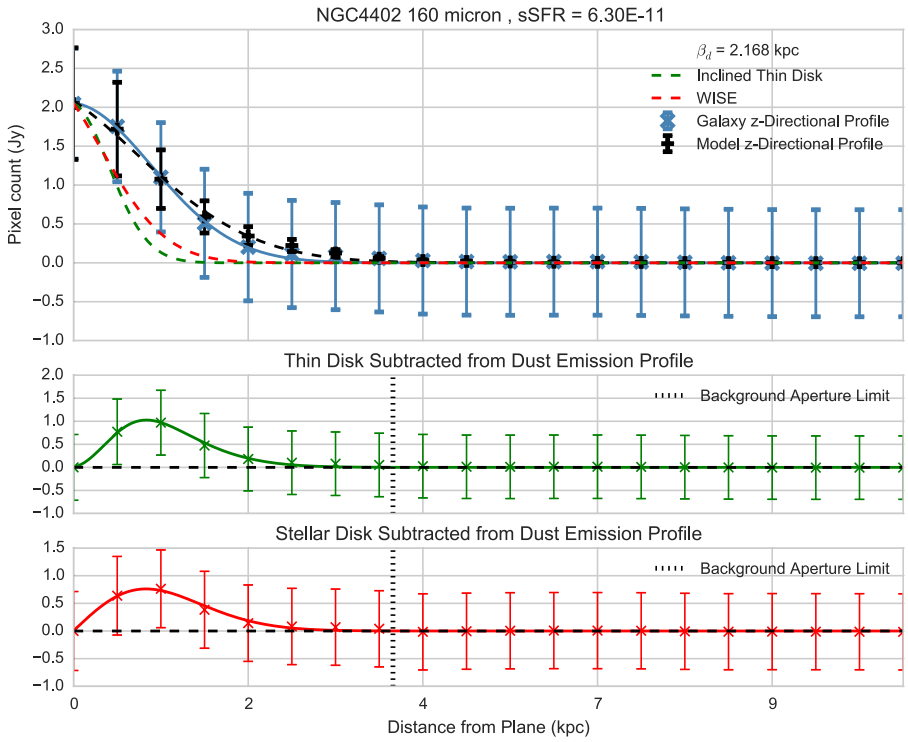
NGC4402 160 micron , sSFR = 6.30E-11
β_d = 2.168 kpc
Inclined Thin Disk
WISE
Galaxy z-Directional Profile
Model z-Directional Profile
Pixel count (Jy)
Thin Disk Subtracted from Dust Emission Profile
Background Aperture Limit
Stellar Disk Subtracted from Dust Emission Profile
Background Aperture Limit
Distance from Plane (kpc)

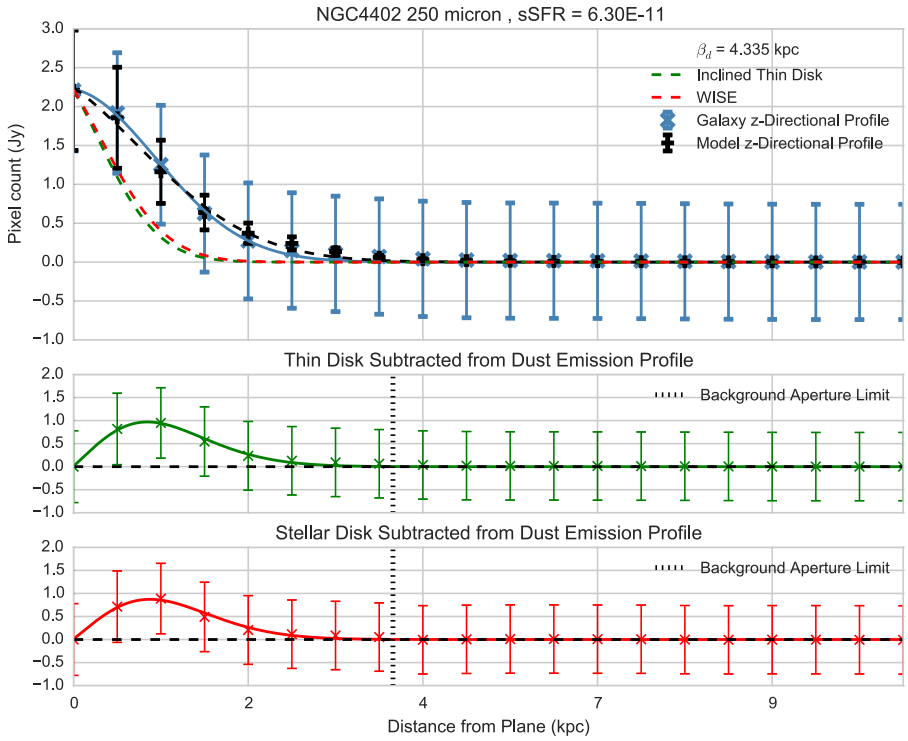
NGC4402 250 micron , sSFR = 6.30E-11
β_d = 4.335 kpc
Inclined Thin Disk
WISE
Galaxy z-Directional Profile
Model z-Directional Profile
Pixel count (Jy)
Thin Disk Subtracted from Dust Emission Profile
Background Aperture Limit
Stellar Disk Subtracted from Dust Emission Profile
Background Aperture Limit
Distance from Plane (kpc)

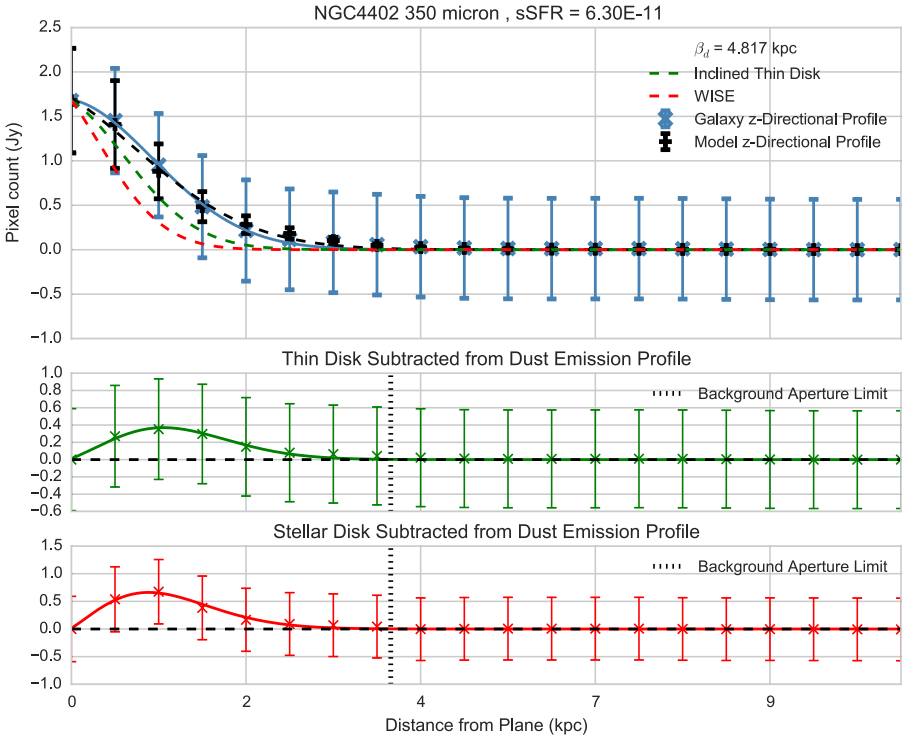
NGC4402 350 micron , sSFR = 6.30E-11
β_d = 4.817 kpc
Inclined Thin Disk
WISE
Galaxy z-Directional Profile
Model z-Directional Profile
Pixel count (Jy)
Thin Disk Subtracted from Dust Emission Profile
Background Aperture Limit
Stellar Disk Subtracted from Dust Emission Profile
Background Aperture Limit
Distance from Plane (kpc)

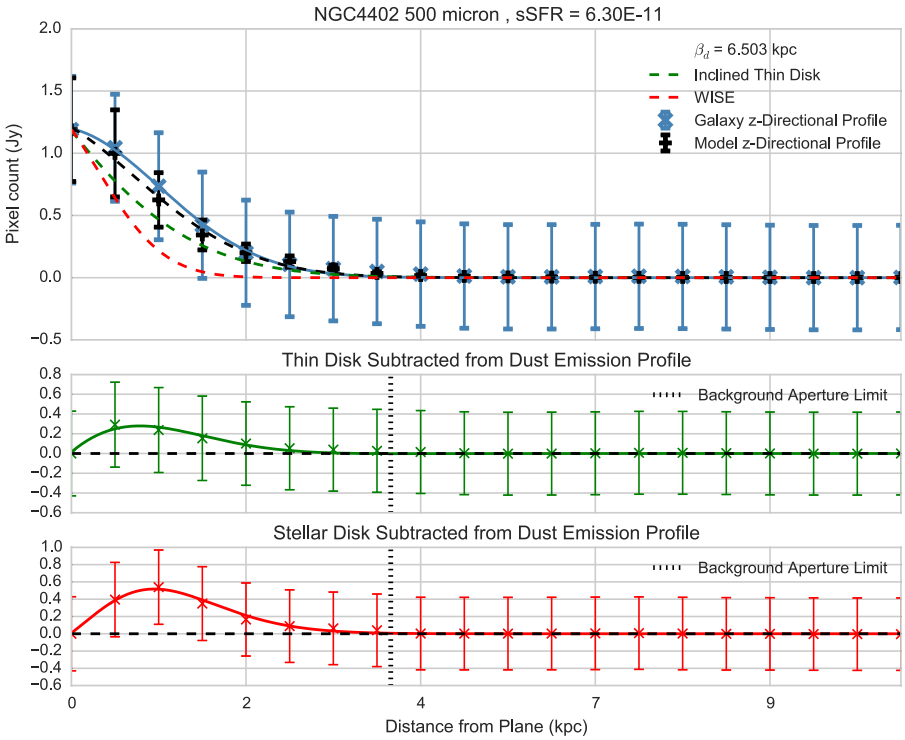
NGC4402 500 micron , sSFR = 6.30E-11
β_d = 6.503 kpc
Inclined Thin Disk
WISE
Galaxy z-Directional Profile
Model z-Directional Profile
Pixel count (Jy)
Thin Disk Subtracted from Dust Emission Profile
Background Aperture Limit
Stellar Disk Subtracted from Dust Emission Profile
Background Aperture Limit
Distance from Plane (kpc)

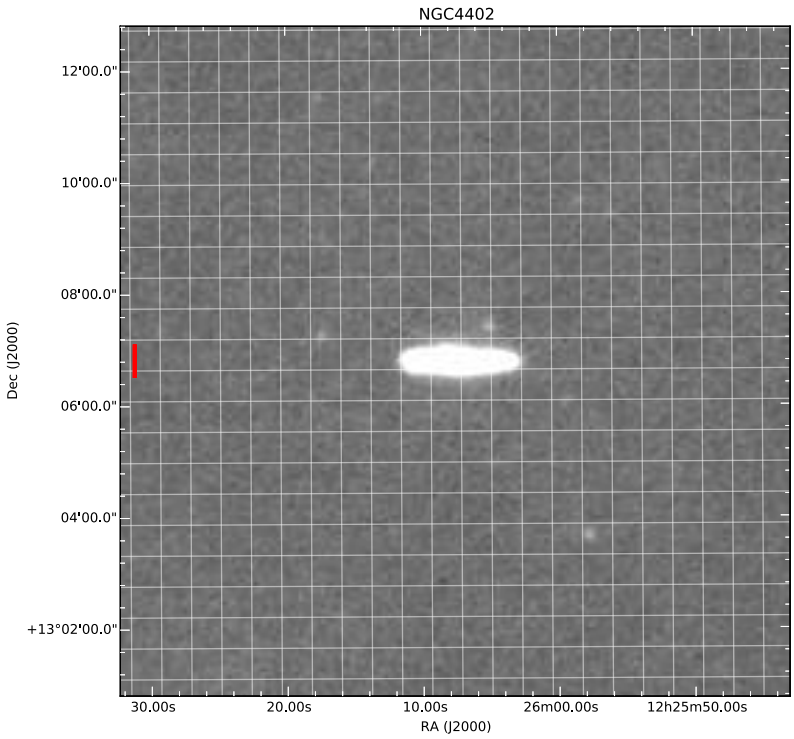

Figure A.161: 100 μm

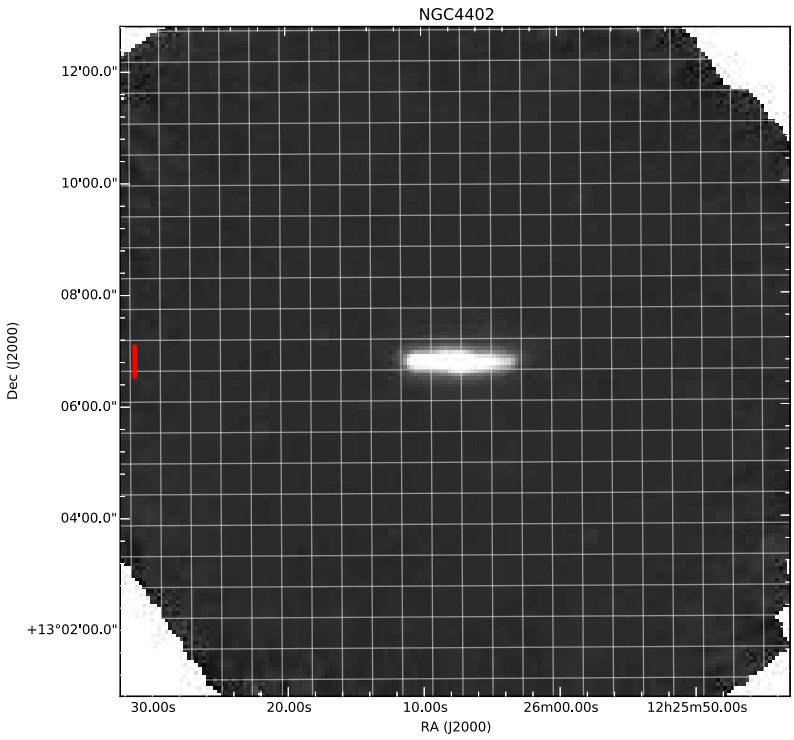

Figure A.162: 160 μm

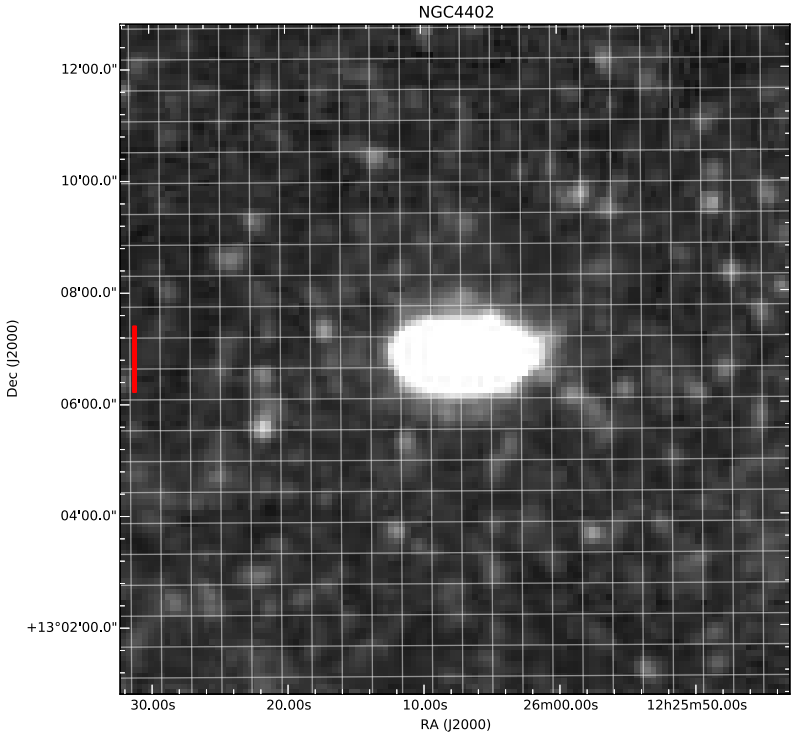

Figure A.163: 250 μm

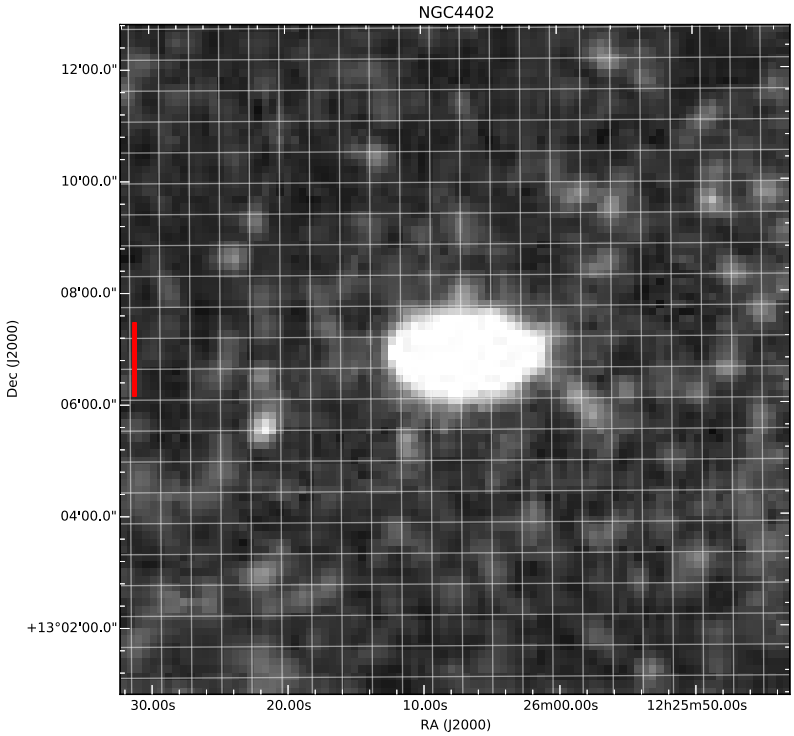

Figure A.164: 350 μm

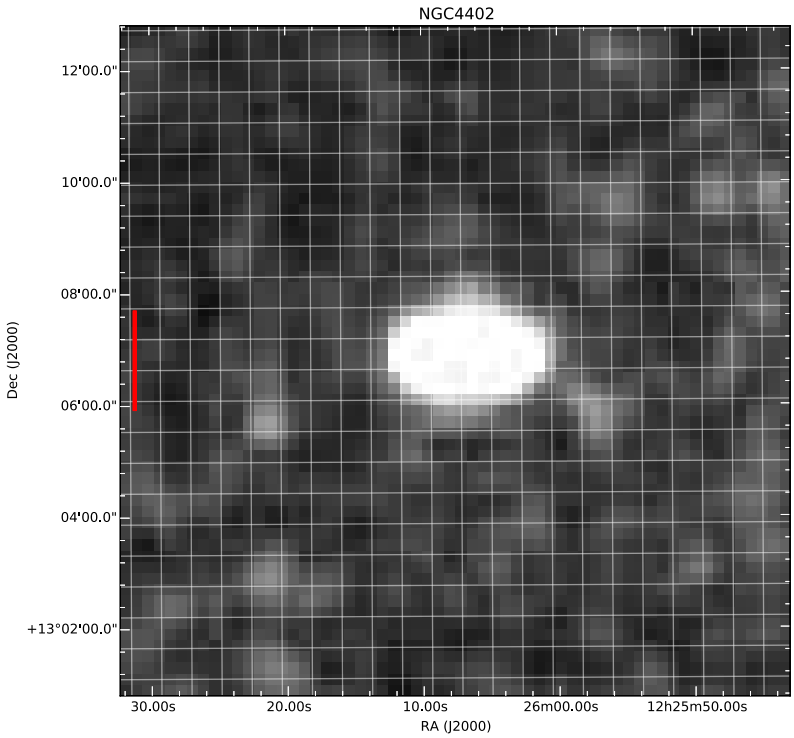

Figure A.165: 500 μm

A.18 NGC4437

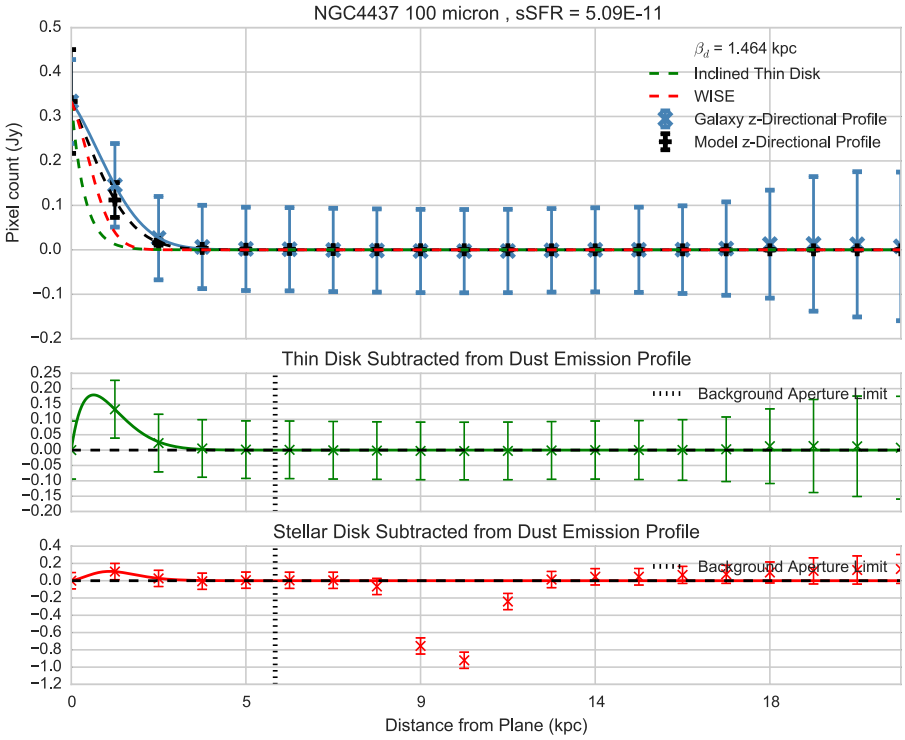
NGC4437 100 micron , sSFR = 5.09E-11
β_d = 1.464 kpc
Inclined Thin Disk
WISE
Galaxy z-Directional Profile
Model z-Directional Profile
Pixel count (Jy)
Thin Disk Subtracted from Dust Emission Profile
Background Aperture Limit
Stellar Disk Subtracted from Dust Emission Profile
Background Aperture Limit
Distance from Plane (kpc)

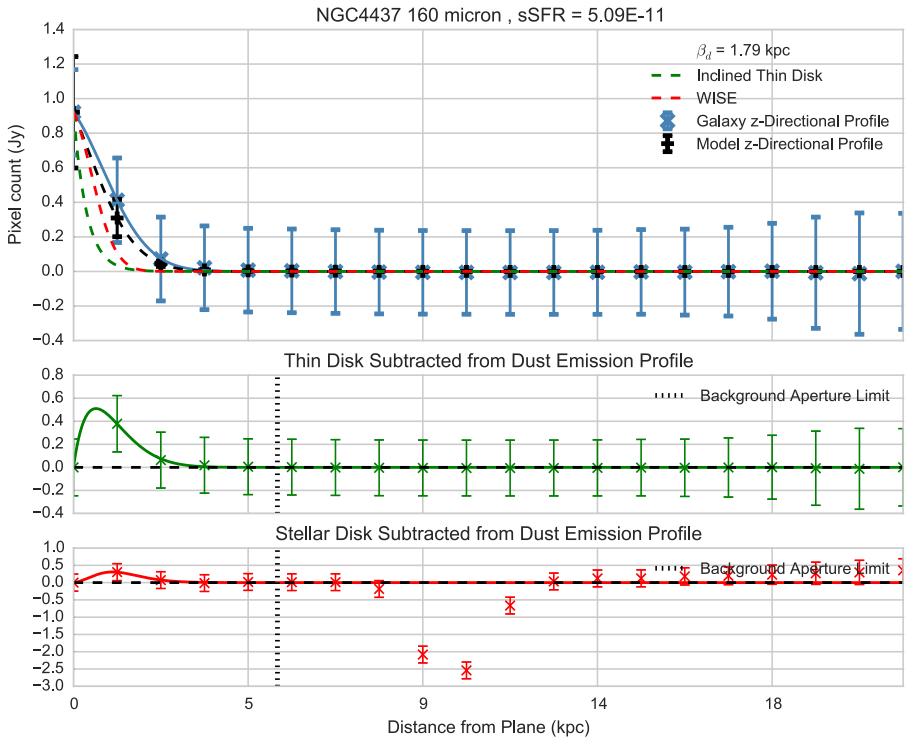
NGC4437 160 micron , sSFR = 5.09E-11
β_d = 1.79 kpc
Inclined Thin Disk
WISE
Galaxy z-Directional Profile
Model z-Directional Profile
Pixel count (Jy)
Thin Disk Subtracted from Dust Emission Profile
Background Aperture Limit
Stellar Disk Subtracted from Dust Emission Profile
Background Aperture Limit
Distance from Plane (kpc)

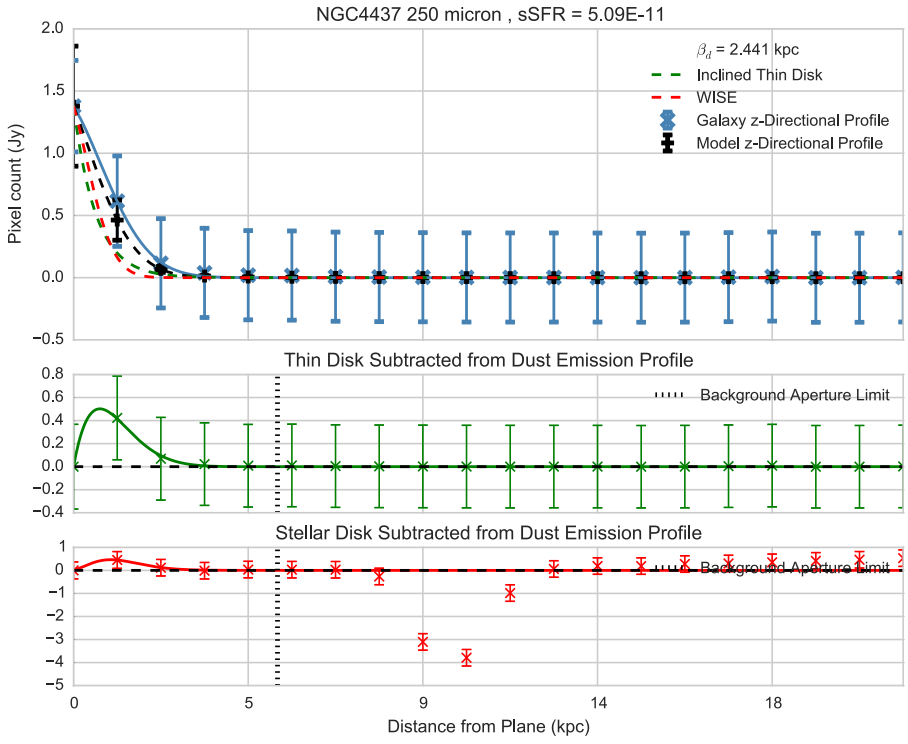
NGC4437 250 micron , sSFR = 5.09E-11
β_d = 2.441 kpc
Inclined Thin Disk
WISE
Galaxy z-Directional Profile
Model z-Directional Profile
Pixel count (Jy)
Thin Disk Subtracted from Dust Emission Profile
Background Aperture Limit
Stellar Disk Subtracted from Dust Emission Profile
Background Aperture Limit
Distance from Plane (kpc)

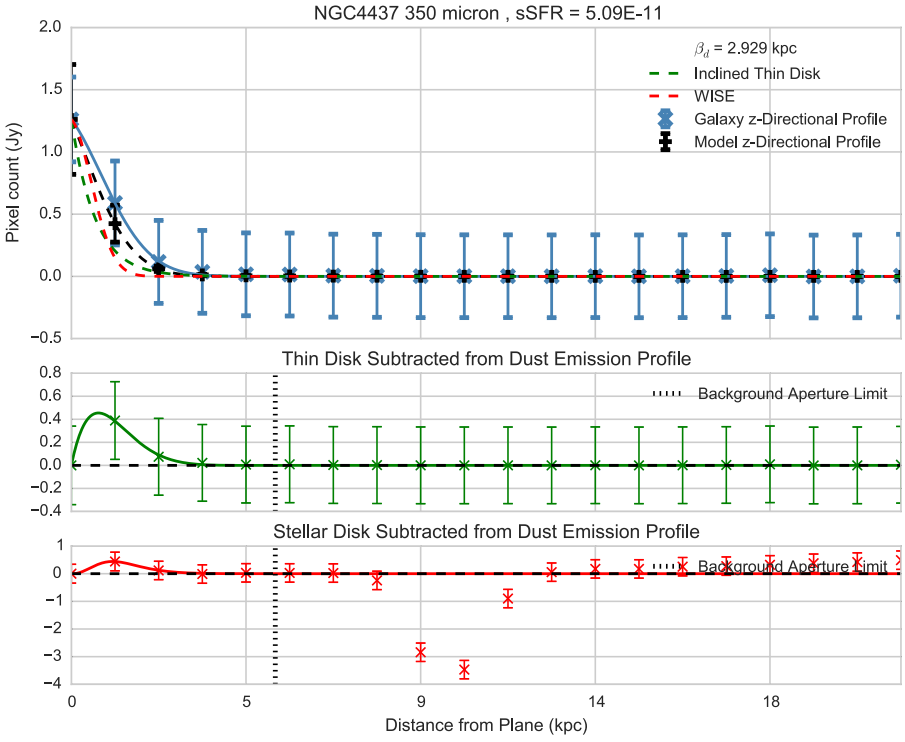
NGC4437 350 micron , sSFR = 5.09E-11
β_d = 2.929 kpc
Inclined Thin Disk
WISE
Galaxy z-Directional Profile
Model z-Directional Profile
Pixel count (Jy)
Thin Disk Subtracted from Dust Emission Profile
Background Aperture Limit
Stellar Disk Subtracted from Dust Emission Profile
Background Aperture Limit
Distance from Plane (kpc)

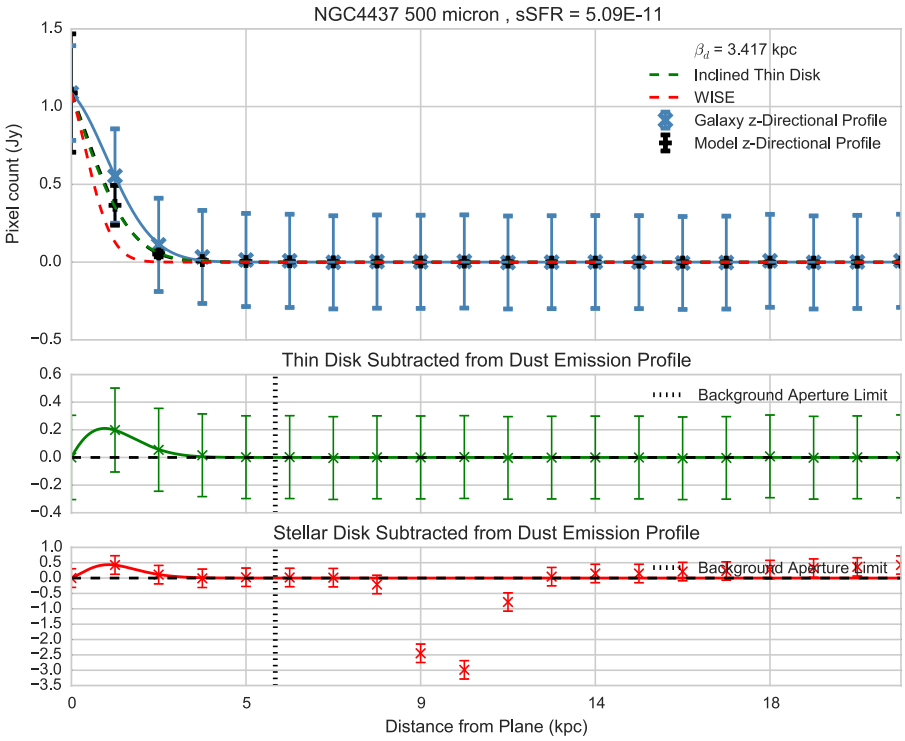
NGC4437 500 micron , sSFR = 5.09E-11
β_d = 3.417 kpc
Inclined Thin Disk
WISE
Galaxy z-Directional Profile
Model z-Directional Profile
Pixel count (Jy)
Thin Disk Subtracted from Dust Emission Profile
Background Aperture Limit
Stellar Disk Subtracted from Dust Emission Profile
Background Aperture Limit
Distance from Plane (kpc)

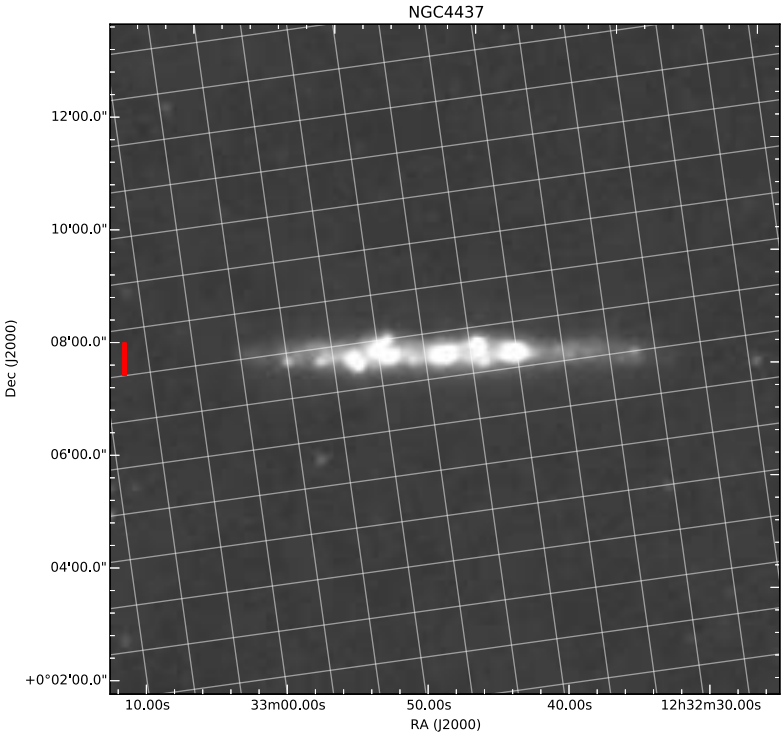

Figure A.166: 100 μm

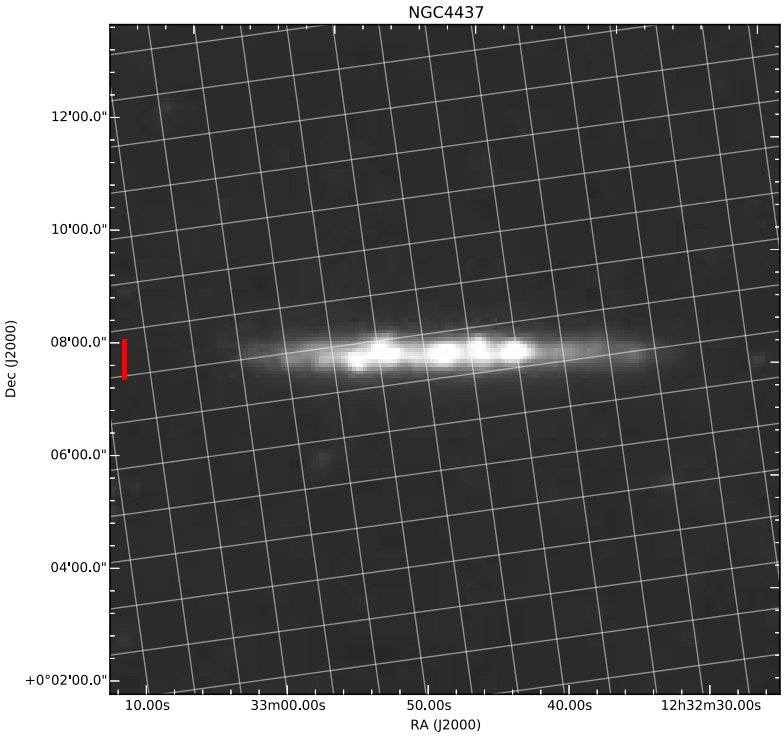

Figure A.167: 160 μm

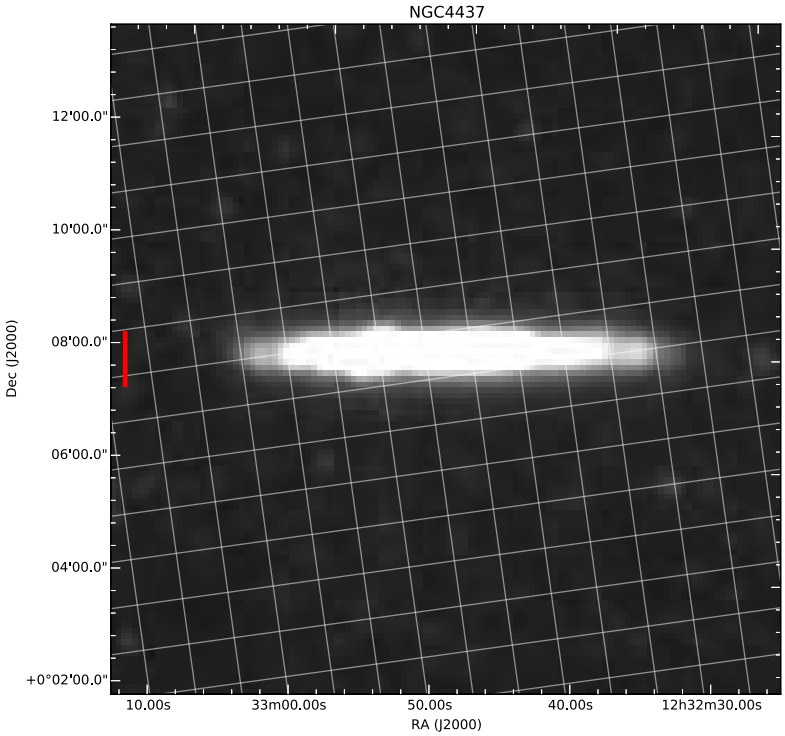

Figure A.168: 250 μm

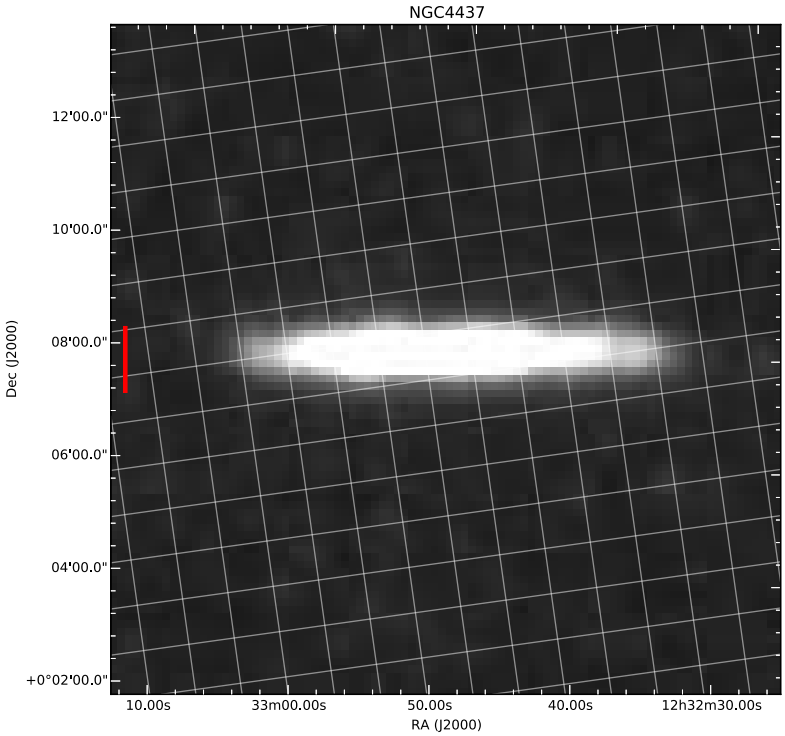

Figure A.169: 350 μm

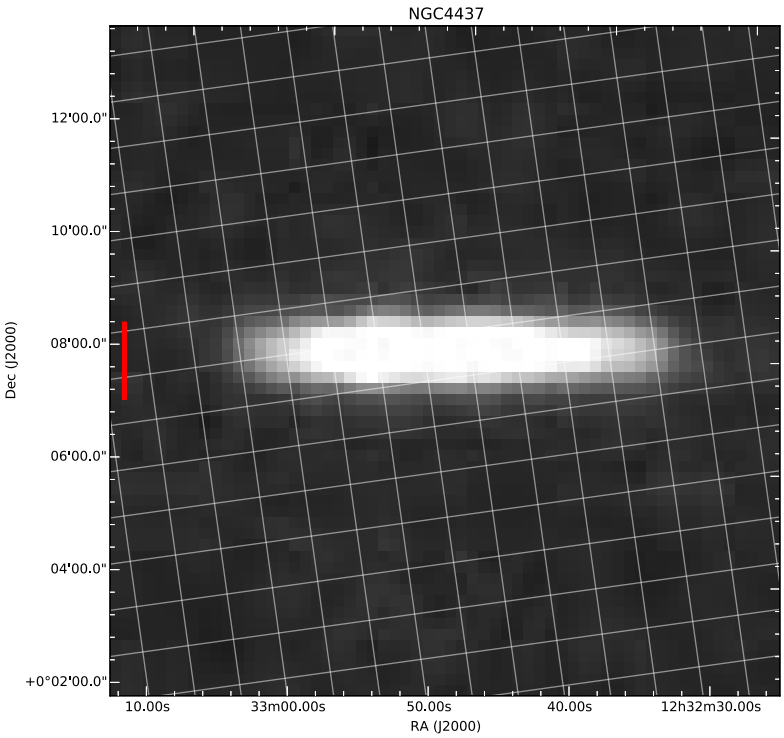

Figure A.170: 500 μm

A.19 NGC4445

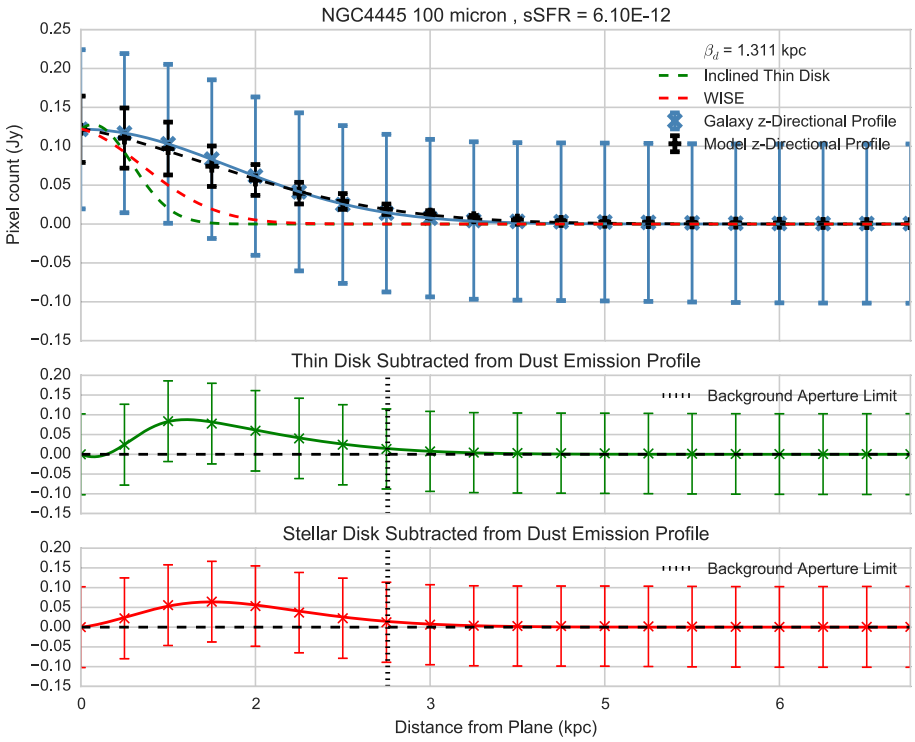
NGC4445 100 micron , sSFR = 6.10E-12
β_d = 1.311 kpc
Inclined Thin Disk
WISE
Galaxy z-Directional Profile
Model z-Directional Profile
Pixel count (Jy)
Thin Disk Subtracted from Dust Emission Profile
Background Aperture Limit
Stellar Disk Subtracted from Dust Emission Profile
Background Aperture Limit
Distance from Plane (kpc)

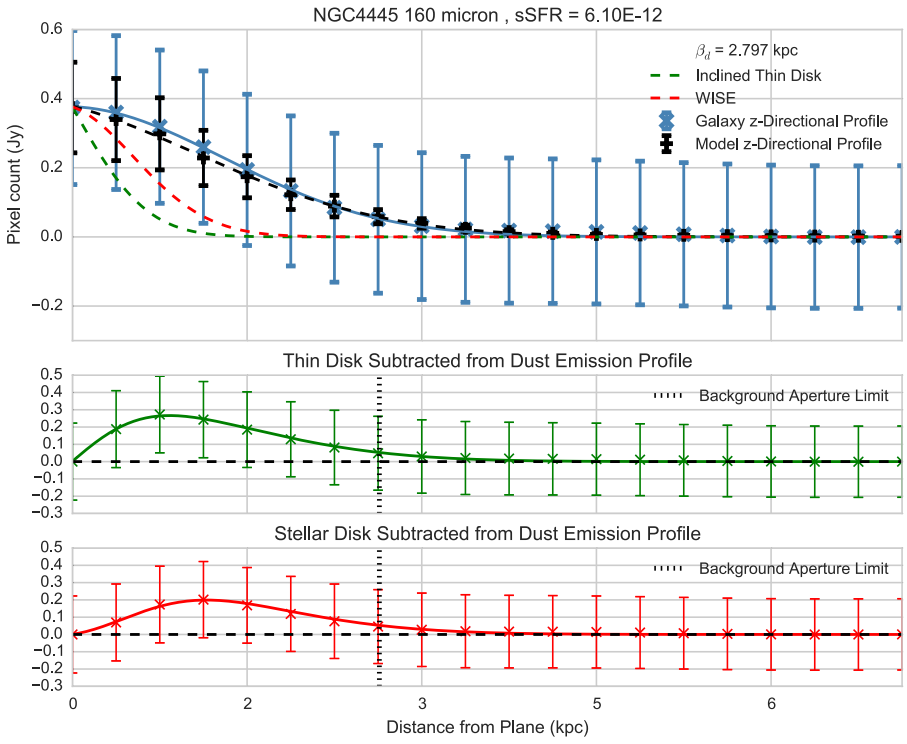
NGC4445 160 micron , sSFR = 6.10E-12
β_d = 2.797 kpc
Inclined Thin Disk
WISE
Galaxy z-Directional Profile
Model z-Directional Profile
Pixel count (Jy)
Thin Disk Subtracted from Dust Emission Profile
Background Aperture Limit
Stellar Disk Subtracted from Dust Emission Profile
Background Aperture Limit
Distance from Plane (kpc)

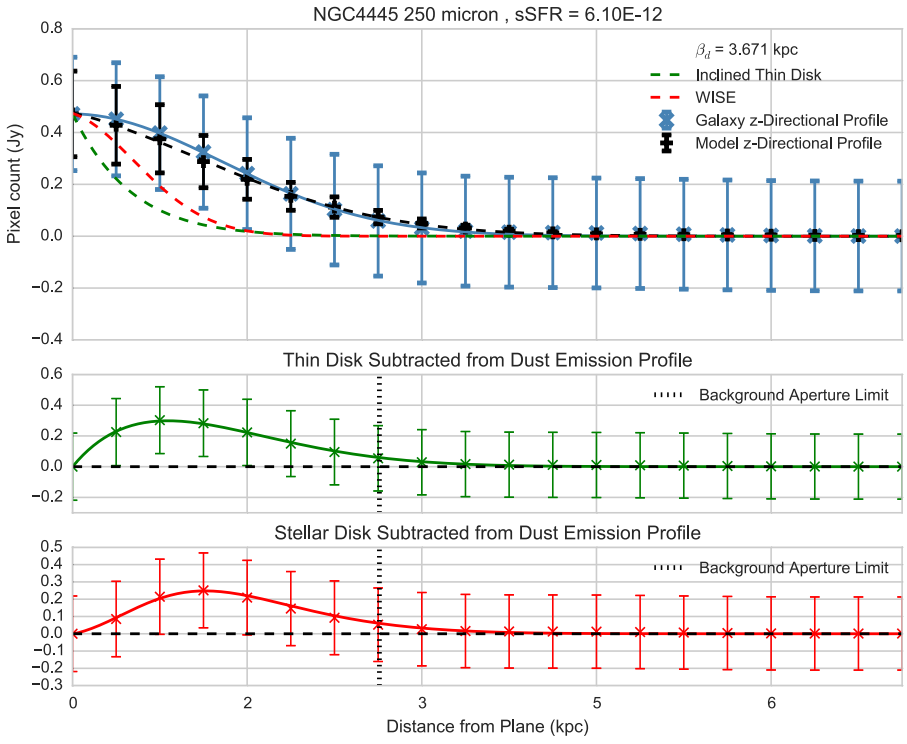
NGC4445 250 micron , sSFR = 6.10E-12
β_d = 3.671 kpc
Inclined Thin Disk
WISE
Galaxy z-Directional Profile
Model z-Directional Profile
Pixel count (Jy)
Thin Disk Subtracted from Dust Emission Profile
Background Aperture Limit
Stellar Disk Subtracted from Dust Emission Profile
Background Aperture Limit
Distance from Plane (kpc)

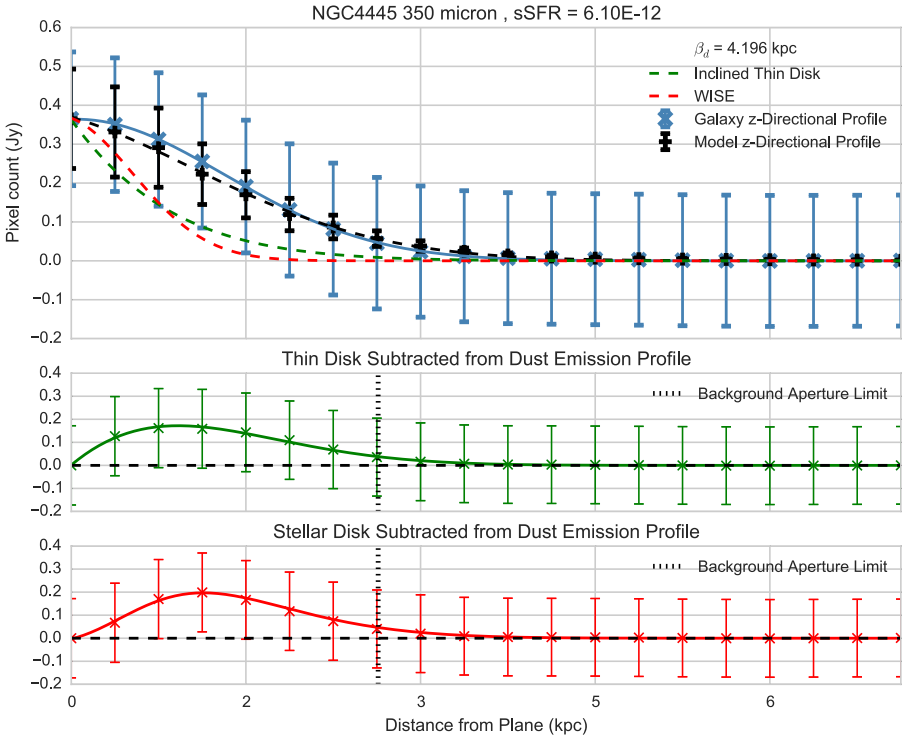
NGC4445 350 micron , sSFR = 6.10E-12
β_d = 4.196 kpc
Inclined Thin Disk
WISE
Galaxy z-Directional Profile
Model z-Directional Profile
Pixel count (Jy)
Thin Disk Subtracted from Dust Emission Profile
Background Aperture Limit
Stellar Disk Subtracted from Dust Emission Profile
Background Aperture Limit
Distance from Plane (kpc)

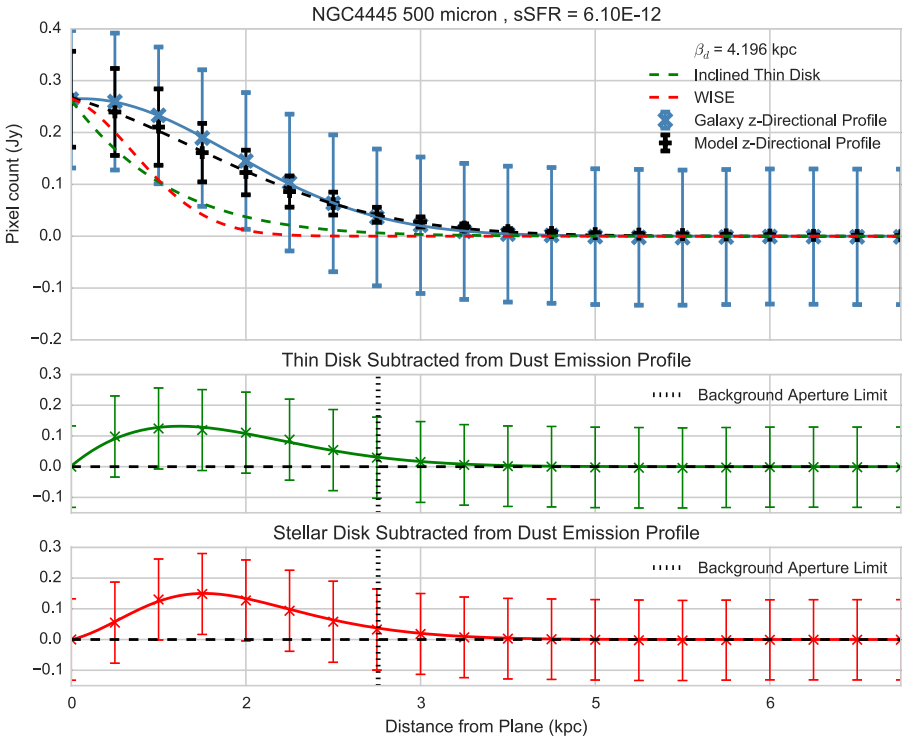
NGC4445 500 micron , sSFR = 6.10E-12
β_d = 4.196 kpc
Inclined Thin Disk
WISE
Galaxy z-Directional Profile
Model z-Directional Profile
Pixel count (Jy)
Thin Disk Subtracted from Dust Emission Profile
Background Aperture Limit
Stellar Disk Subtracted from Dust Emission Profile
Background Aperture Limit
Distance from Plane (kpc)

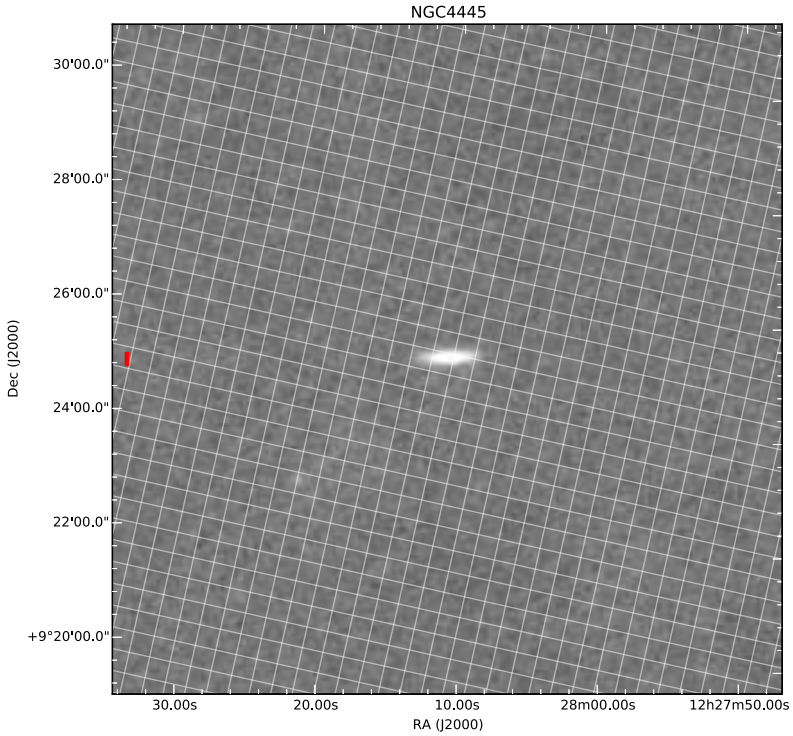

Figure A.171: 100 μm

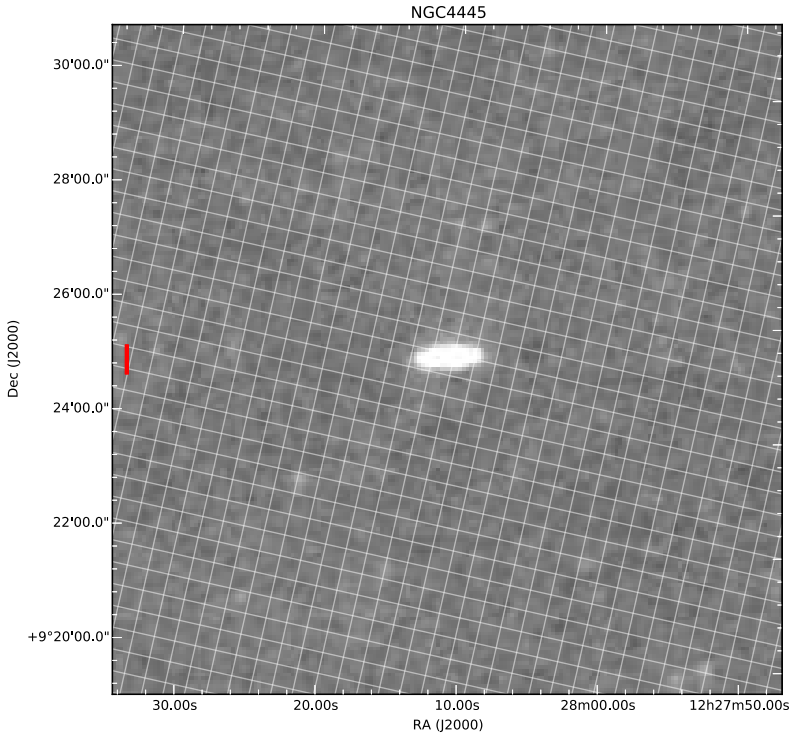

Figure A.172: 160 μm

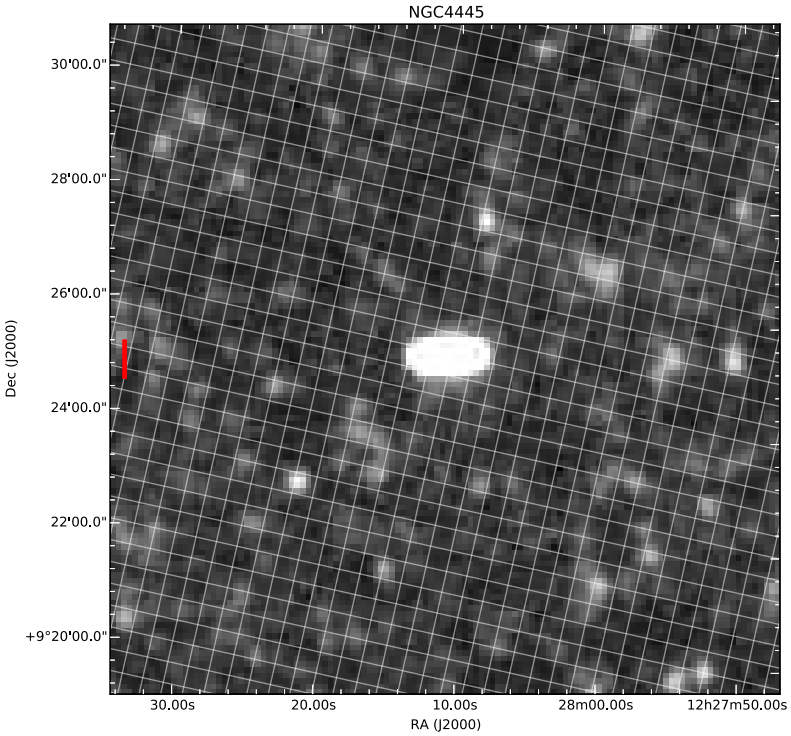

Figure A.173: 250 μm

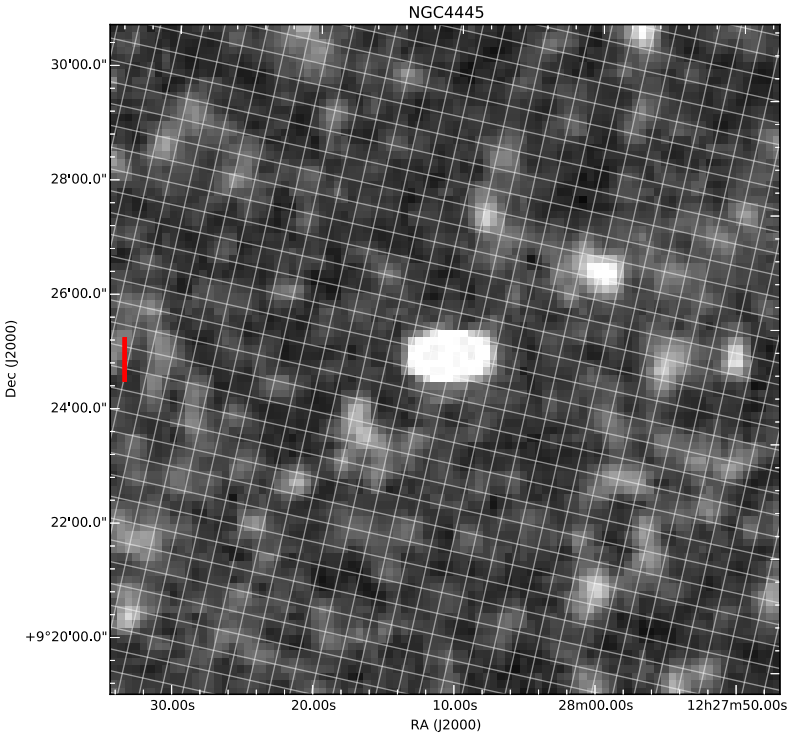

Figure A.174: 350 μm

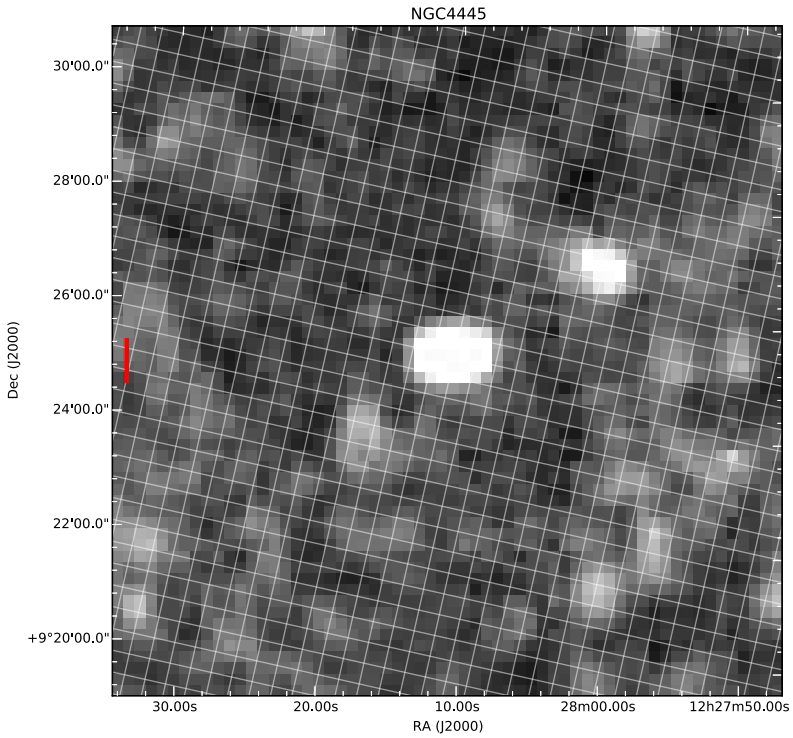

Figure A.175: 500 μm

A.20 NGC4758

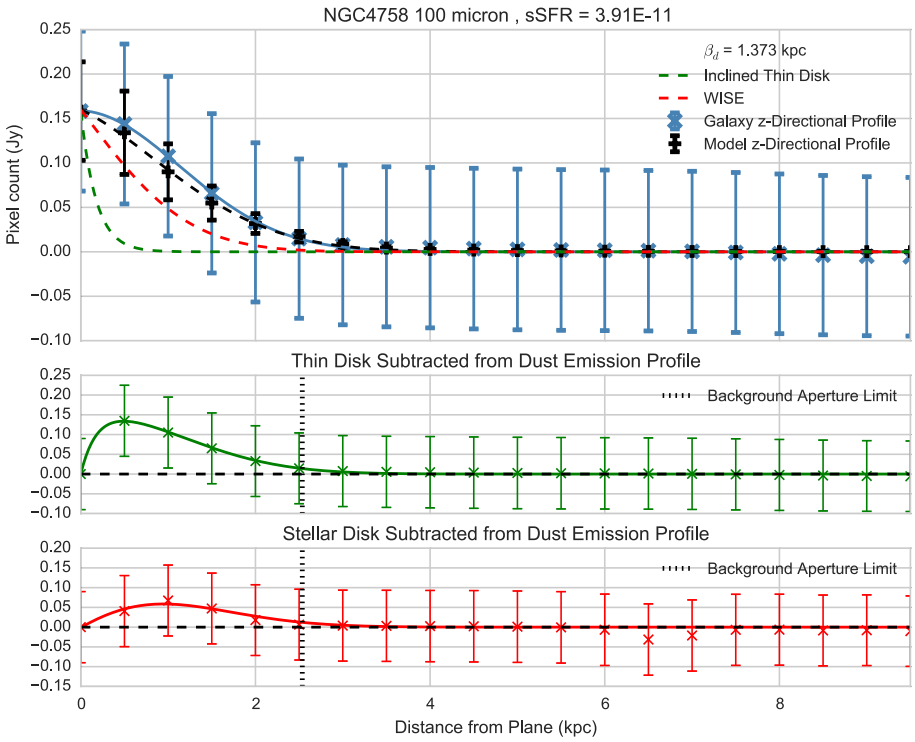
NGC4758 100 micron , sSFR = 3.91E-11
β_d = 1.373 kpc
Inclined Thin Disk
WISE
Galaxy z-Directional Profile
Model z-Directional Profile
Pixel count (Jy)
Thin Disk Subtracted from Dust Emission Profile
Background Aperture Limit
Stellar Disk Subtracted from Dust Emission Profile
Background Aperture Limit
Distance from Plane (kpc)

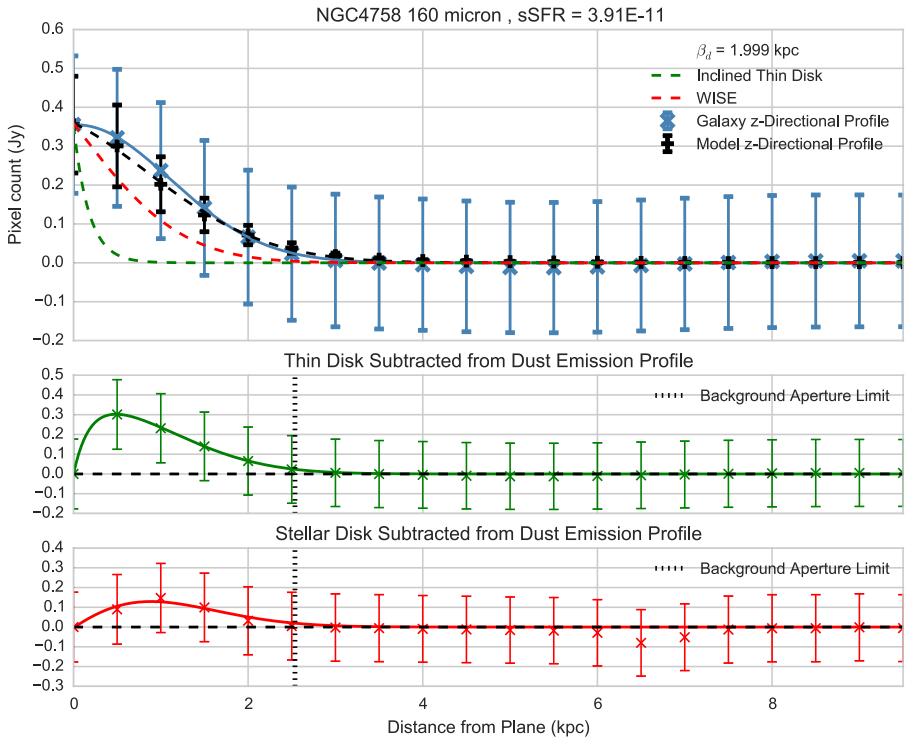
NGC4758 160 micron , sSFR = 3.91E-11
β_d = 1.999 kpc
Inclined Thin Disk
WISE
Galaxy z-Directional Profile
Model z-Directional Profile
Pixel count (Jy)
Thin Disk Subtracted from Dust Emission Profile
Background Aperture Limit
Stellar Disk Subtracted from Dust Emission Profile
Background Aperture Limit
Distance from Plane (kpc)

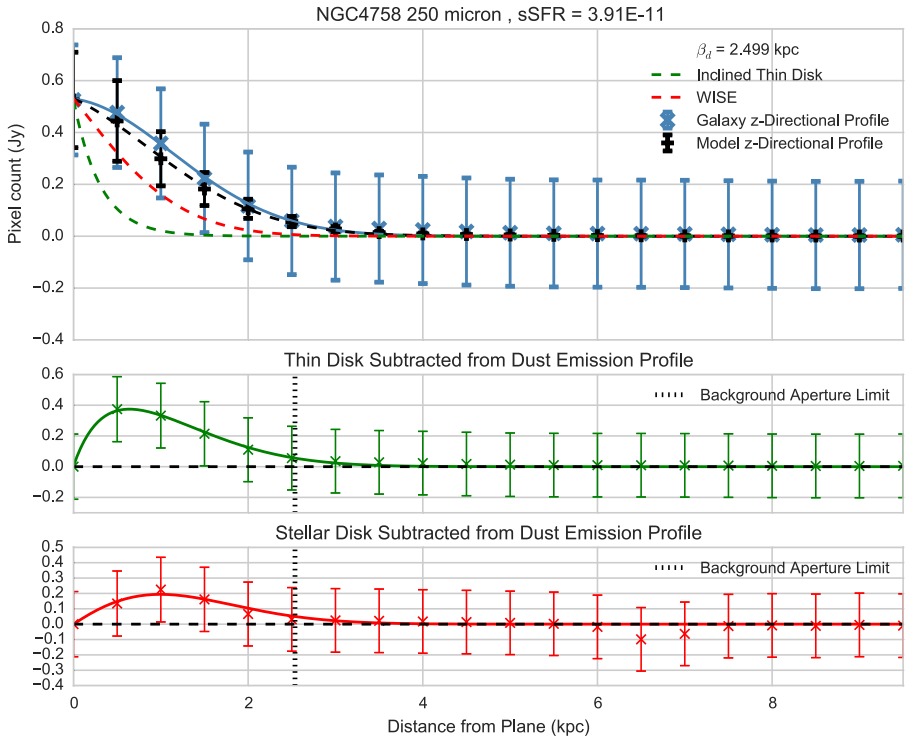
NGC4758 250 micron , sSFR = 3.91E-11
β_d = 2.499 kpc
Inclined Thin Disk
WISE
Galaxy z-Directional Profile
Model z-Directional Profile
Pixel count (Jy)
Thin Disk Subtracted from Dust Emission Profile
Background Aperture Limit
Stellar Disk Subtracted from Dust Emission Profile
Background Aperture Limit
Distance from Plane (kpc)

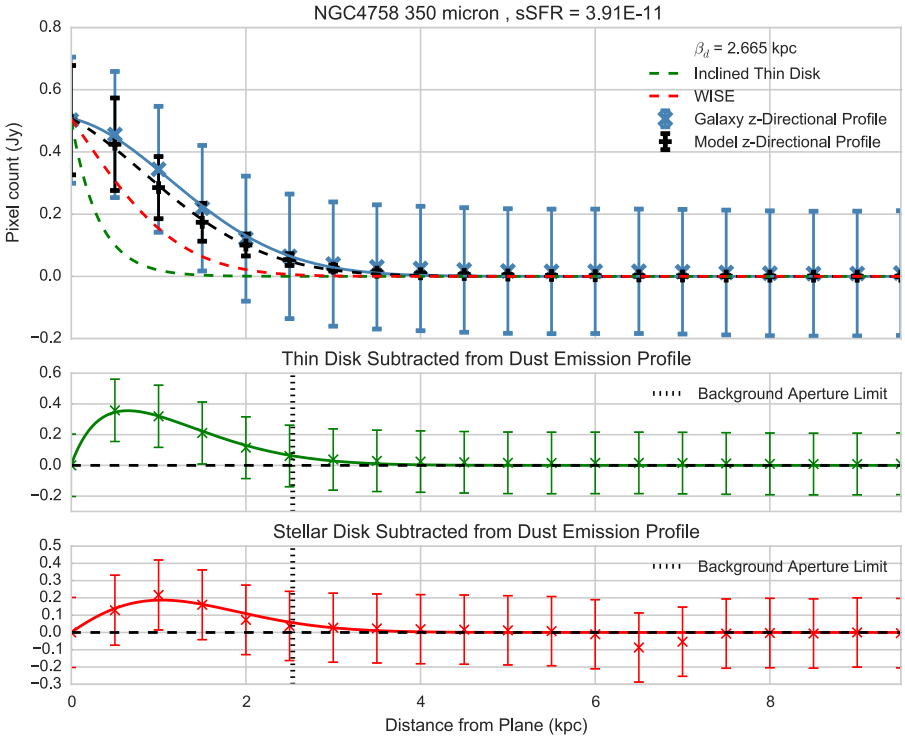
NGC4758 350 micron , sSFR = 3.91E-11
β_d = 2.665 kpc
Inclined Thin Disk
WISE
Galaxy z-Directional Profile
Model z-Directional Profile
Pixel count (Jy)
Thin Disk Subtracted from Dust Emission Profile
Background Aperture Limit
Stellar Disk Subtracted from Dust Emission Profile
Background Aperture Limit
Distance from Plane (kpc)

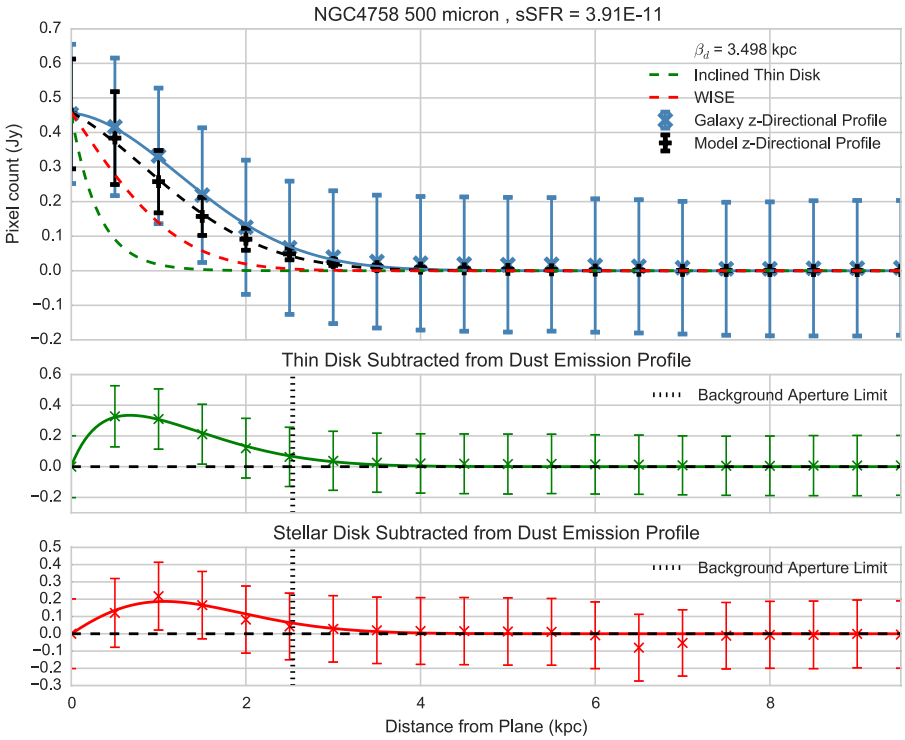
NGC4758 500 micron , sSFR = 3.91E-11
β_d = 3.498 kpc
Inclined Thin Disk
WISE
Galaxy z-Directional Profile
Model z-Directional Profile
Pixel count (Jy)
Thin Disk Subtracted from Dust Emission Profile
Background Aperture Limit
Stellar Disk Subtracted from Dust Emission Profile
Background Aperture Limit
Distance from Plane (kpc)

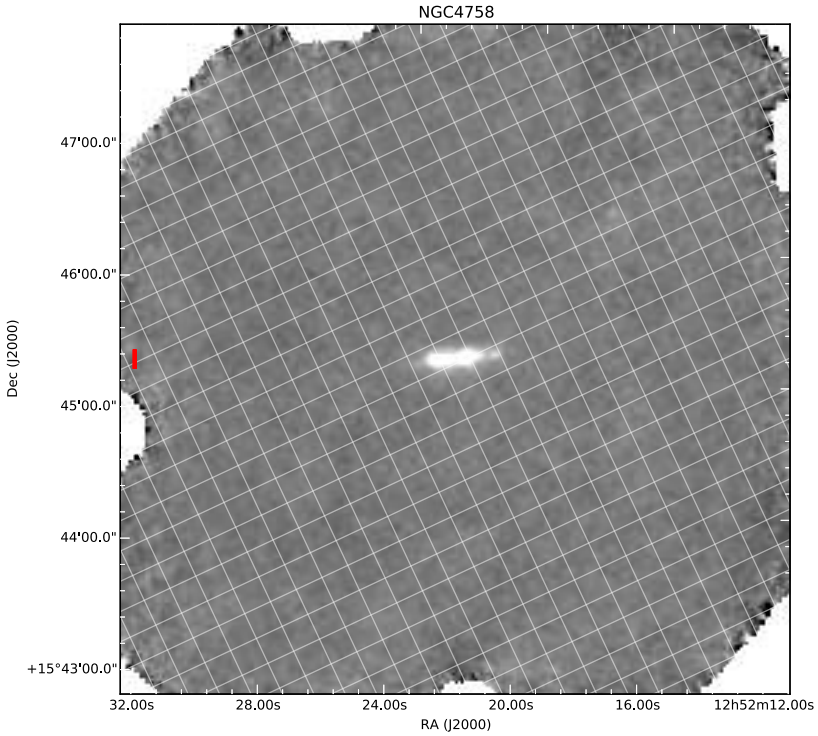

Figure A.176: 100 μm

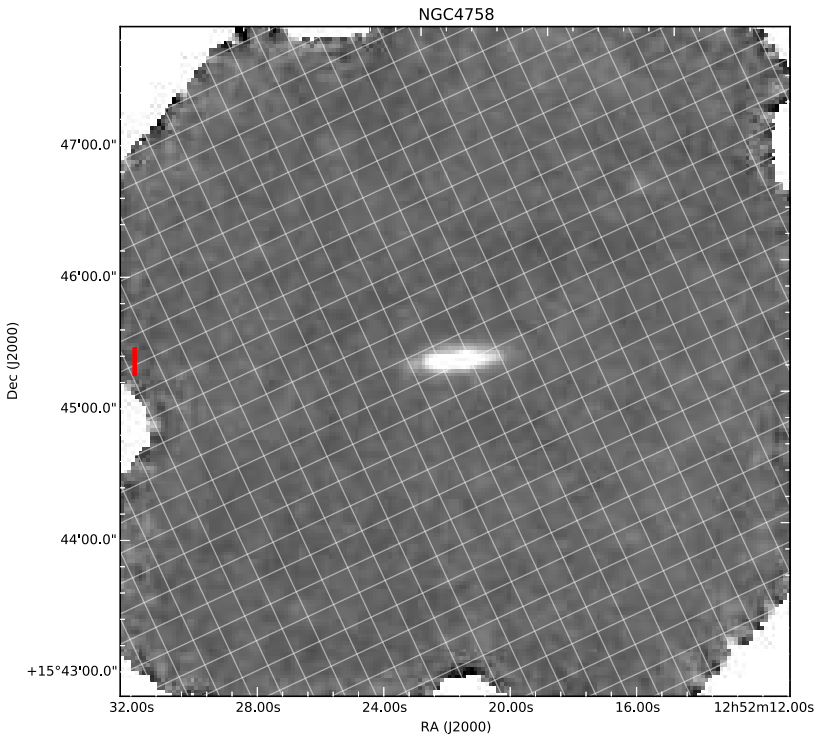

Figure A.177: 160 μm

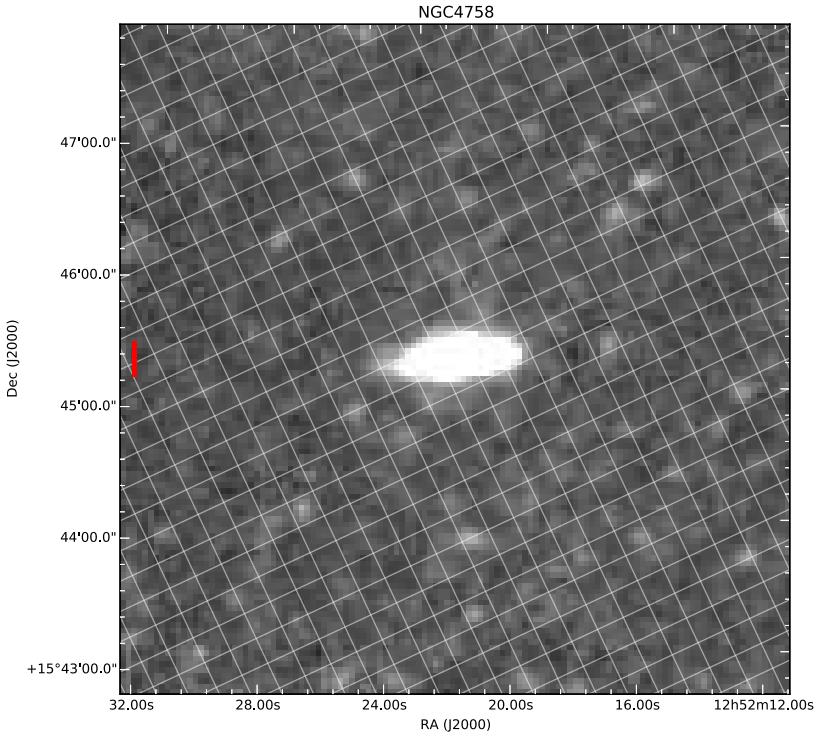

Figure A.178: 250 μm

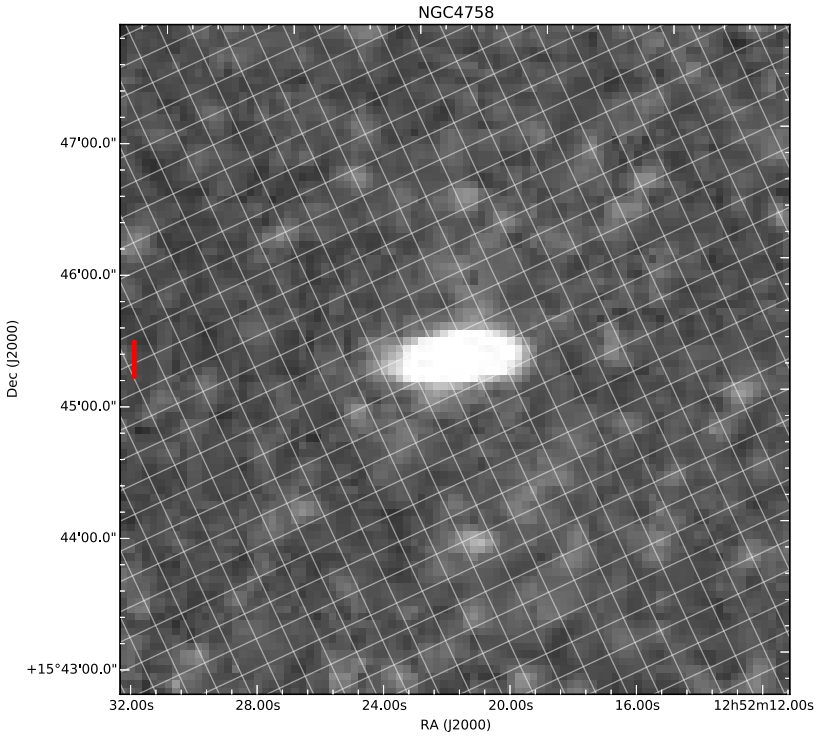

Figure A.179: 350 μm

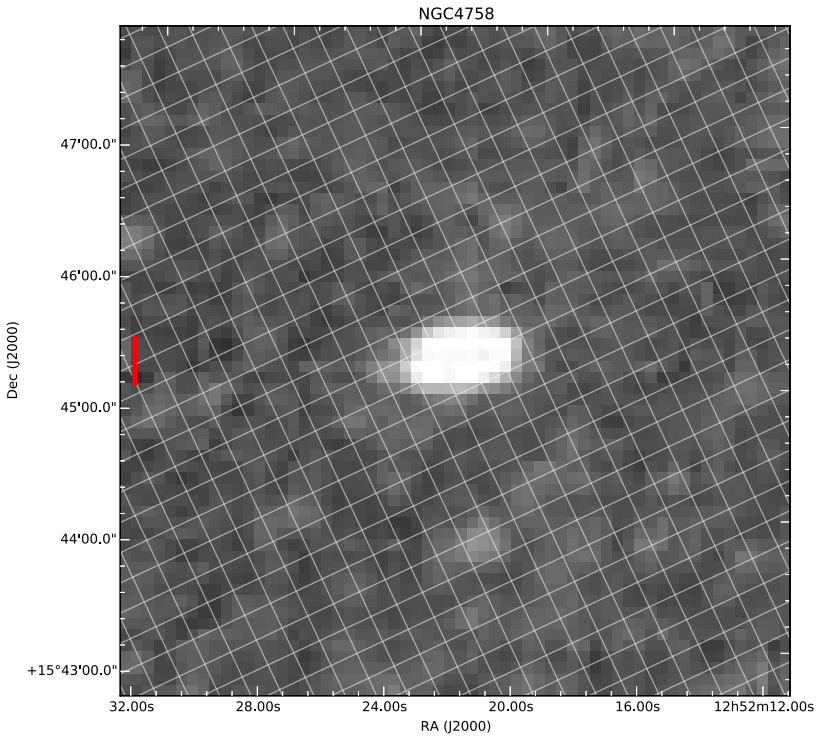

Figure A.180: 500 μm

A.21 NGC5023

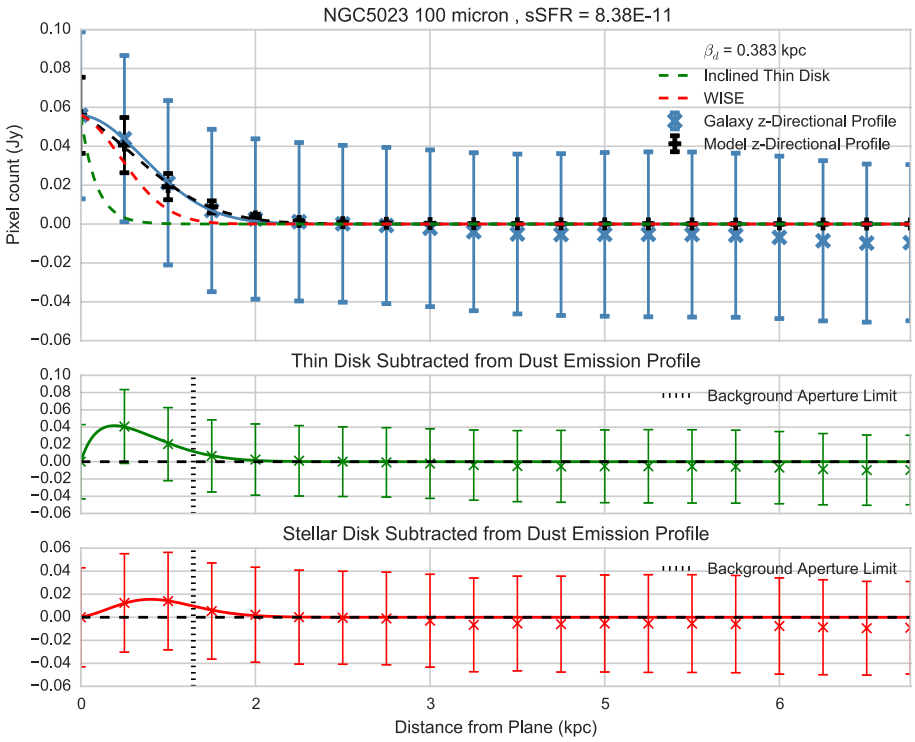
NGC5023 100 micron , sSFR = 8.38E-11
β_d = 0.383 kpc
Inclined Thin Disk
WISE
Galaxy z-Directional Profile
Model z-Directional Profile
Pixel count (Jy)
Thin Disk Subtracted from Dust Emission Profile
Background Aperture Limit
Stellar Disk Subtracted from Dust Emission Profile
Background Aperture Limit
Distance from Plane (kpc)

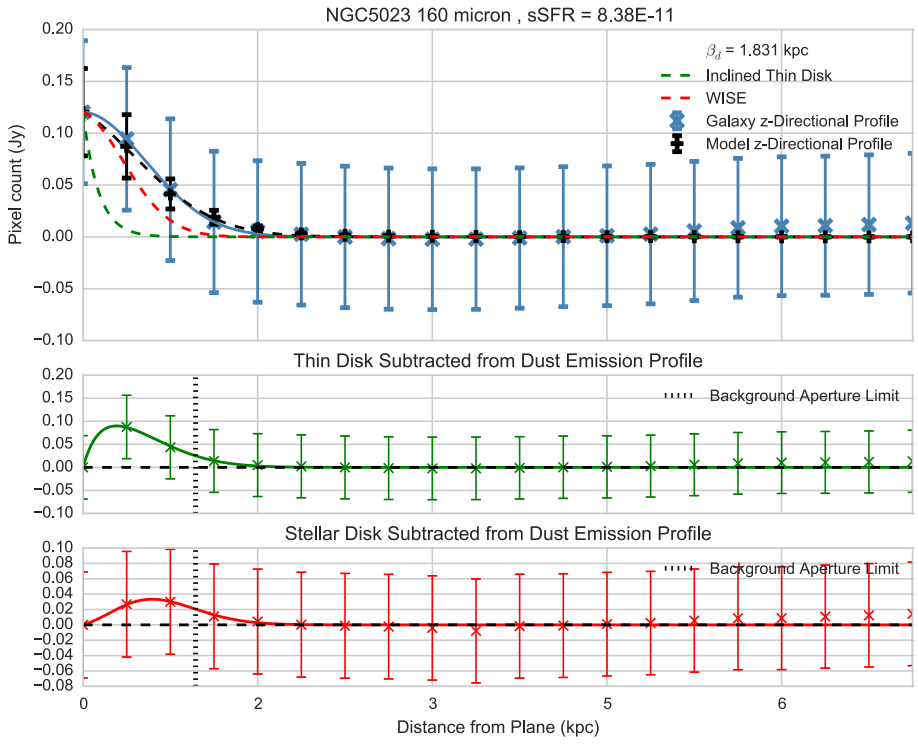
NGC5023 160 micron , sSFR = 8.38E-11
β_d = 1.831 kpc
Inclined Thin Disk
WISE
Galaxy z-Directional Profile
Model z-Directional Profile
Pixel count (Jy)
Thin Disk Subtracted from Dust Emission Profile
Background Aperture Limit
Stellar Disk Subtracted from Dust Emission Profile
Background Aperture Limit
Distance from Plane (kpc)

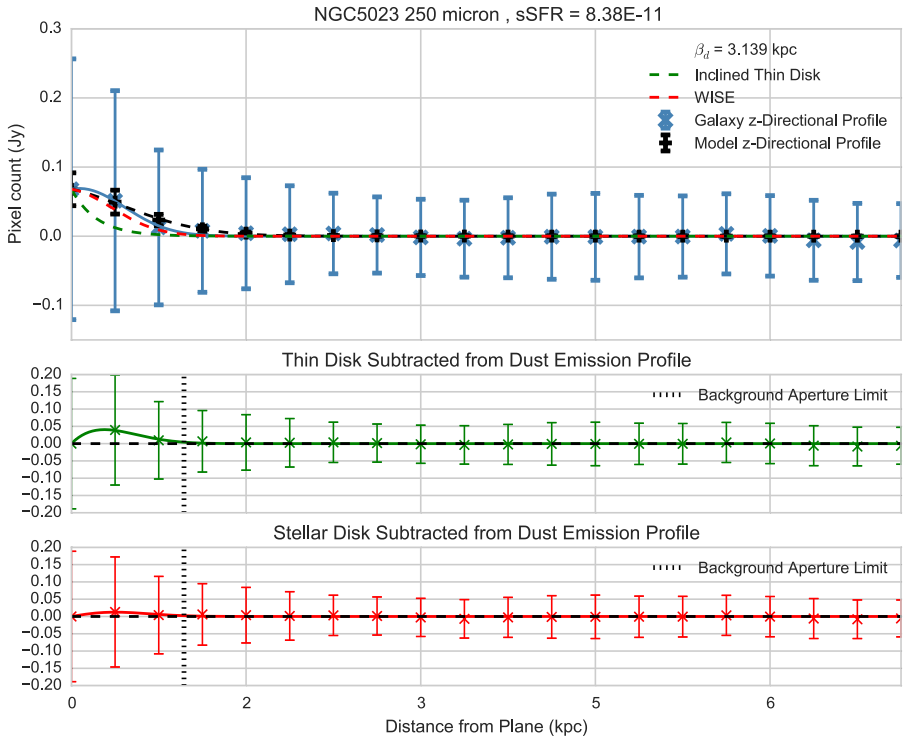
NGC5023 250 micron , sSFR = 8.38E-11
β_d = 3.139 kpc
Inclined Thin Disk
WISE
Galaxy z-Directional Profile
Model z-Directional Profile
Pixel count (Jy)
Thin Disk Subtracted from Dust Emission Profile
Background Aperture Limit
Stellar Disk Subtracted from Dust Emission Profile
Background Aperture Limit
Distance from Plane (kpc)

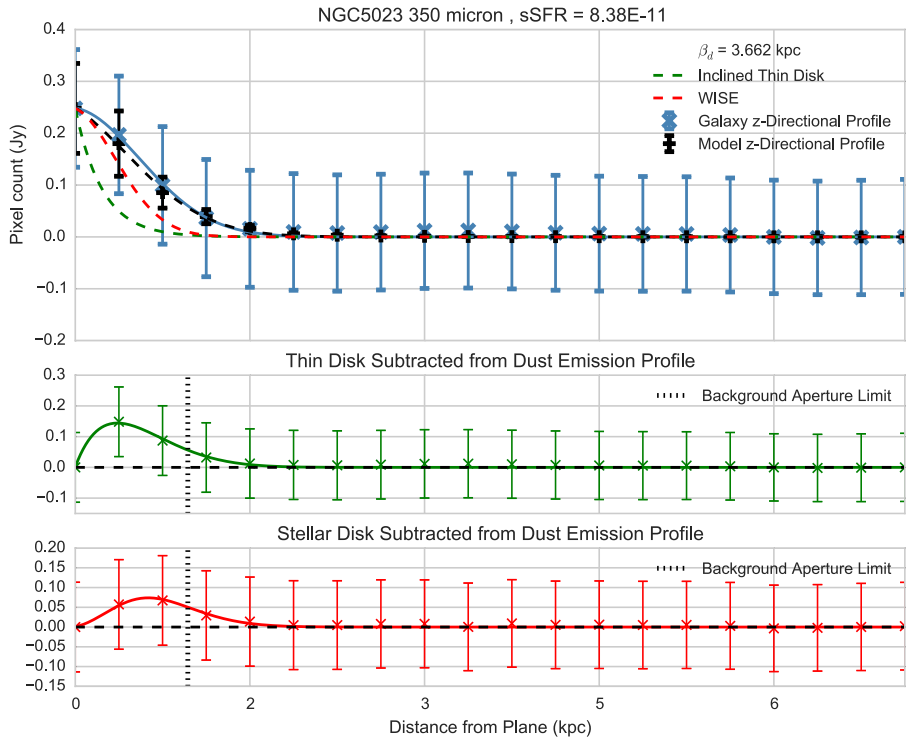
NGC5023 350 micron , sSFR = 8.38E-11
β_d = 3.662 kpc
Inclined Thin Disk
WISE
Galaxy z-Directional Profile
Model z-Directional Profile
Pixel count (Jy)
Thin Disk Subtracted from Dust Emission Profile
Background Aperture Limit
Stellar Disk Subtracted from Dust Emission Profile
Background Aperture Limit
Distance from Plane (kpc)

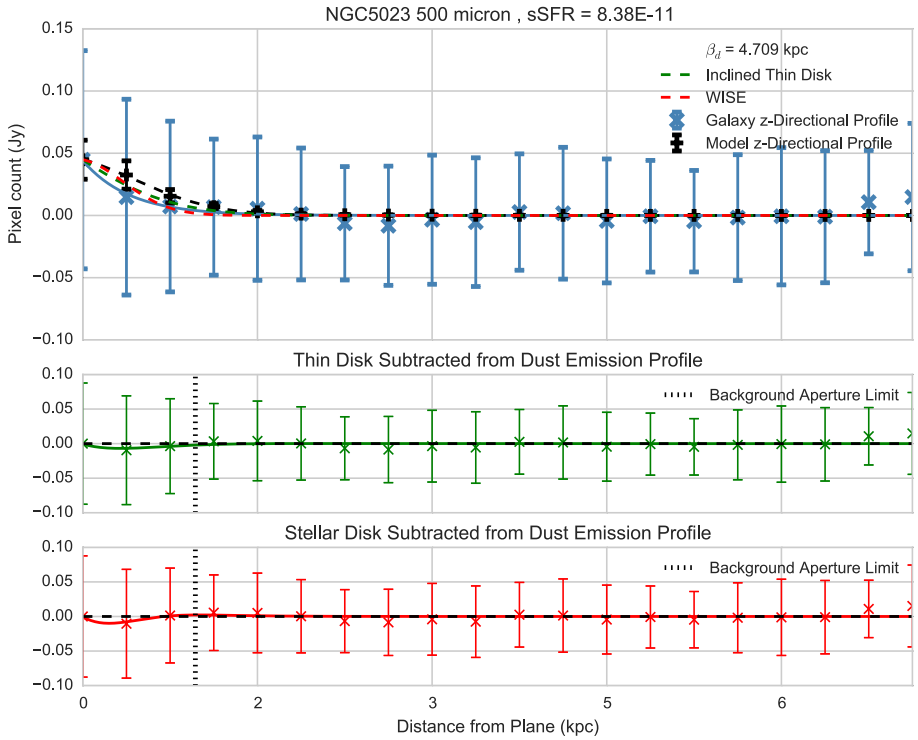
NGC5023 500 micron , sSFR = 8.38E-11
β_d = 4.709 kpc
Inclined Thin Disk
WISE
Galaxy z-Directional Profile
Model z-Directional Profile
Pixel count (Jy)
Thin Disk Subtracted from Dust Emission Profile
Background Aperture Limit
Stellar Disk Subtracted from Dust Emission Profile
Background Aperture Limit
Distance from Plane (kpc)

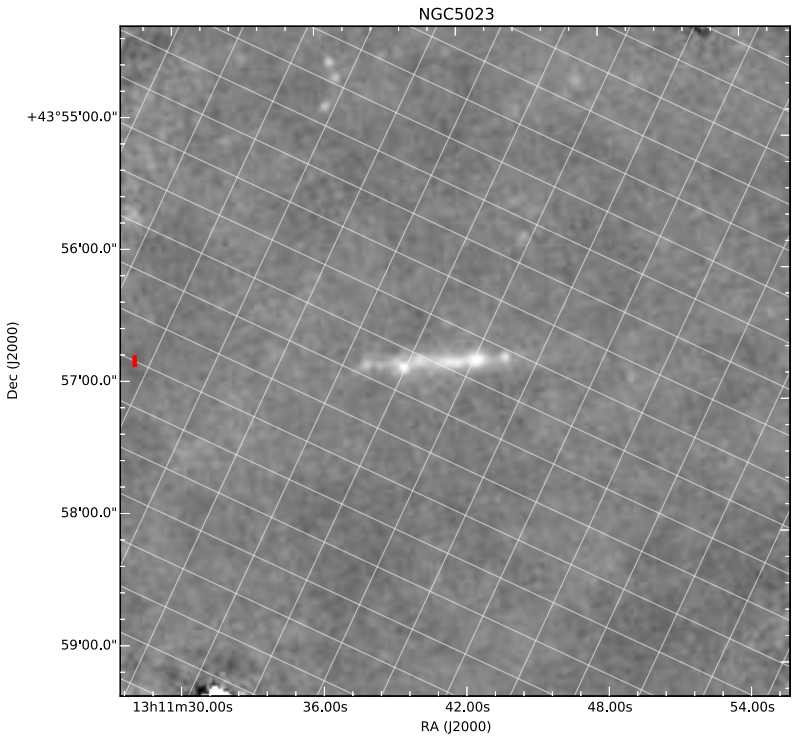

Figure A.181: 100 μm

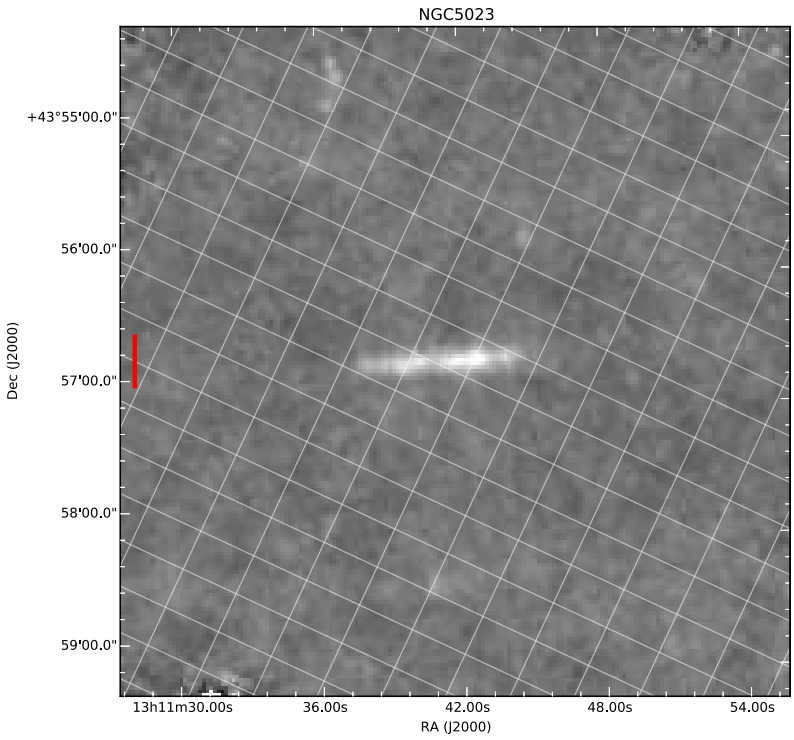

Figure A.182: 160 μm

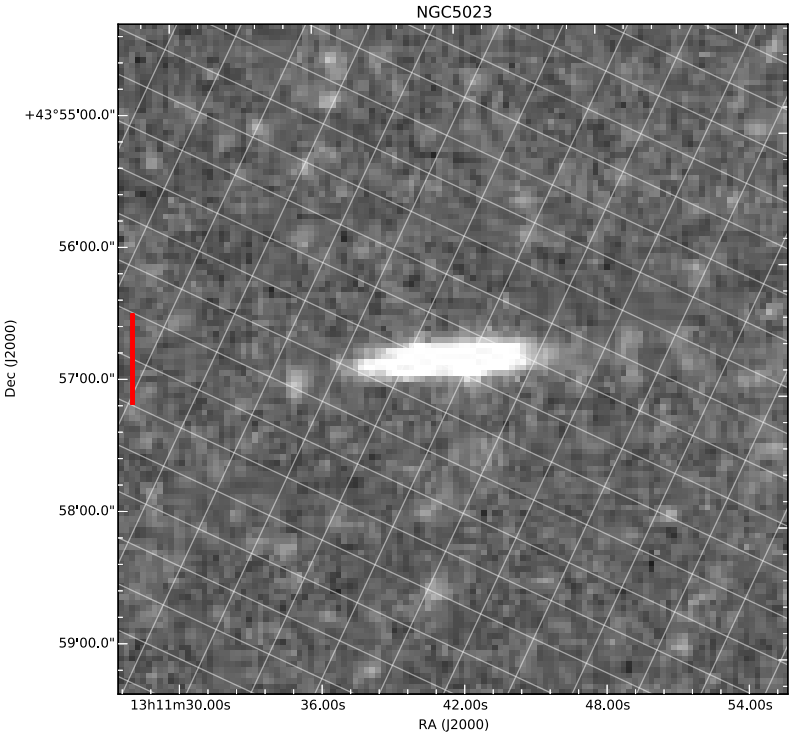

Figure A.183: 250 μm

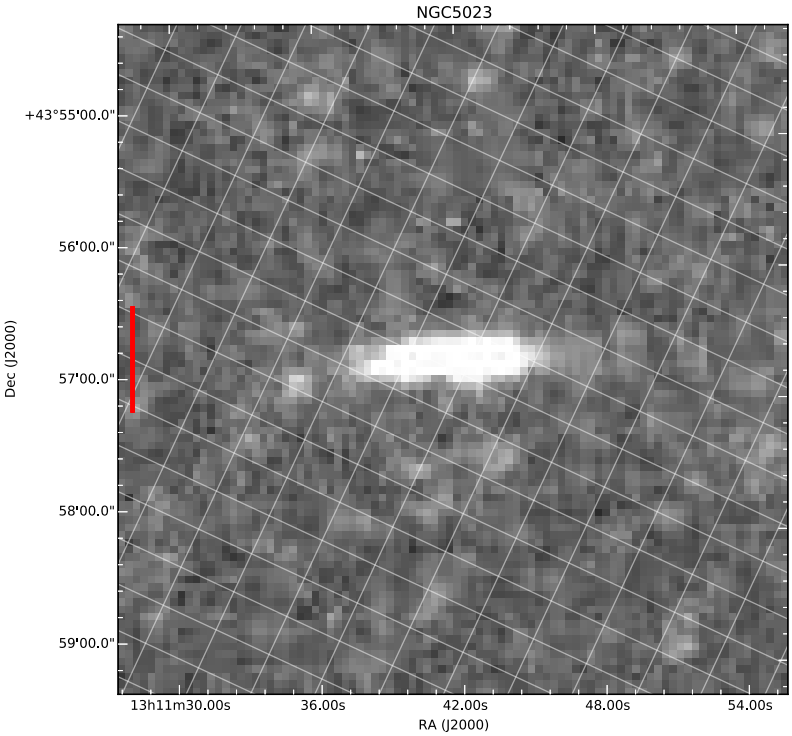

Figure A.184: 350 μm

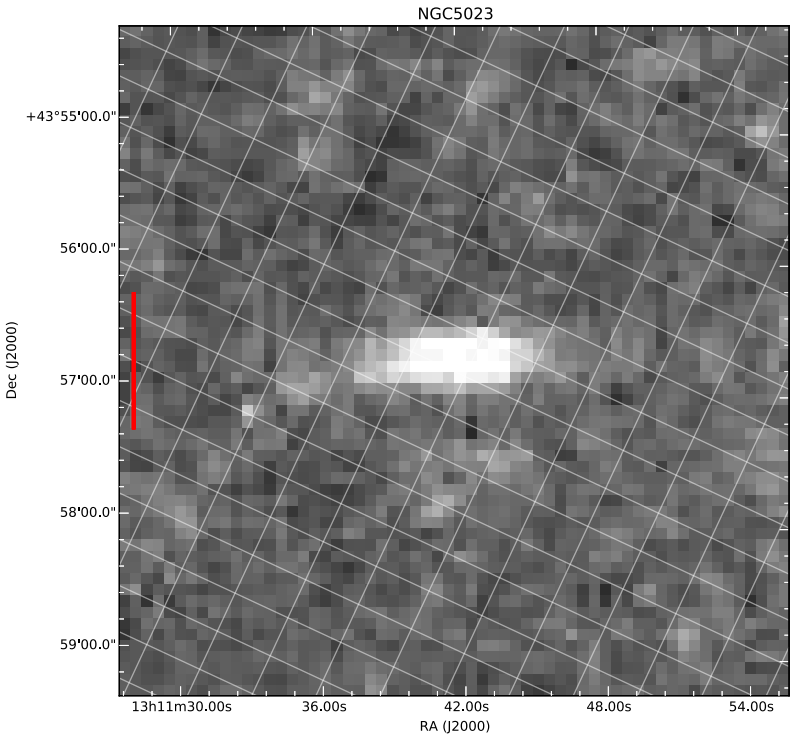

Figure A.185: 500 μm

A.22 NGC5301

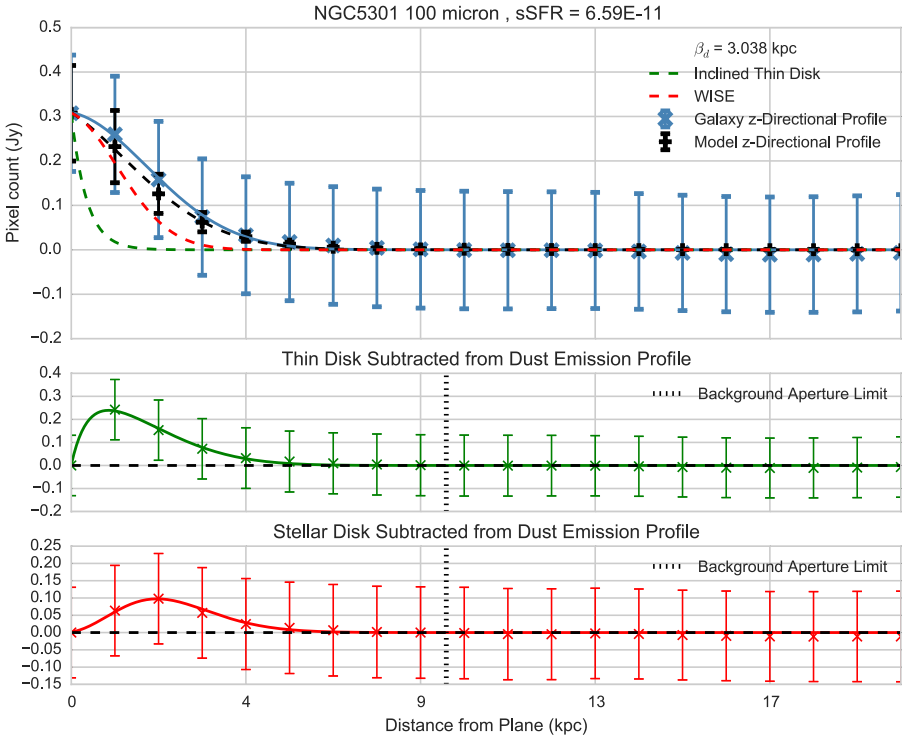
NGC5301 100 micron , sSFR = 6.59E-11
β_d = 3.038 kpc
Inclined Thin Disk
WISE
Galaxy z-Directional Profile
Model z-Directional Profile
Pixel count (Jy)
Thin Disk Subtracted from Dust Emission Profile
Background Aperture Limit
Stellar Disk Subtracted from Dust Emission Profile
Background Aperture Limit
Distance from Plane (kpc)

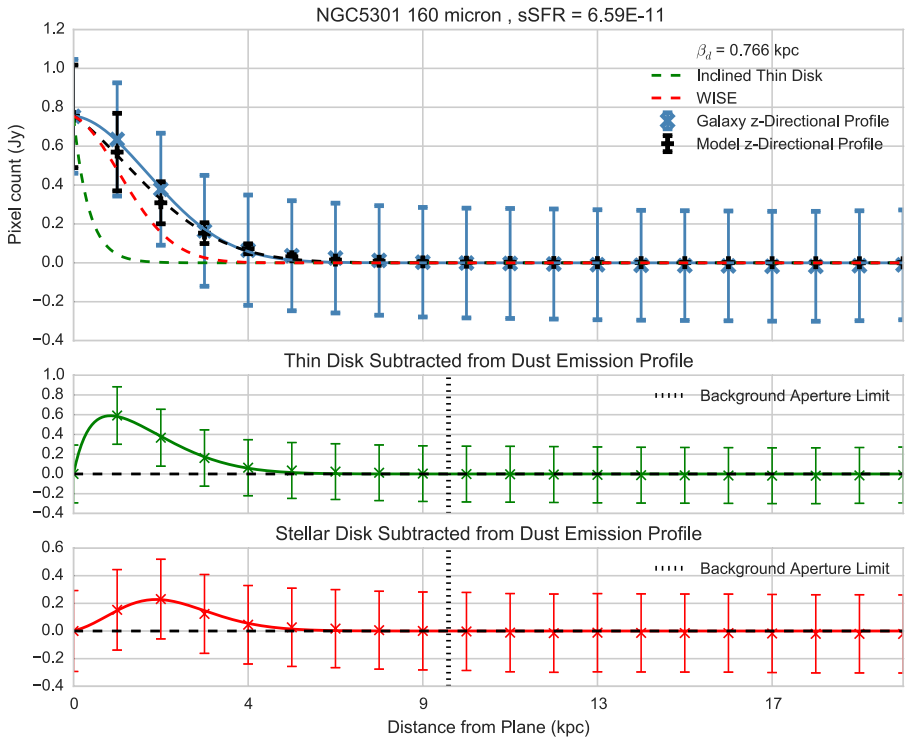
NGC5301 160 micron , sSFR = 6.59E-11
β_d = 0.766 kpc
Inclined Thin Disk
WISE
Galaxy z-Directional Profile
Model z-Directional Profile
Pixel count (Jy)
Thin Disk Subtracted from Dust Emission Profile
Background Aperture Limit
Stellar Disk Subtracted from Dust Emission Profile
Background Aperture Limit
Distance from Plane (kpc)

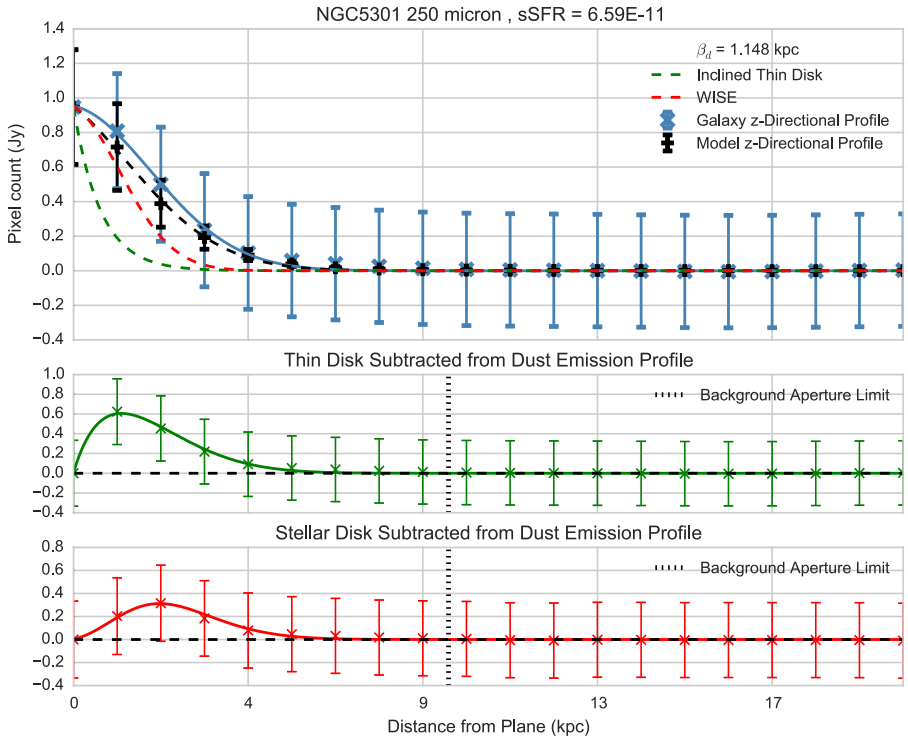
NGC5301 250 micron , sSFR = 6.59E-11
β_d = 1.148 kpc
Inclined Thin Disk
WISE
Galaxy z-Directional Profile
Model z-Directional Profile
Pixel count (Jy)
Thin Disk Subtracted from Dust Emission Profile
Background Aperture Limit
Stellar Disk Subtracted from Dust Emission Profile
Background Aperture Limit
Distance from Plane (kpc)

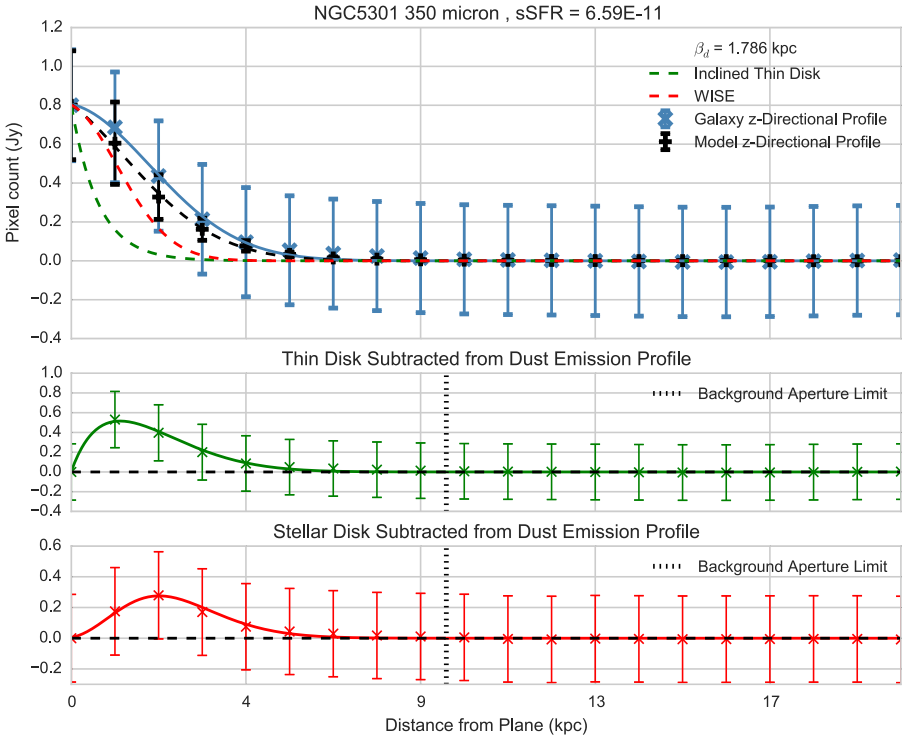
NGC5301 350 micron , sSFR = 6.59E-11
β_d = 1.786 kpc
Inclined Thin Disk
WISE
Galaxy z-Directional Profile
Model z-Directional Profile
Pixel count (Jy)
Thin Disk Subtracted from Dust Emission Profile
Background Aperture Limit
Stellar Disk Subtracted from Dust Emission Profile
Background Aperture Limit
Distance from Plane (kpc)

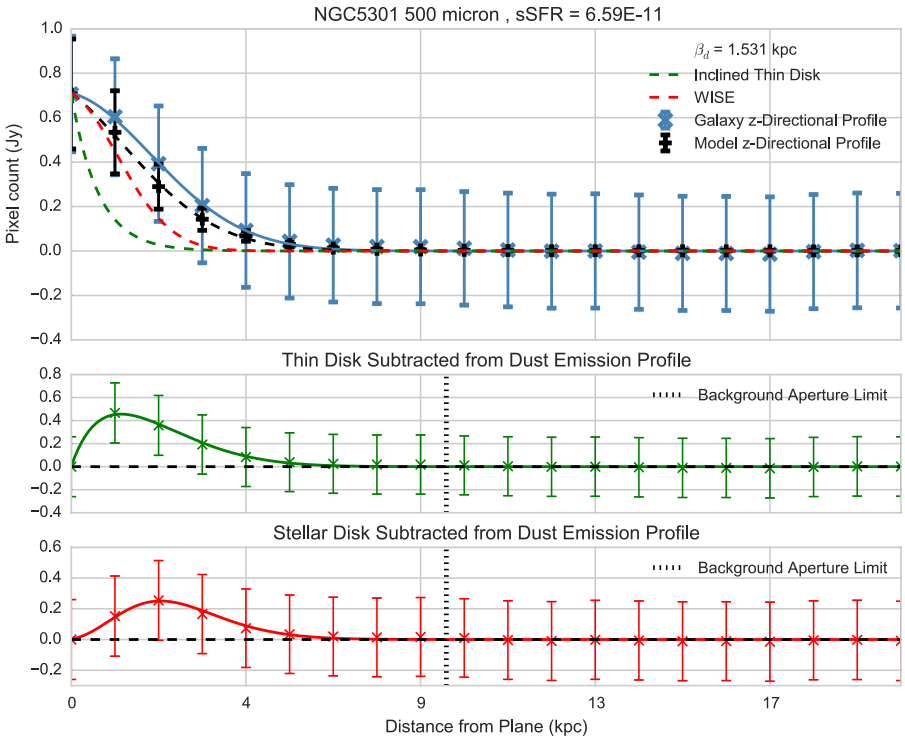
NGC5301 500 micron , sSFR = 6.59E-11
β_d = 1.531 kpc
Inclined Thin Disk
WISE
Galaxy z-Directional Profile
Model z-Directional Profile
Pixel count (Jy)
Thin Disk Subtracted from Dust Emission Profile
Background Aperture Limit
Stellar Disk Subtracted from Dust Emission Profile
Background Aperture Limit
Distance from Plane (kpc)

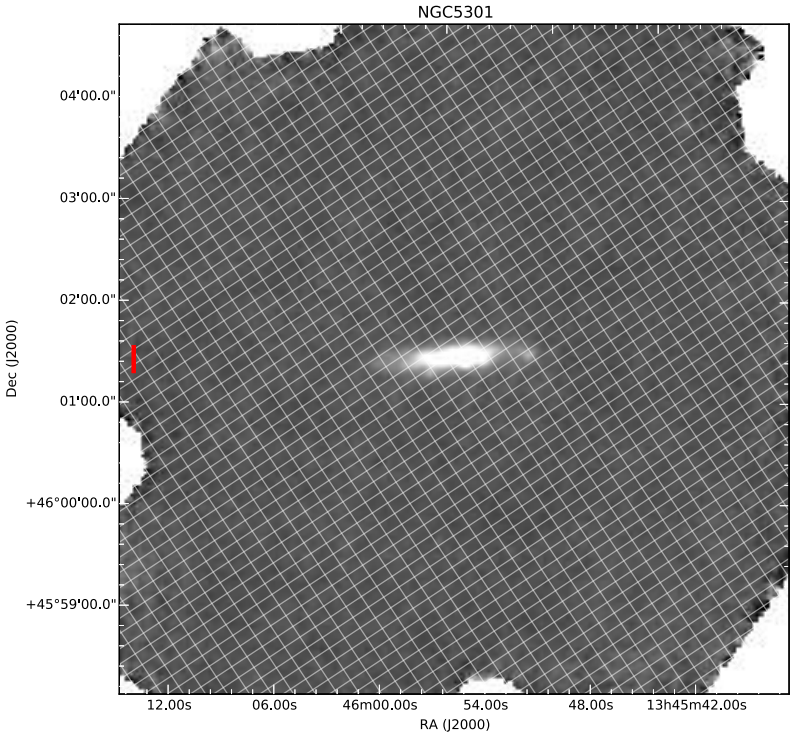

Figure A.186: 100 μm

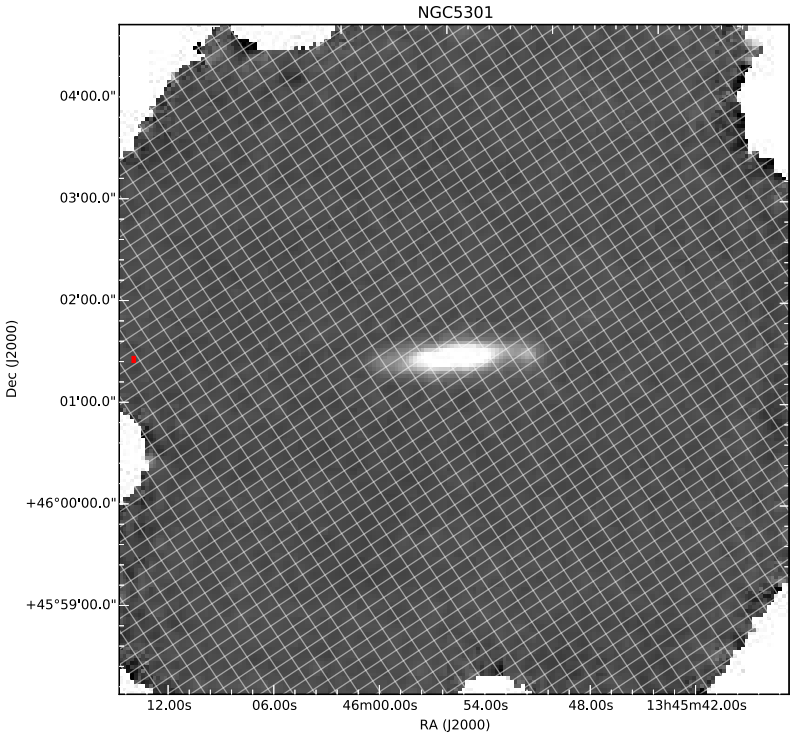

Figure A.187: 160 μm

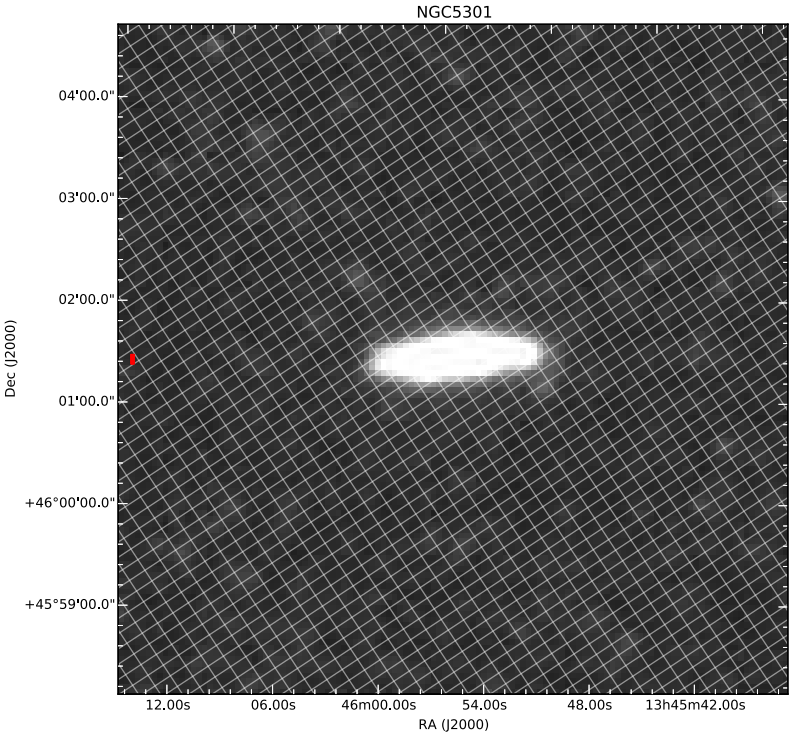

Figure A.188: 250 μm

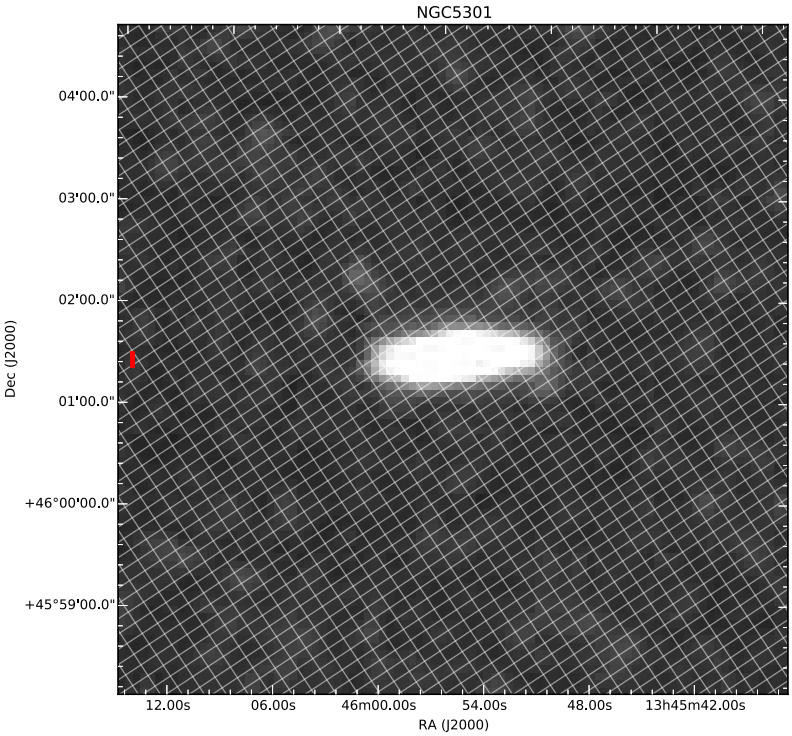

Figure A.189: 350 μm

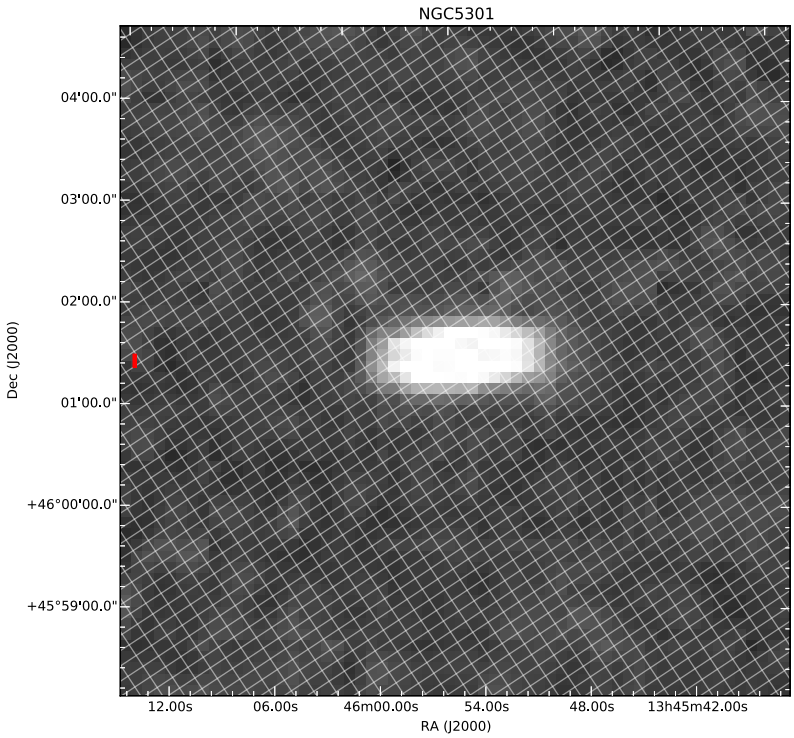

Figure A.190: 500 μm

A.23 NGC5348

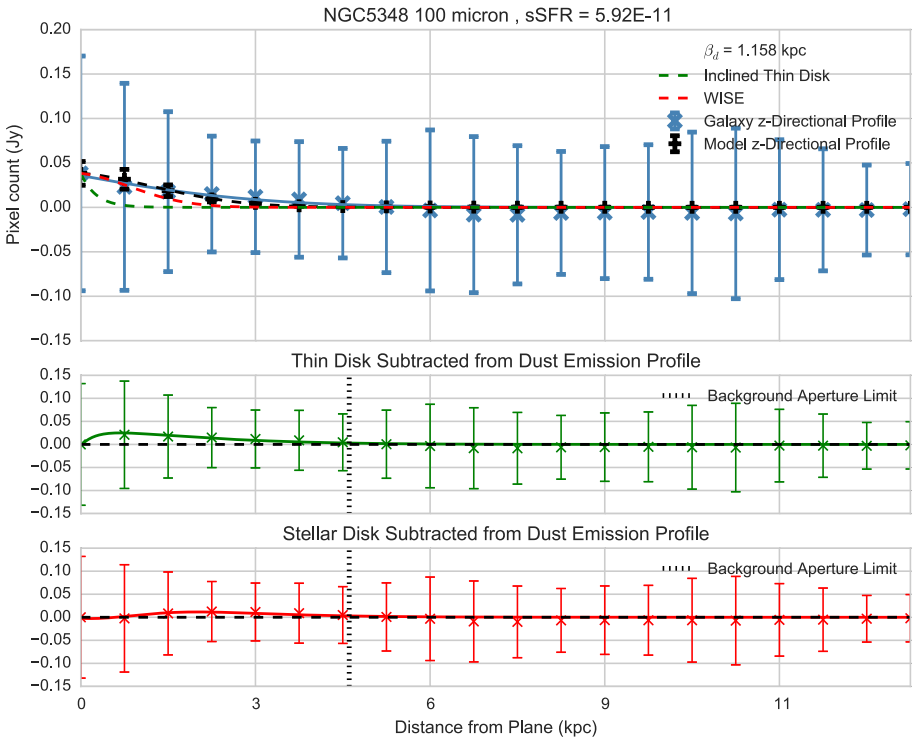
NGC5348 100 micron , sSFR = 5.92E-11
β_d = 1.158 kpc
Inclined Thin Disk
WISE
Galaxy z-Directional Profile
Model z-Directional Profile
Pixel count (Jy)
Thin Disk Subtracted from Dust Emission Profile
Background Aperture Limit
Stellar Disk Subtracted from Dust Emission Profile
Background Aperture Limit
Distance from Plane (kpc)

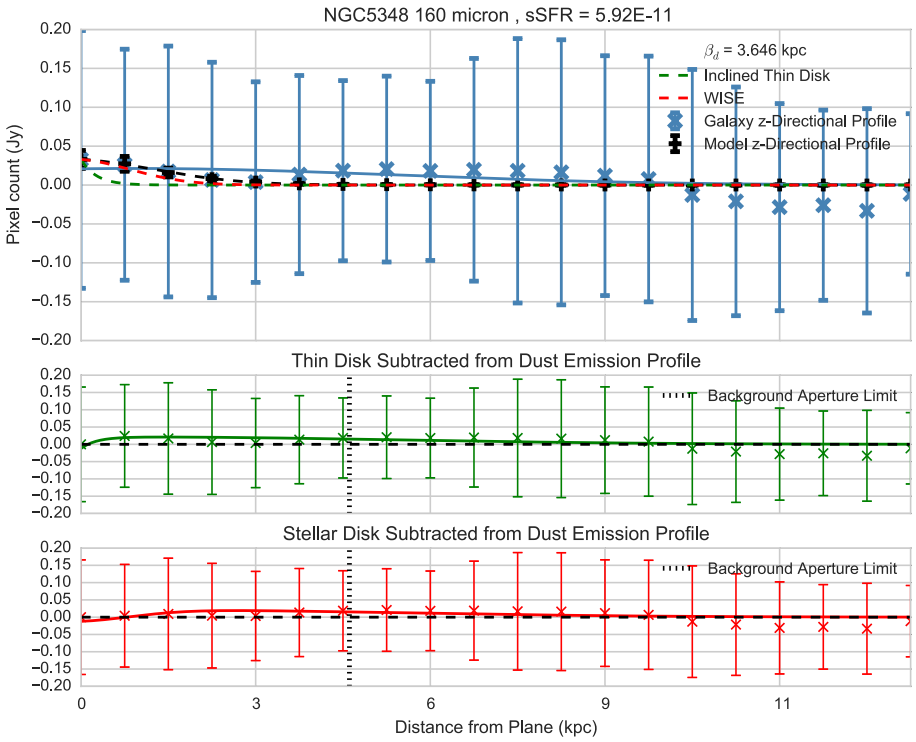
NGC5348 160 micron , sSFR = 5.92E-11
β_d = 3.646 kpc
Inclined Thin Disk
WISE
Galaxy z-Directional Profile
Model z-Directional Profile
Pixel count (Jy)
Thin Disk Subtracted from Dust Emission Profile
Background Aperture Limit
Stellar Disk Subtracted from Dust Emission Profile
Background Aperture Limit
Distance from Plane (kpc)

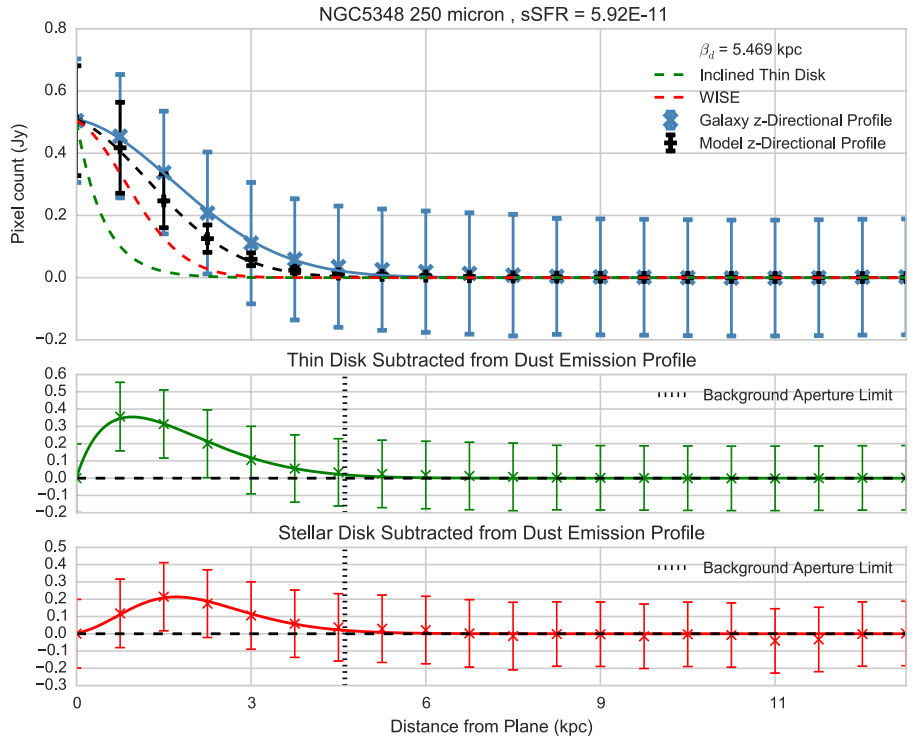
NGC5348 250 micron , sSFR = 5.92E-11
β_d = 5.469 kpc
Inclined Thin Disk
WISE
Galaxy z-Directional Profile
Model z-Directional Profile
Pixel count (Jy)
Thin Disk Subtracted from Dust Emission Profile
Background Aperture Limit
Stellar Disk Subtracted from Dust Emission Profile
Background Aperture Limit
Distance from Plane (kpc)

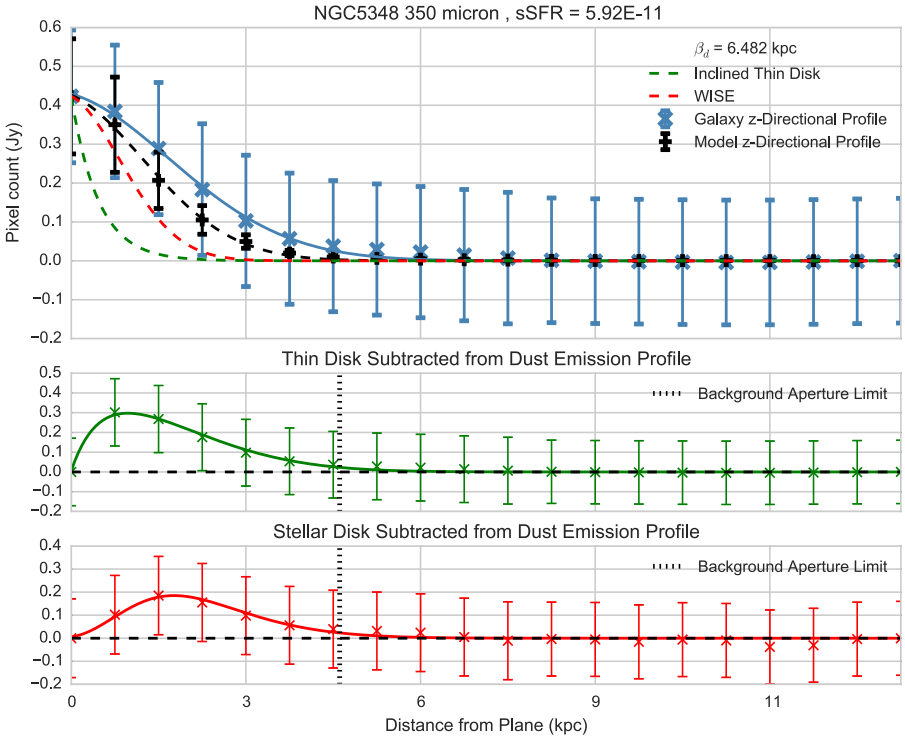
NGC5348 350 micron , sSFR = 5.92E-11
β_d = 6.482 kpc
Inclined Thin Disk
WISE
Galaxy z-Directional Profile
Model z-Directional Profile
Pixel count (Jy)
Thin Disk Subtracted from Dust Emission Profile
Background Aperture Limit
Stellar Disk Subtracted from Dust Emission Profile
Background Aperture Limit
Distance from Plane (kpc)

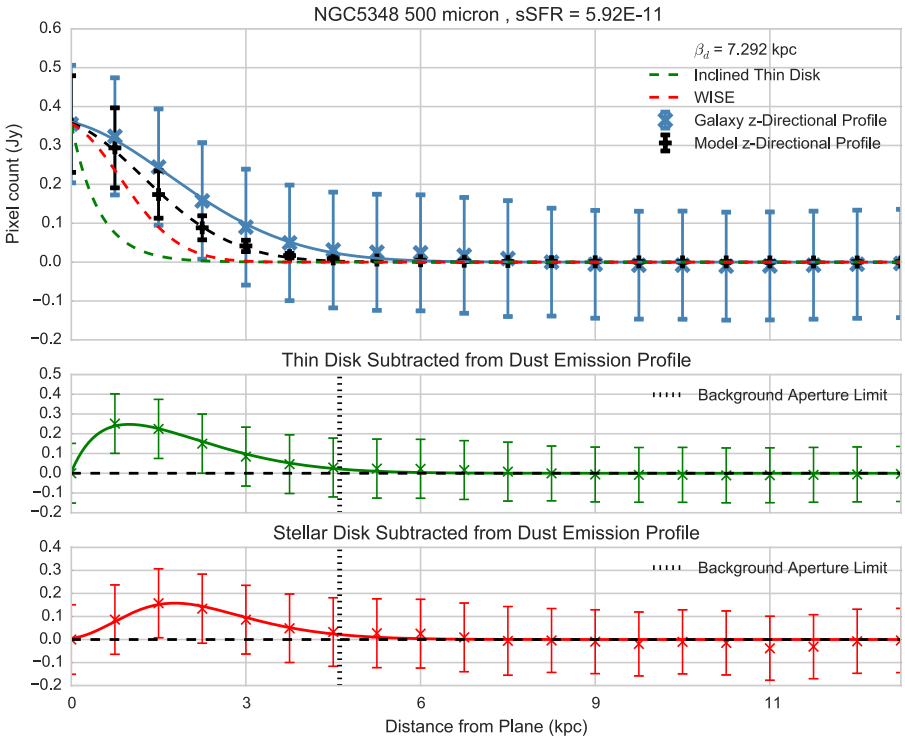
NGC5348 500 micron , sSFR = 5.92E-11
β_d = 7.292 kpc
Inclined Thin Disk
WISE
Galaxy z-Directional Profile
Model z-Directional Profile
Pixel count (Jy)
Thin Disk Subtracted from Dust Emission Profile
Background Aperture Limit
Stellar Disk Subtracted from Dust Emission Profile
Background Aperture Limit
Distance from Plane (kpc)

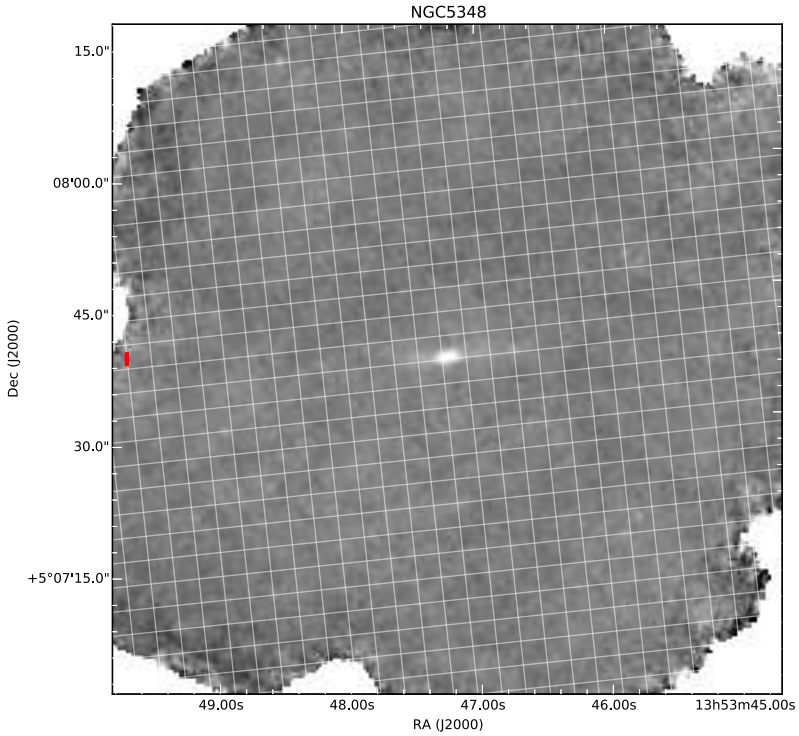

Figure A.191: 100 μm

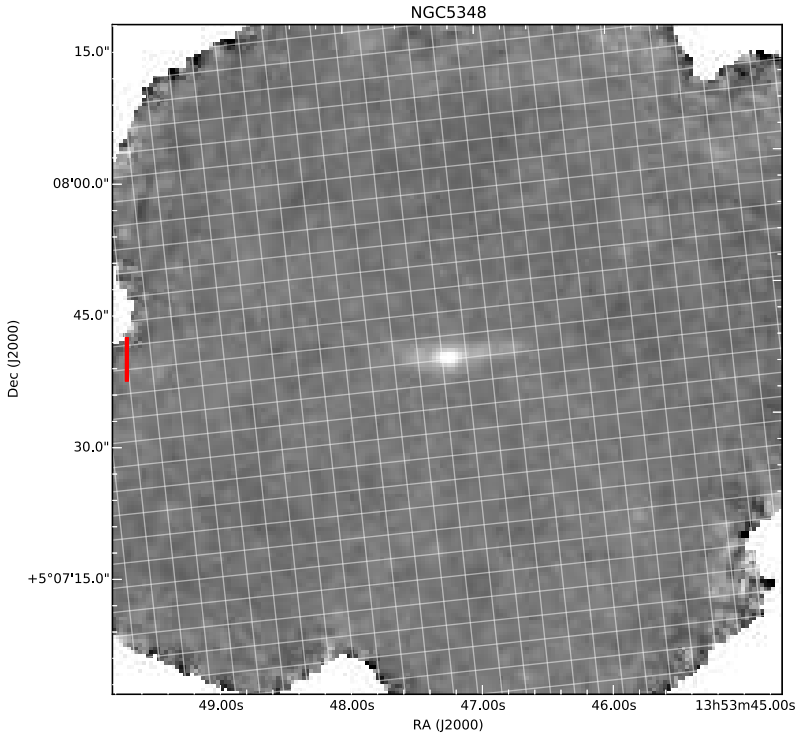

Figure A.192: 160 μm

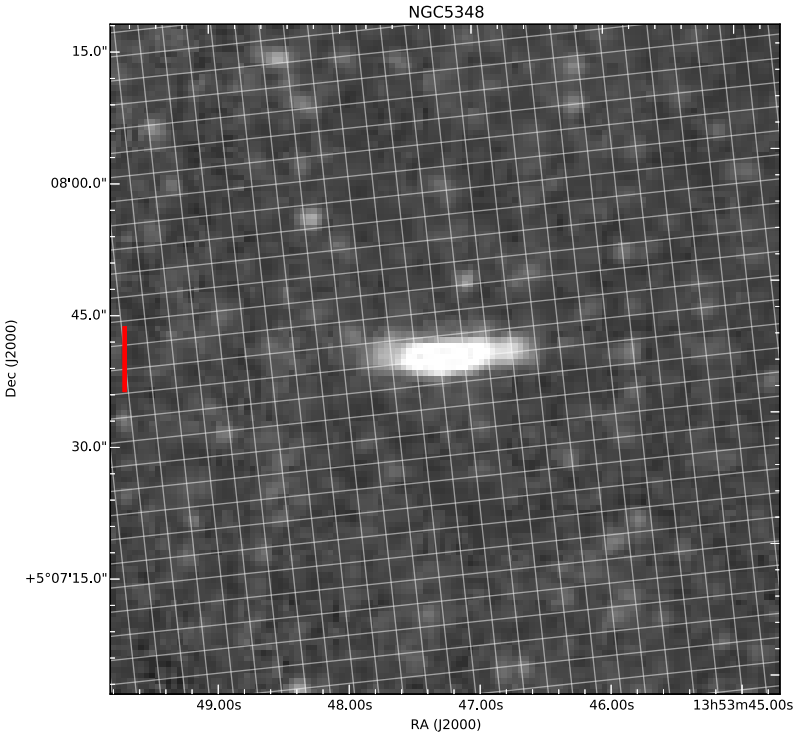

Figure A.193: 250 μm

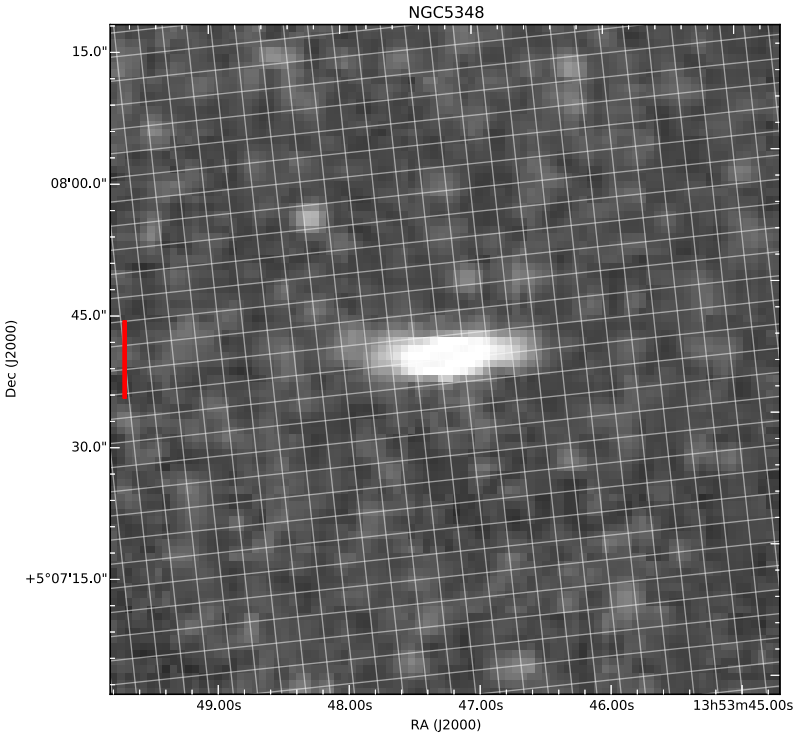

Figure A.194: 350 μm

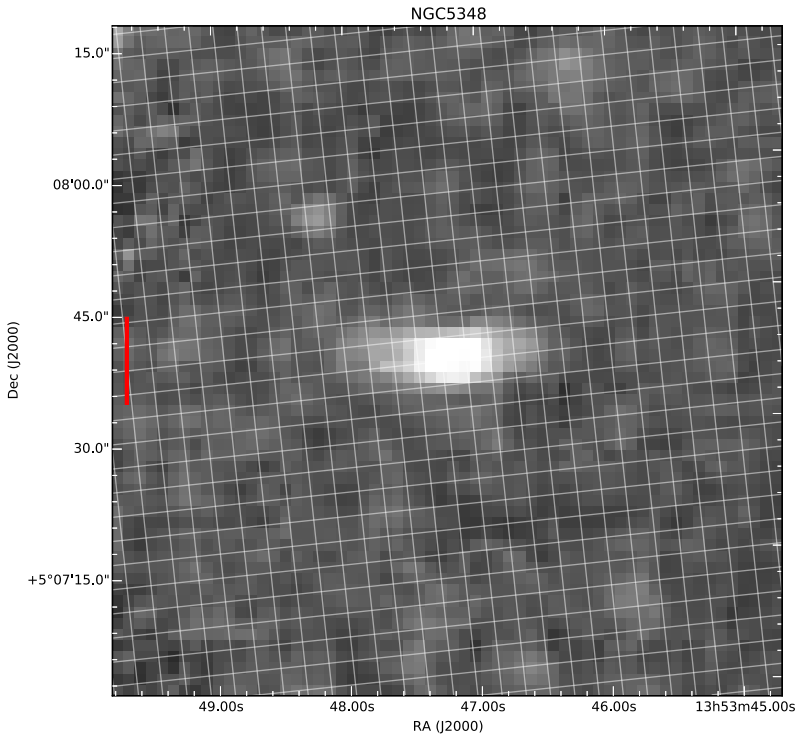

Figure A.195: 500 μm

A.24 NGC5356

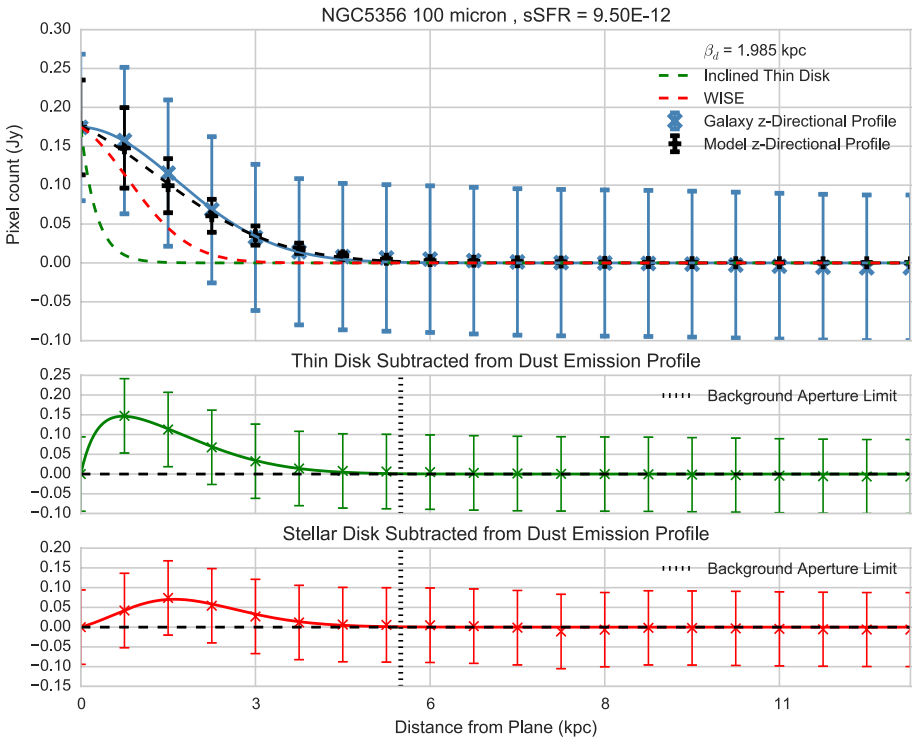
NGC5356 100 micron , sSFR = 9.50E-12
β_d = 1.985 kpc
Inclined Thin Disk
WISE
Galaxy z-Directional Profile
Model z-Directional Profile
Pixel count (Jy)
Thin Disk Subtracted from Dust Emission Profile
Background Aperture Limit
Stellar Disk Subtracted from Dust Emission Profile
Background Aperture Limit
Distance from Plane (kpc)

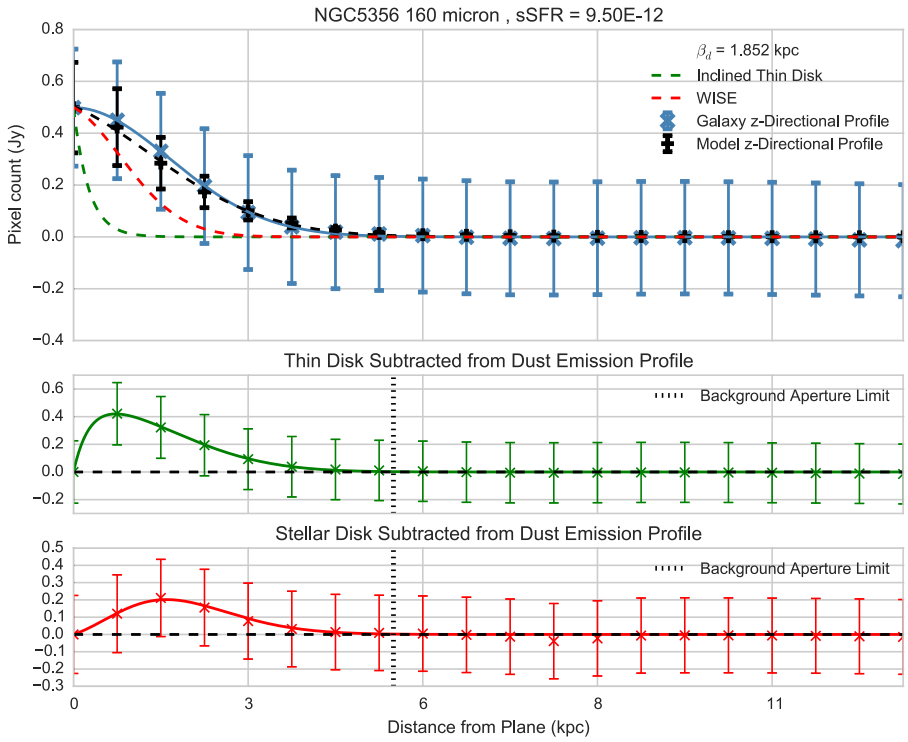
NGC5356 160 micron , sSFR = 9.50E-12
β_d = 1.852 kpc
Inclined Thin Disk
WISE
Galaxy z-Directional Profile
Model z-Directional Profile
Pixel count (Jy)
Thin Disk Subtracted from Dust Emission Profile
Background Aperture Limit
Stellar Disk Subtracted from Dust Emission Profile
Background Aperture Limit
Distance from Plane (kpc)

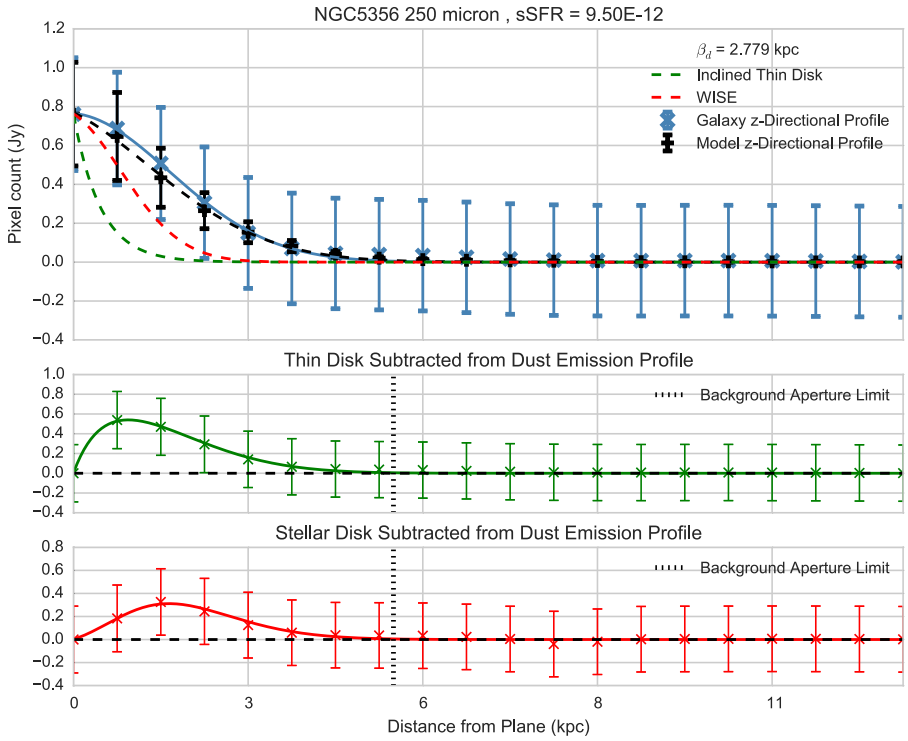
NGC5356 250 micron , sSFR = 9.50E-12
β_d = 2.779 kpc
Inclined Thin Disk
WISE
Galaxy z-Directional Profile
Model z-Directional Profile
Pixel count (Jy)
Thin Disk Subtracted from Dust Emission Profile
Background Aperture Limit
Stellar Disk Subtracted from Dust Emission Profile
Background Aperture Limit
Distance from Plane (kpc)

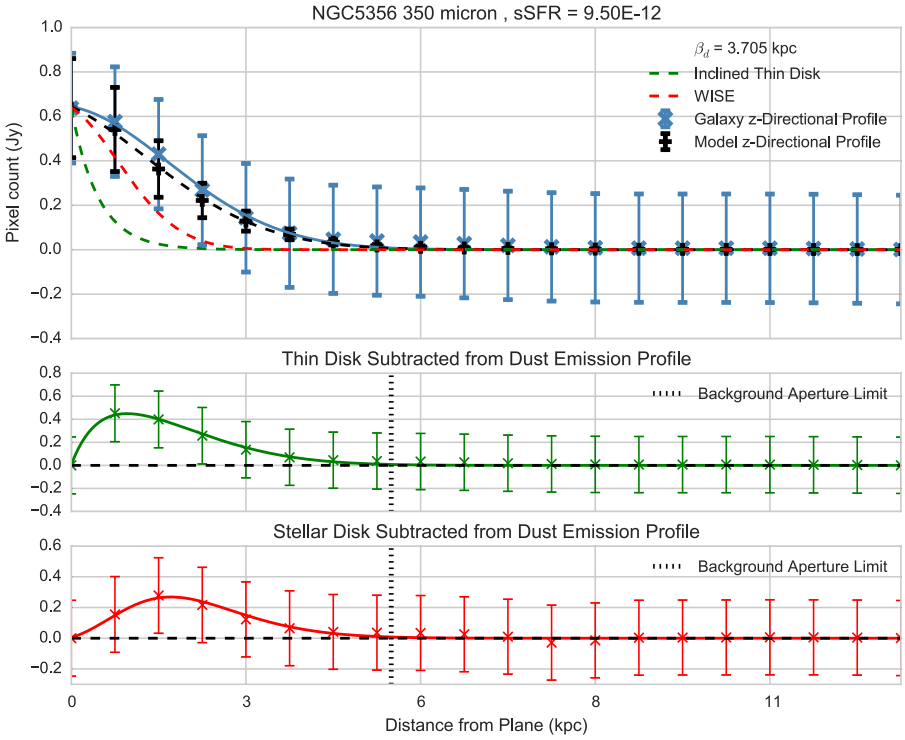
NGC5356 350 micron , sSFR = 9.50E-12
β_d = 3.705 kpc
Inclined Thin Disk
WISE
Galaxy z-Directional Profile
Model z-Directional Profile
Pixel count (Jy)
Thin Disk Subtracted from Dust Emission Profile
Background Aperture Limit
Stellar Disk Subtracted from Dust Emission Profile
Background Aperture Limit
Distance from Plane (kpc)

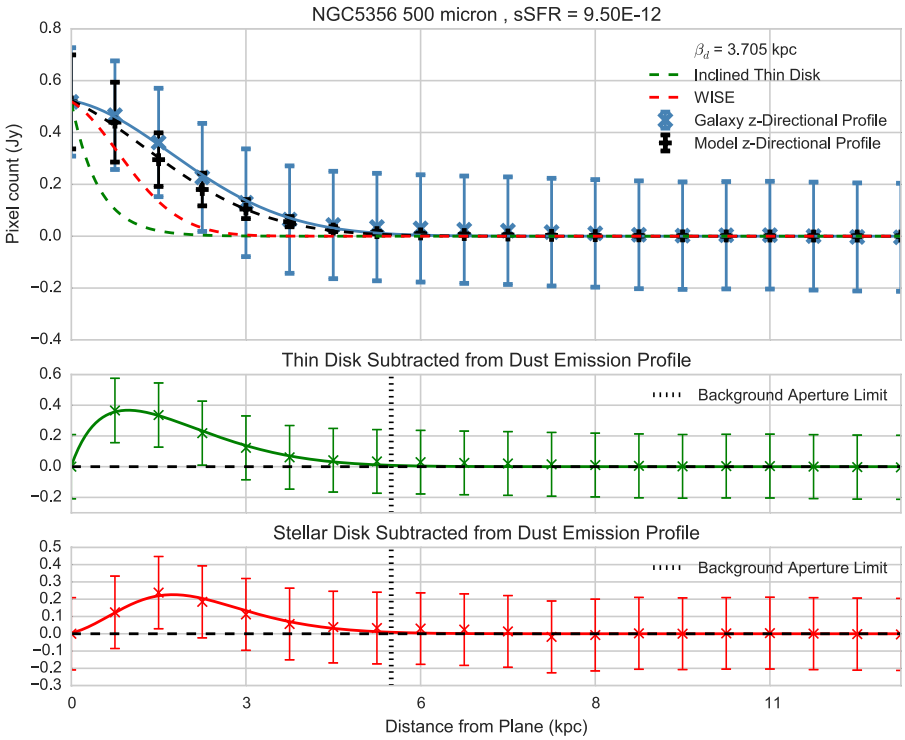
NGC5356 500 micron , sSFR = 9.50E-12
β_d = 3.705 kpc
Inclined Thin Disk
WISE
Galaxy z-Directional Profile
Model z-Directional Profile
Pixel count (Jy)
Thin Disk Subtracted from Dust Emission Profile
Background Aperture Limit
Stellar Disk Subtracted from Dust Emission Profile
Background Aperture Limit
Distance from Plane (kpc)

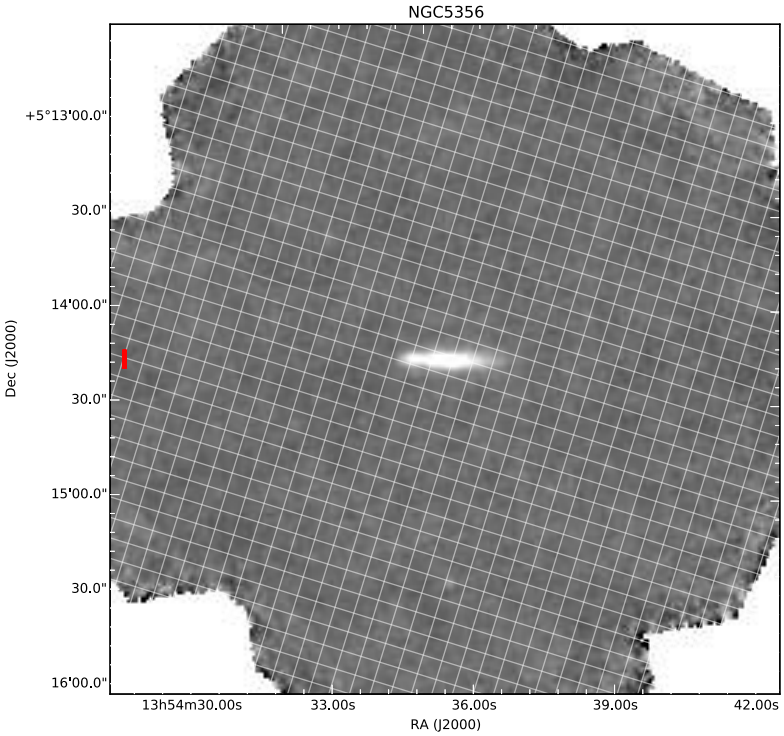

Figure A.196: 100 μm

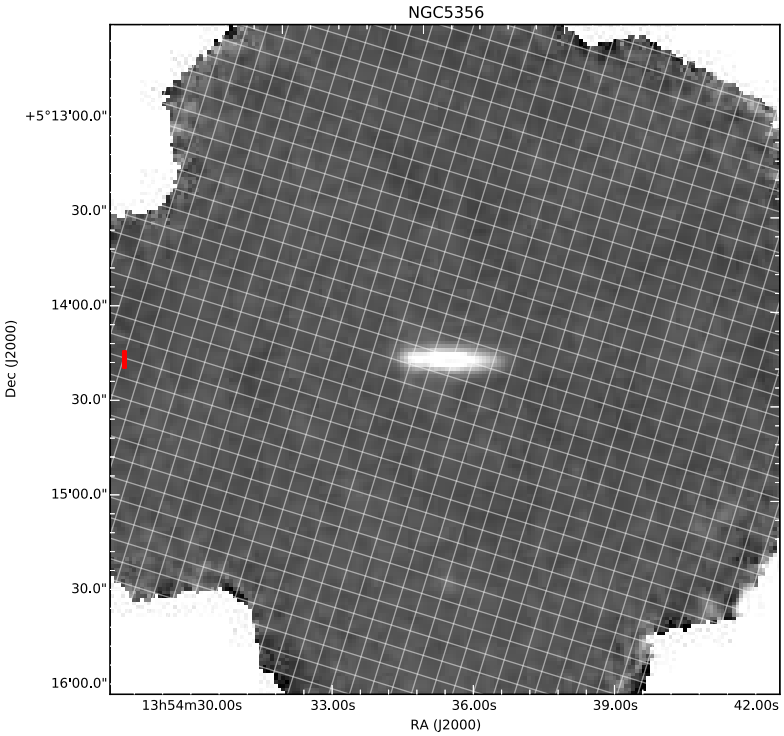

Figure A.197: 160 μm

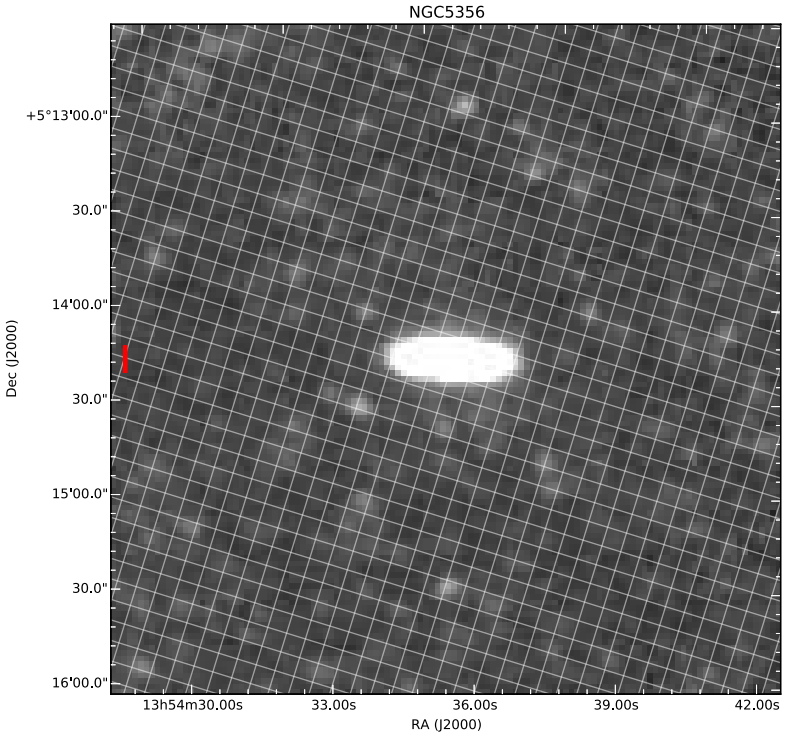

Figure A.198: 250 μm

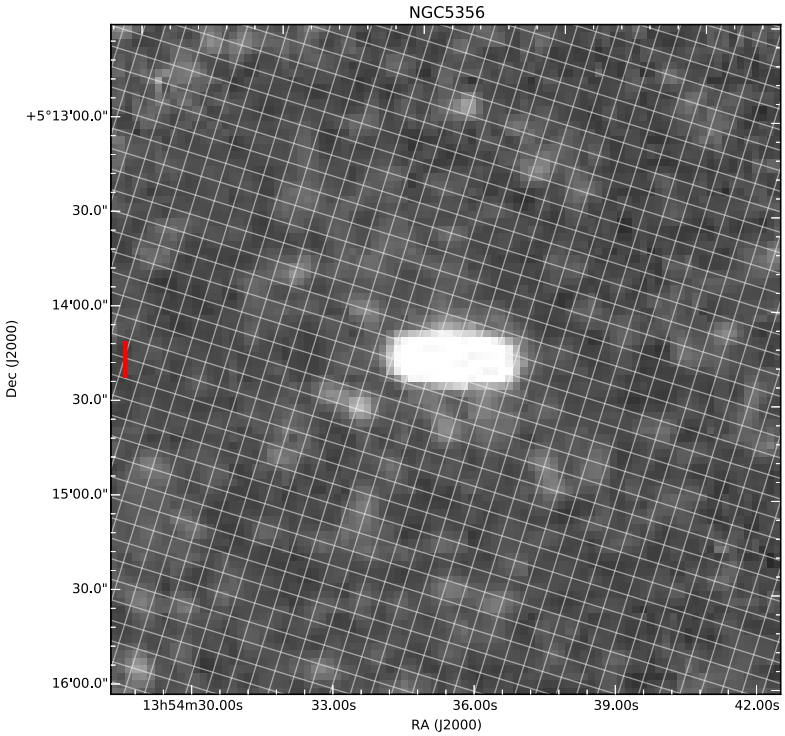

Figure A.199: 350 μm

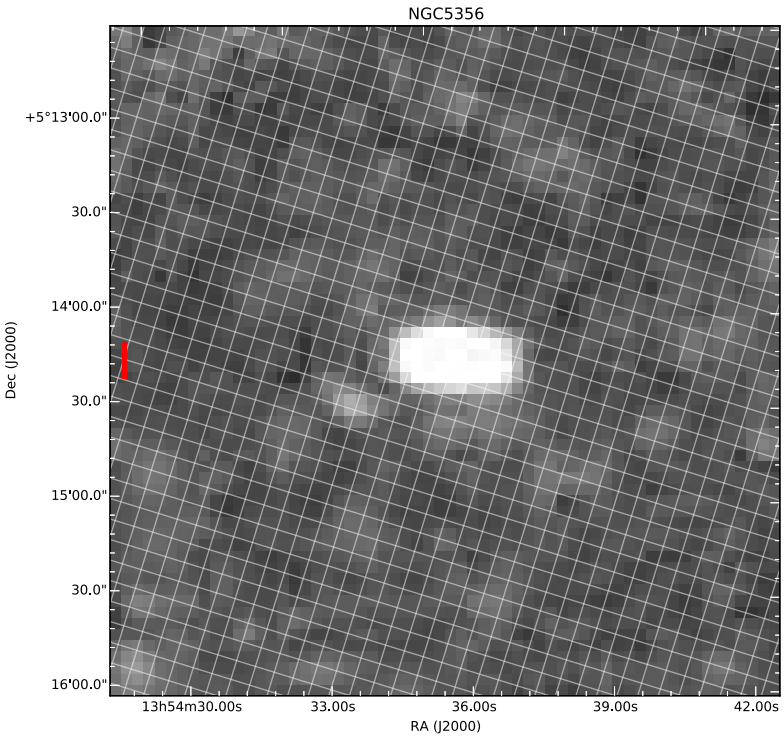

Figure A.200: 500 μm

A.25 NGC5529

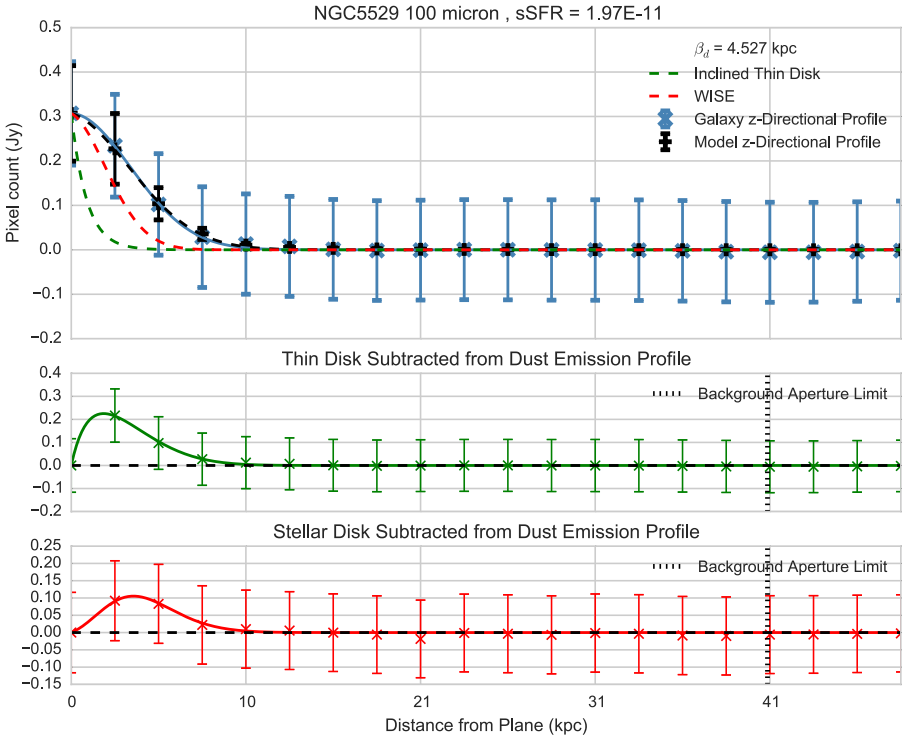
NGC5529 100 micron , sSFR = 1.97E-11
β_d = 4.527 kpc
Inclined Thin Disk
WISE
Galaxy z-Directional Profile
Model z-Directional Profile
Pixel count (Jy)
Thin Disk Subtracted from Dust Emission Profile
Background Aperture Limit
Stellar Disk Subtracted from Dust Emission Profile
Background Aperture Limit
Distance from Plane (kpc)

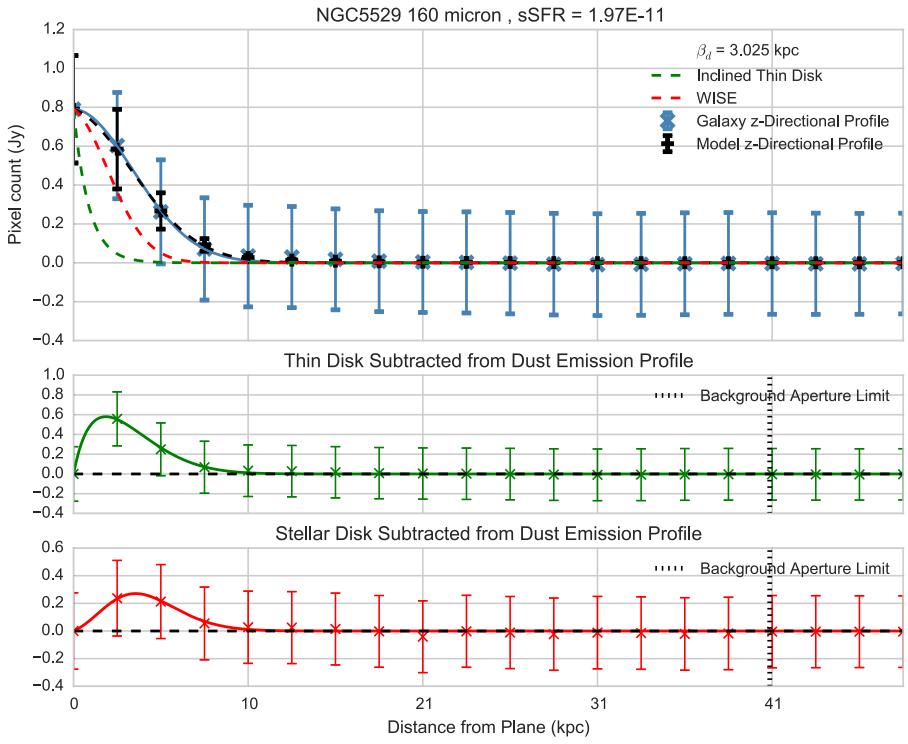
NGC5529 160 micron , sSFR = 1.97E-11
β_d = 3.025 kpc
Inclined Thin Disk
WISE
Galaxy z-Directional Profile
Model z-Directional Profile
Pixel count (Jy)
Thin Disk Subtracted from Dust Emission Profile
Background Aperture Limit
Stellar Disk Subtracted from Dust Emission Profile
Background Aperture Limit
Distance from Plane (kpc)

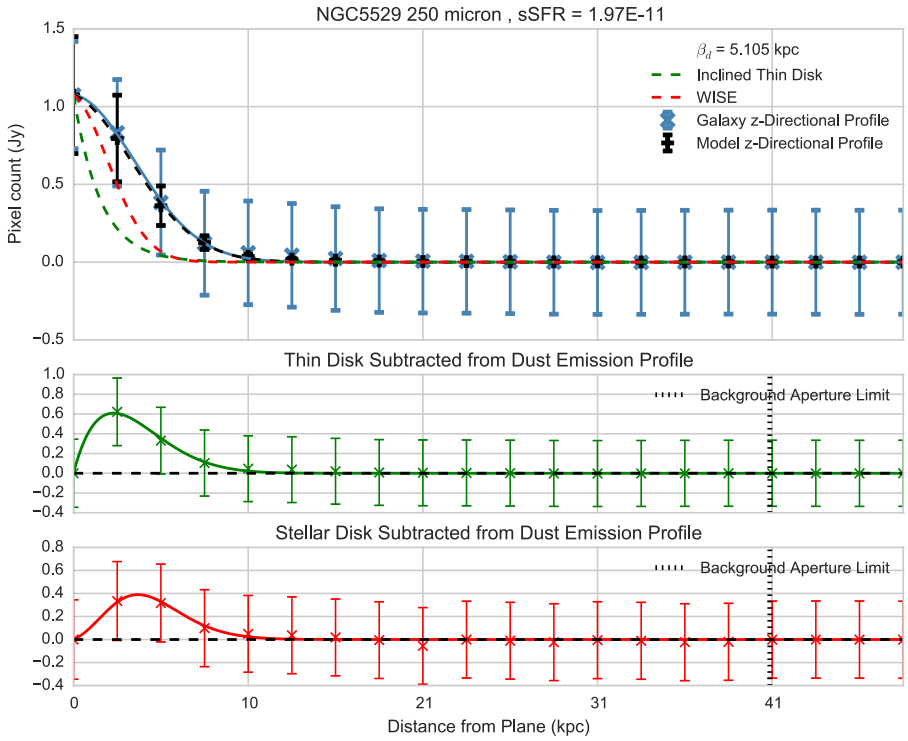
NGC5529 250 micron , sSFR = 1.97E-11
β_d = 5.105 kpc
Inclined Thin Disk
WISE
Galaxy z-Directional Profile
Model z-Directional Profile
Pixel count (Jy)
Thin Disk Subtracted from Dust Emission Profile
Background Aperture Limit
Stellar Disk Subtracted from Dust Emission Profile
Background Aperture Limit
Distance from Plane (kpc)

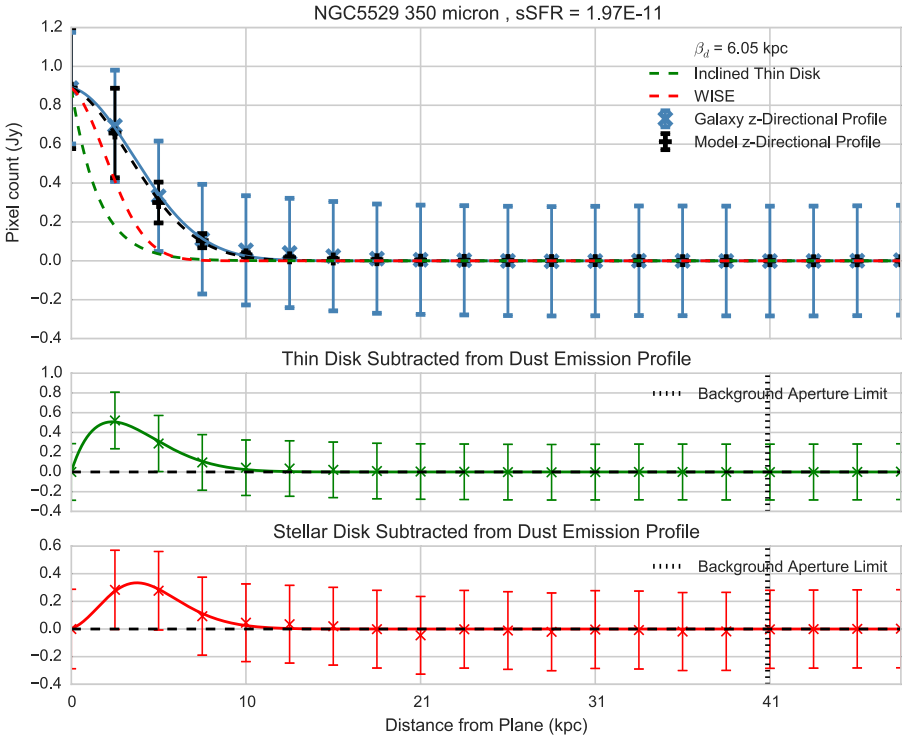
NGC5529 350 micron , sSFR = 1.97E-11
β_d = 6.05 kpc
Inclined Thin Disk
WISE
Galaxy z-Directional Profile
Model z-Directional Profile
Pixel count (Jy)
Thin Disk Subtracted from Dust Emission Profile
Background Aperture Limit
Stellar Disk Subtracted from Dust Emission Profile
Background Aperture Limit
Distance from Plane (kpc)

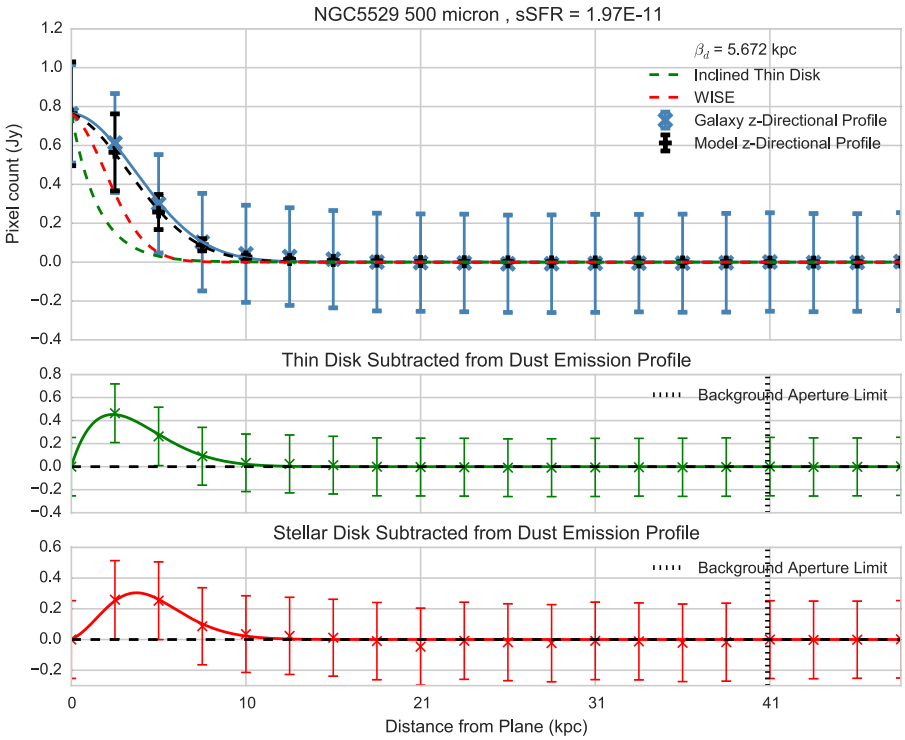
NGC5529 500 micron , sSFR = 1.97E-11
β_d = 5.672 kpc
Inclined Thin Disk
WISE
Galaxy z-Directional Profile
Model z-Directional Profile
Pixel count (Jy)
Thin Disk Subtracted from Dust Emission Profile
Background Aperture Limit
Stellar Disk Subtracted from Dust Emission Profile
Background Aperture Limit
Distance from Plane (kpc)

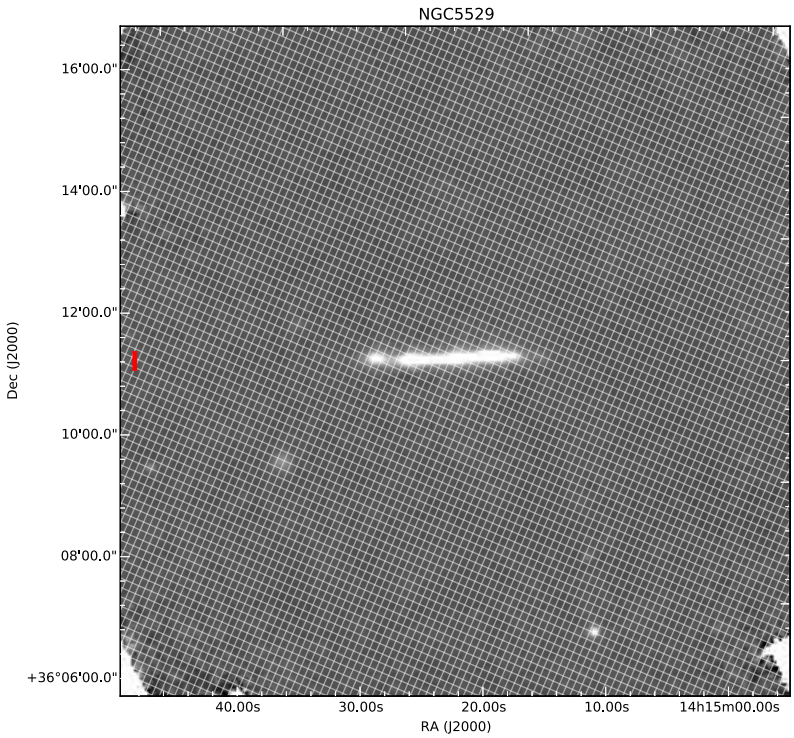

Figure A.201: 100 μm

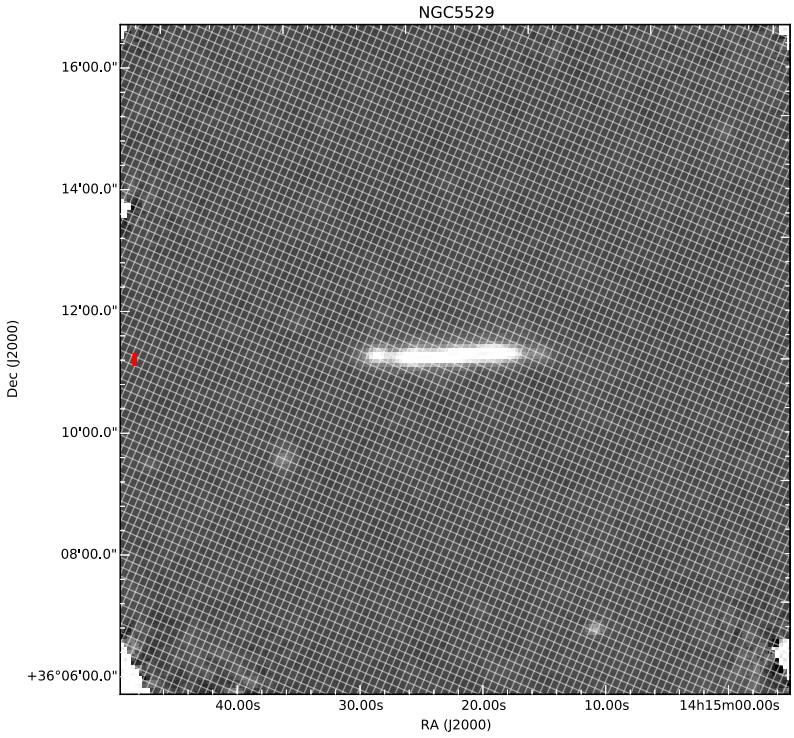

Figure A.202: 160 μm

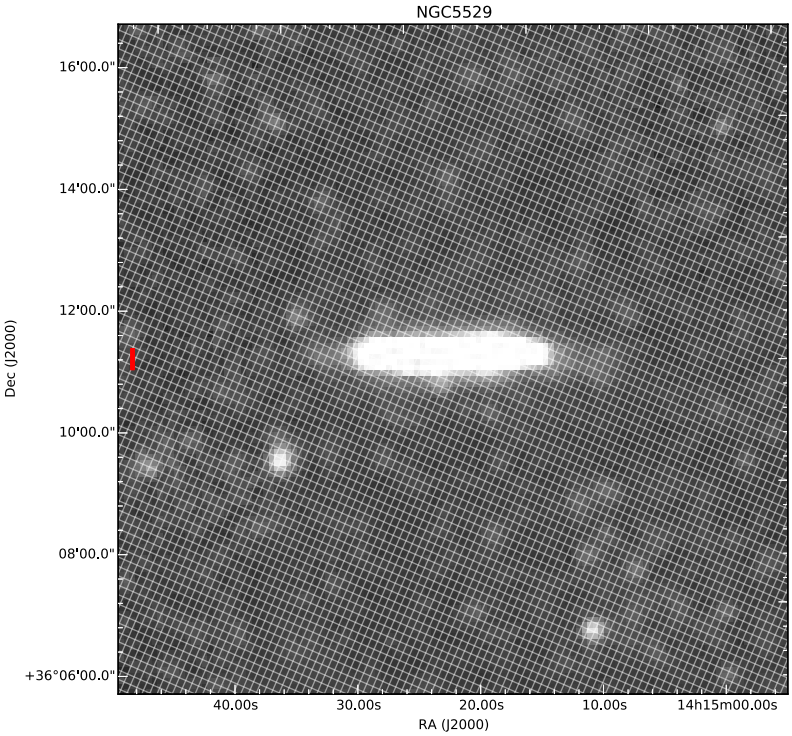

Figure A.203: 250 μm

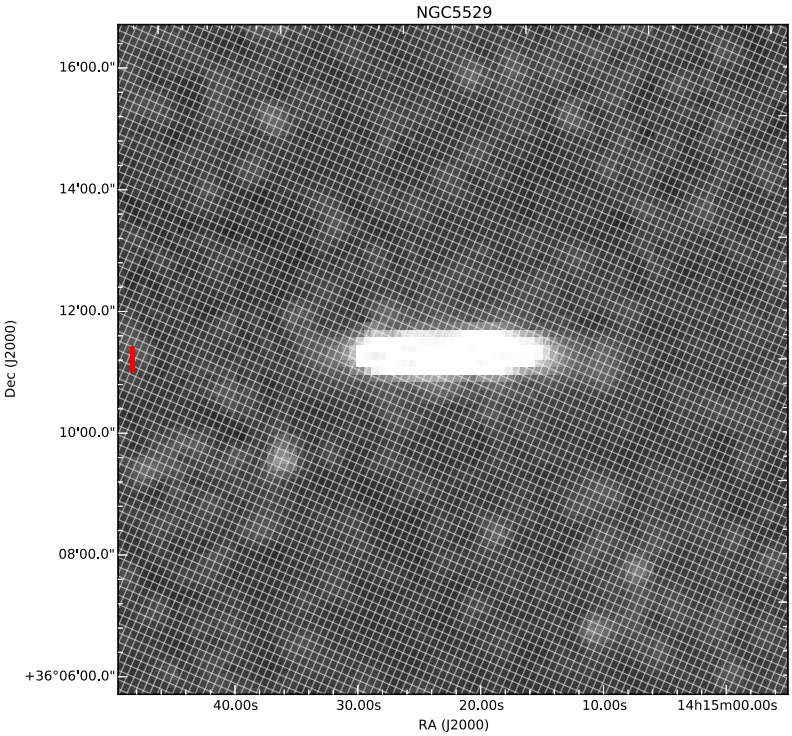

Figure A.204: 350 μm

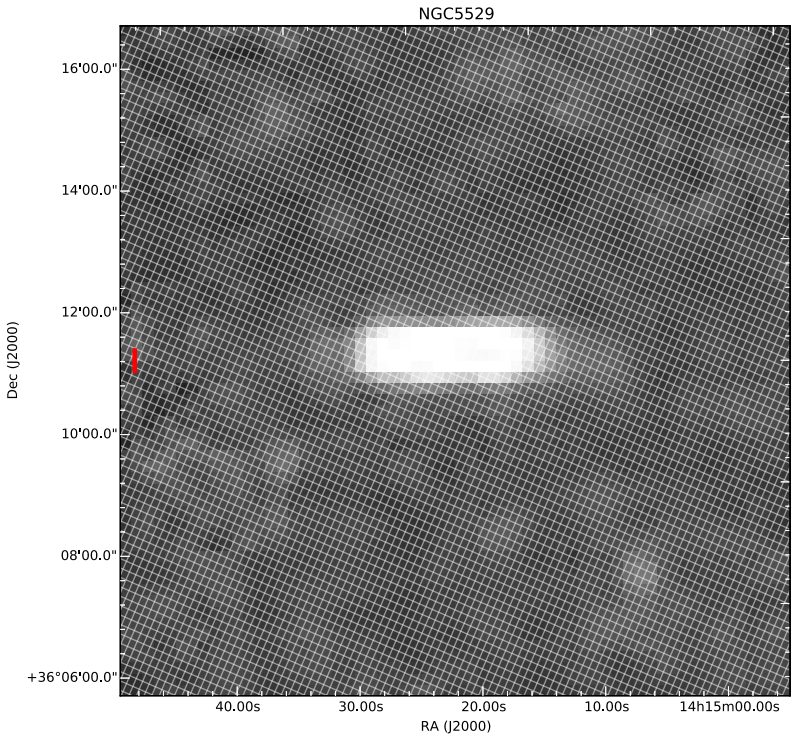

Figure A.205: 500 μm

A.26 NGC5746

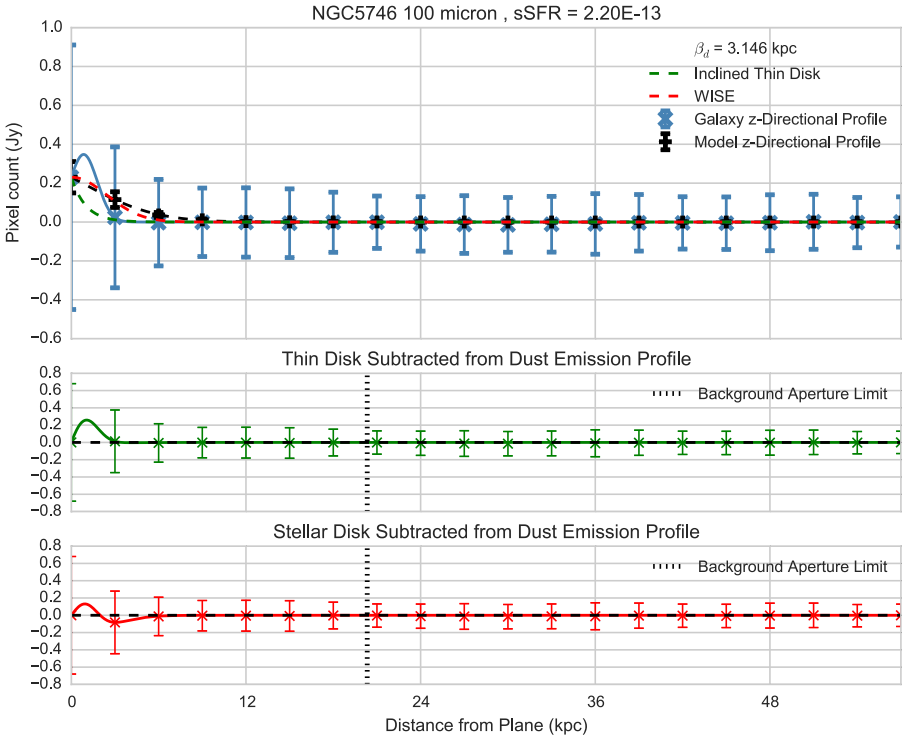
NGC5746 100 micron , sSFR = 2.20E-13
β_d = 3.146 kpc
Inclined Thin Disk
WISE
Galaxy z-Directional Profile
Model z-Directional Profile
Pixel count (Jy)
Thin Disk Subtracted from Dust Emission Profile
Background Aperture Limit
Stellar Disk Subtracted from Dust Emission Profile
Background Aperture Limit
Distance from Plane (kpc)

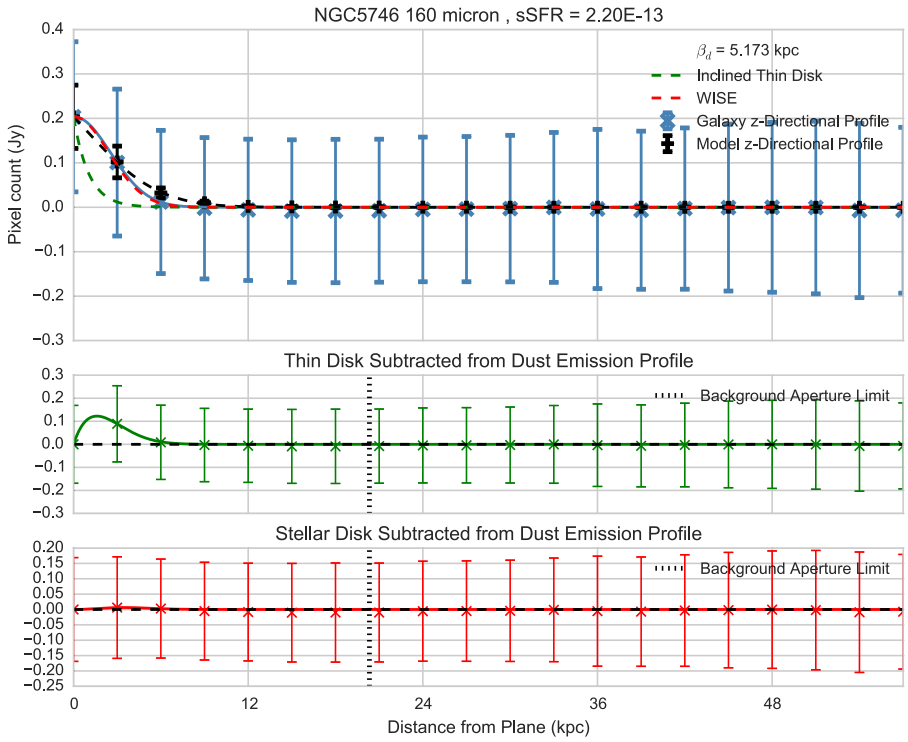
NGC5746 160 micron , sSFR = 2.20E-13
β_d = 5.173 kpc
Inclined Thin Disk
WISE
Galaxy z-Directional Profile
Model z-Directional Profile
Pixel count (Jy)
Thin Disk Subtracted from Dust Emission Profile
Background Aperture Limit
Stellar Disk Subtracted from Dust Emission Profile
Background Aperture Limit
Distance from Plane (kpc)

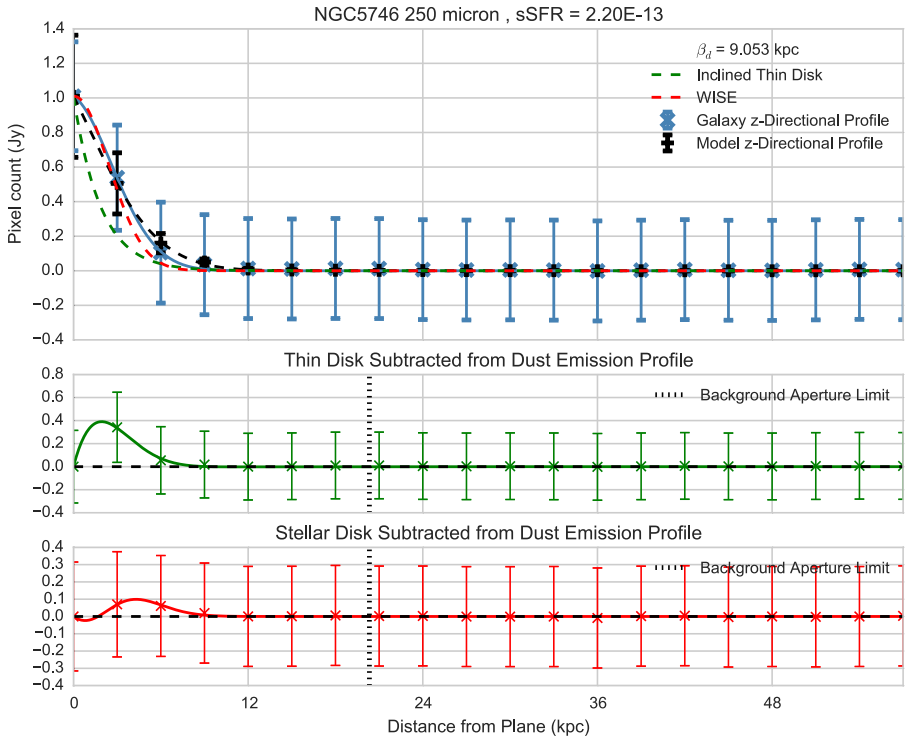
NGC5746 250 micron , sSFR = 2.20E-13
β_d = 9.053 kpc
Inclined Thin Disk
WISE
Galaxy z-Directional Profile
Model z-Directional Profile
Pixel count (Jy)
Thin Disk Subtracted from Dust Emission Profile
Background Aperture Limit
Stellar Disk Subtracted from Dust Emission Profile
Background Aperture Limit
Distance from Plane (kpc)

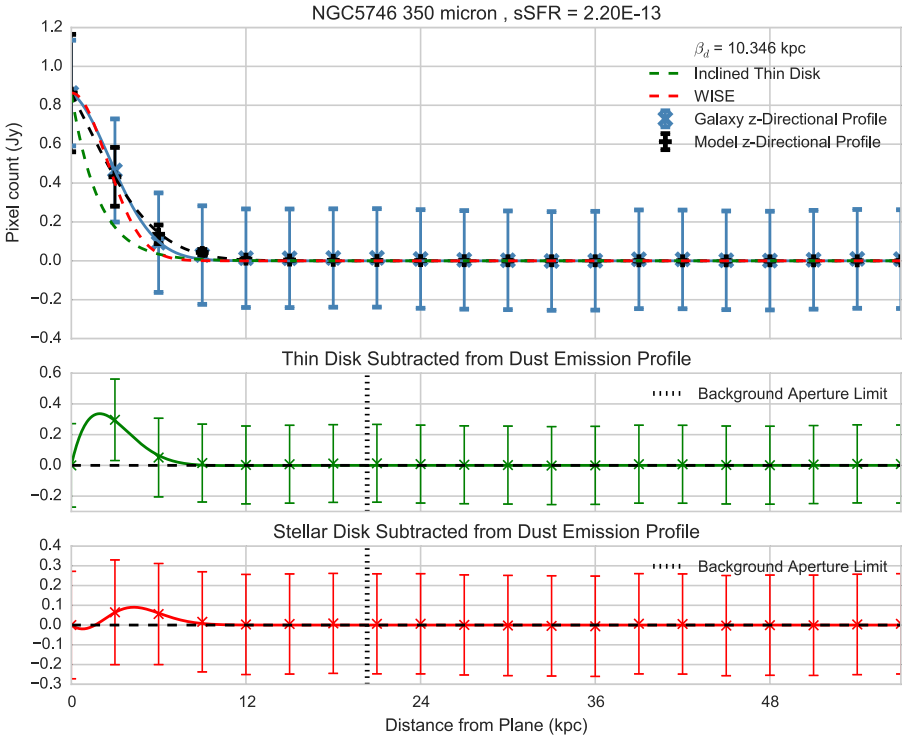
NGC5746 350 micron , sSFR = 2.20E-13
β_d = 10.346 kpc
Inclined Thin Disk
WISE
Galaxy z-Directional Profile
Model z-Directional Profile
Pixel count (Jy)
Thin Disk Subtracted from Dust Emission Profile
Background Aperture Limit
Stellar Disk Subtracted from Dust Emission Profile
Background Aperture Limit
Distance from Plane (kpc)

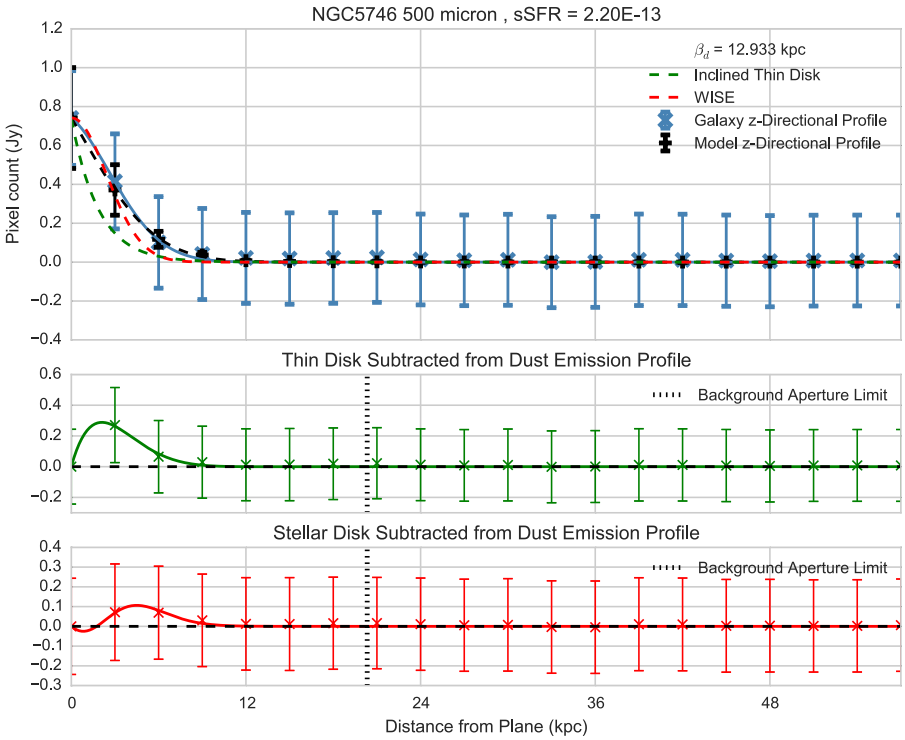
NGC5746 500 micron , sSFR = 2.20E-13
β_d = 12.933 kpc
Inclined Thin Disk
WISE
Galaxy z-Directional Profile
Model z-Directional Profile
Pixel count (Jy)
Thin Disk Subtracted from Dust Emission Profile
Background Aperture Limit
Stellar Disk Subtracted from Dust Emission Profile
Background Aperture Limit
Distance from Plane (kpc)

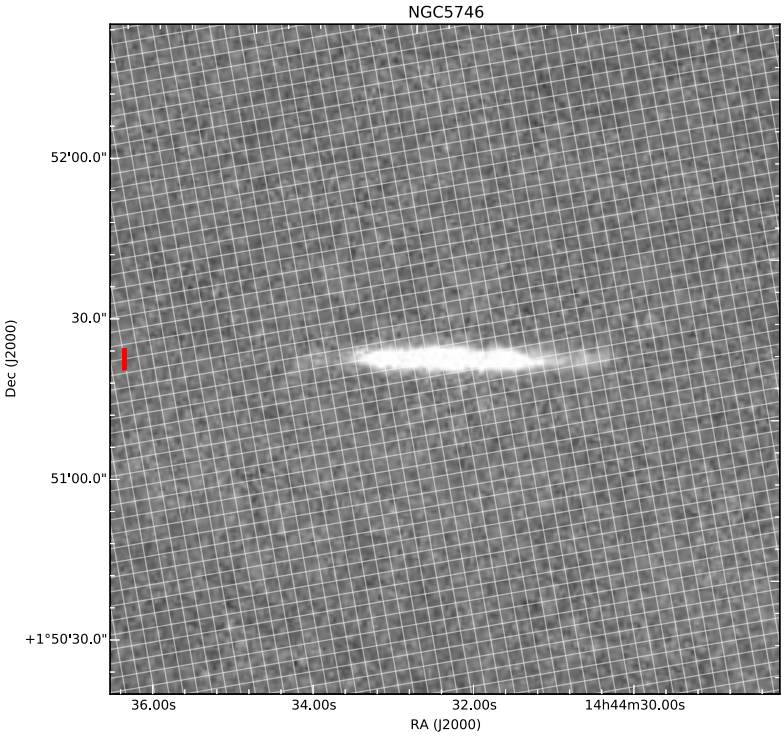

Figure A.206: 100 μm

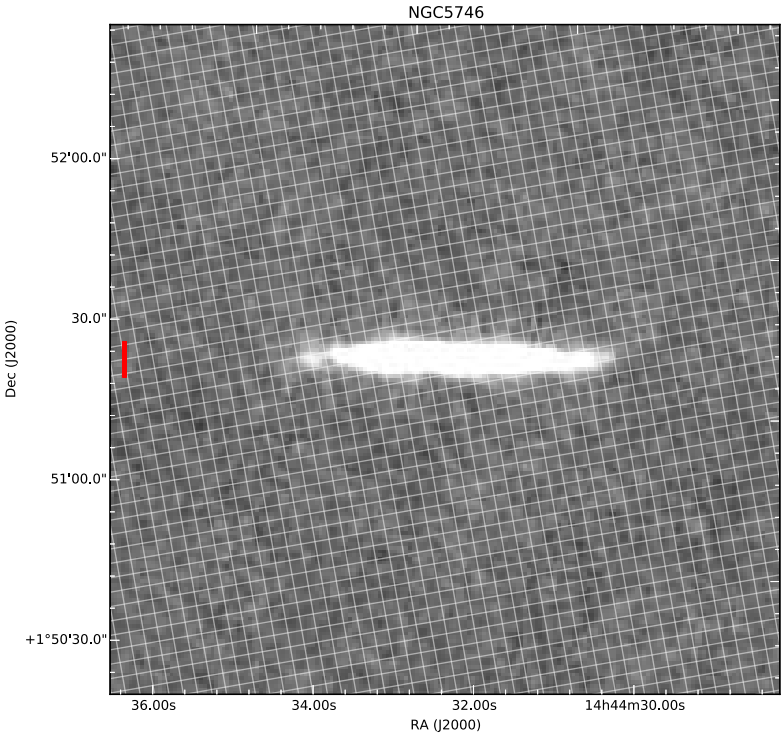

Figure A.207: 160 μm

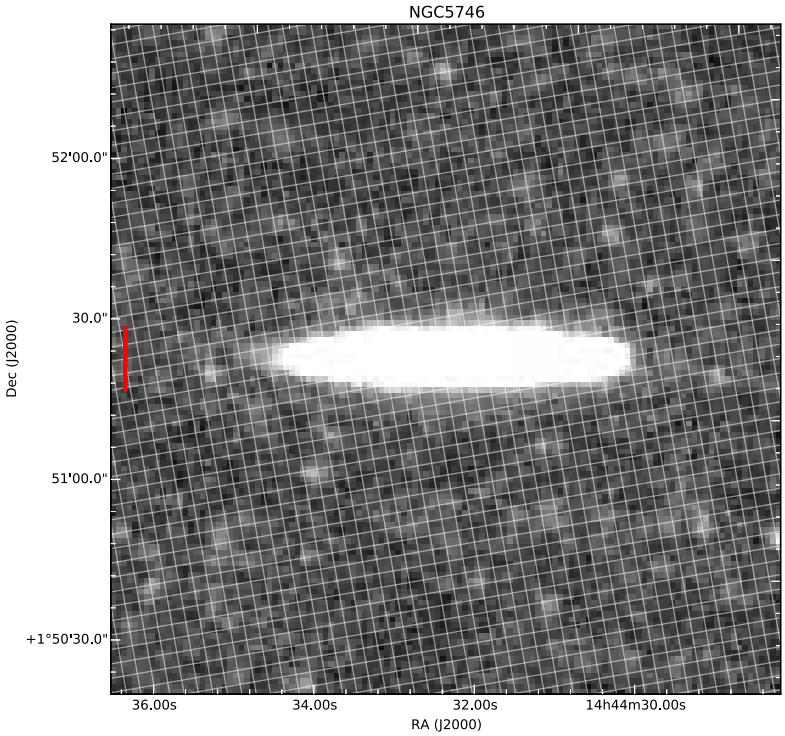

Figure A.208: 250 μm

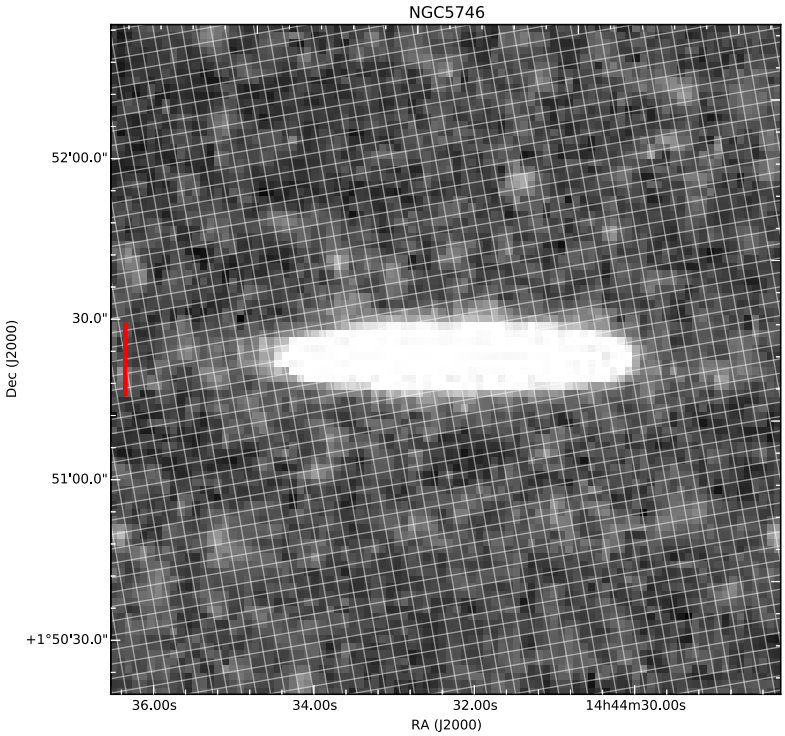

Figure A.209: 350 μm

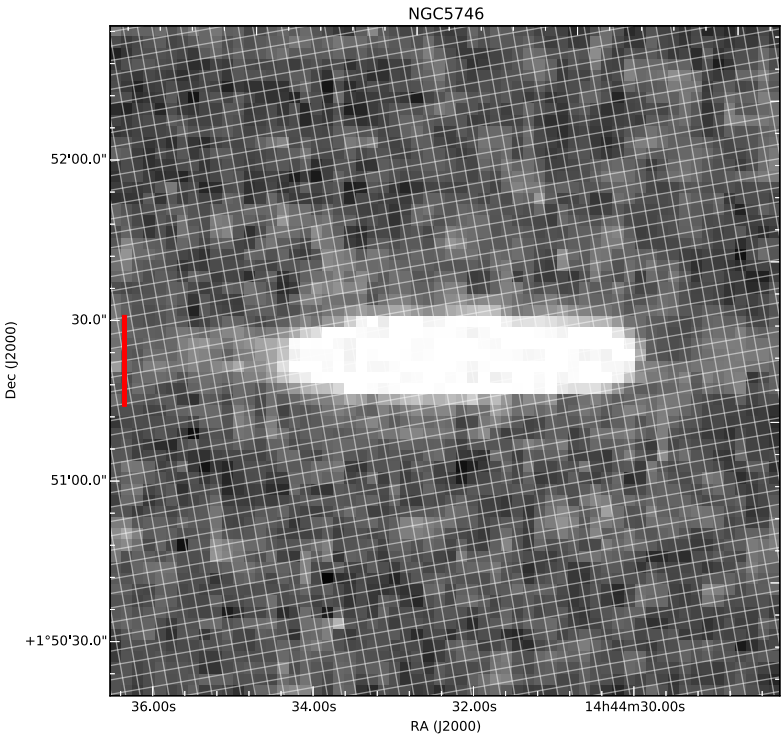

Figure A.210: 500 μm

A.27 NGC5907

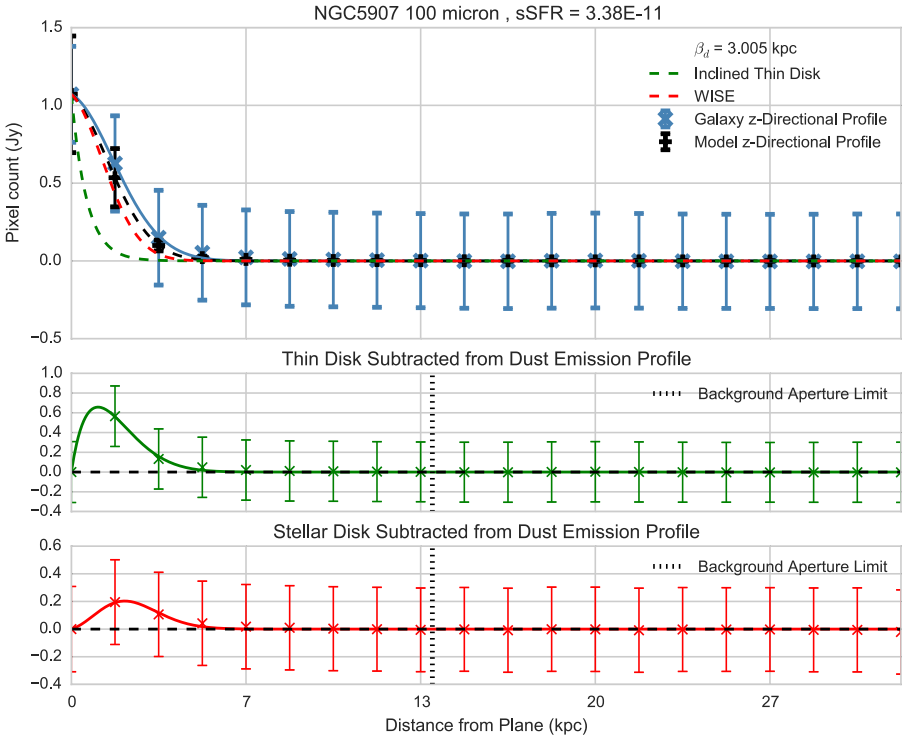
NGC5907 100 micron , sSFR = 3.38E-11
β_d = 3.005 kpc
Inclined Thin Disk
WISE
Galaxy z-Directional Profile
Model z-Directional Profile
Pixel count (Jy)
Thin Disk Subtracted from Dust Emission Profile
Background Aperture Limit
Stellar Disk Subtracted from Dust Emission Profile
Background Aperture Limit
Distance from Plane (kpc)

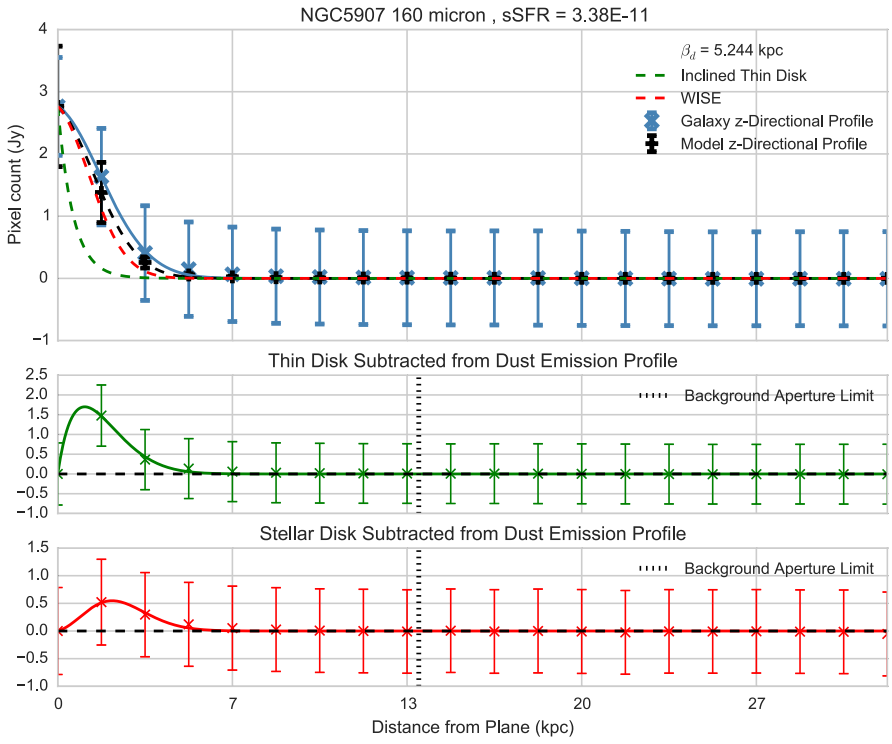
NGC5907 160 micron , sSFR = 3.38E-11
β_d = 5.244 kpc
Inclined Thin Disk
WISE
Galaxy z-Directional Profile
Model z-Directional Profile
Pixel count (Jy)
Thin Disk Subtracted from Dust Emission Profile
Background Aperture Limit
Stellar Disk Subtracted from Dust Emission Profile
Background Aperture Limit
Distance from Plane (kpc)

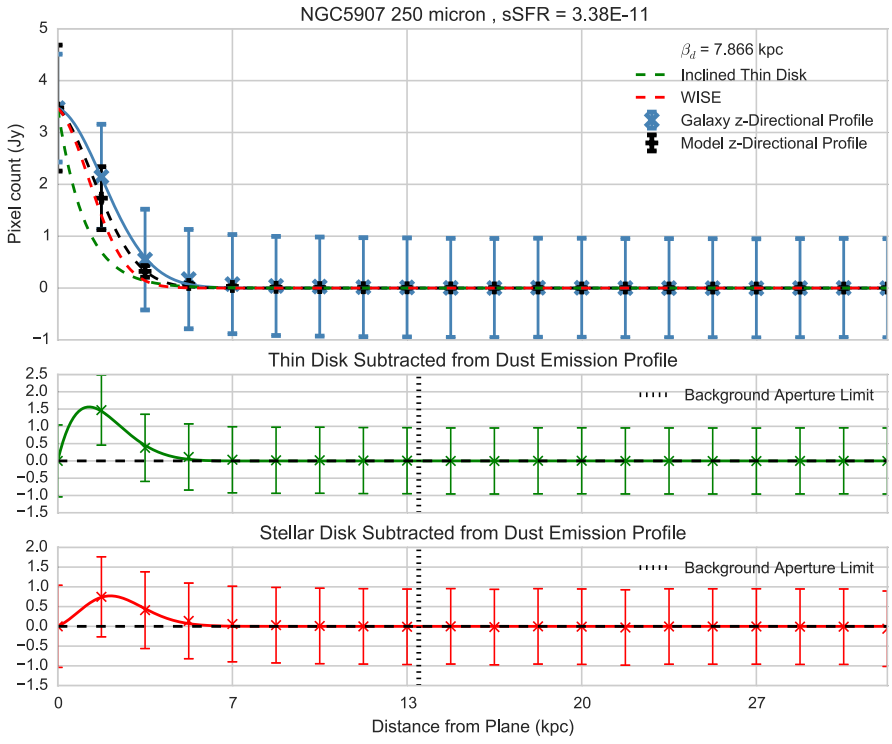
NGC5907 250 micron , sSFR = 3.38E-11
β_d = 7.866 kpc
Inclined Thin Disk
WISE
Galaxy z-Directional Profile
Model z-Directional Profile
Pixel count (Jy)
Thin Disk Subtracted from Dust Emission Profile
Background Aperture Limit
Stellar Disk Subtracted from Dust Emission Profile
Background Aperture Limit
Distance from Plane (kpc)

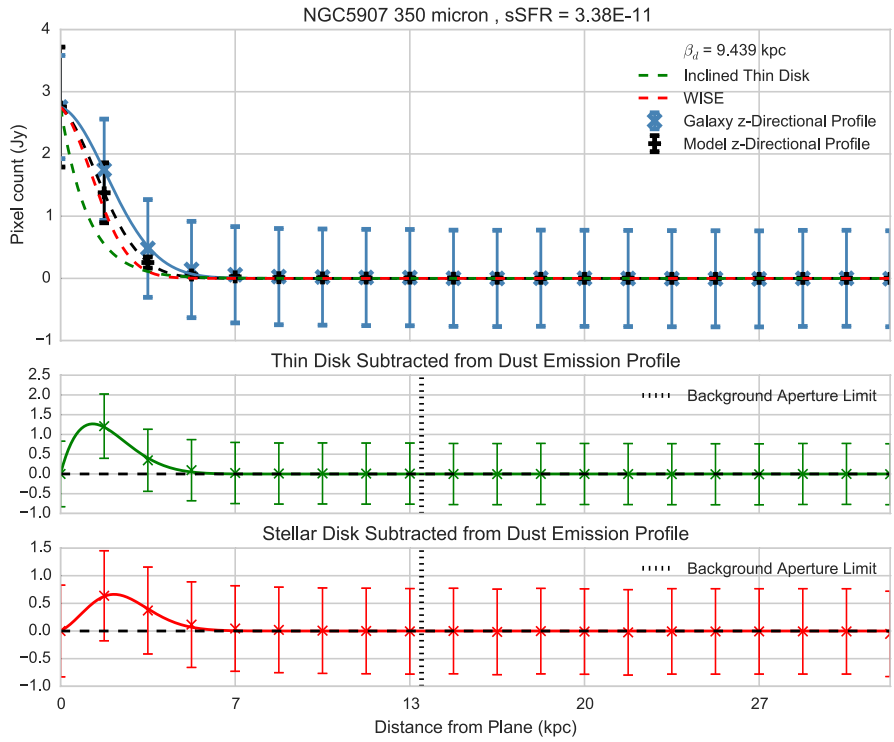
NGC5907 350 micron , sSFR = 3.38E-11
β_d = 9.439 kpc
Inclined Thin Disk
WISE
Galaxy z-Directional Profile
Model z-Directional Profile
Pixel count (Jy)
Thin Disk Subtracted from Dust Emission Profile
Background Aperture Limit
Stellar Disk Subtracted from Dust Emission Profile
Background Aperture Limit
Distance from Plane (kpc)

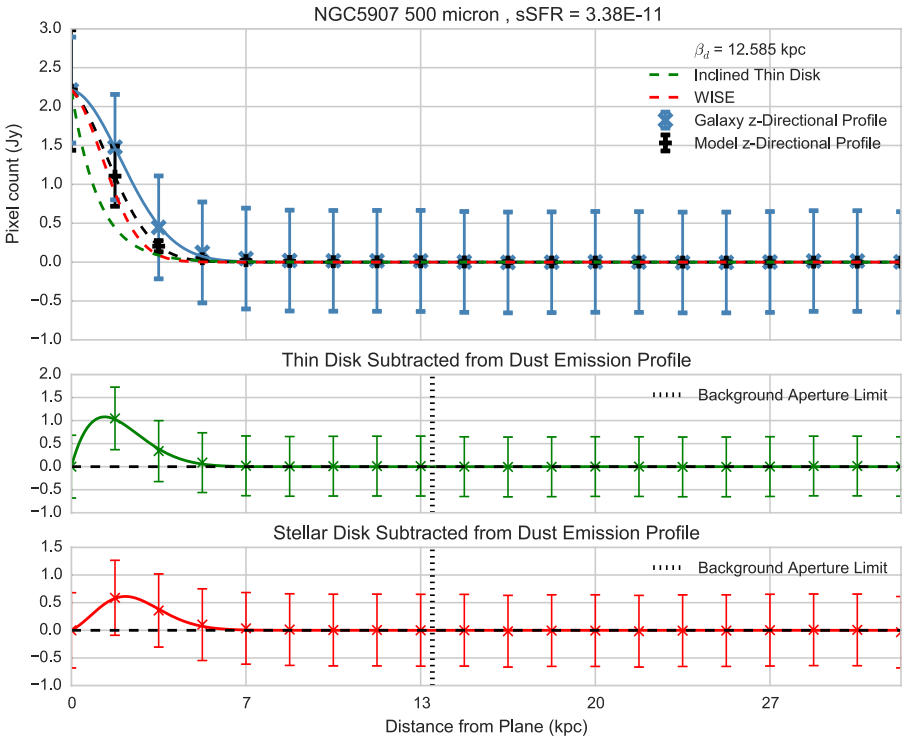
NGC5907 500 micron , sSFR = 3.38E-11
β_d = 12.585 kpc
Inclined Thin Disk
WISE
Galaxy z-Directional Profile
Model z-Directional Profile
Pixel count (Jy)
Thin Disk Subtracted from Dust Emission Profile
Background Aperture Limit
Stellar Disk Subtracted from Dust Emission Profile
Background Aperture Limit
Distance from Plane (kpc)

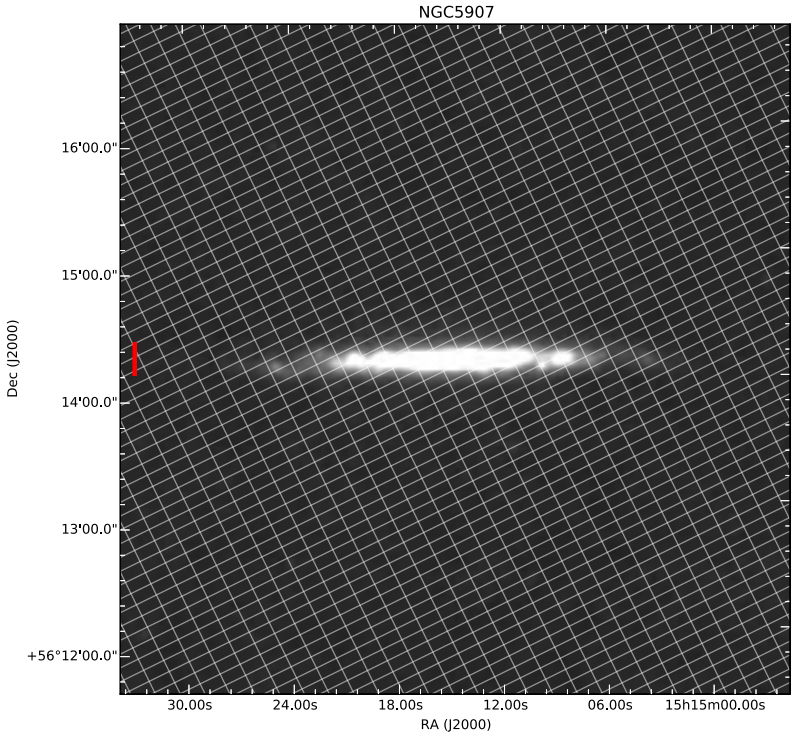

Figure A.211: 100 μm

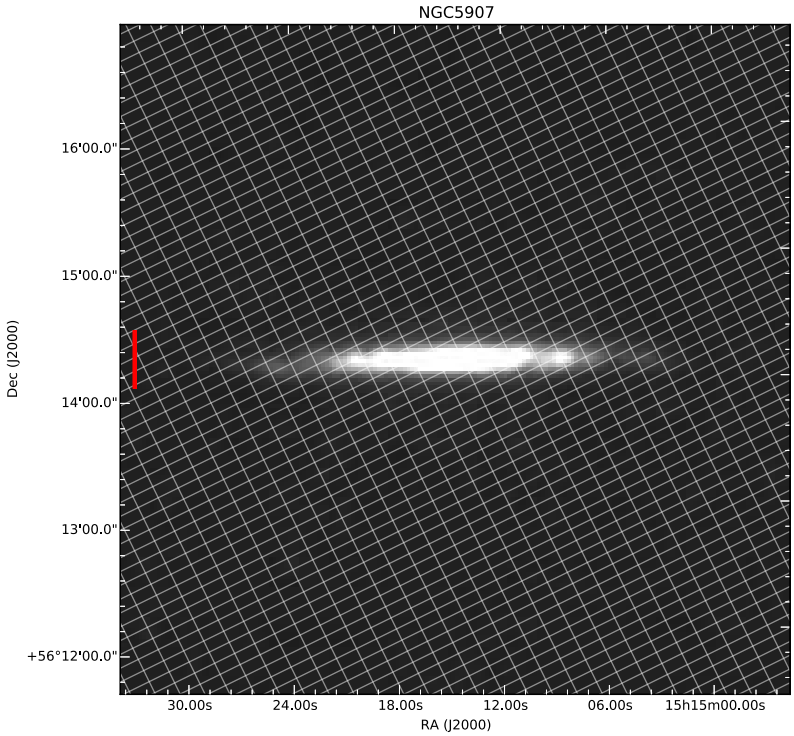

Figure A.212: 160 μm

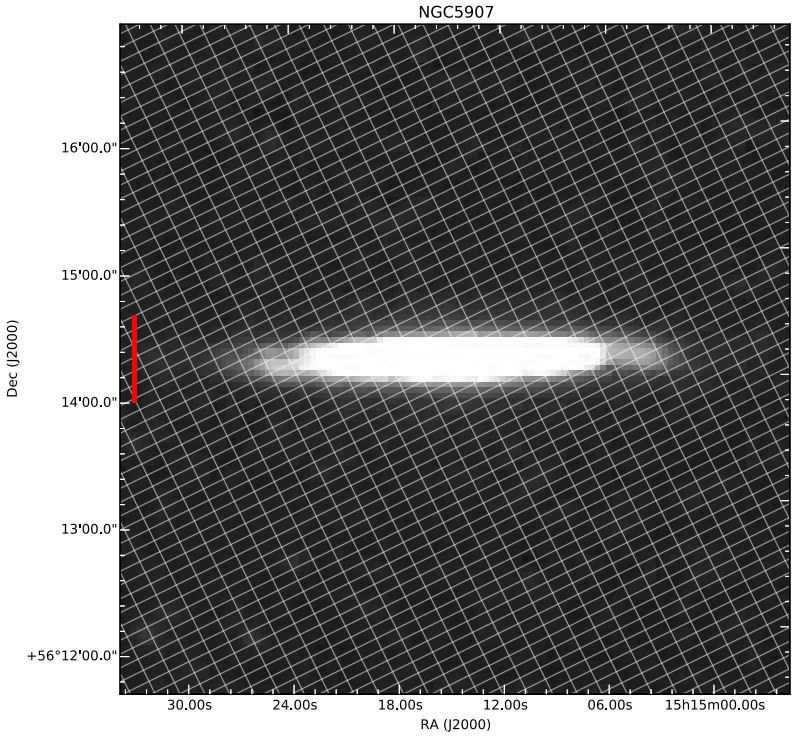

Figure A.213: 250 μm

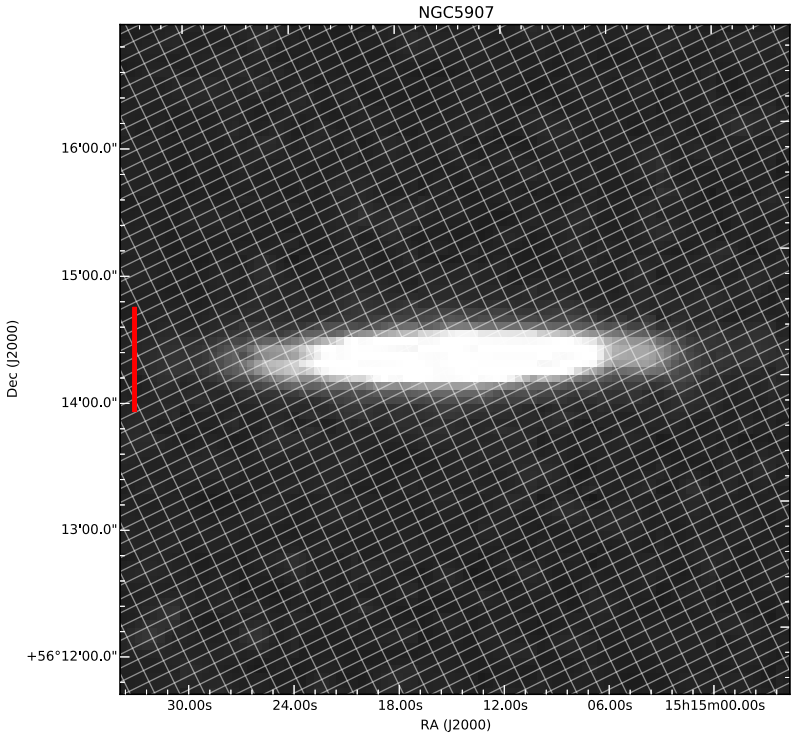

Figure A.214: 350 μm

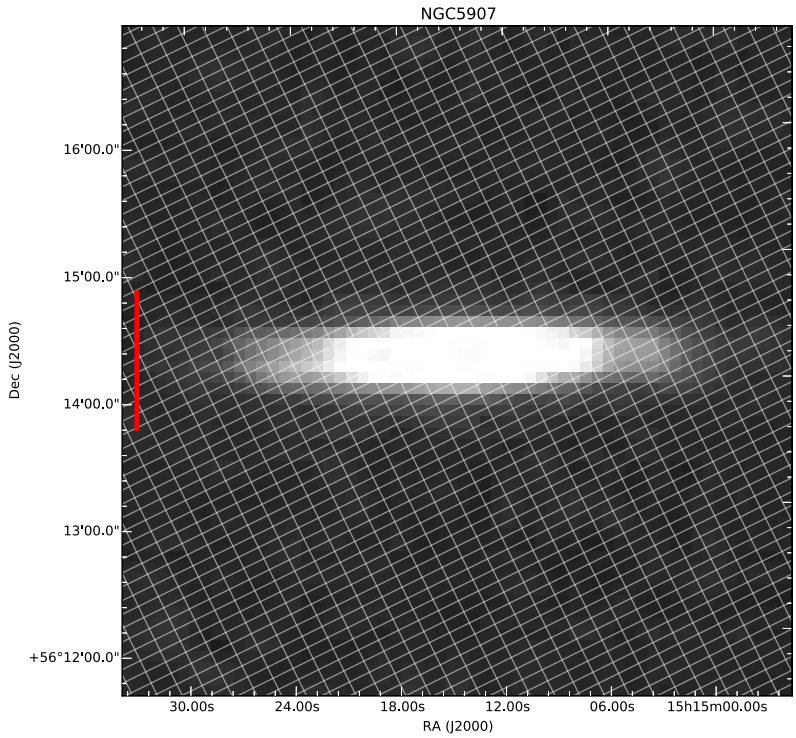

Figure A.215: 500 μm

A.28 NGC7090

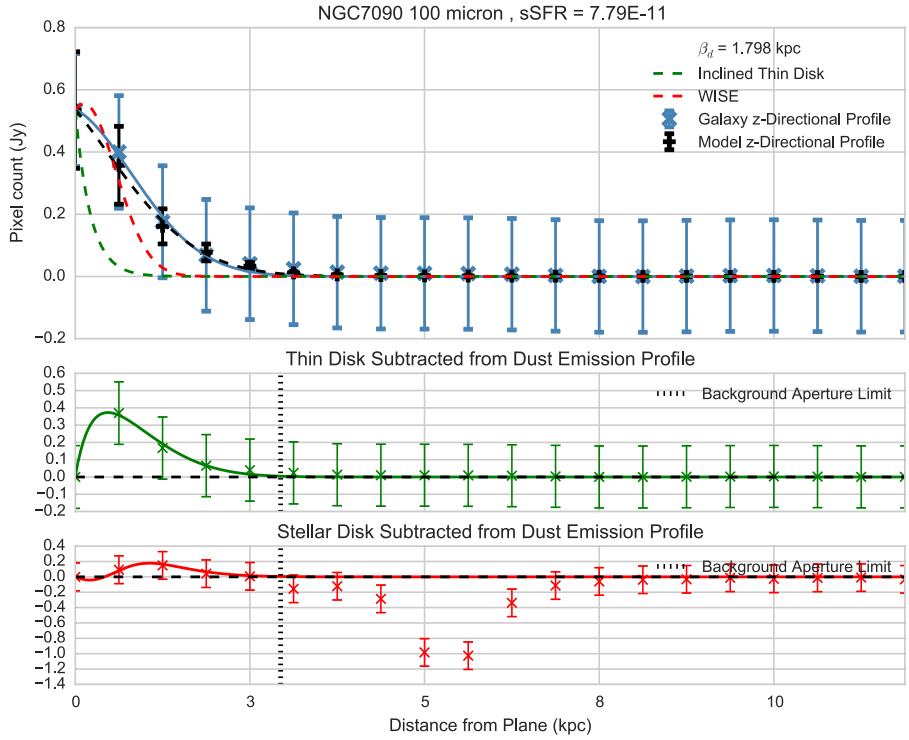
NGC7090 100 micron , sSFR = 7.79E-11
β_d = 1.798 kpc
Inclined Thin Disk
WISE
Galaxy z-Directional Profile
Model z-Directional Profile
Pixel count (Jy)
Thin Disk Subtracted from Dust Emission Profile
Background Aperture Limit
Stellar Disk Subtracted from Dust Emission Profile
Background Aperture Limit
Distance from Plane (kpc)

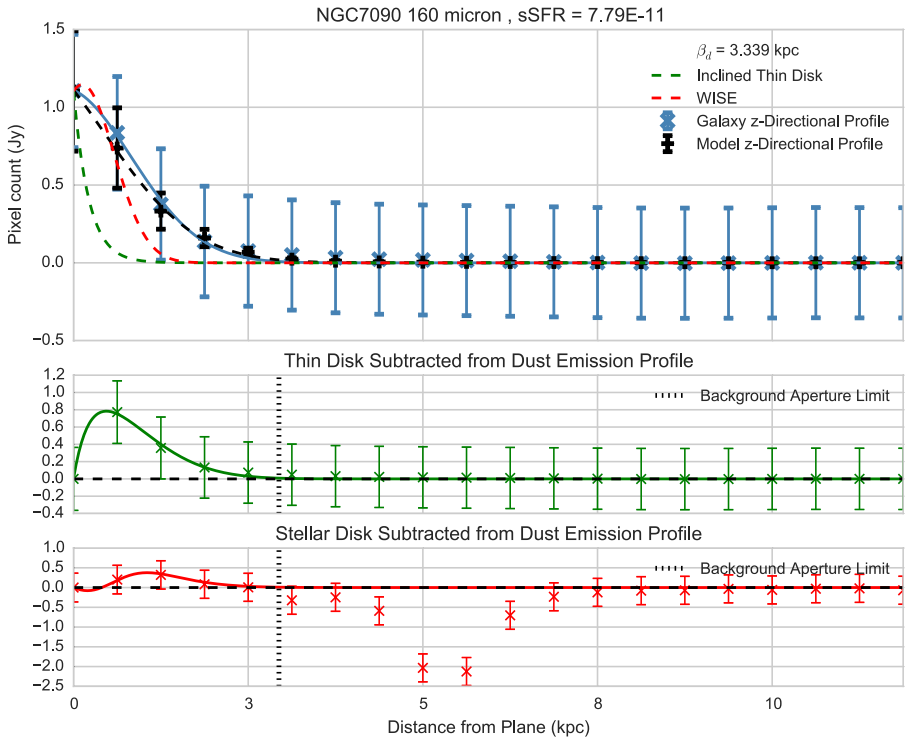
NGC7090 160 micron , sSFR = 7.79E-11
β_d = 3.339 kpc
Inclined Thin Disk
WISE
Galaxy z-Directional Profile
Model z-Directional Profile
Pixel count (Jy)
Thin Disk Subtracted from Dust Emission Profile
Background Aperture Limit
Stellar Disk Subtracted from Dust Emission Profile
Background Aperture Limit
Distance from Plane (kpc)

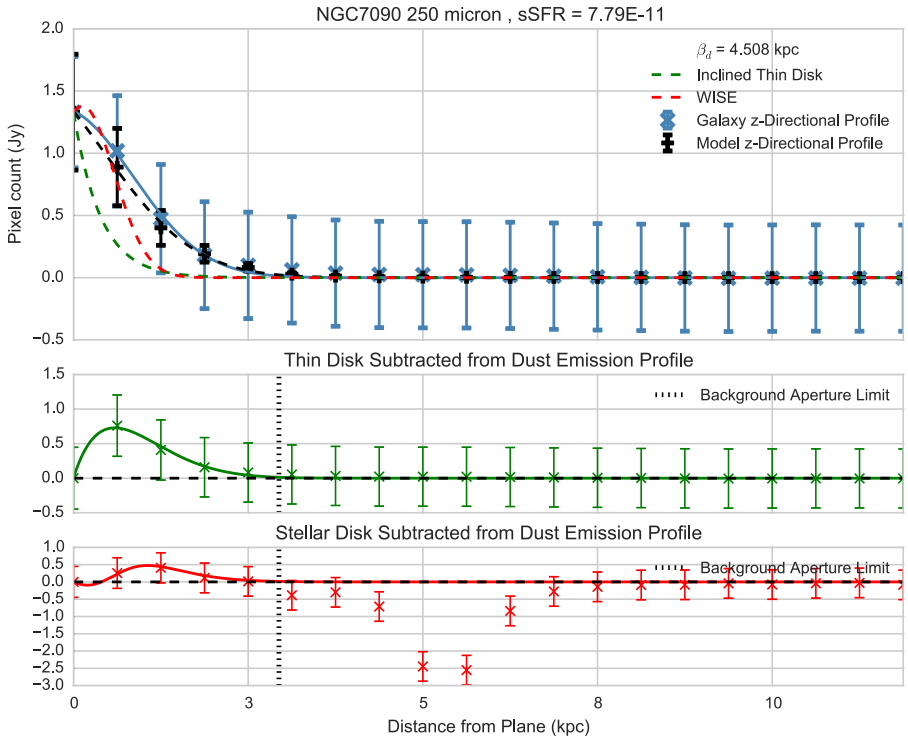
NGC7090 250 micron , sSFR = 7.79E-11
β_d = 4.508 kpc
Inclined Thin Disk
WISE
Galaxy z-Directional Profile
Model z-Directional Profile
Pixel count (Jy)
Thin Disk Subtracted from Dust Emission Profile
Background Aperture Limit
Stellar Disk Subtracted from Dust Emission Profile
Background Aperture Limit
Distance from Plane (kpc)

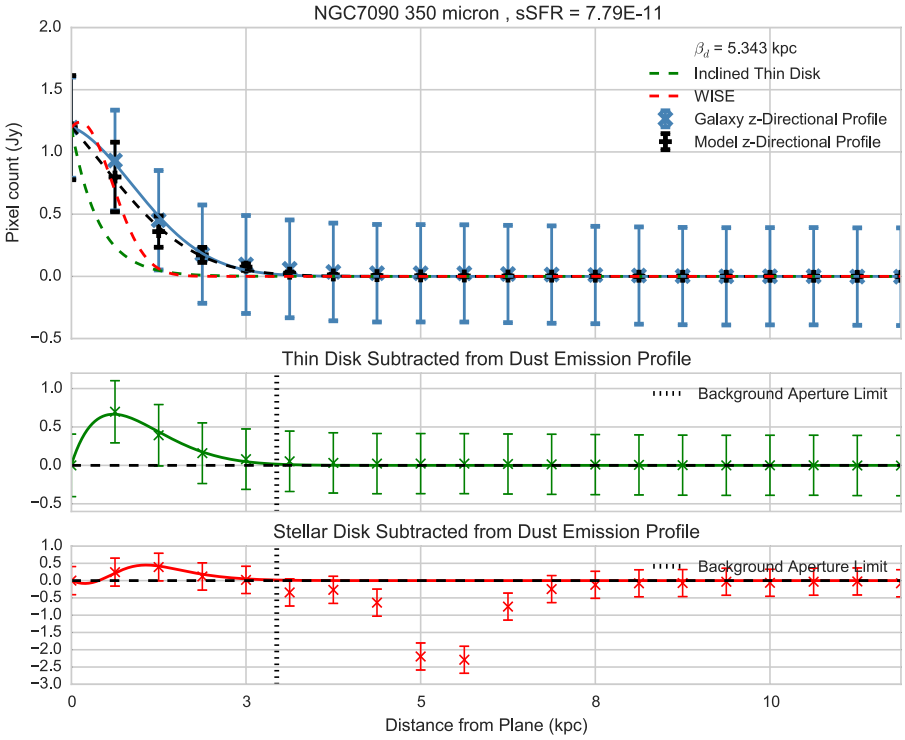
NGC7090 350 micron , sSFR = 7.79E-11
β_d = 5.343 kpc
Inclined Thin Disk
WISE
Galaxy z-Directional Profile
Model z-Directional Profile
Pixel count (Jy)
Thin Disk Subtracted from Dust Emission Profile
Background Aperture Limit
Stellar Disk Subtracted from Dust Emission Profile
Background Aperture Limit
Distance from Plane (kpc)

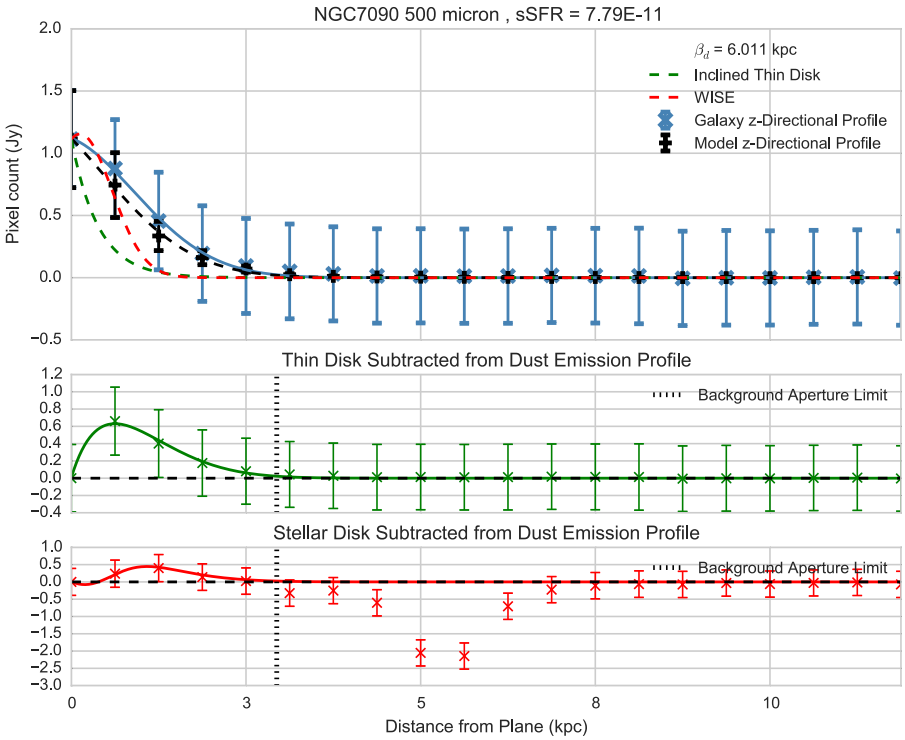
NGC7090 500 micron , sSFR = 7.79E-11
β_d = 6.011 kpc
Inclined Thin Disk
WISE
Galaxy z-Directional Profile
Model z-Directional Profile
Pixel count (Jy)
Thin Disk Subtracted from Dust Emission Profile
Background Aperture Limit
Stellar Disk Subtracted from Dust Emission Profile
Background Aperture Limit
Distance from Plane (kpc)

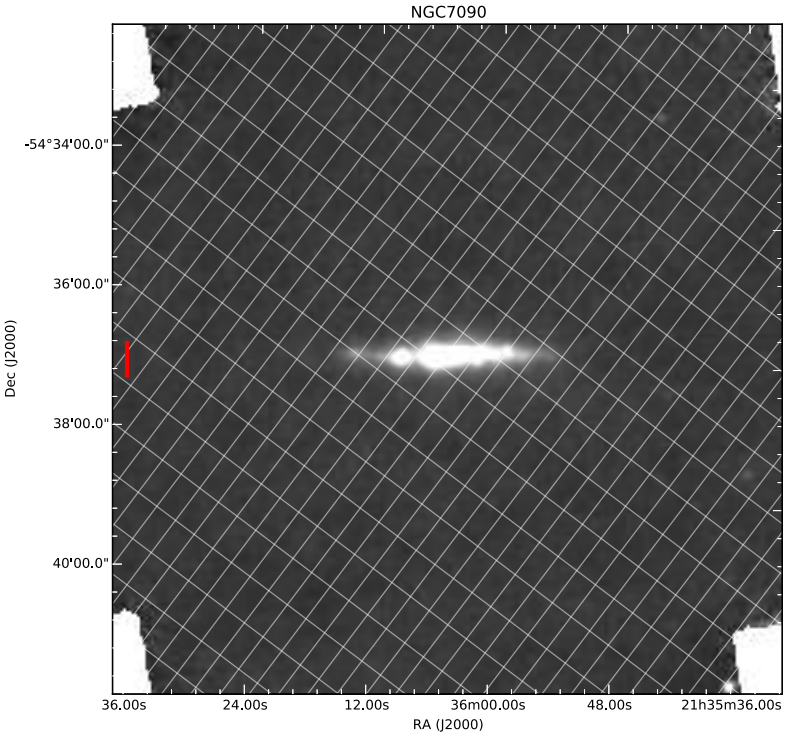

Figure A.216: 100 μm

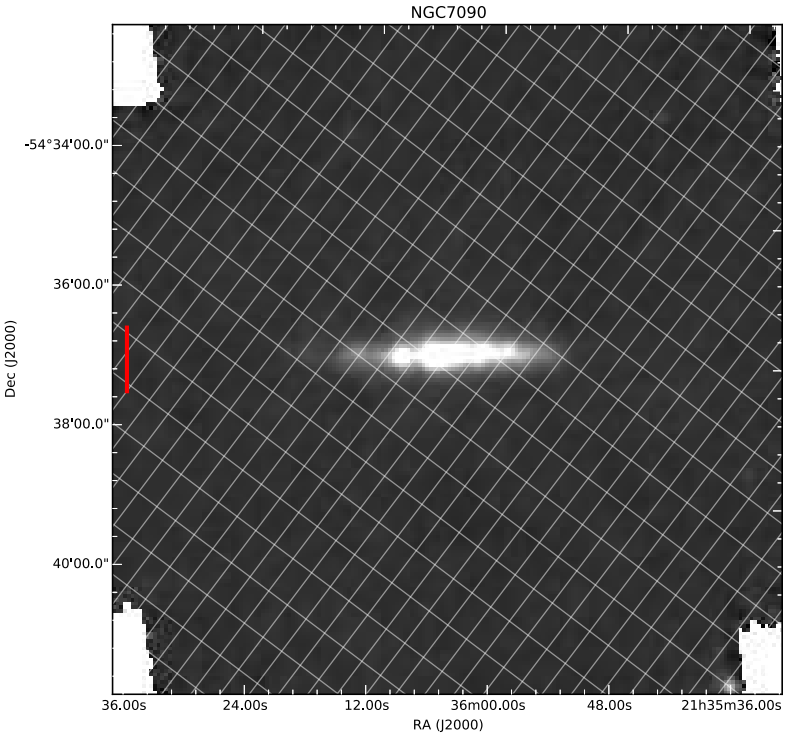

Figure A.217: 160 μm

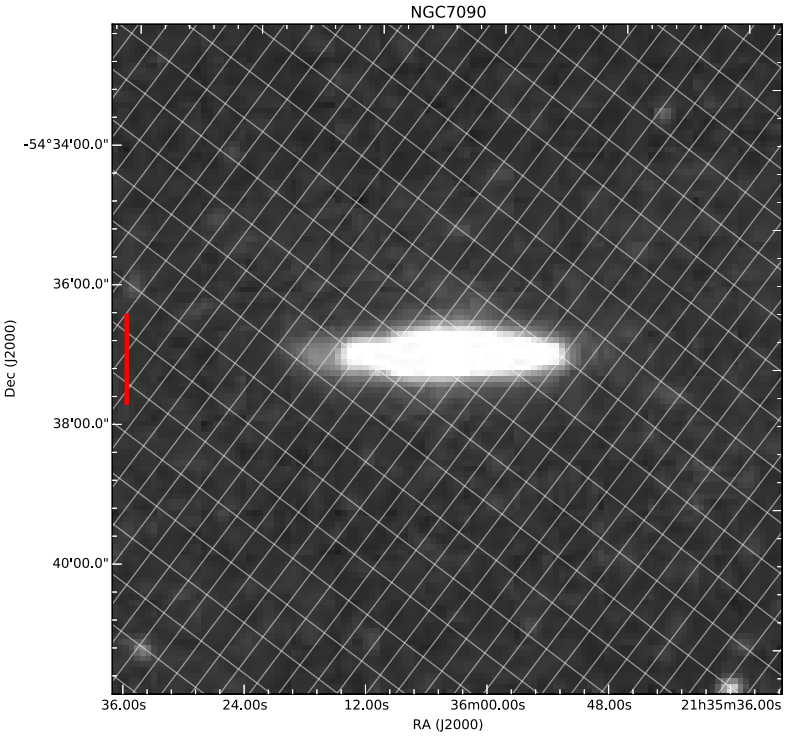

Figure A.218: 250 μm

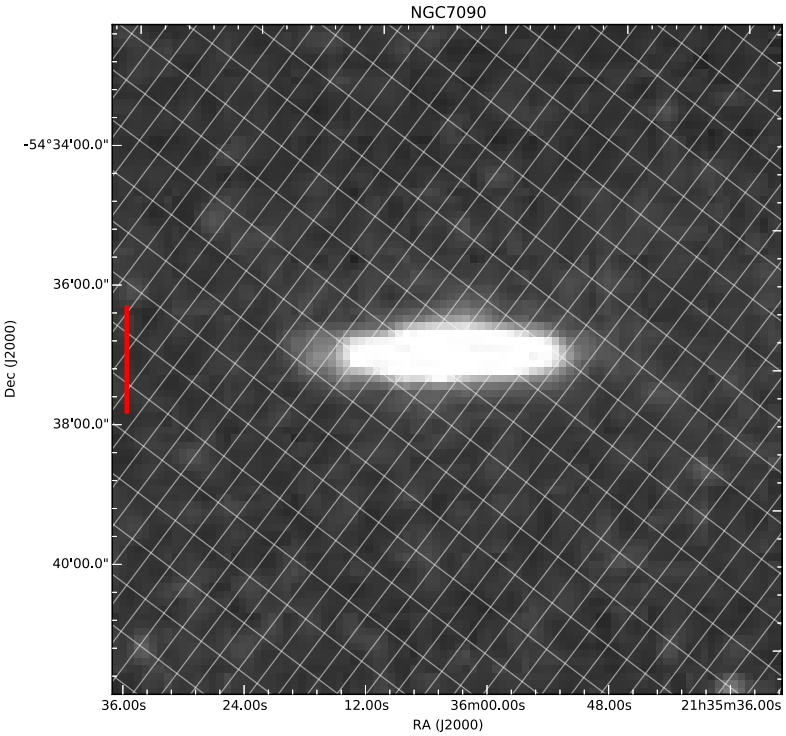

Figure A.219: 350 μm

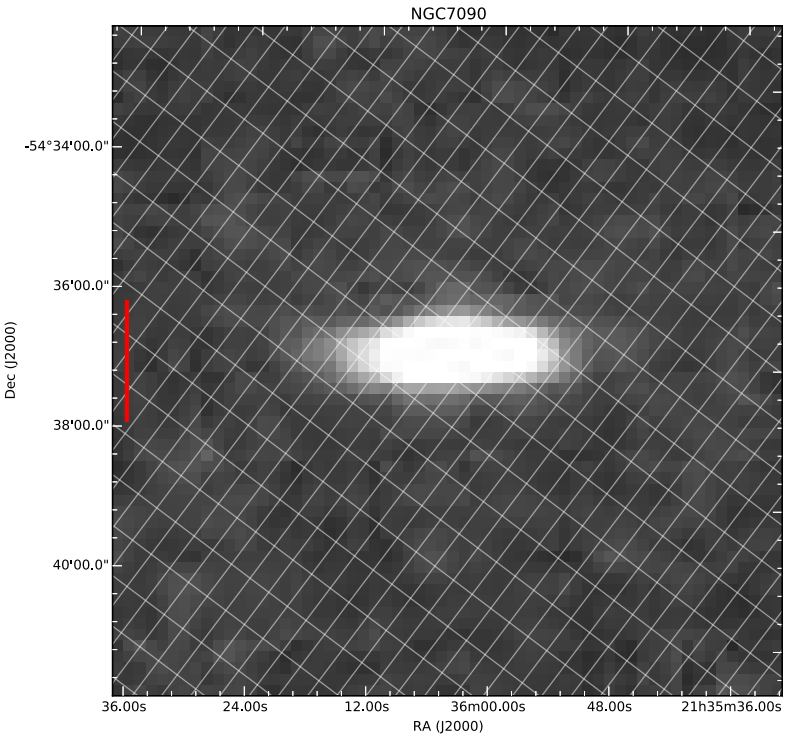

Figure A.220: 500 μm

A.29 UGC07321

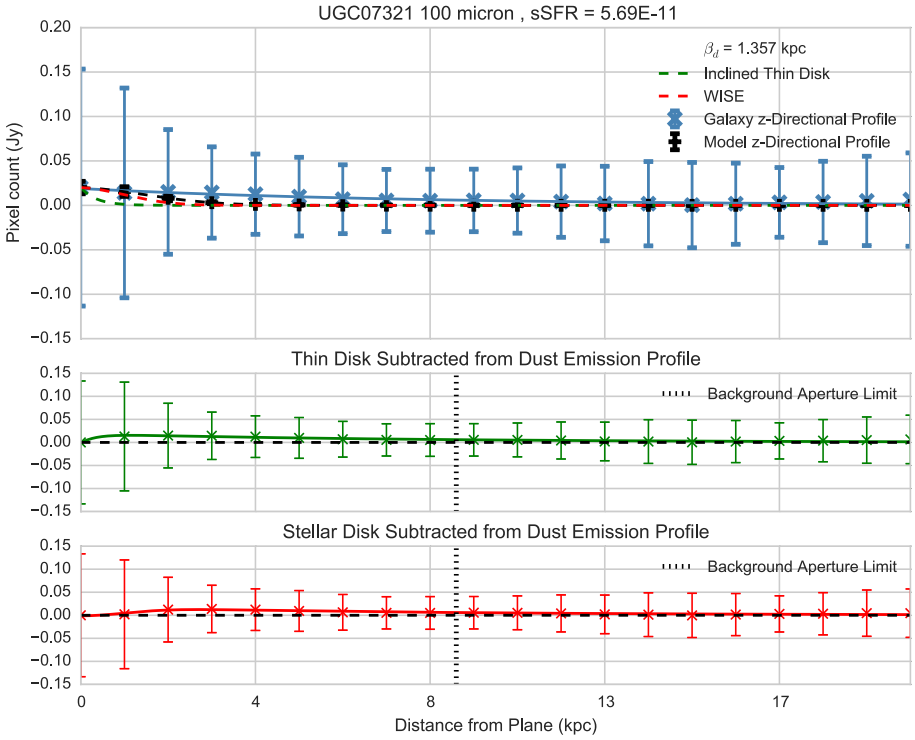

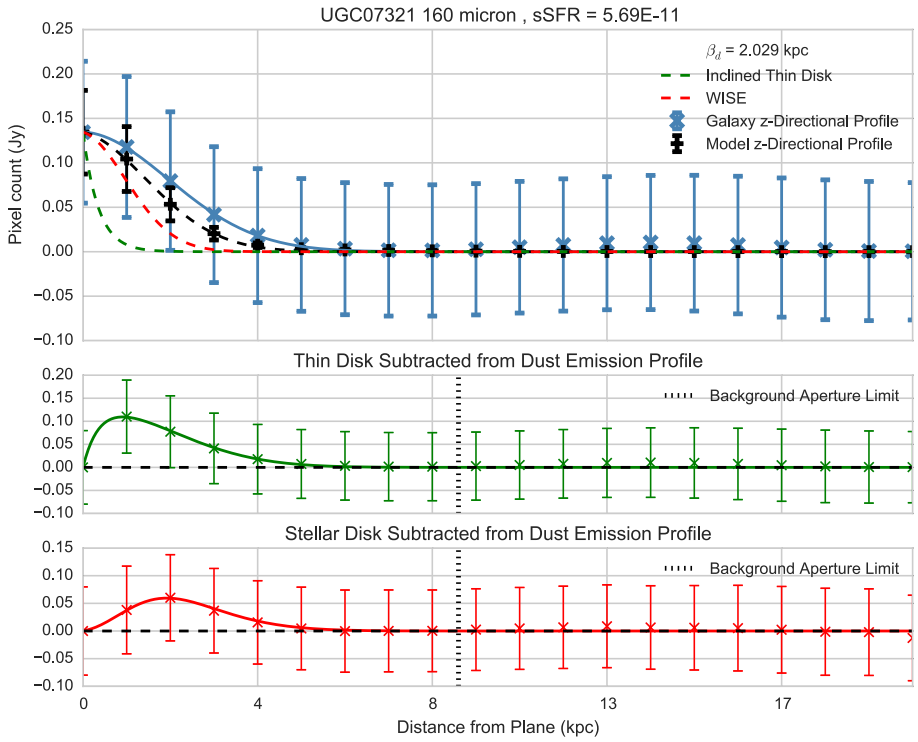
UGC07321 160 micron , sSFR = 5.69E-11
β_d = 2.029 kpc
Inclined Thin Disk
WISE
Galaxy z-Directional Profile
Model z-Directional Profile
Pixel count (Jy)
Thin Disk Subtracted from Dust Emission Profile
Background Aperture Limit
Stellar Disk Subtracted from Dust Emission Profile
Background Aperture Limit
Distance from Plane (kpc)

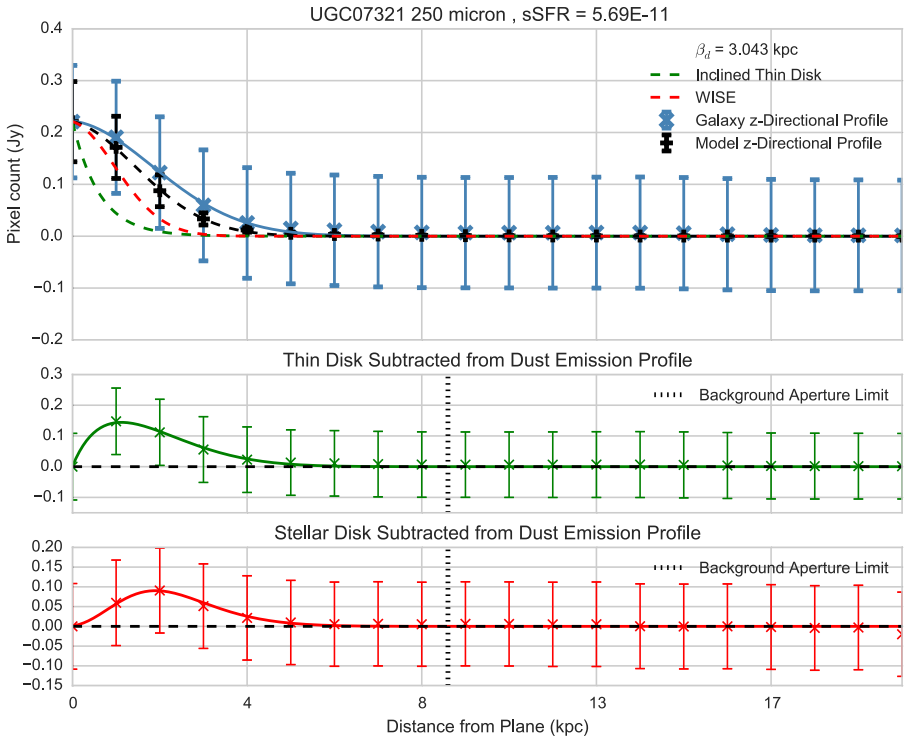
UGC07321 250 micron , sSFR = 5.69E-11
β_d = 3.043 kpc
Inclined Thin Disk
WISE
Galaxy z-Directional Profile
Model z-Directional Profile
Pixel count (Jy)
Thin Disk Subtracted from Dust Emission Profile
Background Aperture Limit
Stellar Disk Subtracted from Dust Emission Profile
Background Aperture Limit
Distance from Plane (kpc)

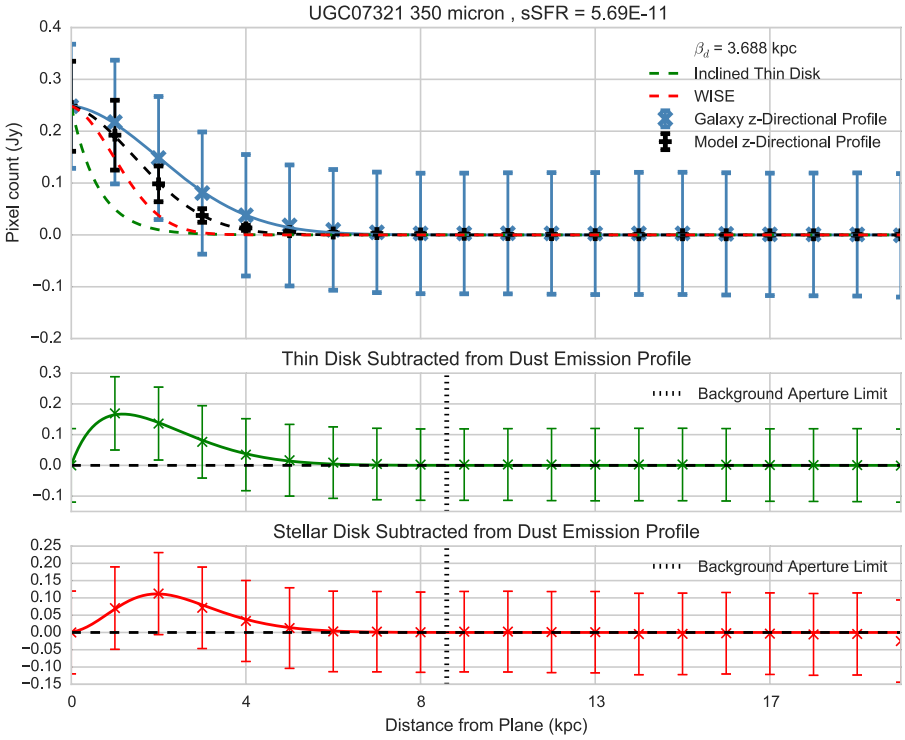
UGC07321 350 micron , sSFR = 5.69E-11
β_d = 3.688 kpc
Inclined Thin Disk
WISE
Galaxy z-Directional Profile
Model z-Directional Profile
Pixel count (Jy)
Thin Disk Subtracted from Dust Emission Profile
Background Aperture Limit
Stellar Disk Subtracted from Dust Emission Profile
Background Aperture Limit
Distance from Plane (kpc)

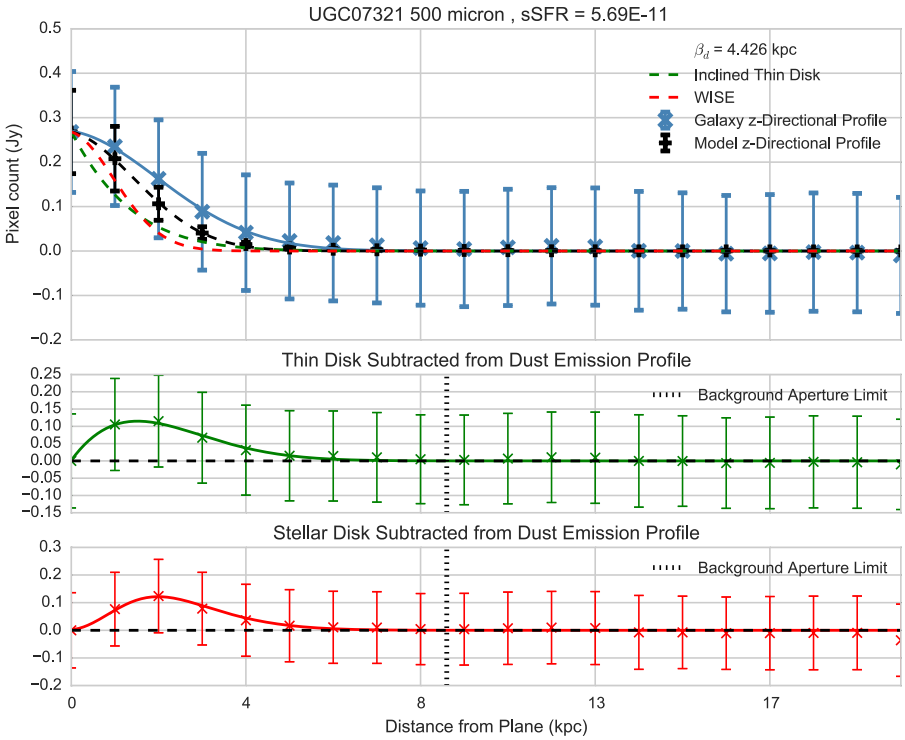
UGC07321 500 micron , sSFR = 5.69E-11
β_d = 4.426 kpc
Inclined Thin Disk
WISE
Galaxy z-Directional Profile
Model z-Directional Profile
Pixel count (Jy)
Thin Disk Subtracted from Dust Emission Profile
Background Aperture Limit
Stellar Disk Subtracted from Dust Emission Profile
Background Aperture Limit
Distance from Plane (kpc)

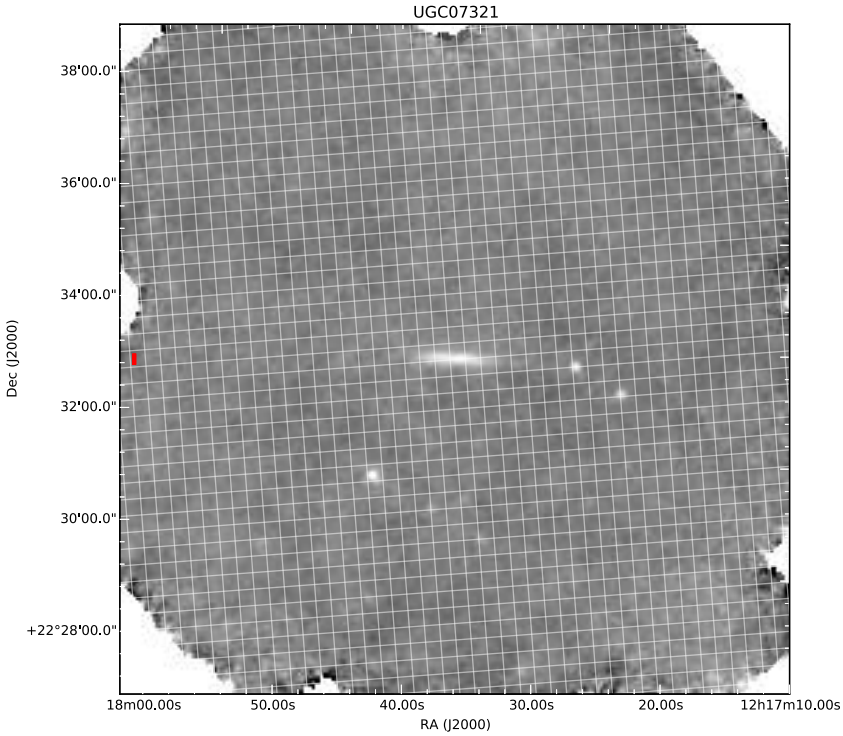

Figure A.221: 100 μm

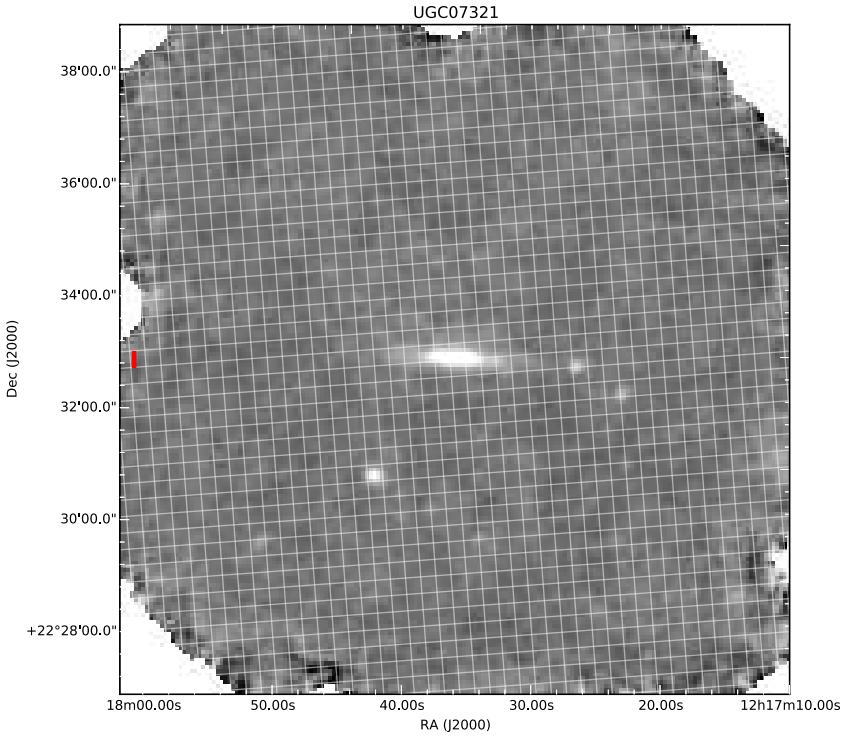

Figure A.222: 160 μm

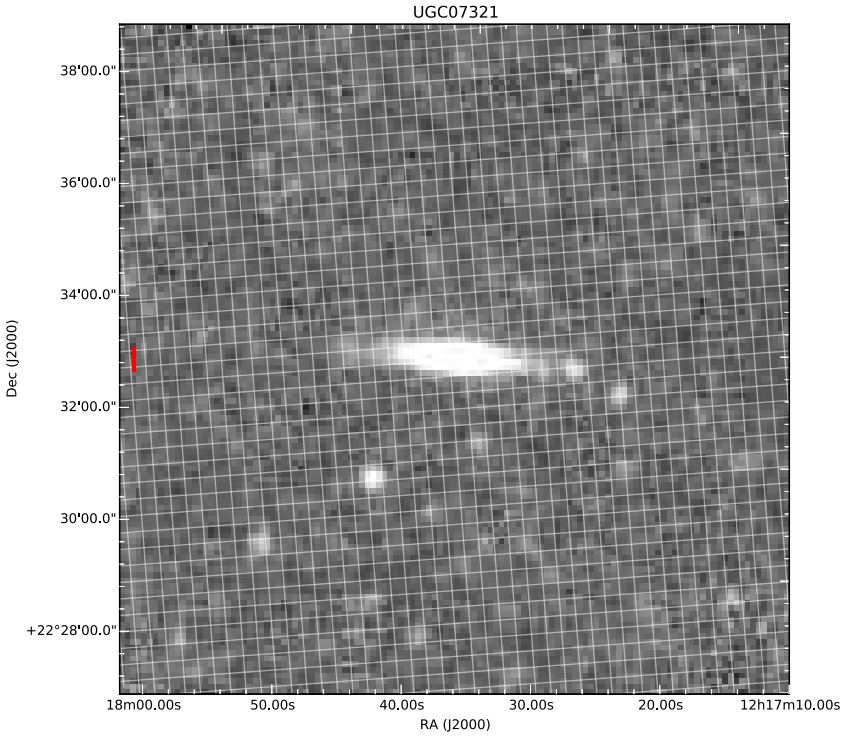

Figure A.223: 250 μm

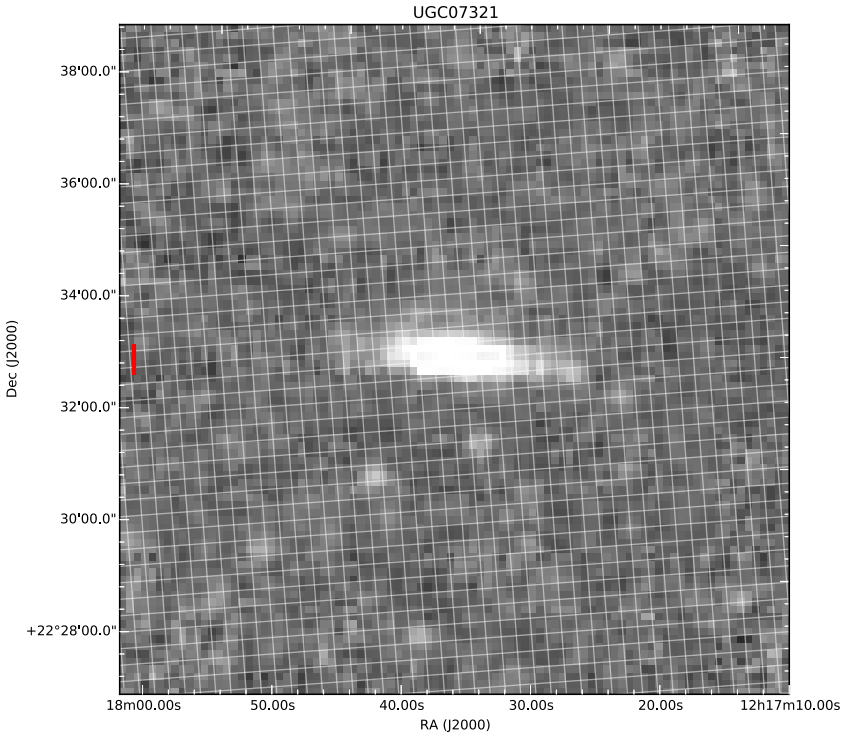

Figure A.224: 350 μm

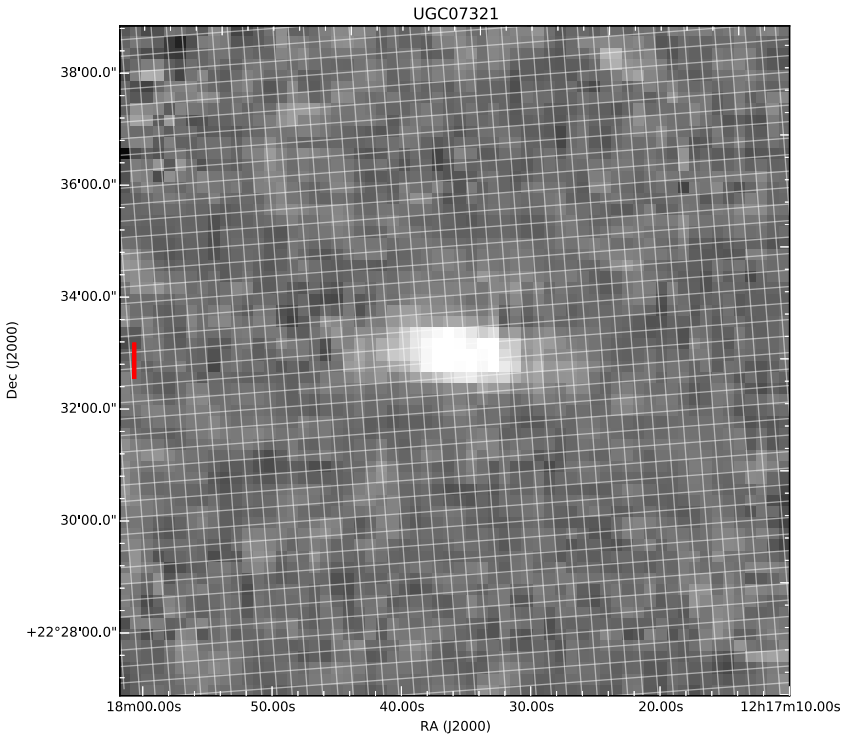

Figure A.225: 500 μm

A.30 UGC07522

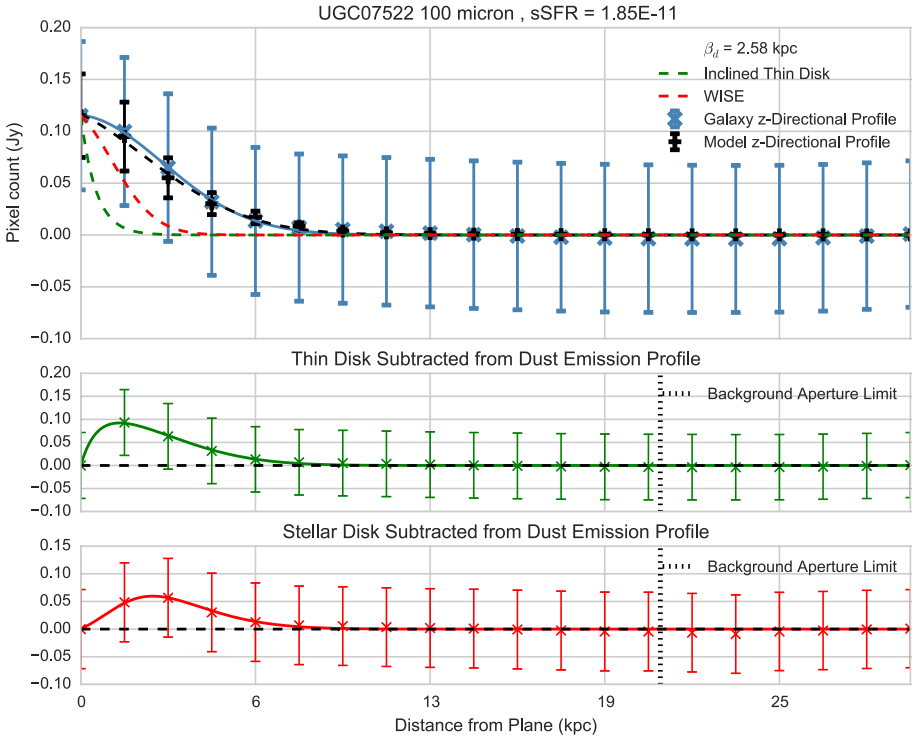

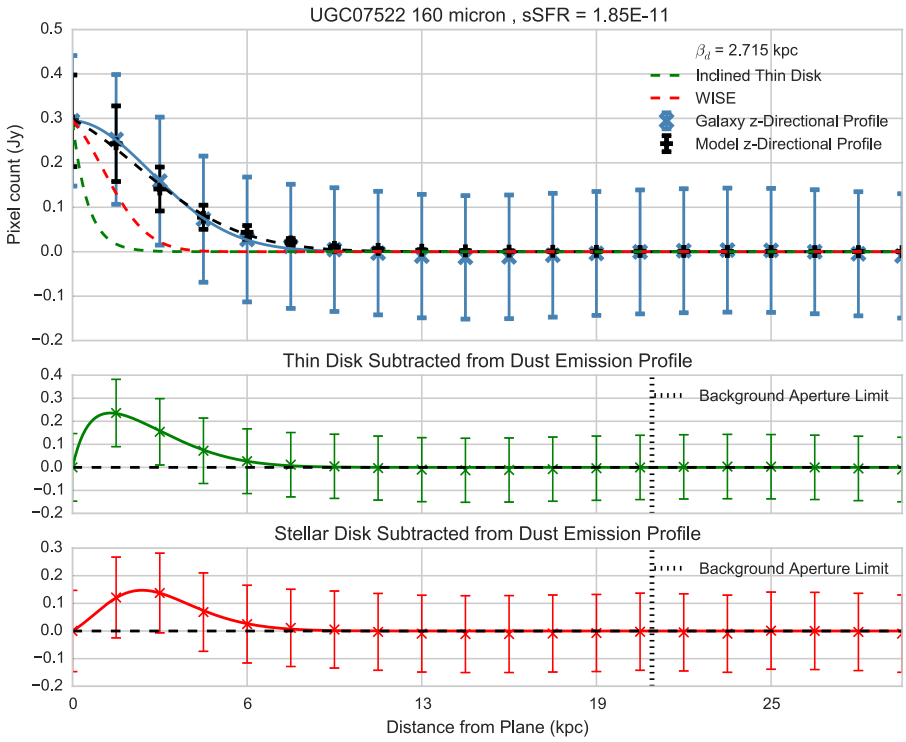
UGC07522 160 micron , sSFR = 1.85E-11
β_d = 2.715 kpc
Inclined Thin Disk
WISE
Galaxy z-Directional Profile
Model z-Directional Profile
Pixel count (Jy)
Thin Disk Subtracted from Dust Emission Profile
Background Aperture Limit
Stellar Disk Subtracted from Dust Emission Profile
Background Aperture Limit
Distance from Plane (kpc)

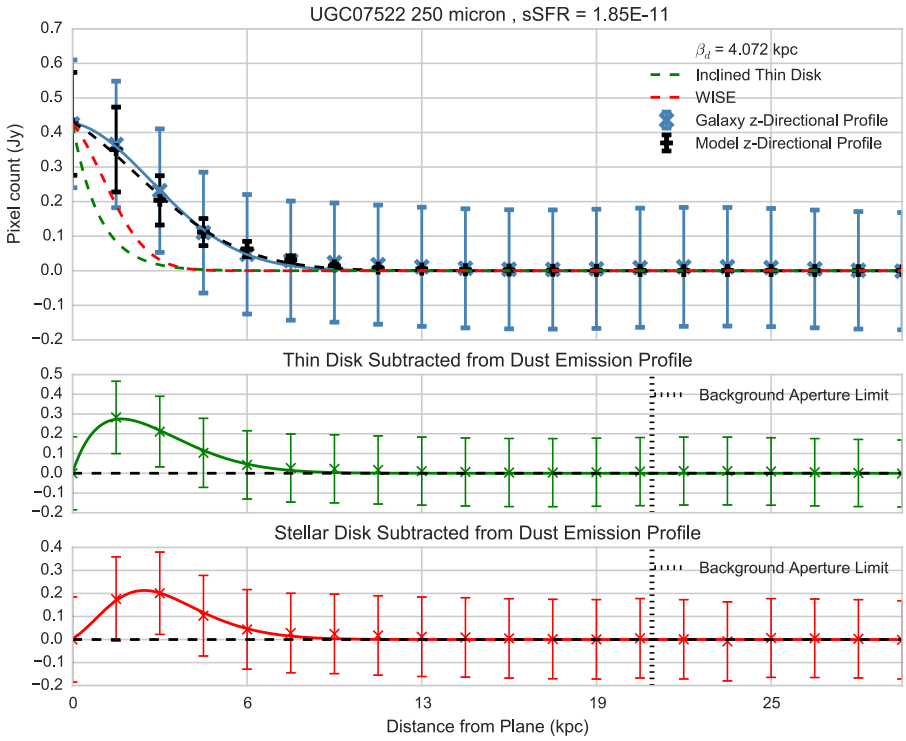
UGC07522 250 micron , sSFR = 1.85E-11
β_d = 4.072 kpc
Inclined Thin Disk
WISE
Galaxy z-Directional Profile
Model z-Directional Profile
Pixel count (Jy)
Thin Disk Subtracted from Dust Emission Profile
Background Aperture Limit
Stellar Disk Subtracted from Dust Emission Profile
Background Aperture Limit
Distance from Plane (kpc)

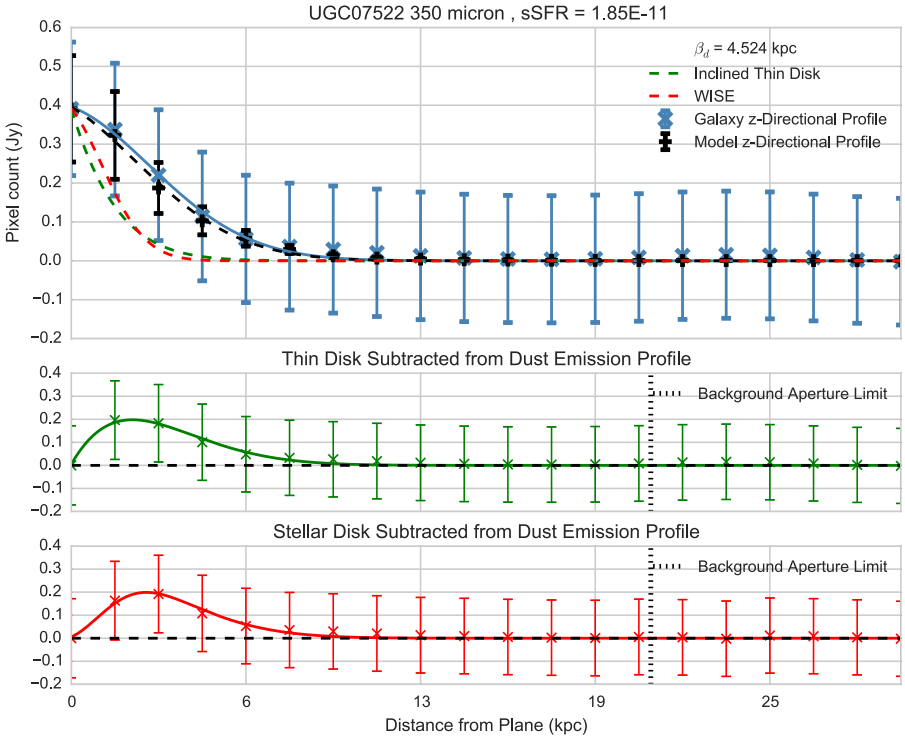
UGC07522 350 micron , sSFR = 1.85E-11
β_d = 4.524 kpc
Inclined Thin Disk
WISE
Galaxy z-Directional Profile
Model z-Directional Profile
Pixel count (Jy)
Thin Disk Subtracted from Dust Emission Profile
Background Aperture Limit
Stellar Disk Subtracted from Dust Emission Profile
Background Aperture Limit
Distance from Plane (kpc)

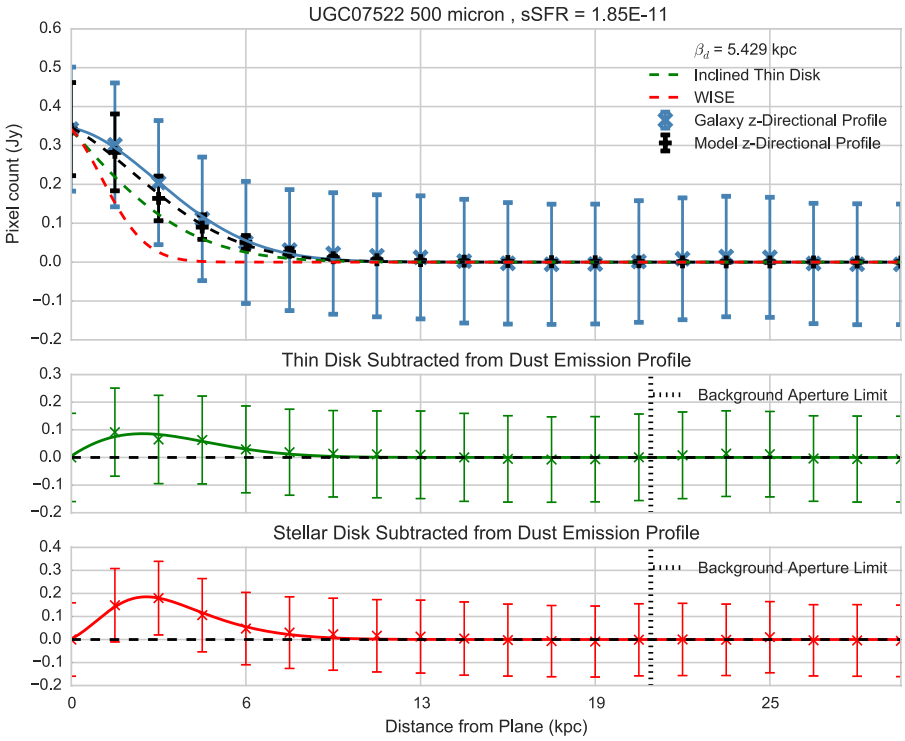
UGC07522 500 micron , sSFR = 1.85E-11
β_d = 5.429 kpc
Inclined Thin Disk
WISE
Galaxy z-Directional Profile
Model z-Directional Profile
Pixel count (Jy)
Thin Disk Subtracted from Dust Emission Profile
Background Aperture Limit
Stellar Disk Subtracted from Dust Emission Profile
Background Aperture Limit
Distance from Plane (kpc)

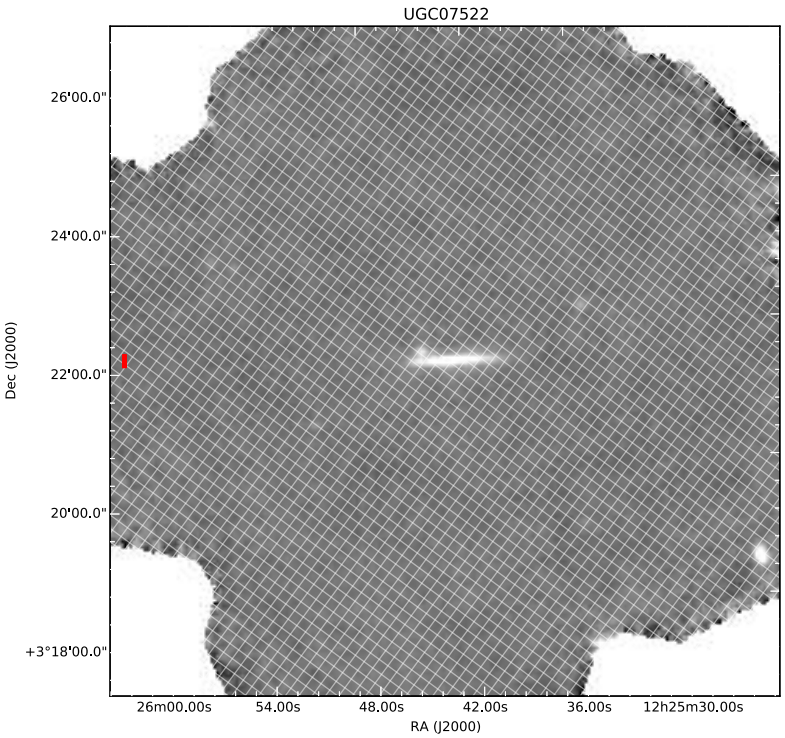

Figure A.226: 100 μm

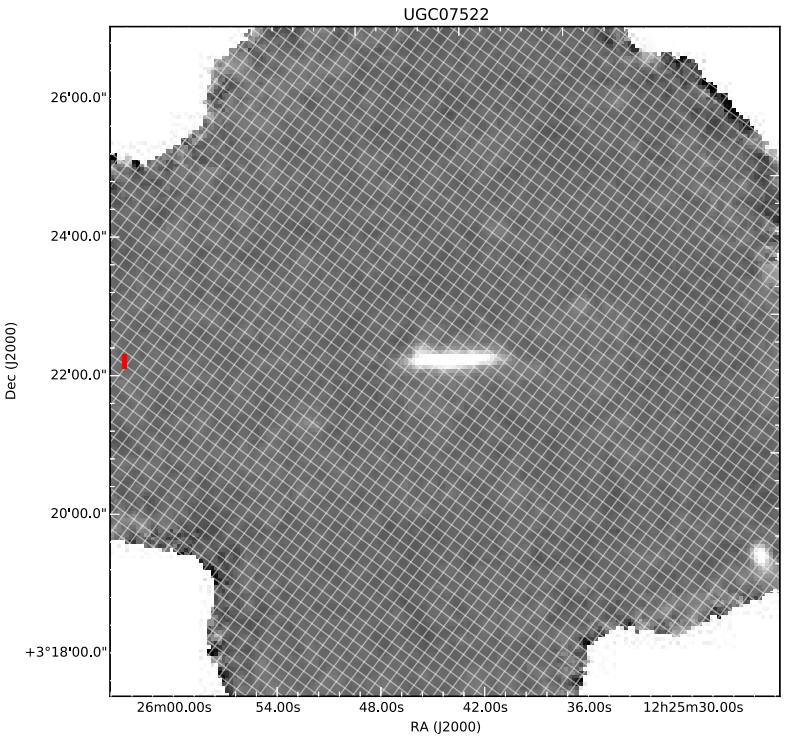

Figure A.227: 160 μm

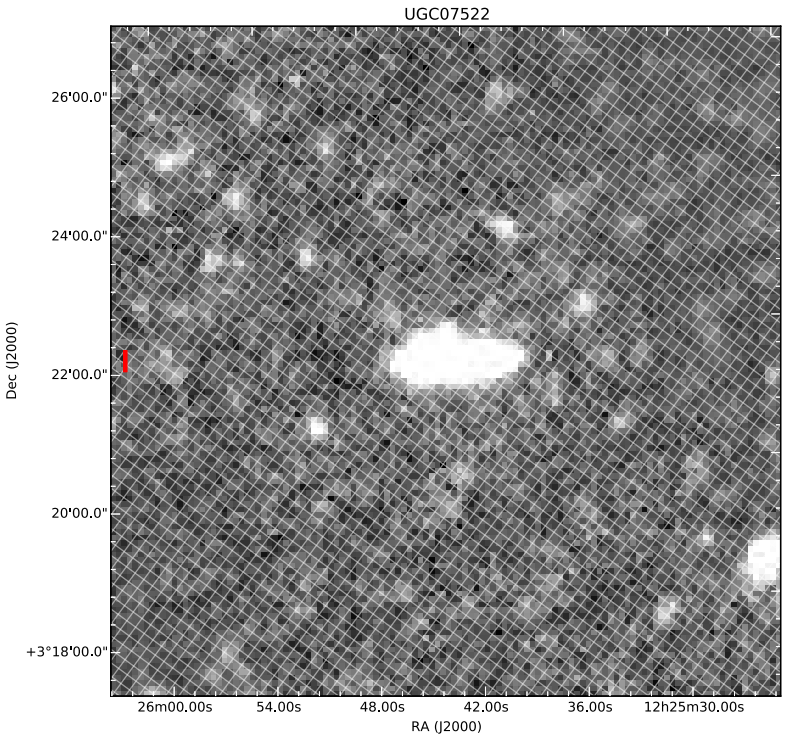

Figure A.228: 250 μm

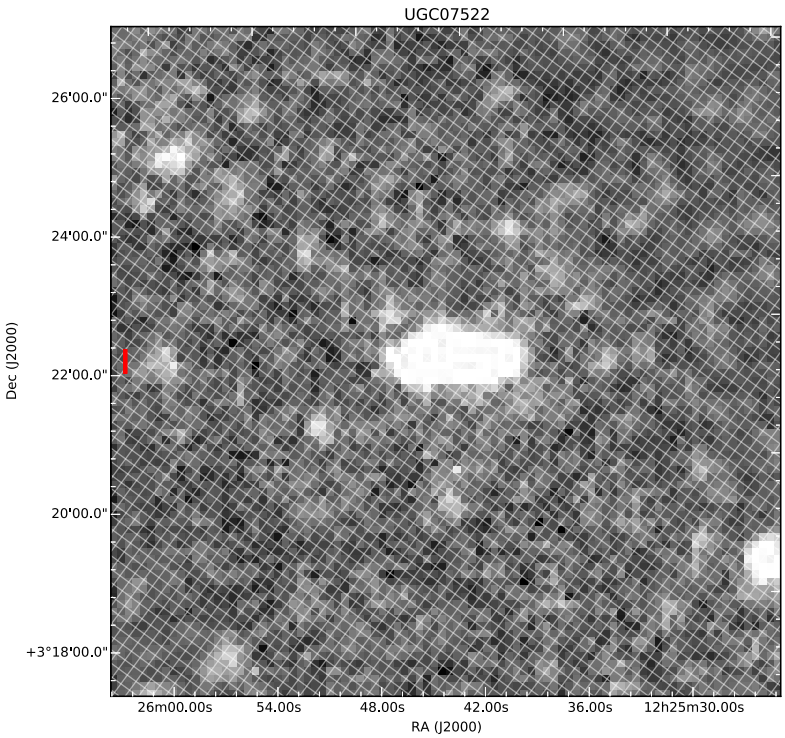

Figure A.229: 350 μm

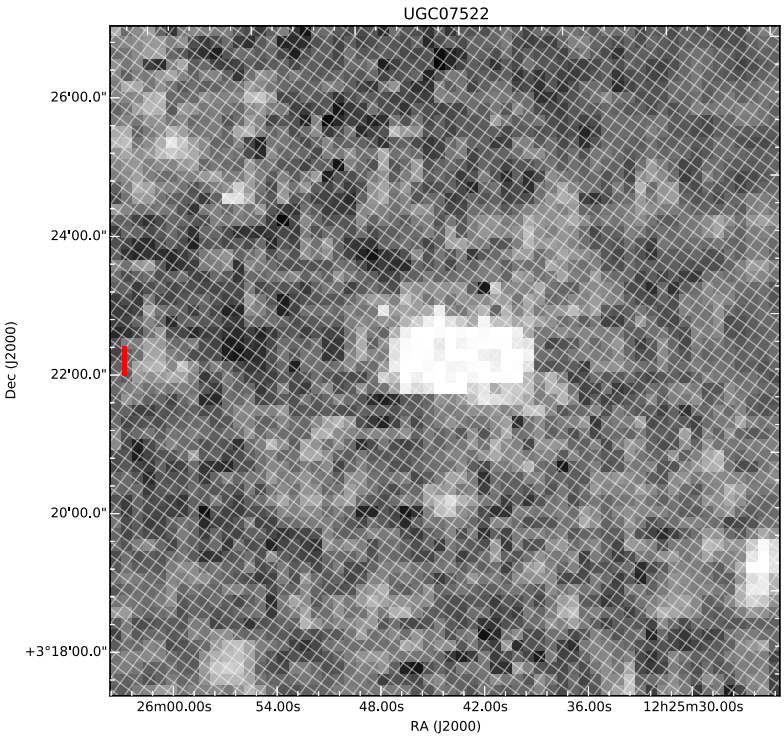

Figure A.230: 500 μm

A.31 UGC07982

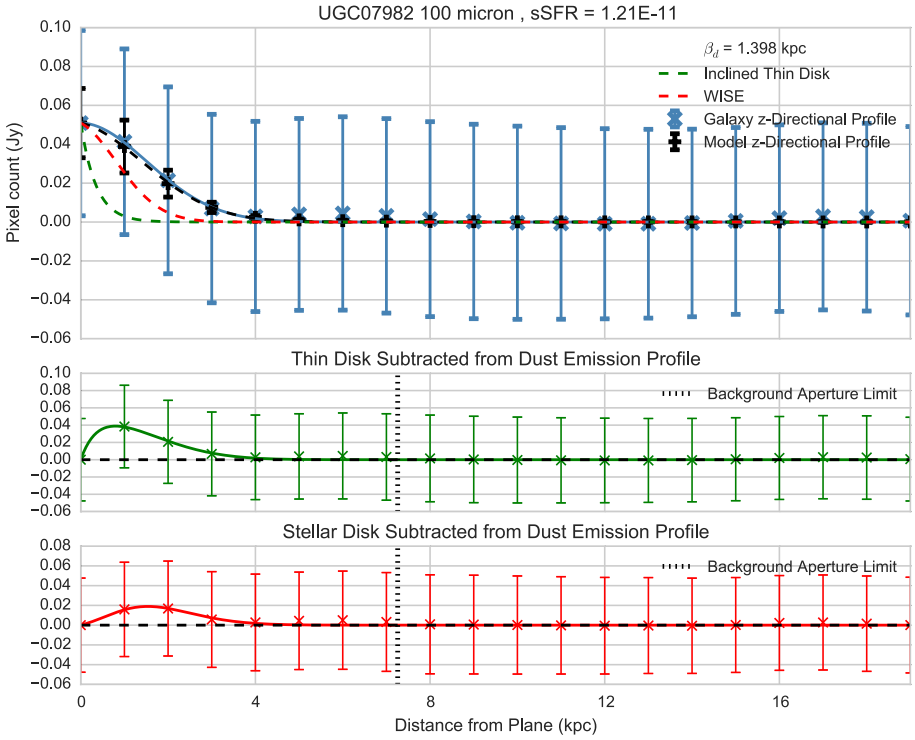

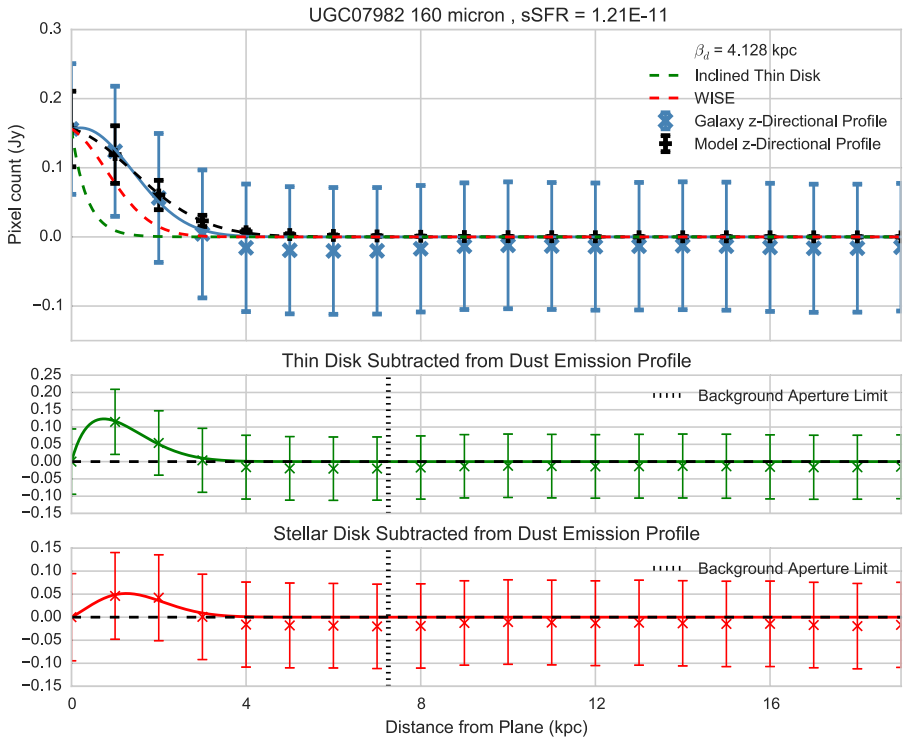
UGC07982 160 micron , sSFR = 1.21E-11
β_d = 4.128 kpc
Inclined Thin Disk
WISE
Galaxy z-Directional Profile
Model z-Directional Profile
Pixel count (Jy)
Thin Disk Subtracted from Dust Emission Profile
Background Aperture Limit
Stellar Disk Subtracted from Dust Emission Profile
Background Aperture Limit
Distance from Plane (kpc)

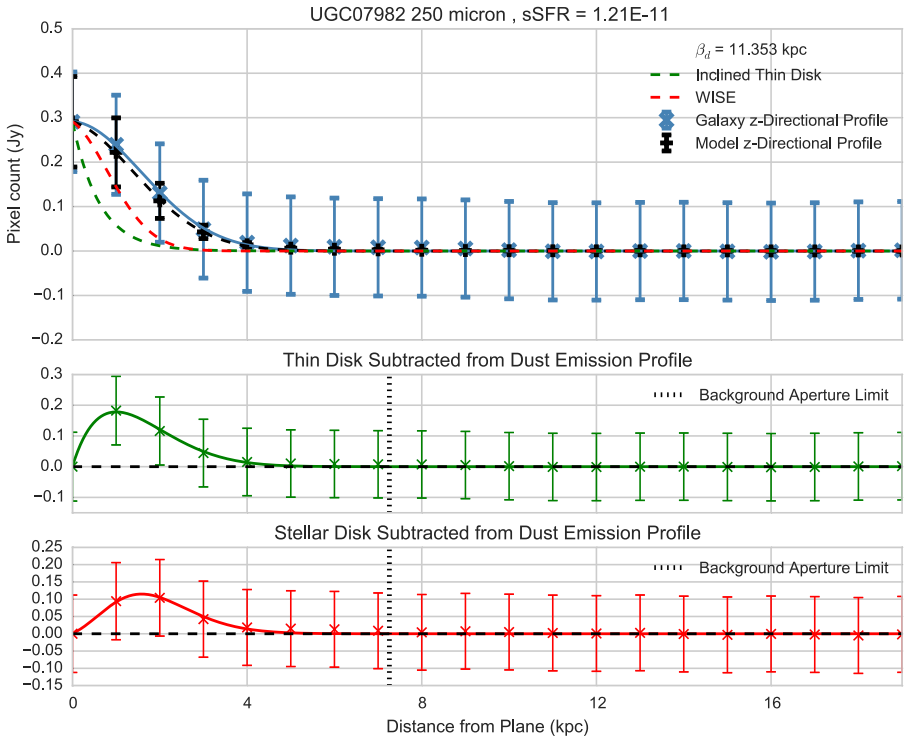
UGC07982 250 micron , sSFR = 1.21E-11
β_d = 11.353 kpc
Inclined Thin Disk
WISE
Galaxy z-Directional Profile
Model z-Directional Profile
Pixel count (Jy)
Thin Disk Subtracted from Dust Emission Profile
Background Aperture Limit
Stellar Disk Subtracted from Dust Emission Profile
Background Aperture Limit
Distance from Plane (kpc)

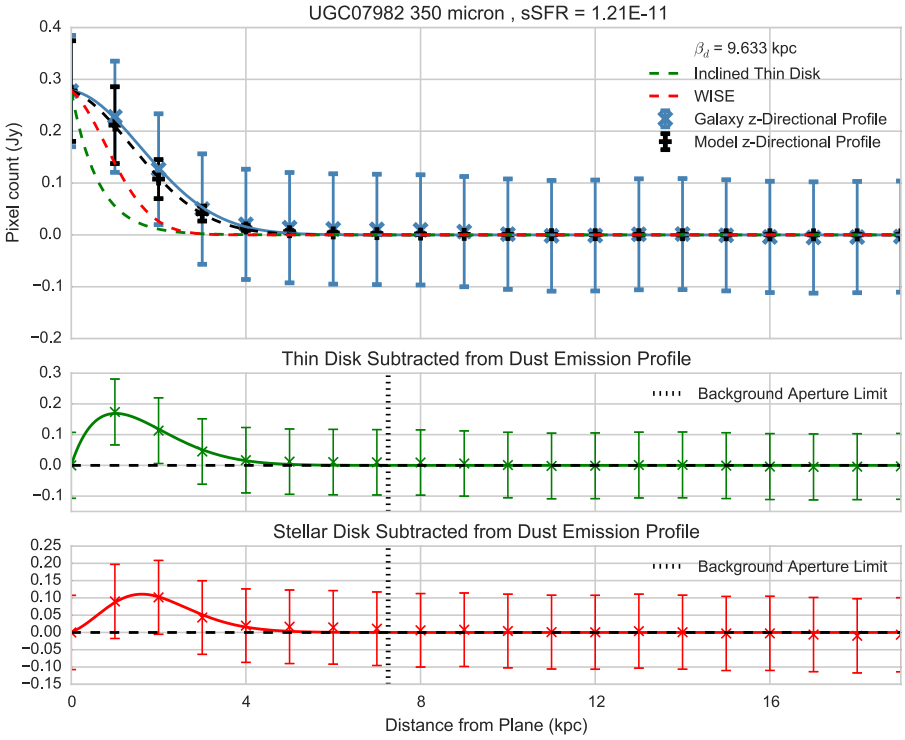
UGC07982 350 micron , sSFR = 1.21E-11
β_d = 9.633 kpc
Inclined Thin Disk
WISE
Galaxy z-Directional Profile
Model z-Directional Profile
Pixel count (Jy)
Thin Disk Subtracted from Dust Emission Profile
Background Aperture Limit
Stellar Disk Subtracted from Dust Emission Profile
Background Aperture Limit
Distance from Plane (kpc)

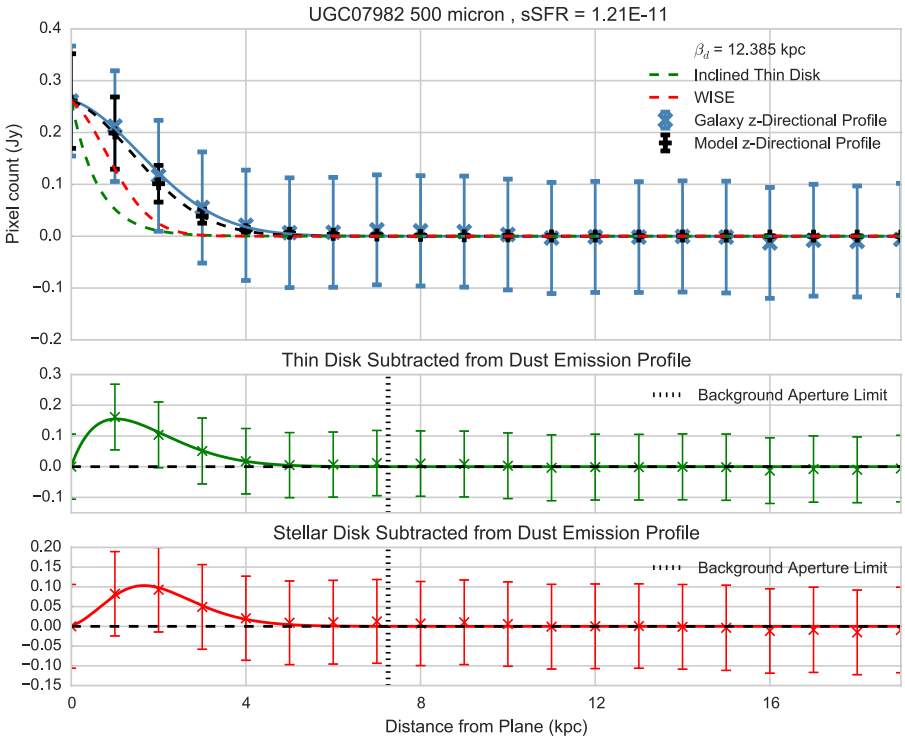
UGC07982 500 micron , sSFR = 1.21E-11
β_d = 12.385 kpc
Inclined Thin Disk
WISE
Galaxy z-Directional Profile
Model z-Directional Profile
Pixel count (Jy)
Thin Disk Subtracted from Dust Emission Profile
Background Aperture Limit
Stellar Disk Subtracted from Dust Emission Profile
Background Aperture Limit
Distance from Plane (kpc)

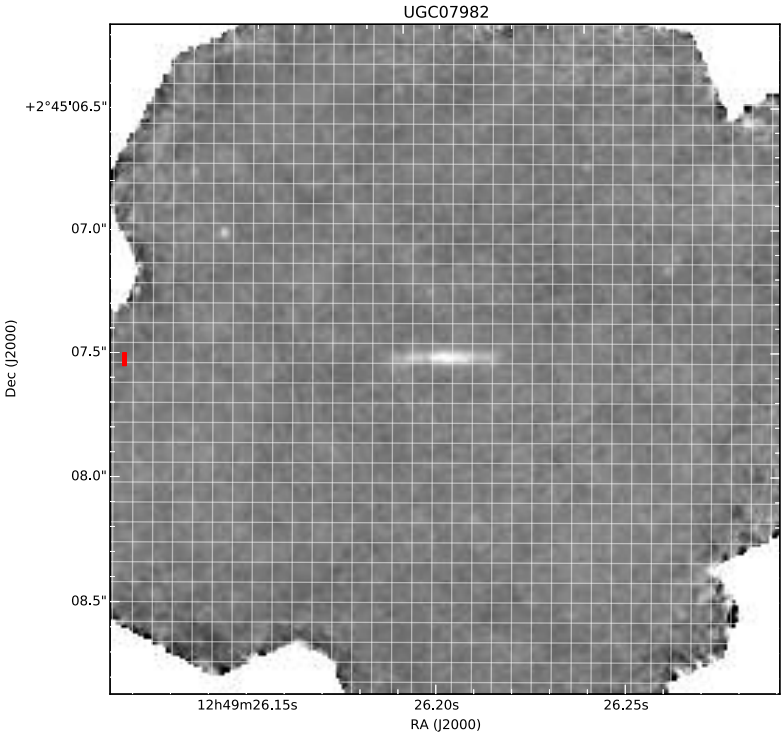

Figure A.231: 100 μm

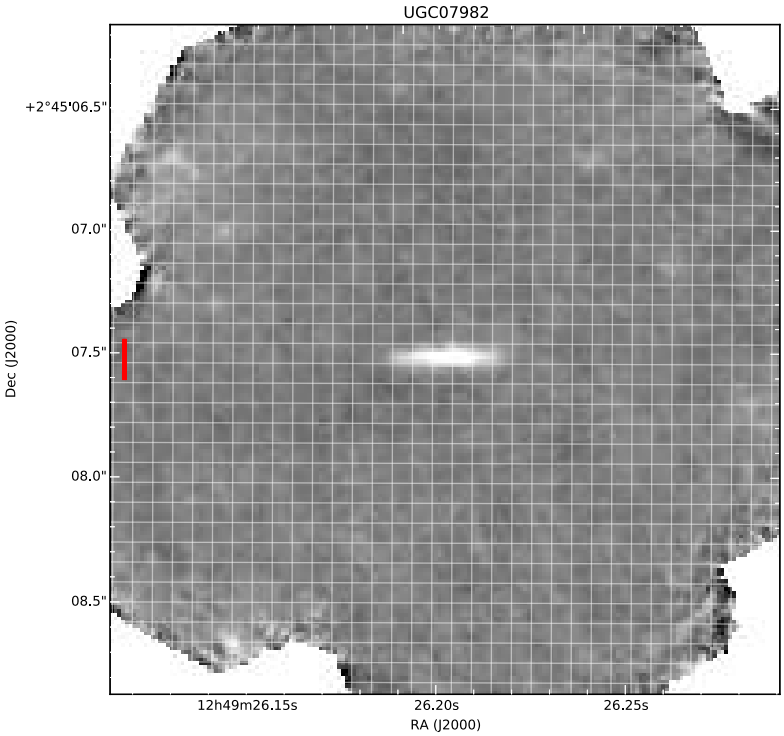

Figure A.232: 160 μm

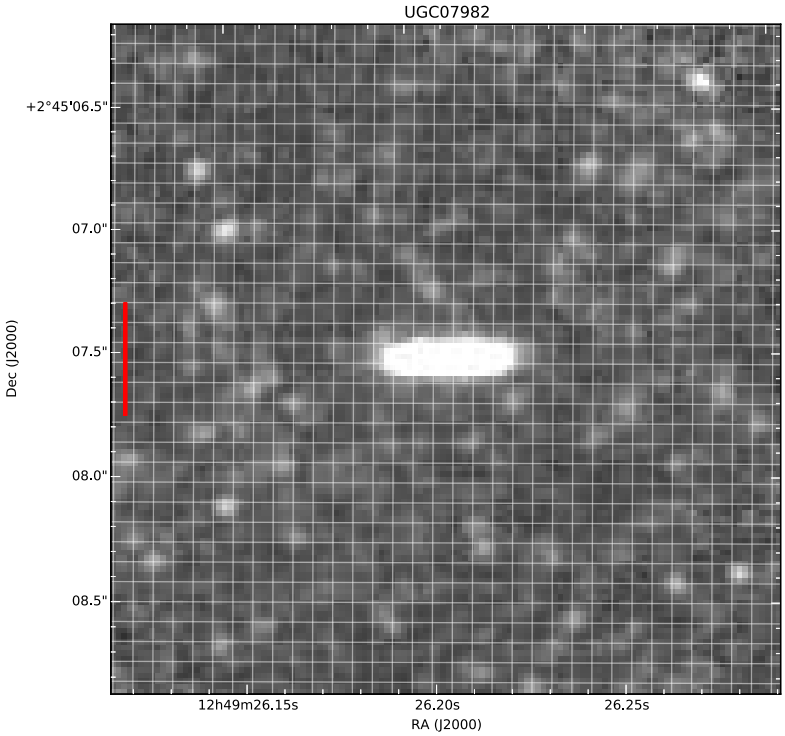

Figure A.233: 250 μm

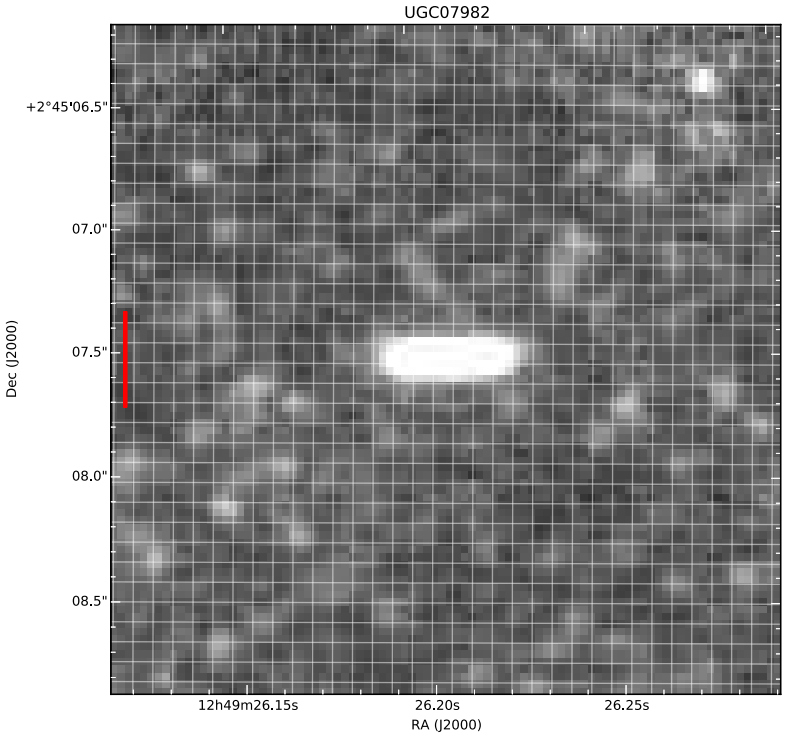

Figure A.234: 350 μm

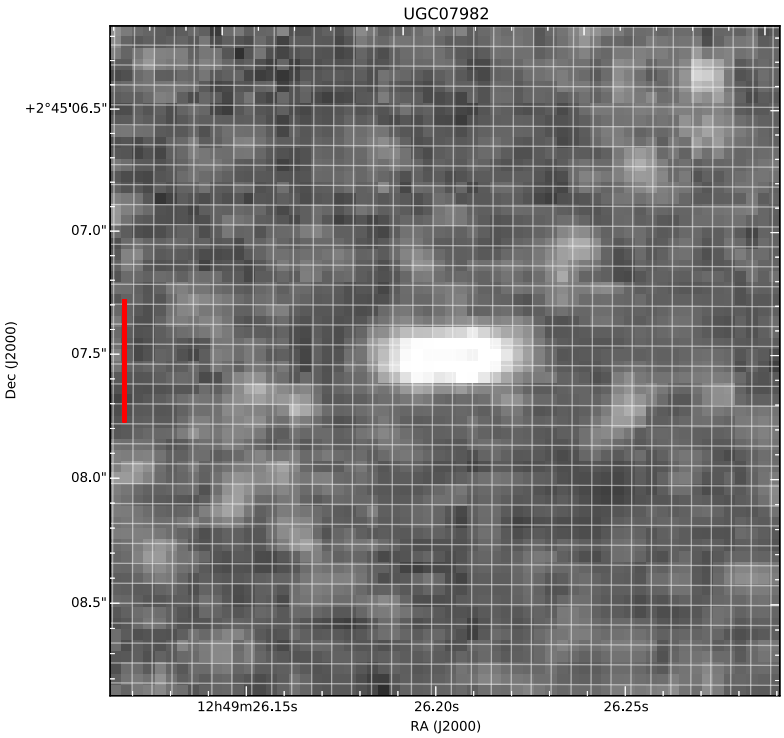

Figure A.235: 500 μm

APPENDIX

B

Plots of the jackknifed brightness profiles at all 5 *Herschel* wavelengths are presented in this Appendix.

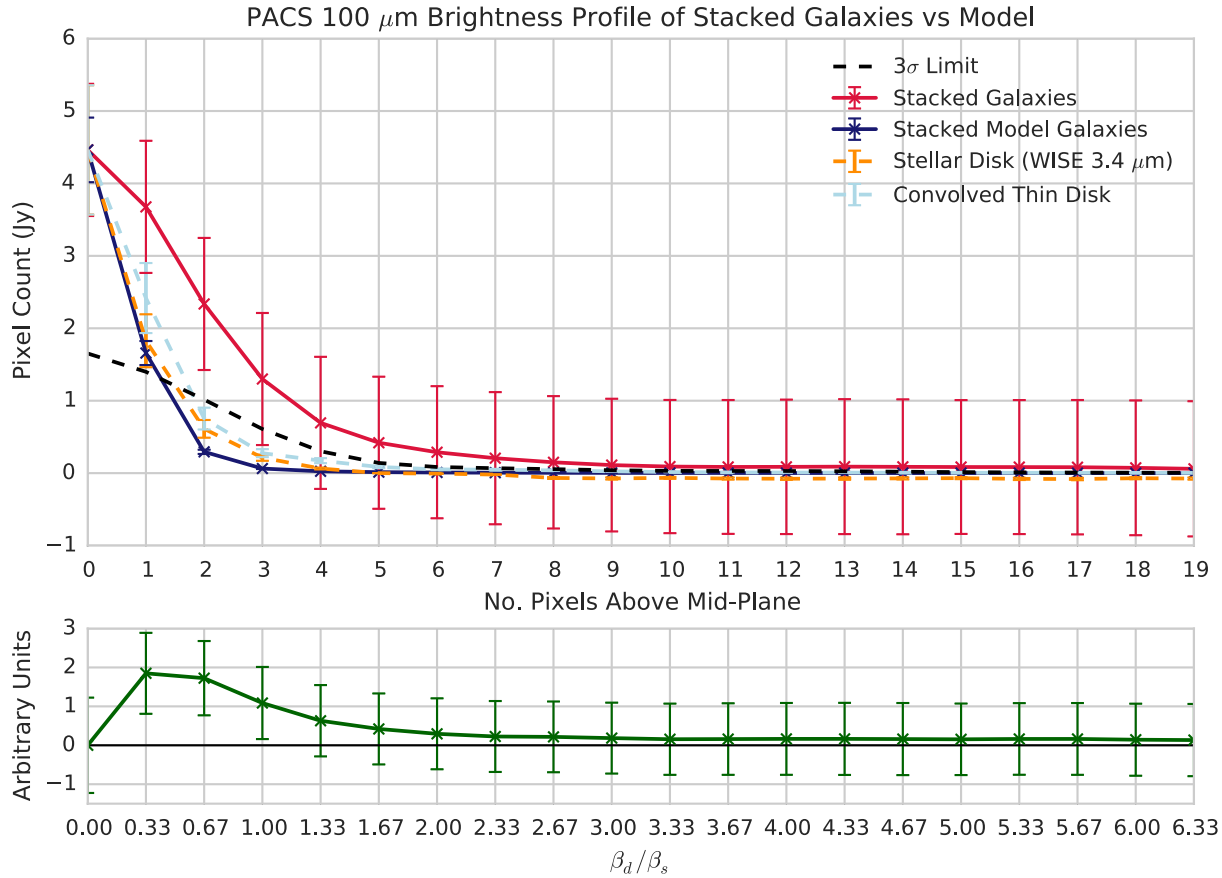

Figure B.1: Upper: Vertical profile of 15 averaged galaxies and models at 100 μm. The profiles have been normalised to match at the peak. The red line shows the value of the summed real galaxy maps using the *Herschel* data, the dark blue line shows the value of the summed models, and the orange dashed line shows the stellar disk profile from the WISE maps. The light blue dashed line represents the profile of an infinitely thin disk convolved with the 500 μm beam processed using the same method, and the black dashed line shows the 3σ noise detection limit. Lower: We subtract the stellar disk profile from the galaxy dust disk profile to see the difference in detected emission and how far the dust extends above the stellar component.

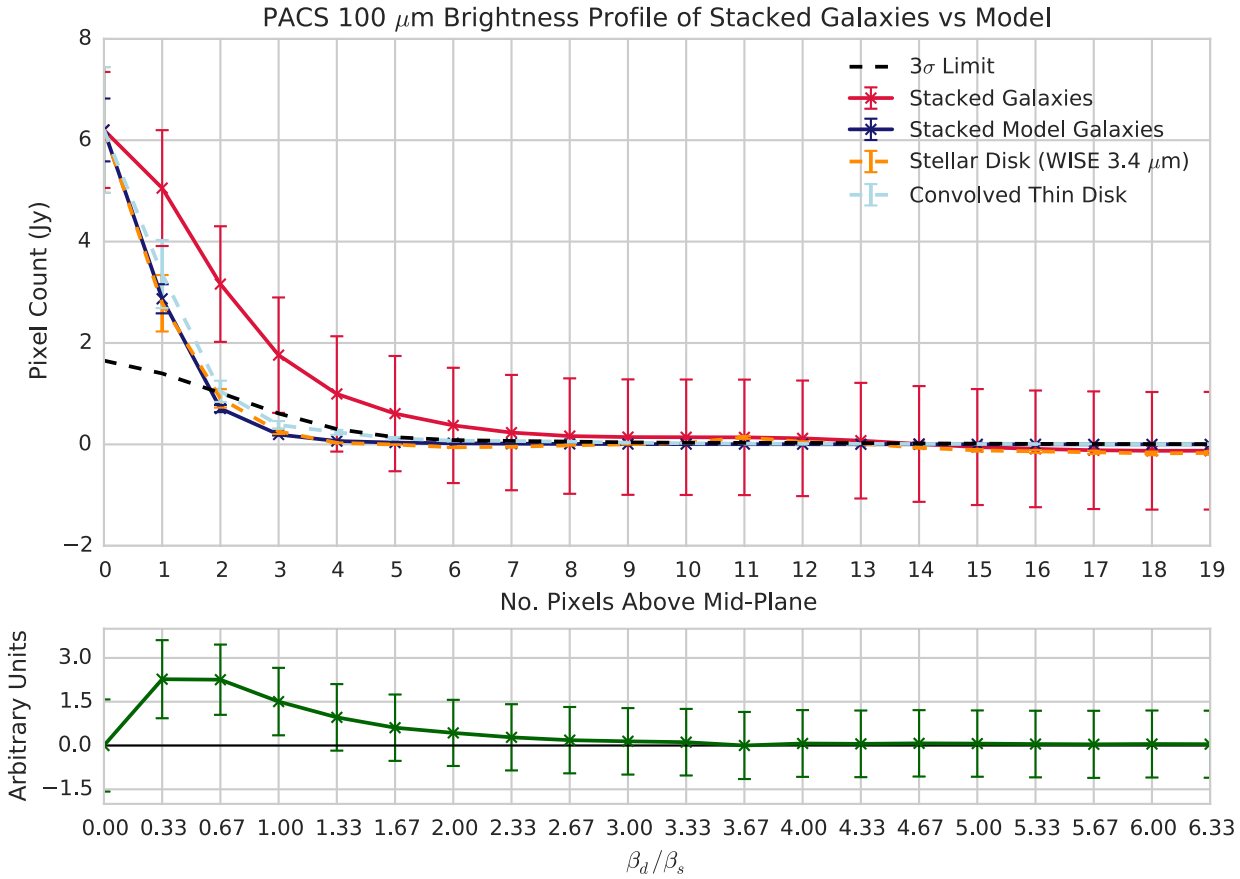

Figure B.2: Upper: Vertical profile of 16 averaged galaxies and models at 100 μm. The profiles have been normalised to match at the peak. The red line shows the value of the summed real galaxy maps using the *Herschel* data, the dark blue line shows the value of the summed models, and the orange dashed line shows the stellar disk profile from the WISE maps. The light blue dashed line represents the profile of an infinitely thin disk convolved with the 500 μm beam processed using the same method, and the black dashed line shows the 3σ noise detection limit. Lower: We subtract the stellar disk profile from the galaxy dust disk profile to see the difference in detected emission and how far the dust extends above the stellar component.

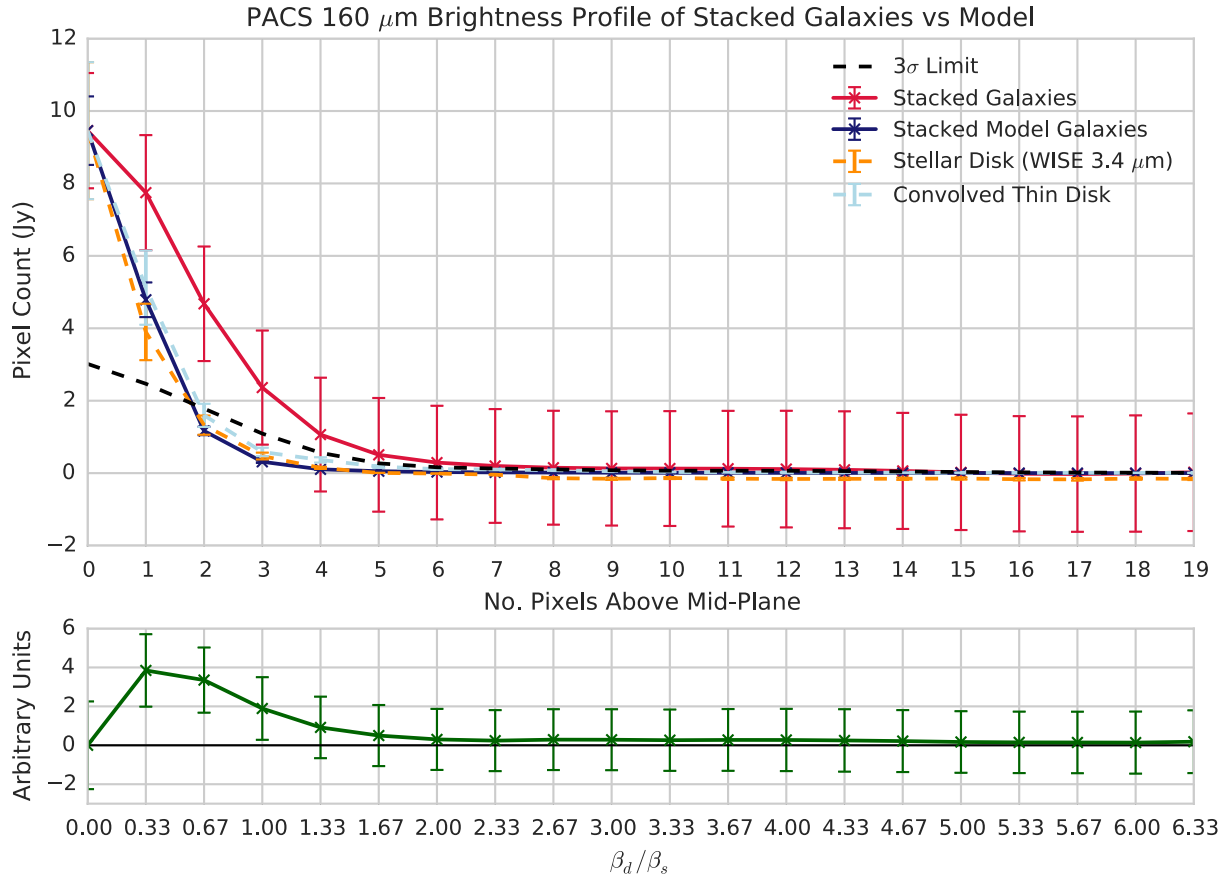

Figure B.3: Upper: Vertical profile of 15 averaged galaxies and models at 160 μm. The profiles have been normalised to match at the peak. The red line shows the value of the summed real galaxy maps using the *Herschel* data, the dark blue line shows the value of the summed models, and the orange dashed line shows the stellar disk profile from the WISE maps. The light blue dashed line represents the profile of an infinitely thin disk convolved with the 500 μm beam processed using the same method, and the black dashed line shows the 3σ noise detection limit. Lower: We subtract the stellar disk profile from the galaxy dust disk profile to see the difference in detected emission and how far the dust extends above the stellar component.

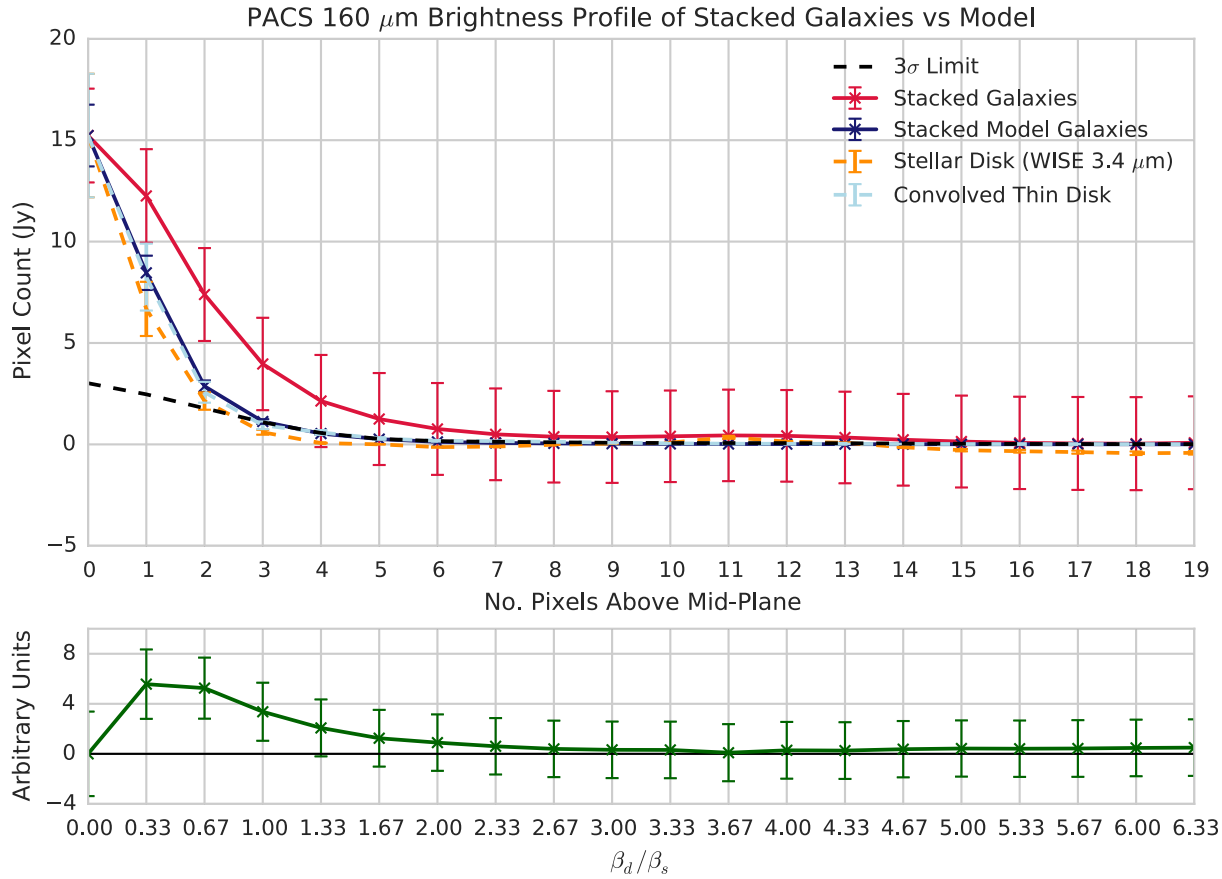

Figure B.4: Upper: Vertical profile of 16 averaged galaxies and models at 160 μm. The profiles have been normalised to match at the peak. The red line shows the value of the summed real galaxy maps using the *Herschel* data, the dark blue line shows the value of the summed models, and the orange dashed line shows the stellar disk profile from the WISE maps. The light blue dashed line represents the profile of an infinitely thin disk convolved with the 500 μm beam processed using the same method, and the black dashed line shows the 3σ noise detection limit. Lower: We subtract the stellar disk profile from the galaxy dust disk profile to see the difference in detected emission and how far the dust extends above the stellar component.

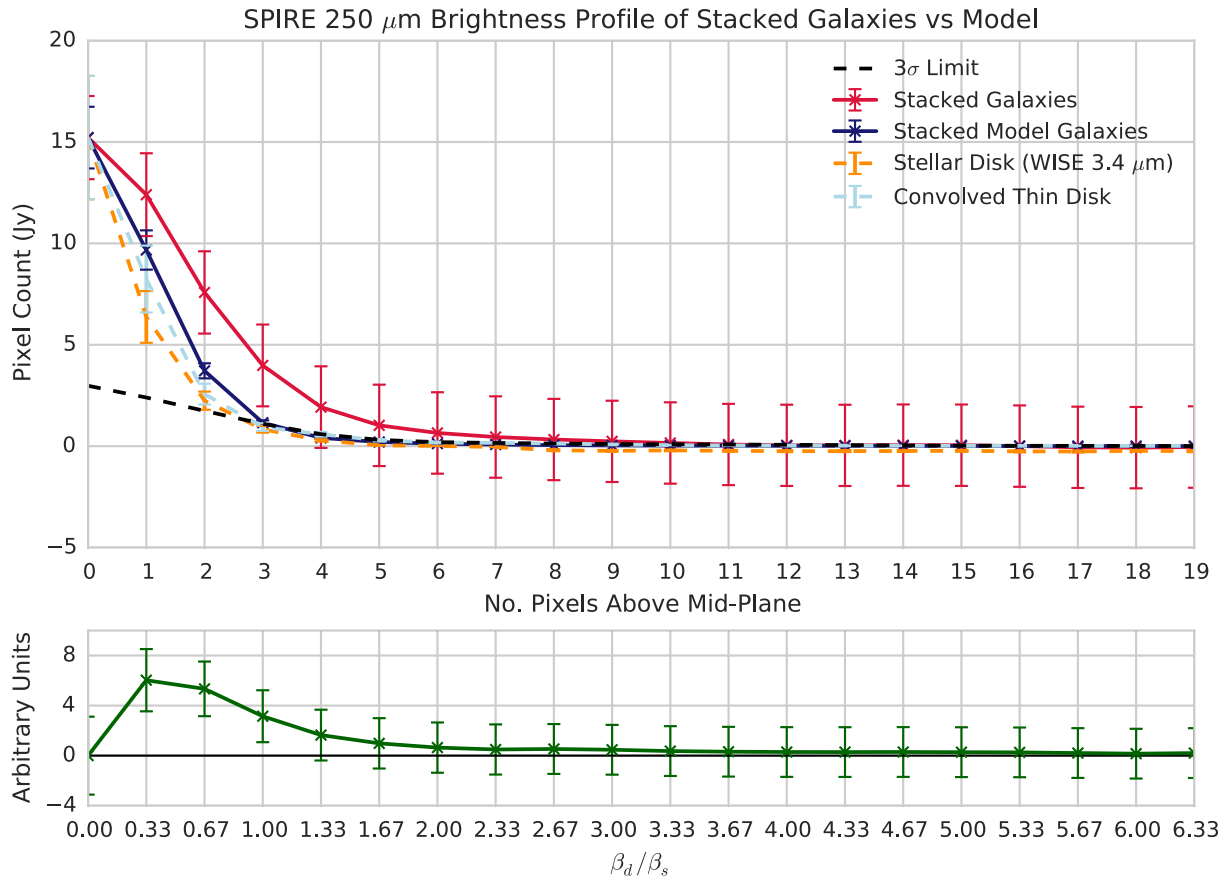

Figure B.5: Upper: Vertical profile of 15 averaged galaxies and models at 250 μm. The profiles have been normalised to match at the peak. The red line shows the value of the summed real galaxy maps using the *Herschel* data, the dark blue line shows the value of the summed models, and the orange dashed line shows the stellar disk profile from the WISE maps. The light blue dashed line represents the profile of an infinitely thin disk convolved with the 500 μm beam processed using the same method, and the black dashed line shows the 3σ noise detection limit. Lower: We subtract the stellar disk profile from the galaxy dust disk profile to see the difference in detected emission and how far the dust extends above the stellar component.

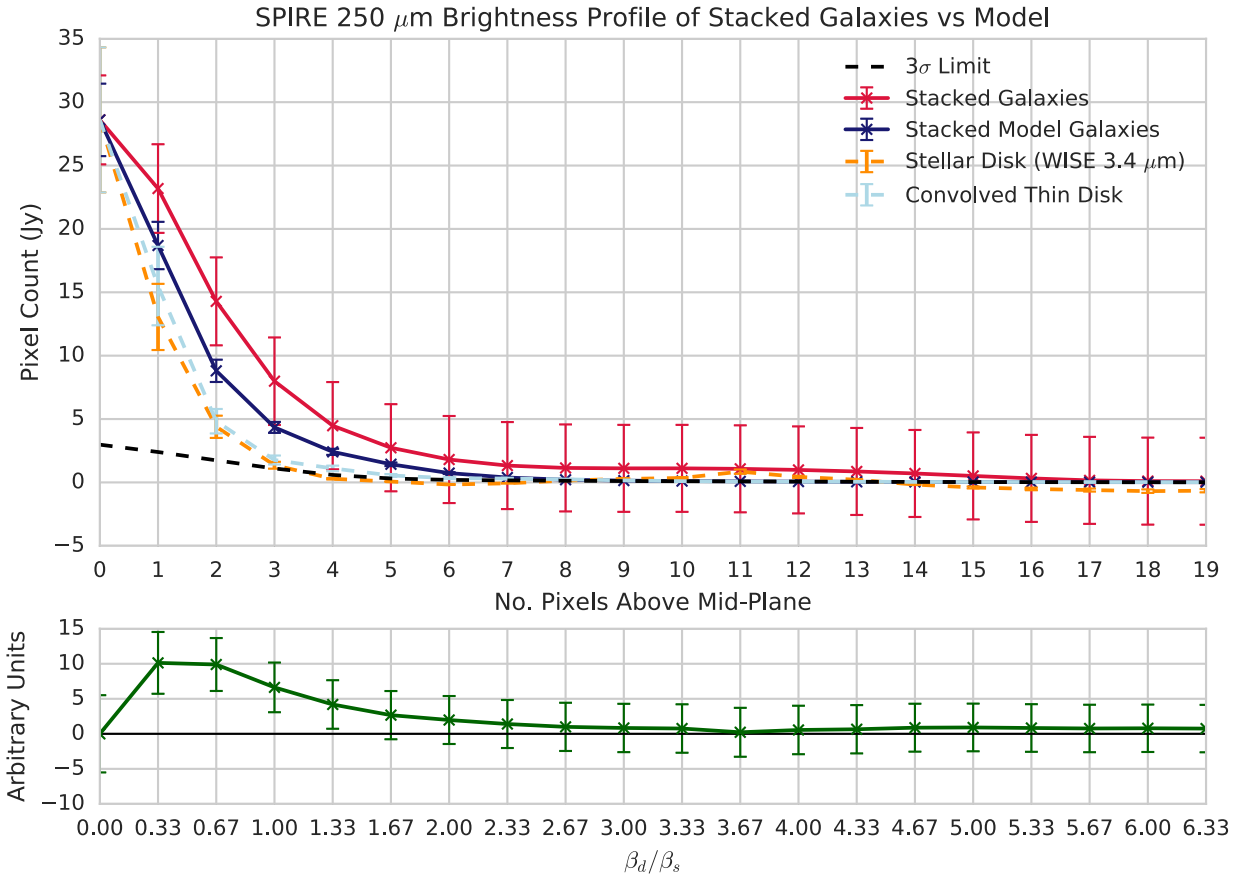

Figure B.6: Upper: Vertical profile of 16 averaged galaxies and models at 250 μm. The profiles have been normalised to match at the peak. The red line shows the value of the summed real galaxy maps using the *Herschel* data, the dark blue line shows the value of the summed models, and the orange dashed line shows the stellar disk profile from the WISE maps. The light blue dashed line represents the profile of an infinitely thin disk convolved with the 500 μm beam processed using the same method, and the black dashed line shows the 3σ noise detection limit. Lower: We subtract the stellar disk profile from the galaxy dust disk profile to see the difference in detected emission and how far the dust extends above the stellar component.

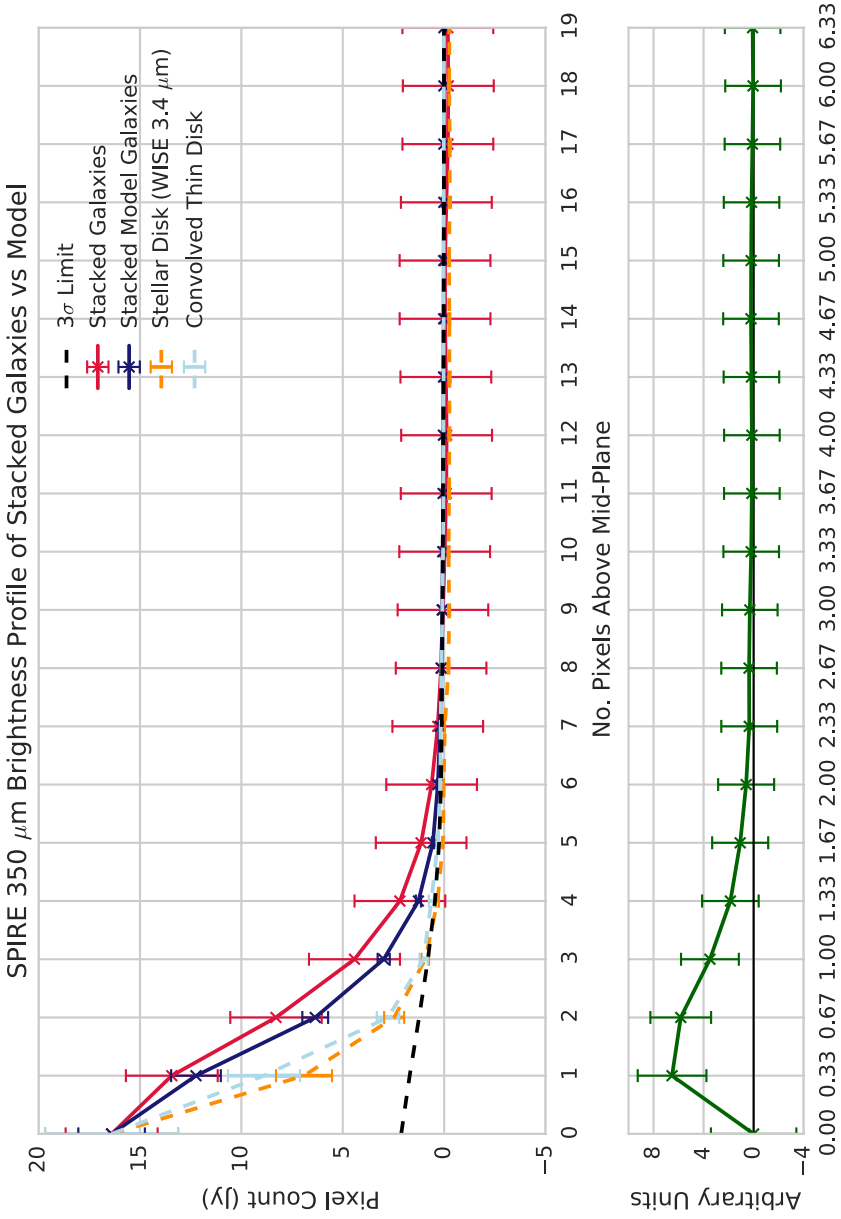

Figure B.7: Upper: Vertical profile of 15 averaged galaxies and models at 350 μm. The profiles have been normalised to match at the peak. The red line shows the value of the summed real galaxy maps using the *Herschel* data, the dark blue line shows the value of the summed models, and the orange dashed line shows the stellar disk profile from the WISE maps. The light blue dashed line represents the profile of an infinitely thin disk convolved with the 500 μm beam processed using the same method, and the black dashed line shows the 3σ noise detection limit. Lower: We subtract the stellar disk profile from the galaxy dust disk profile to see the difference in detected emission and how far the dust extends above the stellar component.

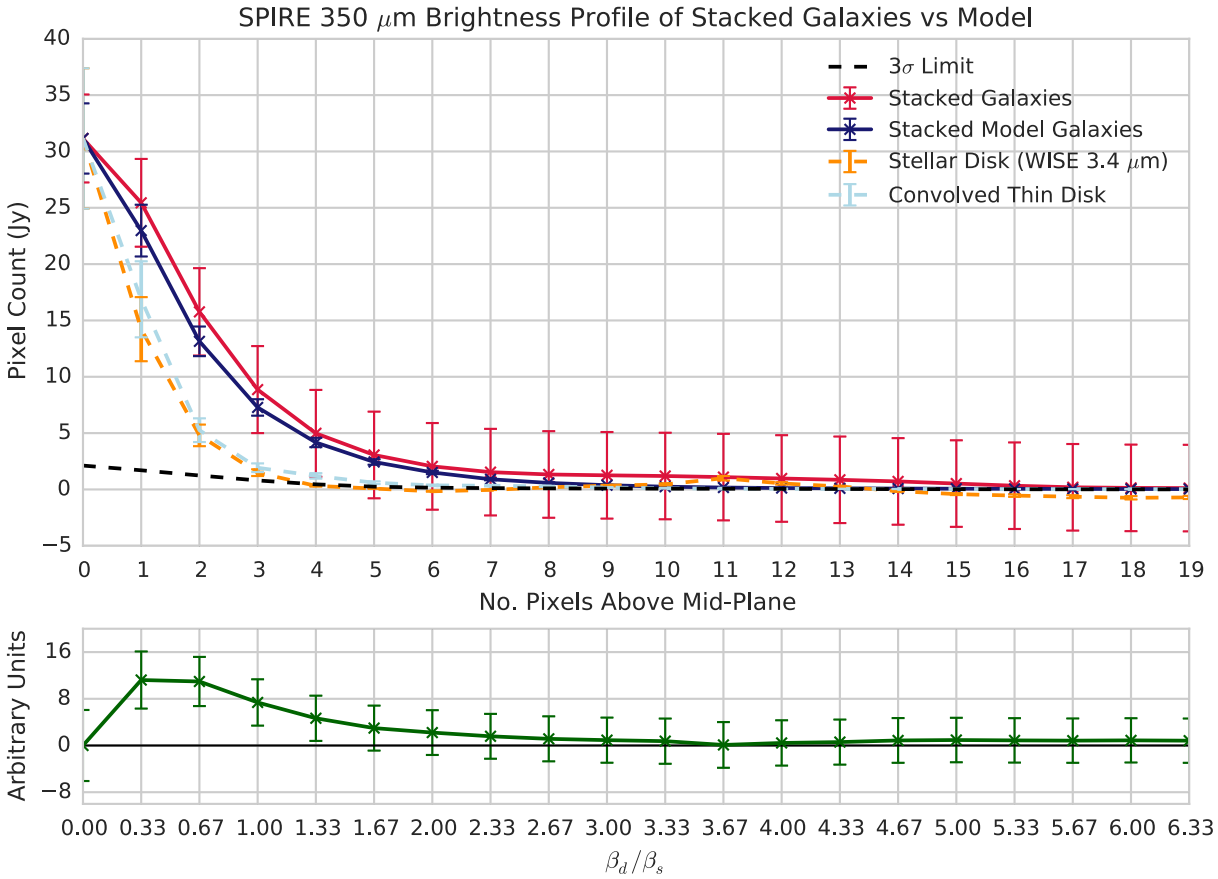

Figure B.8: Upper: Vertical profile of 16 averaged galaxies and models at 350 μm. The profiles have been normalised to match at the peak. The red line shows the value of the summed real galaxy maps using the *Herschel* data, the dark blue line shows the value of the summed models, and the orange dashed line shows the stellar disk profile from the WISE maps. The light blue dashed line represents the profile of an infinitely thin disk convolved with the 500 μm beam processed using the same method, and the black dashed line shows the 3σ noise detection limit. Lower: We subtract the stellar disk profile from the galaxy dust disk profile to see the difference in detected emission and how far the dust extends above the stellar component.

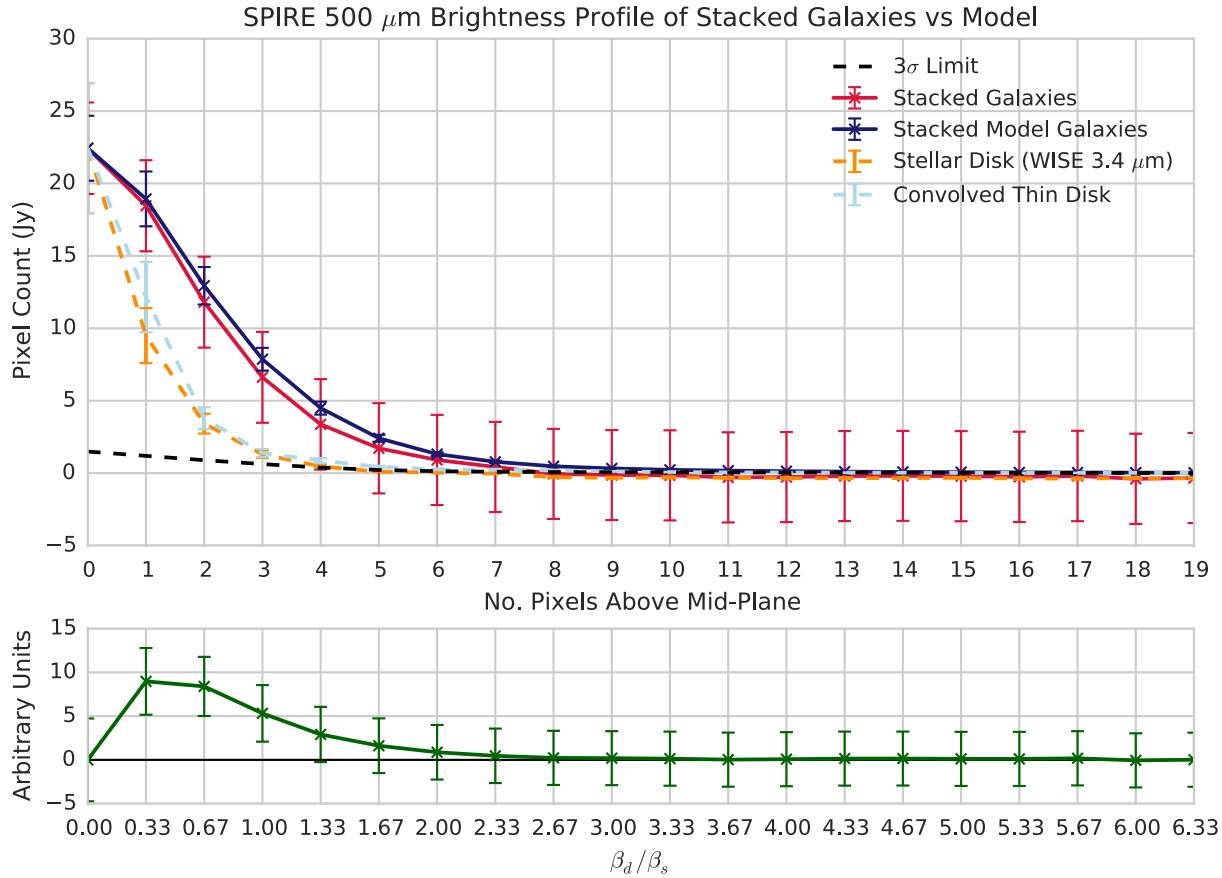

Figure B.9: Upper: Vertical profile of 15 averaged galaxies and models at 500 μm. The profiles have been normalised to match at the peak. The red line shows the value of the summed real galaxy maps using the *Herschel* data, the dark blue line shows the value of the summed models, and the orange dashed line shows the stellar disk profile from the WISE maps. The light blue dashed line represents the profile of an infinitely thin disk convolved with the 500 μm beam processed using the same method, and the black dashed line shows the 3σ noise detection limit. Lower: We subtract the stellar disk profile from the galaxy dust disk profile to see the difference in detected emission and how far the dust extends above the stellar component.

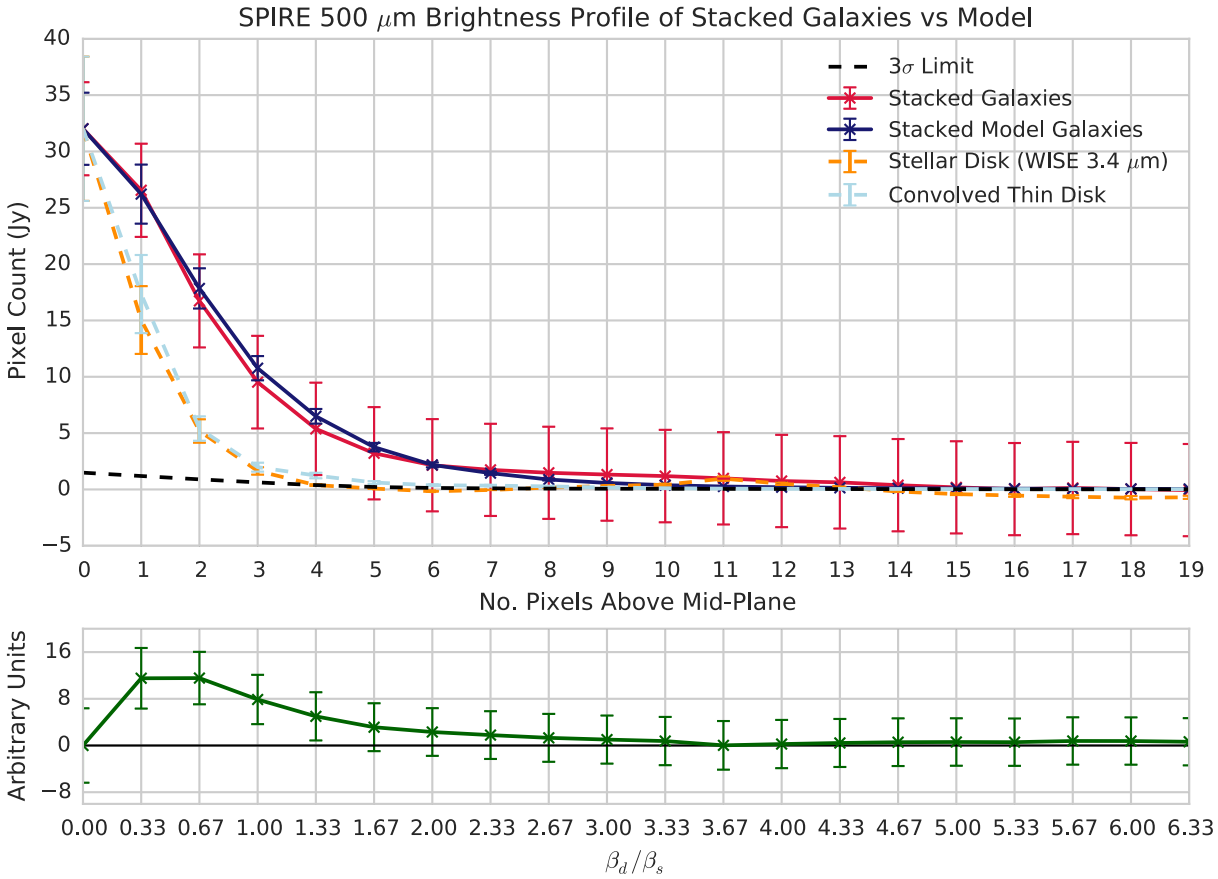

Figure B.10: Upper: Vertical profile of 16 averaged galaxies and models at 500 μm. The profiles have been normalised to match at the peak. The red line shows the value of the summed real galaxy maps using the *Herschel* data, the dark blue line shows the value of the summed models, and the orange dashed line shows the stellar disk profile from the WISE maps. The light blue dashed line represents the profile of an infinitely thin disk convolved with the 500 μm beam processed using the same method, and the black dashed line shows the 3σ noise detection limit. Lower: We subtract the stellar disk profile from the galaxy dust disk profile to see the difference in detected emission and how far the dust extends above the stellar component.